

Microsystems

Mohammad I. Younis

MEMS Linear and Nonlinear Statics and Dynamics

 Springer

MEMS Linear and Nonlinear Statics and Dynamics

MICROSYSTEMS

Series Editors

Roger T. Howe

Stanford University

Antonio J. Ricco

NASA Ames Research Center

For further volumes:

<http://www.springer.com/series/6289>

Mohammad I. Younis

MEMS Linear and Nonlinear Statics and Dynamics

 Springer

Ph.D. Mohammad I. Younis
Department of Mechanical Engineering
State University of New York
Binghamton, NY
USA
myounis@binghamton.edu

ISSN 1389-2134
ISBN 978-1-4419-6019-1 e-ISBN 978-1-4419-6020-7
DOI 10.1007/978-1-4419-6020-7
Springer New York Dordrecht Heidelberg London

Library of Congress Control Number: 2011930834

© Springer Science+Business Media, LLC 2011

All rights reserved. This work may not be translated or copied in whole or in part without the written permission of the publisher (Springer Science+Business Media, LLC, 233 Spring Street, New York, NY 10013, USA), except for brief excerpts in connection with reviews or scholarly analysis. Use in connection with any form of information storage and retrieval, electronic adaptation, computer software, or by similar or dissimilar methodology now known or hereafter developed is forbidden.

The use in this publication of trade names, trademarks, service marks, and similar terms, even if they are not identified as such, is not to be taken as an expression of opinion as to whether or not they are subject to proprietary rights.

Printed on acid-free paper

Springer is part of Springer Science+Business Media (www.springer.com)

*To my parents Ibrahim and Halemah
My wife Ola
and our sons
Ibrahim, Muhmoud, and Mutaz*

Preface

Several decades have passed by since the discovery and development of micro-electro-mechanical systems (MEMS). This technology has reached a level of maturity that, today, several MEMS devices are being used in our every-day life, ranging from accelerometers and pressure sensors in cars, micro-mirrors in Plasma TVs, radio-frequency (RF) switches and microphones in cell phones, and inertia sensors in video games. Fabrication methods of MEMS, such as bulk and surface micromachining, are now well-known and almost standardized. Nowadays, hundreds of foundries around the world offer numerous fabrication services that can translate the imagination of a MEMS designer of a device into reality.

Even with the maturity of fabrication and commercialization, MEMS is still one of the hottest evolving areas in science and engineering, where scientists from across various disciplines investigate, brainstorm, and collaborate to invent smarter devices, develop new technologies, and innovate unique solutions. With the increasing pressure for sensors and actuators of sophisticated functionalities, which are self-powered, self-calibrated, and self-tested, MEMS are expected to remain the sought-after technology of scientists for many years to come.

However, with this growing demand on the MEMS technology come great challenges. Designers are now aiming to achieve complicated objectives while meeting a long list of specifications related to sensitivity, fabrication, system integration, packaging, and reliability. These challenges have created a motivation to seek new solutions and ideas, beyond changing the geometry of devices and making more complex configurations. Researchers are starting to realize the need to look into new methods of improvement and innovation in MEMS beyond the static laws of design and the limitations of linear theories. It is realized now that linear theories are too shallow to allow for bolder ideas and more aggressive design goals. More attention is being directed to investigate deeply the dynamics and motion aspects of MEMS and to explore the hidden opportunities of operating MEMS in the nonlinear regimes.

Most MEMS devices employ a structure or more that undergoes some sort of motion. Accelerometers, gyroscopes, micromirrors, microphones, resonators and oscillators, RF switches and filters, and thermal actuators are few examples of such. Hence, it comes no surprise that the motion characteristic of microstructures affect directly the specifications, quality, and limitations of MEMS devices. Unfortunately,

however, understanding the motion aspects of these devices is not a trivial task, which is one of the reasons that have delayed the research attention in this area.

Many microstructures are highly compliant. When actuated, they undergo large deflection or deformation compared to their dimensions. This amplifies the geometric nonlinearity of the structures. Microstructures are commonly actuated by parallel-plate electrostatic forces, which are inherently nonlinear. When microstructures are driven to motion, they may experience nonlinear dissipation mechanisms, such as squeeze-film damping. These various nonlinear sources in MEMS play significant role in their response and performance. As a result, models and designs based on linear theories can be inadequate, inaccurate, and incorrect. Further, the interaction among inherent coupled-physical domains, such as mechanical, electrostatic, thermal, and fluidic, marks one of the key features of MEMS. This coupling can further complicate the design process. In addition, new phenomena that are common in the microscale range, such as squeeze-film damping and pull-in instability, add to these difficulties. Tackling multiphysics, nonlinear, and dynamic problems can be very challenging especially in the presence of instabilities, such as pull-in, which can cause serious convergence problems in commercial simulation software.

These new challenges facing MEMS designers and researches combined with the growing interest in MEMS and their dynamical behavior have been the motivation behind this book. This book has two main goals: First is to provide the necessary analytical and computational tools that enable students and professionals to model the static and dynamic behavior of MEMS accurately in multiphysics fields and accounting properly for their nonlinearities. The second goal is to present in-depth analysis and treatment for the most common static and dynamic phenomena in MEMS encountered by MEMS engineers and researchers, especially those associated with electrostatic MEMS.

The organization of the book material is as follows: Chapter 1 introduces MEMS, their features, and some of their modeling and simulation challenges and needs. Chapter 2 discusses the basic principles of the vibrations of single- and multiple-degrees-of-freedom systems. Free vibrations and forced vibrations in response to harmonic and arbitrary forcing are discussed. Chapter 3 introduces the common sensing and actuation methods in MEMS. These include electrothermal, piezoelectric, electromagnetic, piezoresistive, and electrostatic methods. The rest of the chapter is dedicated to illustrate the theory of electrostatic transduction in parallel-plate capacitors, torsional actuators, and comb-drive devices. Chapter 4 discusses the basic elements of lumped-parameter modeling, which are the stiffness elements, effective mass, and damping mechanisms including squeeze-film, slide-film, and thermoelastic damping.

Chapter 5 builds on the background of Chaps. 1–4 to introduce the reader to basic principles of nonlinear dynamics and stability analysis as applied to MEMS applications. In doing so, several common phenomena at the microscale are introduced and illustrated, such as pull-in, side instability of comb fingers, collapse due to capillary forces, dynamic pull-in, and hysteresis. Analytical methods, such as linearization and phase diagrams, are illustrated. Then the chapter discusses nonlinear

oscillations with emphasis on the qualitative features and main differences compared to the linear vibrations of Chap. 2.

Moving from lumped-parameter to distributed-parameter modeling, Chap. 6 is dedicated to the most common and essential structures in MEMS: microbeams. Using a Newtonian approach, the chapter starts with a discussion on the derivation of the linear equation of motion and various kinds of boundary conditions. The static problem is discussed followed by illustration of solving the eigenvalue problem to extract the natural frequencies and modeshapes of common beams. Then, forced vibrations and the modal analysis procedure are presented. The second half of the chapter deals with nonlinear models of beams with emphasis on midplane stretching and electrostatic nonlinearities. The Galerkin procedure and reduced-order modeling are then discussed. As an application, universal pull-in curves of electrostatically actuated microbeams are presented. Following the static simulations, methods to solve the eigenvalue problem of beams under electrostatic actuation and the forced vibration response due to AC and DC actuation are discussed. Modeling of Atomic Force Microscopes is then presented. The chapter ends with discussions on the modeling of damping in beams.

Chapters 7 and 8 present special case studies of importance in MEMS, which are treated in some depth both theoretically and experimentally. Chapter 7 discusses the nonlinear dynamics of electrically actuated resonators. Simulation methods, such as the shooting technique and the basin-of-attraction analysis, are introduced and demonstrated. Dynamic pull-in, its utilization, and control are discussed. Chapter 8 deals with a reliability topic, which is the response of MEMS to mechanical shock. Modeling shock in MEMS, its interaction with electrostatic forces and printed circuit boards, and details on experimental testing are presented.

This book can be used by professionals of all levels who aim to model and simulate the behavior of MEMS devices and structures or to improve their design for static and dynamic considerations. In addition, the book serves as an excellent reference to enable full understanding of common MEMS phenomena that face MEMS engineers and researchers, such as squeeze-film damping, buckling, and pull-in instability. The depth of treatment of many of the topics covered in this book should appeal to MEMS researchers and those who consider doing research in related fields.

The book can be used as a text for two courses related to MEMS modeling and design or more specifically for courses in the statics and dynamics of MEMS. Chapters 1–4 and some of the material of Chap. 5 can be used for a first-year graduate or senior undergraduate course. For students who are familiar with mechanical vibrations, many of the materials of Chap. 2 can be assigned for self-reading except for topics specific to MEMS applications, such as MEMS gyroscopes, accelerometers, and band-pass filters. Chapters 5–8 suit a second-year graduate course. In addition, instructors are recommended to add research-oriented projects to encourage students to explore what is new in this highly dynamic field.

The author has relied on introducing and illustrating many new concepts and analytical and numerical approaches through examples instead of introducing them as abstract theories. While this approach does not provide much mathematical rigor, from the author's experience, it is easier for the students to digest. This is especially

true for those outside the mechanical engineering and nonlinear dynamics disciplines. The examples of the book range in their complexity from simple to more difficult and research-oriented ones. These are not intended for beginners in the field but rather for advanced researchers and graduate students. The author aims of such examples to stimulate deep thinking and motivate further research in the field.

A note worth to be mentioned here is regarding the cited references in the book. While the author has attempted to present numerous references for researchers and interested scientists on the various discussed topics, these are not complete lists and do not represent the full spectrum of the state of the art. These references should be considered only as a good starting point for those who want to follow research in related topics.

I would like to express my deep thanks for the people who supported me while writing this book. Many thanks go to my students whose curiosity, thirst, and interest to learn more about this exciting field have inspired me to pursue with this project. I would like to thank my colleagues from the Department of Mechanical Engineering at SUNY Binghamton, Ronald Miles who supported me greatly in my research in MEMS and vibrations, and James Pitarresi, the department chair, who offered great help and supports throughout the period of this project. I would like to thank Professor Stephen Senturia of the MIT for his feedback and fruitful comments on the book draft. I am thankful to Professor Ali Nayfeh of Virginia Tech, whom I am in debited to him for everything nonlinear I know. Thanks also go to Mr. Andrew Willner of Sensata Technologies for his support. Many of the research that I had the opportunity to conduct in the field of dynamics of MEMS have been supported through the Dynamical Systems Program of the National Science Foundation. This support is acknowledged and highly appreciated. I would like to thank my parents, Ibrahim and Halemah, for their continuous encouragement and sacrifices. Last but not least, my deep thanks and appreciation go to my wife Ola, who has supported me continuously and endlessly, especially handling our three boys (Ibrahim, nine; Muhmoud, eight; and Mutaz, one), whom despite being little, like MEMS, are highly sophisticated and nonlinear.

December 2010
Mechanical Engineering
State University of New York at Binghamton

Mohammad I. Younis

Contents

1	MEMS, Their Features, and Modeling Challenges	1
1.1	What Are MEMS and Why They Are Attractive?	1
1.2	Why We Need Modeling and Simulation Tools?	4
1.3	Challenges of MEMS Modeling and Simulations	4
1.4	Coupled-Field MEMS Phenomena	7
1.4.1	Squeeze-Film Damping	7
1.4.2	Thermoelastic Damping	8
1.4.3	Pull-in Instability	8
1.4.4	Stiction Due to Capillary Forces	9
1.5	The State-of-the-Art of MEMS Modeling and Simulations	10
	Problems	11
	References	11
2	Vibrations of Lumped-Parameter Systems	13
2.1	Introduction	13
2.2	Free Vibration of Single-Degree-of-Freedom Systems	14
2.2.1	Undamped Vibration	14
2.2.2	Damped Vibration	18
2.3	Forced Harmonic Excitation of Single-Degree-of-Freedom Systems	22
2.4	Vibrating MEMS Gyroscopes	28
2.5	Base Excitations of SDOF Systems and Accelerometers Principles	32
2.6	Response of SDOF Systems to Arbitrary Excitation	36
2.7	Vibrations of Two-Degree-of-Freedom Systems	40
2.7.1	Undamped Free Vibration and Eigenvalue Problem	40
2.7.2	Modal Analysis	43
2.7.3	Resonances in 2-DOF Systems	47
2.8	Numerical Integration	48

2.9	MEMS Band-Pass Filters	52
	Problems	54
	References	56
3	Sensing and Actuation in MEMS	57
3.1	Electrothermal Actuation	57
3.1.1	U-Shaped Actuator	58
3.1.2	V-Beam Actuator	59
3.1.3	Bimorph Actuator	60
3.2	Piezoelectric Actuation and Detection	61
3.3	Electromagnetic and Magnetic Actuation	65
3.4	Piezoresistive Detection	68
3.5	Electrostatic Actuation and Detection	70
3.5.1	Simple Parallel-Plate Capacitors	72
3.5.2	Torsional Actuators and Micromirrors	78
3.5.3	Comb-Drive Devices	82
3.6	Resonant Sensors	87
	Problems	91
	References	92
4	Elements of Lumped-Parameter Modeling in MEMS	97
4.1	Stiffness of Microstructures	97
4.1.1	Experimental Methods	98
4.1.2	Computational Methods	101
4.1.3	Analytical Methods	101
4.2	Spring–Mass Models	107
4.3	Damping in MEMS	111
4.3.1	Mechanisms of Energy Losses	112
4.3.2	Air Damping Fundamentals	114
4.3.3	Damping Dependence on Pressure: Newell’s Classification	116
4.3.4	Drag Force	117
4.3.5	Squeeze-Film Damping	118
4.3.6	Slide-Film Damping	139
4.3.7	Intrinsic Damping	142
4.3.8	Extracting Damping Coefficients Experimentally	143
	Problems	145
	References	150
5	Introduction to Nonlinear Dynamics	155
5.1	Introduction	155
5.2	Nondimensionalization	157
5.3	Fixed Points and Linearization	161
5.4	Bifurcations of Fixed Points	168
5.4.1	Saddle-Node Bifurcation	169
5.4.2	Transcritical Bifurcation	177

5.4.3	Pitchfork Bifurcation	178
5.4.4	Hopf Bifurcation	182
5.5	Phase Portraits	184
5.5.1	Phase Diagram of a Parallel-Plate Capacitor and the Dynamic Pull-in Concept	190
5.5.2	Phase Diagram of a Double-Sided Capacitor	194
5.6	Step-Input Actuation of Capacitive RF Switches	197
5.7	Dynamics of Torsional Actuators and Micromirrors	201
5.7.1	Single-Degree-of-Freedom Model	202
5.7.2	Two-Degree-of-Freedom Model	206
5.8	Nonlinear Oscillations	211
5.8.1	The Effect of a Constant Force	212
5.8.2	Free Vibration in the Presence of Nonlinearities	216
5.8.3	Forced Harmonic Vibration	217
5.8.4	Parametric Excitation	230
5.8.5	Self-Excited Oscillators	237
5.9	Modal Interaction, Chaos, and Fractal Behavior	239
	Problems	241
	References	245
6	Microbeams	251
6.1	The Linear Equation of Motion	251
6.1.1	Boundary Conditions	254
6.1.2	Beams Made of Different Material Layers	259
6.2	The Static Response	260
6.3	Residual Stresses and Nonideal Supports of Cantilever Microbeams	262
6.4	Natural Frequencies and Modeshapes	267
6.4.1	Nondimensionalization	272
6.4.2	Flexible (Nonideal) Supports	274
6.4.3	Cantilever Beam with a Lumped Mass at the Tip	277
6.5	The Effect of Axial Load on the Natural Frequency and the Buckling Limit	280
6.6	The Orthogonality of Modeshapes	284
6.7	Forced Vibrations and Modal Analysis	286
6.7.1	Undamped Response with no Axial Load	286
6.7.2	Adding Axial Force	290
6.7.3	Adding Damping	291
6.8	A Nonlinear Model of Beams with Midplane Stretching	292
6.9	Other Nonlinear Models of Beams	296
6.10	The Galerkin Discretization and Reduced-Order Modeling	297
6.10.1	The Galerkin Method	297
6.10.2	Beams with Midplane Stretching	299
6.11	Reduced-Order Model of Beams Under Electrostatic Force	302

6.12	The Static Behavior of Beams Under Electrostatic Force	306
6.12.1	Cantilever Microbeams	306
6.12.2	Clamped–Clamped Microbeams	308
6.12.3	Microbeams with Partial Electrodes and Initial Curvature	312
6.13	The Natural Frequencies Under Electrostatic Force	314
6.14	Pull-in Time of RF Switches	319
6.15	Resonators Under AC + DC Excitation	321
6.16	Atomic Force Microscopes	323
6.16.1	Introduction	323
6.16.2	Interaction Forces	325
6.16.3	AFM Models	327
6.16.4	AFM Under Lennard–Jones Force	330
6.17	Beams Under Capillary Forces	338
6.18	Coupled-Field Damping of Beams	343
6.18.1	Squeeze-Film Damping	343
6.18.2	Thermoelastic Damping	344
	Problems	348
	References	352
7	Nonlinear Dynamics of an Electrically Actuated Resonator	359
7.1	The Device and Experimental Setup	359
7.2	Initial Characterization and Parameters Extraction	360
7.3	Experimental Data for Large DC and AC Excitations	363
7.3.1	Primary Resonance	363
7.3.2	Subharmonic Resonance	365
7.4	Simulations Using Long-Time Integration	368
7.5	Simulations Using the Shooting Technique	369
7.5.1	The Shooting Method	369
7.5.2	Results	372
7.6	Basin of Attraction Analysis	376
7.7	Attractors Tracking and the Integrity Factor	379
7.8	Remarks on Resonant Dynamic Pull-in	384
7.9	Mass Detection Application	386
7.10	Controlling Resonant Dynamic Pull-in	391
7.10.1	Introduction	391
7.10.2	Simulation and Experimental Results	392
7.10.3	Integrity Analysis	395
	Problems	397
	References	398
8	Mechanical Shock in MEMS	401
8.1	Introduction	401
8.2	Mechanical Shock	403
8.3	Modeling Shock in Lumped-Parameter Models	405

8.4	The Shock-Response Spectrum	407
8.5	Modeling Shock on Microbeams	409
8.6	Computationally Efficient Approach for Microstructures	411
8.7	High- g Shock Response	413
8.8	The Combined Effect of Shock and Electrostatic Forces	414
8.8.1	Single-Degree-of-Freedom Model	414
8.8.2	Beam Model	418
8.8.3	Switch Application	421
8.8.4	Experiments	421
8.9	Resonators Under Shock	426
8.9.1	Simulations	426
8.9.2	Experimental Results and Comparison with Simulations	429
8.10	The Effect of the PCB Motion	435
	Problems	439
	References	440
Appendix A		443
Index		451

Chapter 1

MEMS, Their Features, and Modeling Challenges

MEMS are devices and systems of distinguished properties and unique characteristics. In this chapter, we attempt to shed light on the main aspects of this technology and its desirable features. Then, we discuss the main challenges that face MEMS engineers in modeling and simulating the static and dynamic behavior of these systems. After that, we give an overview for some of the common phenomena of MEMS that designers and researchers encounter when studying their mechanical behavior. We end the chapter with some remarks on the state-of-the-art of MEMS modeling and simulations.

1.1 What Are MEMS and Why They Are Attractive?

The easiest way to introduce MEMS is to refer to the acronym MEMS itself and what it means. MEMS stands for micro-electro-mechanical-systems. Hence, they are devices in the “micro” scale, in which one or more of their dimensions are in the micrometer range. The “electro” part indicates that they use electric power, for example for actuation and detection, or electronics, for instance for amplifying and filtering signals and for controlling purposes. “Mechanical” means these devices rely on some sort of mechanical motion, action, or mechanism. The word “system” refers to the fact that they function, are designed, and are fabricated as integrated systems and not as individual components. In addition to these features, there are some basic aspects of MEMS that are hidden in the acronym. These can be revealed in this more formal definition of MEMS, which is the integration of mechanical elements, sensors, actuators, and electronics on a common silicon substrate through micro-fabrication technology [1].

This concise definition emphasizes important features of MEMS. The first is the fact that most MEMS are basically sensors and actuators. Examples of MEMS sensors are inertia sensors (accelerometers, gyroscopes), pressure sensors, gas and mass sensors, temperature sensors, force sensors, and humidity sensors. Almost for every physical quantity, there is a MEMS sensor that is developed or being developed to measure it. Examples of actuators are micromirrors to deflect lights in flat-screen

TVs, RF switches and microrelays, microgrippers, and generic force and displacement actuators, such as thermal bimorph actuators and comb-drive electrostatic actuators. Thus, historically speaking, the early generation of MEMS researchers has relied on sensors and actuators journals and conferences to disseminate their research on miniature devices before the introduction of specialized MEMS conferences and journals in the early 1990s. Today, several major MEMS meetings and journals still hold the words sensors, actuators, or transducers in their titles.

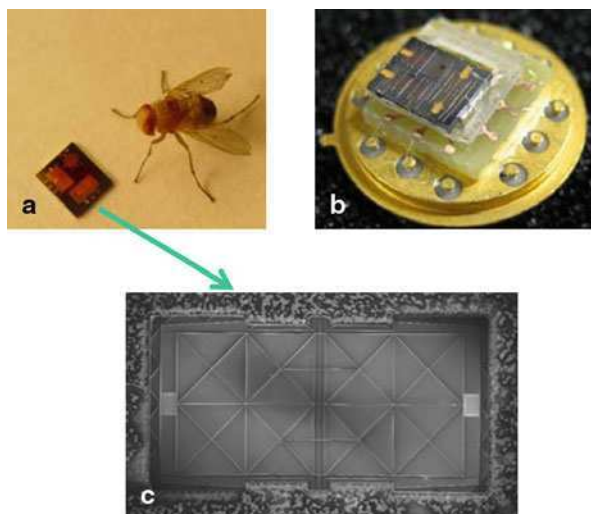
The second feature is that silicon represents the core material of this technology. Silicon substrates are commonly used as the platform where MEMS components are built and electrically bonded, although recently other materials, such as conductive polymers have been utilized [2, 3]. The fabrication of MEMS devices usually starts with single crystal silicon wafers, which come in many standard sizes (4 in, 8 in, and 12 in). Silicon is the preferred material because of its excellent thermal and mechanical properties (small thermal expansion, high melting point, high toughness, and brittleness with no plastic behavior or hysteresis). In addition, silicon has been used for microelectronics long before the MEMS technology. Hence, many of the well-established processes to fabricate microelectronics from silicon have been adopted directly or modified slightly for MEMS. MEMS made of silicon can be integrated easily with other electronics components, which are also made of silicon, on the same chip. Besides silicon, a number of materials are used to realize MEMS structures, such as silicon-oxide, silicon-nitride, polysilicon, gallium arsenide (GaAs), aluminum, and gold. These are grown or deposited as thin-films over the silicon substrate, which are then etched or processed by micro-fabrication techniques [4].

Another key aspect of MEMS devices is the fact that they are made through the micro-fabrication technology, which enables fabricating numerous numbers of them at the same time (batch fabrication). Many of the micro-fabrication processes, such as material deposition, evaporation, and etching, can be applied on multiple silicon wafers at the same time. Each wafer can produce hundreds of MEMS devices. This means that each fabrication batch can produce thousands of MEMS devices all at once. Of course, reaching this level of production is not trivial; micro-fabrication processes need extensive research and optimization for each step to reach stable and reliable level of production. However, once this critical stage is passed, the payoff is thousands of devices at very low cost. MEMS devices have replaced many expensive devices for fractions of the cost. For instance, the Analog Devices airbag accelerometers in cars, which today costs less than a dollar, has replaced bulkier more expensive accelerometers, which cost more than US\$ 50 apiece.

Another important feature of MEMS is the fact that they are systems. This implies that the components of MEMS have to be designed during the design of the whole system. Assembly of individual MEMS components is expensive, cumbersome, and impractical [5]. Also, when designing a microsystem, its fabrication process must be designed too, otherwise the design may not be feasible or cannot be fabricated. Another implication is that system issues, such as packaging, system partitioning into components, stability, and reliability of the products, must be analyzed and taken into consideration during the design and development cycles.

Fig. 1.1 A directional microphone for hearing aids inspired by ears of the fly *Ormia ochracea* [8].

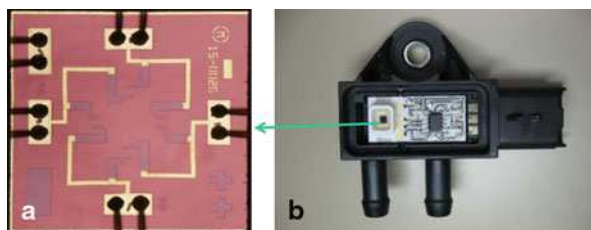
a A picture for the chip containing polysilicon diaphragms next to the fly *Ormia ochracea*, **b** is a packaged microphone, and **c** is a SEM picture of the torsional polysilicon diaphragm, which is the backbone of the directional microphone. (Courtesy of Professor Ronald Miles, Binghamton University.)



The fascination in the MEMS technology comes from their distinguished characteristics. MEMS are characterized by low cost, which is a direct consequence of the batch fabrication. They have lightweight and small size, which is desirable for compactness and convenience reasons. In addition, this has opened the gates for new possibilities of implementing MEMS in many places where large devices do not fit, such as engine of cars and inside the human body. Moreover, they consume very low power, which not only does reduce the operational cost but also enables the development of long-life and self-powered devices that can harvest the small amount of energy they need from the environment during their operation [6, 7]. Furthermore, MEMS devices have enabled many superior performances, smart functionalities, and complicated tasks that cannot be achieved in other technologies. Ultra-sensitive mass detectors, high isolation and low-insertion-loss RF switches, lab-on-a-chip bio-sensors, tiny directional microphones for hearing aids (Fig. 1.1), high-temperature pressure sensors for automobile engines (Fig. 1.2), and precise controlled liquid droplets for ink-jet printers are just few examples.

Fig. 1.2 Differential pressure sensors used in cars and trucks diesel engines emissions systems [9].

a A micro-diaphragm with a piezoresistive 4-gauges bridge, **b** the packaged device. (Courtesy of Sensata Technologies [9])



1.2 Why We Need Modeling and Simulation Tools?

Simulation tools for MEMS represent essential and urgent needs for designers and researchers to advance the technology to the next levels [10]. In the early days of MEMS developments, the majority of research has been directed toward methods of fabrication with little presented on modeling and simulation. Hence, researchers had to rely on either simple analytical formulas based on crude approximations or on complicated finite-element (FE) models using software that are not geared for MEMS. The outcome of either approach was simulation results that contradict or in disagreement with the lab data. This has deepened the problem even more since researchers did not count much on their models predictions and relied more on experimental testing. Hence, a trial-and-error approach has been adopted in which a device is designed; prototypes are fabricated and then tested, and based on the test results the design is modified again, retested and so on. The result has been a very long development cycle, which is costly and time consuming.

The need for modeling and simulation tools for MEMS can be summarized for the following reasons:

- To reduce the design time and cost. Reliable simulation tools can effectively reduce the design cycle from weeks and months to days.
- To allow for more aggressive design goals. Having the right models allows designers to explore the design space more aggressively based on robust knowledge gained from simulation results. This leads to development of devices of higher quality and improved features.
- To optimize the performance of existing devices. Many of the already invented MEMS devices have been designed based on primitive principles as described above. Hence, although some of these devices are well-established and commercialized, there is still a big room for improvement with unexplored possibilities and what-if scenarios. This can lower their cost and lead to smarter and more reliable generation of these devices.
- To design novel devices. This is one of the biggest advantages of simulation tools. They increase our knowledge and help us gain solid understanding of the behavior of MEMS devices and the natural phenomena associated with them. This in turn opens the horizon for new research avenues and novel ideas of devices of distinctive features. Without proper simulation and modeling tools for MEMS, such opportunities are being lost.

1.3 Challenges of MEMS Modeling and Simulations

The need for robust simulation tools and accurate models has been recently recognized by many in the MEMS community. Here, we focus on the mechanical behavior of MEMS devices and mainly their statics and dynamics behavior. There are number of challenges that face MEMS engineers and researchers when attempting to model

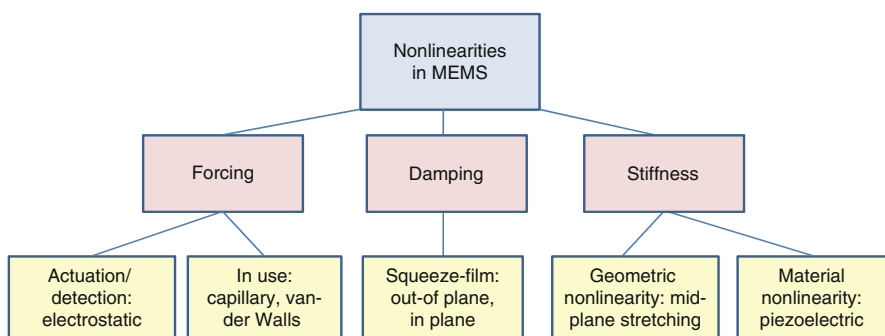


Fig. 1.3 A schematic illustrating some of the common sources of nonlinearities in MEMS

and simulate the mechanical behavior of MEMS devices. These can be classified into three broad categories: nonlinearities, physical fields coupling, and micro-scale phenomena.

Nonlinearities are present in MEMS as in the case of other macro-scale systems. However, in MEMS, nonlinearities can be strong and dominant. Hence, neglecting them in the models can lead to erroneous predictions. There are many sources of nonlinearities in MEMS, which are due to forcing, damping, and stiffness, Fig. 1.3. Forcing can introduce nonlinearities through actuation and detection mechanisms. For example, parallel-plate electrostatic forces are inherently nonlinear (proportional to the inverse of distance squared between the electrodes) and are commonly used for actuation and detection. Also, other nonlinear forces can affect microstructures while they are operated or are in-use, such as capillary forces due to humidity and van-der Waals forces for microstructures in close proximity of each other or the substrate. There are many complicated mechanisms of energy dissipation and damping affecting microstructures. However, the most common mechanism is squeeze-film damping, which is inherently nonlinear (proportional to the inverse of the distance cubed between the close surfaces). It influences structures of large surface area that are close to each other or to the substrate.

Many microstructures are designed to be compliant to deform and undergo specific action or motion. When actuated, microstructures undergo relatively large motion, which amplifies the so-called geometric nonlinearities of the structures [11, 12]. Figure 1.4 shows a schematic for MEMS devices implementing such structures. The deflection of a clamped-clamped beam switch, for example, relative to its thickness is considered large if compared with the relative deflection of a bridge due to the motion of a car across it. Therefore, in the macro-scale world, the vibration of objects, such as bridges and buildings, is considered small compared to their dimensions. Hence, it is common and quite acceptable to apply linear theories to study their deformation and motion. However, the same cannot be said for a microbeam bridge. Because the relative motion is comparable to its thickness and size, geometric nonlinearities, particularly mid-plane stretching, will be induced leading to significant change in its stiffness and dynamical behavior. In addition, using some materials in

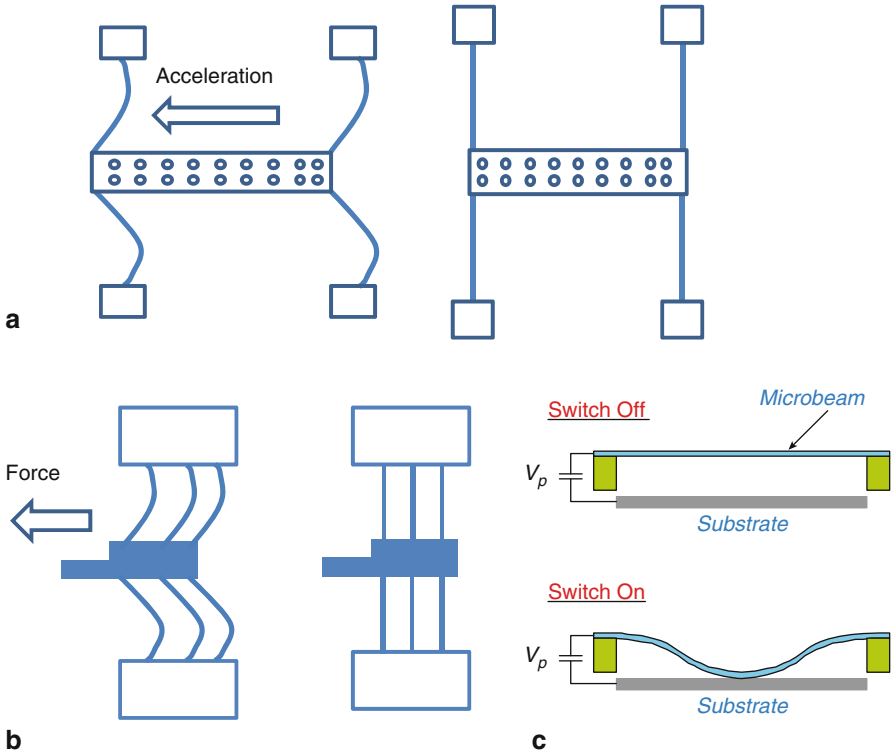


Fig. 1.4 A schematic shows examples of MEMS devices with compliant microstructures exhibiting large deformation. Shown are **a** an accelerometer, **b** a thermal actuator, and **c** a capacitive switch

microstructures can induce nonlinearities, such as piezoelectric materials, which are quadratic in nature [13].

The second challenge of MEMS modeling and simulation is the inherent coupling among various energy domains and physical forces, such as mechanical, fluidic, thermal, and electrical forces. Hence, simulating the behavior of a typical MEMS device requires knowledge in more than one discipline and the ability to deal with the interaction and interface issues among various fields. For example, simulating the dynamic response of a RF MEMS switch to determine its switching time requires a coupled-field model accounting for the electrostatic forces, the structural forces, and the squeeze-film damping (fluidic forces). Adding to this the fact that these forces are nonlinear, simulating the behavior of such a simple device poses serious difficulties for MEMS designers.

The third category of challenges is the micro-scale phenomena, which are unique for MEMS devices and structures. These phenomena can exist in the macro-scale but have negligible effect, such as thermoelastic damping, which was discovered by Zener in the 1930s while conducting research on metallic rods [14]. They can be present in the large scale in limited applications; however they are more common in

MEMS, such as squeeze-film damping, which is primarily known in the big world for hard-disk drives and mechanical bearings. Other micro-scale phenomena can only exist in the micro or small range because of the nature of the involved forces, which are significant only in the very small scale. Examples of these are the pull-in instability associated with capacitive MEMS and the jump-to-contact instability in atomic force microscopes (AFM). MEMS researchers and designers need to be aware of the existence of these phenomena and their influence on the behavior of their devices. Instabilities, such as pull-in, can cause serious numerical difficulties and software problems if one does not have enough background to deal with them.

1.4 Coupled-Field MEMS Phenomena

This section briefly introduces some of the common coupled-fields phenomena in MEMS [10]. Mostly, these are nonlinear and involve coupling among two or more physical fields. In the subsequent chapters, these phenomena will be further analyzed and discussed.

1.4.1 Squeeze-Film Damping

Many MEMS devices employ a parallel-plate capacitor, Fig. 1.5, in which one plate is actuated electrically and its motion is detected by capacitive changes. In order to increase the efficiency of actuation and improve the sensitivity of detection, the distance between the capacitor plates is minimized and the area of the electrode is maximized. Under such conditions, the phenomenon of squeeze-film damping is pronounced. This phenomenon occurs as a result of the massive movement of the fluid underneath the plate, which is resisted by the viscosity of the fluid. This gives rise to a pressure distribution underneath the plate, which may act as a spring and/or a damping force. Squeeze-film damping is the most common and dominant mechanism of MEMS. Studying the effect of squeeze-film damping on a microstructure requires

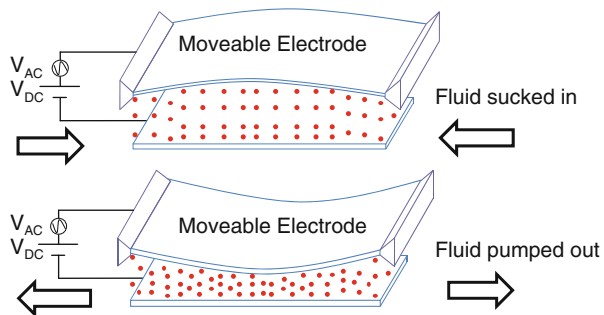


Fig. 1.5 A schematic shows a parallel-plate capacitor pumping fluid in and out its gap while moving up and down

analyzing the behavior of the fluid underneath it and how it reacts with the motion of the microstructure.

1.4.2 Thermoelastic Damping

Thermoelastic damping has been shown to be a possible dominant source of intrinsic damping in MEMS [15, 16]. Thermoelastic damping results from the irreversible heat flow generated by the compression and decompression of an oscillating structure. A structure in bending has one side under tension and the other side under compression at a higher temperature. This variation in temperature causes a thermal gradient inside the material of the structure, which adjusts itself to allow for a thermal equilibrium. However, the energy used in this adjustment cannot be restored (irreversible process) even if the structure returns to its original state of zero-bending stress. Hence, thermoelastic damping is also referred to as internal friction. According to [17], internal friction is defined as “the capacity of a solid to transform its ordered energy of vibration into disordered internal energy.” Investigating thermoelastic damping of microstructures involves at least two physical domains, the structural and thermal domains.

1.4.3 Pull-in Instability

The electric load acting on a capacitor plate is generally composed of a DC polarization voltage and an AC harmonic voltage. The DC component applies an electrostatic force on the plate, thereby deflecting it to a new equilibrium position. In resonators applications, in addition to the DC voltage, an AC component is superimposed to the DC component to vibrate the plate around the equilibrium position. The combined electric load has an upper limit beyond which the mechanical restoring force of the plate can no longer resist its opposing force, thereby leading to a continuous increase in the microstructure deflection and, accordingly, an increase in the electric forces in a positive feedback loop. This behavior continues until a physical contact is made with the stationary electrode. This structural instability phenomenon is known as “pull-in,” and the critical voltage associated with it is called “pull-in voltage” [18]. If pull-in occurs due to DC actuation only, it is called “static pull-in” or just pull-in. If it occurs due to transient DC actuation, AC harmonic loading, or due to transient effects, it is called “dynamic pull-in” [19–22]. Analyzing pull-in requires modeling the coupled structural-electrostatic energy domains.

A key issue in the design of MEMS resonators [18] is to tune the electric load away from the pull-in instability, which leads to collapse of the structure, and hence a failure in the devices. On the other hand, this phenomenon forms the basis of operation for RF MEMS switches [23, 24], Fig. 1.4c, in which the mechanical structure is actuated by a voltage load beyond the pull-in voltage to snap the structure with the fastest speed and minimal time.

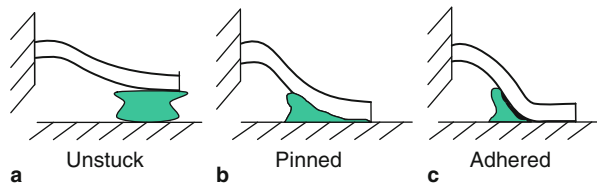
1.4.4 Stiction Due to Capillary Forces

Wet etching of sacrificial layers to release microstructures from the substrate is an important step in the fabrication of many MEMS structures and devices. During drying, the rinse liquid trapped underneath the microstructures creates strong capillary forces pulling them toward the substrate. Humidity can also cause condensation of liquid in working devices. Because of their large surface areas, some microstructures can go down to the substrate if the capillary forces are greater than their restoring forces. If the restoring force of a microstructure cannot resist the capillary force, it collapses hitting the substrate. This is similar to the pull-in instability when the microbeam is actuated by electrostatic forces. Some microstructures get permanently stuck to the substrate if their elastic forces in the collapsed configuration cannot resist both the capillary forces and the adhesion forces induced between the part of the microstructure in contact with the substrate and the substrate (stiction problem) [25–30]. To analyze the effect of capillary forces on microstructures, one needs to solve a coupled-field fluid-structure problem.

To clarify the various instabilities due to capillary forces, we consider as an example a cantilever microbeam with a volume of liquid trapped underneath it, Fig. 1.6. The microbeam under the effect of capillary forces can take one of the following three configurations depending on its stiffness and the capillary force distribution:

- (a) Free-standing configuration: The microbeam is not in contact with the substrate, Fig. 1.6a. In this case, it deflects and maintains equilibrium with the capillary force.
- (b) Pinned configuration: In this case, the capillary force overcomes the stiffness of the cantilever beam causing it to collapse. One of the possible post collapse scenario is that the microbeam makes a contact with the substrate at its tip, where it is pinned and stuck. At this instance, the elastic force of the microbeam is capable of opposing the capillary force underneath; hence, the microbeam stays in this configuration in equilibrium, Fig. 1.6b.
- (c) Adhered (stuck) configuration: In this case, the capillary force is strong enough to overcome the restoring force of the microbeam, which brings it from configuration Fig. 1.6b to Fig. 1.6c, where part of the microbeam becomes adhered to the substrate. The contact length of the cantilever beam varies with the microbeam length, stiffness, and with the distribution of the capillary force.

Fig. 1.6 The possible scenarios for the configuration of a cantilever microbeam under the effect of capillary forces. **a** is unstuck beam, **b** is pinned beam, and **c** is adhered beam



1.5 The State-of-the-Art of MEMS Modeling and Simulations

The state-of-the-art of MEMS modeling and simulation has seen significant progress in recent years. There have been some excellent books on MEMS modeling and design [2, 3, 5, 10, 31–36]. Nevertheless, challenges still exist in this field with a big gap between the models predictions and the experimental data and with many uncertainties and unsolved issues. The following observations can be drawn on the modeling techniques and approaches that are commonly utilized in the literature:

- Many neglect or misrepresent the system nonlinearities. Nonlinearities are sometimes linearized, making the model valid only for small range of motion, or represented incompletely, leading to inaccurate results. More advanced models have been presented recently based on perturbation methods or based on expanding complicated nonlinearities in Taylor series retaining the first few terms. While these models are further steps ahead in complexity compared to linear theories, they have the shortcoming of being valid for weak-nonlinear regimes and local dynamic analysis. Global nonlinear phenomena, such as pull-in and snap-through, may not be predicted using these approximate models.
- Most models employ simplified spring-mass models. They treat compliant structures as rigid bodies and lumped elements instead of continuous systems of distributed mass and stiffness. While these models can be helpful for first-cut designs, they lack sufficient level of accuracy and may not predict complicated dynamical behaviors, such as the effect of higher order modes on the response of microstructures.
- Approximate analytical techniques have been also utilized and applied on distributed parameter models, such as Rayleigh-Ritz techniques. However, more often than not, the convergence of these models and the suitability of the selected trial functions are rarely checked. In addition, many of these techniques are limited to linearized models, which do not account properly for the system nonlinearities.
- The past two decades have seen significant development of FE and computer-aided design CAD software specifically for MEMS devices and structures, for example ANSYS [37], COMSOL [38], Coventor [39], and IntelliSense [40]. Many of these provide the capabilities of tackling nonlinear and multi-physics problems and enable the simulation of the performance of MEMS devices of complex shapes and configurations. Despite their important role in the development and evolution of MEMS, FE software needs to be complemented by other analytical and numerical tools. Using only FE software as black blocks does not provide deep insight and understanding of the various physical aspects associated with MEMS devices. Advanced nonlinear dynamic analysis is hard to be conducted on FE models of numerous degrees of freedom. Many of the analytical and numerical tools of nonlinear dynamics are geared for few-degrees-of-freedom models. Analytical techniques, such as asymptotic methods, phase portraits, shooting and continuation approaches, and stability and bifurcation analysis are hard to be conducted on FE models. Even implementing active control techniques and simulating their effect are cumbersome on FE models. Therefore, analytical models and tools need

to be utilized to understand properly the behavior of MEMS devices, especially those with strong nonlinearities.

Problems

For the below questions, you need to search the internet and do a little research to answer them. There are many resources that you can use, among those you may want to try the below classical MEMS journals:

- (a) Journal of Microelectromechanical systems (JMEMS)
 - (b) Journal of Micromechanics and Micro engineering (JMM)
 - (c) Sensors and Actuators (A) and (B)
 - (d) Microsystem Technologies
1. Give three new examples of MEMS devices that have enabled smart and new functionalities that cannot be achieved using other technologies.
 2. Give three new examples of MEMS devices that have replaced more expensive older devices. Provide quantitative comparisons indicating how much the MEMS devices save.
 3. Provide new examples of multi-physics MEMS devices that involve more than one energy domain in their operation.
 4. Provide new examples of MEMS phenomena that are multi-physics and/or nonlinear, that is they involve multi-physics energy domain and/or nonlinear forces.
 5. Name six MEMS devices that employ a moveable microstructure.
 6. Nanoelectromechanical systems (NEMS) share many similarities with MEMS. Also, they have their own distinctive phenomena, devices, and challenges. Search the net for examples of distinctive NEMS phenomena and devices, which do not exist in the micro-scale or are less common. For this, you need to refer to the Nano technology literature, such as the journals “Nanotechnology” and “Nano Letters.”

References

- [1] www.memsnet.org (MEMS and Nanotechnology Exchange; Reston, Virginia)
- [2] Hsu T R (2008) MEMS and microsystems: Design, manufacture, and nanoscale engineering. Wiley, New York
- [3] Liu C (2006) Foundations of MEMS. Prentice Hall, New Jersey
- [4] Madou M J (2002) Fundamentals of microfabrication: The science of miniaturization. CRC, Boston
- [5] Elwenspoek M (2001) Mechanical microsensors. Springer, New York
- [6] Roundy S, Wright P K, Rabaey J (2003) A study of low level vibrations as a power source for wireless sensor nodes. Computer Communications, 26:1131–1144
- [7] Beeby S P, Tudor M J, White N M (2006) Energy harvesting vibration sources for microsystems applications. Measurement Science Technology, 17:R175–R195
- [8] Miles R N, Su Q, Cui W, Shetye M, Degertekin F L, Bicen B, Garcia C, Jones S, Hall N (2009) A low-noise differential microphone inspired by the ears of the parasitoid fly *Ormia ochracea*. Journal of Acoustics Society of America, 125:2013–2026

- [9] www.sensata.com (Sensata Technologies; Attleboro, MA)
- [10] Senturia S D (2001) *Microsystem design*. Springer, New York
- [11] Nayfeh A, Mook D (1979) *Nonlinear oscillations*. Wiley, New York
- [12] Nayfeh A, Pai P F (2000) *Linear and nonlinear structural mechanics*. Wiley, New York
- [13] Mahmoodi S N, Jalili N, Daqaq M F (2008) Modeling, nonlinear dynamics, and identification of a piezoelectrically actuated microcantilever sensor. *IEEE/ASME Transactions on Mechatronics*, 13(1):58–65
- [14] Zener C (1937) Internal friction in solids: I. Theory of internal friction in reeds. *Physical Review*, 52:230–235
- [15] Lifshitz R, Roukes M L (2000) Thermoelastic damping in micro-and nanomechanical systems. *Physical Review B*, 61:5600–5609
- [16] Zenzhart T V (1990) The effect of thermoelastic internal friction on the Q of micromachined silicon resonators. *Proceeding of IEEE Solid-State Sensors Actuator Workshop*, Hilton Head, South Carolina, pp. 13–16
- [17] Randall R H, Rose F C, Zener C (1939) Intercrystalline thermal currents as a source of internal friction. *Physical Review*, 56:343–348
- [18] Nathanson H C, Newell W E, Wickstrom R A, Davis J R (1967) The resonant gate transistor. *IEEE Transaction Electron Devices*, ED-14(3):117–133
- [19] Krylov S, Maimon R (2004) Pull-in dynamics of an elastic beam actuated by continuously distributed electrostatic force. *Transactions of the ASME*, 126(3):332–342
- [20] Younis M I, Miles R, Jordy D (2006) Investigation of the response of microstructures under the combined effect of mechanical shock and electrostatic forces. *Journal of Micromechanics and Microengineering*, 16:2463–2474
- [21] Nayfeh A H, Younis M I, Abdel-Rahman E M (2007) Dynamic pull-in phenomenon in MEMS resonators. *Nonlinear Dynamics*, 48:153–163
- [22] Alsaleem F M, Younis M I, and Ouakad H M (2009) On the nonlinear resonances and dynamic pull-in of electrostatically actuated resonators. *Journal of Micromechanics and Microengineering*, 19:045013(14pp)
- [23] Rebeiz G M (2003) *RF MEMS: theory, design, and technology*. Wiley, New York
- [24] Varadan V M, Vinoy K J, Jose K A (2003) *RF MEMS and their applications*. Wiley, New York
- [25] De Boer M P, Clews P J, Smith B K, Michalske, T A (1997) Adhesion of polysilicon microbeams in controlled humidity ambient. *Material Research Society Symposium*, 518:131–136
- [26] De Boer M P, Michalske T A (1999) Accurate method for determining adhesion of cantilever beams. *Journal of Applied Physics*, 86(2):817–827
- [27] Mastrangelo C H, Hsu C H (1993) Mechanical stability and adhesion of microstructures under capillary forces. I. Basic Theory. *Journal of Microelectromechanical Systems* 2:33–43
- [28] Mastrangelo C H, Hsu C H (1993) Mechanical stability and adhesion of microstructures under capillary forces. II. Experiments. *Journal of Microelectromechanical Systems*, 2:44–55
- [29] Legtenberg R, Tilmans H A C, Elders J, Elwenspoek M (1994) Stiction of surface micromachined structures after rinsing and drying: Model and investigation of adhesion mechanisms. *Journal of Sensors and Actuators*, 43:230–238
- [30] Tas N, Sonnenberg T, Jansen H, Legtenberg R, Elwenspoek M (1996) Stiction in surface micromachining. *Journal of Micromechanics and Microengineering*, 6:385–397
- [31] Allen J J (2005) *Micro electro mechanical system design*. CRC Press, New York
- [32] Pelesko J A, Bernstein D H (2002) *Modeling MEMS and NEMS*. CRC, Boca Raton
- [33] Bao M (2005) *Analysis and design principles of MEMS devices*. Elsevier, Amsterdam
- [34] Lobontiu N, Garcia E (2004) *Mechanics of microelectromechanical systems*. Springer, New York
- [35] Lobontiu N (2007) *Dynamics of microelectromechanical systems*, Springer, New York
- [36] Kaajakari, V. (2009) *Practical MEMS: Design of microsystems, accelerometers, gyroscopes, RF MEMS, optical MEMS, and microfluidic systems*, Small Gear Publishing, Las Vegas
- [37] <http://www.ansys.com/> (ANSYS Inc.; Canonsburg, PA)
- [38] <http://www.comsol.com/> (COMSOL, Inc.; Burlington, MA)
- [39] <http://www.coventor.com/> (Coventor Inc.; Cary, NC)
- [40] <http://www.intellisensesoftware.com/> (IntelliSense Corp; Woburn, MA)

Chapter 2

Vibrations of Lumped-Parameter Systems

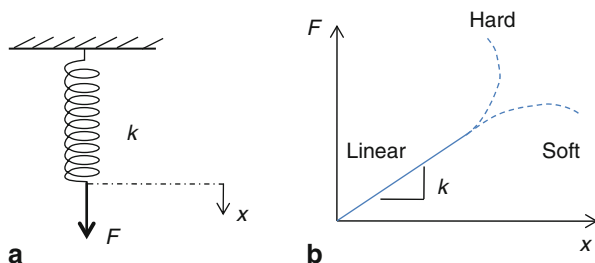
This chapter presents an overview and a refresher on the linear vibration principles of lumped-parameters systems, which are used to model MEMS. Since most microstructures undergo some sort of vibratory motion, the information presented here are fundamental to the understanding of many key aspects of MEMS dynamical behavior. Also, some of the methods to extract the parameters needed to model MEMS devices and structures require knowledge in the principles of vibrations. In addition, this chapter serves as a good introduction to the more advanced topics of nonlinear oscillations that will be discussed in the following chapters. The principles of operation of some MEMS devices, including accelerometers, gyroscopes, and band-pass filters, will be discussed here.

In lumped-parameters systems, MEMS devices are modeled as lumped or concentrated masses, springs, dampers, and point forces. The discussion will start on single-degree-of-freedom (SDOF) systems. The free vibration problem (damped and undamped) will be discussed. Then, forced vibrations due to external point loads and due to base excitations will be addressed. Arbitrary excitation will be also discussed. Finally, the analysis of the vibration of two-degree-of-freedom (2-DOF) systems will be presented. For more in-depth treatment of these topics, the readers are referred to these excellent references in vibrations [1–5].

2.1 Introduction

Vibration can be defined as the study of repetitive motion of objects relative to a stationary frame [1]. There are many examples of vibrations in our everyday life, such as heart beating, cars vibrations on bumpy roads, and the motion of tree branches with wind. In MEMS, most devices employ a microstructure or more that is either driven intentionally to vibrate to achieve sensing or actuation functions, such as microresonators and atomic force microscopes (AFM), or they undergo some sort of vibratory motion when excited by dynamic disturbances, such as when microstructures are subjected to mechanical shock.

Fig. 2.1 **a** A schematic shows a spring being pulled by a force. **b** A force–deflection curve showing a linear regime with a slope k ending with a possible nonlinear hardening or softening behaviors



For vibration to occur there must be an exchange of energy between potential and kinetic energy. Hence, a vibratory system must have a spring-like component that stores the potential energy and converts it to kinetic energy in the form of motion. Complaint structures, such as beams and rods, play the role of springs in MEMS. If the spring is loaded with a force, Fig. 2.1a, and its deflection is measured then a force–displacement curve can be generated, such as that of Fig. 2.1b. Typically, the curve is a straight line for small range of force (linear range). The slope of this line is a constant called the stiffness coefficient of the spring k . Beyond the linear regime, the spring shows a nonlinear force–deflection relationship characterized by either increasing in stiffness (hardening behavior) or decreasing in stiffness (softening behavior) compared to the linear case.

To describe the motion of a system undergoing vibrations, a number of independent coordinates need to be assigned to the system to adequately describe its motion. These are called degrees of freedom (DOFs). For example, a body that undergoes translational and rotational motion in a single plane requires two independent variables to describe its motion, one for translation and one for rotation (unless both are related). If the vibration is induced by initially disturbing the system from its equilibrium position without having a force that continuously acting on it, the vibration is called free vibration (vibration due to initial conditions). If a force acts continuously on the system during motion, the vibration is called forced vibration. Vibration also can be classified as damped or undamped depending on whether the energy of the system is conserved or is being dissipated during vibration. Next, we discuss some of these types of vibrations.

2.2 Free Vibration of Single-Degree-of-Freedom Systems

2.2.1 Undamped Vibration

Many systems that have one mode of motion dominating their response or one principal DOF can be modeled as SDOF systems. In the absence of damping or dissipation mechanisms, a lumped spring–mass system, such as that of Fig. 2.2a, can be used to represent this system. The first step in the vibration analysis is the dynamics, that

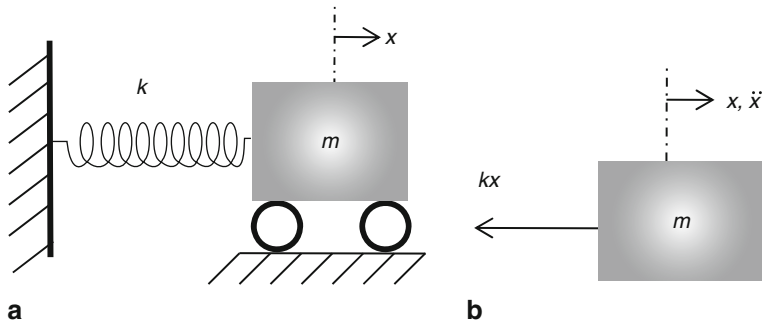


Fig. 2.2 **a** A spring–mass system to model the free vibration of a conservative SDOF system. **b** A diagram showing the forces acting on the mass in the horizontal direction when disturbed to the positive direction to the right

is, we need first to derive the equation of motion for the system. For this, Newton’s second law of motion is used:

$$\sum \vec{F} = m\vec{a} \quad (2.1)$$

where $\sum \vec{F}$ represents the forces acting on the mass m in a specific direction and \vec{a} is the induced acceleration of the mass in that direction. To apply Eq. (2.1) on the system, the mass is assumed displaced in the positive direction (to the right) a distance x . Then, we isolate the mass, label all the forces acting on it, and label the acceleration \vec{a} in the positive direction, which is the same as that of x as shown in Fig. 2.2b. We recall here that the acceleration \vec{a} is the second-time derivative of the displacement, $\vec{a} = \ddot{x}$, where the superscript dot denotes a time derivative. As noted from Fig. 2.2b, when the mass is displaced to the right, there will be a resistance restoring force acting on it to the left, which assuming a linear relationship as in Fig. 2.1b is expressed as

$$\vec{F} = -kx \quad (2.2)$$

where the negative sign in Eq. (2.2) indicates that the force has an opposite direction to the positive displacement to the right. Applying Eq. (2.1) yields

$$-kx = m\ddot{x} \quad (2.3)$$

or after rearranging

$$m\ddot{x} + kx = 0. \quad (2.4)$$

Dividing Eq. (2.4) by m gives

$$\ddot{x} + \omega_n^2 x = 0 \quad (2.5)$$

where $\omega_n^2 = k/m$ and ω_n is called the natural frequency of the system. It has the unit of rad/s. It depends on the “natural” characteristics of the system, mass and stiffness. Equation (2.5) represents a second-order linear differential equation of constant coefficients. To solve this equation, we assume x to be of the form

$$x(t) = ae^{\lambda t} \quad (2.6)$$

where t is the time, a and λ are unknown constants, and e is the exponential constant. Substituting Eq. (2.6) into Eq. (2.5) and dividing by $ae^{\lambda t}$ yields the following characteristic equation for λ :

$$\lambda^2 + \omega_n^2 = 0. \quad (2.7)$$

From Eq. (2.7), $\lambda^2 = \pm i\omega_n$, and hence according to Eq. (2.6) and using the principle of superposition, the total solution of Eq. (2.5) becomes

$$x(t) = a_1 e^{i\omega_n t} + a_2 e^{-i\omega_n t} \quad (2.8)$$

where a_1 and a_2 are the constants of integration that are determined from the initial conditions of the system (its initial velocity and displacement). Alternatively, using Euler’s formulas, Eq. (2.8) can be written as

$$x(t) = A \sin(\omega_n t + \phi) \quad (2.9)$$

where A and ϕ are the constants of integration. Equation (2.9) describes the oscillatory motion of the system of Fig. 2.2a over time with A representing the amplitude of oscillation and ϕ the phase shift. To determine A and ϕ , we assume the system has an initial velocity v_0 and an initial displacement x_0 , that is

$$x(0) = x_0; \quad \dot{x}(0) = v_0. \quad (2.10)$$

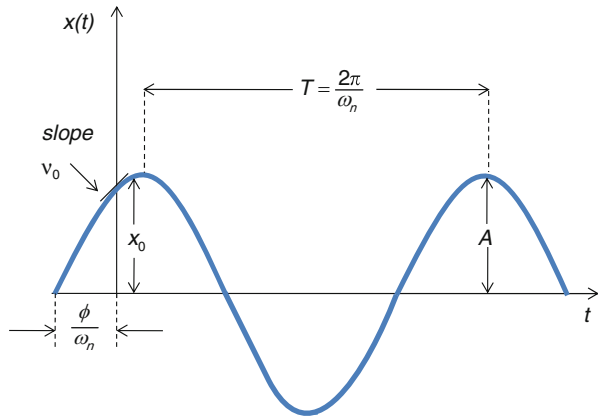
From Eqs. (2.9) and (2.10)

$$A = \sqrt{x_0^2 + (v_0/\omega_n)^2}; \quad \phi = \tan^{-1}(\omega_n x_0/v_0). \quad (2.11)$$

Figure 2.3 shows an example plot of Eq. (2.9) clarifying the terminologies defined above. As seen in the figure, the resulting motion is an oscillatory motion that repeats itself every time interval T . This time is called the natural period. It is related to the natural frequency by $T = 2\pi/\omega_n$ and has the unit of time. As noted, the natural period indicates how “frequent” the motion repeats itself in one cycle T . The inverse of T , f , is also called the natural frequency and it has the unit of (1/s) or Hertz (Hz). Hence,

$$f = \frac{1}{T} = \frac{\omega_n}{2\pi}. \quad (2.12)$$

Fig. 2.3 A portion of the time–history response of the spring–mass system of Fig. 2.2a indicating some of the key vibration features of the system. In the figure, $x_0 > 0$ and $v_0 > 0$



To obtain the mass velocity and acceleration, Eq. (2.9) is derived with respect to time once and twice, respectively, which yields

$$\dot{x}(t) = \omega_n A \cos(\omega_n t + \phi) \quad (2.13)$$

$$\ddot{x}(t) = -\omega_n^2 A \sin(\omega_n t + \phi). \quad (2.14)$$

One can note from Eq. (2.13) that the magnitude of the maximum velocity is $\omega_n A$ with a phase shift $\pi/2$ with respect to the displacement. Also from Eq. (2.14), the magnitude of the maximum acceleration is $\omega_n^2 A$ with a phase shift π with respect to the displacement and $\pi/2$ with respect to the velocity.

Example 2.1: A system operates in vacuum, as in the case of some MEMS resonators, can be modeled as an undamped spring–mass system, such as that of Fig. 2.2. In an experiment to determine the mass and stiffness of the system, its natural frequency was measured and found to be 100 Hz. Then, a new mass was added to the system equals 1 g and the natural frequency was measured again and found to be 90 Hz. Determine the stiffness and mass of this system.

Solution: Given: $f_1 = 100$ Hz, $f_2 = 90$ Hz, $\delta m = 0.001$ kg.
From Eq. (2.12)

$$f_1 = \frac{\omega_1}{2\pi} = \frac{\sqrt{k/m}}{2\pi} \quad (a)$$

$$f_2 = \frac{\omega_2}{2\pi} = \frac{\sqrt{k/(m + \delta m)}}{2\pi}. \quad (b)$$

Dividing Eq. (a) over Eq. (b)

$$\frac{f_1}{f_2} = \frac{\sqrt{k/m}}{\sqrt{k/(m + \delta m)}} = \sqrt{\frac{m + \delta m}{m}}. \quad (c)$$

Squaring Eq. (c)

$$\left(\frac{f_1}{f_2}\right)^2 = \frac{m + \delta m}{m}. \quad (d)$$

Solving for m gives

$$m = \delta m \frac{f_2^2}{f_1^2 - f_2^2}. \quad (e)$$

Substituting the numbers yields $m = 4.3$ g. Solving for k from Eq. (a) gives $k = 1.683$ kN/m.

2.2.2 Damped Vibration

The model presented in Sect. 2.2.1 predicts an oscillatory motion that keeps going forever and never dies out. A more realistic model of vibrating systems should account for the fact that the energy of vibrations dissipates over time through damping mechanisms. One way to account for this is by adding a dashpot or a damper element to the model of Fig. 2.2a. If the damping force \vec{F}_d is assumed linearly proportional to the speed of the mass, as in the case of viscous damping from air, then the damping force can be expressed as

$$\vec{F}_d = -c\dot{x} \quad (2.15)$$

where c is the viscous damping coefficient and the minus sign indicates that the force is a resistance force with a direction opposite to the motion direction. It should be noted here that MEMS damping mechanisms can be more complicated and may be nonlinear, as will be discussed in the next chapter. Figure 2.4 shows a schematic for the model and the corresponding force diagram.

Applying Newton's second law on the system of Fig. 2.4 yields the below equation of motion:

$$m\ddot{x} + c\dot{x} + kx = 0. \quad (2.16)$$

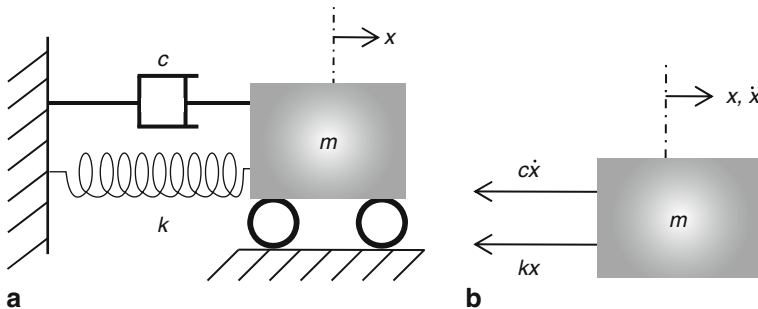


Fig. 2.4 **a** A spring–mass–damper system to model the free vibration of a nonconservative SDOF system. **b** A diagram showing the forces acting on the mass in the horizontal direction when disturbed to the positive direction to the right

Dividing Eq. (2.16) by m yields

$$\ddot{x} + 2\zeta\omega_n\dot{x} + \omega_n^2x = 0 \quad (2.17)$$

where ζ is called the damping ratio, a nondimensional quantity, defined as

$$\zeta = \frac{c}{2m\omega_n}. \quad (2.18)$$

To solve Eq. (2.17), we substitute Eq. (2.6) into Eq. (2.17) and divide the outcome by $ae^{\lambda t}$ to yield

$$\lambda^2 + 2\zeta\omega_n\lambda + \omega_n^2 = 0. \quad (2.19)$$

Solving Eq. (2.19) gives

$$\lambda_{1,2} = -\zeta\omega_n \pm \omega_n\sqrt{\zeta^2 - 1} \quad (2.20)$$

and hence using the principle of superposition, the total solution of Eq. (2.17) is

$$x(t) = a_1e^{\lambda_1 t} + a_2e^{\lambda_2 t}. \quad (2.21)$$

As noted from Eqs. (2.20) and (2.21), the nature of the response depends on whether λ_1 and λ_2 are complex, real, or mix. This in turn depends on the square-root term in Eq. (2.20) and particularly whether ζ is less than one, greater than one, or equal one. Accordingly, the free vibration of damped systems can be classified into the following categories:

1. Overdamped motion ($\zeta > 1$)

As the name suggests, this case indicates too much damping. In this case, λ_1 and λ_2 are pure real numbers. Hence, the solution of the system can be expressed as

$$x(t) = e^{-\zeta\omega_n t} \left[a_1 e^{\omega_n t \sqrt{\zeta^2 - 1}} + a_2 e^{-\omega_n t \sqrt{\zeta^2 - 1}} \right]. \quad (2.22)$$

Figure 2.5 shows a plot of the response of Eq. (2.22) for various damping ratios. As seen in the figure, the response in this case is not oscillatory; the damping is too

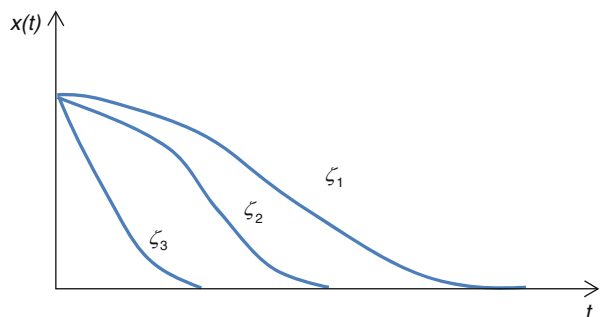
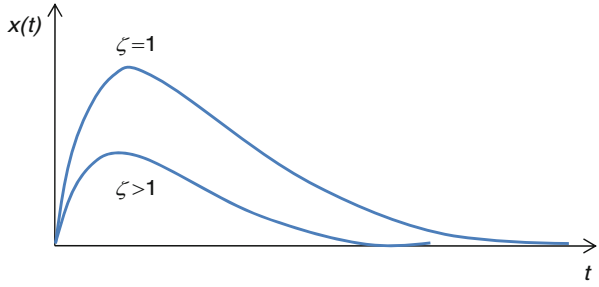


Fig. 2.5 Examples of time-history responses of an overdamped spring-mass-damper system for various damping ratios for $1 < \zeta_1 < \zeta_2 < \zeta_3$. In the figure, $x_0 > 0$ and $v_0 = 0$

Fig. 2.6 A comparison for the response of a spring–mass–damper system between the critically damped and overdamped cases. In the figure, $x_0 = 0$ and $v_0 > 0$



much that the motion dies very quickly without allowing for oscillations. The rate of motion decaying increases with the amount of damping and the value of ζ .

2. Critically damped motion ($\zeta = 1$)

This case is called “critically” damped because it separates two different qualitative behaviors: oscillatory motion for $\zeta < 1$ and non-oscillatory motion for $\zeta > 1$. In this case, Eq. (2.20) gives two real equal roots, $\lambda_{1,2} = -\omega_n$. Hence, the solution of Eq. (2.17) becomes

$$x(t) = e^{-\omega_n t}(a_1 + a_2 t). \quad (2.23)$$

The response of the system in this case is similar to the overdamped case except that decaying of the motion takes longer time. Figure 2.6 compares the response of this case to an overdamped case.

3. Underdamped motion ($0 < \zeta < 1$)

As the name suggests, this case indicates low damping compared to the other two cases. Here, λ_1 and λ_2 are complex numbers. To remind ourselves of this, λ_1 and λ_2 are rewritten from Eq. (2.20) explicitly with the imaginary root i , that is

$$\lambda_{1,2} = -\zeta \omega_n \pm i \omega_n \sqrt{1 - \zeta^2}. \quad (2.24)$$

Hence, the solution for the system motion according to Eq. (2.21) becomes

$$x(t) = e^{-\zeta \omega_n t} \left[a_1 e^{i \omega_n t \sqrt{1 - \zeta^2}} + a_2 e^{-i \omega_n t \sqrt{1 - \zeta^2}} \right]. \quad (2.25)$$

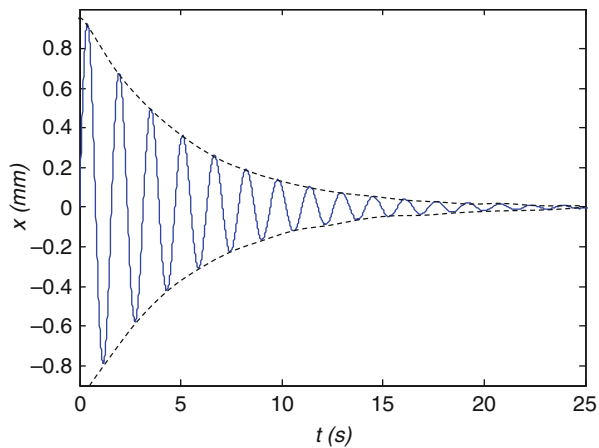
Using Euler’s formula, Eq. (2.25) can be rewritten in the more convenient form as

$$x(t) = A e^{-\zeta \omega_n t} \sin[\omega_d t + \phi] \quad (2.26)$$

where A and ϕ are the amplitude and phase of the response, respectively and $\omega_d = \omega_n \sqrt{1 - \zeta^2}$ is the damped natural frequency of the system. In the case of low values of ζ , $\omega_d \approx \omega_n$. The parameters A and ϕ are determined from the initial conditions of the system. Using Eqs. (2.10) and (2.26) yields

$$\tan(\phi) = \frac{x_0 \omega_d}{v_0 + \zeta x_0 \omega_n}; \quad A = \frac{\sqrt{(x_0 \omega_d)^2 + (v_0 + \zeta x_0 \omega_n)^2}}{\omega_d} \quad (2.27)$$

Fig. 2.7 An example of a time–history response of an underdamped spring–mass–damper system. In the figure, $x_0 = 0$ and $v_0 > 0$



An example of the response obtained from Eq. (2.26) is plotted in Fig. 2.7. The figure shows an oscillatory motion that decays exponentially with time (note the exponential envelope in dashed lines). As noted from Figs. 2.5, 2.6, and 2.7, underdamped motion is the only damped case that can be considered as “true” vibration motion where the moving mass passes through the equilibrium position more than once. Also, underdamped motion is the most common; hence, the majority of vibration analysis and studies are focused on this case.

Before closing this section, we should point out to the fact that in all of the above discussion, we implicitly assumed that the damping ratio ζ or the damping coefficient c to be positive. If otherwise damping is negative then the resulting motion will be unstable vibratory motion (flutter), which usually leads to the collapse or failure of the structure (a famous example of this case is the collapse of the Tacoma Bridge in 1940). A similar note applies on the stiffness k , which must be positive also. In short, both the stiffness and damping of the system must be positive to lead to stable vibration. More on stability issues are discussed in Chap. 5.

Example 2.2: A spring–mass–damper system, Fig. 2.4, has $m = 1$ kg, $k = 100$ N/m, and $c = 1$ kg/s. If the system is given an initial velocity of 10 mm/s while it is in the equilibrium position, determine and plot the response of the system. If the system vibrates, determine the frequency of vibration due to this excitation in Hz.

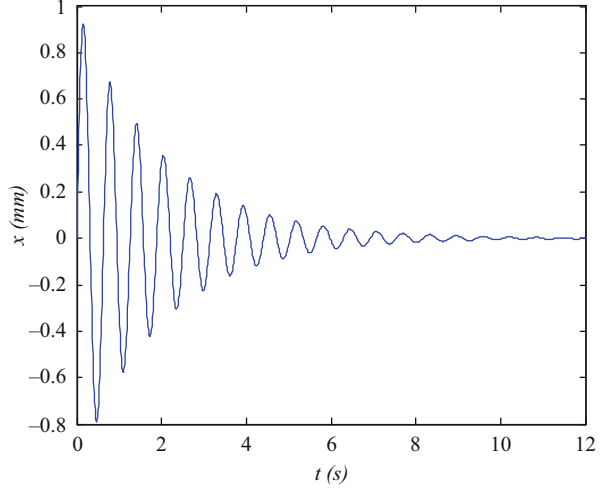
Solution: First, the system needs to be determined if it is overdamped, underdamped, or critically damped. Hence, we need to calculate ζ , but first we calculate ω_n

$$\omega_n = \sqrt{\frac{k}{m}} = \sqrt{\frac{100}{1}} = 10 \text{ rad/s.} \quad (\text{a})$$

From Eq. (2.18)

$$\zeta = \frac{c}{2m\omega_n} = \frac{1}{2(1)(10)} = 0.05. \quad (\text{b})$$

Fig. 2.8 A time–history response of the underdamped system of Example 2.2



Hence, the system is underdamped. It vibrates with ω_d given by

$$\omega_d = \omega_n \sqrt{1 - \zeta^2} = 10 \sqrt{1 - .05^2} = 9.9875 \text{ rad/s} \quad (c)$$

and in Hz

$$f = \frac{\omega_d}{2\pi} = 1.59 \text{ Hz}. \quad (d)$$

As can be seen, for low damping, ω_n and ω_d are almost the same. However, this tiny difference can be translated to hundreds of Hz for microstructures with mega- and gigahertz frequencies.

To determine the response, A and ϕ are calculated from Eq. (2.27)

$$\tan(\phi) = \frac{x_0 \omega_d}{v_0 + \zeta x_0 \omega_n} = \frac{0 \times \omega_d}{v_0 + \zeta x_0 \omega_n} = 0 \Rightarrow \phi = 0 \text{ rad}. \quad (e)$$

$$A = \frac{\sqrt{(x_0 \omega_d)^2 + (v_0 + \zeta x_0 \omega_n)^2}}{\omega_d} = \frac{\sqrt{(0)^2 + (.01 + 0)^2}}{9.9875} = 0.001 \text{ m}. \quad (f)$$

Hence, from Eq. (2.26), the response of the system is expressed as

$$x(t) = .001 e^{-.5t} \sin[9.9875t]. \quad (g)$$

Figure 2.8 shows a plot of the response.

2.3 Forced Harmonic Excitation of Single-Degree-of-Freedom Systems

Harmonic excitation is very common in MEMS through actuation methods, such as electrostatic and piezoelectric actuation. In this section, the forced vibration of a SDOF system, Fig. 2.9a, to a harmonic force excitation is analyzed. From

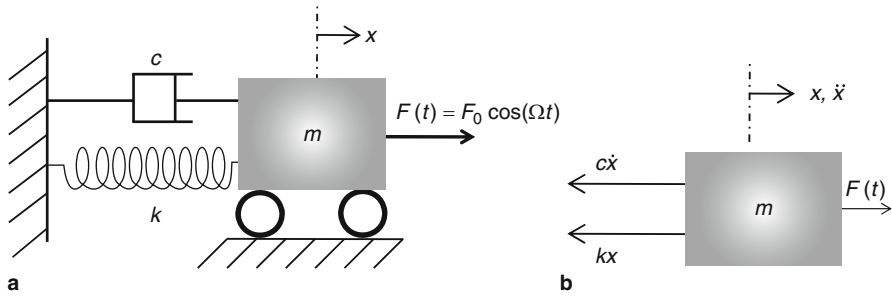


Fig. 2.9 **a** A model for the forced vibration of a spring–mass–damper system. **b** A diagram showing the forces acting on the mass in the horizontal direction when disturbed to the positive direction to the right

the force diagram of Fig. 2.9b, the equation of motion of the system can be written as

$$m\ddot{x} + c\dot{x} + kx = F_0 \cos(\Omega t) \quad (2.28)$$

where F_0 is the harmonic force amplitude and Ω is the excitation frequency. Dividing Eq. (2.28) by m yields

$$\ddot{x} + 2\zeta\omega_n\dot{x} + \omega_n^2x = f_0 \cos(\Omega t) \quad (2.29)$$

where $f_0 = F_0/m$. Equation (2.29) is a nonhomogenous linear differential equation of constant coefficients. Hence, its solution consists of two parts: a homogenous solution x_h and a particular solution x_p . The homogenous solution corresponds to the case when $f_0 = 0$, which is similar to the cases discussed in Sect. 2.2. Thus, depending on the damping ratio, x_h can be calculated by either of Eqs. (2.9), (2.22), (2.23), or (2.26). However, the constant of integrations cannot be calculated based on any of the formulas of Sect. 2.2; they need to be calculated based on relating the initial conditions to the total homogenous and particular solution of the system $x = x_p + x_h$. The homogenous solution represents physically the transient behavior of the system; hence, it decays away leaving only the particular solution, which is also called the steady-state response. To calculate the particular solution, the method of undetermined coefficients is used. Toward this, x_p is expressed as

$$x_p(t) = A_s \cos(\Omega t) + B_s \sin(\Omega t) \quad (2.30)$$

where A_s and B_s are unknown coefficients to be determined. Substituting Eq. (2.30) into Eq. (2.29) and solving for A_s and B_s (see [1] for details) yield

$$A_s = \frac{(\omega_n^2 - \Omega^2)f_0}{(\omega_n^2 - \Omega^2)^2 + 4\zeta^2\omega_n^2\Omega^2}; \quad B_s = \frac{2\zeta\omega_n\Omega f_0}{(\omega_n^2 - \Omega^2)^2 + 4\zeta^2\omega_n^2\Omega^2}. \quad (2.31)$$

A more convenient way to express this solution is through writing it in the form of an amplitude X and a phase θ as

$$x_p(t) = X \cos(\Omega t - \theta) \quad (2.32)$$

where

$$X = \frac{f_0}{\sqrt{(\omega_n^2 - \Omega^2)^2 + (2\zeta\omega_n\Omega)^2}} \quad (2.33)$$

$$\theta = \tan^{-1} \left(\frac{2\zeta\omega_n\Omega}{\omega_n^2 - \Omega^2} \right). \quad (2.34)$$

If the forcing function in Eq. (2.28) is of the form $F_0 \sin(\Omega t)$, then the cosine is replaced with sine in Eq. (2.32), whereas Eq. (2.33) and Eq. (2.34) still apply. Equation (2.32) indicates an important fact for linear systems, that is if the system is excited with a frequency Ω , it responds with the same frequency.

For convenience, the excitation frequency is normalized with respect to the natural frequency. This is a more meaningful way to describe the excitation frequency as a ratio of the natural frequency than just saying it as an absolute number, which does not reveal much unless it is known how far it is from the natural frequency. Thus, a normalized frequency ratio is introduced as $r = \Omega/\omega_n$. Accordingly, Eqs. (2.33) and (2.34) are rewritten as

$$\frac{X}{f_0/\omega_n^2} = \frac{1}{\sqrt{(1 - r^2)^2 + (2\zeta r)^2}} \quad (2.35)$$

$$\theta = \tan^{-1} \left(\frac{2\zeta r}{1 - r^2} \right). \quad (2.36)$$

Note that the ratio $X/(f_0/\omega_n^2)$ is the dynamic steady-state response due to the harmonic force normalized to the static deflection of the system due to an equivalent static force of the same magnitude as the harmonic force (note that $f_0/\omega_n^2 = F_0/m\omega_n^2 = F_0/k = \delta$, where δ is a constant). Therefore, this ratio indicates how much the response of the system is being amplified due to the dynamic effect. Note also that both sides of Eq. (2.35) are nondimensional.

Mostly in forced-vibration problems, the interest is in the steady-state response. In this case, Eq. (2.35) and (2.36) play key rule in revealing the vibration features of the system. Figures 2.10, 2.11, and 2.12 show plots of these equations while varying the damping ratio and the normalized excitation frequency. The following notes can be observed from Fig. 2.10:

- All the curves start from $X/k = 1$, which corresponds to very low excitation frequencies compared to the natural frequency. This range of excitation is called quasi-static. It is a stiffness-dominated range with slight effect from damping or inertia. By exciting the system near this range, one can extract the stiffness coefficient of the system if the amplitude of vibration is measured.
- The normalized response of all the curves become small and approach zero as r increases beyond $r = 2$. This range is called inertia-dominated range with slight effect from damping or stiffness. For sensor applications in MEMS, this range is not of much benefit since the system responds very weakly to the input excitation.

Fig. 2.10 Frequency–response curves of spring–mass–damper system showing the normalized steady-state amplitude versus the normalized excitation frequency for various values of damping ratio

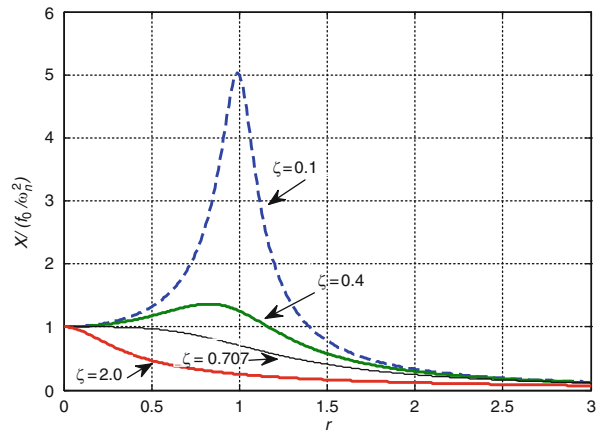
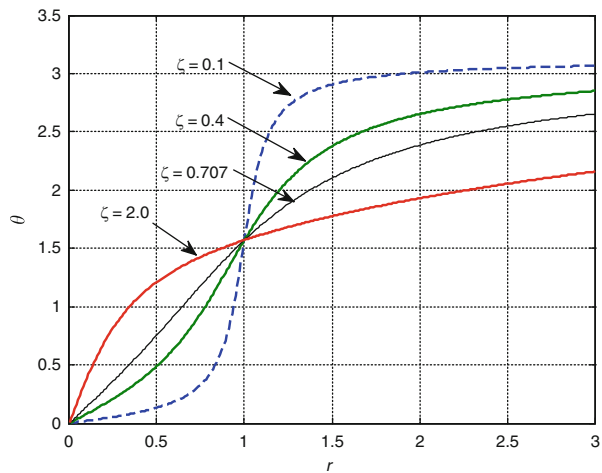
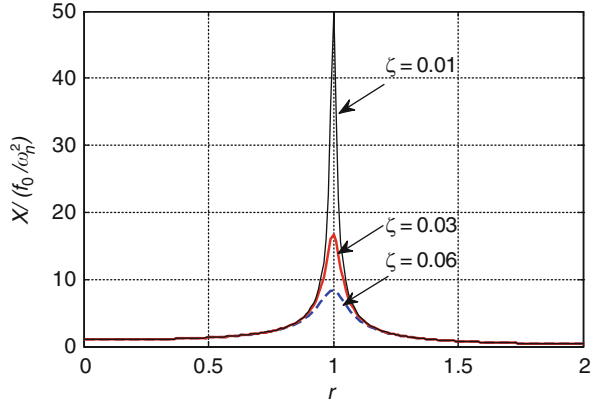


Fig. 2.11 The phase angle of a spring–mass–damper system versus the normalized excitation frequency for various values of damping ratio



- For the range near $0.5 < r < 1.5$, the curves of small ζ (0.4 and 0.1) peak in their value near $r = 1$. This corresponds to the so-called **resonance** phenomenon. It occurs when the excitation frequency is equal to the natural frequency and results in the maximum response for systems of low damping. Resonance is very important concept in vibration and MEMS as well. On the other hand, the curves of large ζ (0.707 and 2) do not show any peak in their response. It turns out that all the curves of $\zeta < 0.707$ have peak amplitudes somewhere close to $r = 1$ whereas all the curves of $\zeta > 0.707$ do not have any peaks. Because this range of r is very sensitive to damping, it is called damping dominated.
- While resonance most often corresponds to the maximum response of the system, it is not always the case, especially for large damping. In fact one can see that the maximum response for $\zeta = 0.4$ is shifted slightly to the left. In general, the

Fig. 2.12 Frequency–response curves for smaller values of the damping ratio



frequency corresponding to the peak response Ω_{peak} is given by

$$\Omega_{\text{peak}} = \omega_n \sqrt{1 - 2\zeta^2}. \quad (2.37)$$

For small values of ζ , the peak, resonance, and natural frequencies are almost the same.

From Fig. 2.11, the following can be noted:

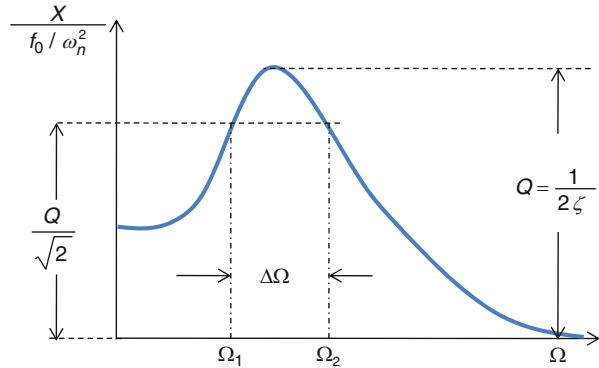
- All the curves pass through $\theta = \pi/2$ at $r = 1$. This represents another indication of resonance corresponding to $\pi/2$ phase shift.
- For values of $r \ll 1$, $\theta \approx 0$. This means that for very small excitation frequencies, the response is almost in phase with the excitation force.
- For values of $r \gg 1$, $\theta \approx \pi$. This means that for large excitation frequencies, the response is 180° out of phase with the excitation force.

Figure 2.12 shows frequency–response curves for small values of ζ . Many MEMS resonators and sensors are operated in such conditions with even lower values of damping ratios. As seen in the figure, the curves become very sharp and narrow near resonance. In sensors, the interest is to achieve the highest response to give strong signal as an indication of what is being measured. The sharpness of resonance is commonly expressed in terms of a quantity called the quality factor Q , which is related to the damping ratio by

$$Q = \frac{1}{2\zeta}. \quad (2.38)$$

A rough estimation for the quality factor can be taken from the height of the resonance peak, as shown in Fig. 2.13. Another quantity of interest for sensors applications is the width of the resonance spike. As noted from Fig. 2.12, it is very hard to operate a resonator at the exact location of resonance for very small values of ζ . Therefore, it is desirable to have the width of the spike as large as possible. A standard way to measure this width is through a quantity called bandwidth $\Delta\Omega$. To calculate the bandwidth, a

Fig. 2.13 A frequency–response curve illustrating the concepts of quality factor and bandwidth



horizontal line is drawn intersecting with the frequency–response curve at a height of $Q/\sqrt{2}$ as shown in Fig. 2.13. The height $Q/\sqrt{2}$ represents the vibration amplitude that corresponds to half the maximum power (power is proportional to the amplitude squared). In decibel, this height represents -3 dB. The points of intersection, called half-power points, are labeled Ω_1 and Ω_2 . The bandwidth is then expressed as [2]

$$\Delta\Omega = \Omega_2 - \Omega_1 = 2\zeta\omega_n. \quad (2.39)$$

Hence, from Eq. (2.38) and Eq. (2.39)

$$Q = \frac{\omega_n}{\Delta\Omega}. \quad (2.40)$$

Equation (2.40) is used to measure the quality factor, which more accurate than depending on measuring the height of the resonance peak. Equation (2.40) indicates that achieving high quality factor is on the expense of a good bandwidth and vice versa. This poses a challenge for MEMS and sensors applications. One way to overcome this and to achieve both high-quality factor and wide bandwidth is through using band-pass filters as sensors, as will be explained in Sect. 2.9.

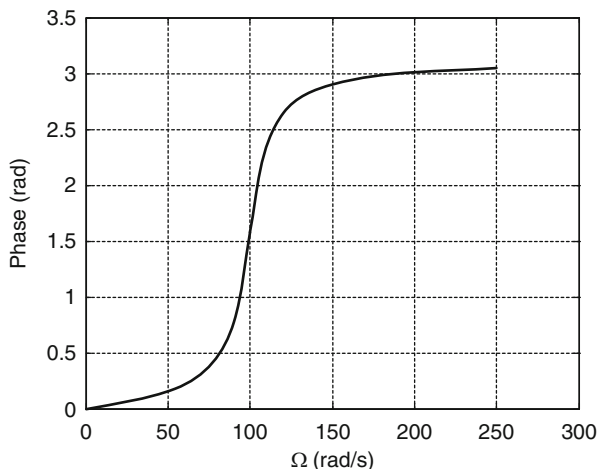
Example 2.3: Figure 2.14 shows the measured phase angle of the steady-state response of the system of Fig. 2.9a for a harmonic force of various excitation frequencies. If the system is then driven by $F(t) = 200\cos(10t)$, calculate the steady-state amplitude of the system assuming $m = 1$ kg.

Solution: Based on Fig. 2.14, we note that the response has a phase shift $\pi/2$ when $\Omega = 100$ rad/s. This indicates resonance, which means that the natural frequency of the system is also 100 rad/s. Since the excitation frequency is given to be 10 rad/s, this means that $r = 10/100 = 0.1$. Hence, this is a quasi-static excitation case, in which knowing the damping is not important. According to Fig. 2.10, in this case

$$\frac{X}{f_0/\omega_n^2} \approx 1. \quad (a)$$

Accordingly, $f_0 = F_0/m = 200$ N/kg and from (a) $X \approx 0.02$ m.

Fig. 2.14 A measured phase response for the system of Example 2.3



Example 2.4: Calculate the maximum response of the system of Example 2.2 if it is driven by a harmonic force of amplitude 10 N.

Solution: We recall from Example 2.4 that $\omega_n = 10$ rad/s, $\zeta = 0.05$. Since the system is lightly damped, its maximum response occurs at resonance when $r = 1$. From Eq. (2.35)

$$\frac{X}{f_0/\omega_n^2} = \frac{1}{2\zeta}. \quad (a)$$

Substituting $f_0 = F_0/m = 10$ N/kg yields

$$\frac{X}{10/10^2} = \frac{1}{2(.05)} \Rightarrow X = 1 \text{ m}. \quad (b)$$

2.4 Vibrating MEMS Gyroscopes

As an application for the previous section, we study here the vibration response of MEMS gyroscopes. A gyroscope is a device that captures the rotational motion of a body. More specifically, it is a device that measures the angular velocity of a body about a certain axis of rotation. Gyroscopes have wide range of uses in vehicle control applications, such as anti-rollover and antiskid control systems, aviation, navigation, space applications, robotics, and military applications, such as for missiles navigation. Conventional gyroscopes rely on large structures, such as tuning forks or spinning disks that are free to rotate in specific directions. Also, they may contain complicated components, such as bearings and rotating rings. Hence, the classical gyroscopes are bulky, expensive, and unreliable.

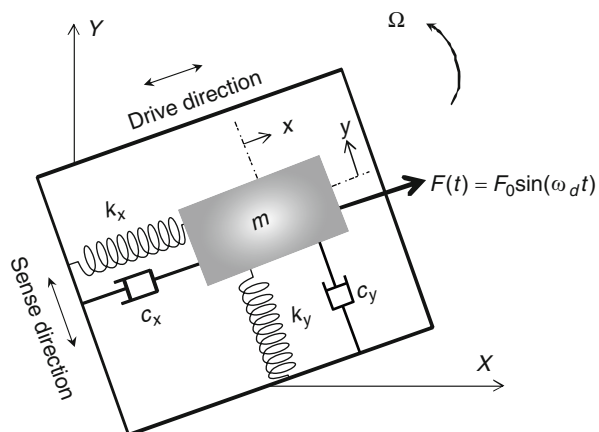
The technology of MEMS with the advantages of batch fabrication, small size, and low price has offered an attractive alternative to conventional gyroscopes. Almost all MEMS gyroscopes rely on vibrating mechanical elements that are driven to oscillate in the plane of the chip and to respond to rotation by another vibratory motion also in the same plane. This simple motion in a single plane and the fact that MEMS gyroscopes do not require complicated rotating parts or bearings have led to simplified and compact designs that can be easily fabricated using micromachining techniques.

MEMS gyroscopes have enabled smart generations of new technologies and applications, especially in consumer electronics, which would not have been possible before. MEMS gyroscopes are currently being used in video and still cameras and other portable electronics to help in the stabilization of their performance and to reduce the effect of human body motion and shaking. In addition, they are being used for interactive video games and head-mounted displays to sense and guide rotational motions.

The main principle of MEMS gyroscopes is the transfer of energy between two modes of vibrations, the drive and the sense modes, through the so-called Coriolis acceleration. Coriolis acceleration is an apparent acceleration that arises in a rotating frame and is proportional to the rate of rotation. The proof mass of MEMS gyroscopes can be driven and sensed using many methods; however, the most common is through electrostatic transduction. A major challenge in MEMS gyroscope is the fact that the generated Coriolis acceleration is very small. Hence, it is challenging to fabricate a small gyroscope of small mass with high sensitivity. More information on MEMS gyroscopes can be found in [6–8]. Next, we demonstrate through an example the basic dynamical and vibration features of a typical MEMS gyroscope.

Example 2.5: Consider the model of a vibratory MEMS gyroscope of Fig. 2.15. Derive the equations of motion of the device. Then, solve for the response of the

Fig. 2.15 A model of a typical MEMS vibratory gyroscope



device when undergoing a rotational motion and derive an analytical expression for the device's sensitivity.

Solution: To derive the equations of motion, we need to apply Newton's second law, which requires determining the acceleration of the mass. The acceleration can be determined by taking twice the derivative of the position vector of the mass with respect to time as measured from a stationary frame of reference (the X - Y frame in Fig. 2.15). An additional frame (the x - y frame in Fig. 2.15) is also introduced, which rotates with the plane of the vibrating mass with an angular velocity Ω . Both the stationary and rotating frames are assumed to share the same origin. The position vector \vec{R} of the mass can be written in terms of the x - y frame as

$$\vec{R} = x\hat{b}_1 + y\hat{b}_2 \quad (a)$$

where \hat{b}_1 and \hat{b}_2 are the unit vectors along the x and y coordinates, respectively. To find the velocity of the mass, the position vector is derived using the role of the time derivative of a rotating vector [9], which is

$$\frac{{}^{X-Y}d\vec{R}}{dt} = \frac{{}^{x-y}d\vec{R}}{dt} + {}^{x-y}\vec{\omega} \times \vec{R} \quad (b)$$

where ${}^{X-Y}d\vec{R}/dt$ refers to the time derivative of the vector with respect to the inertial frame, ${}^{x-y}d\vec{R}/dt$ is the local derivative of the vector with respect to the rotating frame, ${}^{x-y}\vec{\omega}$ is the rotational speed of the rotating frame (here assumed equal $\Omega\hat{b}_3$), and \times refers to the cross product operation. Applying Eq. (b) on Eq. (a) yields the velocity vector \vec{V} :

$$\vec{V} = \dot{x}\hat{b}_1 + \dot{y}\hat{b}_2 + \Omega\hat{b}_3 \times (x\hat{b}_1 + y\hat{b}_2) \Rightarrow \vec{V} = (\dot{x} - \Omega y)\hat{b}_1 + (\dot{y} + \Omega x)\hat{b}_2. \quad (c)$$

Similarly, taking one more time derivative of the velocity vector of Eq. (c) while applying the derivative role of Eq. (b) yields the acceleration vector \vec{a}

$$\vec{a} = (\ddot{x} - \dot{\Omega}y - 2\dot{y}\Omega - \Omega^2x)\hat{b}_1 + (\ddot{y} + \dot{\Omega}x + 2\dot{x}\Omega - \Omega^2y)\hat{b}_2 \quad (d)$$

where $\dot{\Omega}$ is the angular acceleration. One can also arrive to Eq. (d) by applying directly the five-term acceleration formula for rotating frames [9].

Based on Eq. (d), and by considering the forces on the mass of Fig. 2.15, the equations of motion of the mass in the x and y directions can be written, respectively, as

$$-k_x x - c_x \dot{x} + F_0 \sin(\omega_d t) = m(\ddot{x} - \dot{\Omega}y - 2\dot{y}\Omega - \Omega^2x) \quad (e)$$

$$-k_y y - c_y \dot{y} = m(\ddot{y} + \dot{\Omega}x + 2\dot{x}\Omega - \Omega^2y) \quad (f)$$

where F_0 and ω_d are the driving force amplitude and frequency, respectively. Equations (e) and (f) represent two coupled differential equations. The coupling comes from the terms involving $\dot{\Omega}$ and the two terms with “2” ($2\dot{y}\Omega$ and $2\dot{x}\Omega$), which are

nothing but the Coriolis acceleration terms. Equations (e) and (f) can be simplified by assuming constant angular speed, hence $\dot{\Omega} = 0$. Also, since Ω is usually much smaller than the natural frequencies of the system, the terms involving Ω^2 can be dropped. Further, because the sense mode response y is much smaller than the response of the directly-excited drive mode x , the term $2\dot{y}\Omega$ can be dropped. Under these simplifications, Eqs. (e) and (f) are reduced to

$$m\ddot{x} + k_x x + c_x \dot{x} = F_0 \sin(\omega_d t) \quad (g)$$

$$m\ddot{y} + k_y y + c_y \dot{y} = -2m\Omega \dot{x}. \quad (h)$$

Equation (g) can be solved independently of Eq. (h). Then the solution is substituted into Eq. (h), which is then solved for the sense-mode response y . To proceed, Eq. (g) is divided by m , hence it becomes

$$\ddot{x} + 2\zeta_x \omega_x \dot{x} + \omega_x^2 x = f_x \sin(\omega_d t) \quad (i)$$

where $\omega_x = \sqrt{k_x/m}$, $\zeta_x = c_x/(2m\omega_x)$, and $f_x = F_0/m$. The solution of Eq. (i) is given by

$$x(t) = X \sin(\omega_d t - \phi) \quad (j)$$

where

$$X = \frac{f_x/\omega_x^2}{\sqrt{(1-r_x^2)^2 + (2\zeta_x r_x)^2}}; \quad \phi = \tan^{-1} \left(\frac{2\zeta_x r_x}{1-r_x^2} \right) \quad (k)$$

and $r_x = \omega_d/\omega_x$. To find the sense-mode response, Eq. (j) is substituted into Eq. (h), which after dividing by m becomes

$$\ddot{y} + \omega_y^2 y + 2\zeta_y \omega_y \dot{y} = f_y \cos(\omega_d t - \phi) \quad (l)$$

where $\omega_y = \sqrt{k_y/m}$, $\zeta_y = c_y/(2m\omega_y)$, and $f_y = -2\Omega\omega_d X$. Hence, the amplitude of the sense-mode response can be written as

$$Y = \frac{f_y/\omega_y^2}{\sqrt{(1-r_y^2)^2 + (2\zeta_y r_y)^2}} = \left(\frac{2m\Omega\omega_d X}{k_y} \right) \frac{1}{\sqrt{(1-r_y^2)^2 + (2\zeta_y r_y)^2}} \quad (m)$$

where $r_y = \omega_d/\omega_y$. The sensitivity of the gyroscope is defined as the induced sense-mode amplitude (output) divided to the rotational speed (input), that is

$$\frac{Y}{\Omega} = \left(\frac{2m\omega_d X}{k_y} \right) \frac{1}{\sqrt{(1-r_y^2)^2 + (2\zeta_y r_y)^2}}. \quad (n)$$

One can see from Eq. (n) that the sensitivity is proportional to the oscillating mass, which puts some restrictions on the level of miniaturization that can be achieved

for MEMS gyroscopes. To achieve the highest sensitivity, X needs to be as large as possible. Hence, the mass usually is driven at resonance, $r_x = 1$. Also, resonance in the sense mode, $r_y = 1$, maximizes the sensitivity. This means that for maximum sensitivity $\omega_d = \omega_y = \omega_x$. Hence, substituting $r_x = 1$ in Eq. (k) and then substituting the outcome and $r_y = 1$ into Eq. (n) yield the below simplified expression for the sensitivity

$$\frac{Y}{\Omega} = \frac{2m\omega_d F_0 Q_x Q_y}{k_x k_y} \quad (o)$$

where $Q_x = 1/2\zeta_x$ and $Q_y = 1/2\zeta_y$ are the quality factors of the drive and sense modes, respectively. It is clear that high-quality factors are desirable to improve sensitivity.

Due to fabrication imperfections and environmental effects, it is extremely difficult to fabricate a gyroscope with $\omega_y = \omega_x$ and to lock the driving frequency exactly at resonance. This is known as the frequency mismatch problem in the literature [6–8]. Adding more DOFs to the design of MEMS gyroscopes can alleviate this problem [8].

2.5 Base Excitations of SDOF Systems and Accelerometers Principles

Base excitation, also called support excitation, refers to the case when a structure or a device is placed on top of a moving floor with some damping and stiffness characteristics, such as isolation rubber floors. Also, it models the case when a structure is supported through elastic mountains, which can act as springs and dampers, such as shock absorbers in cars. When the floor or the supports move, they cause vibration to the structure, which is influenced by the stiffness and damping properties of the floor or the supports.

The above description refers to the classical scenarios for base excitation. In MEMS, base excitation represents a more common case. Flexible structures of MEMS in handheld devices and machinery components are excited into vibration through their supports. Essentially, any MEMS chip that contains a flexible structure will base-excite that structure if the chip is placed in an application where it moves. The flexibility of the structure plays the role of a spring, which is actuated from the base. MEMS accelerometers, gyroscopes, and pressure sensors inside a car are subjected to base excitation whenever the car hits a bump or even undergoes slight vibration. Accelerometers, including MEMS type, are intentionally designed to detect the motion properties of a moving base or a structure. In addition, several kinds of AFM rely on exciting a cantilever beam from its support, such as the tapping mode AFM.

Currently, there is considerable interest in harvesting energy from environmental vibrations. This can be done by designing flexible structures to be mounted over

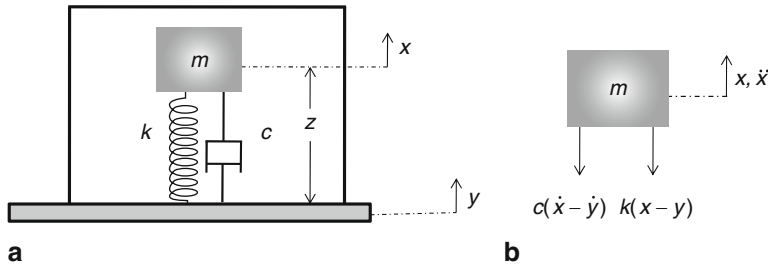


Fig. 2.16 **a** A packaged device modeled as a spring–mass–damper system subjected to base excitation. **b** A diagram showing the forces acting on the mass when disturbed to the positive direction upward

a floor or a machine that undergoes slight vibration, for example a microwave or a dishwasher, such that the structures will be base-excited to vibration. Then the kinetic energy of the excited structures is converted into electricity through piezoelectric, electrostatic, or electromagnetic mechanisms [10, 11].

Figure 2.16a shows a schematic for a packaged device, for example an accelerometer, containing a flexible structure placed over a base that moves with displacement $y(t)$. Figure 2.16b shows a free-body diagram for the mass indicating the forces acting on it when displaced from its equilibrium position upward. Note here that the gravitational force of the weight is not included since it affects only the equilibrium position with no influence on the dynamic response (this is true for linear systems only). Based on Fig. 2.16b, the equation of motion of the mass can be written as

$$m\ddot{x} + k(x - y) + c(\dot{x} - \dot{y}) = 0 \quad (2.41)$$

where x is the absolute deflection of the mass. In MEMS applications, usually the structure is suspended a small distance above the substrate. Hence, an excessive support excitation can lead to a contact between the structure and the substrate, which may lead to the device failure. Thus, it is important to monitor the relative deflection $z(t)$ of the structure with respect to the moving base, which is expressed as $z = y - x$. In addition, transduction mechanisms, such as electrostatic and piezoelectric, depend on this relative deflection. Writing Eq. (2.41) in terms of z yields

$$m\ddot{z} + c\dot{z} + kz = -m\ddot{y}. \quad (2.42)$$

The base is assumed to have harmonic excitation in the form of

$$y = Y \cos(\Omega_b t) \quad (2.43)$$

where Y denotes the amplitude of the base excitation and Ω_b is its frequency. Substituting Eq. (2.43) into Eq. (2.42) and dividing the outcome by m yields

$$\ddot{z} + 2\zeta\omega_n\dot{z} + \omega_n^2 z = \Omega_b^2 Y \cos(\Omega_b t). \quad (2.44)$$

Equation (2.44) looks similar to Eq. (2.29) with $f_0 = \Omega_b^2 Y$. Defining $r = \Omega_b/\omega_n$ and using Eqs. (2.35) and (2.36) result in the below expression for the steady state relative response:

$$z(t) = Z \cos(\Omega_b t - \theta) \quad (2.45)$$

where

$$\frac{Z}{Y} = \frac{r^2}{\sqrt{(1-r^2)^2 + (2\zeta r)^2}} \quad (2.46)$$

and θ is as defined in Eq. (2.36).

The nondimensional ratio Z/Y represents an amplification factor indicating how much relative displacement is induced in the structure compared to the input displacement. Figure 2.17 shows a plot for Z/Y based on Eq. (2.46) for various damping ratios. It is observed that at resonance, the relative displacement reaches a maximum value for damping ratios below 0.707. For small values of r , Z/Y is very small. It is noted also that all the curves converge to $Z/Y \approx 1$ as r exceeds 3. Based on this interesting observation, the device shown in Fig. 2.16 can be used to measure the displacement of the base by relating it directly to the relative displacement of the mass, which can be transformed into a voltage signal for instance through piezoelectric, magnetic, or electrostatic methods. This is again provided that $r > 3$, which means that the natural frequency of the device should be at least below one-third of that of the frequency being measured. This implies that the device and its moving mass should be bulky and large to satisfy this requirement, which puts practical limitations on the use of such devices. This kind of measurement devices is called seismometer.

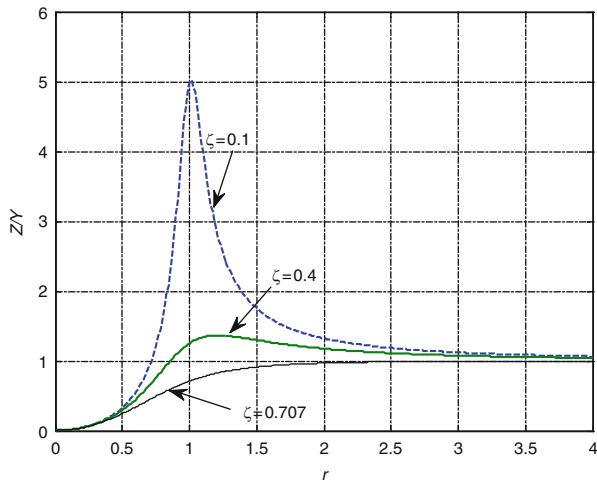


Fig. 2.17 A plot for the relative deflection of a structure excited from the base normalized to the amplitude input

Now consider the quantity $z(t)\omega_n^2$. From Eq. (2.45), it can be written as

$$z(t)\omega_n^2 = \frac{\Omega_b^2 Y \cos(\Omega_b t - \theta)}{\sqrt{(1-r^2)^2 + (2\zeta r)^2}}. \quad (2.47)$$

Recall that $\ddot{y} = -\Omega_b^2 Y \cos(\Omega_b t - \theta)$, hence according to Eq. (2.47)

$$z(t)\omega_n^2 = \frac{-\ddot{y}}{\sqrt{(1-r^2)^2 + (2\zeta r)^2}}. \quad (2.48)$$

Note that as $r \rightarrow 0$; $\frac{1}{\sqrt{(1-r^2)^2 + (2\zeta r)^2}} \rightarrow 1$. Hence, from Eq. (2.48), in this case the relative displacement is proportional to the base acceleration as $|z(t)\omega_n^2| = |\ddot{y}|$.

The previous observation represents the basic principle of **accelerometers**. By measuring the relative deflection of the structure inside the accelerometer through a transduction mechanism, for instance electrostatic or piezoelectric, the acceleration of the base is determined. This is provided again that r is sufficiently small. To further quantify this condition, we plot in Fig. 2.18 the ratio $\frac{1}{\sqrt{(1-r^2)^2 + (2\zeta r)^2}}$ for small range of r for various values of ζ . As noted from the figure, this ratio remains equal to unity for the largest range of r when $\zeta = 0.707$. Hence, by tuning the damping of the accelerometer to be near this damping ratio, the maximum operating range of the device is achieved. It is agreed on that for accurate measurements, r must be less than 0.2. This means that the natural frequency of the accelerometer should be at least five times higher than the measured frequency. This implies that the mass of the

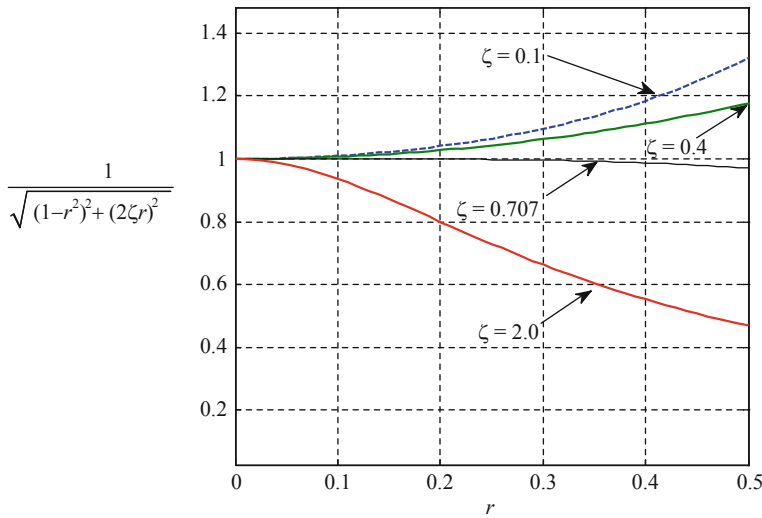


Fig. 2.18 A plot for the coefficient of \ddot{y} versus the normalized frequency for various values of damping ratios

accelerometer should be small enough to satisfy this condition. It turns out that this requirement in addition to the requirement of high damping near critical are easily satisfied via the MEMS technology. Through MEMS, the size of the accelerometer is made very small making the useful range of the accelerometer very large. Also, through the naturally existing squeeze-film damping, achieving critical damping is neither difficult nor costly in the micro scale. Therefore, no wonder that MEMS accelerometers were among the first and most successful MEMS devices that made it to commercialization.

2.6 Response of SDOF Systems to Arbitrary Excitation

Sections 2.3 and 2.4 deal with forced vibration, in which a system is constantly being excited by a harmonic force. In many situations, systems can be excited by nonharmonic and even nonperiodic forces, which may last for limited duration of time. A common example in the macro and micro applications is the mechanical shock force, which is induced on a structure when dropped on the ground. This force can take the shape of a pulse, for example triangle or half-sine, of limited duration, corresponding to the time of contact between the body and the ground. As a result of such a force, a flexible structure can get excited and undergo oscillatory motion over several cycles before the motion dies out due to damping.

In this section, we discuss the response of SDOF systems subjected to an arbitrary excitation based on the convolution integral approach without going into derivations details. For an undamped system, such as that of Fig. 2.2a, subjected to a force $F(t)$ of an arbitrary profile, Fig. 2.19, the response of the system can be expressed as

$$x(t) = \frac{1}{m\omega_n} \int_0^t F(\tau) \sin[\omega_n(t - \tau)] d\tau. \quad (2.49)$$

For an underdamped system, such as that of Fig. 2.4a, subjected to $F(t)$, the response of the system is calculated by

$$x(t) = \frac{1}{m\omega_d} \int_0^t F(\tau) e^{-\zeta\omega_n(t-\tau)} \sin[\omega_d(t - \tau)] d\tau. \quad (2.50)$$

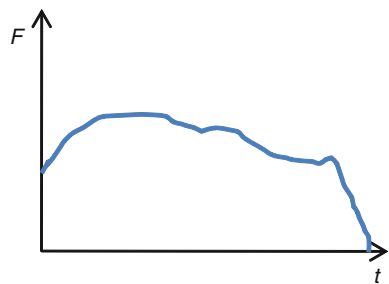


Fig. 2.19 An example of a force of arbitrary profile

Equations (2.49) and (2.50) predict the total response of the system due to the applied force assuming trivial initial conditions. For other initial conditions, Eqs. (2.49) and (2.50) represent only the particular solution for the equation of motion due to the force. The total response will then be composed of Eq. (2.49) or Eq. (2.50) plus the homogenous solution (corresponding to zero force). From relating the total solution to the initial conditions, the constants of integration of the homogenous solution are determined. This is further clarified in Example 2.7. Calculating the integrals in Eqs. (2.49) and (2.50) can be difficult analytically. Hence, numerical approaches, such as the trapezoidal method, can be used, which are found readily in software, such as Mathematica [12] and Matlab [13].

Example 2.6: Calculate the response of an undamped SDOF system, Fig. 2.2a, when subjected to a suddenly applied constant force F_0 (step force), Fig. 2.20. Assume trivial initial conditions for the system.

Solution: The equation of motion for this system is written as

$$m\ddot{x} + kx = F(t) \quad (2.51)$$

where $F(t)$ is an arbitrary force. Hence, applying Eq. (2.49) yields

$$x(t) = \frac{1}{m\omega_n} \int_0^t F_0 \sin[\omega_n(t - \tau)] d\tau = \frac{-F_0}{m\omega_n} \frac{\cos[\omega_n(t - \tau)]}{-\omega_n} \Big|_0^t \quad (2.52)$$

$$\Rightarrow x(t) = \frac{F_0}{k} [1 - \cos(\omega_n t)]. \quad (2.53)$$

Example 2.7: Calculate the response of an undamped SDOF system, Fig. 2.21, dropped to the ground from a distance h . This problem models the drop test used in the industry to test the survivability of portable devices and electronics including MEMS.

Solution: At the instant the system touches the ground, the spring will be pushed upward from its base. Also, at that moment, the whole system will be under the influence of the gravity acceleration $-g$, where the negative sign indicates that the acceleration is in a direction opposite to x (downward). This is similar to the base

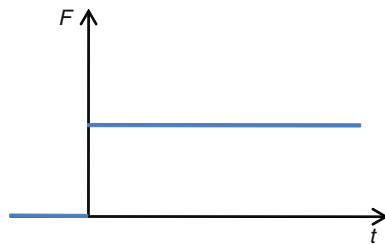


Fig. 2.20 A step force applied at time zero

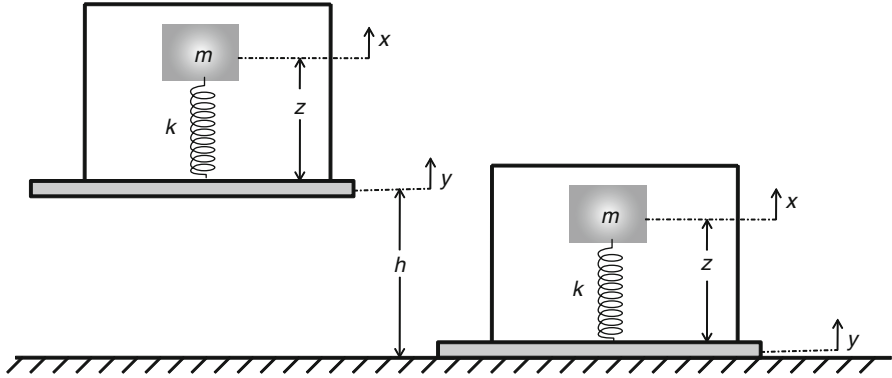


Fig. 2.21 A model for a drop test of a packaged device of Example 2.7

excitation problem of Sect. 2.4, except that the force here is not harmonic but arbitrary (constant). From Eq. (2.42), the equation of motion for this system is expressed as

$$m\ddot{z} + kz = -m\ddot{y} = mg = F_0 \quad (2.54)$$

which is similar to the case of Example 2.6 except that here the system is not initially at rest. The initial velocity of the system at the time of contact v_0 can be found from equating the potential energy mgh to the kinetic energy $mv_0^2/2$, which gives

$$v_0 = \sqrt{2gh}. \quad (2.55)$$

The total solution for Eq. (2.54) is composed of a particular solution given by Eq. (2.53) and a homogeneous solution given by Eq. (2.9), that is

$$x(t) = \frac{F_0}{k}[1 - \cos(\omega_n t)] + A \sin(\omega_n t + \phi). \quad (2.56)$$

Substituting $F_0 = mg$, $k = m\omega_n^2$, using the initial conditions $x_0 = 0$ and Eq. (2.55), and solving for A and ϕ yield

$$x(t) = \frac{g}{\omega_n^2}[1 - \cos(\omega_n t)] + \frac{\sqrt{2gh}}{\omega_n} \sin(\omega_n t). \quad (2.57)$$

To find the instantaneous acceleration for the mass, Eq. (2.57) is differentiated twice with respect to time:

$$\ddot{x}(t) = g \cos(\omega_n t) - \omega_n \sqrt{2gh} \sin(\omega_n t). \quad (2.58)$$

Alternatively, Eq. (2.58) can be written as

$$\ddot{x}(t) = g \sqrt{1 + \frac{2h\omega_n^2}{g}} \sin \left[\omega_n t + \tan^{-1} \left(\frac{-g}{\omega_n v_0} \right) \right]. \quad (2.59)$$

Hence, the maximum acceleration magnitude is given by

$$|\ddot{x}_{\max}| = g \sqrt{1 + \frac{2h\omega_n^2}{g}}. \quad (2.60)$$

We note from Eq. (2.60) that the maximum induced acceleration increases with the height of drop h and the natural frequency of the system.

Example 2.8: A more accurate model for the shock force induced from the impact of a system with the ground is achieved by modeling it as a pulse force or acceleration of finite duration. As an example, consider a rectangular pulse force of amplitude F_0 and duration t_1 , Fig. 2.22. Calculate the response of the undamped system of Fig. 2.2a to this force pulse assuming trivial initial conditions.

Solution: The force of Fig. 2.22 can be expressed as

$$F(t) = \begin{cases} F_0 & 0 \leq t \leq t_1 \\ 0 & t_1 \leq t \end{cases}. \quad (2.61)$$

Since the force is split into two parts, the response of the system is also split into two parts. For the first time period, $0 \leq t \leq t_1$ the scenario looks exactly like the case of Example 2.6 (the system is always under the influence of F_0 during this time interval). Hence, the response of the system in this interval is given by Eq. (2.53). For the second time interval, $t_1 \leq t$, the convolution integral, Eq. (2.49), is applied as

$$x(t) = \frac{1}{m\omega_n} \int_0^{t_1} F_0 \sin[\omega_n(t - \tau)] d\tau + \frac{1}{m\omega_n} \int_{t_1}^t 0 \times \sin[\omega_n(t - \tau)] d\tau \quad (2.62)$$

where the integral has been split into two parts to account for the discontinuity of the force over time, as expressed in Eq. (2.61). Calculating the above integrals yields

$$x(t) = \frac{F_0}{k} \{ \cos[\omega_n(t - t_1)] - \cos(\omega_n t) \}. \quad (2.63)$$

In summary, the response of the system is given by

$$x(t) = \begin{cases} \frac{F_0}{k} [1 - \cos(\omega_n t)] & 0 \leq t \leq t_1 \\ \frac{F_0}{k} \{ \cos[\omega_n(t - t_1)] - \cos(\omega_n t) \} & t_1 \leq t \end{cases}. \quad (2.64)$$

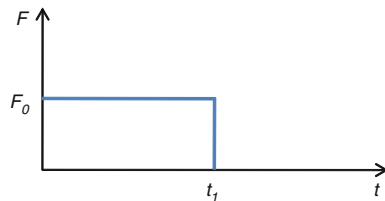


Fig. 2.22 A rectangular pulse that can be used to model shock forces

2.7 Vibrations of Two-Degree-of-Freedom Systems

This section presents an introduction to an important topic, which is the vibration of multi-DOF systems. This topic is too big to be covered in a single section or even in a single chapter. Here, we attempt to go over the basic elements of this subject, which have direct applications in MEMS. For more in-depth coverage of this topic, the reader is referred to any of these books [1–5].

We focus next on systems that need two independent coordinates to describe their motions. These are called 2-DOF systems. Figure 2.23 shows examples of such. Note that for each system, two independent coordinates are needed to fully describe the motion, which can be translational or rotational coordinates. Examples of such systems in MEMS include filters made of two coupled oscillators, gyroscopes, directional microphones, and devices placed over flexible printed-circuit boards.

2.7.1 Undamped Free Vibration and Eigenvalue Problem

As with SDOF systems, we start by analyzing the free vibration of 2-DOF systems. To illustrate the procedure, we consider as an example the system shown in Fig. 2.24. The first step in the analysis is to write the equations of motion for the system. Typically, this can be done using Lagrange's or energy approaches for complicated multi-DOF systems. These are outside the scope of this book. Hence, whenever it is possible, we

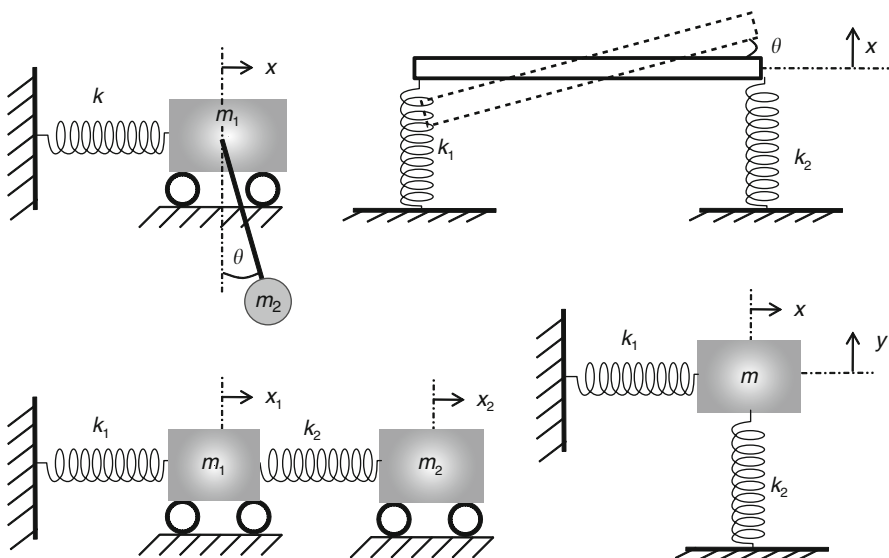


Fig. 2.23 Examples of 2-DOF systems

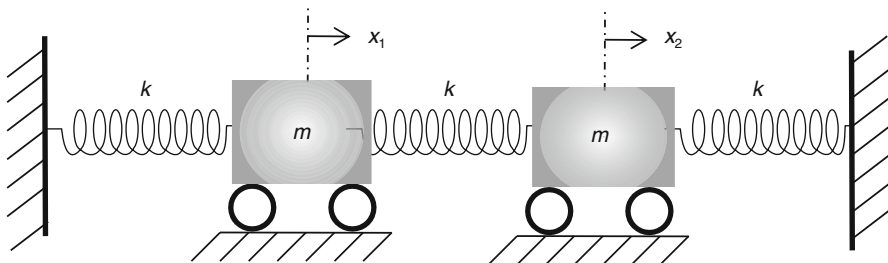


Fig. 2.24 A 2-DOF system

will use the Newtonian or force-diagram approach. In this approach, each mass is separated from the system and all the forces acting on it in the considered directions of motion are considered. In this example, the masses move in the horizontal direction, hence the horizontal forces are analyzed. Assuming each mass is displaced to the positive direction to the right, the resistance forces will be as depicted in Fig. 2.25.

Based on Fig. 2.25, the equation of motion of each mass is written as

$$-kx_1 + k(x_2 - x_1) = m\ddot{x}_1 \Rightarrow m\ddot{x}_1 + 2kx_1 - kx_2 = 0 \quad (2.65)$$

$$-kx_2 - k(x_2 - x_1) = m\ddot{x}_2 \Rightarrow m\ddot{x}_2 - kx_1 + 2kx_2 = 0. \quad (2.66)$$

Equations (2.65) and (2.66) are two coupled linear second-order differential equations. The fact that they are coupled means that we cannot solve one equation independently from the other; both need to be solved simultaneously. For convenience, we cast them in a matrix format as

$$\underbrace{\begin{bmatrix} m & 0 \\ 0 & m \end{bmatrix}}_{[m]} \underbrace{\begin{Bmatrix} \ddot{x}_1 \\ \ddot{x}_2 \end{Bmatrix}} + \underbrace{\begin{bmatrix} 2k & -k \\ -k & 2k \end{bmatrix}}_{[k]} \underbrace{\begin{Bmatrix} x_1 \\ x_2 \end{Bmatrix}} = \underbrace{\begin{Bmatrix} 0 \\ 0 \end{Bmatrix}} \quad (2.67)$$

where $[m]$ is called the mass matrix and $[k]$ is called the stiffness matrix. To solve the system of Eq. (2.67), we assume

$$\begin{aligned} x_1 &= X_1 e^{i\omega t} \\ x_2 &= X_2 e^{i\omega t} \end{aligned} \quad (2.68)$$

where i is the imaginary root. This is equivalent to assuming that each mass vibrates in harmony with the other; hence, they vibrate with the same frequency ω but with

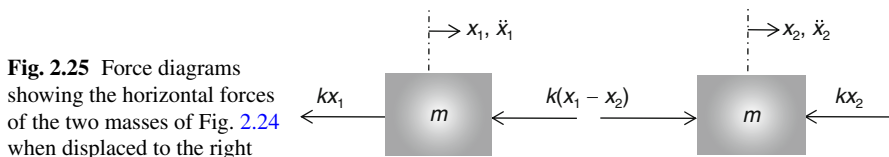


Fig. 2.25 Force diagrams showing the horizontal forces of the two masses of Fig. 2.24 when displaced to the right

different amplitudes, X_1 and X_2 for mass one and two, respectively. Substituting Eq. (2.68) into Eq. (2.67), dividing by $e^{i\omega t}$, and regrouping the coefficients yield

$$[k] - \omega^2[m] \{X\} \Rightarrow \begin{bmatrix} 2k - \omega^2 m & -k \\ -k & 2k - \omega^2 m \end{bmatrix} \begin{Bmatrix} X_1 \\ X_2 \end{Bmatrix} = \begin{Bmatrix} 0 \\ 0 \end{Bmatrix}. \quad (2.69)$$

Equation (2.69) is a homogenous algebraic system of equations in X_1 and X_2 . Multiplying both sides by the inverse of the matrix $[k] - \omega^2[m]$ yields simply that X_1 and X_2 are zeros (trivial solution) meaning no vibrations. Our only hope for not ending with this result is to reconsider the matrix $[k] - \omega^2[m]$ and assume that this matrix is non-invertible (singular matrix). Mathematically this means its determinant must be equal to zero.

To summarize, to obtain nontrivial solutions, we need to solve Eq. (2.69) as an eigenvalue problem by first setting the determinant of $[k] - \omega^2[m]$ equal to zero. This yields the following quadratic (characteristic) equation in ω^2 :

$$(2k - \omega^2 m)^2 - k^2 = 0. \quad (2.70)$$

Solving Eq. (2.70) for ω^2 yields the so-called eigenvalues

$$\omega^2 = \frac{k}{m}; \quad \omega^2 = \frac{3k}{m}. \quad (2.71)$$

Taking the square roots yields

$$\begin{aligned} \omega_1 &= \sqrt{\frac{k}{m}}; & \omega_2 &= \sqrt{\frac{3k}{m}}; \\ \omega_3 &= -\sqrt{\frac{k}{m}}; & \omega_4 &= -\sqrt{\frac{3k}{m}}. \end{aligned} \quad (2.72)$$

The positive roots, ω_1 and ω_2 , are the natural frequencies of the system. This is a major feature characterizing 2-DOF systems compared to SDOF systems; they have two natural frequencies instead of one. To proceed, we need to solve for the ratio of X_1 with respect to X_2 , the so-called eigenvectors or modeshapes, for each eigenvalue. For this, each value of ω^2 in Eq. (2.71) is substituted into Eq. (2.69). Then, one of the two resulting equations in X_1 and X_2 is solved to determine the ratio X_1/X_2 . The second equation is dependent on the first, hence one needs to use only one of the two equations. Substituting $\omega^2 = k/m$ and adopting the first equation (first row) gives

$$\left(2k - \frac{k}{m} \times m\right) X_1 - kX_2 = 0 \Rightarrow \frac{X_1}{X_2} = 1. \quad (2.73)$$

From Eq. (2.73), we say that the first eigenvector v_1 corresponding to the natural frequency ω_1 is equal $v_1 = \begin{Bmatrix} 1 \\ 1 \end{Bmatrix}$. This means that for some initial conditions, if the system happens to vibrate in ω_1 only, then the ratio of the displacement of the first mass to the second mass is equal 1. In another word, if the first mass is displaced a

distance one unit to the right, the second mass will also be displaced a one unit to the right. This is the meaning of the eigenvector or modeshape.

Similarly, substituting $\omega^2 = 3k/m$ and adopting the first equation give

$$\left(2k - \frac{3k}{m} \times m\right) X_1 - kX_2 = 0 \Rightarrow \frac{X_1}{X_2} = -1. \quad (2.74)$$

From Eq. (2.74), the second eigenvector v_2 corresponding to the natural frequency ω_2 is equal to $v_2 = \begin{Bmatrix} 1 \\ -1 \end{Bmatrix}$. This means that for some initial conditions, if the system happens to vibrate in ω_2 only, then the ratio of the displacement of the first mass to the second mass is equal -1 . In another word, if the first mass is displaced a distance one unit to the right, the second mass will also be displaced a one unit to the left. We should mention here that an eigenvector is arbitrary within a constant. So if we multiply it by any number α , it remains the same eigenvector. What really matters is the ratio between the individual elements of the eigenvector and not their absolute values.

After finding the natural frequencies and modeshapes, the free response of each mass can be expressed in term of those as

$$\begin{aligned} \begin{Bmatrix} x_1(t) \\ x_2(t) \end{Bmatrix} &= B_1 \begin{Bmatrix} 1 \\ 1 \end{Bmatrix} e^{i\omega_1 t} + B_2 \begin{Bmatrix} 1 \\ 1 \end{Bmatrix} e^{-i\omega_1 t} \\ &+ B_3 \begin{Bmatrix} 1 \\ -1 \end{Bmatrix} e^{i\omega_2 t} + B_4 \begin{Bmatrix} 1 \\ -1 \end{Bmatrix} e^{-i\omega_2 t} \end{aligned} \quad (2.75)$$

where B_1 – B_4 are constants of integration, which are determined from the initial conditions of the system. Equivalently, Eq. (2.75) can be rewritten as

$$\begin{Bmatrix} x_1(t) \\ x_2(t) \end{Bmatrix} = A_1 \begin{Bmatrix} 1 \\ 1 \end{Bmatrix} \sin(\omega_1 t + \phi_1) + A_2 \begin{Bmatrix} 1 \\ -1 \end{Bmatrix} \sin(\omega_2 t + \phi_2) \quad (2.76)$$

where also the constants A_1 , A_2 , ϕ_1 , and ϕ_2 are determined from the initial conditions of the system, for example Eq. (2.77) below:

$$x_1(0) = x_{10}; \quad x_2(0) = x_{20}; \quad \dot{x}_1(0) = v_{10}; \quad \dot{x}_2(0) = v_{20}. \quad (2.77)$$

Substituting Eq. (2.77) in either Eq. (2.75) or Eq. (2.76), four algebraic equations are obtained for the constant of integrations, which are then solved simultaneously.

2.7.2 Modal Analysis

Modal analysis is the key procedure to study the damped and forced vibrations of multi-DOF systems. In this procedure, the coupled system of differential equations governing the vibration of a multi-DOF system is decoupled into independent SDOF

systems, which can be solved using the information in Sects. 2.2–2.6. To illustrate the procedure, consider the below undamped multi-DOF system subjected to the force vector $\{F(t)\}$:

$$[m]\{\ddot{x}\} + [k]\{x\} = \{F(t)\}. \quad (2.78)$$

In Eq. (2.78), the matrices $[m]$ and $[k]$ are generally not diagonal, and hence the equations of motion are coupled. To decouple them, a transformation is used that transforms the physical coordinates $\{x\}$ into “modal coordinates” $\{y\}$ as

$$\{x\} = [s]\{y\} \quad (2.79)$$

where the transformation matrix $[s]$ is composed of the normalized eigenvectors of the system v_j^n , calculated as in Sect. 2.7.1, being put in columns as

$$[s] = [v_1^n v_2^n v_3^n \dots]. \quad (2.80)$$

The normalization of the eigenvectors is done as below

$$\{v_j^n\}^T [m] \{v_j^n\} = 1 \quad (2.81)$$

where the superscript T denotes transpose.

Next, we substitute Eq. (2.79) into Eq. (2.78) and multiply the outcome by $[s]^T$

$$[s]^T [m] [s] \{\ddot{y}\} + [s]^T [k] [s] \{y\} = [s]^T \{F(t)\}. \quad (2.82)$$

It turns out that the following facts are true for Eq. (2.82) and the transformation matrix $[s]$:

- $[s]^{-1} = [s]^T [m]$.
- $[s]^T [m] [s] = [I]$, where $[I]$ is the identity matrix.
- $[s]^T [k] [s] = [\Lambda]$, where $[\Lambda]$ is a diagonal matrix composed of the eigenvalues of the system, that is $[\Lambda] = \begin{bmatrix} \omega_1^2 & & \\ & \omega_2^2 & \\ & & \dots \end{bmatrix}$.

Thus, our objective of getting diagonal matrices is achieved. The individual SDOF equations due to the transformation are written as

$$\begin{aligned} \ddot{y}_1 + \omega_1^2 y_1 &= f_1 \\ \ddot{y}_2 + \omega_2^2 y_2 &= f_2 \\ \vdots \quad \quad \quad & \end{aligned} \quad (2.83)$$

where $f_1, f_2 \dots$ are the modal forces. For a 2-DOF system, they are given by

$$\begin{Bmatrix} f_1(t) \\ f_2(t) \end{Bmatrix} = [s]^T \begin{Bmatrix} F_1(t) \\ F_2(t) \end{Bmatrix}. \quad (2.84)$$

Equations (2.83) are solved as presented in Sects. 2.2–2.6 for their homogenous part (transient) and forcing part (steady state). For the transient behavior, the modal initial conditions, for instance for a 2-DOF system, are calculated by

$$\begin{aligned} \begin{Bmatrix} y_1(0) \\ y_2(0) \end{Bmatrix} &= [s]^T [m] \begin{Bmatrix} x_1(0) \\ x_2(0) \end{Bmatrix}; \\ \begin{Bmatrix} \dot{y}_1(0) \\ \dot{y}_2(0) \end{Bmatrix} &= [s]^T [m] \begin{Bmatrix} \dot{x}_1(0) \\ \dot{x}_2(0) \end{Bmatrix}. \end{aligned} \quad (2.85)$$

Once the modal coordinates are obtained, Eq. (2.79) is used to transform back to the physical coordinates.

A final note is regarding damping. Damping can pose challenges to modal analysis unless it is of proportional type. This is more of a mathematical concepts, which means that the damping matrix $[c]$ depends on the mass and stiffness matrices, that is $[c] = \alpha[m] + \beta[k]$, where α and β are constants. We refer to [1–5] for further information on proportional damping. In addition, damping ratios can be imposed directly on Eq. (2.83) through experience or measurements [1]. Hence, the damped modal equations become

[illegible]

Each equation above is dealt with as explained in Sects. 2.3–2.6.

Example 2.9: Consider the system of Fig. 2.24. Assume a harmonic force $F_1 = \cos(\Omega t)$ is acting on the first mass only and that the modal damping ratios for the first and second modes of vibrations are 0.05, 0.02, respectively. Consider $m = 1$ kg and $k = 100$ N/m. Calculate the steady-state response of each mass as a function of Ω and plot their response for $\Omega = 15$ rad/s.

Solution: This is a forced vibration of a 2-DOF system. One method to solve it is using modal analysis. Hence, the first step is to **calculate the matrix** $[s]$. From Sect. 2.7.1, we obtained v_1 and v_2 . So the next step is to normalize them according to Eq. (2.81). This means, we need to evaluate α to satisfy Eq. (2.81), that is

$$\alpha \{v_1^n\}^T [m] \alpha \{v_1^n\} = 1 \Rightarrow \alpha^2 [1 \quad 1] \begin{bmatrix} m & 0 \\ 0 & m \end{bmatrix} \begin{Bmatrix} 1 \\ 1 \end{Bmatrix} = 1 \Rightarrow \alpha = \frac{1}{\sqrt{2m}}. \quad (\text{a})$$

Hence,

$$v_1^n = \frac{1}{\sqrt{2m}} \begin{Bmatrix} 1 \\ 1 \end{Bmatrix}. \quad (\text{b})$$

Similarly,

$$v_2^n = \frac{1}{\sqrt{2m}} \begin{Bmatrix} 1 \\ -1 \end{Bmatrix}. \quad (\text{c})$$

The transformation matrix is written as

$$s = \frac{1}{\sqrt{2m}} \begin{bmatrix} 1 & 1 \\ 1 & -1 \end{bmatrix}. \quad (d)$$

The second step is to calculate the modal forces according to Eq. (2.84):

$$\begin{Bmatrix} f_1(t) \\ f_2(t) \end{Bmatrix} = [s]^T \begin{Bmatrix} \cos(\Omega t) \\ 0 \end{Bmatrix} = \frac{1}{\sqrt{2m}} \begin{Bmatrix} \cos(\Omega t) \\ \cos(\Omega t) \end{Bmatrix}. \quad (e)$$

Next, the modal equations are written according to Eq. (2.86). Substituting the values of k , ζ_1 , ζ_2 , and m and recalling the values of ω_j^2 from Sect. 2.7.1 yield

$$\begin{aligned} \ddot{y}_1 + 2\zeta_1\omega_1\dot{y}_1 + \omega_1^2 y_1 &= f_1 \Rightarrow \ddot{y}_1 + \dot{y}_1 + 100y_1 = \frac{\cos(\Omega t)}{\sqrt{2}} \\ \ddot{y}_2 + 2\zeta_2\omega_2\dot{y}_2 + \omega_2^2 y_2 &= f_2 \Rightarrow \ddot{y}_2 + 0.7\dot{y}_2 + 300y_2 = \frac{\cos(\Omega t)}{\sqrt{2}}. \end{aligned} \quad (f)$$

Equations (f) are solved according to Eqs. (2.32)–(2.34) as below:

$$\begin{aligned} y_1(t) &= Y_1 \cos(\Omega t - \theta_1) \\ y_2(t) &= Y_2 \cos(\Omega t - \theta_2) \end{aligned} \quad (g)$$

where

$$\begin{aligned} Y_1 &= \frac{1/\sqrt{2}}{\sqrt{(100 - \Omega^2)^2 + (\Omega)^2}} \\ Y_2 &= \frac{1/\sqrt{2}}{\sqrt{(300 - \Omega^2)^2 + (.7\Omega)^2}} \end{aligned} \quad (h)$$

$$\begin{aligned} \theta_1 &= \tan^{-1} \left(\frac{\Omega}{100 - \Omega^2} \right) \\ \theta_2 &= \tan^{-1} \left(\frac{0.7\Omega}{300 - \Omega^2} \right). \end{aligned} \quad (i)$$

Transforming back to the physical coordinates using Eq. (2.79) yields

$$\begin{Bmatrix} x_1 \\ x_2 \end{Bmatrix} = \frac{1}{\sqrt{2}} \begin{bmatrix} 1 & 1 \\ 1 & -1 \end{bmatrix} \begin{Bmatrix} Y_1 \cos(\Omega t - \theta_1) \\ Y_2 \cos(\Omega t - \theta_2) \end{Bmatrix}. \quad (j)$$

Substituting for the values of Y_1 and Y_2 gives the final expressions for x_1 and x_2 :

$$x_1(t) = \frac{\cos(\Omega t - \theta_1)}{2\sqrt{(100 - \Omega^2)^2 + (\Omega)^2}} + \frac{\cos(\Omega t - \theta_2)}{2\sqrt{(300 - \Omega^2)^2 + (.7\Omega)^2}} \quad (k)$$

$$x_2(t) = \frac{\cos(\Omega t - \theta_1)}{2\sqrt{(100 - \Omega^2)^2 + (\Omega)^2}} - \frac{\cos(\Omega t - \theta_2)}{2\sqrt{(300 - \Omega^2)^2 + (.7\Omega)^2}}. \quad (l)$$

Figure 2.26 shows the response of each mass in time.

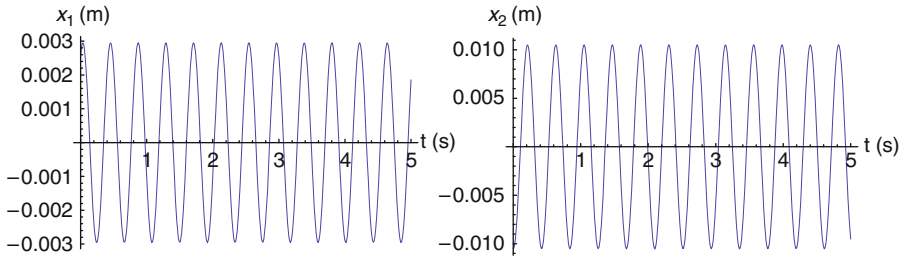


Fig. 2.26 The time–history response of the first and second mass of Example 2.9

2.7.3 Resonances in 2-DOF Systems

In a 2-DOF system, there are two resonance frequencies (and in an n -DOF systems, there are n resonance frequencies). They occur when the system is excited near one of its natural frequencies. For example, for the system described in Sect. 2.7.1 and in Example 2.9, we should expect resonances near $\Omega = 10$ rad/s and 17.3 rad/s. The next example illustrates this further.

Example 2.10: Plot the frequency–response curves of the system of Example 2.9 and show its resonances.

Solution: The responses are given in Eqs. (k) and (l) in Example 2.9. To plot the frequency–response curves, we need to rewrite the response expression in terms of amplitude and phase. For simplicity, we let

$$A_1 = \frac{1}{2\sqrt{(100 - \Omega^2)^2 + (\Omega)^2}}; \quad A_2 = \frac{1}{2\sqrt{(300 - \Omega^2)^2 + (.7\Omega)^2}}. \quad (\text{a})$$

Then, using trigonometric identities of the cosine of the sum of two angles, it can be shown that

$$x_1(t) = X_1 \sin[\Omega t + \Phi_1]; \quad x_2(t) = X_2 \sin[\Omega t + \Phi_2]; \quad (\text{b})$$

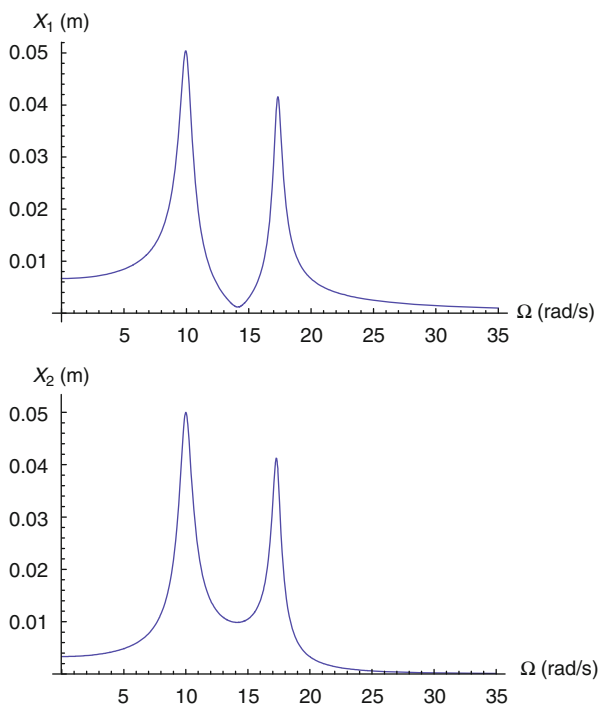
where

$$X_{1,2} = \sqrt{A_1^2 + A_2^2 \pm 2A_1 A_2 \cos(\theta_1 - \theta_2)} \quad (\text{c})$$

$$\Phi_{1,2} = \tan^{-1} \left(\frac{A_1 \sin(\theta_1) \pm A_2 \sin(\theta_2)}{A_1 \cos(\theta_1) \pm A_2 \cos(\theta_2)} \right). \quad (\text{d})$$

Figure 2.27 shows the frequency–response curve obtained from Eqs. (a) and (c). It is clear that both masses exhibit resonant behaviors near the natural frequencies of the system at $\Omega = 10$ rad/s and $\Omega = 17.3$ rad/s.

Fig. 2.27 Frequency–response curves of the first and second mass of Example 2.9



2.8 Numerical Integration

In the previous sections, we discussed analytical techniques to solve for the response of systems to initial conditions and to forcing, harmonic and arbitrary. The analytical results and expressions can reveal valuable information about the response without even plugging numbers. However, in many situations, such as in the presence of nonlinearities, analytical solutions may not be available or possible. Even if the analytical solutions are available, it is recommended to check the validity of these using numerical techniques and software. Numerical techniques, such as the Runge-Kutta method, can be used to integrate the equation of motion in time, and hence solve the equation of motion numerically.

This section gives an introduction to the numerical integration techniques using the software Mathematica [12] and Matlab [13]. These will be used and referred to more frequently in the subsequent chapters. In Matlab, there are many ordinary-differential equations (ODE) solvers, such as *ode45* and *ode23*. To use those, the user needs to write a main program, an *m* file, to input the various parameters of the problem and to process the obtained solutions, and a subprogram, another *m* file, which contains the equations of motion written in state-space representation. In Mathematica, one can use the command *NDSolve*, which does not require casting the equations in state-space format. Without further introduction, we demonstrate the use of these in the following examples.

Example 2.11: Write Matlab and Mathematica codes to simulate the response of a spring–mass–damper system to a generic excitation force using numerical integration. Then, solve Example 2.2 and compare to the analytical results.

Solution:

1. **Matlab:** To solve this problem in Matlab, the equation of motion needs to be rewritten in state-space representation, which is to transform the equation of motion into a system of first-order differential equations in time. Consider below the general SDOF equation normalized by the mass:

$$\ddot{x} + \frac{c}{m}\dot{x} + \frac{k}{m}x = \frac{F(t)}{m}. \quad (a)$$

To write Eq. (a) in a state-space form, we let $x_1 = x$ and $x_2 = \dot{x}$. Then Eq. (a) becomes:

$$\begin{aligned} \dot{x}_1 &= x_2; \\ \dot{x}_2 &= -\frac{c}{m}x_2 - \frac{k}{m}x_1 + \frac{F(t)}{m}. \end{aligned} \quad (b)$$

The below Matlab code is used to find the response of Example 2.2. The code yields the same results as shown in Fig. 2.8.

- (a) The main Program (the *m* file is called *main1*).

```
%This program solves the response of a SDOF system to
% a generic force.
%Below is the solution for example 2.2 using
%numerical time integration.
clear all;clc;close all
global m k c F %This is to make those parameters
%identified in both the main program and the
%subprogram.
m=1;
k=100;
c=1;

%Tint is the time interval for the time integration
%(start and end).
tend=12;
Tint=[0 tend];

%Below are the initial conditions of the system.
x0=0;
v0=0.01;
Int=[x0 v0];

%This the main time integration command. It calls
%a subroutine that we build in a separate m-file,
%called eq1. The output will be two vectors: t:
%refers to the time vector and x1: refers to the
%displacement vector.
[t,x1]=ode45('eq1',Tint,Int);
```



```
%Below is the plot of the solution in mm.
plot(t,x1(:,1)*1000);xlabel('t(s)');ylabel('x (mm)');
```

- (b) The subroutine program (the *m* file is called *eq1*).

```
%This is the subprogram or subroutine where the
%equations of motion are entered.
%The subroutine must be named as it was called in
%the main program (in this case it must be
%named 'eq1'
function dxdt(eq1(t,x)
global m k c
F=0; %This is the forcing in the system.
%The equations of motion below are written in
%state-space form.
dxdt=[x(2);
      -k/m*x(1)-c/m*x(2)+F/m];
```

2. **Mathematica:** Below are the command lines to solve this problem (note that in Mathematica multiplication is expressed using a space between the various variables and numbers):

```
tend=12;
x0=.0;
v0=0.01;
m=1;
k=100;
c=1;
solution(Flatten[NDSolve[{x''[t]+c/m x'[t]+k/m
x[t]==0,x[0]==x0,x'[0]==v0},x[t], {t,tend},MaxSteps→109]];
Plot[Evaluate[(x[t])*1000 /.solution],
{t,0,tend},PlotRange→All,AxesLabel→{"t (s)","x (mm)"}]
```

Example 2.12: Solve Example 2.6 using numerical integration assuming $F_0 = 10$ N, $m = 1$ kg, and $k = 100$ N/m and compare to the analytical results.

Solution: $\omega_n = \sqrt{k/m} = 10$ rad/s. Hence, the analytical solution Eq. (2.53) becomes

$$x(t) = 0.1[1 - \cos(10t)]. \quad (\text{a})$$

1. **Matlab:** We use similar *m*-files of the previous example with slight modifications for this problem input. Figure 2.28 shows the results. Below are the used code:

- (a) The main program (the *m* file is called *main2*).

```
%Below is the solution for example 2.12 using numerical
time integration.
clear all;clc;close all
global m k c
m=1;
k=100;
c=0;
```

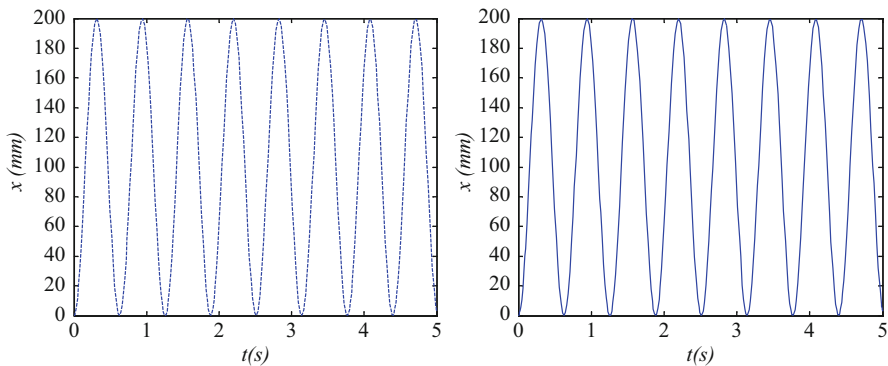


Fig. 2.28 A comparison of the time history response of Example 2.12 obtained analytically (*left*) to that obtained using time integration (*right*)

```
tend=5;
Tint=[0 tend];

x0=0;
v0=0.01;
Int=[x0 v0];
[t,x1]=ode45('eq2',Tint,Int);

%Below is the plot of the numerical solution in mm.
plot(t,x1(:,1)*1000);xlabel('t (s)');ylabel('x (mm)');

%Below is the plot of the analytical solution in mm.
Xanalyt=0.1*(1-cos(10*t));
figure; plot(t,Xanalyt*1000,'--');
xlabel('t (s)');ylabel('x (mm)');
```

- (b) The subroutine program (the *m* file is called *eq2*).

```
%This is the subprogram named 'eq2'
%function dxdt(eq2(t,x)
global m k c
F=10*stepfun(t,0); %This defines a unit-step function
%multiplied by 10.
%The equations of motion below are written in state-
%space presentation.
dxdt=[x(2);
      -k/m*x(1)-c/m*x(2)+F/m];
```

2. **Mathematica:** The same command lines of Example 2.11 can be used after adjusting the damping and the forcing as below:

```
solution=Flatten[NDSolve[{x''[t]+c/m x'[t]+k/m
x[t]==10 UnitStep[t], x[0]==x0, x'[0]==v0}, x[t],
{t,tend},MaxSteps->10^9]];
```

2.9 MEMS Band-Pass Filters

Perhaps one of the earliest researched MEMS devices since the beginning of the technology is the MEMS band pass filter. Since the mid-sixties, Nathanson and coworkers at Westinghouse demonstrated in a series of papers the attractive features of electrostatically actuated microbeams, called resonant gate transistors, such as their high-quality factors, their excellent thermal properties, and their desirable band-pass filter characteristics [14, 15]. This is in addition to the more significant advantage of their ability to interface with integrated electronics at the board level (on-chip integration), which is essential for miniaturization. This cannot be achieved with conventional off-chip bulky filters. Nathanson et al. [14, 15] have noticed that the distinctive large response of these microbeams when driven near their resonance frequencies qualify them as distinguished band pass filters, which pass signals at frequencies within a certain range near resonance and attenuate signals at frequencies outside this range. Nowadays, MEMS filters are commonly used in communication systems, such as wireless and cellular applications. They come in various designs and shapes, and not necessarily based on coupled vibrating systems.

In addition to realizing a band-pass filter from the vibration of a single microstructure near resonance, Nathanson et al. [15] have proposed the use of coupled multiple filters to improve their performance. This is achieved by mechanically connecting more than one vibrating microstructure of close resonant frequencies to each other through a weak mechanical coupler, for example Fig. 2.29. The bandwidth of the filter is then determined by the stiffness of the mechanical coupler. This has the effect of widening the bandwidth of the filter and improving the roll-off from the pass-band to the stop-band (making the transition from the resonance regime to nonresonant regime steeper and faster). In recent years, many studies have been presented on MEMS filters to increase their operating frequency and improve their overall performance, see for instance [16–18].

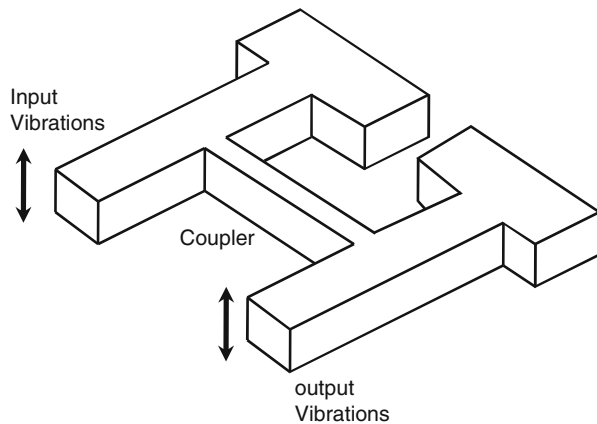


Fig. 2.29 Schematic of one of the possible configurations of a MEMS band-pass filter

Fig. 2.30 The response of a band-pass filter showing some of its key parameters

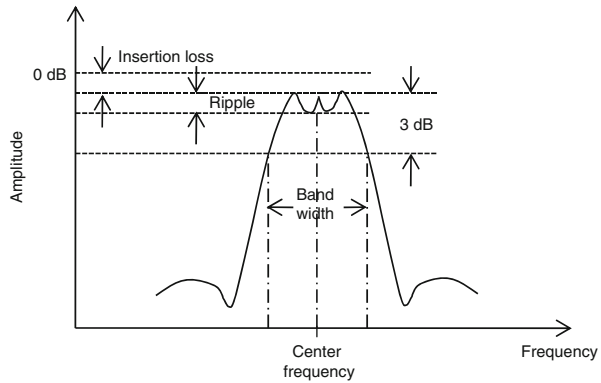


Figure 2.30 shows an example of the response of a band-pass filter explaining some of its main characteristics. A good band pass filter in general has a high-quality factor, low insertion loss (insertion loss is the ratio of output to input signals of the filter; it measures the reduction of the signal power as it passes the filter), flat pass band (minimum ripples), and sharp or rapid roll off from the pass-band to stop band.

Example 2.13: Consider the 2-DOF model of a band-pass filter of Fig. 2.31. Assume $m = 0.1$ g, $k = 1$ N/m, $c = 0.6$ g/s and $F = 0.1$ μ N. Calculate the response of the second unforced mass (output) for (a) $\delta k = 0.06$ N/m and (b) $\delta k = 0.1$ N/m.

Solution: The equation of motion of the system can be written as

$$m\ddot{x}_1 + c\dot{x}_1 + (k + \delta k)x_1 - \delta kx_2 = F \cos \Omega t \quad (a)$$

$$m\ddot{x}_2 + c\dot{x}_2 + (k + \delta k)x_2 - \delta kx_1 = 0. \quad (b)$$

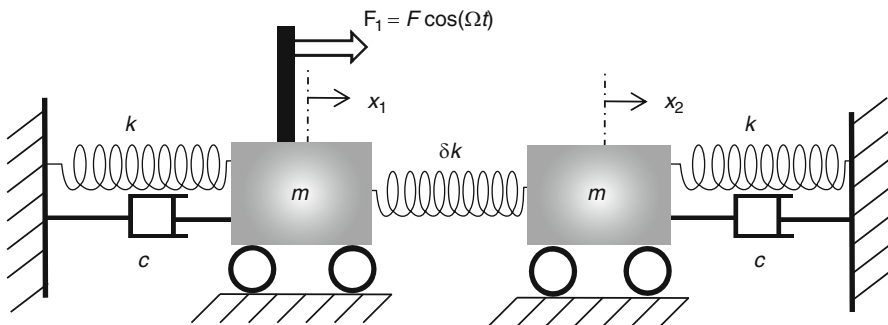


Fig. 2.31 A model of a two coupled microstructures acting as a band-pass filter

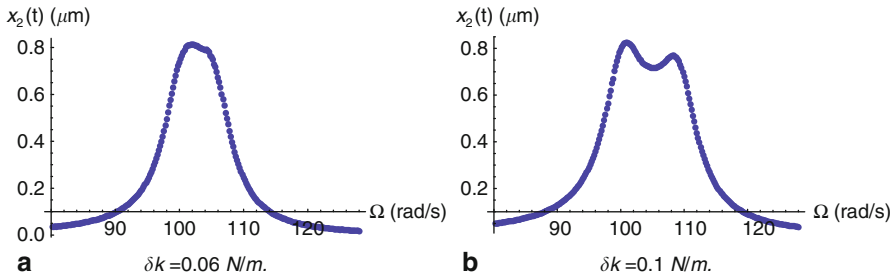


Fig. 2.32 The response of the unforced mass of Fig. 2.31 showing a band-pass filter characteristic

Using modal analysis as in Sect. 2.7.1, it is found that the natural frequencies of the system are expressed as

$$\omega_1 = \sqrt{\frac{k}{m}}; \quad \omega_2 = \sqrt{\frac{(k + 2\delta k)}{m}}. \quad (c)$$

Hence, one can see that the larger the value of δk is the larger the separation between the two frequencies is, which means a wider bandwidth. Equations (a) and (b) can be solved using modal analysis, similar to Sect. 2.7.2, or can be integrated numerically directly, as in Sect. 2.8. Here we choose to use the second method as an exercise toward learning the procedure for the more complicated nonlinear problems. In this method, a for-loop is built to run over several values of excitation frequencies. At each excitation frequency, a numerical integration of the equations of motion is carried out over a sufficient period of time that guarantees that the system reaches steady-state response (one can check this visually by plotting the time history response for a single excitation frequency). Then, the maximum value of the response over the last oscillation period of the time response is calculated. This represents a single point on the frequency response at the current excitation frequency of the for-loop. Repeating this for several values of the excitation frequency yields the complete frequency-response curve. The results are depicted in Fig. 2.32. Note that the bandwidth has increased with the increase of δk .

Problems

1. For the SDOF system of Fig. 2.4a, given $m = 1$ kg, $k = 100$ N/m, and assuming the system has trivial initial conditions, calculate and plot the response of the system for the following cases:
 - (a) $c = 0$ kg/s.
 - (b) $c = 2$ kg/s.
 - (c) $c = 20$ kg/s.
 - (d) $c = 40$ kg/s.
 - (e) Verify your results in (a)–(d) using numerical integration for the equation of motion, as in Sect. 2.8, using Matlab or Mathematica.

2. For the SDOF system of Fig. 2.9a, given $m = 10$ kg, $k = 4000$ N/m, and $c = 200$ kg/s, calculate
 - (a) The undamped natural frequency.
 - (b) The damped natural frequency.
 - (c) The resonance frequency.
 - (d) The peak frequency (where the amplitude of the response is maximum).
 - (e) The steady-state amplitude of the response at resonance.
 - (f) The peak steady-state amplitude (at the peak frequency).
 - (g) Verify your results in (e) and (f) using numerical integration for the equation of motion, as in Sect. 2.8, using Matlab or Mathematica.
3. Assume the device of Fig. 2.16a, with $m = 0.01$ kg, $k = 100$ N/m, and $c = 0.2$ kg/s, is subjected to a harmonic base excitation of amplitude 10 mm. Calculate the maximum steady-state relative deflection of the device with respect to the base for:
 - (a) Excitation frequency equals 10 Hz.
 - (b) Excitation frequency equals 30 Hz.
 - (c) Excitation frequency at resonance.
4. Solve Example 2.8 assuming a triangular pulse force, Fig. 2.33, instead of the rectangular pulse of Fig. 2.22. (Hint: you may want to use Mathematica to carry out the convolution integrals).
5. For the 2-DOF system of Fig. 2.34, write the equations of motion for the system and then calculate
 - (a) The natural frequencies of the system.
 - (b) The corresponding mode shapes.
 - (c) The transformation matrix S .
 - (d) The amplitude of the steady-state response of each mass for $\Omega = 10$ rad/s assuming $m = 1$ kg and $k = 100$ N/m.
 - (e) Verify your results in (d) using numerical integration for the equation of motion, as in Sect. 2.8, using Matlab or Mathematica.
 - (f) The values of Ω that will cause resonance for the system.
6. Consider the band-pass filter of Example 2.13. Investigate the variation of the damping coefficient c on the performance of the filter.

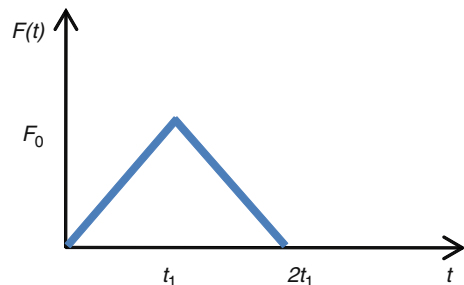


Fig. 2.33 Schematic of a triangular pulse for Problem 4

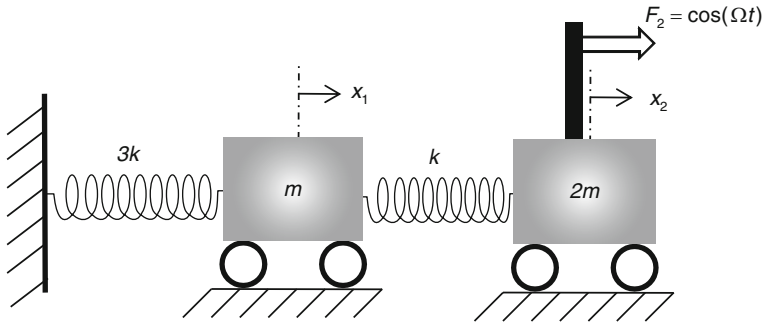


Fig. 2.34 The two-DOF system of Problem 5

References

- [1] Inman D J (2008) Engineering vibration. Third Edition, Prentice Hall, New Jersey
- [2] Thomson W T, Dahleh M D (1998) Theory of vibration with applications. Fifth Edition, Prentice Hall, New Jersey
- [3] Rao S S (2004) Mechanical vibrations. Fourth Edition, Prentice Hall, New Jersey
- [4] Meirovitch L (2001) Fundamentals of vibrations. Fourth Edition, McGraw Hill, New York
- [5] Balachandran B, Magrab E (2009) Vibrations. Second Edition, Cengage Learning, Toronto
- [6] Yazdi N, Ayazi F, Najafi K (1998) Micromachined inertial sensors. *Proceedings of the IEEE*, 86(8):1640–1659
- [7] Liu K, Zhang W, Chen Wn, Li K, Dai F, Cui F, Wu X, Ma G, Xiao Q (2009) The development of micro-gyroscope technology. *Journal of Micromechanics and Microengineering*, 19:113001(29pp)
- [8] Acar C, Shkel A (2009) MEMS vibratory gyroscopes. Springer, New York
- [9] L. Meirovitch (1970) *Methods of analytical dynamics*. McGraw-Hill, New York
- [10] Roundy S, Wright P K, Rabaey J (2003) A study of low level vibrations as a power source for wireless sensor nodes. *Computer Communications*, 26:1131–1144
- [11] Stephen N G (2006) On energy harvesting from ambient vibration. *Journal of Sound and Vibration*, 293:409–25
- [12] www.wolfram.com (Wolfram Research, Inc.; Champaign, IL)
- [13] www.mathworks.com (Mathworks; Natick, MA)
- [14] Nathanson H C, Wickstrom R A (1965) A resonant-gate silicon surface transistor with high-Q band-pass properties. *Applied physics letters*, 7(4):84–86
- [15] Nathanson H C, Newell W E, Wickstorm R A, Davis J R (1967) The resonant gate transistor. *IEEE Transaction on Electron Devices*, ED-14(3):117–133
- [16] Bannon F D, Clark J R, Nguyen C T-C (2000) High-Q HF microelectromechanical filters. *IEEE Journal of Solid-State Circuits*, 35:512–526
- [17] Lin L, Nguyen C T-C, Howe R T, Pisano A P (1992) Microelectromechanical filters for signal processing. In *Proceeding IEEE Micro Electro Mechanical Systems MEMS 1992*, Travemunde, Germany, pp. 226–231
- [18] Varadan V M, Vinoy K J, Jose K A (2003) RF MEMS and their applications, Wiley, New York

Chapter 3

Sensing and Actuation in MEMS

There are number of common transduction methods in MEMS. Some transform a change of a physical quantity, such as pressure and temperature, into an electric signal that can be measured. These are called sensing or detection methods. They include piezoelectric, piezoresistive, and electrostatic methods. Also, comes under this category the so-called resonant sensors, which detect the change in the resonance frequencies of microstructures upon sensing. Other transduction methods convert an input energy into a motion of a microstructure. These are called actuation methods, which include electrothermal, electromagnetic, piezoelectric, and electrostatic. Among the transduction methods, electrostatic actuation and detection are considered the most common in MEMS. Hence, electrostatic transduction will be under extensive investigations in the upcoming chapters. Next, basic knowledge on the most common transduction methods in MEMS is introduced.

3.1 Electrothermal Actuation

Electrothermal transduction methods are mainly used for actuation of MEMS and less commonly used for sensing. Electrothermal actuation is primarily suitable for deformable and flexible microstructures to achieve a desirable motion. This method relies on heating a microstructure by passing an electric current I either through the microstructure itself or through resistors deposited on it. Because of the resistance of the microstructure or the deposited resistor to the electric current, Joule heating is induced according to

$$P = I^2 R \quad (3.1)$$

where P is the generated power and R is the electrical resistance of the microstructure or the deposited resistor. In general, for a conductor of length L and cross-section area A , R is expressed as

$$R = \frac{\rho^E L}{A} \quad (3.2)$$

where ρ^E is the resistivity, which is a material property of the conductor.

Thermal actuation has the advantages of being simple, compatible with other electronics, of high energy density, and can achieve large deflection of microstructures. However, it has a major disadvantage of being too slow since it depends on achieving thermal equilibrium in the microstructure, which is a relatively slow process. Hence, it becomes difficult and inefficient to excite a microstructure with high frequency vibration using this method [1]. Also, it consumes high power because of the Joule heating. In addition, most of this power can be lost in the environment with little impact on the motion of the structure (low efficiency). Temperature sensitivity to the environment is another disadvantage. Finally, the induced heat and temperature rise due to thermal actuation can cause many complications for the surrounding electronics as well as in the packaging stage of the device. Below is a discussion for the common mechanisms of thermal actuation.

3.1.1 *U-Shaped Actuator*

This actuator is also called a hot/cold-arm actuator, two-arm actuator, a pseudobimorph actuator, and a laterally-driven electro-thermal actuator [2–7]. It is mainly used for in-plane or lateral actuation with respect to the substrate. The principle of actuation in this method relies on passing a current through a U-shaped microstructure of two arms of different geometrical properties, such that the resistance to the current flow, and hence the generated Joule heating in each arm, is different from the other. This causes thermal expansion in the arm of more generated heat with respect to the other arm causing deflection and motion of the whole microstructure. An example of this method of actuation is shown in Fig. 3.1, which is realized by making one of the arms thinner than the other. When a current passes through the arms, the thin arm has higher resistance to current flow, according to Eq. (3.2), so it becomes hotter and expands more than the thick arm. Large thermal stresses develop in the hot arm. This differential stress between the arms cause the entire system to deflect [2]. Also, a similar behavior can be realized by designing the two arms to be of different lengths while keeping their thickness and cross-section area the same [3]. To increase the induced force of this actuation method, an array of actuators can be stacked together to generate the desired level of force [4].

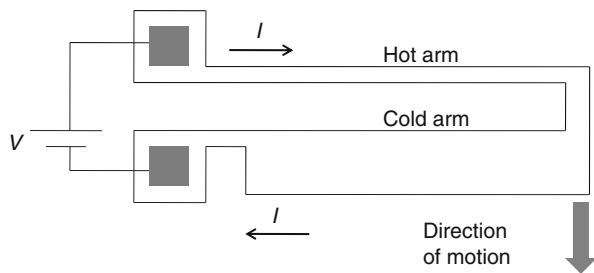


Fig. 3.1 A schematic shows an example of a U-shaped thermal actuator

3.1.2 V-Beam Actuator

The V-beam actuator [8–13] is also used mainly for in-plane or lateral actuation, Fig. 3.2b. The simplicity of design of this actuator is one of its major advantages. It is made of a bent or V-shaped beam. When a current passes through the bent beam, its temperature rises due to the generated Joule heating. This causes thermal expansion for the beam that tends to expand in the easiest and less resistance direction, which by design is made to be the lateral direction. Note from Fig. 3.2b that the beam is made to be compliant in the lateral direction and stiff in the out-of-plane direction. The generated force of the beam turns out to show good linearity with the current. By stacking more bent beams in parallel and connecting them to a push arm, larger force can be generated. One common application for such a mechanism is to push optical fibers to be aligned together to pass a signal [11–13]. Figure 3.3 shows an illustration of this application.

Another way of achieving the lateral actuation can be based on using a straight clamped–clamped microbeam. Then, by passing an electric current such that the heat induced in the microbeam generates compressive forces beyond its buckling limit, the microbeam buckles to yield large forces [14]. Assuming a constant new temperature T of the microbeam across its length due to this heating, the induced thermal force F_t on the beam can be expressed as

$$F_t = \alpha EA(T - T_0) \quad (3.3)$$

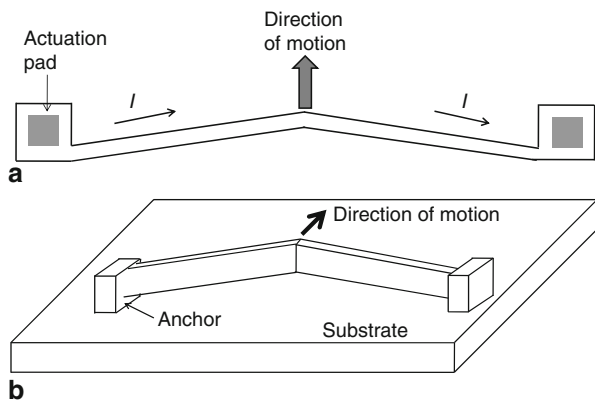


Fig. 3.2 Schematic shows a V-beam thermal actuator from the top view (a) and 3-D view (b)

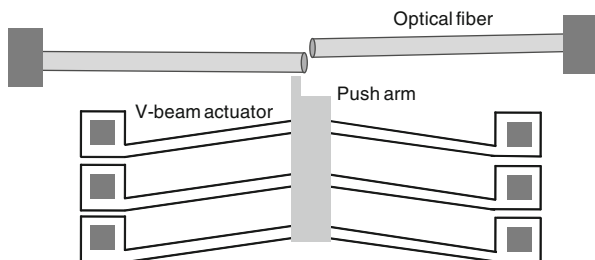


Fig. 3.3 A schematic illustrating the use of an array of V-beam thermal actuators to line-up two optical fibers to pass an optical signal

where α is the thermal expansion coefficient of the microbeam, E is its modulus of elasticity and T_0 is its original temperature before heating.

3.1.3 Bimorph Actuator

Unlike the previous two actuators, bimorphs actuators [15, 16] are generally utilized for out-of-plane actuation. They are also called bimetallic actuator because they are based on using two materials of different thermal expansion coefficients to form a microstructure or a microbeam, cantilever or clamped–clamped. Typically, thermal resistors are embedded within the surface of the microstructure such that when a current passes, heat is induced in the resistors, thereby heating one layer of the structure more than the other. Because the two layers are bonded and restrained together, the entire structure bends due to the thermal expansion, Fig. 3.4. Reference [16] presents detailed analytical solution that relates the radius of curvature of a deformed bimorph cantilever due to the temperature rise from heating to the material and geometrical properties of the two materials composing the cantilever.

The embedded heating resistor can either span the entire length of the beam being heated or span part of it. In the second case, there is a possibility that only portion of the microbeam be heated due to the thermal resistors, depending on the geometry and material of the microbeam as well as the frequency of actuation if it is harmonic actuation [1]. In reference [1], detailed thermal and mechanical analysis is presented for a thermal bimorph cantilever microbeam actuated by a harmonic thermal actuation. The analysis shows several cases when the microbeam becomes thermally too long, that is being not efficiently responsive to the thermal actuation, for example when the frequency of excitation becomes relatively larger.

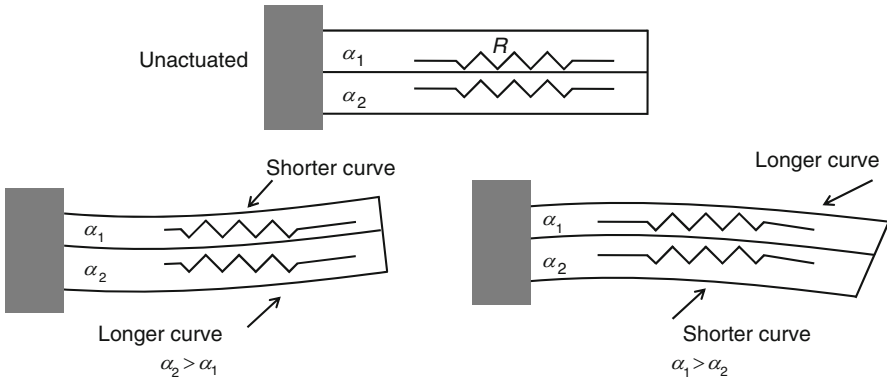


Fig. 3.4 A schematic illustrating the principle of the thermal bimorph actuator. When a current passes through the resistors, heat is generated causing thermal expansion in the layers of the beam. Because the bonded layers have different thermal expansion coefficients α , curvature deformation of the whole beam occurs such that the layer of larger α will have a longer curved portion compared to the other layer

3.2 Piezoelectric Actuation and Detection

Piezoelectricity refers to the ability of a material to generate an electrical potential under the application of mechanical stress or vice versa, that is to convert the applied electrical potential into mechanical stress or strain. Piezoelectricity was discovered by the Curie brothers in 1880. It comes from the Greek word “piezo,” which means press. Piezoelectric materials have been commonly used for both sensors and actuators applications in the macro scale and in recent years in MEMS applications. Figure 3.5 shows a schematic illustrating the basic principle of piezoelectricity and its basic use for sensing and actuation. Common piezoelectric materials are lead zirconate titanate (PZT), quartz, zinc oxide, and polyvinylidene difluoride (PVDF). Generally, piezoelectric materials are brittle. Care should be taken when packaging them. They are rarely used alone, but rather they are usually attached to flexible structures to be used for actuation and sensing. Piezoelectric materials cannot sustain high temperature operation. Piezoelectric actuation can generate large displacement. Piezoelectric sensing is considered self-powered because of the ability to generate voltage under stress.

The constitutive equations governing the behavior of piezoelectric materials under stress and electric field can be expressed as [17–19]

$$\{S\}_{6 \times 1} = [s]_{6 \times 6}\{T\}_{6 \times 1} + [d]_{6 \times 3}\{E\}_{3 \times 1} \quad (3.4)$$

where $\{S\}$ and $\{T\}$ are the mechanical strain and stress vectors of the material, respectively (three normal components and three shear components), $[s]$ is the compliance matrix, which is the inverse of the stiffness matrix, $[d]$ is the matrix of piezoelectric constants, and $\{E\}$ is the applied electric field vector along the three orthogonal directions (x , y , and z or 1, 2, and 3 directions). The unit of the components of T is Newton (N)/m², S is m²/N, d is Coulomb (C)/N, and E is Volt (V)/m.

Equation (3.4) can be considered as the actuation-mode version. Another version of the constitutive equations for the sensing mode is written as

$$\{D\}_{3 \times 1} = [d]_{3 \times 6}\{T\}_{6 \times 1} + [\varepsilon]_{3 \times 3}\{E\}_{3 \times 1} \quad (3.5)$$

where $\{D\}$ is the vector of electrical displacements or polarization (charge per unit area), of units C/m², and $[\varepsilon]$ is the matrix of dielectric constants (permittivity) of units Farad (F)/m or (C)/(mV).

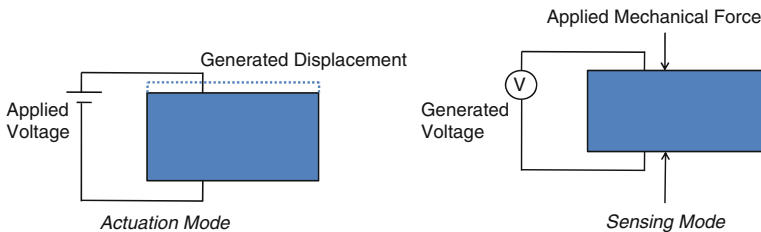


Fig. 3.5 Piezoelectricity in both sensing and actuation modes

Equations (3.4) and (3.5) are very complicated to deal with in their primitive form and usually require finite-element analysis to be solved. However, they can be simplified significantly under some assumptions and special cases (see reference [17], Chap. 7 and reference [18], Chap. 21 for more details about the reduction of the constitutive equation). In MEMS, for example, it is common to have a thin piezoelectric layer attached to a flexible structure, such as a beam or a membrane that can easily bend under an applied moment or force (this is also called piezoelectric bimorph). Figure 3.6a shows as an example a cantilever beam actuator with a thin layer of piezoelectric material deposited on top. When powered with a voltage source, an electric field E_3 is generated across and perpendicular to the piezoelectric layer (the 3 direction). This causes an elongation and strain S_1 across the length of the piezoelectric layer (the 1 direction). Because it is bonded to the flexible cantilever, the whole structure bends as shown in the figure. Such an actuation has been proposed to be used for micromirror applications [20]. In this case, Eq. (3.4) is reduced to

$$S_1 = d_{31} E_3 = d_{31} \frac{V}{t_p} \quad (3.6)$$

where t_p is the thickness of the piezoelectric layer. More generally, if in addition to the applied voltage there is an applied stress T_1 in the (1 direction), such as that from an external vertical force or bending moment, the total strain because of both effects becomes

$$S_1 = s_{11} T_1 + d_{31} E_3 \quad (3.7)$$

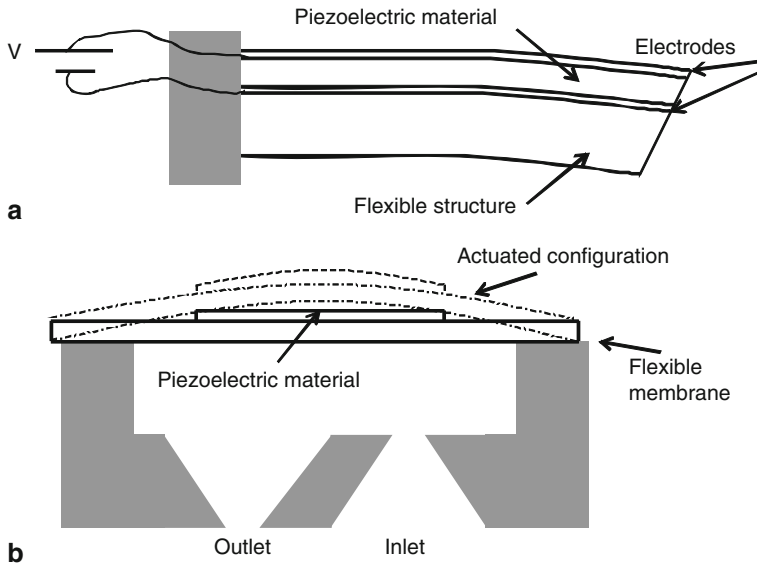


Fig. 3.6 Examples of piezoelectric actuators commonly used in MEMS. (a) A cantilever beam actuator. (b) A membrane used for pumping applications

where s_{11} is the compliance (inverse of Young's modulus E_y). When the piezoelectric layer is deposited on a fully clamped plate or membrane, the resulting motion can be utilized for micropumping application to pump fluids, Fig. 3.6b. The flow rate of pumping in this case depends on how fast the membrane can respond to the actuation, which depends on its natural frequency [21, 22].

For sensing application, an external force/moment on a structure, such as that of Fig. 3.6a, induces a stress T_1 in the (1 direction) in the piezoelectric layer, which generates polarity D_3 across the piezoelectric layer. This translates into generated voltage that can be measured. In this case, Eq. (3.5) is reduced to

$$D_3 = d_{31}T_1. \quad (3.8)$$

More generally, if in addition to the external applied stress there is an applied electric field E_3 in the (3 direction), the total polarity is then expressed as

$$D_3 = d_{31}T_1 + \varepsilon_{33}E_3. \quad (3.9)$$

Examples of sensing application in MEMS include a piezoelectric accelerometer, made of a cantilever microbeam with a piezoelectric patch deposited near its clamped end [23, 24], and a piezoelectric gyroscope [18]. Piezoelectric materials are also commonly used for resonant sensors and resonators, especially Quartz. In addition, piezoelectric materials are heavily investigated for harvesting energy from environmental vibrations [25–27]. Typical properties of common piezoelectric materials are shown in Table 3.1 [17–19] (care should be taken in using these numbers; the range of variations among them and that of an actual used piezoelectric film can be large).

Equations (3.4)–(3.9) assume linear behavior of the piezoelectric material. Recent researches have shown that piezoelectric materials can exhibit quadratic nonlinear behavior [28–30]. Experimental work has indicated that when driving a cantilever microbeam, such as Fig. 3.6a, into large vibration, it exhibits softening behavior because of the quadratic nonlinearity introduced from the piezoelectric material [30]. According to [30], the constitutive equation for a cantilever microbeam bimorph actuator can be written as

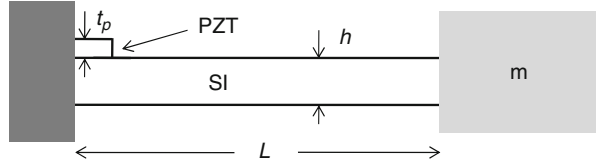
$$T_1 = E_y S_1 + \frac{\alpha_1}{2} S_1^2 - d_{31} E_y E_3 \quad (3.10)$$

where α_1 is the quadratic nonlinear coefficient of the piezoelectric material. On the other hand, when exciting clamped–clamped microbeams into large vibration, another geometric nonlinearity, mid-plane stretching, can be activated. This has an opposite hardening effect on the dynamic response, which can dominate the softening effect of the piezoelectric material [31, 32].

Table 3.1 Typical properties of common piezoelectric materials

Material	$d_{31} (\times 10^{-12} \text{ C/N})$	$E_y \text{ (GPa)} = 1/s_{11}$	$\varepsilon_{33} (\times 8.85 \times 10^{-12} \text{ F/m})$
PZT	190	49	1,800
Quartz	0, ($d_{11} = 2.3$)	87	4.5
Zinc Oxide	11	210	10
PVDF	15	2	10

Fig. 3.7 A piezoelectric accelerometer



Example 3.1: Figure 3.7 shows an accelerometer made of a cantilever beam of length L , thickness h , and width b with a proof mass at its tip of mass m . Attached to the cantilever beam near its fixed end a layer of PZT of thickness t_p and length across the length of beam, which is much smaller than L . Assuming the accelerometer is subjected to a slow-varying acceleration, which can be approximated as a constant a , find an analytical expression relating the induced voltage V across the PZT layer to the acceleration.

Solution: Since this is a sensing problem, and because there is no additional applied electric field E_3 , Eq. (3.8) is used. The applied acceleration on the proof mass can be modeled as a point force $F=ma$ applied at the tip of the cantilever microbeam. This force causes a bending moment M on the beam, $M=FL$. The bending moment results on an axial stress on the cantilever microbeam T_1 with a maximum value near its fixed support. The maximum stress can be calculated as

$$T_1 = \frac{Mh}{2I_c} \quad (a)$$

where I_c is the moment of inertia of the cross section, which is given by $I_c = bh^3/12$. Because the length of the PZT layer is much smaller than the beam, we assume the maximum stress across the PZT layer to be constant and equal to the maximum bending stress of the cantilever beam. Thus, according to Eq. (3.8), the generated polarity across the PZT layer is

$$D_3 = d_{31} \frac{Mh}{2I_c} = d_{31} \frac{6(ma)L}{bh^2}. \quad (b)$$

The equivalent voltage due to the generated polarity can be calculated according to

$$D_3 = \epsilon_{33} E_3 = \epsilon_{33} \frac{V}{t_p}. \quad (c)$$

Hence, the final expression relating the voltage to the acceleration is given by

$$V = \frac{6d_{31}t_pmaL}{\epsilon_{33}bh^2}. \quad (d)$$

3.3 Electromagnetic and Magnetic Actuation

Electromagnetic and magnetic transduction methods have been long used in the macro-world for sensing and actuation applications, for example for loud speakers. They have been also increasingly investigated for MEMS applications, and particularly for actuation. The major advantages of electromagnetic and magnetic actuation include large forces and moments, large displacement, and the requirement of low driving voltage compared to other actuation techniques, such as electrostatic actuation. On the other hand, they consume high power because of the large current used in the case of electromagnetic actuation. Also, their fabrication is complex (usually requires inductive components to generate magnetic flux and may involve fabrication of coils, deposition of magnetic material, etc).

Electromagnetic actuation refers to the fact that the method requires electricity to induce the magnetic effect whereas “magnetic” actuation refers to the use of permanent magnet, which does not require electricity to operate (hard magnet). In MEMS, various versions of actuations have been used including strictly electromagnetic actuation, magnetic actuation, and electromagnet-magnetic actuation. Electromagnetic and magnetic actuations have been also used as an aid to other actuation methods, such as electrostatic [33] and electrothermal [34].

The simplest form of electromagnetic actuation relies on the so-called Lorentz force. In this method, when a conductor carrying an electric current I is exposed to an external magnetic field B , Lorentz force F_L is induced according to

$$\vec{F}_L = L \vec{I} \times \vec{B} \quad (3.11)$$

where L is the conductor length and \times refers to the cross product operation. The right-hand rule needs to be applied to determine the direction of F_L , that is to align the thumb of the right hand along the direction of I , the rest of the fingers along the direction of B , then the resultant force is normal to both vectors pointing outside the hand. By varying the direction of the current, bi-directional force or actuation can be realized. As an example, electromagnetic actuation is used to induce buckling in clamped-clamped microbeams [35, 36] by passing electric current through them while being exposed to an external magnetic field, Fig. 3.8a. Also, out-of-plane resonators and filters [37] can be excited using this method when passing an alternating current through a circuit on the microstructure, Fig. 3.8b. If a coil is deposited on a microstructure, such as cantilever beam, then Lorentz forces will be induced of equal magnitude and opposite directions, corresponding to the opposite directions of the passing current in the various sections of the coil. These forces cancel each other. However, a net moment will be induced [38], which is utilized to actuate the structure, Fig. 3.8c.

Actuation based on the electromagnetic force generated between a permanent magnet and a coil has been also utilized in MEMS. For instance, it is used in RF switches [33], micropumping [39, 40], and in generic microactuators [41, 42]. By reversing the current direction in the coil, repulsive and attractive forces can be generated (bi-directional actuation). An example of such configuration is depicted in

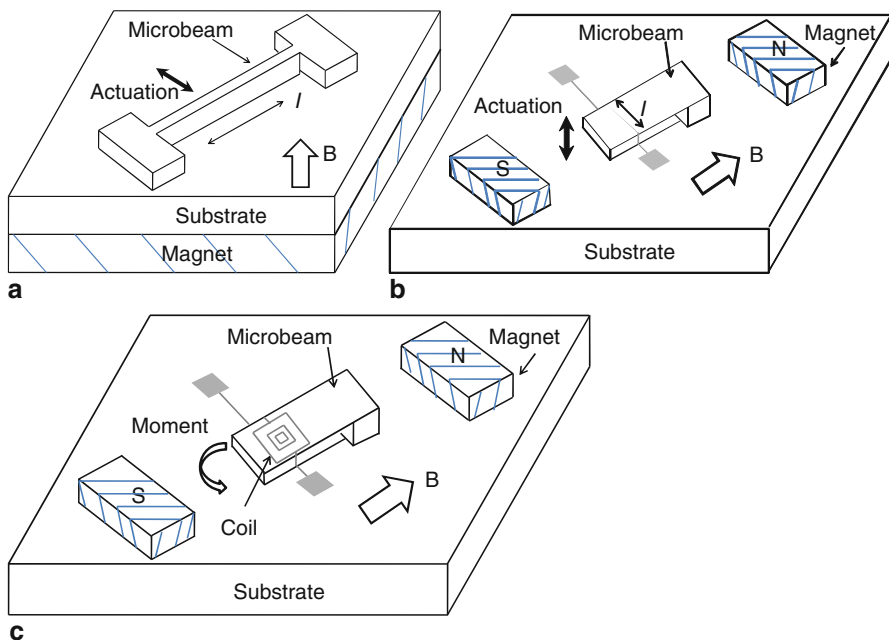


Fig. 3.8 Examples of electromagnetic actuation using Lorentz forces. Figure part **a** shows in-plane actuator, **b** and **c** show out-of-plane actuators

Fig. 3.9 showing a cantilever microbeam carrying a magnet at its tip. Underneath the magnet, a planar coil is printed on the substrate. In other possible configurations, the coil is deposited on the microstructure while the magnet is placed on the substrate. The generated force F_z in the vertical direction z can be approximated in this case as [39–42]

$$F_z = M_z V_m \frac{\partial B_z}{\partial z} \quad (3.12)$$

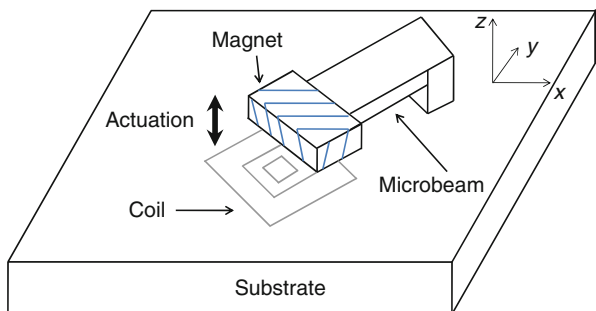
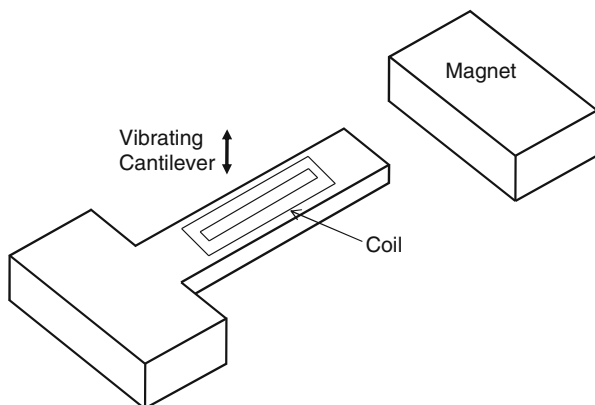


Fig. 3.9 Electromagnetic actuation using magnetic-coil forces

Fig. 3.10 An example for energy harvesting from ambient vibration according to Faraday's law of induction between a moving coil and a permanent magnet



where M_z is the magnetization, V_m is the volume of the magnet, and B_z is the vertical magnet flux density generated by the coil. Usually, more accurate estimation of this force requires finite-element analysis and more complicated models [43].

Electromagnetic–magnetic interaction between a magnet and a coil has been also explored for power generation and energy harvesting [44–46]. In this method, a coil is patterned on a microstructure, such as a cantilever microbeam, Fig. 3.10. A permanent magnet is placed next to the tip of the cantilever and the coil. When the microbeam is base-excited from a vibration source from the ambient, it vibrates. Hence, its coil cuts through the magnetic flux from the magnet. This induces voltage in the coil in accordance with the so-called Faraday's law. According to Faraday's law of induction, an electromotive force (EMF) is produced around a closed path, which is proportional to the rate of change of the magnetic flux through any surface bounded by that path. Hence, an electrical current is induced in any closed circuit when the magnetic flux through a surface bounded by the conductor changes due to the motion of the conductor. The electromotive force ε^{emf} in (volt) can be expressed as

$$\varepsilon^{\text{emf}} = NBL_p\dot{z} \quad (3.13)$$

where L_p is the practical coil length, B is the magnetic flux density produced by the magnet (Weber) through a single loop, \dot{z} is the relative velocity of the cantilever with respect to the magnet (speed across the flux lines), and N is the number of coil turns. This induced voltage has been also used for detection, for example for the motion of a cantilever microbeam actuator [37].

In addition to the above mentioned mechanisms of actuation, there others mechanisms of transductions based on magnetism, for example using strictly permanent magnets [47] and magnetostrictive films [48]. A good review of these can be found in [48].

3.4 Piezoresistive Detection

We discuss briefly in this section a detection method that is commonly used for pressure sensors and accelerometers, which is piezoresistive detection. As the prefix “piezo” suggests, this principle is related to stress. Essentially, piezoresistivity is defined as the change in electrical resistance of solids due to the change in their strain in response to an applied stress. According to Eq. (3.2), the resistance can vary due to changes in geometry (length, cross section) or the material property (resistivity). Piezoresistive detection relies on the change of the resistivity of the material upon an applied stress. In piezoresistive materials, the change in resistivity due to an applied stress has much more effect on the resistance compared to that due to the change in geometry (sensors based on the resistance change due to geometry are called strain gauges).

Silicon piezoresistors and polysilicon patches are commonly used in microsensors. Resistivity of silicon depends on its method of doping. P-type doped silicon is more sensitive than n-type. This adds restrictions in fabrications. Like piezoelectricity, the relationship between stress and change in resistance of piezoresistive materials can be very complicated, especially for doped silicon, which is anisotropic material [17, 49]. However, this relationship can be simplified in the case of well-characterized cubic materials of diagonal resistivity tensor (see [18], Chap. 18) and for thin piezoresistive strips that are commonly used in MEMS, Fig. 3.11. In this case, the in-plane stresses, transversal and longitudinal, are the most important components. The change in resistance ΔR in this case can be expressed as

$$\frac{\Delta R}{R} = \pi_L \sigma_L + \pi_T \sigma_T \quad (3.14)$$

where σ_L and σ_T are the longitudinal and transversal stresses, respectively, and π_L and π_T are the longitudinal and transversal piezoresistive coefficients, which are material properties. Another way to write Eq. (3.14) is to relate the change in resistance to the change in strain, that is

$$\frac{\Delta R}{R} = G_L S_L + G_T S_T \quad (3.15)$$

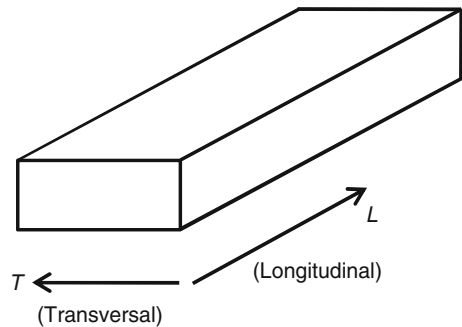


Fig. 3.11 Schematic of a piezoresistor strip

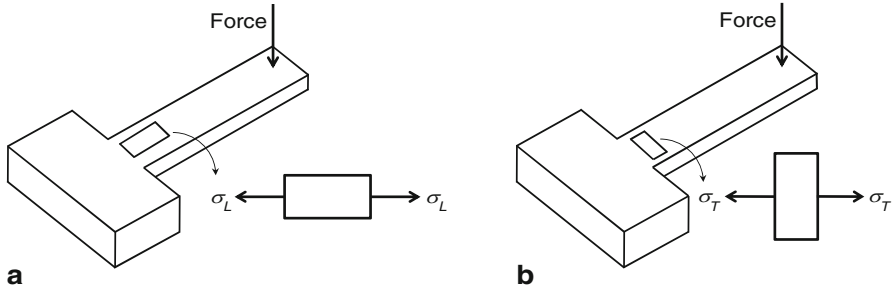


Fig. 3.12 Scenarios of piezoresistor strips subjected to **a** longitudinal stress and **b** transversal stress

where S_L and S_T are the longitudinal and transversal strains, respectively, and G_L and G_T are the longitudinal and transversal gauge factors, which are also material properties.

Longitudinal and transversal strains are often present at the same time. However, one of them can dominate the other [17, 18]. Examples of such scenarios are depicted in Fig. 3.12. Note in the figure that the piezoresistive patches are placed near the clamped edge of the cantilever beam, where the bending stress, and hence the induced strain, is maximum. For a cantilever beam of length L , width b , and thickness h , the maximum stress σ_{\max} is expressed as

$$\sigma_{\max} = \frac{(FL)h}{2I_c} \quad (3.16)$$

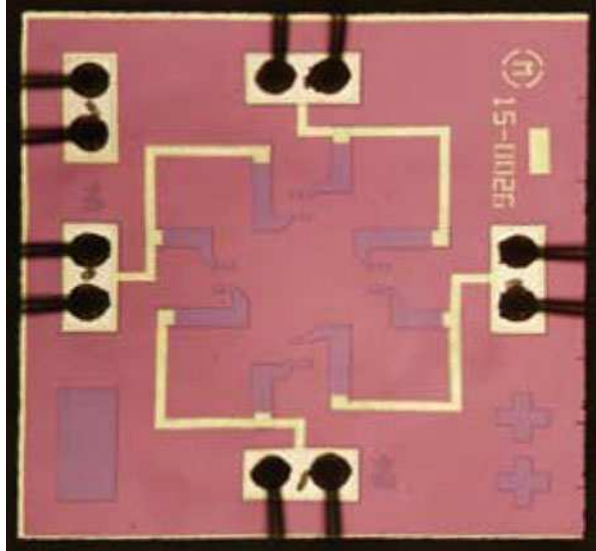
where I_c is the moment of inertia of the cross-section, which is given by $I_c = bh^3/12$. Hence, neglecting the contraction of the strip (the Poisson's effect), and assuming a unilateral stress, the normalized change of resistance can be expressed as

$$\begin{aligned} \frac{\Delta R}{R} &= \pi_L \frac{(FL)h}{2I_c} \quad \text{for case (a)} \\ \frac{\Delta R}{R} &= \pi_T \frac{(FL)h}{2I_c} \quad \text{for case (b).} \end{aligned} \quad (3.17)$$

Piezoresistive patches are either deposited on the structure, such as the case of polysilicon strips, or doped, such as the case of p-type silicon on n-type structure.

A major disadvantage of this sensing method is the strong temperature dependence on resistivity. To minimize this effect, usually a group of piezoresistive stripes are used to form a Wheatstone bridge. This minimizes the temperature dependence. Figure 3.13 shows a picture of four piezoresistors forming a Wheatstone bridge on top of micro-diaphragm used for pressure sensing [50].

Fig. 3.13 A micro-diaphragm used for differential pressure sensors showing four piezoresistors forming a Wheatstone bridge. (Courtesy of Sensata Technologies [50])



3.5 Electrostatic Actuation and Detection

Electrostatic transduction is the most common actuation and sensing method in MEMS because of its simplicity and high efficiency. Two of the classical successful MEMS devices have been relying on this method: the Analog Devices accelerometers for airbag deployments, which use capacitive detection to sense the motion, and the micromirror in the digital mirror display DMD for projection displays by Texas Instruments, which relies on electrostatic actuation. Other examples of microdevices employing this method include microphones, pressure sensors, temperature sensors, RF switches, band-pass filters, and resonators. MEMS devices utilizing electrostatic transduction are also called electrostatic MEMS.

Electrostatic transduction relies on simple capacitors of parallel plate electrodes. These can be easily fabricated using surface micromachining. Electrostatic transduction does not require any special material, such as piezoelectric materials, deposition of any patches, such as piezoresistors, or any external field sources, such as electromagnetic transduction. It only requires a voltage source, which is readily available on most IC and electronics circuits. Also, it is characterized by very low power consumption. Power dissipation requires passing a current in a circuit beside the voltage source. A parallel-plate capacitor is an open-circuit component that does not typically pass a current. In the case of an AC or variable voltage, a small amount of current is induced in the capacitor circuit, which is proportional to the rate of change of the voltage [17].

Electrostatic actuation depends on the attractive force between the two plates of a capacitor to generate a force or displacement. Electrostatic actuation offers high energy density, high mechanical flexibility, and well controlled force. Also, it is

considered fast actuation method, compared for instance to electrothermal actuation, since the time constant for charging a capacitor is small. In electrostatic or capacitive sensing, a physical quantity, such as pressure or acceleration, changes the capacitance values of the parallel-plate capacitor. Using an electronic circuitry, this change is related to the physical quantity being measured. The main disadvantage of electrostatic actuation and detection is their nonlinearity, especially for out-of-plane capacitors. This limits the controlled travel range of actuators and can result in unexpected collapse, short circuit, stiction, and functional failure of sensors. Also, the large driving voltage for actuation applications, such as in RF switches, is another limitation.

The most common forms of electrostatic sensing and actuation are based on either simple parallel-plate capacitors or comb-drive configuration of multiple interdigitated or non-interdigitated fingers. Because these depend somehow on the electrostatic forces generated between parallel electrodes, we discuss next some of the basic mathematical relationships related to these. Toward this, consider the parallel-plate capacitor shown in Fig. 3.14. The two plates can have any arbitrary shape. Here, the electric field lines between the two plates are assumed to be perpendicular to the plates even near edges. This means that the fringe effect of the electric field is neglected. This is also equivalent to assuming infinite plates. The capacitor is powered by a voltage source V , which can be time varying, as shown in the figure.

Because of the power source, the capacitor is charged according to

$$Q = C(\eta)V \quad (3.18)$$

where Q is the electrical charge of the capacitor, C is its capacitance, and η is a variable representing the degree of freedom of the moveable electrode of the capacitor. The potential energy stored in the capacitor E_c can be expressed as

$$E_c = \frac{1}{2}C(\eta)V^2. \quad (3.19)$$

To derive a relationship for the electrostatic force, an expression of the coenergy stored in the capacitor is derived. Then the electrostatic force is taken to be the negative gradient of the coenergy [18]. Alternatively, the relationship can be derived by

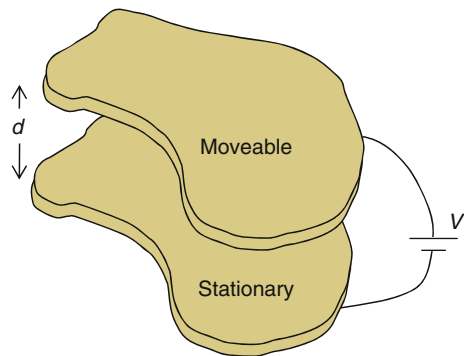


Fig. 3.14 A parallel-plate capacitor of arbitrary shape electrodes

considering the total electric potential energy of the battery-capacitor system. Then, the electrostatic force is taken to be the negative of the gradient of the potential energy [49, 51]. This is consistent with the practice of deriving expressions for conservative forces in the Lagrangian mechanics. Here we follow the second approach. Toward this, the initial energy of the battery that is hooked-up to the capacitor is assumed to be E_0 . When connected to the capacitor, the battery provides the electrical charge Q and an electrical potential $-QV$, which is negative since it is lost from the battery. Hence, the new potential energy of the battery E_b is reduced to

$$E_b = E_0 - QV = E_0 - CV^2. \quad (3.20)$$

Thus, the total potential energy of the system E is equal to that from the battery and the capacitor, that is

$$E = E_b + E_c = E_0 - CV^2 + \frac{1}{2}CV^2 = E_0 - \frac{1}{2}CV^2. \quad (3.21)$$

The attractive force F between the two electrodes of the capacitor can be obtained according to

$$F = -\frac{\partial E(\eta)}{\partial \eta} = \frac{1}{2} \frac{\partial C(\eta)}{\partial \eta} V^2. \quad (3.22)$$

For electrodes of simple geometries, an analytical expression can be found for C . However, for electrodes of complicated geometry, finite-element or boundary-element analysis can be used to characterize the dependence of C on the displacement η . Then, curve fitting is used to extract a simple analytical expression for $C(\eta)$ that can be used in Eq. (3.22) [18].

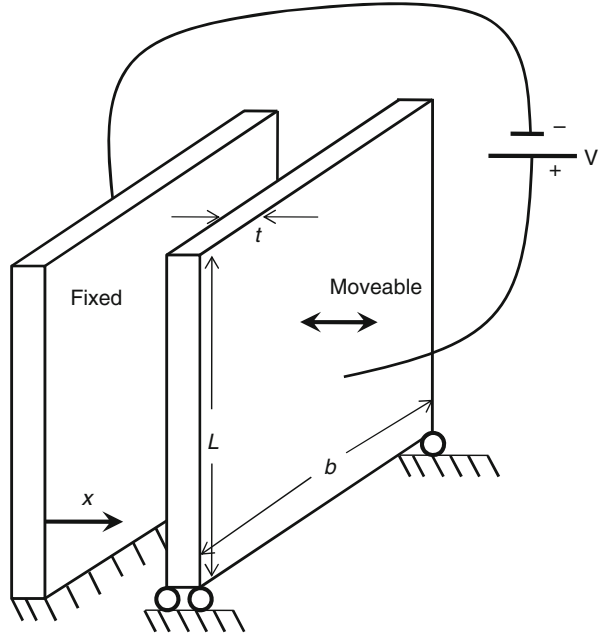
3.5.1 Simple Parallel-Plate Capacitors

Next, we consider the special case of a capacitor formed by two parallel rectangular plates, in which one of them is kept stationary while the other is allowed to move only toward the stationary electrode, Fig. 3.15. Hence, $\eta = x$, where x is the variable distance between the two electrodes. Each electrode has a width b and length L . By solving the Laplace equation governing the electrostatic potential between the two rectangular plates [52], the capacitance of the capacitor, neglecting the fringing effect, can be expressed as

$$C(x) = \epsilon_r \epsilon_o \frac{A}{x} = \epsilon_r \epsilon_o \frac{Lb}{x} \quad (3.23)$$

where A is the overlap area between the two electrodes (in this case $A = Lb$), ϵ_r is the relative permittivity of the gap space medium with respect to the free space (equal unity in air), and ϵ_o is the dielectric constant in free space,

Fig. 3.15 A parallel-plate capacitor of rectangular electrodes



$\epsilon_o = 8.85 \times 10^{-12}(\text{C}^2/\text{Nm}^2)$. Substituting Eq. (3.23) into Eq. (3.22) yields the below expression for the attractive force between the two electrodes

$$F = \frac{-\epsilon_r \epsilon_o A V^2}{2x^2} \quad (3.24)$$

where the minus sign in Eq. (3.24) indicates that the force on the movable electrode is of an opposite sign to the positive x direction (an attractive force between the two electrodes).

One can note from Eq. (3.24) that the parallel-plate electrostatic force is inherently nonlinear in terms of the electrodes separation. Typically in MEMS, the movable electrode is a flexible structure, such as a beam or a plate. Hence, when deflected a distance x due to the electrostatic force, the resorting force of the structure tends to oppose the electrostatic force (acts as a spring). If the electrostatic force is not too big, equilibrium between the resorting and electrostatic force is achieved. However, if the voltage load is increased too much, then the electrostatic force overcomes the resorting force of the structure leading to its collapse, where it hits the stationary electrode. This phenomenon is known in electrostatic MEMS as the **pull-in** instability [53, 54]. If the collapse of the structure is associated with inertia effect due to its motion or is caused by an AC harmonic excitation, it is referred to as **dynamic pull-in** [55–64]. More on dynamic pull-in is presented in Chap. 5.

In sensing application, pull-in is undesirable. It leads to the collapse of the moveable electrode into the stationary electrode leading to short circuit, stiction, and un-functionality of the sensor. The moveable electrode in this case is supposed to

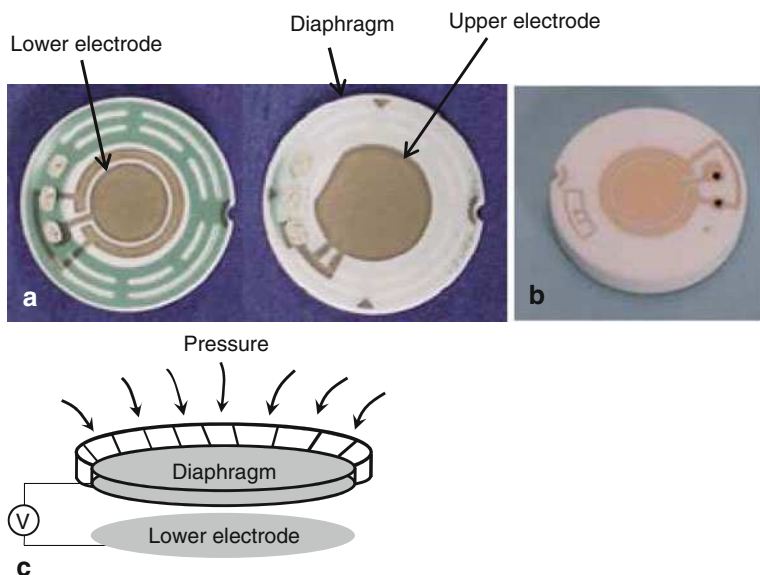


Fig. 3.16 A capacitive sensor fabricated by Sensata Technologies [50]. **a** Taken apart. **b** Assembled. **c** Schematic

deflect slightly in response to the external effect to cause a measureable change in capacitance. Examples of devices working on this principle are depicted in Fig. 3.16 for a pressure sensor and Fig. 3.17 for an accelerometer. Another sensing application relies on vibrating the structure near resonance, the so-called **resonance sensors and resonators**, using a DC voltage source superimposed to an AC harmonic load, Fig. 3.18. Electrically actuated resonators have been proposed as RF band-pass filters since the mid-sixties [53, 54]. In resonant sensors, an external effect, such as mass or temperature, changes the resonance frequency of the structure, which is related to the physical quantity being measured. Also here, pull-in can damage the device. So in either case, capacitive or resonant sensor, designers need to tune the voltage load such that it is away and safe from pull-in.

For some MEMS actuation applications, it is desirable to deflect the structure by a small well-controlled displacement or angular motion. In this case also, the voltage actuation should be below the pull-in threshold. However, many actuators rely on pull-in to achieve reliable actuation in short time. **RF switches** and microrelays use this actuation method, Fig. 3.19a. RF switches are commonly used for wireless, communications, and radar applications. Pull-in in this case provides fast actuation method with large stroke. This in turn helps achieve high isolation (isolation is the amount of output signal when the switch is off) and low insertion loss (insertion is characterized by the amount of losses in the signal output line when the switch is on). In addition, capacitive switches are characterized by low on-resistance (resistive switching), high on-capacitance, and a much broader operating temperature range than silicon electronic devices. These make RF switches a major component of MEMS in general and electrostatic MEMS in particular [65–67]. Another classical

Fig. 3.17 A capacitive accelerometer fabricated by Sensata Technologies [50]. **a** Taken apart. **b** Assembled. **c** Schematic

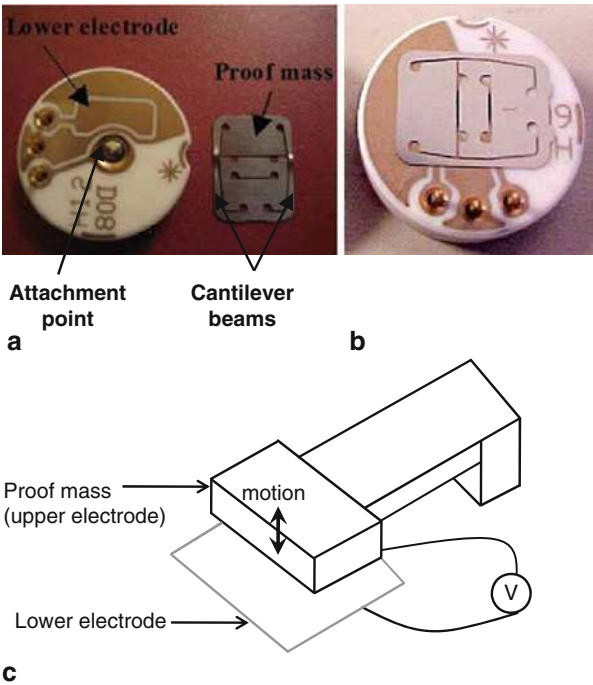


Fig. 3.18 Schematic of a resonant sensor actuated by parallel-plate electrostatic forces

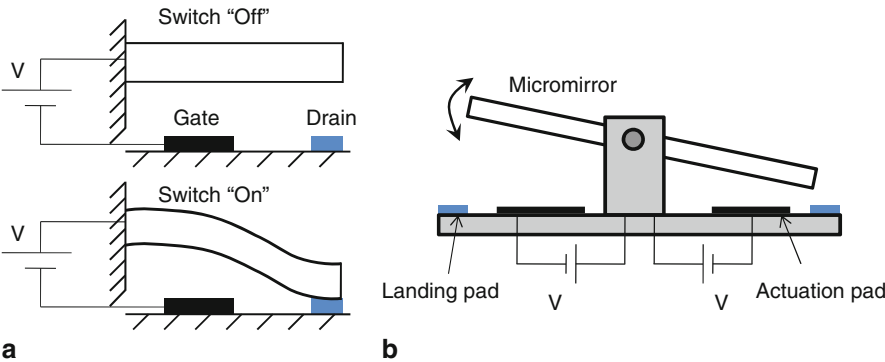
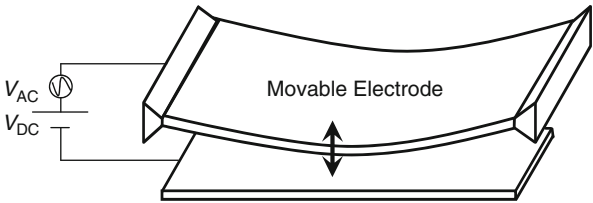


Fig. 3.19 Examples of capacitive actuators. **a** RF switch. **b** Micromirror

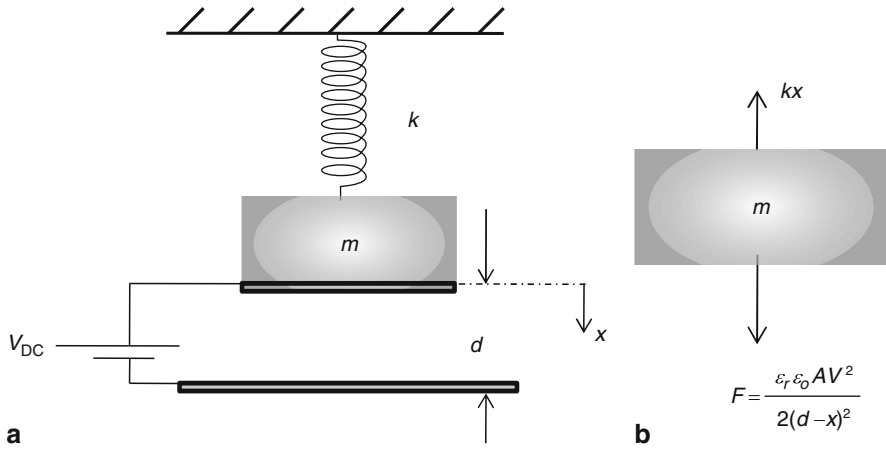


Fig. 3.20 A model of a parallel-plate capacitor. **a** Spring-mass system. **b** Free body diagram

example of pull-in use is the actuation of the Deformable Mirror Device DMD or the **micromirror**, Fig. 3.19b, of Texas Instruments. The micromirror is actuated beyond pull-in in angular motion to deflect and reflect incident lights [18].

To gain some insight into the pull-in phenomenon, we consider the spring-mass system shown in Fig. 3.20a. This represents a model for a parallel-plate capacitor, where the moveable electrode of mass m is a flexible structure, such as a beam, of stiffness k , which forms the upper electrode of the capacitor. The stationary electrode is placed a distance d underneath the flexible electrode. The capacitor is biased by a DC voltage V_{DC} , which pulls the flexible electrode downward a distance x . In this case, the electrostatic force acting on the upper electrode is expressed as

$$F = \frac{\varepsilon A V^2}{2(d-x)^2} \quad (3.25)$$

where ε is the dielectric constant of the gap medium ($\varepsilon = \varepsilon_r \varepsilon_o$). A restoring force of the structure kx is induced to oppose the electrostatic force, which leads to a new equilibrium position of the structure. Figure 3.20b shows a free body diagram of the structure (the effect of weight is neglected because in microstructures it is very small compared to the actuation force). Hence, the equation governing the equilibrium position x can be written as

$$kx = \frac{\varepsilon A V^2}{2(d-x)^2}. \quad (3.26)$$

Equation (3.26) is a cubic equation in x with three possible solutions. It turns out that one of the three solutions predicts $x > d$, and hence it is nonphysical and discarded (the structure cannot penetrate and move below the lower electrode). Of the other two physical solutions, one represents unstable solution, meaning that practically the

structure cannot hold into this position (this is similar to the equilibrium position of an inverted pendulum, more in Chap. 5). So we are left with one physical solution ($x < d$) that is stable, which represents the “real” deflection of the upper electrode in response to the DC load.

One easy approach to explore the solutions of Eq. (3.26) is to plot the right-hand and left-hand sides of the equation and then look for their intersection, which give the solutions of the equation. Then, one can get an exact solution of Eq. (3.26) near the intersection by providing an initial guess of the solution from the plot to a numerical solver. Figure 3.21 shows such plots for various values of V_{DC} much lower than the pull-in voltage V_{pull} , lower than V_{pull} , equal V_{pull} , and larger than V_{pull} . When $V_{DC} < V_{pull}$, Fig. 3.21a, b, we can see that the restoring and electrostatic force curves intersect each other in two locations. The location at smaller values of force and deflection represents the stable solution whereas the other one is the unstable solution. One can see that as V_{DC} is increased, both solutions approach each other. Eventually, when $V_{DC} = V_{pull}$, Fig. 3.21c, both coalesce at $x = d/3$. Substituting $x = d/3$ in Eq. (3.26), an analytical expression for the pull-in voltage V_{pull} is

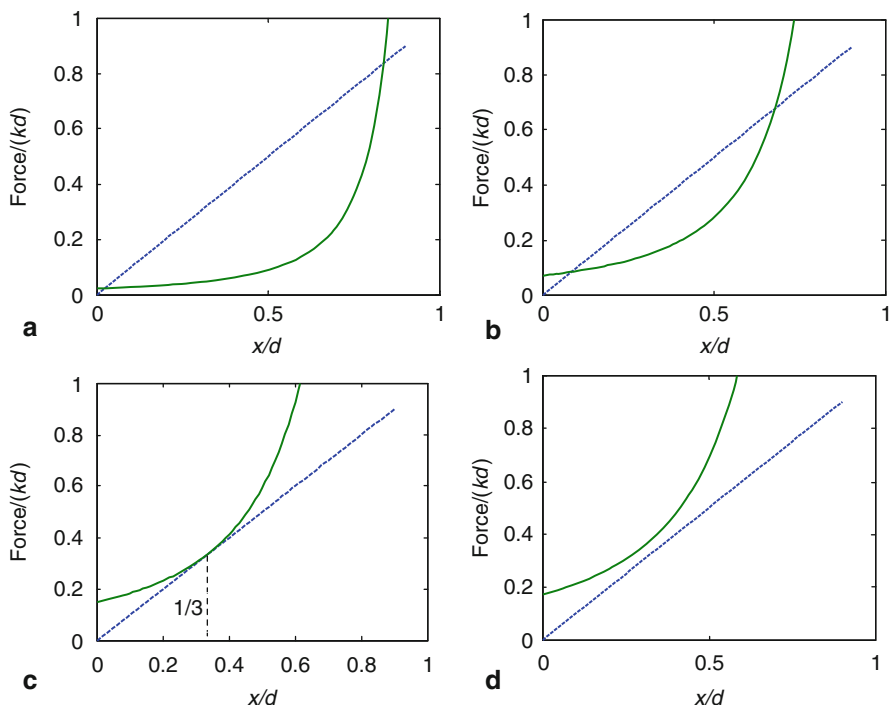
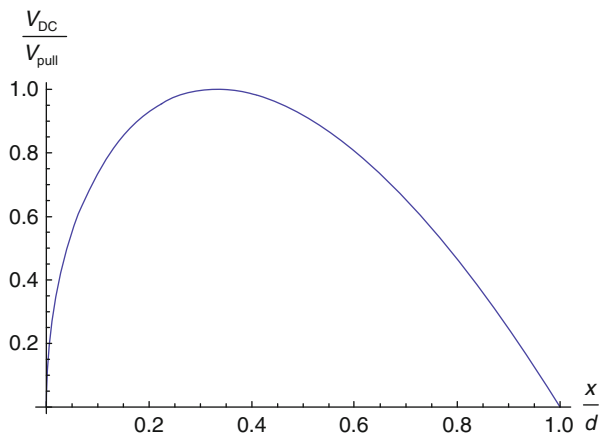


Fig. 3.21 Plots for the linear restoring force of a microstructure (*dashed straight line*) versus the nonlinear electrostatic force (*solid curve*) for various values of DC loads. **a** $V_{DC} \ll V_{pull}$. **b** $V_{DC} < V_{pull}$. **c** $V_{DC} = V_{pull}$. **d** $V_{DC} > V_{pull}$. In the figures, the forces are normalized with respect to kd and x is normalized with respect to d

Fig. 3.22 A plot of Eq. (3.28) showing the two possible solutions of the simple capacitor



obtained:

$$V_{\text{pull}} = \sqrt{\frac{8kd^3}{27\epsilon A}} \quad (3.27)$$

Equation (3.27) applies for all structures with almost linear restoring force (see e.g., [54]). Beyond pull-in, as seen in Fig. 3.21d, the two curves do not intersect indicating that there are no equilibrium solutions.

Another way to view the solution of Eq. (3.26) is to solve for V in terms of x as

$$V_{\text{DC}} = \sqrt{2kx(d-x)^2/(\epsilon A)}. \quad (3.28)$$

One can then plot Eq. (3.28) for several values of x , which is sort of an indirect way to view the solutions. An example of the possible results is shown in Fig. 3.22. Again, of the two curves of x , the smaller one represents stable solutions and the larger one represents unstable solutions. Both meet at the pull-in voltage.

3.5.2 Torsional Actuators and Micromirrors

Electrostatically actuated torsional micromirrors form the backbone of the DLP chip, which is the essential element to the technology of video and image projections and flat-screen TV's of Texas Instrument [68]. Each mirror, also called Deformable Mirror Device DMD, represents one image pixel on the chip. The chip contains approximately two million of these mirrors. The mirror reflects the incident light thousands of time per second in a digital on-off fashion. In this method, the mirror is brought to the on position by actuating it beyond pull-in so that it reflects the light at a precise angle. The mirror is then brought back to its original position, the off position, by sufficiently reducing the actuation voltage. By controlling the frequency of the

on-off actuation, and hence the light reflection, different color scale is realized. In addition to their application in the DLP chip, torsional actuators have been explored thoroughly for various switching, scanning, and optical applications.

An expression of the electrostatic torque that actuates a torsional actuator can be derived as follows. Consider the torsional actuator of Fig. 3.23. The actuator is composed of an upper plate of length $2a_3$, width b , and thickness t . The plate is connected to two torsional springs, each of length l , width w , and thickness t . An electrode of width b is deposited on the plate a distance a_1 from its center line such that its length is $a_2 - a_1$ as shown in the figure. A lower electrode is placed underneath the upper electrode a distance d on the substrate. Next, an expression of the electrostatic force acting on a small portion of the upper electrode of length dx is calculated. Under the assumptions of negligible fringing effect, infinitely wide plates (parallel-plate approximation), and a small tilting angle α , this portion of the electrode and the one directly underneath it can be treated as two parallel plates. Hence, according to Eq. (3.25), the force is expressed as

$$dF = \frac{\epsilon b V^2 dx}{2(d - x\alpha)^2}. \quad (3.29)$$

Then, the electrostatic torque M_e is calculated according to [69, 70]

$$M_e = \int_{a_1}^{a_2} x dF = \int_{a_1}^{a_2} \frac{\epsilon b V_{DC}^2 x}{2(d - \alpha x)^2} dx. \quad (3.30)$$

Carrying out the integration in Eq. (3.30) yields

$$M_e = \frac{\epsilon b V_{DC}^2}{2\alpha^2} \left[\frac{d}{d - a_2\alpha} - \frac{d}{d - a_1\alpha} + \ln \left(\frac{d - a_2\alpha}{d - a_1\alpha} \right) \right]. \quad (3.31)$$

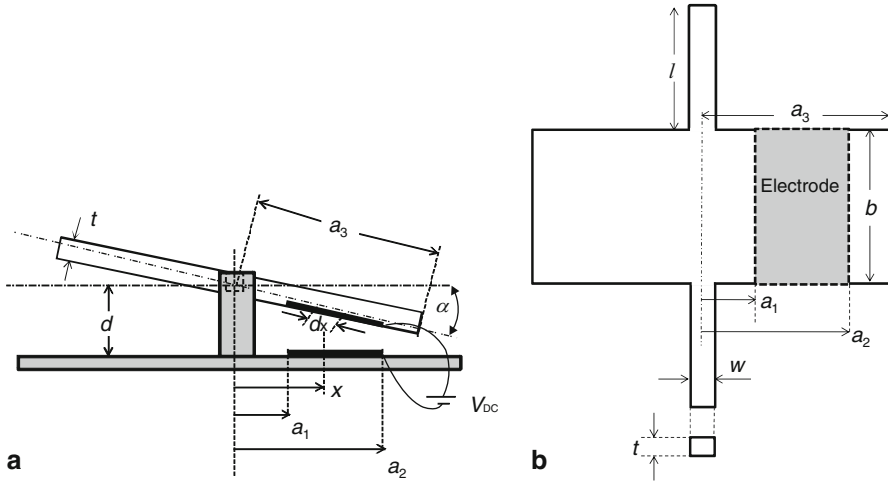


Fig. 3.23 Schematic of a torsional actuator: **a** is a front view and **b** is a top view

Another way to derive Eq. (3.31) is to start from the polar form of the Laplace equation of the electrostatic force. Then by calculating the electrostatic field and charge density on the plates, the electrostatic pressure and torque are obtained [71]. A more convenient form of the electrostatic torque can be obtained by normalizing α with respect to its maximum possible value $\alpha_{\max} = d/a_3$ and defining

$$\theta = \frac{\alpha}{\alpha_{\max}}. \quad (3.32)$$

Also, the following normalized ratios are introduced:

$$\gamma = \frac{a_1}{a_3}; \quad \beta = \frac{a_2}{a_3}. \quad (3.33)$$

Substituting Eq. (3.32) and Eq. (3.33) into Eq. (3.31) yields

$$M_e = \frac{\varepsilon b V_{\text{DC}}^2}{2\alpha_{\max}^2 \theta^2} \left[\frac{1}{1 - \beta\theta} - \frac{1}{1 - \gamma\theta} + \ln \left(\frac{1 - \beta\theta}{1 - \gamma\theta} \right) \right]. \quad (3.34)$$

In the special case that the electrode spans the whole length of the actuator, $a_1 = \gamma = 0$, $a_2 = a_3$ and $\beta = 1$. Then, Eq. (3.34) is reduced to

$$M_e = \frac{\varepsilon b V^2}{2\alpha_{\max}^2 \theta^2} \left[\frac{\theta}{1 - \theta} + \ln(1 - \theta) \right]. \quad (3.35)$$

When an electrostatic torque is applied on the upper plate of the actuator, an opposing restoring torque M_{mech} from the torsional springs is induced to counter this torque. The restoring torque can be written as

$$M_{\text{mech}} = K_t \alpha = K_t \alpha_{\max} \theta \quad (3.36)$$

where K_t is the effective torsional spring coefficient of the two torsional springs. Thus, the actuator reaches an equilibrium state at the tilted angle α . The equation of equilibrium can be written as

$$K_t \alpha_{\max} \theta = \frac{\varepsilon b V_{\text{DC}}^2}{2\alpha_{\max}^2 \theta^2} \left[\frac{1}{1 - \beta\theta} - \frac{1}{1 - \gamma\theta} + \ln \left(\frac{1 - \beta\theta}{1 - \gamma\theta} \right) \right]. \quad (3.37)$$

Each side of Eq. (3.37) can be plotted for a given voltage to show the possible intersection of the two curves, and thus, the solutions of the equation. As in the simple parallel-plate capacitor, one of the solutions turns out to be stable and the other larger one to be unstable. Alternatively, an expression for V can be solved in terms of θ as

$$V_{\text{DC}} = \sqrt{\frac{2K_t \alpha_{\max}^3 \theta^3}{\varepsilon b \left[\frac{1}{1 - \beta\theta} - \frac{1}{1 - \gamma\theta} + \ln \left(\frac{1 - \beta\theta}{1 - \gamma\theta} \right) \right]}}. \quad (3.38)$$

Similar to the simple capacitor of Fig. 3.20, there is a limit of actuation voltage beyond which the restoring torques of the torsional springs cannot oppose the electrostatic torque leading to the pull-in phenomenon and the collapse of the actuator on the substrate. Hence, when plotting Eq. (3.38), both stable and unstable curves meet and are terminated at the pull-in voltage. For the special case of a full-electrode actuator, pull-in occurs at $\theta = 0.4404$. For all other cases, pull-in occurs at an approximate angle of [72]

$$\theta_{\text{pull}} \cong \frac{0.4404}{1 + 0.322\delta^{2.117}} \quad (3.39)$$

where $\delta = a_1/a_2$. The pull-in voltage can be calculated according to [72]

$$V_{\text{pull}} \cong \sqrt{\frac{0.8275 K_t d^3}{\epsilon b a_2^3}} (1 - \delta^2)^{-0.5} (1 + 0.6735 \delta^{1.931})^{-0.3244}. \quad (3.40)$$

In the case of an electrode spanning the whole length of the actuator ($a_1 = \delta = 0$), the expression is reduced to

$$V_{\text{pull}} = 0.90967 \sqrt{\frac{K_t d^3}{\epsilon b a_2^3}}. \quad (3.41)$$

Example 3.2: Consider the MMV torsional actuator of Degani et al. [71] of the parameters in the table below.

$K_t \times 10^{-3}$ (Nm)	a_1 (μm)	a_2 (μm)	a_3 (μm)	d (μm)	b (μm)
0.0143087	430	580	600	3.42	1,300

- Evaluate the normalized equilibrium angle θ for $V_{\text{DC}} = 12$ V.
- Plot V_{DC} versus θ .
- Calculate V_{pull} and θ_{pull} from Eqs. (3.39) and (3.40) and compare the results to the plot of (b).

Solution:

- First, we plot both sides of Eq. (3.37) to show the intersection of the curves and the two possible solutions, Fig 3.24a. Using the command “FindRoot” in the software Mathematica with an initial guess $\theta = 0.1$ gives $\theta = 0.075064$.
- Using Eq. (3.38), a plot of V_{DC} versus θ is obtained, Fig. 3.24b, showing the stable and unstable solutions at each voltage value. From the figure, once can see that the pull-in voltage is approximately at $V_{\text{pull}} \approx 20$ V at $\theta_{\text{pull}} \approx 0.4$.
- Using Eq. (3.39) gives $\theta_{\text{pull}} = 0.376$. Also using Eq. (3.40) gives $V_{\text{pull}} = 19.5$ V.

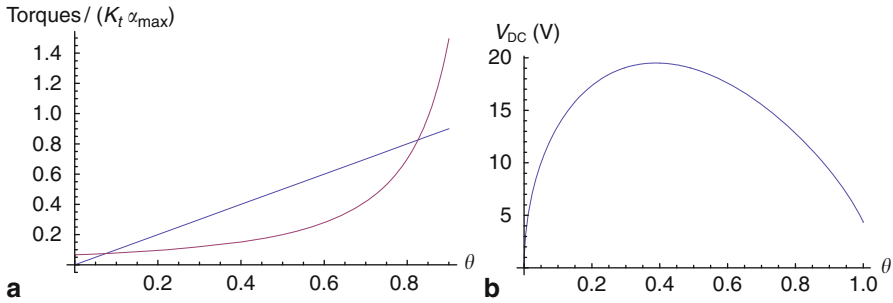


Fig. 3.24 **a** A plot of the normalized mechanical and electrostatic torque curves versus the normalize angle θ . **b** A plot of V_{DC} versus θ

3.5.3 Comb-Drive Devices

Comb-drive devices are also commonly used in MEMS for sensing and actuation. Among the various applications, they have been implemented in accelerometers [73], microgrippers [74], resonators [75, 76], filters [77], generic force actuators [78, 79], two dimensional microstagers [80], and micromirrors [81, 82]. Comb-drive devices commonly rely on interdigitated fingers. Non-interdigitated fingers are also utilized, however their capacitance is hard to be calculated analytically and usually finite-element analysis is needed for their characterization (see e. g., [83]). Here, we focus on devices with interdigitated fingers.

Comb-drive devices rely on two comb structures, a stationary and a moveable one that is connected to flexible structures (springs or tethers). The flexible structures are made to be compliant in the direction of the desirable displacement and stiff in the orthogonal directions to limit motion in these directions. Each comb consists of interdigitated fingers. The stationary and moveable fingers form parallel-plate capacitors among each other. Comb-drive devices can have many configurations, such as rotary, in which one circular-shape comb moves in rotational motion with respect to the stationary comb. There is also out-of-plane types, in which one comb moves out-of-plane with respect to the other, and in-plane devices, where one comb moves in the same plane as the stationary one and the substrate. The most common are the in-plane devices. These can be classified into two categories: transverse and longitudinal, Fig. 3.25 [17]. In either case, each moveable finger is sandwiched between two fixed fingers, where portion of its surface overlap with those of the fixed fingers, Fig. 3.25. This causes capacitive and electrostatic interaction among the fingers resulting in an actuation and/or detection mechanism.

In the case of the transverse comb-drive, Fig. 3.25a, the moveable comb moves in transverse direction to the longitudinal axis of the fingers (along the x -axis in the figure). Figure 3.26 shows a closer look at one of the moveable finger as it is sandwiched between two stationary fingers. As seen in the figure, the moveable finger represents an electrode for two parallel-plate capacitors with two stationary fingers, thereby forming one capacitor to its right and another one to its left. If the finger

Fig. 3.25 Transverse (a) and longitudinal (b) in-plane comb-drive devices

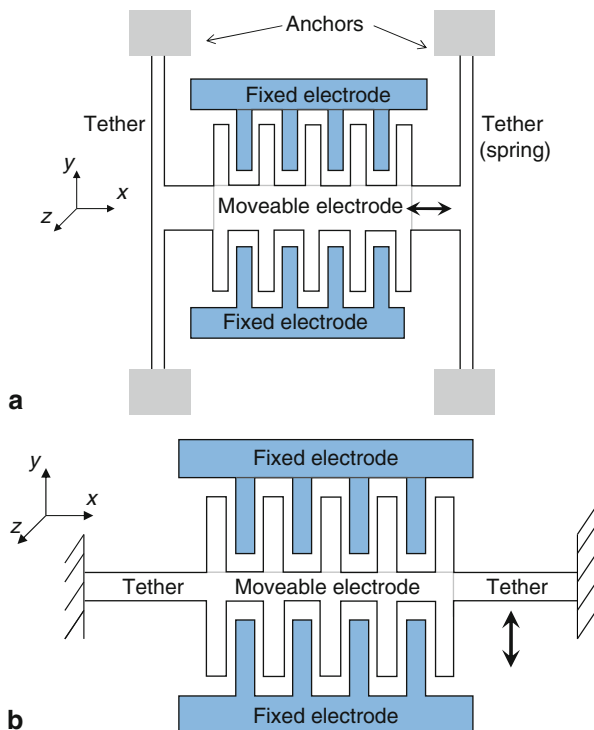
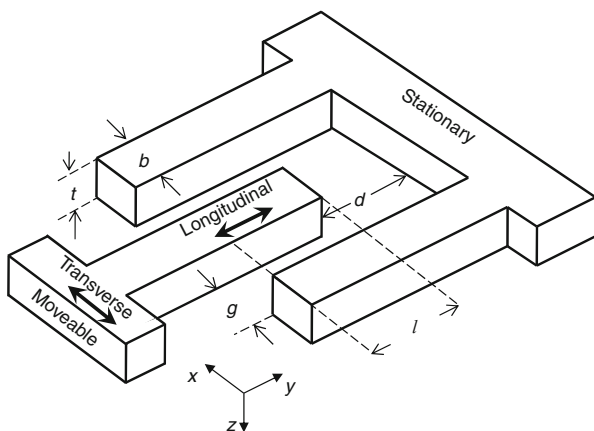


Fig. 3.26 A moveable finger sandwiched between two stationary fingers illustrating the two possible modes of motion of the finger



moves a positive distance x (to the left), then the capacitance of the left capacitor C_{left} and right capacitor C_{right} are expressed as

$$C_{\text{left}} = \frac{\varepsilon(lt)}{g - x};$$

$$C_{\text{right}} = \frac{\varepsilon(lt)}{g + x}$$
(3.42)

where l , t , and g are as shown in Fig. 3.26. Note that in the case of no displacement, $x = 0$, and $C_{\text{left}} = C_{\text{right}}$. If $x \neq 0$ then $C_{\text{left}} - C_{\text{right}} = 2\varepsilon(lt)x/(g^2 - x^2)$. This differential capacitance can be used to sense the motion of the moveable comb. To increase the value of the induced capacitance, the number of comb fingers is increased.

If the capacitors are biased by a voltage V , then two electrostatic forces will be generated on the moveable finger. One acts on its left side F_{left} in the positive x direction and an opposite one acts on its right side F_{right} . The magnitudes of these forces are expressed according to Eq. (3.24) as

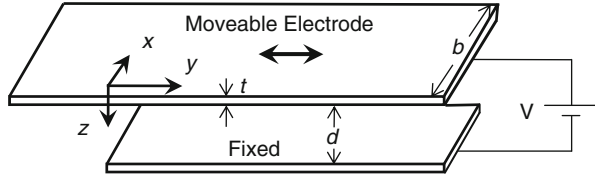
$$\begin{aligned} F_{\text{left}} &= \frac{\varepsilon(lt)V^2}{2(g-x)^2}; \\ F_{\text{right}} &= \frac{\varepsilon(lt)V^2}{2(g+x)^2}. \end{aligned} \quad (3.43)$$

If $x = 0$, the electrostatic forces acting on the moveable finger cancel each other. If $x \neq 0$, a resultant force $F_{\text{right}} - F_{\text{left}}$ will act on the moveable finger. There is a limit on the maximum stable displacement of the comb before the electrostatic force overcomes the elastic resorting force from the tethers before it snaps, pulls-in, to the stationary combs. More on this issue is discussed in Chap. 5.

The transverse comb-drive represents the backbone of the classical ADXL-50 accelerometer of Analog Devices, which is used in automobiles for airbags deployments [73, 84]. In this device, the moveable comb represents a proof mass that is sensitive to acceleration. If a car moves at a constant velocity (zero acceleration), the fingers of the proof mass will be centered between the stationary electrodes, thereby creating zero differential capacitance. If the car undergoes an acceleration or deceleration a , the proof mass will be subjected to a force ma , where m is its mass, and will move a distance x . This force is balanced by the force from the tethers kx , where k is the spring constant of the tethers. Due to the deflection of the proof mass, a differential capacitance is generated. The capacitance value is then measured and used in a feedback circuit designed to apply a voltage load on the fingers, which generates a balancing electrostatic force on the proof mass that restores it to its original position ($x = 0$). The value of the voltage load used for balancing the electrostatic force is taken as a measurement of the acceleration. Thus, the ADXL-50 accelerometer is also called a force-balanced accelerometer.

In the case of a longitudinal comb-drive, Fig. 3.25b, the moveable comb moves parallel to the longitudinal axis of the fingers (along the y -axis in the figure, see also Fig. 3.26). Also here each moveable finger represents one side of two parallel-plates capacitors with the stationary fingers. When a bias voltage is applied between the stationary and moveable fingers, lateral electrostatic forces are induced on the moveable fingers, which move them in the lateral direction along the y -axis. To derive expressions for these forces, consider the parallel-plate capacitor shown in Fig. 3.27, where the upper moveable electrode is allowed to slide parallel to the lower stationary electrode and is constrained to move in all other directions. The capacitance of the

Fig. 3.27 Parallel-plate capacitor showing lateral (in-plane) motion of the upper electrode



parallel-plate capacitor, neglecting the fringing of the electric field, is expressed as

$$C(y) = \epsilon_r \epsilon_o \frac{A}{d} = \epsilon \frac{yb}{d} \quad (3.44)$$

where yb represents the overlapping area between the two electrodes and d is the width of the gap separating the two electrodes, which is constant in this case. Because of the power source, the capacitor is charged according to Eq. (3.18) and stores energy according to Eq. (3.19). The total potential energy of the battery-capacitor system is given by Eq. (3.21). Substituting Eq. (3.44) into Eq. (3.21) yields

$$E(y) = E_0 - \epsilon \frac{yb}{2d} V^2. \quad (3.45)$$

An expression for the lateral electrostatic force F_y affecting the moveable finger is expressed as

$$F_y = \frac{-\partial E(y)}{\partial y} = \frac{1}{2} \frac{\partial C(\eta)}{\partial \eta} V^2 = \frac{\epsilon b V^2}{2d}. \quad (3.46)$$

One can note from Eq. (3.46) that the electrostatic force along the length of the finger is independent from its length and depends on its width. This force tends to increase the overlap among the fingers while being constant in magnitude. The fact that this force remains constant during actuation and that it is independent of the displacement is very desirable. This makes the longitudinal comb-drive actuators capable of providing linear well-controlled actuation. This, in addition to its high-quality factor in air compared to the basic parallel-plate actuators, makes it attractive for resonators actuation [75–77].

For the case of a longitudinal moveable finger sandwiched between two stationary fingers, Fig. 3.26, there are two capacitive forces generated on the moveable finger from the two nearby stationary electrodes with the electrode area of each capacitor is ty and the gap width g . For n number of moveable fingers, the total electrostatic force F_y^{Tot} acting on the moveable comb drive is

$$F_y^{\text{Tot}} = n \times 2 \times \frac{\epsilon t V^2}{2g} = \frac{n \epsilon t V^2}{g}. \quad (3.47)$$

It is worth to mention that each movable finger in this case is also affected by the side parallel-plate electrostatic forces along the x -direction given in Eq. (3.45). In the ideal situation, these forces cancel each other, since the moveable finger is supposed

to be centered exactly in between them. However, due to fabrication imperfections, a resultant force can be induced along the x -direction. If it is large enough, it can cause the moveable electrode to stick to the stationary fingers. Even if the finger is centered precisely between the stationary fingers, there is a limit on the amount of voltage that can be exerted on the finger before it loses stability and gets stuck to the sides (see Example 5.9). This phenomenon is known as the side instability or side sticking [78–80]. In addition, dynamic disturbances combined with the electrostatic force can lead to such instability [85]. Side instability limits the maximum amount of voltage load that can be applied on the fingers. In addition to the side instability, there is also the front instability [80] due to the parallel-plate force acting between the front side of the finger (of length b and thickness t) and the stationary electrode. This instability occurs when the moveable finger moves too close to the stationary electrode (d becomes too small in Fig. 3.26). Hence, it causes the moveable finger to stick to the stationary fingers causing short circuit problems and stiction failure. This instability also limits the maximum actuation voltage and the displacement that the comb-drive fingers can move before being caught with stiction. For n moveable fingers, the total front force F_y^{Front} acting on the comb drive is written as

$$F_y^{\text{Front}} = n \frac{\epsilon b t V^2}{2d^2}. \quad (3.48)$$

The force in Eq. (3.48) plus that of Eq. (3.47) are summed and used to study the stability of the comb-drive and the maximum allowable voltage below the front instability.

Example 3.3: A comb-drive actuator has 10 moveable fingers with $t = 2 \mu\text{m}$ and $g = 2 \mu\text{m}$. The stiffness of the tethers holding the moveable comb was measured and found to be $k = 0.01 \text{ N/m}$. Calculate and plot the deflection of the comb when actuated by a voltage load ranging from 0 to 10 V. Neglect the effect of side and front sticking.

Solution: The forces on the comb-drive are due to the actuating lateral electrostatic force and the opposing elastic force from the tethers. Hence, the equilibrium equation of the comb is written as

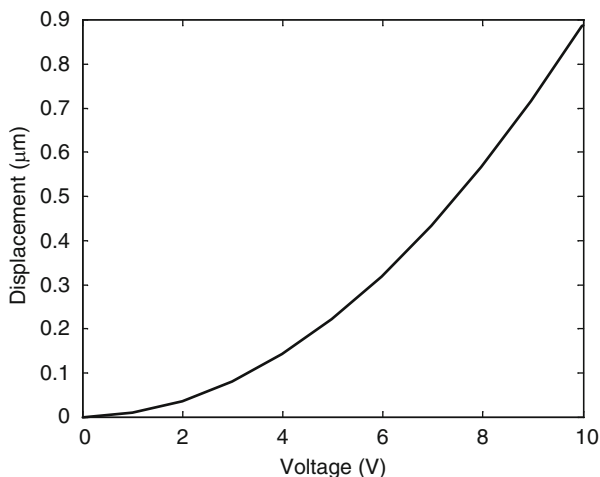
$$ky = \frac{n\epsilon t V^2}{g}. \quad (a)$$

From which the actuated displacement y is expressed as

$$y = \frac{n\epsilon t V^2}{kg} = \frac{1}{k} F_y^{\text{Tot}}. \quad (b)$$

It is clear from Eq. (b) that the deflection is linearly proportional to the voltage squared and to the electrostatic force. This is unlike the case of parallel-plate capacitive actuation, where the deflection and force are related nonlinearly (see Eq. (3.26)). As pointed previously, this is one of the major advantages of comb-drive actuators. A plot for the deflection-voltage curve is shown in Fig. 3.28.

Fig. 3.28 Voltage versus displacement curve of a comb-drive lateral actuator



3.6 Resonant Sensors

Resonant sensors [86–89] refer to the class of sensors that employ a structure vibrating at resonance (called resonators). The structure can be a cantilever beam, a clamped–clamped beam (bridge), a diaphragm, or can have any other shapes. A change in a physical parameter in the sensor’s environment, such as pressure, temperature, force, acceleration, and gas concentration, varies either the stiffness of the structure, such as by inducing axial stress on it, or its mass. This shifts the resonance frequency of the structure. The amount of frequency shift is taken as a direct measurement of the physical parameter. A major attractive characteristic of resonant sensors is the fact that the frequency shift is a readily digital signal output (the resonance frequency provides an output in the form of pulses that can be transmitted to a digital processor and decoded by counting pulses over a specified interval [86]). Hence, the digital output can be connected directly to digital signal processing without the need for analog-to-digital converters (these are complex and expensive). In addition, resonant sensors offer other attractive advantages over conventional sensors, such as high sensitivity and resolution, low-power consumption, and long-term stability.

Single crystal silicon is commonly used for MEMS resonators because of its excellent mechanical properties, low intrinsic damping due to its purity, the ability to batch process at low cost, and the compatibility with electronic components. Also, silicon-based sensors possess excellent dynamic and temperature characteristics compared to conventional piezoresistive sensors. In addition, MEMS resonators have been also made of grained polycrystalline silicon (polysilicon) (e.g., [90, 91]), due to its ease of micromachining.

There are two major features for resonant sensors that designers should take into account: the quality factor of the resonator and its temperature stability [88]. It is desirable for the resonator to have a high quality factor, or in another words low

damping. This simplifies the feedback control electronics, minimizes the sensitivity to the variations in electrical parameters and the drive electronics, and gives a high resolution. This also means a very low unwanted mechanical coupling to the external world, which gives high accuracy and long-term stability. Many external and internal dissipation mechanisms can influence the quality factor. These are discussed in the next chapter. Also, it is desirable to have a low temperature sensitivity to ensure accurate measurements of the physical parameters of interest. Factors affecting the temperature sensitivity of the resonator include its composing materials and their properties, such as their thermal expansion, the vibration mode (transversal, torsional, longitudinal), and the excitation and detection mechanisms. For example, thermal excitation and piezoresistive detection increase temperature sensitivity.

Most resonant sensors rely on a feedback circuitry, such as a phase-locked controller, that keeps track of the resonance frequency of the resonator and ensure operating at resonance while the natural frequency of the resonator changes during the detection of the physical parameter. A feedback controller requires an active detection of the resonance frequency of the resonator and its motion. Also, an excitation or actuation mechanism is needed to bring the resonator to vibrations. Figure 3.29 illustrates the basic components of a resonant sensor, which are the resonator, the excitation unit, the detection unit, and the feedback circuitry [88].

The excitation-detection methods for MEMS resonators, arranged from common to less common, are [87–89] electrostatic excitation and capacitive detection, piezoelectric excitation and detection, electrothermal excitation and piezoresistive detection (e.g., [1]), optical heating and detection, magnetic excitation and detection, and any mix and match among these. Details about these mechanisms have been mostly described in the previous sections.

Electrostatic excitation can be through parallel-plate capacitor (e.g., [90]) or a comb-drive actuator (e.g., [92]). In either case, a DC voltage is superimposed to an AC harmonic load. The addition of the DC component prevents driving the structure at twice the AC-forcing frequency. This is undesirable because half-frequency elements have to be introduced in the resonator's circuit to maintain driving the

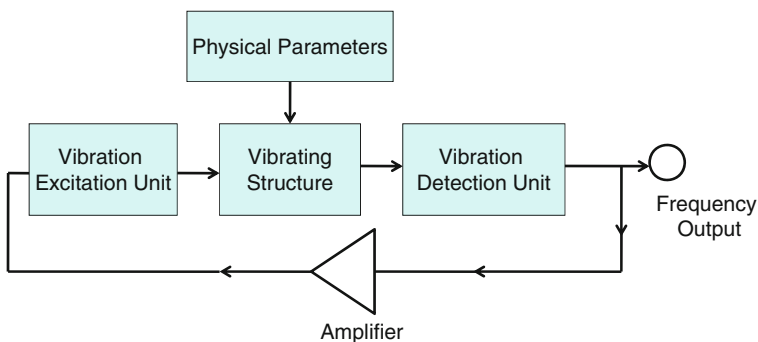


Fig. 3.29 The essential components of a resonant sensor

microstructure at resonance, which complicates the feedback circuitry and adds to the cost of the devices. To clarify this, consider an AC harmonic load of amplitude V_{AC} and frequency Ω that is superimposed to a DC load V_{DC} . The total electrostatic force is proportional to $[V_{DC} + V_{AC} \cos(\Omega t)]^2$, which can be expanded as $V_{DC}^2 + 0.5V_{AC}^2[\cos(2\Omega t) - 1] + 2V_{DC}V_{AC} \cos(\Omega t)$. If $V_{DC} = 0$ then the frequency of excitation will be twice that of the AC load. However, by superimposing a DC component, which is selected to be much larger than the AC component ($V_{DC} \ll V_{AC}$), the term $2V_{DC}V_{AC} \cos(\Omega t)$ dominates the excitation force leading to a direct excitation at the frequency of the AC load. The capacitive detection of motion is achieved through a sensing circuit, which can be the same as the excitation circuit (single port) or independent of the excitation circuit (two ports). The sensing circuit monitors the generated current i due to the fluctuation of the capacitance of the variable capacitor ($i = V_p \frac{\partial C}{\partial t} \frac{\partial x}{\partial t}$ where V_p is the polarization voltage of the sensing circuit, C is the capacitance, x is the moveable electrode displacement, and t is time). One can see that electrostatic excitation and detection is easily realized. However, some of the common problems of this method are the significant effect of squeeze-film damping, the requirement of a DC source, and the pull-in instability in the case of parallel-plate capacitors.

The most common use of resonant sensors has been for mass detection, force-based detection, and pressure sensing. Howe and Muller first demonstrated a resonant mass sensor to detect vapors [92]. Since then, numerous resonant sensors have been proposed to detect chemical and biological materials [1, 93, 94]. Recently, resonant sensors have been demonstrated to detect extremely small masses, such as atoms, through scaling the resonators down to the Nano range [95, 96]. Force-based detection refers to the detection of a physical parameter due to an induced axial force or strain on a microstructure resonator, such as a clamped-clamped bridge. This class of sensors is also called micro resonant force gauges [89]. The axial force or strain can be induced on the resonator directly due to changes in the surrounding physical parameter, such as pressure, weight, and temperature. However, a more common use of a force sensor is to embed it into another structure, such as a diaphragm, which is subjected directly to the physical parameter, which can be pressure, acceleration, and mass flow. When the diaphragm is exposed to the physical parameter, it deflects and strains. This causes an axial stress to be induced on the embedded resonator, thereby changing its resonance frequency. A well-known example of this technique has been used for pressure sensors [89, 97]. Figure 3.30 shows a schematic illustrating a resonant-based pressure sensor. In such applications, the microbeam resonator is placed inside a sealed vacuum cavity made of silicon. The vacuum housing provides isolation from environmental effects, such as dust and vapor, which disturb the microbeam motion. It also improves the quality factor for better resolution and stable operation. The housing is exposed to the external effect to be detected and, at the same time, is integrated with the boundaries of the resonating microbeam. Thus, the microbeam and the surrounding shell are considered as the resonant sensor [90].

Example 3.4: Consider a resonant mass sensor modeled as an undamped spring-mass system as shown in Fig. 3.31a of mass m and stiffness k . When the resonator

Fig. 3.30 A resonant-based pressure sensor

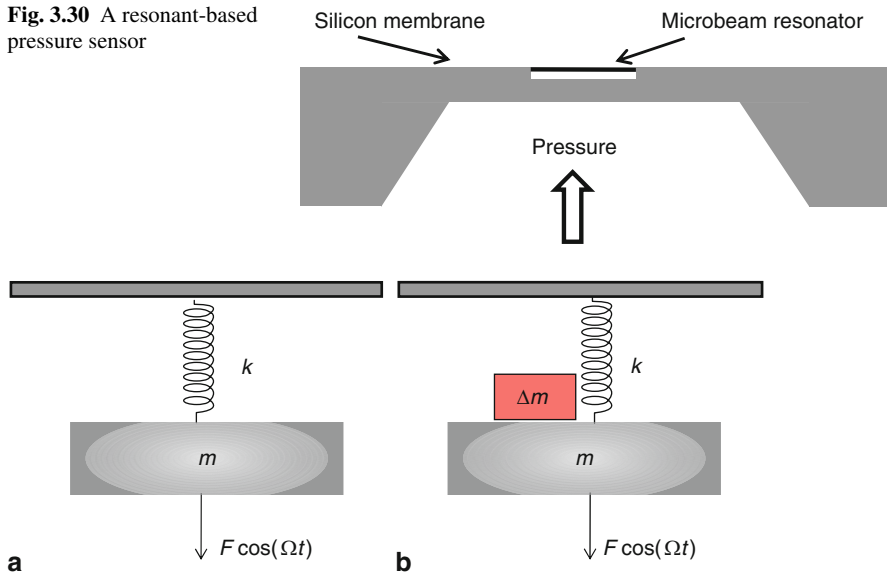


Fig. 3.31 A model of a resonant mass sensor **a** before detecting mass and **b** after detecting mass

picks up mass Δm , Fig. 3.31b, such as gas molecules or viruses, its natural frequency, and hence its resonance frequency changes. Derive an analytical expression for the detected mass of the resonator in terms of this frequency shift in Hz.

Solution: Before adding mass, the natural frequency of the resonator ω_{n1} in rad/s is expressed as

$$\omega_{n1} = \sqrt{\frac{k}{m}}. \quad (a)$$

After adding the mass, the new natural frequency ω_{n2} becomes

$$\omega_{n2} = \sqrt{\frac{k}{m + \Delta m}}. \quad (b)$$

Dividing (a) over (b) yields

$$\left(\frac{\omega_{n1}}{\omega_{n2}}\right)^2 = 1 + \frac{\Delta m}{m} \quad \text{or} \quad \frac{\Delta m}{m} = \left(\frac{\omega_{n1}}{\omega_{n2}}\right)^2 - 1. \quad (c)$$

Substituting for $m = k/\omega_{n1}^2$ above yields

$$\Delta m = \frac{k}{\omega_{n1}^2} \left[\left(\frac{\omega_{n1}}{\omega_{n2}}\right)^2 - 1 \right] = \Delta m = k \left[\frac{1}{\omega_{n2}^2} - \frac{1}{\omega_{n1}^2} \right]. \quad (d)$$

Recalling that $\omega_n = 2\pi f$ (Hz) and substituting in (d) yield

$$\Delta m = \frac{k}{4\pi^2} \left[\frac{1}{f_{n2}^2} - \frac{1}{f_{n1}^2} \right]. \quad (e)$$

Problems

1. Shown below is a bulk silicon accelerometer with doped piezoresistive material of gauge factor G near the clamped end of the beam. Derive an expression for the normalized change in resistance as a function of the sensed acceleration a . Assume the beam has a width W .
2. In Problem 1 and Fig. 3.32, assume that instead of the piezoresistive patch, a PZT layer of thickness t_p is deposited in the same location near the clamping edge of the cantilever beam. Derive an analytical expression for the induced voltage across the PZT layer as a function of the sensed acceleration.
3. Estimate the number of comb fingers needed to move a longitudinal comb-drive actuator a displacement of $2\text{ }\mu\text{m}$ along the direction of the longitudinal axis of the fingers when biased by 5 V . Assume for each finger $t = 2\text{ }\mu\text{m}$ and $g = 2\text{ }\mu\text{m}$. Also, assume that the tethers of the comb drive have an estimated effective stiffness coefficient of $k = 0.02\text{ N/m}$.
4. Compare the pull-in voltage of the two parallel-plate capacitors shown in Fig. 3.33.
5. A cantilever microbeam of stiffness 0.01 N/m and fundamental natural frequency equal 5 kHz . Calculate the shift in its natural frequency if it is used as a resonant

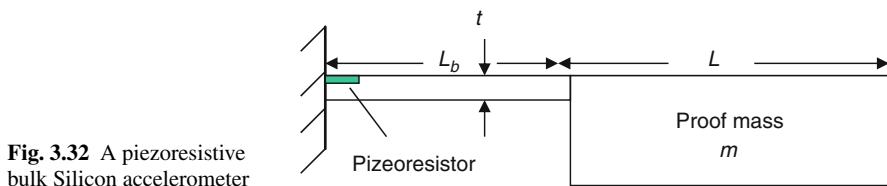


Fig. 3.32 A piezoresistive bulk Silicon accelerometer

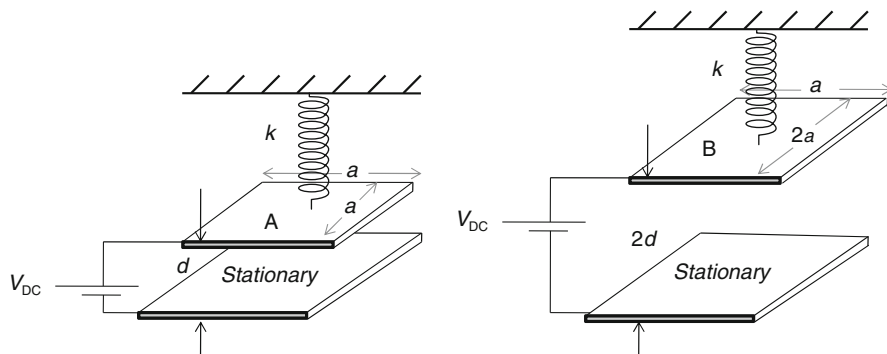


Fig. 3.33 Parallel-plate capacitors

mass sensor when detecting a substance of mass 100 picogram (picogram is 10^{-12} of g).

6. Consider the torsional actuator of the parameters in the table below.

$K_t \times 10^{-3}$ (Nm)	a_1 (μm)	a_2 (μm)	a_3 (μm)	d (μm)	b (μm)
0.02	400	500	600	3.0	1,000

- Evaluate the normalized angle θ for $V_{\text{DC}} = 8$ V.
- Plot V_{DC} versus θ .
- Calculate V_{pull} and θ_{pull} from Eqs. (3.39) and (3.40) and compare the results to the plot of (b).

References

- [1] Lange D, Brand O, Baltes H (2002) CMOS cantilever sensor systems: atomic-force microscopy and gas sensing applications, Springer, Berlin
- [2] Lerch P, Slimane C K, Romanowicz B, Renaud P (1996) Modelization and characterization of asymmetrical thermal micro-actuators. *Journal of Micromechanics and Microengineering*, 137:134–137
- [3] Chi S P, Hsu W (1997) An electro-thermally and laterally driven polysilicon microactuator. *Journal of Micromechanics and Microengineering*, 7:7–13
- [4] Corntois J H, Bright V M (1997) Applications for surface-micromachined polysilicon thermal actuators and arrays. *Sensors and Actuators A*, 58:9–25
- [5] Huang Q-A, Ka N, Lee S (1999) Analysis and design of polysilicon thermal flexure actuator. *Journal of Micromechanics and Microengineering*, 9:64–70
- [6] Guckel H, Klein J, Christenson T, Skrobis K, Laudon M, Lovell E G (1992) Thermo-magnetic metal flexure actuators. In: *Proceeding of Solid-State Sensor and Actuator Workshop*, Hilton Head, pp. 73–75
- [7] Keller C G, Howe R T, (1995) Nickel-filled HEXSIL thermally actuated tweezers. In: *Proceeding of the IEEE International Conference on Solid-State Sensors and Actuators (Transducers' 95)*, Stockholm, Sweden, pp. 376–379
- [8] Noworolski J M, Klaassen E H, Logan J R, Peterson K E, Maluf N I (1996) Process for in-plane and out-of-plane single-crystal-silicon thermal microactuators. *Sensors and Actuators A*, 55: 65-9
- [9] Lott C D, McLain T W, Harb J N and Howell L L (2002) Modeling the thermal behavior of a surface-micromachined linear-displacement thermomechanical microactuator. *Sensors and Actuators A*, 101:239–250
- [10] Que L, Park J-S and Gianchandani Y B (2001) Bent-beam electrothermal actuators: I. Single beam and cascaded devices. *Journal of Microelectromechanical Systems*, 10:247–54
- [11] Maloney J M, Schreiber D S, DeVoe D L (2004) Large-force electrothermal linear micromotors. *Journal of Micromechanics and Microengineering*, 14:226–234
- [12] Cochran K R, Fan L, DeVoe D L (2005) High-power optical microswitch based on direct fiber actuation. *Sensors and Actuators A: Physical*, 119(2):512–519
- [13] Sassen W P, Henneken V A, Tichem M, Sarro P M (2008) An improved in-plane thermal folded V-beam actuator for optical fiber Alignment. *Journal of Micromechanics and Microengineering*, 18:075033 (9pp)
- [14] Chiao M, and Lin L (2000) Self-buckling of micromachined beams under resistive heating. *Journal of Microelectromechanical Systems*, 9(1):146–151
- [15] Riethmuller W, Benecke W (1988) Thermally excited silicon microactuators. *IEEE Transactions on Electron Devices*, 35(6):758–763

- [16] Chut W-H, Mehregany M, Mullen R L (1993) Analysis of tip deflection and force of a bimetallic cantilever microactuator. *Journal of Micromechanics and Microengineering*, 3:4–7
- [17] Liu C (2006) *Foundations of MEMS*. Prentice Hall, New Jersey
- [18] Senturia S D (2001) *Microsystem design*. Springer, New York
- [19] Perumont A (2006) *Mechatronics: dynamics of electromechanical and piezoelectric systems*. Springer, Netherland
- [20] Cheng H-M, Ewe I M T S, Chiu G T-C, Bashir R (2001) Modeling and control of piezoelectric cantilever beam micro-mirror and micro-laser arrays to reduce image banding in electrophotographic processes. *Journal of Micromechanics and Microengineering*, 11:487–498
- [21] Gerlach T, Wurmus H (1995) Working principle and performance of the dynamics miropump. *Sensor and Actuators A*, 50:135–140.
- [22] Olsson A, Stemme G, Stemme E (1995) A valve-less planar fluid pump with two pump chambers. *Sensor and Actuators A*, 46–47:549–556
- [23] Motamedi M E, Andrews A P, Brower E (1982) Accelerometer sensor using piezoelectric ZnO thin films. In *Proceeding of the IEEE Ultrasononic Symposium*, 1:303–307.
- [24] DeVoe D L, Pisano A P, Surface micromachined piezoelectric accelerometers (PiXLs). *Journal of Microelectromechanical Systems*, 10(2):180–186
- [25] Roundy S, Wright P K (2004) A piezoelectric vibration based generator for wireless electronics. *Smart Material and Structures*, 13:1131–1142
- [26] Erturk A, Inman D J (2008) Issues in mathematical modeling of piezoelectric energy harvesters. *Smart Materials and Structures*, 17:065016(14pp).
- [27] duToit N E, Wardle B L, Kim S-G (2005) Design considerations for MEMS-scale piezoelectric mechanical vibration energy harvesters. *Integrated Ferroelectrics*, 71:121–160
- [28] Guyomar D, Aurelle N, Eyraud L (1997) Piezoelectric ceramics nonlinear behavior. Application to Langevin Transducer. *Journal of Physics III France*, 7:1197–1208
- [29] Wing Q-M, Zhang Q, Xu B, Liu R, Cross E (1999) Nonlinear piezoelectric behavior of ceramic bending mode actuators under strong electric fields. 86:3352–3360
- [30] Mahmoodi S N, Jalili N, Daqaq M F (2008) Modeling, nonlinear dynamics, and identification of a piezoelectrically actuated microcantilever sensor. *IEEE/ASME Transactions on Mechatronics*, 13(1):58–65
- [31] Dick A J, Balachandran B, DeVoe D L, Mote C D Jr (2006) Parametric identification of piezoelectric microscale resonators. *Journal of Micromechanics and Microengineering*, 16:1593–1601
- [32] Li H, Preidikman S, Balachandran B, Mote C D Jr (2006) Nonlinear free and forced oscillations of piezoelectric microresonators. *Journal of Micromechanics and Microengineering*, 16:356–367
- [33] Cho I-J, Song T, Baek S-H, Yoon E (2005) A low-voltage and low-power RF MEMS series and shunt switches actuated by combination of electromagnetic and electrostatic forces. *IEEE Transactions on Microwave Theory and Techniques*, 53(7):2450–2457
- [34] Cao A, Kim J, Lin L (2007) Bi-directional electrothermal electromagnetic actuators. *Journal of Micromechanics and Microengineering*, 17:975–982
- [35] Han J S, Ko J S, Kim Y T, Kwak B M (2002) Parametric study and optimization of a micro-optical switch with a laterally driven electromagnetic microactuator. *Journal of Micromechanics and Microengineering*, 12:939–947
- [36] Park S, Hah D (2008) Pre-shaped buckled-beam actuators: theory and experiment. *Sensors and Actuators A*, 148:186–192
- [37] Greywall D (1999) Micromechanical RF filters excited by the Lorentz force. *Journal of Micromechanics and Microengineering*, 9:78–84.
- [38] Lobontiu N, Garcia E (2004) *Mechanics of Microelectromechanical Systems*. Springer, New York
- [39] Yufeng S, Wenyan C, Feng C, Weiping Z (2006) Electro-magnetically actuated valveless micropump with two flexible diaphragms. *International Journal of Advanced Manufacturing Technology*, 30:215–220

- [40] Chang H-T, Lee C-Y, Wen C-Y, Hong B-S (2007) Theoretical analysis and optimization of electromagnetic actuation in a valveless microimpedance pump. *Microelectronics Journal*, 38:791–799
- [41] Lagorce L K, Brand O, Allen M G (2002) Magnetic microactuator based on polymer magnets. *Journal of Microelectromechanical Systems*, 8(1):2–9
- [42] Cho H J, Ahn C H (2002) A bidirectional magnetic microactuator using electroplated permanent magnet arrays. *Journal of Microelectromechanical Systems*, 11(1):78–84
- [43] De S K, Aluru N R (2006) A hybrid full-Lagrangian technique for the static and dynamic analysis of magnetostatic MEMS. *Journal of Micromechanics and Microengineering*, 16:2646–2658
- [44] Mizuno M, Chetwynd D G (2003) Investigation of a resonance microgenerator. *Journal of Micromechanics and Microengineering*, 13:209–216
- [45] Külah H, Najafi K (2008) Energy scavenging from low-frequency vibrations by using frequency up-conversion for wireless sensor applications. *IEEE Sensors Journal*, 8(3):261–268
- [46] Pei-Hong Wanga, Xu-Han Dai, Dong-Ming Fang, Xiao-Lin Zha (2007) Design, fabrication and performance of a new vibration-based electromagnetic micro power generator. *Microelectronics Journal* 38:1175–1180
- [47] Judy J, Muller R (1996) Magnetic microactuation of torsional polysilicon structures. *Sensors and Actuators A*, 53:392–397
- [48] Niarchos D (2003) Magnetic MEMS: key issues and some applications. *Sensors and Actuators A*, 109:166–173
- [49] Bao M (2005) *Analysis and design principles of mems devices*. Elsevier, Amsterdam
- [50] www.sensata.com (Sensata Technologies; Attleboro, MA)
- [51] Seeger J I, Boser B E (2003) Charge control of parallel-plate, electrostatic actuators and the tip-in instability. *Journal of Microelectromechanical Systems*, 12(5):656–671
- [52] Pelesko J A, Bernstein D H (2002) *Modeling MEMS and NEMS*. CRC, Boca Raton
- [53] Nathanson H C, Wickstrom R A (1965) A resonant-gate silicon surface transistor with high-Q band-pass properties. *Applied Physics Letters*, 7(4):84–86
- [54] Nathanson H C, Newell W E, Wickstrom R A, Davis J R (1967) The resonant gate transistor. *IEEE Transaction on Electron Devices*, ED-14(3)
- [55] Ananthasuresh G K, Gupta R K, Senturia S D (1996) An approach to macromodeling of MEMS for nonlinear dynamic simulation. In *Proceeding ASME International Conference of Mechanical Engineering Congress and Exposition (MEMS)*, Atlanta, GA, 401–407
- [56] Krylov S, Maimon R (2004) Pull-in dynamics of an elastic beam actuated by continuously distributed electrostatic force. *ASME Journal of Vibrations and Acoustics*, 126(3):332–342
- [57] De S K, Aluru N R (2006) Complex Nonlinear oscillations in electrostatically actuated microstructures. *Journal of Microelectromechanical Systems*, 15:355–369
- [58] Lenci S, Rega G (2006) Control of pull-in dynamics in a nonlinear thermoelasticelectrically actuated microbeam. *Journal of Micromechanics and Microengineering*, 16:390–401
- [59] Luo A C, Wang F Y (2004) Nonlinear dynamics of a Micro-electro-mechanical system with time-varying capacitors. *Journal of Vibration and Acoustics*, 126:77–83
- [60] Elata D, Bamberger H (2006) On the dynamic pull-in of electrostatic actuators with multiple degrees of freedom and multiple voltage sources. *Journal of Microelectromechanical Systems*, 15:131–140
- [61] Fargas-Marques A, Casals-Terre J, Shkel A M (2007) Resonant pull-in condition in parallel-plate electrostatic actuators. *Journal of Microelectromechanical Systems*, 16(5):1044–1053
- [62] Seeger J I, Boser B E (2002) Parallel-plate driven oscillations and resonant pull-in. In: *Proceeding of the Solid-State Sensor, Actuator and Microsystems Workshop*, pp. 313–316
- [63] Nayfeh A H, Younis M I, Abdel-Rahman E M (2007) Dynamic pull-in phenomenon in MEMS resonators. *Journal of Nonlinear Dynamics*, 48:153–163
- [64] Alsaleem F, Younis M I, Ouakad H (2009) On the nonlinear resonances and dynamic pull-in of electrostatically actuated resonators. *Journal of Micromechanics and Microengineering*, 19:045013(1–14)

- [65] Tilmans H A, Raedt W D, Beyne E (2003) MEMS for wireless communications: from RF-MEMS components to RF-MEMS-SIP. *Journal of Micromechanics and Microengineering*, 13:139–163
- [66] Rebeiz G M (2003) RF MEMS: Theory, design, and technology. Wiley, New York
- [67] Varadan V M, Vinoy K J, Jose K A (2003) RF MEMS and their applications, Wiley, New York
- [68] <http://www.dlp.com> (Texas Instruments; Dallas, Texas)
- [69] Jaecklin V P, Linder C, de Rooij N F (1994) Line-addressable tensional micromirrors for light modulator arrays. *Sensors and Actuators A*, 41–42:324–329
- [70] Zhang X M, Chau F S, Quan C, Lam Y L, Liu A Q (2001) A study of the static characteristics of a torsional micromirror. *Sensors and Actuators A*, 90:73–81
- [71] Degani O, Socher E, Lipson A, Leitner T, Setter D J, Kaldor S, Nemirovsky Y (1998) Pull-in study of an electrostatic torsion microactuator, *Journal of Microelectromechanical Systems*, 7(4): 373–379
- [72] O. Degani, Y. Nemirovsky, “Design Considerations of Rectangular Electrostatic Torsion Actuators Based on New Analytical Pull-in Expressions,” *Journal of Microelectromechanical Systems*, 11(1):20–26
- [73] Goodenough F (1991) Airbags boom when IC accelerometers sees 50 G. *Electronic Design*, 39:45–56
- [74] Kim C J, Pisano A P, Muller R S, Lim M G (1990) Polysilicon microgripper. In proceeding of the IEEE Solid-State Sensor and Actuator Workshop, Hilton Head, Island, SC, pp 48–51
- [75] Tang W C, Nguyen T C, Howe R T (1989) Laterally driven polysilicon resonant microstructures. *Sensors Actuators A*, 20:25–32
- [76] Tang W C, Nguyen T C, Judy M W, Howe R T (1990) Electrostatic-comb drive of lateral polysilicon resonators. *Sensors Actuators A*, 21–23:328–331
- [77] Lin L, Nguyen C T-C, Howe R T, Pisano A P (1992) Microelectromechanical filers for signal processing. In Proceeding of the IEEE Micro-Electro-Mechanical Systems, Travemunde, Germany, 226–231
- [78] Hirano T, Furuhashi T, Gabriel K J, Fujita H (1992) Design, fabrication, and operation of submicron gap comb-drive microactuators. *Journal of Microelectromechanical Systems*, 1(1):52–59
- [79] Legtenberg R, Groeneveld A W, Elwenspoek M (1996) Comb-drive actuators for large displacements. *Journal of Micromechanics and Microengineering*, 6:320–329
- [80] Jaecklin V P, Lindert C, de Rooij N F, Moret J M (1992) Micromechanical comb actuators with low driving voltage. *Journal of Micromechanics and Microengineering*, 2:250–255
- [81] Kim J, Christensen D, Lin L (2005) Monolithic 2-D Scanning Mirror Using Self-Aligned Angular Vertical Comb Drives. *IEEE Photonics Technology Letters*, 17(11):2307–2309
- [82] Xie H, Pan Y, Fedder G K (2003) A CMOS-MEMS mirror with curled hinge comb drives. *Journal of Microelectromechanical Systems*, 12(4):450–457
- [83] Zhang W, Turner K L (2005) Application of parametric resonance amplification in a single-crystal silicon micro-oscillator based mass sensor. *Sensors and Actuators A*, 122:23–30
- [84] Kovacs G T (1998) Micromachined transducers sourcebook. McGraw-Hill, New York
- [85] Younis M I, Miles R, Jordy D (2006) Investigation of the response of microstructures under the combined effect of mechanical shock and electrostatic forces. *Journal of Micromechanics and Microengineering*, 16:2463–2474
- [86] Langdon R M (1985) Resonator sensors-a review. *Journal of Physics E: Scientific Instruments*, 18:103–115
- [87] Elwenspoek M, Wiegerink R (2001) Mechanical microsensors. Springer, Verlag.
- [88] Stemme G (1991) Resonant silicon sensors. *Journal of Micromechanics and Microengineering*, 1:113–125
- [89] Tilmans H A, Elwenspoek M, Fluitman J H (1992) Micro resonant force gauges. *Sensors and Actuators A*, 30:35–53
- [90] Tilmans H A, Legtenberg R (1994) Electrostatically driven vacuum-encapsulated polysilicon resonators. Part II. Theory and performance. *Sensors and Actuators A*, 45:67–84

- [91] Zook J D, Burns D W, Guckel H, Sniegowski R L, Engelstad R L, Feng Z (1992) Characteristics of polysilicon resonant microbeams. *Sensors and Actuators A*, 35:290–294
- [92] Howe R T, Muller U S (1986) Resonant microbridge vapor sensor. *IEEE Trans. Electron Devices*, ED-33:499–506
- [93] Thundat T, Wachter E A, Sharp S L, Warmack R J (1995) Detection of mercury vapor using resonating micro-cantilevers. *Applied Physical Letters*, 66:1695–1697
- [94] Ilic B, Czaplewski D, Zalalutdinov M, Craighead H G, Neuzil P, Campagnolo C, Batt C (2001) Single cell detection with micromechanical oscillators. *Journal of Vacuum Science & Technology B (Microelectronics and Nanometer Structures)*, 19:2825–2828
- [95] Waggoner P S, Craighead H G (2007) Micro- and nanomechanical sensors for environmental, chemical, and biological detection. *Lab on a Chip*, 7:1238–1255, doi:10.1039/b707401h
- [96] Chiu H-Y, Hung P, Postma H W, Bockrath M (2008) Atomic-scale mass sensing using carbon nanotube resonators. *Nano Letters*, 8(12):4342–4346
- [97] Burnes D W, Zook J D, Horning R D, Herb W R, Guckel H (1995) Sealed-cavity resonant microbeam pressure sensor. *Sensors and Actuators A*, 48:179–186

Chapter 4

Elements of Lumped-Parameter Modeling in MEMS

In this chapter, we discuss the various elements of lumped-parameter modeling in MEMS devices. These include the stiffness of microstructures, the inertia elements, and the damping mechanisms of energy dissipation in microstructures. The forces affecting microstructures due to actuation and detection are another element, which is the subject of Chap. 3. The discussion here is focused mainly on linear modeling; nonlinear modeling is introduced in the following chapter.

It is worth to note that while lumped-parameter models are easy and convenient, they may not be accurate or capable of capturing the full dynamical picture of the system. Hence, lumped-parameter models should be used for first-cut analysis to gain basic understanding of the system, which may not be realized using more complicated models. To seek more accurate quantitative results however, more complicated distributed-parameter models should be used in combination with analytical techniques, if possible, and numerical techniques, such as finite-element methods.

4.1 Stiffness of Microstructures

Determining the stiffness properties of microstructures is essential to model their behavior and analyze their motion. For lumped-parameter modeling, this means determining an equivalent stiffness coefficient of the microstructure, k , which can be used as a spring constant in the model. A spring-like behavior results from a variety of microstructures configurations depending on their geometry, materials properties, and boundary conditions. Microstructures can behave linearly or nonlinearly depending on many parameters, such as their geometry and loading conditions. This section assumes linear behavior, in which case a single constant stiffness coefficient is sufficient for modeling. Extraction of nonlinear stiffness coefficients is not discussed in this chapter. Methods for nonlinear system identifications based on perturbation models can be found for example in [1] and [2]. In the following chapters, we discuss some of the methods to extract nonlinear stiffness coefficients, for instance based on the Galerkin decomposition.

The stiffness coefficient of a microstructure can be obtained experimentally, computationally, and analytically. If possible, one should make use of all the possible and available techniques and compare among them to come up with an accurate estimation. One key fact to keep in mind is that a stiffness coefficient depends on the kind of force or moment that affects the microstructure. For example, k of a cantilever actuated by distributed load is different from that due to a point load at the tip. Hence, when extracting k using experimental, computational, or analytical method, it is important to account for this fact in comparison with what the device experiences in the actual operating conditions. Nevertheless, the extracted coefficients due to different loads can be related and one can infer one by knowing the other. For example, one can determine k of a cantilever beam actuated by distributed load if given k of the beam when actuated by a point load at the tip. Another key factor is the influence of residual stresses. These can significantly affect the stiffness of microstructures of immovable edges, such as clamped–clamped beams, and hence need to be accounted for properly in the stiffness estimation.

4.1.1 Experimental Methods

Experimental techniques for extracting stiffness are mostly based on static measurements. For example, applying a force at the tip of a microstructure and measuring its displacement result in a force–displacement curve. The slope of the curve’s linear regime gives the linear stiffness coefficient. This can be done using an atomic force microscope (AFM) or a Nano-indentation machine. Figure 4.1 shows an example of the results obtained to extract the effective stiffness of two cantilever beams carrying a proof mass of the capacitive accelerometer of Fig. 3.17. Also, experimental techniques can be utilized to extract parameters to be used in analytical formulas to calculate the stiffness coefficients. For example, stress–strain curves can be used

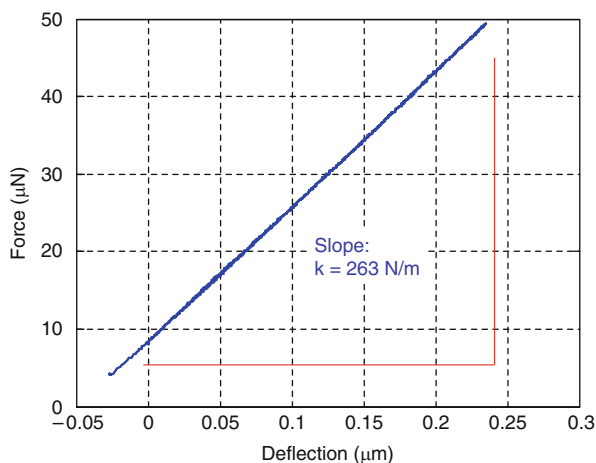


Fig. 4.1 Experimentally measured force–deflection curve of the cantilever beams of a capacitive accelerometer using a Nano-indentation machine

to extract Young's modulus, which is then implemented in the stiffness formulas. Another example is the so-called M-Test, pioneered by Osterberg and Senturia [3]. In this test, an array of electrostatically actuated microstructures, such as cantilever and clamped-clamped microbeams, of various lengths is tested to determine their pull-in voltages. From the results, the amount of residual stress and Young's modulus of the thin films on the chip are determined. These are then used in the appropriate analytical formulas to extract k of the microstructures on the chip.

In addition to static measurements, dynamic measurements can also be utilized, although they are more complicated and require prior knowledge of other parameters of the system, such as inertia. For instance, the microstructure can be actuated by a random or sinusoidal excitation and its dynamic response is measured, for example optically using a laser Doppler vibrometer, or by other methods, such as capacitive detection. The actuation can be through any readily embedded actuation method, if any, such as electrostatic, electrothermal, and piezoelectric actuation. Exciting a microstructure with a shaker, as the case in the macro world, can be less useful for MEMS since it is hard to reach high excitation frequencies, close to the natural frequencies of microstructures. There are other experimental techniques to extract frequency–response curves and the natural frequencies of microstructures, including those without an embedded actuation mechanism, such as the excitation using pulses generated of a PZT transducer [4] and a bulk acoustic wave hammer generated by a pulsed ultrasonic transducer [5]. Figure 4.2 depicts an example of a frequency–response curve. From the figure, the fundamental natural frequency, corresponding to the maximum amplitude response, can be read. If the mass of the microstructure is known, k can be estimated. Also, in the quasi-static regime, particularly the response near very small frequency can be used. The amplitude in this case is $X_0/(F/k)$, where F is the amplitude of excitation and X_0 is the static response of the microstructure to an equivalent static force. Hence, if X_0 is known from previous static measurements, an estimation of k can be obtained.

Additional experimental techniques can be utilized for **electrostatic MEMS**. In the case of longitudinal comb-drive actuators, measurements of the deflection of the actuator versus the driving voltage, as shown in Example 3.2, can yield the effective

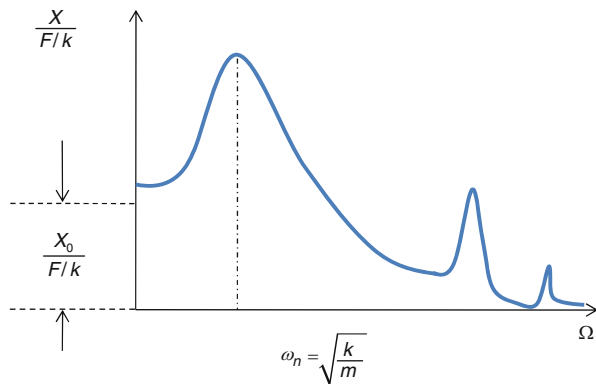
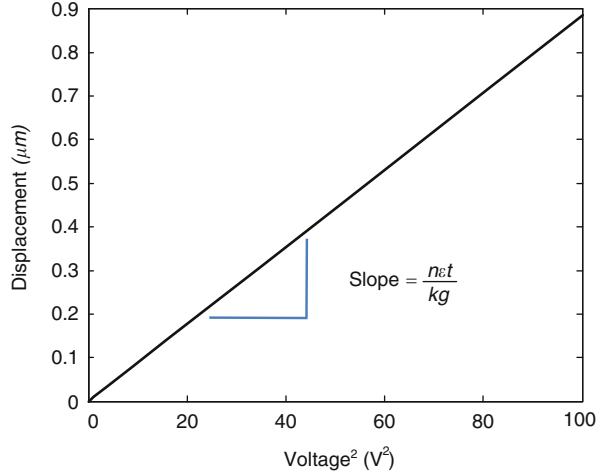


Fig. 4.2 An example of a frequency–response curve due to a dynamic testing of a microstructure

Fig. 4.3 Displacement versus the driving voltage (squared) of a comb-drive actuator



stiffness of the tethers of the actuator, if the other parameters, such as the thickness of each finger and their numbers are known [6]. As an example, consider the replot of Fig. 3.24 in Fig. 4.3, but with the voltage squared. Recall that the deflection and the voltage are related according to

$$y = \left(\frac{n\epsilon t}{kg} \right) V^2. \quad (4.1)$$

From the slope of the straight line, k can be obtained. In the case of parallel-plate capacitors, the pull-in voltage can be utilized [7]. Using Eq. (3.27), and assuming the other parameters of the equation are known, k can be obtained according to

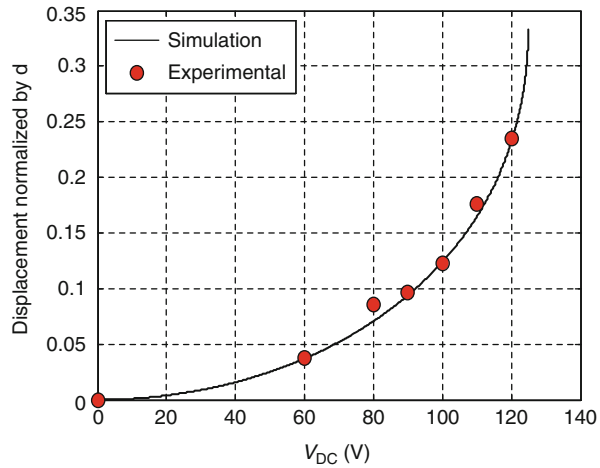
$$k = \frac{27\epsilon A V_{\text{pull}}^2}{8d^3}. \quad (4.2)$$

However, one should be careful before using this equation. First, pull-in is usually measured experimentally by applying a step voltage load. The pull-in of this case is called dynamic or transient pull-in, which is typically below that of Eq. (3.27). In vacuum, transient pull-in can be as low as 92% of the value of Eq. (3.26). Because of this and the fact that pull-in is a single measurement with many possibilities of errors, it is recommended, in addition to Eq. (4.2), to rely on measuring the deflection of the moveable electrode for various values of actuation voltage. According to Eq. (3.26), the deflection of the moveable electrode for a given voltage load is given by

$$x^3 - 2dx^2 + d^2x - \frac{\epsilon A V_{\text{DC}}^2}{2k} = 0. \quad (4.3)$$

By solving Eq. (4.3) for each voltage value, considering the smallest solution (since the other two are either unstable or nonphysical), and fitting the results with the measured $V_{\text{DC}}-x$ curve, a value of k can be obtained. Figure 4.4 shows an example

Fig. 4.4 An example of measured and simulated displacement versus the driving voltage of the capacitive accelerometer of Fig. 3.17



of measured $V_{DC}-x$ points and the fitted curve according to Eq. (4.3). Also, one can read the pull-in voltage from the same figure, which is near 123 V. Hence, based on the figure, one can use Eq. (4.3) and double check the result with Eq. (4.2). Similar procedure can be followed for torsional actuators and mirrors based on Eq. (3.40) or Eq. (3.41) (see Problem 1).

4.1.2 Computational Methods

Computational methods, such as finite-element and finite-difference methods, can be also used to determine the stiffness of microstructures. A model is built for the microstructure. Then a small force, to ensure linear response, either distributed or point load depending on the intended application is applied and the deflection of the microstructure is obtained at the desired location of interest, such as the tip of cantilever-like structures or the center of diaphragm-like structures. The slope of the deflection–force curve represents the linear stiffness coefficient k , or based on one data point, $k = F/\delta$, where δ is the static deflection corresponding to the force F . For electrostatic MEMS, the assumed force is taken to be fully distributed on the microstructure (pressure) to imitate the effect of the electrostatic force [3, 8]. In addition to the static simulation, one can also determine the natural frequency of the microstructure computationally. Then, if the mass of the microstructure is known, k is evaluated.

4.1.3 Analytical Methods

If the microstructure has a simple geometry, or at least can be approximated as one, then analytical formulas can be used to estimate its stiffness coefficient. These

formulas are derived by solving the differential equation governing the displacement of the structure when subjected to a specific force, point or distributed load. Then, by relating the maximum deflection of the microstructure δ to the applied force F , the stiffness coefficient is calculated by $k = F/\delta$. Another method to calculate k is based on the energy method of Castigliano, which is discussed in details in [9, 10]. Table 4.1 presents the linear stiffness coefficient for some of the common configurations of MEMS structures. Caution must be taken when using the table. First, the coefficients in the table are intended for linear problems only. Second, when calculating the natural frequencies of these structures, an appropriate effective mass, which is discussed next section, should be used. The effective mass, like the stiffness coefficient, varies depending on the loading type.

It is very often in MEMS to have a microstructure supported by more than one flexible microstructure. For example, the proof mass of inertia sensors, such as comb-drive and bulk-micromachined accelerometers, is usually supported by more than one beam to help stabilize and control its motion. These microstructures can be treated as springs connected in series or in parallel. Based on this, an equivalent spring constant can be extracted to represent them in lumped modeling. The rules for equivalent springs are the following: If two springs of stiffness coefficients k_1 and k_2 share the same nodal (tip) displacement, Fig. 4.5a, they are said to be acting in parallel and their equivalent stiffness coefficient k_p is given by

$$k_p = k_1 + k_2. \quad (4.4)$$

If on the other hand the two springs are actuated by the same force, Fig. 4.5b, they are said to be acting in series and their equivalent stiffness coefficient k_s is given by

$$\frac{1}{k_s} = \frac{1}{k_1} + \frac{1}{k_2}. \quad (4.5)$$

The same rules apply for more than two springs. One can note that parallel configuration results in higher overall stiffness whereas a series configuration lowers the total stiffness.

A final note to be mentioned is regarding calculating the effective stiffness of torsional actuators, such as that of Fig. 3.23. Typically, the upper plate of the actuator is supported by two torsional springs, which act in parallel. Each spring is made of a bar of a rectangular cross section, Fig. 3.23b, of width w and thickness t , where $w > t$. The effective stiffness of each spring can be calculated according to case 2 of Table 4.1, where J_P is given by [11]

$$J_P = \frac{1}{3}t^3w \left(1 - \frac{192t}{\pi^5w} \sum_{n=0}^{\infty} \frac{1}{[2n+1]^5} \tanh \left[\frac{(2n+1)\pi w}{2t} \right] \right). \quad (4.6)$$

The summation in Eq. (4.6) converges very quickly; within two terms, high accuracy is obtained.

Table 4.1 The linear stiffness coefficient k of some of the common structure configurations in MEMS. The unit of k for all loading types is force/length. For wide beams ($b > 5h$) of cases 3–9, replace E with $E/(1 - \nu^2)$, where ν is the Poisson’s ratio. When calculating the natural frequency of a flexible structure alone, use an “effective” mass for the structure


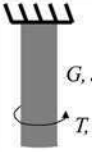
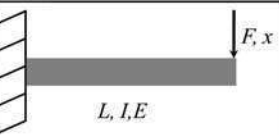
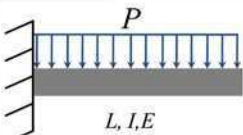
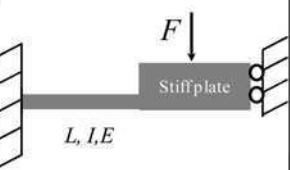
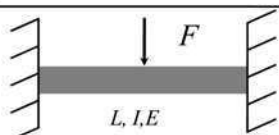
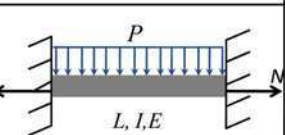
1) Axially loaded bar	 <p>E, A, L F, x</p>	$k = \frac{EA}{L}$ <p>E: Modulus of elasticity A: Area of cross section L: Length of bar</p>
2) Rod under torque	 <p>G, J_p, L T, θ</p>	$k = \frac{GJ_p}{L}$ <p>J_p: Polar moment of inertia of the cross section G: Shear modulus L: Length of rod</p>
3) Cantilever beam under point load at the tip	 <p>L, I, E F, x</p>	$k = \frac{3EI}{L^3}$ <p>E: Modulus of elasticity I: Moment of inertia of the cross section L: Length of bar</p>
4) Cantilever beam under uniformly distributed pressure	 <p>L, I, E P</p>	$k = \frac{8EI}{L^3}$
5) A cantilever beam with a stiff plate at the tip (fixed-guided beam)	 <p>L, I, E F Stiff plate</p>	$k = \frac{12EI}{L^3}$
6) Clamped-clamped beam under a point load in the middle	 <p>L, I, E F</p>	$k = \frac{192EI}{L^3}$
7) Clamped-clamped beam under uniformly distributed pressure load and an axial force	 <p>L, I, E P N</p>	$k = \frac{384EI}{L^3} + \frac{8.32N}{L}$ <p>N: axial force in Newton. *[12]</p>

Table 4.1 (continued)

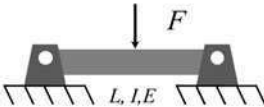
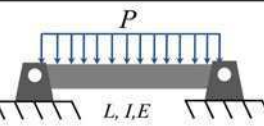
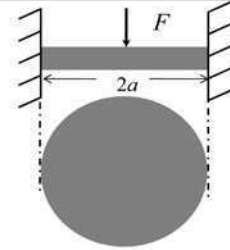
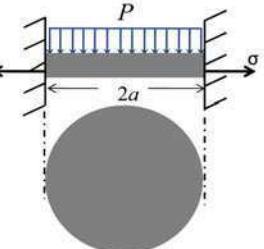
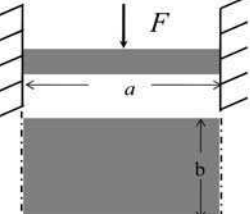
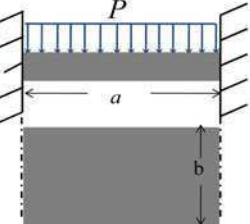
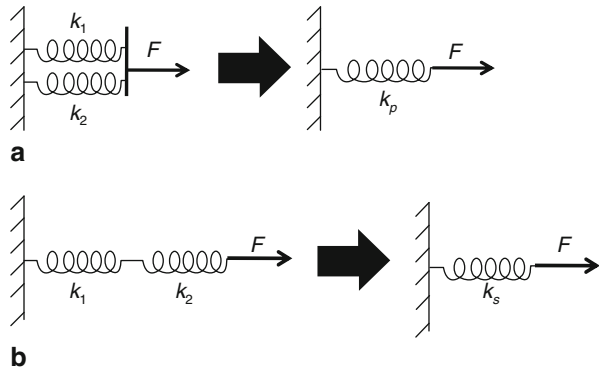
8) Hinged-hinged beam under a point load in the middle		$k = \frac{48EI}{L^3}$										
9) Hinged-hinged beam under uniformly distributed pressure load and an axial force		$k = \frac{384EI}{5L^3}$										
10) Clamped circular plate with a point load in the middle		$k = \frac{4.189Eh^3}{a^2(1-\nu^2)}$ <p>E: Modulus of elasticity h: Thickness of the plate a: Radius of the plate ν: Poisson's ratio</p> <p>*[13]</p>										
11) Clamped circular plate under a uniform pressure and radial in-plane stress.		$k = \frac{16\pi Et^3}{3a^2(1-\nu^2)} + 4\pi\sigma t$ <p>σ: in-plane stress (force/area)</p> <p>*[14]</p>										
12) Fully clamped rectangular plate with a point load in the middle		$k = \frac{Eh^3}{12\alpha a^2(1-\nu^2)}$ <p>a: Length of the plate b: Width of the plate</p> <table><tr><td>b/a</td><td>1</td><td>1.4</td><td>1.8</td><td>2</td></tr><tr><td>α</td><td>0.0056</td><td>0.0069</td><td>0.0072</td><td>0.00722</td></tr></table> <p>*[13]</p>	b/a	1	1.4	1.8	2	α	0.0056	0.0069	0.0072	0.00722
b/a	1	1.4	1.8	2								
α	0.0056	0.0069	0.0072	0.00722								
13) Fully clamped rectangular plate with uniformly distributed load		$k = \frac{aEh^3}{\alpha b^3}$ <p>a: Length of the plate b: Width of the plate</p> <table><tr><td>a/b</td><td>1</td><td>1.4</td><td>1.8</td><td>2</td></tr><tr><td>α</td><td>0.0138</td><td>0.0226</td><td>0.0267</td><td>0.0277</td></tr></table> <p>*[15]</p>	a/b	1	1.4	1.8	2	α	0.0138	0.0226	0.0267	0.0277
a/b	1	1.4	1.8	2								
α	0.0138	0.0226	0.0267	0.0277								

Fig. 4.5 Equivalent springs for **a** parallel and **b** series configuration



Example 4.1: Consider a clamped–clamped microbeam, which forms one side of a capacitor [8], of length $L = 510 \mu\text{m}$, thickness $h = 1.5 \mu\text{m}$, width $b = 100 \mu\text{m}$, and air-gap width $d = 1.18 \mu\text{m}$. Consider $E = 154 \text{ GPa}$ and $\rho = 2,330 \text{ kg/m}^3$. Assuming linear behavior of the microbeam and using a lumped parameter model, estimate the pull-in voltage for the below cases:

- (a) Assuming zero axial strain.
- (b) Assuming 10^{-5} axial strain.
- (c) Assuming 10^{-2} axial strain.

Solution: For this problem, we need to use Eq. (3.27):

$$V_{\text{pull}} = \sqrt{\frac{8kd^3}{27\varepsilon A}}. \quad (\text{a})$$

The above requires the calculation of the stiffness coefficient k . Since the electrostatic force acts as a kind of uniformly distributed load on the microbeam, we refer to case 7 of Table 4.1:

$$k = \frac{384EI}{L^3} + \frac{8.32N}{L}. \quad (\text{b})$$

The area moment of inertia I for a rectangular cross section is calculated as

$$I = \frac{bh^3}{12}. \quad (\text{c})$$

The axial strain ε is related to the axial force N as

$$N = (bh)E\varepsilon. \quad (\text{d})$$

Since this is a wide beam ($b > 5h$), then E should be replaced with $E/(1 - \nu^2)$ in Eqs. (b) and (d). Plugging the numbers in Eqs. (a)–(d) yield the following answers:

Case	k (N/m)	V_{pull} (V)
(a)	13.78	3.86
(b)	17.92	4.4
(c)	4,155	66.94

The results of the above table are close to these reported in [8] and are less accurate compared to the results based on distributed-parameter and nonlinear models.

Example 4.2: Write down an expression for the pull-in voltage of the stiff plate shown in Fig. 4.6 if it forms an upper electrode of a parallel-plate capacitor with a distance d from the lower electrode.

Solution: Figure 4.6 shows a stiff plate connected to four cantilever beams. Since the tip of each cantilever undergoes the same deflection upon the motion of the proof mass, they can be modeled as four springs in parallel. The stiffness of each can be calculated according to case 5 of Table 4.1. Hence,

$$k_p = 4k = 4 \times \frac{12EI}{L^3} = 4 \times \frac{12E\left(\frac{wt^3}{12}\right)}{L^3} = \frac{4Ewt^3}{L^3}. \quad (\text{a})$$

Hence, according to Eq. (3.27)

$$V_{\text{pull}} = \sqrt{\frac{8\left(\frac{4Ewt^3}{L^3}\right)d^3}{27\varepsilon A}} = \sqrt{\frac{32Ewt^3d^3}{27L^3\varepsilon A}}. \quad (\text{b})$$

Example 4.3: Consider the torsional actuator of Xio et al. [16] of the parameters in the table below. The actuator is supported by two torsional springs, each of a rectangular cross section of $t = 4.26 \mu\text{m}$, $w = 23.4 \mu\text{m}$, and $l = 1,220 \mu\text{m}$. Assume the shear modulus of the springs $G = 73 \text{ GPa}$, calculate the pull-in voltage of the device.

a_1 (μm)	a_2 (μm)	a_3 (μm)	d (μm)	b (μm)
0	700	700	21.2	700

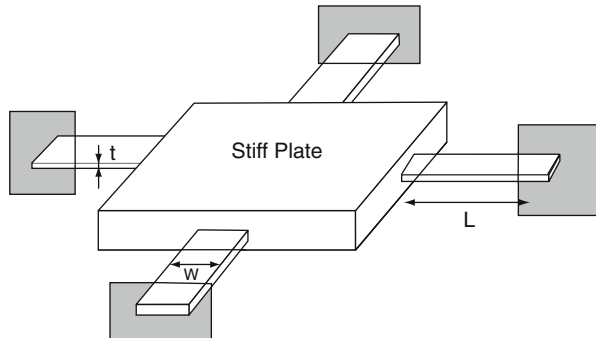


Fig. 4.6 A stiff plate supported by four cantilever beams

Solution: The pull-in voltage can be found from Eq. (3.41). For this, we need to determine K_t . Because of the two parallel springs, K_t can be expressed according to case 2 of Table 4.1 as

$$K_t = 2 \left(\frac{GJ_p}{l} \right) \quad (a)$$

where J_p is calculated from Eq. (4.6). Substituting the numbers gives that $K_t \approx 6.39 \times 10^{-8} \text{ Nm}$ and $V_{\text{pull}} = 15.4 \text{ V}$.

4.2 Spring–Mass Models

A spring–mass model is considered the backbone of lumped-parameter modeling. Such a model aims to capture both the static and the undamped dynamic behavior of the system in the neighborhood of the natural frequency of interest, which is usually the fundamental natural frequency [8]. There are several methods to construct a spring–mass model. One method, called the Galerkin’s method [17], is based on expressing the dynamics of the structure in terms of the dominant or excited mode-shape(s) $\phi_i(x)$ multiplied by the modal coordinate or generalized variable(s) $u_i(t)$, where x is the spatial location on the structure and t is time. Hence, the displacement of the microstructure $w(x, t)$ is expressed as

$$w(x, t) = \sum_i^n \phi_i(x) u_i(t) \quad (4.7)$$

where n is the number of assumed activated or dominant modes. The modeshapes are taken to be the undamped–unforced of the microstructure. It is common to use a single modeshape, which is the fundamental mode. The modeshapes can be estimated analytically for simple microstructures, such as beams, plates, and diaphragms. For complicated microstructures, it can be calculated from a finite-element analysis. In addition to the modeshapes, one needs to calculate the corresponding natural frequencies (ω_i , $i = 1, \dots, n$). This is also done using either analytical methods for simple structures or finite-element methods for complicated geometry. Then, the equations of motion of the microstructure are written as

$$\ddot{u}_i + \omega_i^2 u_i = f_i; \quad i = 1, \dots, n \quad (4.8)$$

where f_i is the modal force, which is the force that affects the particular mode, and is related to the actual force per unit length F by $f_i = \int_L \phi_i F dx$. Equation (4.8) can be solved analytically or numerically, depending on f_i . This approach is further clarified in Chap. 6 when studying distributed-parameter systems.

Another method to construct a spring–mass model is to use the preknowledge of the stiffness coefficient of a microstructure, from the techniques discussed in Sect. 4.1, and the natural frequency of the system near the mode of interest to calculate

an effective mass for the system. The effective mass refers to the fact that for a flexible microstructure of distributed mass, not all of its portions may participate in a particular mode of motion nor do they necessarily participate in the same proportion. For example, in the case of a cantilever beam, the mass near the support almost does not contribute to the motion. The natural frequency of the microstructure can be determined experimentally, by finite-element methods, and by energy and Rayleigh's quotient methods [18]. The effective mass is then calculated according to

$$m_{\text{eff}} = \frac{k}{\omega_i^2}. \quad (4.9)$$

For example, the effective mass of the capacitive sensor of Fig. 3.17 was estimated by measuring the natural frequency of the system using a laser Doppler vibrometer, which came near 192 Hz [19]. Then, the stiffness of the cantilever beams of the device was determined as explained in Fig. 4.4, which was near $k = 215 \text{ N/m}$. Hence, the effective mass of the cantilevers-proof mass system was calculated according to Eq. (4.9) and found to be $= 215/(2\pi \times 192)^2 = 0.148 \text{ mg}$. Another example, Ijntema et al. [8] calculated the natural frequency of a clamped-clamped microbeam including the effects of DC voltage and axial load using Rayleigh's quotient method. Then, using the formula of case 7 of Table 4.1 and Eq. (4.9), they estimated the effective mass. A third example, the natural frequency of a cantilever microbeam, which is obtained analytically based on a distributed parameter model, can be expressed as $3.52\sqrt{EI/(L^3m)}$, where m is the total mass of the beam. The stiffness coefficient of the cantilever, according to case 3 of Table 4.1, is $k = 3EI/L^3$. Hence, based on Eq. (4.9), the effective mass of the cantilever microbeam is

$$m_{\text{eff}} = \frac{k}{\omega_i^2} = \frac{3EI/L^3}{3.52^2 EI/L^3 m} = 0.242m.$$

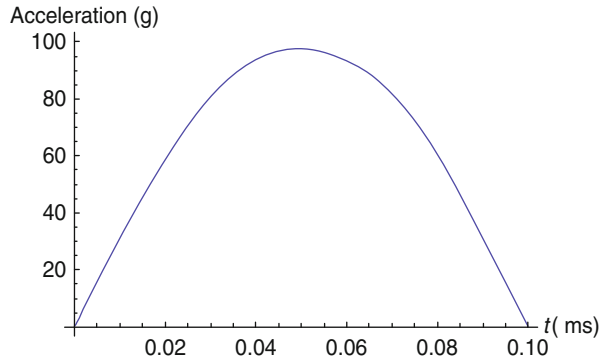
One should note that this effective mass of the cantilever beam should be used in a spring-mass model to simulate cases when the beam is loaded at its tip or when a mass attached to its tip. In the case of a distributed force, another effective mass should be calculated according to case 4 of Table 4.1, which is

$$m_{\text{eff}} = \frac{8EI/L^3}{3.52^2 EI/L^3 m} = 0.646m.$$

Example 4.4 below clarifies further this point.

Example 4.4: Mechanical shock affects microstructures in the form of supports excitation and can be modeled as a uniformly distributed force. Use an undamped single-degree-of-freedom model to calculate the response of a cantilever microbeam to the half-sine acceleration (shock) pulse shown in Fig. 4.7. Assume the microbeam made of silicon with density $\rho = 2,332 \text{ kg/m}^3$ and modulus of elasticity $E = 169 \text{ GPa}$. Assume the microbeam of length $L = 900 \mu\text{m}$, thickness $h = 1.0 \mu\text{m}$, and width $b = 100 \mu\text{m}$.

Fig. 4.7 An acceleration pulse



Solution: The force affecting the cantilever beam is a uniformly distributed load expressed as the mass of the beam times the pulse acceleration. One approach to solve this example is to use the effective mass $0.646m$ and the stiffness coefficient of case 4 of Table 4.1 $k = 8EI/L^3$. Hence, the equation of motion governing the tip deflection x of the cantilever becomes

$$(0.646m)\ddot{x} + \left(\frac{8EI}{L^3}\right)x = mG(t) \quad (a)$$

where $G(t) = a \sin\left(\frac{\pi}{T}t\right)u(t) + a \sin\left[\frac{\pi}{T}(t - T)\right]u(t - T)$ is the mathematical representation for the half-sine pulse of maximum magnitude a and duration T and $u(t)$ is the Heave-side function. From Fig. 4.7, $a = 100 \text{ g}$ ($g = 9.81 \text{ m/s}^2$) and $T = 0.1 \text{ ms}$. Equation (a) can be solved using the convolution integral approach of Sect. 2.6 or it can be integrated numerically in time. The results are shown in Fig. 4.8. Another approach to solve the problem is to use Eqs. (4.7) and (4.8) and express the response

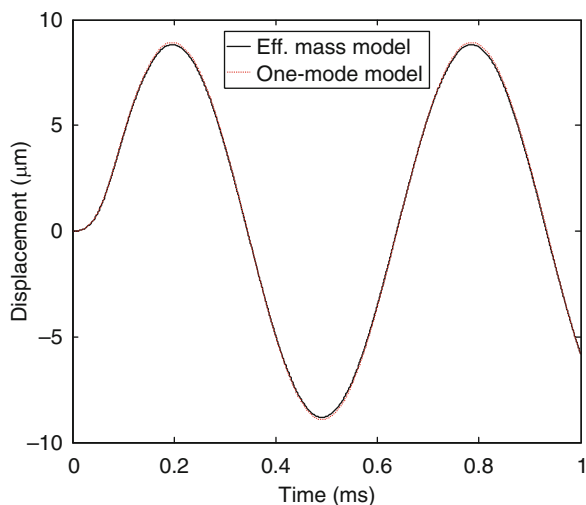


Fig. 4.8 The response of a cantilever beam to acceleration pulse using two lumped-parameter models

in terms of the first mode of the microbeam $\phi(x)$ and the corresponding modal coordinate $u_1(t)$. The first modeshape of a cantilever microbeam can be expressed analytically as

$$\begin{aligned}\phi(x) = & \cosh\left[1.875\frac{x}{L}\right] - \cos\left[1.875\frac{x}{L}\right] \\ & + 0.734\left(\sin\left[1.875\frac{x}{L}\right] - \sinh\left[1.8751\frac{x}{L}\right]\right).\end{aligned}\quad (b)$$

The first natural frequency is expressed as $3.52\sqrt{EI/(L^3m)}$. Hence, according to Eq. (4.8), the modal equation is expressed as

$$\ddot{u}_1 + 3.52^2 \frac{EI}{mL^3} u_1 = \frac{m}{L} \int_0^L G(t)\phi(x)dx = mG(t)(0.783). \quad (c)$$

Note that when dividing Eq. (a) by the coefficient 0.646 m, Eq. (c) becomes the same as Eq. (a), except that the forcing term of Eq. (a) is twice that of Eq. (c). Equation (a) can be solved analytically or integrated numerically in time to yield $u_1(t)$. Then, to obtain the displacement at the cantilever tip, Eq. (4.7) is used:

$$w(L) = \phi_1(L)u_1(t) = 2u_1(t). \quad (d)$$

Figure 4.8 shows the results of both approaches.

Another approximate method to estimate the effective mass is the so-called the Rayleigh's method [20–22]. To illustrate this method, consider as an example the case of a cantilever beam of mass m with a proof mass at the tip of mass m_p , Fig. 4.9. We would like to determine an equivalent mass for the cantilever beam and then determine the natural frequency of the system. For this, the kinetic energy KE of the cantilever beam is written in the form of

$$KE = \frac{1}{2} m_{\text{eff}} \dot{w}^2(L) \quad (4.10)$$

where $\dot{w}(L)$ is the velocity of the cantilever tip. The deflection of the beam $w(x)$ due to a point load P (since the effect of the proof mass resembles a point load) can be expressed as [10]

$$w(x) = \frac{x^2(3L - x)}{2L^3} w(L) \quad (4.11a)$$

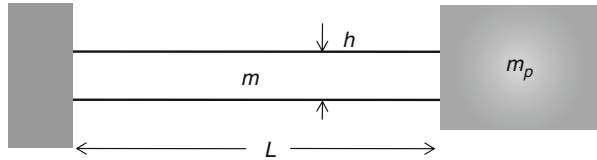


Fig. 4.9 A cantilever beam carrying a proof mass at the tip

where $w(L) = PL^3/(3EI)$. Next, an approximation is made to calculate the velocity of the beam by differentiating Eq. (4.11a) with respect to time while keeping x fixed, that is

$$\dot{w}(x) = \frac{x^2(3L - x)}{2L^3} \dot{w}(L). \quad (4.11b)$$

The kinetic energy of the whole microbeam can be calculated as

$$KE = \int_0^L \dot{w}^2(x) dm = \int_0^L \hat{m} \dot{w}^2(x) dx \quad (4.12)$$

where \hat{m} is the mass per unit length. Substituting Eq. (4.11b) into (4.12) yields

$$KE = \int_0^L \hat{m} \left[\frac{x^2(3L - x)}{2L^3} \dot{w}(L) \right]^2 dx = \frac{1}{2} \left(\frac{33m}{140} \right) \dot{w}^2(L). \quad (4.13)$$

Equating the outcome of Eq. (4.13) to Eq. (4.10) gives $m_{\text{eff}} = 0.236m$, which is close to what is found using Eq. (4.9) combined with Table 4.1. The natural frequency of the system of Fig. 4.9 is $\omega = \sqrt{k/(0.236m + m_p)}$. It is noted here that the mass of the cantilever can have a considerable impact on the natural frequency if it is comparable to that of the proof mass. In general, it is acceptable to ignore the mass of the cantilever if the ratio $m_p/m > 2.3$ [13]. More on this is in Sect. 6.4.3.

Following a similar procedure, the effective mass can be calculated for other macrostructures. Table 4.2 presents results for selected cases. The Rayleigh's method has been used commonly to estimate the effective stiffness of comb-drive actuators, which are composed of the tethers and the shuttle mass [6, 23–26].

4.3 Damping in MEMS

Damping in MEMS devices strongly affects their performance, design, and control. Damping influences the behavior of MEMS in various ways, depending on their design criteria and operating conditions. For instance, in microaccelerometers, high damping (near critical) is desirable to achieve the widest range of operation and

Table 4.2 The effective mass (or inertia element) of selected microstructures when carrying concentrated masses [21]

Case	Effective Inertia Element
Cantilever beam with a mass at the tip	$m_{\text{eff}} = 0.236m$
Clamped-clamped beam with a mass at the center	$m_{\text{eff}} = 0.375m$
Simply-supported beam with a mass at the center	$m_{\text{eff}} = 0.486m$
Bar in axial motion with a mass at the tip	$m_{\text{eff}} = 0.333m$
Rod in twisting motion with a mass at the tip	$I_{\text{eff}} = 0.333I_r^a$

^a I_r refers to the polar mass moment of inertia of the rod

prevent large resonance responses due to external disturbances, which may result in a mechanical or an electrical failure. On the other hand, in resonant sensors, a high quality factor is required for achieving high sensitivity and resolution. Hence, it is essential to understand the damping mechanisms in MEMS devices to optimize their designs. This section presents an introduction to some of the common dissipation mechanisms in MEMS with a focus on viscous damping, since it is the most common and dominant mechanism.

4.3.1 Mechanisms of Energy Losses

There are several mechanisms of energy dissipation in MEMS, Fig. 4.10. These can be classified into extrinsic or external, which are related to the environment of the moving structure, and intrinsic or internal, which are related to the material of the structure itself and its method of fabrication. Intrinsic losses in MEMS, especially for single-crystal materials like silicon, are very low and their contribution to the total damping is almost negligible compared to extrinsic losses. However, they become important when attempting to achieve extremely high quality factors of resonators by minimizing or eliminating the extrinsic sources of damping. In this case, the quality factor is capped by the intrinsic losses. The most common extrinsic dissipation mechanisms include losses into the surrounding fluid due viscous damping, losses due to acoustic radiation, and losses into the structure mounts. Each source of energy loss can be described quantitatively in terms of a corresponding quality factor Q_j . The total quality factor Q can be expressed in terms of the individual quality factors as

$$\frac{1}{Q} = \frac{1}{Q_1} + \frac{1}{Q_2} + \cdots = \sum_j \frac{1}{Q_j}. \quad (4.14)$$

It is clear from Eq. (4.14) that the total quality factor is limited by the smallest component Q_j , i.e., Q cannot exceed any of its components Q_j . Hence, when analyzing

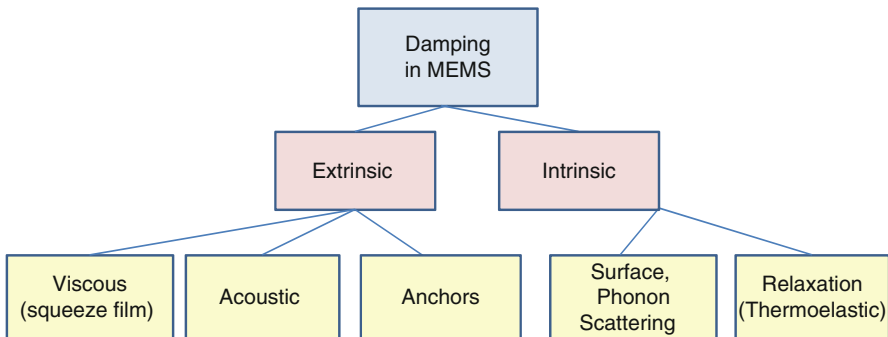


Fig. 4.10 Damping mechanisms in MEMS

damping in MEMS, a vital step is to determine the dominant dissipation mechanism since it controls the overall damping. The quality factor can be defined as in Chap. 2. It is also defined as [27]

$$Q = 2\pi \frac{\text{maximum energy stored in one period}}{\text{dissipated energy per period}}. \quad (4.15)$$

Support losses, also called anchor losses, arise from uncanceled shear forces and moments at the end supports, which transfer energy from the vibrating structure to the substrate through propagating waves. According to Hao et al. [28], the contribution from the shear forces on the losses are much greater than those of the moments. Based on this and assuming the supports of vibrating microbeams to be 2-D semi-infinite and infinite thin plates, Hao et al. [28] derived the below analytical expressions for supports losses of cantilever Q_s^{cn} and clamped–clamped Q_s^{cl} microbeams:

$$Q_s^{\text{cn}} = \alpha_{\text{cn}} \left(\frac{L}{t} \right)^3 \quad (4.16)$$

$$Q_s^{\text{cl}} = \alpha_{\text{cl}} \left(\frac{L}{t} \right)^3 \quad (4.17)$$

where L and t are the length and thickness of the microbeams, respectively, and α_{cn} and α_{cl} are coefficients for the cantilever and clamped–clamped microbeams, which depend on the mode of vibration and the Poisson's ratio. Assuming a Poisson's ratio = 0.28, the coefficients are given in Table 4.3 for several vibration modes. Hosaka et al. [29] predicted $\alpha_{\text{cn}} = 2.17$ for the first mode of vibration of a cantilever beam, which is close to the value in Table 4.3.

Support losses can be minimized by building a symmetric resonator so that it vibrates in a balanced way without moving its center of mass. Hence, the sums of the forces and moments due to the excitation are zero over a period of oscillation [30]. Support losses can also be minimized by a proper design of the vibrating structure and its mounting mechanism, such as a double-ended tuning fork or a triple beam structure [27], and by isolating the vibrating element from the mount using a mechanical isolation mechanism. According to Zook et al. [31], such special designs might introduce complicated modes of motion. Hence, they recommend designing resonators having fundamental natural frequencies much greater than the vibration modes in the supporting structure.

Acoustic radiation results from sound waves generated by the movement of the mechanical element in a direction normal to its surface. This mechanism can be

Table 4.3 The coefficients of anchor losses to be used with Eqs. (4.16) and (4.17)

Mode no.	1	2	3	4	5
α_{cn}	2.081	0.173	0.064	0.033	0.02
α_{cl}	0.638	0.223	0.114	0.069	0.046

significant if the acoustic wavelength is equal to or less than a typical dimension of the mechanical element, which is uncommon in MEMS.

Viscous or air damping in MEMS usually takes one of three forms: drag, sliding, and squeezed film. The last two are related to the motion of microstructures in proximity to each other or to the substrate and the former is related to the generic motion of a microstructure in air while being away from any nearby surfaces. Among all damping sources, viscous damping is the most significant source of energy loss in MEMS.

4.3.2 Air Damping Fundamentals

Before we start discussion about air and viscous damping in MEMS, it is fruitful to introduce some of the key concepts. The first one is the so-called Navier–Stokes equation in fluid. This equation results from the application of Newton’s second law on a control volume of fluid. It describes the motion of the volume of fluid in the presence of body forces, such as gravity, net pressure acting on the volume, inertia forces, and viscous forces. Navier–Stokes is a nonlinear 3D partial-differential equation, which is very challenging to be solved even numerically. Special cases, assumptions, and simplifications have to be made to reduce it to simpler equations that can be easily solved numerically and even analytically. Toward this, normalization of the equation variables has been made to enable comparison among the contribution of the various forces in the equation. This results in a number of nondimensional or universal numbers. One of them, which is of special importance in MEMS, is the Reynolds number Re . It is a measure for the strength of the inertial forces compared to viscous forces and is defined as

$$Re = \frac{u\rho L}{\mu} \quad (4.18)$$

where u is the speed of fluid, ρ and μ are the density and viscosity of the fluid, respectively, and L is a characteristic length, for example the diameter of the tube where the fluid flows. The flows of fluid can be classified into laminar or turbulent depending on this number. If $Re < 2,300$, the flow is said to be laminar (fluid flows in parallel layers with no mixing among them), otherwise it is said to be turbulent (chaotic) or in transient state to turbulence. In MEMS, Re typically is much less than unity, and hence the flow is always laminar. This indicates that it is safe to neglect the effect of inertia forces of the fluid in MEMS since they are much less than the viscous forces.

Next, we discuss parameters related to pressure. Pressure has too many units (it should be given the award of the physical variable with the most units!). Before getting deeper into the topic, it is good to remind ourselves with some of the popular units and conversions of pressure. Table 4.4 summarizes some of these.

The second parameter of interest is the mean free-path of gases λ . It is defined as the average distance that a gas particle travels between two successive collisions.

Table 4.4 Some of the common units of pressure and their conversion factors

To convert	Into	Multiply by
bar	Pa or N/m ²	1×10^5
psi	Pa	6,894.75
atmosphere	bar	1.01295
torr or mm Hg	Pa	133.3

One can think of this parameter as a measure of the crowdedness of a volume of gas; the more gas molecules exist in a certain volume, the shorter the distance a gas molecule can travel without collision. The formula for λ is

$$\lambda = \frac{K_B T}{\sqrt{2} \pi d^2 P} \quad (4.19)$$

where K_B is the Boltzmann constant ($K_B = 1.380 \times 10^{-23}$ J/K), T is the absolute temperature (in Kelvin K), d is the diameter of the gas molecule, and P is the pressure. For air in ambient pressure and $T = 300$ K, the mean free path under these conditions is approximately $\lambda_0 = 0.07 \mu\text{m}$. As expected, λ is inversely proportional to pressure. For convenience, λ at any pressure other than the ambient pressure P_0 can be expressed as a ratio of its value at ambient pressure λ_0 , that is:

$$\lambda = \frac{\lambda_0 P_0}{P}. \quad (4.20)$$

As an example, λ for air at a reduced pressure of $P = 100$ Pa, is calculated as

$$\lambda = \frac{101.3 \times 10^3}{100} \times 0.07 \times 10^{-6} = 71 \mu\text{m}.$$

As noted above, λ under reduced pressure is comparable to typical dimensions of microstructures. Hence, in MEMS applications involving interaction with gas, questions may be raised of whether the gas should be modeled as continuum or as individual molecules.

A key parameter that helps address this issue is the Knudsen number K_n [32], which is defined as

$$K_n = \frac{\lambda}{H} \quad (4.21)$$

where H is a characteristic length related to the physical problem. For example, it can be the diameter of a sphere moving into the fluid or it can be the separation distance between the two electrodes of a capacitor, as in the case of MEMS. Based on the Knudsen number, the flow can be divided into four regimes [33]: Continuum flow when $K_n < 0.01$, slip flow when $0.01 < K_n < 0.1$, transitional flow when $0.1 < K_n < 10$, and free molecular flow when $K_n > 10$. In the continuum regime, the fluid is governed by the Navier–Stokes equations. Slip flow can be described by modifying the zero-velocity boundary conditions in Navier–Stokes equations to account for the slip of the flow near the solid boundaries [34]. The flow in the transitional regime is a more subtle issue that needs special treatment [35]. In the molecular regime, the intermolecular collisions can be neglected and the fluid is governed by the Boltzmann transportation equation.

4.3.3 Damping Dependence on Pressure: Newell's Classification

Many MEMS devices are designed to operate at reduced pressure or in near vacuum conditions, such as resonant sensors. Others are designed to operate near atmospheric pressure. When studying air damping, it is vital to understand how damping and quality factors vary with pressure. In 1968, Newell [36] identified several regimes for the dependence of quality factor on pressure. His description is still considered qualitatively valid. Newell [36] studied the effect of damping on miniaturizing cantilever resonators. He divided the pressure range from vacuum to atmospheric pressure into three regimes, Fig. 4.11. In the first regime, A, the pressure is very low, near vacuum, which Newell predicted it to be in the ranges of hundreds of Pascal (Pa). Latter experimental research [31, 37] has suggested that this regime exists below 10 Pa. Here, air-damping has negligible effect and the damping is dominated by intrinsic damping, which depends on the material and is independent from pressure. Newell remarked that modeling intrinsic damping might be challenging, and hence he recommended using experimental and empirical methods to predict it.

In the second regime, B, the pressure is higher, approximately in the range from 10 to 1,000 Pa. In this regime, air damping is dominant and the quality factor is very sensitive to pressure. Here, air molecules are so apart from each other that they do not interact. Air damping occurs due to momentum transfer during collision of the molecules with the moving structure. In this regime, Newell applied the Christian's model [38], derived by studying the effect of a moving rigid plate on changing the linear momentum of the gas molecules, and predicted Q to be

$$Q = \left(\frac{\pi}{2}\right)^{3/2} \rho t f \sqrt{\frac{R_0 T}{M_0}} \frac{1}{P} \quad (4.22)$$

where ρ , t , and f , are the density, thickness, and resonance frequency (in Hz) of the vibrating beam, respectively, R_0 is the universal gas constant, T is the absolute temperature, and M_0 is the molecular mass of the gas. This formula has been proven inaccurate quantitatively in predicating the quality factor. Many recent models have

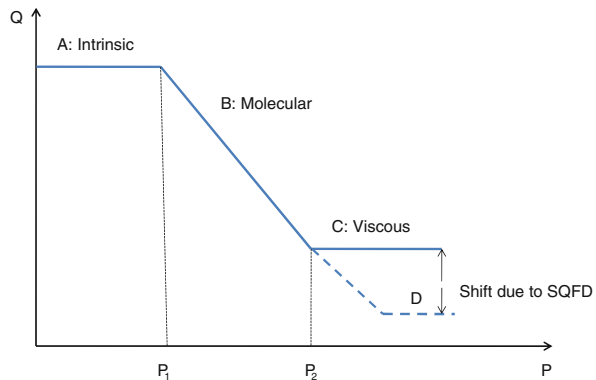


Fig. 4.11 Schematic illustrating Newell's classification of the dependence of quality factor on pressure [36]

presented improvement over this formula with better agreement with experimental data [39–41]. However, all models have predicted a qualitatively similar behavior and a drop of the quality factor with pressure that is proportional to $1/P$.

In the third regime, C, the pressure is higher, approximately above a thousand Pa up to atmospheric pressure. In this case, air molecules interact with each other and the air acts as a viscous fluid. This viscous damping is independent of pressure. Using Stokes' law, and assuming the cantilever beam to be isolated from any nearby surfaces, Newell provided the below expression for Q of the cantilever:

$$Q = \frac{b\sqrt{E\rho}}{24\mu} \left(\frac{t}{L} \right)^2 \quad (4.23)$$

where b and E are the width and Young's modulus of the beam, respectively, and μ is the viscosity coefficient of the fluid (air).

Newell recognized that in reality, microstructures and resonators may not be isolated in space, but can exist in close proximity to other surfaces and to the substrate. Based on the drop in pressure in a viscous fluid flowing through a parallel-walled duct, Newell derived the below modified expression for Q :

$$Q = \frac{b\sqrt{E\rho}}{\mu} \left(\frac{t}{L} \right)^2 \left(\frac{d}{b} \right)^3 \quad (4.24)$$

where d is the distance separating the cantilever beam from the other surface or the substrate. Equation (4.24) is in fact a model for the so-called squeeze-film damping (SQFD). It is valid for $d < (1/3)b$. Although more accurate models came in recent years to model SQFD, one can see that Eq. (4.24) still predicts an accurate dependence of the quality factor on the separation distance, particularly that damping is proportional to $1/d^3$, which agrees with most of the latter developed models.

As pointed previously, the classification of Newell is still considered an accurate qualitative description of damping dependence on pressure. Several experimental works have yielded similar curves to Fig. 4.11 [31, 37]. However, quantitatively, Newell's formula failed to estimate accurately the quality factor, especially in the case of microstructures moving close to other nearby surfaces (SQFD effect). Next, some of the common models for air damping in MEMS are discussed.

4.3.4 Drag Force

When a microstructure moves in free space in air, apart from any nearby surfaces, its motion is resisted by a drag force. Since MEMS are characterized by low Reynolds numbers with the inertia forces small compared to viscous forces, most models in the literature have been based on the so-called Stock's equation, which is a simplification of the more complicated Navier–Stokes equation. Some of the works have been based on the simple problem of calculating the drag force of a sphere moving in fluid. If

a vibrating sphere at frequency ω of a diameter b moves with a velocity u , then the drag force on the sphere, neglecting the effect of added mass, is given by

$$F = \beta_1 u \quad (4.25)$$

where the damping coefficient β_1 is given by

$$\beta_1 = 3\pi\mu b + \frac{3}{4}\pi b^2\sqrt{2\rho\mu\omega} \quad (4.26)$$

and μ and ρ are the viscosity and density of the fluid, respectively. One can see from Eq. (4.25) that the damping force is linearly proportional to the speed of the sphere. This model for damping force applies to most bodies vibrating in free space in air. The parameter β_1 is either calculated analytically for simple shapes as in the sphere case or measured experimentally.

Hosaka et al. [29] and Blom et al. [37] modeled a resonating beam as a series or string of spheres (beads) connected to each other. They calculated the drag force on the beam and estimated the damping coefficient in this case, of unit kg/s, to be β_1/b , where b is taken to be the width of the beam instead of the diameter of the sphere. Bao [42] also modeled the beam as a string of dishes with the diameter of the dishes equal the width of the beam and found the damping coefficient of the beam to be 8μ . It is observed from Eq. (4.26) and the derived expressions for the beams that the damping coefficient is always proportional to μ , which is similar to the prediction of Newell in Eq. (4.23).

4.3.5 Squeeze-Film Damping

Squeeze-film damping (SQFD) is considered the most common and dominant dissipation mechanism in MEMS. Many devices employ microstructures of big surface-to-volume ratio, such as microbeams and microplates. These are typically suspended a small distance above the substrate to allow for their free motion when actuated or while sensing. Many are fabricated using surface micromachining. They are released to motion by etching the underneath thin layer of oxide separating them from the substrate. Others are fabricated by bulk-micromachining, which also results in big bulk masses suspended above the substrate a distance, which is considered small compared to the size of the bulk masses. There are also microstructures that move in proximity to each other, such as comb-drive fingers. In addition, electrostatic MEMS typically employ a parallel-plate capacitor, in which one plate is actuated electrically and its motion is detected by capacitive changes. In order to increase the efficiency of actuation and improve the sensitivity of detection, the distance between the capacitor plates is minimized and the area of the electrode is maximized. In all of these scenarios, the common feature is that microstructures of big surface areas come too close to each other, thereby “squeezing” the air in between them in and out. This gives rise to the phenomenon of SQFD.

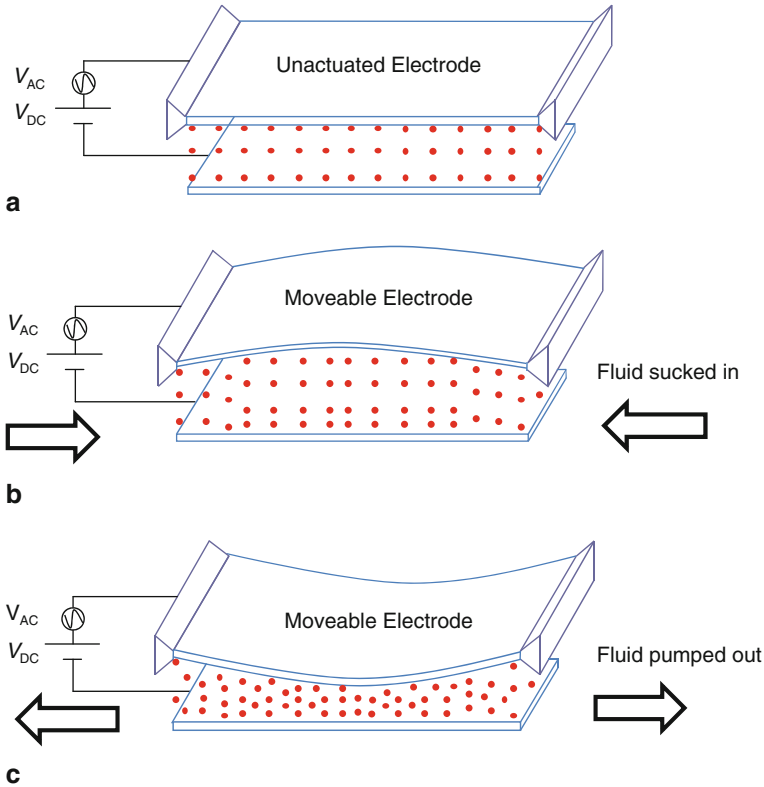


Fig. 4.12 A schematic shows a parallel plate capacitor sucking and pumping fluid in and out its gap while moving (a–c) illustrating the squeeze-film effect

This phenomenon occurs because of the massive movement of the fluid trapped between the microstructure and the substrate or the other microstructure. For example, consider the parallel-plate capacitor of Fig. 4.12a. During actuation, when the upper plate moves up, Fig. 4.12b, the pressure inside the air gap decreases, and hence air from outside the gap is sucked into inside. When the plate moves down, it pumps away the air underneath to the outside of the gap. Because of the small distance between the electrodes and their big surface area, the motion of the air is resisted by its viscosity, i.e., the air experiences friction with the walls of the electrodes (notice that in the big world air is considered almost ideal or non viscous, but things are different in the micro scale). This “friction” causes energy dissipation from both the air and the moveable electrode. Therefore, viscous damping in many MEMS devices corresponds to SQFD. Also, the pressure distribution underneath the plate can act in addition to the damping force as a spring force. It has been shown that the damping force dominates the spring force at low frequencies, whereas the spring force dominates the damping force at high frequencies. Figure 4.13a shows the simulated deflection of the upper electrode of Fig. 4.12a and the corresponding pressure

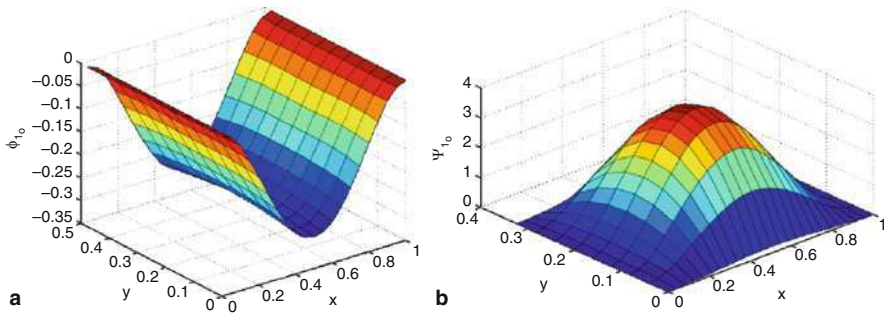


Fig. 4.13 The first mode shape of the upper electrode of a parallel-plate capacitor (a) and the corresponding pressure distribution underneath it (b). (Copyright 2004, IOP Publishing Ltd [43])

distribution underneath it, as calculated by coupled-field finite-element model [43]. As seen from Fig. 4.13b, higher pressure is built up toward the center of the plate, where the deflection is maximum.

4.3.5.1 Approaches to Model SQFD

There are at least three approaches in the literature to model SQFD. All of them have predicted that SQFD is inversely proportional to the cubic distance separating the moving structure from the substrate or the other nearby surfaces. The first approach targets the molecular regime B of Fig. 4.11, also called the rarefied gas regime, and utilizes statistical thermodynamics. It is based on studying the effect of collisions of the moving structure on the individual molecules of the gas, such as their effect in changing the molecules momentum and energy. For instance, Kàdàr et al. [39] and Li et al. [40] modified the Christian model [38] by improving the distribution function of the velocity molecules to reflect more the physics of the problem. Bao et al. [41] used an energy-transfer model to study the effect of a moving structure on changing the kinetic energy of the gas molecules. They derived an equation for the quality factor, similar to that of Christian [38], but modified by a correction factor, which is proportional to the gap width and the inverse of the plate length. This modification has resulted in a better agreement with the experimental data of Zook et al. [31].

The second and third approaches target the vicious regime D of Fig. 4.11 and assume the gas to be continuum. However, attempts have been made to extend the validity of these approaches to regime B through the effective viscosity concept, as discussed latter. These approaches are based on the so-called Reynolds equation, which is derived from the Navier–Stokes equation. The second and third approaches are more popular than the first one since they give sufficient accuracy among an extended range of pressure with high computational efficiency.

The second approach simplifies the Reynolds equation by assuming it to be incompressible [44]. This means that the spring effect of the gas is neglected. This

simplification reduces the equation to a simple Poisson's equation, which can be solved either analytically for simple shapes or numerically (e.g., finite-element methods) for complicated shapes. Starr [44] modeled a capacitive parallel-plate accelerometer using a linearized Reynolds equation. As an example, Starr [44] used the finite-element package ANSYS to calculate the pressure distribution underneath a plate with a hole. He also derived an exact expression for the damping force of a circular disk and an approximate expression for the damping force of a rectangular plate. Chu et al. [45] modeled the dynamic behavior of parallel-plate electrostatic microgripper using a lumped spring–mass model. They used the expressions of Starr [44], modified by replacing the initial air-gap width by the variable distance between the plates.

The third approach employs the full compressible Reynolds equation. Blech [46] followed the work of Griffin et al. [47] and solved analytically the linearized Reynolds equation in the case of oscillating rigid plates of rectangular and circular shapes with trivial pressure boundary conditions and derived analytical expressions for the spring and damping forces. Andrews et al. [48] conducted experiments on parallel-plate electrostatic microstructures and simulated their dynamic behavior with a spring–mass–damper model. The spring constant was composed of a structural component extracted from the measured resonance frequency at vacuum and a pressure component calculated from the Blech model [46]. The damping constant was also calculated from the Blech model.

Veijola et al. [49] investigated the behavior of a capacitive accelerometer, which employs a proof mass supported by a cantilever beam. They simulated its dynamic behavior with a spring–mass–damper model with a parallel-plate electrostatic force. The damping coefficient was calculated using the Blech model [46]. They accounted for the slip-flow condition by using an effective viscosity coefficient. Darling et al. [50] overcame the limitation of the Blech model [46], which was derived only for trivial pressure boundary conditions, by solving the linearized compressible Reynolds equation for arbitrary venting conditions in the case of rigid plates. Their solution scheme is based on Green's function.

While most of the literature has been focused on rigid bodies, some works have been also presented for flexible microstructures. For example, Hosaka et al. [29] utilized the expression of Starr [44] to model SQFD on a resonating beam. Yang et al. [51] simulated the dynamic behavior of an electrostatic clamped–clamped microbeam. They used the finite-element package ABAQUS to extract the fundamental free modeshape of the microbeam. They fed this modeshape as a harmonic deflection in the linearized Reynolds equation, modified to account for the slip condition. Then they solved the Reynolds equation over time using finite-difference and Runge–Kutta integration codes. From the results, they extracted effective damping and spring coefficients to be used in a spring–mass–damper model. Then, they calculated the quality factors and the resonance frequencies of two microbeams and compared the results with experiments.

Hung and Senturia [52] developed a reduced-order model to simulate the dynamics of a clamped–clamped microbeam proposed as a pressure sensor. They used the Galerkin method to discretize the two coupled partial-differential equations: the

Euler-beam equation with the electric and squeeze-film forces and the nonlinear Reynolds equation, modified to account for the slip condition. The global basis functions were extracted using data produced from a few runs of a fully meshed and slow finite-difference method. McCarthy et al. [53] studied the dynamic behavior of an electrostatic cantilever microswitch. They used a finite-difference scheme to solve two coupled equations, the Euler-beam equation with electrostatic forcing and the compressible Reynolds equation, modified to account for the slip condition. Nayfeh and Younis [43] and Younis and Nayfeh [54] used perturbation techniques to solve the compressible Reynolds equation for microbeams and microplates actuated by electrostatic forces. They fed the solution into the structural equation and solved the resulting equation using a finite-element method. They compared their predicted quality factor of a clamped–clamped microbeam to the experimental data of Legtenberg and Tilmans [55] and found good agreement.

Research in SQFD is still evolving. What has been reviewed above is only a partial list of contributions. Numerous works on SQFD have been conducted in the past six years, which are not reviewed here.

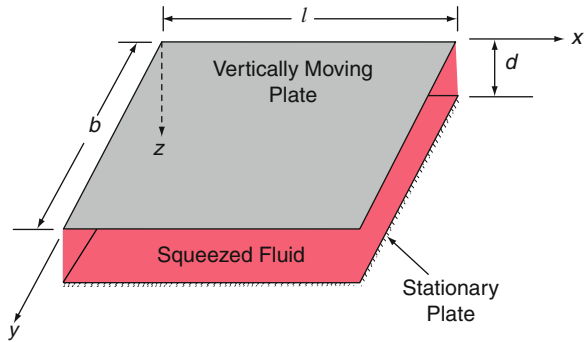
4.3.5.2 The Reynolds Equation

As discussed, the continuum-based approaches to model SQFD are based on the Reynolds equation. The derivation of the Reynolds equation is based on a number of assumptions, which are essential to the understanding of its validity and limitations. The following are the most common [32, 56]:

1. The fluid is Newtonian (the shear stress is directly proportional to the velocity).
2. The fluid obeys the ideal gas law.
3. The inertia and body forces are negligible compared to the viscous and pressure forces.
4. The variation of pressure across the fluid film is negligibly small.
5. The flow is laminar.
6. The width of the gap separating the two surfaces or plates, where the gas is trapped inside, is very small compared to the lateral extent of the plates.
7. The fluid can be treated as continuum and does not slip at the boundaries.
8. The system is isothermal.

Under these assumptions, the Reynolds equation is derived as follows [32, 56]. Without any loss of generality, consider two parallel rectangular plates (Fig. 4.14) separated by a gap of width d . Assume that one plate is moving vertically while the other plate is stationary. The plate has a length l and a width b . A simplified form of the Navier–Stokes equations is obtained by an order-of-magnitude analysis, in which higher-order inertia and gravitation terms are dropped from the original equations. Then, the simplified equations are integrated across the gap width to obtain expressions for the fluid velocities. The results are substituted into the continuity equation to yield a primitive form of the Reynolds equation in terms of pressure and density. Finally, assuming isothermal conditions and ideal gas law, the density

Fig. 4.14 Two parallel rigid plates with fluid trapped in between them



is expressed in terms of pressure, which in turn is substituted into the Reynolds equation to obtain the following standard form of Reynolds equation:

$$\frac{\partial}{\partial x} \left(H^3 P \frac{\partial P}{\partial x} \right) + \frac{\partial}{\partial y} \left(H^3 P \frac{\partial P}{\partial y} \right) = 12\mu \left(H \frac{\partial P}{\partial t} + P \frac{\partial H}{\partial t} \right). \quad (4.27)$$

In Eq. (4.27), x and y are the positions along the length and width of the plate, respectively, t is time, H is the variable distance between the two plates, P is the total pressure, and μ is the viscosity coefficient of the fluid. It is noted that the Reynolds equation is a nonlinear partial-differential equation involving two variables H and P . It is also time varying and two-dimensional in space.

4.3.5.3 Limitations and Correction Factors of Reynolds Equation

In practical MEMS applications, the aforementioned assumptions of the Reynolds equation might not be completely satisfied. In fact, some assumptions are inherently violated in certain designs, making the predictions of the Reynolds equation suspect. These violations and their effects have been studied and correction factors have been proposed to enable the use of a modified version of the Reynolds equation.

As an example, in some MEMS devices, the ratio of the gap width to the plate length or width is not sufficiently large, which violates assumption #6. In such cases, the Reynolds equation in its original form is inaccurate. Other issues like acoustic radiations and nondeveloped flow at the edges become important. Schrag and Wachutka [57] compared results of the damping and spring forces obtained using the Reynolds equation with results obtained using the Navier–Stokes-based finite-element program for different ratios of the plate length and width to the gap width. The results show erroneous predictions of the Reynolds equation for ratios 5 and 10, whereas the results are in good agreement for ratio of 100. Veijola et al. [58] compared results of a modified Reynolds equation including acoustic edge effects with results of the original Reynolds equation. They found that the damping force predicted with the modified model is 1.07 and 2.0 of that predicted with the unmodified Reynolds equation when the length-to-gap ratio was 100 and 7, respectively.

A similar observation was also reported by Vemuri et al. [59] who showed that the percentage error in the original Reynolds equation increases with decreasing plate length.

However, perhaps the most significant violation is related to the continuum assumption (assumption 7). Many MEMS devices are designed to operate at very low pressure with a very small gap between the capacitor electrodes. Under such conditions, the Knudsen number is closer to the noncontinuum regimes, making the use of the Reynolds equation suspect. Fortunately, recent extensive research has extended the validity of the Reynolds equation to the noncontinuum regimes, thereby enabling description of the flow using a single model. This is achieved by using the so-called “effective viscosity coefficient” μ_{eff} , which depends directly on the Knudsen number.

Various models have been proposed for μ_{eff} since the beginning of the 20th century, when Knudsen presented a correction coefficient based on his research on the gas flow in capillary tubes [49]. His coefficient has been used recently by Andrews et al. [48] and gave good results. Another well-known correction factor was presented by Burgdorfer [34]. He accounted for the slip-flow regime by modifying the boundary conditions to take into account, to the first-order approximation, the slip velocities. His modified Reynolds equation has been widely used, examples are found in [52] and [53]. However, the Knudsen model is limited to the range $0 < K_n < 1$ [32]. Thanks to the active research in MEMS, many other models have been proposed in the last two decades. Summary of these models and comparison among some of them are given by [58] and [33]. Table 4.5 lists some of these. Although all models give close results, the model of Veijola et al. [49] tends to be more accurate because it is valid over a wider range of K_n . Their model is an empirical approximation of the more

Table 4.5 A list of effective viscosity models. The parameter α is the accommodation coefficient (approximately equal one) and Q is a coefficient related to the Poiseuille flow

Author (s)	Year	Effective viscosity	Derived from
Knudsen	1906	$\frac{\mu}{1 + \frac{K_n(K_n + 2.507)}{0.1474(K_n + 3.095)}}$	Gas flow in capillary tubes
Burgdorfer [34]	1959	$\frac{\mu}{1 + 6K_n}$	Navier–Stokes Eqs. + slip flow
Hsia and Domoto [61]	1983	$\frac{\mu}{1 + 6K_n + 6K_n^2}$	Experimental data fitting
Fukui and Kaneko [60]	1988	$\frac{\mu D}{6Q(d)}; D = \frac{\sqrt{\pi}}{2K_n}$	Boltzmann equation
Seidel et al. [62]	1993	$\frac{0.7\mu}{0.7 + K_n}$	Experimental data fitting
Mitsuya [63]	1993	$\frac{\mu}{1 + 6\frac{2-\alpha}{\alpha}K_n + \frac{8}{3}K_n^2}$	Navier–Stokes Eqs. + slip flow
Andrews and Harris [48]	1995	$\frac{\mu}{1 + 6.8636K_n^{0.9906}}$	Experimental data fitting
Veijola et al. [49]	1995	$\frac{\mu}{1 + 9.638K_n^{1.159}}$	Fukui and Kaneko model [60]

complicated expression proposed by Fukui and Kaneko [60] based on the Boltzmann transport equation.

4.3.5.4 Rigid-Bodies Models

As discussed previously, the continuum approaches to model SQFD are based on the Reynolds equation. There have been two major approaches to solve this equation for the case of rigid bodies (assuming the microstructure to be undeformable). One is attributed to Blech [46], which solves the compressible form of Reynolds equation and the other is attributed to Starr [44], which deals with the incompressible Reynolds equation. Both approaches assume small variation in pressure and small motion, and hence, are based on the linearized equation. Thus, their results might be inaccurate for large displacement and nonlinear behaviors. Next, we outline both approaches for selected cases.

The Compressible-Gas Model

Blech [46] presented analytical solutions for the linear SQFD problem in the cases of rectangular and circular rigid plates. Next, the rectangular plate case is outlined following the notations of Li and Hughes [33]. Consider the parallel plates of Fig. 4.15. The upper plate is moveable with dimensions as shown. We assume that the origin of the coordinate system is located at the center of the upper plate. The pressure underneath the upper plate is governed by Eq. (4.27). Next, we assume small displacement $z(t)$ compared to the original gap width d and small pressure change across the upper plate $\Delta p(x, y, t)$ compared to the original static pressure in the gap P_a . Hence, the total displacement and pressure are expressed, respectively, as

$$H(t) = d + z(t) \quad (4.28a)$$

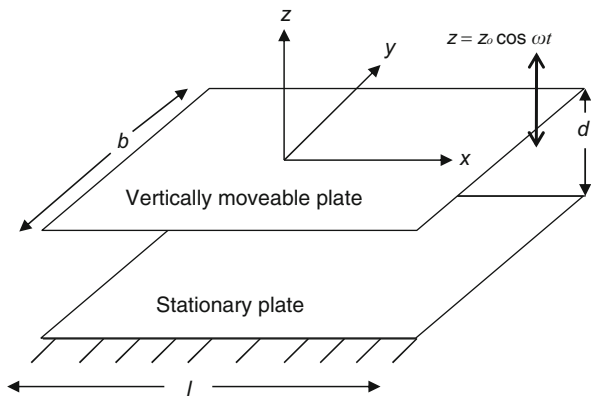


Fig. 4.15 Two parallel rigid plates with the upper plate moving harmonically

$$P(x, y, t) = P_a + \Delta p(x, y, t). \quad (4.28b)$$

Substituting Eqs. (4.28a) and (4.28b) into Eq. (4.27) and dropping the nonlinear terms yield

$$\frac{\partial^2(\Delta p)}{\partial x^2} + \frac{\partial^2(\Delta p)}{\partial y^2} = \frac{12\mu}{d^3 P_a} \left(d \frac{\partial(\Delta p)}{\partial t} + P_a \frac{\partial z}{\partial t} \right). \quad (4.29)$$

The plate is open or vented from all of its sides. Hence, the pressure along its edges has to be the same as the ambient pressure P_a , meaning no pressure differential across the plate near the edges. Therefore, the pressure boundary conditions of Eq. (4.29) are written as

$$\Delta p = 0 \quad \text{at} \quad x = \pm l/2 \quad \text{and} \quad y = \pm b/2. \quad (4.30)$$

The displacement $z(t)$ is assumed to be harmonic of the form $z(t) = z_0 \cos \omega t$, where z_0 and ω are the amplitude and frequency of motion, respectively. For convenience, the following normalized variables are introduced:

$$\hat{p} = \frac{\Delta p}{P_a}; \quad \eta = \frac{z}{d}; \quad \tau = \omega t. \quad (4.31)$$

Also, the normalized harmonic motion becomes $\eta(\tau) = \eta_0 \cos \tau$, where $\eta_0 = z_0/d$. Substituting Eq. (4.31) into Eq. (4.30) yields

$$\frac{\partial^2 \hat{p}}{\partial x^2} + \frac{\partial^2 \hat{p}}{\partial y^2} - \alpha \frac{\partial \hat{p}}{\partial \tau} = \alpha \frac{\partial \eta}{\partial \tau} \quad (4.32)$$

where $\alpha = 12\omega\mu/P_a d^2$. The solution of Eq. (4.32) is based on separating space and time (separation of variables) and assuming the solution to be composed of two components, one in phase with the response (and the excitation), which will yield the spring component, and the other in phase with the velocity of the response, which will give the damping component. Accordingly, the solution can be expressed as

$$\hat{p}(x, y, \tau) = \phi_1(x, y) \cos \tau + \phi_2(x, y) \sin \tau \quad (4.33)$$

where ϕ_1 and ϕ_2 are to be determined. Substituting Eq. (4.33) into Eq. (4.32) yields

$$\frac{\partial^2 \phi_1}{\partial x^2} + \frac{\partial^2 \phi_1}{\partial y^2} - \alpha \phi_2 = 0 \quad (4.34)$$

$$\frac{\partial^2 \phi_2}{\partial x^2} + \frac{\partial^2 \phi_2}{\partial y^2} + \alpha \phi_1 = -\alpha \eta_0. \quad (4.35)$$

The boundary conditions of ϕ_1 and ϕ_2 are also trivial, as in Eq. (4.30). Next, ϕ_1 and ϕ_2 are expanded in series as

$$\phi_1 = \sum_{\substack{m,n \\ \text{odd}}} a_{mn} \cos\left(\frac{m\pi x}{a}\right) \cos\left(\frac{n\pi y}{b}\right) \quad (4.36)$$

$$\phi_2 = \sum_{\substack{m,n \\ \text{odd}}} b_{mn} \cos\left(\frac{m\pi x}{a}\right) \cos\left(\frac{n\pi y}{b}\right) \quad (4.37)$$

where only odd numbers of m and n are used due to the requirement of symmetry in both x and y . Substituting Eqs. (4.36) and (4.37) into Eqs. (4.34) and (4.35), multiplying by $\cos\left(\frac{m\pi x}{a}\right) \cos\left(\frac{n\pi y}{b}\right)$, and integrating from $-l/2$ to $l/2$ in x and from $-b/2$ to $b/2$ in y give the below linear algebraic equations:

$$\left(\frac{m^2}{a^2} + \frac{n^2}{b^2}\right) \pi^2 a_{mn} + \alpha b_{mn} = 0 \quad (4.38)$$

$$\left(\frac{m^2}{a^2} + \frac{n^2}{b^2}\right) \pi^2 b_{mn} - \alpha a_{mn} = \frac{16\alpha\eta_0}{mn\pi^2} (-1)^{\frac{m+n}{2}-1}. \quad (4.39)$$

Solving Eqs. (4.38) and (4.39) gives

$$\begin{aligned} a_{mn} &= \frac{-16\alpha\eta_0}{mn\pi^2 \left(\left(\frac{m^2}{a^2} + \frac{n^2}{b^2} \right)^2 \pi^4 + \alpha^2 \right)} (-1)^{\frac{m+n}{2}-1}; \\ b_{mn} &= \frac{16\alpha\eta_0 \left(\frac{m^2}{a^2} + \frac{n^2}{b^2} \right)}{mn \left(\left(\frac{m^2}{a^2} + \frac{n^2}{b^2} \right)^2 \pi^4 + \alpha^2 \right)} (-1)^{\frac{m+n}{2}-1}. \end{aligned} \quad (4.40)$$

The force induced from the fluid on the plate is obtained by integrating the pressure difference Δp across the plate over its area, that is

$$\begin{aligned} F = P_a \int_{-l/2}^{l/2} \int_{-b/2}^{b/2} \hat{p} dx dy &= \cos \tau \int_{-l/2}^{l/2} \int_{-b/2}^{b/2} P_a \phi_1 dx dy \\ &+ \sin \tau \int_{-l/2}^{l/2} \int_{-b/2}^{b/2} P_a \phi_2 dx dy. \end{aligned} \quad (4.41)$$

The equation of motion of the plate of mass M , when influenced by the fluid only can be expressed as

$$M\ddot{z} + c\dot{z} + kz = 0 \Rightarrow M\ddot{z} = -c\dot{z} - kz \quad (4.42)$$

where c and k are the damping and stiffness coefficient from the fluid, respectively. Substituting $z(t) = z_0 \cos \omega t$ in Eq. (4.42) yields

$$M\ddot{z} = c\omega(d\eta_0)\sin \tau - k(d\eta_0)\cos \tau. \quad (4.43)$$

Equating the coefficients of $\cos \tau$ and $\sin \tau$ of Eq. (4.43) and Eq. (4.41) yields

$$c = \frac{P_a}{\omega d\eta_0} \int_{-l/2}^{l/2} \int_{-b/2}^{b/2} \phi_2 dx dy; \quad k = -\frac{P_a}{d\eta_0} \int_{-l/2}^{l/2} \int_{-b/2}^{b/2} \phi_1 dx dy. \quad (4.44)$$

Substituting Eq. (4.40) into Eqs. (4.37) and (4.38), then substituting the outcome into Eq. (4.44), and carrying out the integrals result in the below analytical expressions for the stiffness and damping coefficients due to SQFD:

$$k = \frac{64\sigma^2 P_a A}{\pi^8 d} \sum_{\substack{m,n \\ \text{odd}}} \frac{1}{(mn)^2 \left\{ (m^2 + \beta^2 n^2)^2 + \frac{\sigma^2}{\pi^4} \right\}} \quad (4.45)$$

$$c = \frac{64\sigma P_a A}{\pi^6 \omega d} \sum_{\substack{m,n \\ \text{odd}}} \frac{m^2 + \beta^2 n^2}{(mn)^2 \left\{ (m^2 + \beta^2 n^2)^2 + \frac{\sigma^2}{\pi^4} \right\}} \quad (4.46)$$

where $A = lb$ is the area of the plate, $\beta = b/l$, and σ is the so-called squeeze number defined as

$$\sigma = \frac{12A\omega\mu}{P_a d^2}. \quad (4.47)$$

The series in Eqs. (4.45) and (4.46) converge fast, so even one term can yield acceptable results (see Example 4.6). Of course, in all of the above expressions, μ should be replaced with μ_{eff} for low values of pressure depending on the Knudsen number.

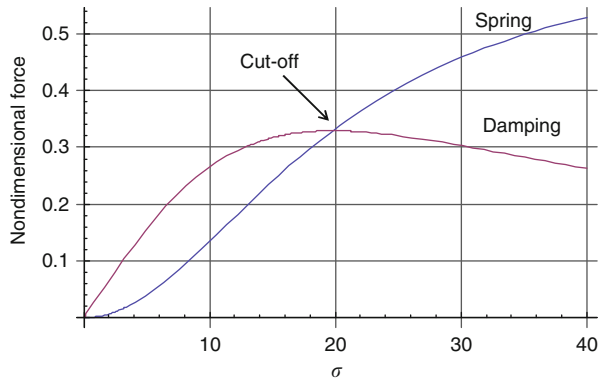
The squeeze-number of Eq. (4.47) represents a measurement of the compressibility of the fluid. According to [48], it “represents the ratio of the gas velocity needed to be set up between the two plates to ensure no compression, to the velocity which can be achieved under viscous flow.” A low squeeze number means that the gas is squeezed without compression (incompressible fluid) and it can escape the gap easily. In another words, the oscillation is too slow that the gas can go in and out the gap without experiencing the compression. According to Eq. (4.45), when $\sigma \rightarrow 0$ this means $k \rightarrow 0$, i.e., no spring contribution. In this case, according to Eq. (4.46), c is approximated as

$$c = \frac{0.8\mu A^2}{d^3(1 + \beta^2)}. \quad (4.48)$$

A high squeeze number means that the gas is trapped in the gap and cannot escape. In another words, the oscillation is too fast to allow the gas to escape. In this case, the spring contribution of the gas becomes significant. This spring constant can be modeled to act in parallel with the spring constant of the microstructure itself.

In between the two extreme values of σ , the squeezed fluid has both spring and damping effects. Which one is dominant or how they are compared against each other depends on the so-called cut-off frequency ω_c . This is the value of frequency at which both the spring force and the damping force are equal. Below ω_c , the spring force is lower than the damping force, and above it the spring force dominates the damping force. A plot of the nondimensional damping and spring forces versus the squeeze number are depicted in Fig. 4.16 for a square plate. The figure indicates that the cut-off frequency is near $\sigma = 20$. As seen, if σ is much lower than the cut-off squeeze number σ_c , corresponding to ω_c , then the spring effect is negligible. Blech

Fig. 4.16 A plot of the nondimensional damping force $[c\omega d/(P_a A)]$ and spring force $[kd/(P_a A)]$ versus the squeeze number for the case of a square plate



[46] presented an analytical approximation for σ_c as

$$\sigma_c = \pi^2(1 + \beta^2). \quad (4.49)$$

Using Eq. (4.49) with $\beta = 1$ gives $\sigma_c = 19.7$, which is close to that of Fig. 4.16.

Belch [46] has also derived an analytical solution for circular disks. However, the solution looks complicated and not very practical. Also, Darling et al. [50] has extended the Blech solution for plates of other pressure boundary conditions. Also, the derived analytical solutions seem not easy to use. One method to simplify the analytical solution of the Reynolds equation is to assume incompressible fluid. This of course means neglecting the stiffness or spring effect of SQFD. How good this assumption depends on σ as explained before.

Similar analytical work based on the linearized compressible Reynolds equation has been conducted for **torsional actuators and micromirrors** [50, 64]. Pan et al. [64] solved the equation analytically using Fourier series and using a double-sine series approach, similar to Blech [46]. They obtained analytical expressions of double series from both approaches that yield almost the same results. Pan et al. [64] also concluded that using one term in the obtained double series yields accurate results. They validated their analytical expressions by comparing their results to experimental data and finite-difference simulations of the nonlinear Reynolds equation. Following Pan et al. [64], for a mirror such as that of Fig. 3.23, the expressions for the torsional stiffness coefficient k_{tsq} and torsional damping coefficient c_{tsq} due to SQFD can be expressed, respectively, as

$$k_{tsq} = \frac{4l_m w_m^3 P_a \sigma^2}{\pi^4 d} \frac{1}{\left(\pi^2 + \frac{4\pi^2}{\beta^2}\right)^2 + \sigma^2} \quad (4.50)$$

$$c_{tsq} = \left(\frac{4l_m w_m^3 P_a \sigma}{\pi^4 d \omega} \right) \frac{\pi^2 + \frac{4\pi^2}{\beta^2}}{\left(\pi^2 + \frac{4\pi^2}{\beta^2}\right)^2 + \sigma^2} \quad (4.51)$$

where $l_m = b$ (see Fig. 3.23), $w_m = 2a_3$, $\beta = w_m/l_m$, and σ is the squeeze number defined as $\sigma = 12l_m^2 \omega \mu / P_a d^2$. Hence, the total induced torque T_d on the mirror due

to SQFD can be written as

$$T_d = k_{tsq}\alpha + c_{tsq}\dot{\alpha} \quad (4.52)$$

where α is the titling angle of the mirror. In the case of small σ , k_{tsq} can be neglected.

The Incompressible-Gas Model

When it is reasonable to assume the gas incompressible, the Reynolds equation, Eq. (4.27), can be simplified by setting the variation in pressure with time equal to zero. This leads to a Poisson's equation that can be easily solved analytically for simple cases or numerically using many of the available software that deals with this equation. Under this condition, Eq. (4.27) becomes

$$\frac{\partial}{\partial x} \left(H^3 P \frac{\partial P}{\partial x} \right) + \frac{\partial}{\partial y} \left(H^3 P \frac{\partial P}{\partial y} \right) = 12\mu P \frac{\partial H}{\partial t}. \quad (4.53)$$

As an example, we derive next the damping coefficient for a long rectangular beam of length l , much longer than its width b [65]. We consider the same notation as Fig. 4.15 and the linear case of Eq. (4.29). By dropping the variation of pressure with time, the equation becomes

$$\frac{\partial^2(\Delta p)}{\partial x^2} + \frac{\partial^2(\Delta p)}{\partial y^2} = \frac{12\mu}{d^3} \frac{\partial z}{\partial t}. \quad (4.54)$$

Since the length of the beam is much larger than its width, it is assumed that the pressure variation across the width is more significant than it is across the length, and hence, the variation across the length can be neglected. Hence, the equation is further simplified to

$$\frac{\partial^2(\Delta p)}{\partial y^2} = \frac{12\mu}{d^3} \frac{\partial z}{\partial t}. \quad (4.55)$$

Integrating for Δp twice and using $\Delta p = 0$ at $y = \pm b/2$ yield

$$\Delta p = \frac{6\mu}{d^3} \frac{\partial z}{\partial t} \left[y^2 - \frac{b^2}{4} \right]. \quad (4.56)$$

Finally, the total damping force on the beam can be calculated as

$$F_{SQFD} = \iint_A \Delta p dx dy = \int_{-b/2}^{b/2} \frac{6\mu}{d^3} \frac{\partial z}{\partial t} \left(y^2 - \frac{b^2}{4} \right) l dy = -\frac{b^3 l \mu}{d^3} \frac{\partial z}{\partial t} \quad (4.57)$$

where the negative sign indicates that the force opposes the positive motion. Hence, the damping coefficient in this case is given by

$$c = \frac{b^3 l \mu}{d^3}. \quad (4.58)$$

Table 4.6 Damping coefficients [N/(m/s)] of selected cases assuming incompressible fluid. In the table, d refers to the gap width separating the structure from the substrate or the other nearby structure, μ is the viscosity coefficient, which can be replaced by an effective viscosity coefficient. The formulas are obtained from [42], [44], [66], and the references therein

Case	Damping coefficient
1. Long rectangular beam of length L	$\frac{\mu b^3 l}{d^3}$
2. Rectangular plate of length L and width b	$\frac{\mu l b^3}{d^3} f(b/l)$; see Table 4.7 for $f(b/l)$
3. Circular plate of radius R	$\frac{3\pi \mu R^4}{2d^3}$
4. Annular plate of inner radius r and outer radius R	$\frac{3\pi \mu R^4}{2d^3} G(r/R)$; $G(\beta) = 1 - \beta^4 + \frac{(1 - \beta^2)^2}{\ln(\beta)}$
5. Uniformly perforated thin plate of area A (without the holes) with N circular holes, each of radius r_0 and assuming a cell surrounding the hole of radius r_c	$\frac{3\mu A^2}{2\pi d^3 N} k(\beta)$; $\beta = r_0/r_c$; $k(\beta) = 4\beta^2 - \beta^4 - 4 \ln(\beta) - 3$

Starr [44] has derived analytical solutions for rectangular plates and circular disks and provided correction factors for the cases of large displacement and compressible fluid. The analytical solutions along with those of other cases are provided in Table 4.6. The correction factors for a rectangular plate are given in Table 4.7. These cases are derived in details in [42]. One note worth to be mentioned is regarding the damping coefficient for the rectangular plate case. The formula in the table yields close results to that of the Blech model of Eq. (4.48). For example, for the case of a square plate, $f(b/l = 1)$ according to Table 4.7 is equal 0.42. Hence, the total damping coefficient is $0.42\mu A^2/d^3$, which is close to that of the Blech model of $0.4\mu A^2/d^3$.

A final note on Table 4.6 is regarding the damping coefficient of the perforated rectangular plate (case 5). This formula is derived under the assumptions of infinite thin plate, circular holes, and that the gas does not experience any resistance when it escapes from the holes. This formula is merely an approximation. Factors, such as the finite dimensions of the plate, the gas resistance through the holes, especially for thick plates, and the undeveloped flow near the edges need to be taken into account for more accurate results [67, 68]. The use of perforations in microstructures is common in MEMS. It serves two purposes: One is to allow easier access for the etchant solution to get to the sacrificial layer underneath the microstructure for the purpose of releasing it. Second, it relieves and reduces the effect of SQFD. The study of Homentcovschi and Miles [68], however, has indicated that because of

Table 4.7 The function f for the case of a rectangular plate of Table 4.6 [44]

b/l	0.1	0.2	0.3	0.4	0.5	0.6	0.7	0.8	0.9	1
$f(b/l)$	0.94	0.87	0.81	0.75	0.69	0.63	0.57	0.52	0.47	0.42

the resistance of the gas through the holes, there is an optimum number of holes to be used to ensure the maximum reduction of damping.

Example 4.5: Consider the square plate of Fig. 4.17a of length $l = 200 \mu\text{m}$. The plate has $N = 16$ uniformly distributed circular holes, each hole of a radius $r_0 = 3 \mu\text{m}$.

- Find the ratio of the SQFD coefficient of the perforated plate to that of a solid plate (without the perforation).
- Repeat (a) assuming the number of holes has increased to $N = 25$.
- Repeat (a) assuming the radius of the hole has increased to $r_0 = 6 \mu\text{m}$.

Solution: The solution of such a problem starts by dividing the plate into N square cells, each of width w . Since the total area of the plate is $A = l^2$, the area of each square cell is A/N . The width of the cell is $w = \sqrt{A/N} = 50 \mu\text{m}$. Next, each square cell is replaced by an equivalent circular cell of the same area as the square cell, Fig. 4.17a. The radius of the circular cell r_c is calculated as $r_c = w/\sqrt{\pi} = 28.2 \mu\text{m}$. This way, the plate is represented by annuluses, Fig. 4.17c. Then, in preparation to use the formula of case 5 of Table 4.6, the ratio $\beta = r_0/r_c$ and the corresponding function $k(\beta)$ are calculated. These are found for this studied case to be $\beta = 3/28.2 = 0.106$ and $k(0.106) = 6$. Finally, using the formula in Table 4.6:

$$c_{\text{perf}} = \frac{3\mu A^2}{2\pi d^3 N} k(\beta) = \frac{3\mu(200 \times 10^{-6})^4}{2\pi d^3 (16)} \times 6 = \frac{2.87 \times 10^{-16} \mu}{d^3}. \quad (\text{a})$$

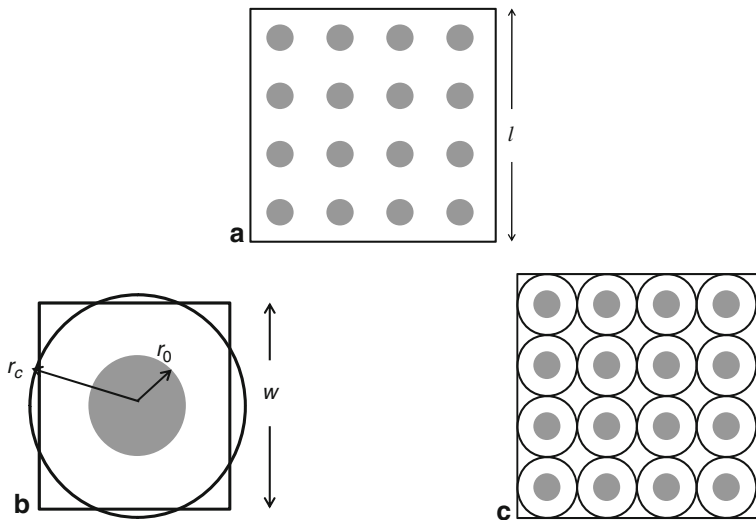


Fig. 4.17 a A perforated square plate. b A single circular cell, which is an equivalent to a square cell. c The approximation of the area of the plate into circular cells

In the case of no perforation, the damping coefficient is found from case 2 of Table 4.6 as

$$c_{\text{solid}} = \frac{\mu l b^3}{d^3} f(b/l) = \frac{\mu (200 \times 10^{-6})^4}{d^3} \times 0.42 = \frac{6.72 \times 10^{-16} \mu}{d^3}. \quad (\text{b})$$

- (a) The solution in this case is obtained by dividing the answer of Eq. (a) over Eq. (b):

$$c_{\text{perf}}/c_{\text{solid}} = 0.427. \quad (\text{c})$$

Therefore, the perforations have reduced the SQFD effect by more than half.

- (b) When the number of holes are increased to $N=25$, the answer becomes

$$c_{\text{perf}}/c_{\text{solid}} = 0.234. \quad (\text{d})$$

This is even more significant reduction.

- (c) Doubling the radius of the hole should also reduce the damping, in this case the ratio becomes

$$c_{\text{perf}}/c_{\text{solid}} = 0.24. \quad (\text{e})$$

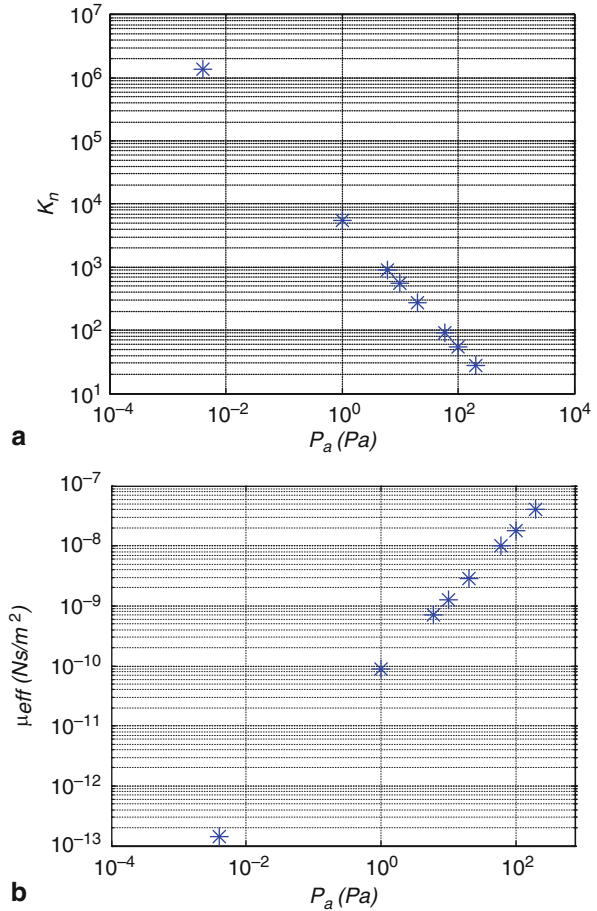
Example 4.6: In this example, we use a spring–mass–damper model to study the damping characteristic of a clamped–clamped microplate, similar to Fig. 4.12, actuated by electrostatic forces and used as a resonant sensor [55, 69]. The microplate is made of silicon with density $\rho = 2,332 \text{ kg/m}^3$ and modulus of elasticity $E = 166 \text{ GPa}$. The plate has a length $l = 210 \mu\text{m}$, thickness $h = 1.5 \mu\text{m}$, width $b = 100 \mu\text{m}$, and gap width separating it from the substrate $d = 1.18 \mu\text{m}$. The microplate is placed in a package, where the pressure is reduced according to the below values:

$$P_a = \{4 \times 10^{-5}, 0.01, 0.06, 0.1, 0.2, 0.6, 1.0, 2.0\} \text{ mbar}.$$

Experimentally, the fundamental natural frequency of the microplate was measured and found near $f = 322 \text{ kHz}$, a tensile residual strain was measured and found to be $S = 0.0000404$, and the quality factor of the microplate was measured in vacuum and found to be $Q_{\text{vac}} = 18,000$. Assume the mean free path of air at ambient pressure $\lambda_0 = 0.064 \mu\text{m}$ and the viscosity coefficient of air $\mu_{\text{air}} = 1.82 \times 10^{-5} \text{ Ns/m}^2$. Also, assume the microplate to be rigid of open sides, so that the model of Blech [46] applies. Consider the microplate is operated near its fundamental natural frequency.

1. Plot the Knudsen number for the given values of pressure.
2. Use the model of Viejola et al. [49] to calculate and plot the effective viscosity coefficient.
3. Calculate and plot the squeeze number assuming the microplate to be excited at resonance (at its natural frequency). Also, calculate the cut-off squeeze number.
4. Calculate and plot the damping coefficient of the microplate assuming compressible and incompressible gas and compare the two results.
5. Calculate the total quality factor of the microplate and plot the results against pressure. Compare to the below measured values of quality factor [55]:
 $Q_{\text{exp}} = \{12,600, 12,000, 8,000, 2,800, 1,800, 900, 550, 270\}.$
6. Calculate the change of natural frequency, if any, with the pressure and plot the results.

Fig. 4.18 The variation of
a the Knudsen number and
b the effective viscosity
 coefficient for various values
 of air pressure



Solution:

1. The Knudsen number is calculated according to Eq. (4.21). First, λ needs to be calculated according to Eq. (4.20). The results are shown in Fig. 4.18a. It is clear that for all pressure values, the microplate is operated in the molecular regime.
2. The effective viscosity coefficient is given according to Table 4.5 as

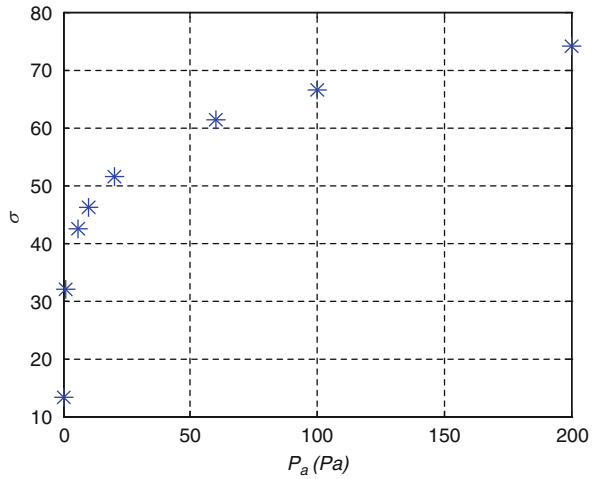
$$\mu_{\text{eff}} = \frac{\mu}{1 + 9.638 K_n^{1.159}}. \quad (\text{a})$$

Using the data from part (1), the results are depicted in Fig. 4.18b.

3. The squeeze number is calculated according to Eq. (4.47). Note that $\omega = 2\pi f$. The results are depicted in Fig. 4.19. The cut-off squeeze number is calculated from Eq. (4.49) as

$$\sigma_c = \pi^2(1 + \beta^2) = \pi^2[1 + (100/210)^2] = 12.11. \quad (\text{b})$$

Fig. 4.19 The squeeze number versus pressure



Based on Eq. (b) and Fig. 4.19, it is concluded that the gas for most of the pressure range behaves as compressible.

4. Under the compressible gas assumption, the Belch model, Eq. (4.46), can be used. Using only one term in the series, the formula becomes

$$c_{\text{com}} = \frac{64\sigma P_a A}{\pi^6 \omega d} \times \frac{1 + \beta^2}{(1 + \beta^2)^2 + \frac{\sigma^2}{\pi^4}}. \quad (\text{c})$$

Under the incompressible gas assumption, either Eq. (4.48) or the Starr's model of case 2 of Table 4.6 can be used. Either way, the formula is written as

$$c_{\text{inc}} = \frac{\mu l b^3}{d^3} \times 0.7. \quad (\text{d})$$

The results of both approaches are depicted in Fig. 4.20. As expected, the results of the two approaches deviate considerably since the incompressible assumption is invalid in this case.

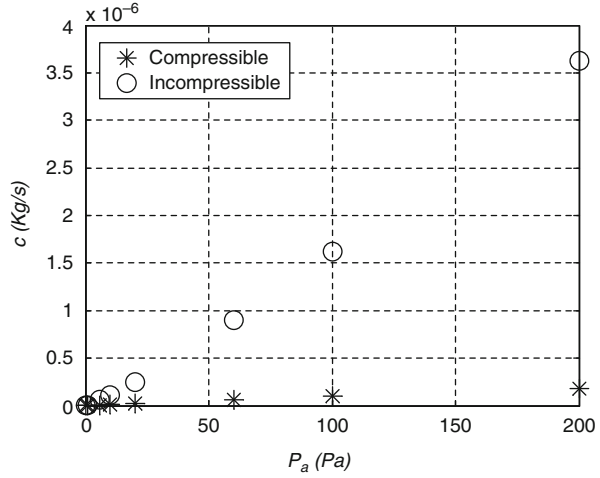
5. The total quality factor is calculated according to Eq. (4.14) to account for the contribution from SQFD, Q_{SQFD} , and to the other losses Q_L :

$$\frac{1}{Q} = \frac{1}{Q_{\text{SQFD}}} + \frac{1}{Q_L}. \quad (\text{e})$$

The quality factor due to the other losses is the same as the measured quality factor in vacuum. Hence, $Q_L = Q_{\text{vac}} = 18,000$. The quality factor Q_{SQFD} is calculated as $Q_{\text{SQFD}} = 1/2\zeta$, where ζ is given by Eq. (2.18). Hence,

$$Q_{\text{SQFD}} = \frac{1}{2\zeta} = \frac{m\omega}{c}. \quad (\text{f})$$

Fig. 4.20 The calculated damping coefficient using two models versus pressure



The mass, m , in this case is the effective mass, m_{eff} , which is calculated according to Eq. (4.9): $m_{\text{eff}} = k/\omega^2$, where k is calculated as clarified below in part #6. Finally, using the results of Eq. (c) in Eq. (f) and then the outcome in Eq. (e), the total quality factor is calculated. The results are shown in Fig. 4.21, labeled as Q_{th} , and compared to the experimental data, Q_{exp} . As seen, the agreement is good. To improve further the results, the flexibility of the plate and the correct pressure boundary conditions need to be considered [43].

- Since the gas mostly behaves as compressible, some change in the resonance frequency is expected with increasing the pressure. To estimate this, first, the

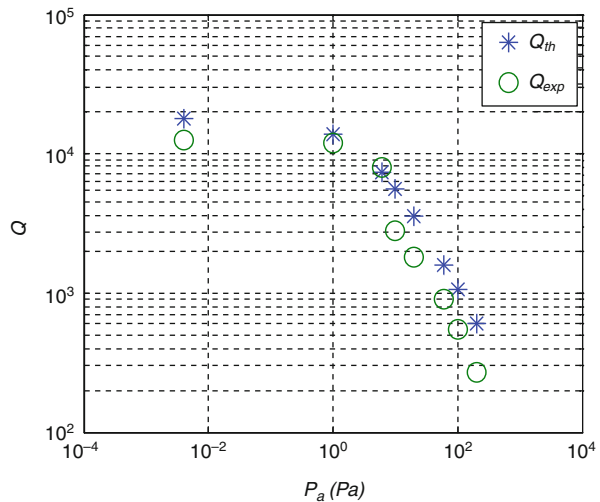


Fig. 4.21 The calculated and experimentally measured quality factor versus pressure

stiffness of the microplate needs to be calculated according to case 7 of Table 4.1:

$$k = \frac{384EI}{L^3} + \frac{8.32N}{L} \quad (g)$$

where $I = (bh^3)/12$ and $N = SEbh$. Then, the stiffness coefficient due to SQFD, k_{SQFD} is calculated according to Eq. (4.45). Using one term in the series leads to

$$k_{SQFD} = \frac{64\sigma^2 P_a A}{\pi^8 d} \times \frac{1}{(1 + \beta^2)^2 + \frac{\sigma^2}{\pi^4}}. \quad (h)$$

The total stiffness is then calculated as the sum of Eq. (g) and Eq. (h), since both act in parallel on the microplate. Finally, the new natural frequency ω_{SQFD} is calculated as

$$\omega_{SQFD} = \sqrt{\frac{k_{SQFD} + k}{m_{\text{eff}}}}. \quad (i)$$

The results are depicted in Fig. 4.22. As seen in the figure, SQFD has shifted the natural frequency near 1.5 kHz from vacuum to $P_a = 200$ Pa. This can be significant shift for resonance sensors if not accounted for properly in calibration.

4.3.5.5 The Nonlinearity of Squeeze-Film Damping

The models discussed in the previous sections are all based on the assumptions of small pressure variation and small motion, which lead to the linearized Reynolds equation. However, if the motion of the structure is large, it results in considerable change in pressure, and hence in nonlinear behavior. To model this, the original

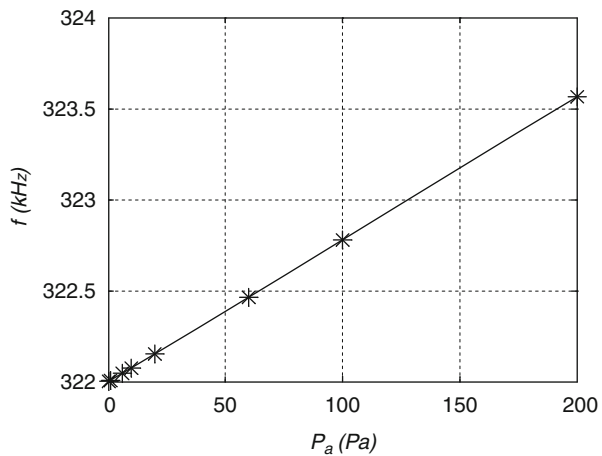


Fig. 4.22 The calculated variation in natural frequency due to SQFD versus pressure

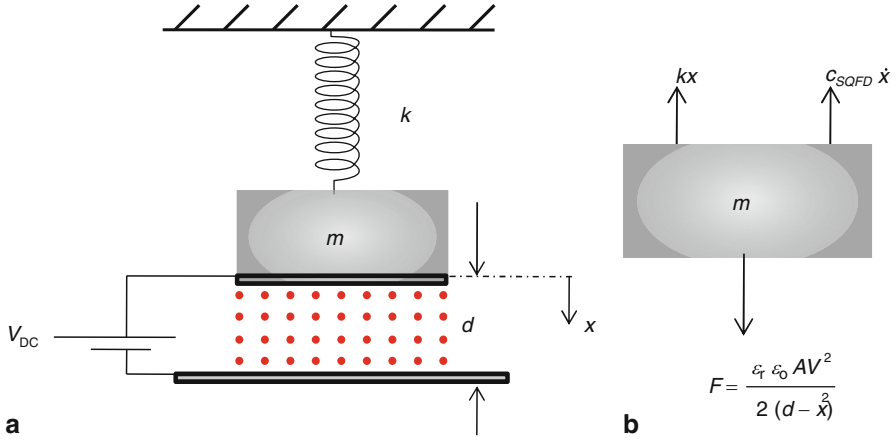


Fig. 4.23 A model of a parallel-plate capacitor under the effect of SQFD, **a** is a schematic of the model and **b** is a free-body diagram

nonlinear Reynolds equation, Eq. (4.27), coupled with a nonlinear structural equation needs to be solved simultaneously.

Recent experimental data [70, 71] have suggested that, for lumped-parameter modeling, the nonlinear dependence of the damping may be captured by a damping coefficient of the form

$$c_{\text{non}} = \frac{\alpha}{[H(x)]^3} \quad (4.59)$$

where α is a parameter that depends on the surface of the structure and the viscosity coefficient of the gas and $H(x)$ is the variable distance between the structure and the substrate. Note that $H(x)$ is taken to be constant ($H = d$) in the linearized model whereas in the nonlinear model it is variable and depends on the displacement of the structure. Several approaches have been proposed for the form of Eq. (4.59). One approach is to assume that the models of Blech [46] and Starrs [44] are still valid for nonlinear behavior if the gap width d is replaced by $H(x)$. To illustrate this, consider as an example the parallel-plate capacitor of Fig. 4.23a. The force diagram of this model is shown in Fig. 4.23b. Based on the figure, the equation of motion of the system can be written as

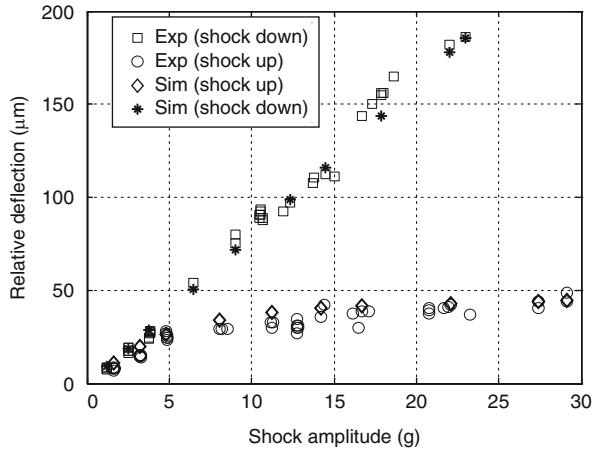
$$m\ddot{x} + c_{\text{non}}\dot{x} + kx = F_{\text{elec}} \quad (4.60)$$

where F_{elec} is the parallel-plate electrostatic force. Using the Belch model, the nonlinear SQFD can be modeled, using one term in the series, as

$$c_{\text{non}} = \frac{768\mu A^2}{\pi^6(d-x)^3} \times \frac{1 + \beta^2}{(1 + \beta^2)^2 + \frac{\sigma^2}{\pi^4}}. \quad (4.61)$$

Equations (4.60) and (4.61) have been used to simulate the large response of the capacitive accelerometer of Fig. 3.17 when subjected to a full-sine acceleration pulse

Fig. 4.24 Simulation results (*stars and diamonds*) and experimental data (*circles and squares*) of the proof mass deflection of a capacitive accelerometer when subjected to a full-sine acceleration pulse. The linear response corresponds to that of the proof mass when it moves away from the substrate, and the nonlinear curve represents its response when it moves toward the substrate. (Reprinted with permission. Copyright 2007, IOP Publishing Ltd [71])



[71]. Figure 4.24 shows the results indicating good agreement between theory and experiment.

If the lumped mass can be modeled as a rectangular plate, then using the Starrs model, the nonlinear coefficient becomes:

$$c_{\text{non}} = \frac{\mu l b^3}{(d - x)^3} f(b/l). \quad (4.62)$$

Chu et al. [45] used Eq. (4.62) to model the dynamic behavior of parallel-plate electrostatic microgripper. For other complicated structures, Eq. (4.59) can be curve-fitted with experimental data to find α . For a full electrode torsional mirror, such as that of Fig. 3.23 with $a_1 = 0$ and $a_2 = a_3$, Sattler et al. [72] derived the below nonlinear expression for the SQFD coefficient

$$c_{\text{non}} = \frac{A a_3^2}{d^3} \frac{1 + \theta^2}{(1 - \theta^2)^2} \quad (4.63)$$

where A is a coefficient calibrated from experimental measurements and the rest of variables are as defined in Fig. 3.23.

4.3.6 Slide-Film Damping

A number of MEMS devices rely on the in-plane motion of microstructures parallel to the substrate, such as comb-drive and electrothermal actuators. The interaction of the gas underneath and above the structure with its motion causes dissipation of energy. There are two main models for the fluid motion in such scenarios: The Couette model and the Stokes model. Both models are derived from the Navier–Stokes equation assuming one-dimensional incompressible flow and that the structure and

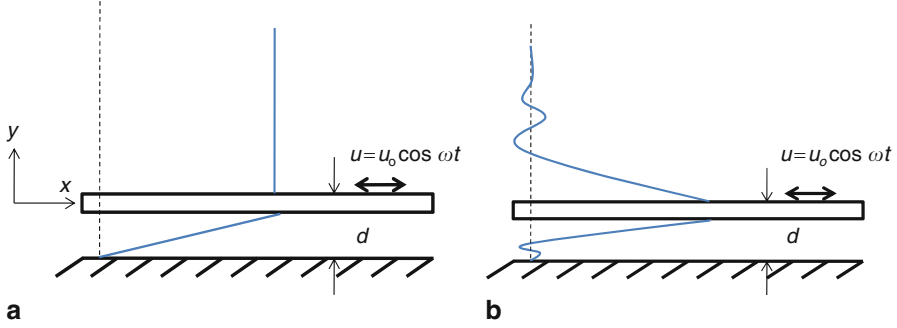


Fig. 4.25 Velocity profile across a laterally moving structure using **a** a Couette model and **b** a Stokes model for the fluid

the substrate are infinite plates. The Couette model assumes linear variation of the velocity below the structure starting from zero on the substrate to the same velocity of the structure on the structure, Fig. 4.25a. Above the structure, the velocity of the gas is assumed the same as that of the structure even for a very large distance above it. Hence, the gas above the structure always moves with it and does not contribute to damping. The Stokes model on the other hand does assume variation for the velocity of the gas both below and above the structure with a nonlinear velocity profile, Fig. 4.25b. While both models predict close results for the damping contribution due to the gas underneath the structure, they deviate when the contribution of the gas above the structure becomes measureable. In this case, the Couette model overestimates the quality factor. This was first remarked by Tang et al. [73] when comparing the measured quality factor of a comb-drive resonator to that predicted using the Couette model. Cho et al. [74] latter used the Stokes model and showed a better agreement with the experimental data. The discussion of this section follows the work of Cho et al. [74].

Whether a Couette model is a good approximation or not depends on the parameter δ , which is a measurement of the distance over which the motion amplitude decreases by the exponential constant e . It is defined as

$$\delta = \sqrt{\frac{2\mu}{\rho\omega}} \quad (4.64)$$

where μ is the viscosity of the fluid, ρ its density, and ω is the frequency of oscillation of the structure. The Couette model applies accurately when $\delta \gg d$, where d is the gap width between the structure and the substrate. Figure 4.26a shows the variation of δ with the frequency f in kHz for air at typical ambient conditions. As seen, when f is large, δ gets closer to typical ranges of d .

The damping coefficient c_{sd} due to the gas underneath the structure is expressed according to Stokes model as [74]

$$c_{sd} = \frac{\mu A}{d} \times Factor \quad (4.65)$$

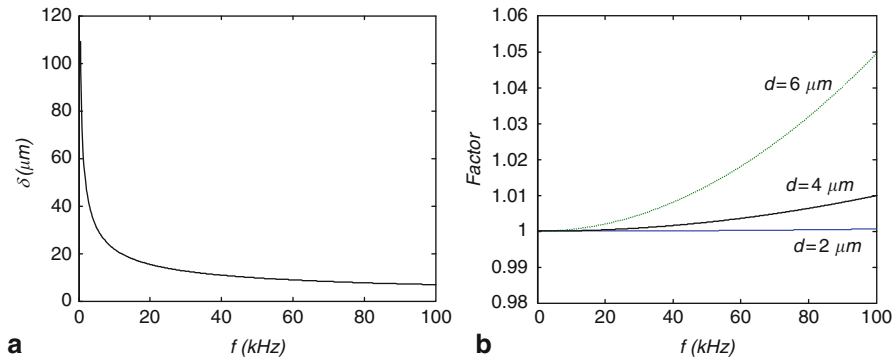


Fig. 4.26 The variation of δ (a) and the amplification factor (*Factor*) (b) with the frequency of oscillation f

where

$$Factor = \beta d \times \frac{\sin(2\beta d) + \sinh(2\beta d)}{\cosh(2\beta d) - \cos(2\beta d)} \quad (4.66)$$

where $\beta = 1/\delta$ and A is the surface area of the structure. When $\delta \gg d$, the multiplication factor (*Factor*) approaches unity. Thus, the damping coefficient due to the gas underneath the structure converges to that assuming a Couette model c_{cd} :

$$c_{cd} = \frac{\mu A}{d}. \quad (4.67)$$

Figure 4.26a shows the variation of *Factor* with the frequency for various values of d . As noted, for small values of d , the *Factor* is equal unity for almost all ranges of frequency. It increases then with larger values of d . The damping coefficient due to the gas above the structure $c_{s,above}$ is expressed according to the Stokes model as [74]

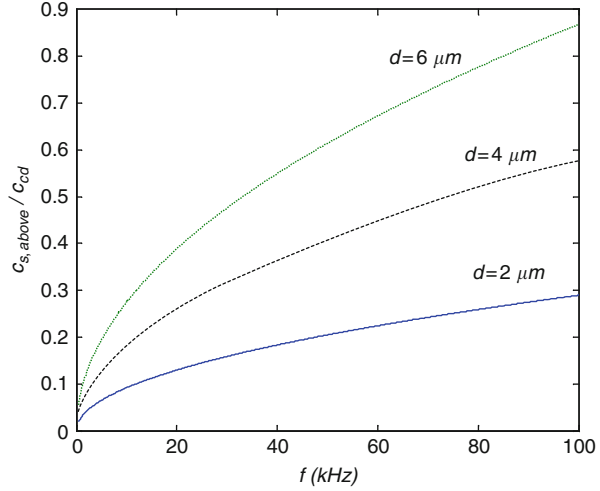
$$c_{s,above} = \mu A \beta. \quad (4.68)$$

One way to quantify the contribution of the gas above the structure is to normalize it to that due to the gas underneath the structure. Figure 4.27 shows a plot for the ratio $c_{s,above}/c_{cd}$ versus f for various values of d . As noted, the contribution of the gas above the substrate increases with d and f .

Example 4.7: A lateral comb-drive resonator of an effective area $A = 4 \times 10^{-8} \text{ m}^2$, an effective spring constant $k = 0.5 \text{ N/m}$, and a gap separation from the substrate $d = 2 \text{ } \mu\text{m}$ is operated at resonance at a frequency $f = 10 \text{ kHz}$. Calculate the quality factor of the device. Ignore the contribution from the motion of the fingers against each other.

Solution: The quality factor Q is contributed in general from the gas underneath the structure and above it. Since d and f are small, according to Fig. 4.26b, a Couette model applies for the gas below the structure. Also, according to Fig. 4.27, the gas

Fig. 4.27 The damping contribution from the gas above the structure normalized to that of the gas below the structure using the Couette model



above the structure contributes slightly to the damping. Hence, the quality factor is expressed as

$$Q = m\omega \left(\frac{1}{c_{cd}} + \frac{1}{c_{s,above}} \right) = m\omega \left(\frac{d}{\mu A} + \frac{1}{\mu A \beta} \right). \quad (a)$$

The mass is calculated as $m = k/\omega^2$. Plugging the numbers yields $Q = 20.25$. If $c_{s,above}$ is ignored, then $Q = 22.1$.

4.3.7 Intrinsic Damping

Intrinsic damping in MEMS is in general much lower than extrinsic damping due to environmental and external effects. Extrinsic damping mechanisms can be minimized by a proper design of devices and their operating conditions. For example, SQFD can be minimized by increasing the distance between the capacitor electrodes, perforating the structures, and encapsulating the devices at a very low pressure. Support losses also can be minimized by a proper design of the vibrating structure and its mounting mechanism. Intrinsic mechanisms on the other hand are more difficult to control because they depend primarily on the material and geometric properties of the structures. Intrinsic damping increases significantly with miniaturization of devices and can limit the quality factors of microstructures in the micro and sub-micro scales.

Intrinsic damping in MEMS is still a very active research topic. There are many mechanisms that contribute to intrinsic damping; however the exact contribution of each of them is still unclear. Examples of these mechanisms are [75] phonon–phonon scattering; phonon–phonon–electron scattering; and surface losses, such as

losses due to thin film, metal layer, oxide layer, and water layer. There is also energy dissipation due to the relaxation phenomenon. This mechanism is characterized by a peak and a relaxation time (this process is also called Debye relaxation). Examples of this category are thermoelastic relaxation, defect relaxation, and grain-boundary relaxation. Recent studies have shown that thermoelastic damping can be a dominant source of intrinsic damping in MEMS.

Thermoelastic damping, also called internal friction, can occur in any material subjected to cyclic stress [76]. This mechanism becomes a very significant source of energy loss when the period of cyclic stress approaches a structure's thermal constant. In a thermoelastic solid [77], the strain and temperature are coupled through the material thermal expansion coefficient. This coupling provides an energy dissipation mechanism, which allows the system to relax to equilibrium. The relaxation is achieved through the irreversible heat flow across the material of structure with different temperature zones. An example is the case of a structure in bending, in which one of its side is under tension, with cooler temperature, and the other side is under compression, with higher temperature.

The first to realize the importance of thermoelastic damping and analyze it rigorously is Zener [78], who gave an analytical approximation for the quality factors of metallic beams due to thermoelastic damping. Roszhart [76] showed experimentally that thermoelastic damping can limit the quality factors of devices in the micro scale. He used the Zener [78] model to calculate the quality factors of solid-state resonators and found good agreement with the measurements. Other experimental works showing thermoelastic damping as a dominant source of energy loss in MEMS are also reported in [79, 80].

Lifshitz and Roukes [77] solved exactly the problem of thermoelastic damping of beams and derived an analytical expression for the quality factors. They calculated the quality factors of various microbeams and found that their model yields results close to that of the Zener [78] model. The thermoelastic problem in microplates has been also investigated recently [81]. More analysis of this topic in beams is presented in Sect. 6.18.2.

4.3.8 Extracting Damping Coefficients Experimentally

Despite the effort of the previous sections to present analytical expressions to predict damping due to various sources, these remain only approximations and rough estimates with many sources of inaccuracies and errors. Essentially, there are always the possibilities for unaccounted sources of energy dissipation that may be overlooked or underestimated in the modeling, which may in reality contribute significantly to the dynamic response. Therefore, in addition to the analytical prediction, if possible, one should seek to quantify energy losses and to estimate equivalent damping coefficients experimentally.

Measurement of damping is however not an easy task. Unlike stiffness and mass, which can be determined through static tests and measurements, damping requires

dynamic testing, which is in general more difficult to conduct and control. For linear damping mechanisms, there are two main approaches to estimate damping coefficients. The first and most common in MEMS relies on measuring the dynamic steady-state response of the structure for various values of frequency, thus generating a frequency–response curve. Such a curve can be generated either using random excitation test or through frequency-sweep tests. Then, by measuring the half-power points, also called the 3-dB down points if the response is plotted in the log scale in dB, the damping ratio and quality factor are determined as explained in Fig. 2.13 and Eqs. (2.38)–(2.40).

The second approach, called the logarithmic decrement approach [20], depends on measuring the transient response of the structure when subjected to a sudden force, such as a step input voltage or an acceleration pulse. As an example, consider the transient response shown in Fig. 4.28a. By measuring the ratio of any two successive amplitudes X_1, X_2 , the logarithmic decrement δ is calculated as

$$\delta = \log \left(\frac{X_1}{X_2} \right). \quad (4.69)$$

Then, it can be shown that the damping ratio ζ is calculated as [20]

$$\zeta = \frac{\delta}{\sqrt{\delta^2 + 4\pi^2}}. \quad (4.70)$$

Because Eqs. (4.69) and (4.70) rely on only two measurements of amplitude, it can yield inaccurate results. A more accurate way to estimate δ and hence ζ is to measure multiple successive amplitudes X_1, X_2, \dots, X_j . Then, by plotting the natural logarithm of X_j versus j , a straight line is obtained, the slope of which represents a more accurate estimate for δ . Figure 4.28b shows an example of such plot based on Fig. 4.28a.

A third approach that can be used is to curve-fit a simulated frequency–response curve using a spring–mass–damper model to that measured experimentally by adjusting the value of the damping coefficient. This requires however a preknowledge

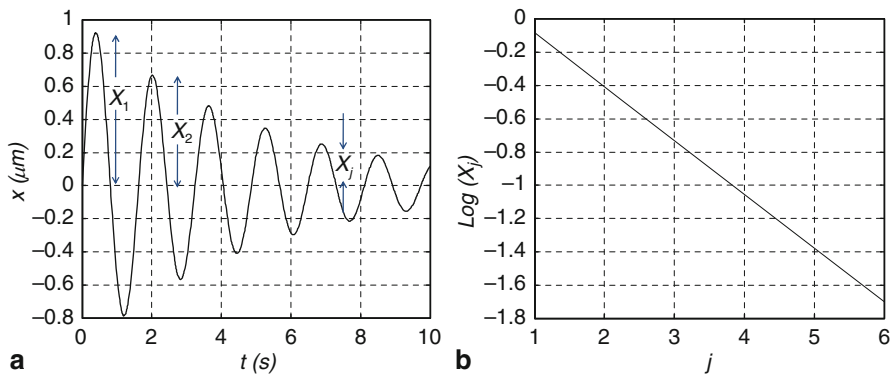


Fig. 4.28 **a** The transient response of a damped oscillator. **b** The logarithmic of the various amplitudes versus their order number

of the other model parameters, which are the effective mass and the stiffness. To estimate the damping coefficient in a nonlinear damping model, for example due to SQFD, curve fitting techniques for the predicted dynamic response based on the nonlinear model of the system to the experimental data need to be used. For example, in the case of SQFD, Eq. (4.59) can be used with experimental data to find α .

Example 4.8: Calculate the damping coefficient of the transient response of Fig. 4.28a using the logarithmic decrement approach based on two measurements of amplitudes and also based on multiple measurements.

Solution: From Fig. 4.28a, the first two amplitudes are estimated as $X_1 = 0.92$ and $X_2 = 0.67$. Hence, according to Eq. (4.69) $\delta = 0.325$. Plugging this value in Eq. (4.70) gives $\zeta = 0.054$. The other approach is to measure multiple amplitudes and to plot their natural logarithm versus their order number, as shown in Fig. 4.28b. Based on the figure, the absolute value of the slope of the line gives $\delta = 0.324$, which yields $\zeta = 0.052$.

Problems

- 1. Consider the measured parameters of the T-type torsional actuator of Degani et al. [82] in the below table. Estimate the effective stiffness of the actuator. Then, plot the response of the actuator for various values of voltage load up to pull-in.

V_{pull} (V)	a_1 (μm)	a_2 (μm)	a_3 (μm)	d (μm)	b (μm)
11.5	430	680	700	4.55	1,300

- 2. Shown in Fig. 4.29 are clamped–clamped, cantilever, and pinned–pinned microbeams, respectively. Each is assumed to form the upper electrode of a capacitor of a gap width d . All microbeams have a rectangular cross section of width b and have the same material properties. Using lumped-parameter modeling, compare the pull-in voltage of the microbeams.

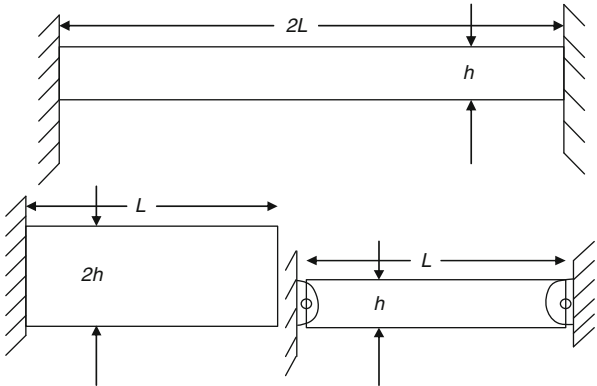


Fig. 4.29 Microbeams of different geometry forming the upper electrode of capacitors

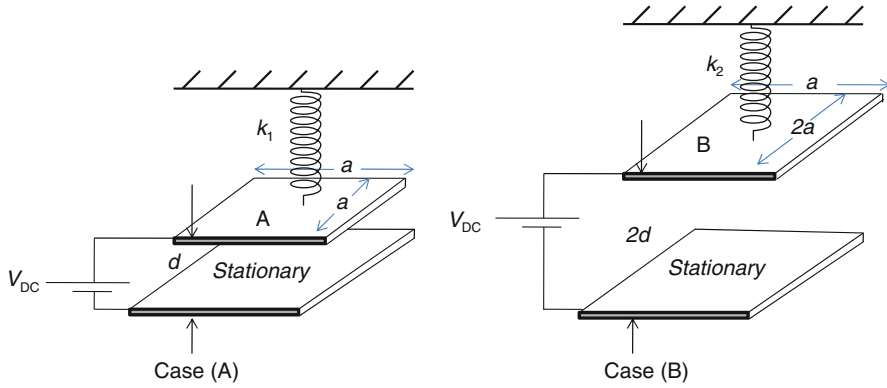


Fig. 4.30 Two parallel-plate capacitors

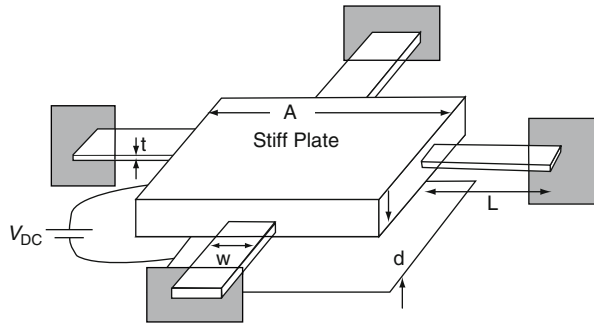
3. Figure 4.30 shows two parallel plate capacitors employed in pressure sensors.
 - (a) Using the Belch model, determine which plate of the two will experience the larger SQFD effect?
 - (b) Experimentally, it was found that the upper plate has the same pull-in voltage in both cases. Let $V_{DC} = 0$, under the action of a uniform distributed pressure load P above the upper plate, determine which plate of the two will have the larger deflection due to this pressure load?
4. Use a lumped spring–mass–damper model to study the damping characteristic of a clamped–clamped microplate, similar to Fig. 4.12, actuated by electrostatic forces and used as a resonant sensor [55, 69]. The microplate is made of silicon with density $\rho = 2,332 \text{ kg/m}^3$ and modulus of elasticity $E = 166 \text{ GPa}$. The plate has a length $L = 310 \text{ }\mu\text{m}$, thickness $h = 1.5 \text{ }\mu\text{m}$, width $b = 100 \text{ }\mu\text{m}$, and gap width separating it from the substrate $d = 1.18 \text{ }\mu\text{m}$. The microplate is placed in a package, where the pressure is reduced according to the below values:

$$P_a = \{4 \times 10^{-5}, 0.01, 0.06, 0.1, 0.2, 0.6, 1.0, 2.0\} \text{ mbar.}$$

Experimentally, the fundamental natural frequency of the microplate was measured and found near $f = 163 \text{ kHz}$, a tensile residual strain was measured and found to be $S = 0.0000404$, and the quality factor of the microplate was measured in vacuum and found to be $Q_{vac} = 17,000$. Assume the mean free path of air at ambient pressure $\lambda_0 = 0.064 \text{ }\mu\text{m}$ and the viscosity coefficient of air $\mu_{air} = 1.82 \times 10^{-5} \text{ Ns/m}^2$. Also, assume the microplate rigid of open sides, so that the model of Blech [46] applies. Consider the microplate is operated near its fundamental natural frequency.

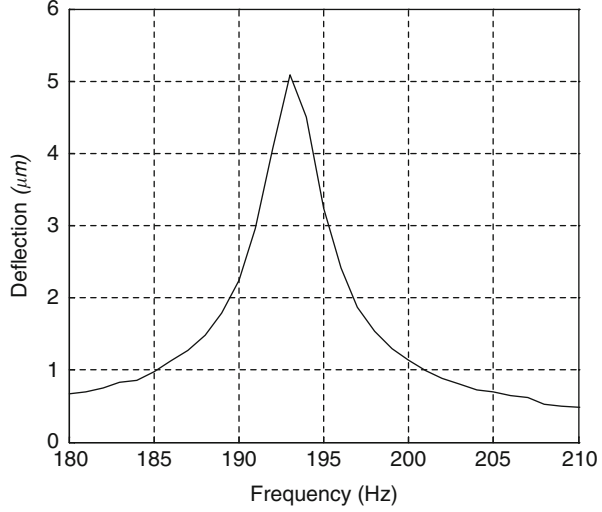
- (a) Plot the Knudsen number for the given values of pressure.
- (b) Use the model of Viejola et al. [49] to calculate and plot the effective viscosity coefficient.

Fig. 4.31 A stiff plate capacitor



- (c) Calculate and plot the squeeze number assuming the microplate to be excited at resonance (at its natural frequency). Also, calculate the cut-off squeeze number.
 - (d) Calculate and plot the damping coefficient of the microplate assuming compressible and incompressible gas and compare the two results.
 - (e) Calculate the total quality factor of the microplate and plot the results against pressure. Compare to the below measured values of quality factor [55].
 $Q_{\text{exp}} = \{18,000, 9,950, 1,800, 850, 450, 188, 110, 60\}$;
 - (f) Calculate the change of natural frequency, if any, with the pressure and plot the results.
 - (g) Calculate the pull-in voltage of the microplate. Compare to the reported measurement of 13.8 V.
5. Figure 4.31 shows a schematic of a stiff square plate made of silicon and anchored through four cantilever beams from its four sides as shown. The plate forms one side of a capacitor. Assume $a = L = 200 \mu\text{m}$, $d = t = 2 \mu\text{m}$, and $w = 10 \mu\text{m}$. The natural frequency of the plate was measured and found to be 10 kHz.
 - (a) Calculate the pull-in voltage of the plate.
 - (b) Calculate the damping coefficient of the microplate assuming compressible and incompressible gas and compare the two results.
6. Figure 4.32 shows a measured frequency–response curve of the capacitive accelerometer of Fig. 3.17 at a pressure = 214 mtorr. The proof mass of the device is suspended a distance $d = 42 \mu\text{m}$ from the substrate. The pull-in voltage of the device was measured and found near 115 V. Assume the proof mass dimensions, which are the same as the electrode area, to be $9 \text{ mm} \times 4.4 \text{ mm}$.
 - (a) From Fig. 4.31, estimate the quality factor of the device.
 - (b) Calculate the effective stiffness of the beams connected to the proof mass.
 - (c) Use the Blech model [46] with an appropriate effective viscosity coefficient and calculate the quality factor analytically. Compare to your answer in (a).

Fig. 4.32 A measured frequency–response curve of a capacitive accelerometer



7. Consider the SQFD problem of a circular rigid plate of radius R vibrating against the substrate, which is separated from the plate a distant d . Assuming incompressible gas underneath the plate and that the pressure varies radially across it, the linearized Reynolds equation in polar coordinates can be written as

$$\frac{1}{r} \frac{\partial}{\partial r} \left(r \frac{\partial [\Delta p(r)]}{\partial r} \right) = \frac{12\mu}{d^3} \frac{\partial z}{\partial t} \quad (a)$$

where r is the radial distance on the circular plate from its center, Δp is the net gauge pressure across the thickness of the plate, and $z(t)$ is the small displacement of the plate. Assume the plate to be open from all edges with the below pressure boundary conditions:

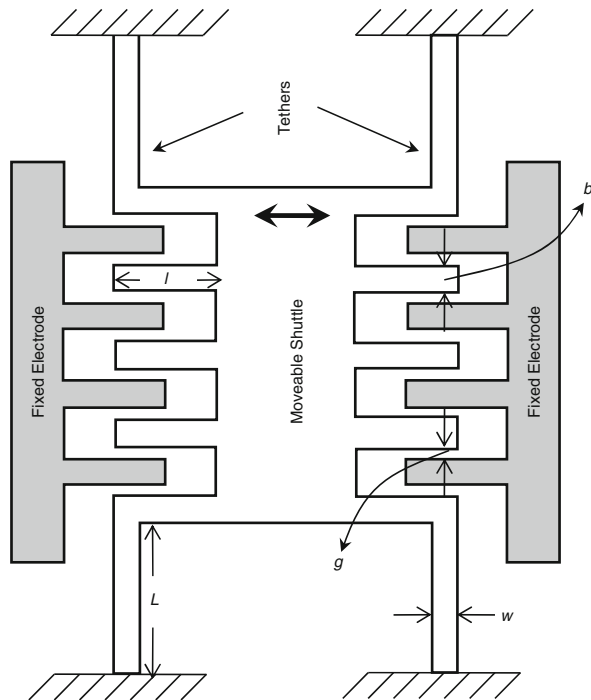
$$\Delta p(R) = 0; \quad \frac{\partial [\Delta p(0)]}{\partial r} = 0. \quad (b)$$

Derive an analytical expression for the damping coefficient of the circular plate due to the SQFD. Your answer should be the same as case 3 of Table 4.6.

8. Figure 4.33 shows the top view of a transversal comb-drive actuator of six active fingers. The actuator is made of a moveable shuttle connected to four cantilever beams, which act as springs. Each cantilever has a length $L = 100 \mu\text{m}$, width $w = 5 \mu\text{m}$, and a depth $h = 20 \mu\text{m}$. Each moveable finger has a length $l = 100 \mu\text{m}$, width $b = 10 \mu\text{m}$, and a depth $h = 20 \mu\text{m}$, and is separated from the stationary finger a distance $g = 1 \mu\text{m}$. The device is suspended above the substrate a distance $d = 2 \mu\text{m}$. Assume the device is made of silicon with Young's modulus $E = 166 \text{ GPa}$ and density $\rho = 2,330 \text{ kg/m}^3$.

- (a) Calculate the effective stiffness coefficient of the cantilevers assuming the moveable shuttle as a stiff plate.

Fig. 4.33 A transversal comb-drive actuator



- (b) Calculate the deflection of the shuttle mass if the device is biased by a DC voltage of 20 V.
- (c) Calculate the quality factor of the device when operated in air assuming the surface area of the shuttle $A = 4 \times 10^{-8} \text{ m}^2$. Assume the device is operated at its resonance frequency $f = 20 \text{ kHz}$. Neglect the contribution of the damping from the fingers.
9. Consider the torsional mirror of Pan et al. [64] of the parameters in the table below. The equation of motion of the micromirror can be expressed as

$$I_m \ddot{\alpha} + c_{\text{tsq}} \dot{\alpha} + K_t \alpha = T_e \quad (\text{a})$$

where I_m is the mass moment of inertia of the mirror, c_{tsq} is the SQFD coefficient, K_t is the torsional stiffness coefficient, and T_e is the external applied torque. Assume the mirror is operated in air at the atmospheric pressure.

$K_t \times 10^{-7} \text{ (Nm)}$	$l_m \text{ (}\mu\text{m)}$	$w_m \text{ (}\mu\text{m)}$	$I_m \text{ (kg m}^2\text{)}$	$d \text{ (}\mu\text{m)}$
4.49	1,500	1,400	5.51×10^{-15}	42

- (a) Calculate the squeeze number and show that it is small, therefore k_{tsq} can be neglected.
- (b) Calculate the SQFD coefficient c_{tsq} .

- (c) Calculate and plot the time response of the mirror to a harmonic external torque $T_e = (4.84 \times 10^{-9}) \sin(\Omega t)$ for an excitation frequency $\Omega = 1.44$ kHz.
 - (d) Calculate and plot the frequency–response curve of the mirror to a harmonic external torque $T_e = (4.84 \times 10^{-9}) \sin(\Omega t)$ for various values of Ω .
10. Consider a square plate of length $l = 400 \mu\text{m}$. The plate has $N = 36$ uniformly distributed circular holes, each hole of a radius $r_0 = 4 \mu\text{m}$.
- (a) Find the ratio of the SQFD coefficient of the perforated plate to that of a solid plate (without the perforation).
 - (b) Repeat (a) assuming the number of holes has increased to $N = 49$.
 - (c) Repeat (a) assuming the radius of the hole has increased to $r_0 = 8 \mu\text{m}$.

References

- [1] Malatkar P and Nayfeh A H (2003) A parametric identification technique for single-degree-of-freedom weakly nonlinear systems with cubic nonlinearities. *Journal of Vibration and Control*. 9: 317–36
- [2] Dick A J, Balachandran B, DeVoe D L, and Mote C D Jr (2006) Parametric identification of piezoelectric microscale resonators. *Journal of Micromechanics and Microengineering*. 16:1593–1601
- [3] Osterberg P M and Senturia S D (1997) M-Test: A test chip for MEMS material property measurement using electrostatically actuated structures. *Journal of Microelectromechanical Systems*. 6:107–118
- [4] Wang X D, Li N, Wang T, Liu M W, and Wang L D (2007) Dynamic characteristic testing for MEMS micro-devices with base excitation. *Measurement Science and Technology*. 18: 1740–1747
- [5] Lai W P and Fang W (2002) Novel bulk acoustic wave hammer to determinate the dynamic response of microstructures using pulsed broad bandwidth ultrasonic transducers. *Sensors and Actuators A*. 96: 43–52
- [6] Legtenberg R, Groeneveld A W, and Elwenspoek M (1996) Comb-drive actuators for large displacements. *Journal of Micromechanics and Microengineering*. 6: 320–329
- [7] Gupta R K and Senturia S D (1997) Pull-in time dynamics as a measure of absolute pressure. *Proceedings of the IEEE Micro Electro Mechanical Systems, MEMS '97*: pp. 290–294
- [8] Ijntema D J and Tilmans H A (1992) Static and dynamic aspects of an air-gap capacitor. *Sensors and Actuators A*. 35:121–128
- [9] Lobontiu N and Garcia E (2004) *Mechanics of Microelectromechanical Systems*. Springer, New York
- [10] Mische C R and Budynas R G (2008) *Shigley's Mechanical Engineering Design*, 8th edition. McGraw-Hill, New York
- [11] Timoshenko S P and Goodier J N (1970) *Theory of Elasticity*. McGraw-Hill, New York
- [12] Pamidighantam S, Puers R, Baert K, and Tilmans H (2002) Pull-in voltage analysis of electrostatically actuated beam structures with fixed-fixed and fixed-free end conditions. *Journal of Micromechanics and Microengineering*. 12: 458–464
- [13] Balachandran B and Magrab E (2009) *Vibrations*, 2nd edition. Cengage Learning, Toronto
- [14] Osterberg P, Yie H, Cai X, White J, and Senturia, S (1994) Self-consistent simulation and modeling of electrostatically deformed diaphragms. *Proceedings of the IEEE Workshop on Micro Electro Mechanical Systems MEMS 94*, Oiso, Japan, 28–32.

- [15] Young W and Budynas R (2002) Roark's Formulas for Stress and Strain, 7th edition. McGraw Hill, New York
- [16] Xiao Z, Sun Y, Li B, Lee S, Sidhu K S, Chin K K, and Farmer K R (2004) Natural Frequency Shift of Rectangular Torsion Actuators due to Electrostatic Force. Proceeding of NSTI-Nanotech. 1:0-9728422-7-6
- [17] Nayfeh A H, Younis M I, and Abdel-Rahman E M (2005) Reduced-order models for MEMS applications. *Nonlinear Dynamics*. 41:211–236
- [18] Meirovitch L (2001) Fundamentals of Vibrations. McGraw Hill, New York
- [19] Alsaleem F, Younis M I, Ouakad H (2009) On the nonlinear resonances and dynamic pull-in of electrostatically actuated resonators. *Journal of Micromechanics and Microengineering*, 19:045013(1–14)
- [20] Thomson W T and Dahleh M D (1998) Theory of Vibration with Applications, 5th edition. Prentice Hall, New Jersey
- [21] Palm W (2007) Mechanical Vibration. Wiley, New York
- [22] Lobontiu N (2007) Dynamics of Microelectromechanical Systems. Springer, New York
- [23] Tang W C, Nguyen T C and Howe R T (1989) Laterally driven polysilicon resonant microstructures. *Sensors Actuators A*. 20:25–32
- [24] Tang W C, Nguyen T C, Judy, M W, and Howe R T (1994) Electrostatic-comb drive of lateral polysilicon resonators. *Sensors Actuators A*. 21–23: 328–331
- [25] Lin L, Nguyen C, Howe R T, and Pisano A P (1992) Micro Electromechanical Filers for Signal Processing. Proceeding IEEE Micro-Electro-Mechanical Systems, Travemunde, Germany, pp: 226–231
- [26] Hirano T, Furuhashi T, Gabriel K J, and Fujita H (1992) Design, fabrication, and operation of submicron gap comb-drive microactuators. *Journal of Micromechanical systems*. 1–1: 52–59
- [27] Tilmans H A, Elwespoek M, and Fluitman J H (1992) Micro resonant force gauges. *Sensors and Actuators A*. 30: 35–53
- [28] Hao Z, Erbil A, and Ayazi F (2003) An analytical model for support loss in micromachined beam resonators with in-plane flexure vibrations. *Sensors and Actuators A*. 109: 156–164.
- [29] Hosaka H, Itao K, and Kuroda S (1995) Damping characteristics of beam-shaped micro-oscillators. *Sensors and Actuators A*. 49:87–95
- [30] Corman T, Enoksson P, and Stemme G (1997) Gas damping of electrostatically excited resonators. *Sensors and Actuators A*. 61: 249–255
- [31] Zook J D, Burns D W, Guckel H, Sniegowski J J, Engelstad R L, and Feng Z (1992) Characteristics of polysilicon resonant microbeams. *Sensors and Actuators A*. 35: 290–294
- [32] Khonsari M M and Booser E R (2001) Applied Tribology. Wiley, New York
- [33] Li G and Hughes H (2000) Review of viscous damping in micro-machined structures. Proceedings of SPIE in micromachined devices and components VI, Bellingham, Washington, 4176: 30–46
- [34] Burgdorfer A (1959) The influence of the molecular mean free path on the performance of hydrodynamic gas lubricated bearing. *Journal of Basic Engineering*. 81: 94–99
- [35] Beskok A and Karniadakis G E (1996) A model for rarefied internal gas flows. *Journal of Fluid Mechanics*. 10: 1–37
- [36] Newell W E (1968) Miniaturization of tuning forks. *Science*. 161: 1320–1326
- [37] Blom F R, Bouwstra S, Elwespoek M, Fluitman J H J (1992) Dependence of the quality factor of micromachined silicon beam resonators on pressure and geometry. *Journal of Vacuum and Science Technology B*. 10: 19–26
- [38] Christian R G (1966) The theory of oscillating-vane vacuum gauges. *Vacuum*. 16: 175–178
- [39] Kadar Z, Kindt W, Bossche A, and Mollinger J (1996) Quality factor of torsional resonators in the low-pressure region. *Sensors and Actuators A*. 53: 299–303
- [40] Li B, Wu H, Zhu C, and Liu J (1999) The theoretical analysis on damping characteristics of resonant microbeam in vacuum. *Sensors and Actuators A*. 77: 191–194
- [41] Bao M, Yang H, Yin H, and Sun Y (2002) Energy transfer model for squeeze-film air damping in low vacuum. *Journal of Micromechanics and Microengineering*. 12: 341–346
- [42] Bao M (2005) Analysis and Design Principles of MEMS Devices. Elsevier, Amsterdam

- [43] Nayfeh A H and Younis M I (2004) A new approach to the modeling and simulation of flexible microstructures under the effect of squeeze-film damping. *Journal of Micromechanics and Microengineering*. 14: 170–181
- [44] Starr J B (1990) Squeeze-film damping in solid-state accelerometers. *Proceeding of the IEEE Solid-State Sensor and Actuator Workshop*, Hilton Head Island, South Carolina, 44–47
- [45] Chu P B, Nelson P R, Tachiki M L, and Pister K S (1996) Dynamics of polysilicon parallel-plate electrostatic actuators. *Sensors and Actuators A*. 52: 216–220
- [46] Blech J J (1983) On isothermal squeeze films. *Journal of Lubrication Technology A*. 105: 615–620
- [47] Griffin W S, Richardson H H, and Yamanami S (1966) A study of fluid squeeze-film damping. *Journal of Basic Engineering*. 88: 451–456.
- [48] Andrews M, Harris I, and Turner G (1993) A comparison of squeeze-film theory with measurements on a microstructure. *Sensors and Actuators A*. 36: 79–87
- [49] Veijola T, Kuisma H, Lahdenpera J, and Ryhanen T (1995) Equivalent-circuit model of the squeezed gas film in a silicon accelerometer. *Sensors and Actuators A*. 48: 239–248
- [50] Darling R B, Hivick C and, Xu J (1998) Compact analytical modeling of squeeze film damping with arbitrary venting conditions using a Green's function approach. *Sensors and Actuators A*. 70: 32–41
- [51] Yang Y J, Gretillat M A, and Senturia S D (1997) Effect of air damping on the dynamics of nonuniform deformations of microstructures. *International Conference on Solid State Sensors and Actuators, TRANSDUCERS '97*, Chicago, Illinois, 2: 1093–1096
- [52] Hung E S and Senturia S D (1999) Generating efficient dynamical models for microelectromechanical systems from a few finite-element simulations runs. *Journal of Microelectromechanical Systems*. 8: 280–289
- [53] McCarthy B, Adams G, McGruer N, and Potter D (2002) A dynamic model, including contact bounce of an electrostatically actuated microswitch. *Journal of Microelectromechanical Systems*. 11: 276–283
- [54] Younis M I and Nayfeh A H (2007) Simulation of squeeze-film damping of microplates actuated by large electrostatic load. *ASME Journal of Computational and Nonlinear Dynamics*. 2: 232–241
- [55] Legtenberg R and Tilmans H A (1994) Electrostatically driven vacuum-encapsulated polysilicon resonators. Part I. Design and fabrication. *Sensors and Actuators A*. 45: 57–66
- [56] Harmrock B J (1994) *Fundamentals of Fluid Film Lubrication*. McGraw-Hill, New York
- [57] Schrag G and Wachutka G (2002) Physically based modeling of squeeze film damping by mixed-level system simulation. *Sensors and Actuators A*. 97: 193–200
- [58] Veijola T, Ruokonen K, and Tittonen I (2001) Compact model for the squeezed-film damping including the open border effects. *Proceeding of the Forth Conference on Modeling and Simulation of Microsystems, MSM'01*, Hilton Head Island, South Carolina, pp. 76–79
- [59] Vemuri S, Fedder G K, and Mukherjee T (2000) Low-order squeeze film model for simulation of MEMS devices. *Proceeding of the Third Conference on Modeling and Simulation of Microsystems, MSM'00*, San Diego, pp. 205–208
- [60] Fukui S and Kaneko R (1988) Analysis of ultra-thin gas film lubrication based on linearized Boltzman equation: first report-derivation of a generalized lubrication equation including thermal creep flow. *Journal of Tribology*. 253–262:299–303
- [61] Hsia Y T and Domoto G A (1983) An experimental investigation of molecular rarefaction effects in gas lubricated bearings at ultra-low clearance. *Journal of Lubrication Technology: Transaction of the ASME*. 105: 120–130
- [62] Seidel H, Riedel H, Kolbeck R, Mück G, Kupke W, and Kupke W (1990) Capacitive silicon accelerometer with highly symmetric design. *Sensors and Actuators A*. 23: 312–315
- [63] Mitsuya Y (1993) Modified Reynolds equation for ultra-thin film gas lubrication using 1.5-order slip-flow model and considering surface accommodation coefficient. *Journal of Lubrication Technology: Transaction of the ASME*. 115: 289–294
- [64] Pan F, Kubby J, Peeters E, Tran A T, and Mukherjee S (1998) Squeeze film damping effect on the dynamic response of a MEMS torsion mirror. *Journal of Microelectromechanical Systems*. 8: 200–208

- [65] Furlani E P (1999) Theory and simulation of viscous damped reflection phase gratings. *Journal of Physics D: Applied Physics*. 32: 412–416
- [66] Gabrielson T (1993) Mechanical-thermal noise in micromachined acoustic and vibration sensors. *IEEE Transaction on Electron Devices*. 40: 903–909
- [67] Bao M, Yang H, Sun Y, French P J (2003) Modified Reynold's equation and analytical analysis of squeeze-film air damping of perforated structures. *Journal of Micromechanics and Microengineering*. 13: 795–800
- [68] Homentcovschi D, Miles R N (2005) Viscous damping of perforated planar micromechanical structures. *Sensors and Actuators A*. 119: 544–552
- [69] Tilmans H A and Legtenberg R (1994) Electrostatically driven vacuum-encapsulated polysilicon resonators. Part II. Theory and performance. *Sensors and Actuators A*. 45: 67–84
- [70] Krylov S and Maimon R (2004) Pull-in dynamics of an elastic beam actuated by continuously distributed electrostatic force. *ASME Journal of Vibrations and Acoustics*. 126–3: 332–342
- [71] Younis M I, Alsaleem F M, Miles R, and Su Q (2007) Characterization for the performance of capacitive switches activated by mechanical shock. *Journal of Micromechanics and Microengineering*. 17: 1360–1370
- [72] Sattler R, Plotz F, Fattinger G, Wachutka G (2002) Modeling of an electrostatic torsional actuator demonstrated with an RF MEMS switch. *Sensors and Actuators A*. 97–98: 337–346
- [73] Tang W C, Nguyen T C, and Howe R T (1989) Laterally driven polysilicon resonant microstructures. *Sensors Actuators A*. 20, 25–32.
- [74] Cho Y H, Pisano A, and Howe R T (1994) Viscous damping model for laterally oscillating microstructures. *Journal of Microelectromechanical Systems*. 3: 81–87
- [75] Cleland A N (2003) *Foundations of Nanomechanics*. Springer, Berlin
- [76] Roszhart T V (1990) The effect of thermoelastic internal friction on the Q of micromachined silicon resonators. *Proceedings of the IEEE technical Digest of Solid-State Sensors and Actuators Workshop*, Hilton Head, South Carolina, pp. 13–16
- [77] Lifshitz R and Roukes M L (2000) Thermoelastic damping in micro- and nanomechanical systems. *Physical Review B*. 61: 5600–5609
- [78] Zener C (1937) Internal friction in solids: I. Theory of internal friction in reeds. *Physical Review*. 52: 230–235
- [79] Duwel A, Gorman J, Weinstein M, Borenstein J, and Ward P (2003) Experimental study of thermoelastic damping in MEMS gyros. *Sensors and Actuators A*. 103: 70–75
- [80] Evoy S, Oikhovets A, Sekaric L, Parpia J M, Craighead H G, and Carr D W (2000) Temperature-dependent internal friction in silicon nanoelectromechanical systems. *Applied Physics Letter*. 77: 2397–2399
- [81] Nayfeh A H and Younis M I (2004) Modeling and simulations of thermoelastic damping in microplates. *Journal of Micromechanics and Microengineering*. 14: 1711–1717
- [82] Degani O, Socher E, Lipson A, Leitner T, Setter D J, Kaldor S, and Nemirovsky Y (1998) Pull-In Study of an Electrostatic Torsion Microactuator. *Journal of Micromechanics and Microengineering*. 7: 373–379

Chapter 5

Introduction to Nonlinear Dynamics

This chapter presents an introduction to fundamental concepts in nonlinear dynamics, which are essential for modeling and testing the mechanical behavior of MEMS devices. Because nonlinear dynamics is a wide topic, the focus here is on subjects that are most common and relevant to MEMS. Basic analytical techniques to analyze and tackle nonlinear systems are presented. Several applications on MEMS devices demonstrating phenomena at the microscale level are discussed. The aim of this chapter is to give MEMS researchers fundamental background on the subject. This should lead to proper understanding of the behavior of microsystems and enable the development of modeling methodologies that can capture the essence of the static and dynamic aspects of MEMS devices behaving nonlinearly.

5.1 Introduction

The dynamic behavior of most systems can be generally considered nonlinear except for a small range of variations of their parameters, in which case linear behavior can be assumed. This is true for both the macro and micro worlds. However, at the microscale, the strong influence of several sources of nonlinearities makes the possibility of operating within the linear regime difficult and of less benefit and the likelihood of triggering nonlinear behavior high.

There are many sources of nonlinearities in MEMS, which can be due to forcing, damping, and stiffness, Fig. 5.1. Forcing can introduce nonlinearities through actuation and detection mechanisms, such as the case of parallel-plate electrostatic forces. Also, nonlinear forces can affect microstructures while in-use, such as in the case of capillary forces due to humidity and van-der Waals forces for structures in close proximity of each other or to the substrate. Some of the damping mechanisms, such as squeeze-film damping, are inherently nonlinear, as discussed in Sect. 4.3.5. Many microstructures are compliant because of the large surface-to-volume ratio. When actuated, they undergo relatively large deformation, which amplifies the so-called geometric nonlinearities of the structures resulting in nonlinear stiffness effect. In addition, the use of some materials can induce material and stiffness-related nonlinear behavior, such as piezoelectric materials, which are quadratic in nature.

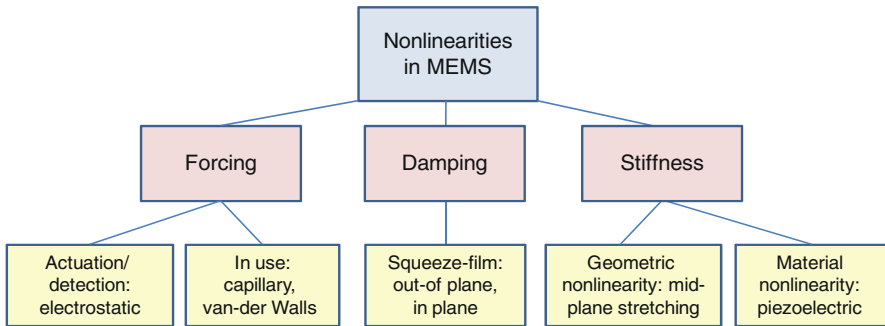


Fig. 5.1 A schematic illustrating some of the common sources of nonlinearities in MEMS

Using linear theories to study nonlinear systems can lead to wrong predictions and erroneous judgments. Linear theories fail to capture and explain many behaviors in MEMS, which are observed experimentally. Phenomena, such as hysteresis and jumps in frequency responses, coexistence of more than one stable state, sensitivity to initial conditions, and escape from a potential well (as in the case of dynamic pull-in) are all nonlinear and cannot be captured based on linear theories. Therefore, nonlinear theories and models need to be utilized for correct and accurate results. One of the major differences between linear and nonlinear theories is the fact that the many of the powerful mathematical methods and tools that apply on linear theories do not apply for nonlinear theories. The superposition principle, Fourier analysis, and Laplace transformation are all inapplicable.

The approaches to analyze nonlinear systems can be classified into qualitative and quantitative. The qualitative approach was first introduced by Henry Poincaré (1854–1912), who is considered the father of nonlinear dynamics, when he presented his geometric qualitative approach of dynamics while studying celestial mechanics [1]. In this method, the interest is to know whether a solution is stable or not in the neighborhood of a known solution of the differential equation without actually solving it. Using this approach, many important characteristics can be revealed about the dynamic behavior of the system. This method is easy to implement; however, it does not provide quantitative results and precise knowledge of the state of the system at a given time. This method is presented in Sect. 5.5 when discussing phase portraits.

A number of quantitative approaches have been developed to solve nonlinear differential equations. In the close neighborhood of equilibrium points, there is the linearization approach, which assumes small disturbances around equilibrium. For weak nonlinearities, perturbation and asymptotic approaches can be used. For strong nonlinearities, numerical approaches need to be utilized. These include finite-element and finite difference methods, direct time integration of the equations of motion, which is discussed in Sect. 2.7, continuation approaches, and shooting techniques to find periodic motions [2]. Some of these methods are introduced in this chapter and in the following ones. For highly complicated dynamical systems, such as chaotic

systems, several other methods need to be used collectively to reveal the nature of the dynamics, such as Lyapunov exponents, Poincaré sections, and power spectra. These methods as well as chaotic systems will not be discussed here, but details about them can be found in [2].

5.2 Nondimensionalization

Nondimensionalization and normalization refer to the process of transforming an equation into a nondimensional equation and its variables into normalized nondimensional variables. As an outcome of this process, the various variables of the system are lumped together in a few nondimensional parameters. The behavior of the system then can be described completely and compactly by understanding the influence of each nondimensional parameter.

Normalization and nondimensionalization serve many important purposes in MEMS. First, it helps identify the influence and strength of the various variables of the system by comparing them against each other and against basic elements of the system. For example, for a cantilever microbeam, a tip deflection of $1\text{ }\mu\text{m}$ can be viewed small if compared to its length, which is in the hundreds of micrometer range. However, if the microbeam is actuated toward the substrate, then the same deflection is now considered large if compared to the distance separating it from the substrate, which is in the range of $1\text{--}2\text{ }\mu\text{m}$. Also, nondimensionalization helps gauge the strength of the various nondimensional parameters governing the behavior of the system. In a nondimensional equation, some parameters may appear negligibly small compared to others, such as the Reynolds number in microfluidic applications. Also, some parameters may appear weak with some influence to suggest using approximate analytical methods, such as identifying that the nonlinearities of the system are weak and then using perturbation techniques to solve the equation. Other parameters may appear dominant with significant influence on the system behavior, thereby demanding special numerical treatment.

The second advantage of nondimensionalization is that it enables characterizing a system in terms of generalized variables and universal parameters that are applicable for generic systems and not confined to a specific one. It also facilitates understanding the characteristic of systems of different properties. For example, a quality factor of 1,000 is considered high for a resonator whereas a quality factor of 5 is considered low, regardless of the size and type of the resonator. The third advantage is computational. Many of the available software and computer packages are not designed to deal with small numbers, such as these of MEMS. Deflections in the microscale and masses in the nanogram can be considered small numbers, which are negligible or below the tolerance limits of the software. Hence, MEMS equations and variables usually introduce computational difficulties and can lead to the divergence of software packages. This problem is solved when dealing with nondimensional equations and variables. Finally, as mentioned before, nondimensionalization maps the design space from numerous variables into few nondimensional parameters. These can

adequately characterize the behavior of the system and make it easier to see how the various variables interact with each other and how they affect the system. Next, the nondimensionalization procedure is demonstrated through some examples.

Example 5.1: Consider the spring–mass–damper system of Fig. 5.2. The spring force in the system is nonlinear and is expressed as

$$F = k_1x + k_2x^2 + k_3x^3. \quad (a)$$

Assume the system initially at rest and is pulled a distance x_0 to the right. Derive an appropriate nondimensional equation of motion for the system.

Solution: The dimensional equation of motion for the system is written as

$$m\ddot{x} + k_1x + k_2x^2 + k_3x^3 + c\dot{x} = 0. \quad (b)$$

The variables of the system, displacement x and time t , need to be replaced by nondimensional variables by normalizing them with respect to constants relevant to the system. The choice of relevant constants is not necessary a unique one. There can be more than one way to normalize a variable and this should not affect the process. In the problem at hand, the dependent variable x is proposed to be normalized with respect to the initial deflection x_0 . One may also choose to normalize x with respect to other characteristic lengths related to the problem, such as the length of the body or the maximum allowable displacement. The independent variable t is proposed to be normalized with respect to the natural period of the system $T = \sqrt{m/k_1}$. Other choices could be any time constant of relevance to the problem, such as the duration of a shock force or the time constant for the temperature to reach steady-state value. Thus, the nondimensional variables \hat{x} and \hat{t} are introduced and defined as

$$\hat{x} = \frac{x}{x_0}; \quad \hat{t} = \frac{t}{T}. \quad (c)$$

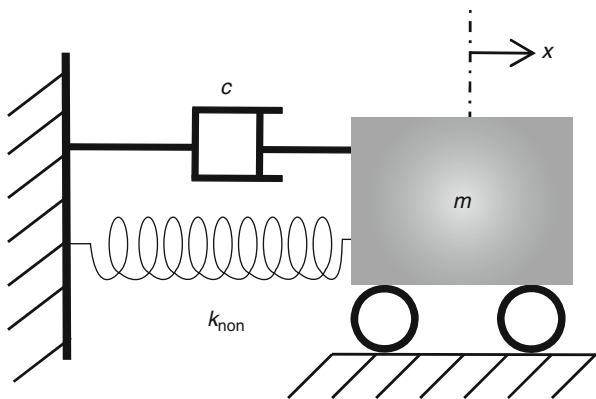


Fig. 5.2 A spring–mass–damper system with a nonlinear spring

The derivatives in the original equation need to be redefined in terms of the nondimensional variables. Here, the derivative with respect to time is written as

$$\frac{d}{dt} = \frac{d}{d(T\hat{t})} = \frac{1}{T} \frac{d}{d\hat{t}}; \quad \frac{d^2}{dt^2} = \frac{d^2}{d(T\hat{t})^2} = \frac{1}{T^2} \frac{d^2}{d\hat{t}^2}. \quad (d)$$

The next step is to substitute Eqs. (c) and (d) into Eq. (b):

$$\frac{mx_0}{T^2} \frac{d^2 \hat{x}}{d\hat{t}^2} + k_1 x_0 \hat{x} + x_0^2 k_2 \hat{x}^2 + x_0^3 k_3 \hat{x}^3 + \frac{cx_0}{T} \frac{d\hat{x}}{d\hat{t}} = 0. \quad (e)$$

To make Eq. (e) nondimensional, the whole equation is multiplied by $T^2/(mx_0) = 1/(k_1 x_0)$, which yields

$$\frac{d^2 \hat{x}}{d\hat{t}^2} + \hat{x} + \frac{x_0 k_2}{k_1} \hat{x}^2 + \frac{x_0^2 k_3}{k_1} \hat{x}^3 + \frac{c}{\sqrt{mk_1}} \frac{d\hat{x}}{d\hat{t}} = 0. \quad (f)$$

Equation (f) can be rewritten as

$$\frac{d^2 \hat{x}}{d\hat{t}^2} + \hat{x} + \alpha_q \hat{x}^2 + \alpha_c \hat{x}^3 + \mu \frac{d\hat{x}}{d\hat{t}} = 0 \quad (g)$$

where the nondimensional parameters in Eq. (g) are defined as

$$\alpha_q = \frac{x_0 k_2}{k_1}; \quad \alpha_c = \frac{x_0^2 k_3}{k_1}; \quad \mu = \frac{c}{\sqrt{mk_1}}. \quad (h)$$

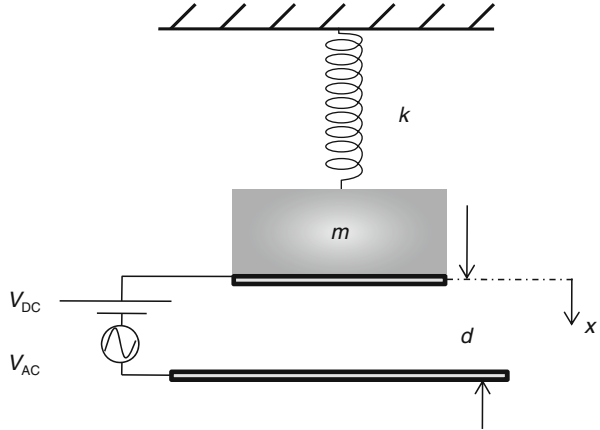
The nondimensional parameters α_q and α_c represent measurements of the strength of the nonlinear spring forces compared to the linear spring force. Based on these parameters, the quadratic and cubic nonlinearities of the system can be judged to be weak or strong. The parameter μ represents a ratio of the damping force to the linear spring force. Also, based on this parameter, the system is judged to be lightly or heavily damped.

Equation (g) is solved with the nondimensional initial condition

$$\hat{x} = 1; \quad \frac{\partial \hat{x}}{\partial \hat{t}} = 0; \quad \text{at } \hat{t} = 0. \quad (i)$$

Example 5.2: Consider the single-degree-of-freedom (1-DOF) model of a parallel-plate capacitor shown in Fig. 5.3, in which the mass is actuated by a DC load V_{DC} superimposed to an AC harmonic load V_{AC} . Derive an appropriate nondimensional equation for the system.

Fig. 5.3 A model of a parallel-plate capacitor with harmonic excitation



Solution: The dimensional equation of motion for the system is written as

$$m\ddot{x} + kx = \frac{\varepsilon A [V_{DC} + V_{AC} \cos(\Omega t)]^2}{2(d - x)^2} \quad (a)$$

where ε is the dielectric constant of the gap medium, A is the electrode area, and Ω is the AC frequency. Next, the variables of the system, x and t , are normalized. Since the gap width d is of importance in this problem, an obvious choice is to normalize x with respect to d . The variable t is normalized with respect to the natural period of the system $T = \sqrt{m/k}$. Thus, the nondimensional variables \hat{x} and \hat{t} are defined as

$$\hat{x} = \frac{x}{d}; \quad \hat{t} = \frac{t}{T}. \quad (b)$$

The derivatives with respect to time are redefined as in Eq. (d) of Example 5.1. Hence, upon substitution, Eq. (a) becomes

$$\frac{md}{T^2} \frac{d^2 \hat{x}}{d\hat{t}^2} + kd\hat{x} = \frac{\varepsilon A [V_{DC} + V_{AC} \cos(\Omega T \hat{t})]^2}{2d^2(1 - \hat{x})^2}. \quad (c)$$

Multiplying by $T^2/md = 1/kd$ yields

$$\frac{d^2 \hat{x}}{d\hat{t}^2} + \hat{x} = \frac{\beta [V_{DC} + V_{AC} \cos(\hat{\Omega} \hat{t})]^2}{(1 - \hat{x})^2} \quad (d)$$

where the nondimensional frequency $\hat{\Omega}$ and the parameter β are defined as

$$\hat{\Omega} = \Omega T = \frac{\Omega}{\sqrt{k/m}}; \quad \beta = \frac{\varepsilon A}{2kd^3}. \quad (e)$$

The parameter β is dimensional. It can be left as is in the equation for convenience to allow direct alteration of the voltage terms in the nondimensional equation. Alternatively, it can be replaced by a nondimensional number by normalizing the voltage

terms. One way to do this is by normalizing V_{DC} and V_{AC} with respect to the pull-in voltage of the device, V_{pull} . Thus, nondimensional voltage loads are defined as

$$\hat{V}_{DC} = \frac{V_{DC}}{V_{pull}}; \quad \hat{V}_{AC} = \frac{V_{AC}}{V_{pull}}. \quad (f)$$

Substituting Eq. (f) into Eq. (d) yields

$$\frac{d^2 \hat{x}}{d\hat{t}^2} + \hat{x} = \frac{\hat{\beta} [\hat{V}_{DC} + \hat{V}_{AC} \cos(\hat{\Omega} \hat{t})]^2}{(1 - \hat{x})^2} \quad (g)$$

where the nondimensional parameter $\hat{\beta}$ is defined as

$$\hat{\beta} = \frac{\varepsilon A V_{pull}^2}{2kd^3}. \quad (h)$$

Note that to excite the system of Eq. (g) at resonance, $\hat{\Omega}$ should be close to unity, which is the normalized natural frequency.

5.3 Fixed Points and Linearization

This section discusses finding the equilibrium points of a dynamical system and analyzing their stability. Also, the method of linearization around equilibrium positions is presented, in which the dynamics of the system in a small neighborhood round the equilibrium positions are analyzed. The discussion here is restricted to the so-called autonomous systems, which do not have an explicit dependence on time in the dynamical equation. The discussion of this section follows the derivations in [2].

Consider the dynamical system governed by the below system of first-order differential equations written in state-space representation

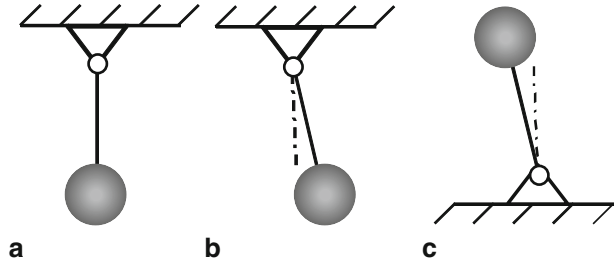
$$\dot{x} = F(x, \mu) \quad (5.1)$$

where $x(t)$ is a vector describing the state of the system in time t , F is a vector representing the right-hand side of the state-space equations, and μ is a constant, called the control parameter, which can be tuned to control the dynamics of the system, such as the voltage load or the damping constant. The equilibrium positions of Eq. (5.1), also called stationary or fixed points, can be found by assuming a constant solution vector $x = X$, which does not depend on time. Substituting $x = X$ in Eq. (5.1) gives the equilibrium equation

$$F(X, \mu) = 0. \quad (5.2)$$

Solving Eq. (5.2) yields the equilibrium vector X . Each equilibrium point can be stable or unstable. The question of stability is very important for dynamical systems.

Fig. 5.4 **a** An unperturbed pendulum. **b** The pendulum perturbed from its stable equilibrium position. **c** An inverted pendulum perturbed from its unstable equilibrium position



Roughly speaking, if for all initial conditions in the close neighborhood of an equilibrium point the system state converges to the equilibrium point or stay confined and close to it as time approaches infinity, the equilibrium point is said to be stable, otherwise, it is considered unstable. For example, a swinging pendulum, Fig. 5.4a, has at least two equilibrium positions, one is stable, Fig. 5.4b, and the other is unstable, Fig. 5.4c. If the system is perturbed from the stable equilibrium position, Fig. 5.4b, then, in the presence of damping, the system converges back to this equilibrium position as time goes on. On the other hand, any small perturbation in the unstable position, Fig. 5.4c, makes the system diverge away and never comes back to the same equilibrium point.

Therefore, analyzing the stability of equilibrium points boils to addressing these questions: How the system behaves when perturbed from equilibrium? Does the ensuing motion remain confined to the neighborhood of the equilibrium points? To answer these questions from a mathematical stand, a small dynamic disturbance $\eta(t)$ is superimposed to the equilibrium solutions and then is monitored to see if it grows or diminishes as time goes on. Thus, the state of the system near equilibrium points at a given time and in the presence of the disturbance is expressed as

$$x(t) = X + \eta(t). \quad (5.3)$$

Equation (5.3) is then substituted into Eq. (5.1), which yields

$$\dot{\eta} = F(X + \eta, \mu). \quad (5.4)$$

Next, Eq. (5.4) is expanded in Taylor series. In the linearization method, only the linear terms are retained and the higher order terms (H.O.T.) are dropped. The results of this expansion becomes

$$\dot{\eta} = \underbrace{F(X; \mu)}_{\text{From Eq.(5.2)=0}} + \nabla_x F(X; \mu)\eta + \underbrace{\text{H.O.T.}}_{\text{Neglected}} \Rightarrow \quad (5.5)$$

$$\dot{\eta} = A\eta \quad (5.6)$$

where $A = \nabla_x F(X; \mu)$ is the Jacobian, first derivative, matrix evaluated at the equilibrium positions and the control parameter. Hence, A is really a matrix of constants.

For a system of differential equations

$$\begin{aligned}\dot{x}_1 &= F_1(x_1, x_2, \dots) \\ \dot{x}_2 &= F_2(x_1, x_2, \dots) \\ &\vdots\end{aligned}\tag{5.7}$$

the Jacobian matrix $\nabla_x F$ is calculated as

$$\nabla_x F = \begin{pmatrix} \frac{\partial F_1}{\partial x_1} & \frac{\partial F_1}{\partial x_2} & \dots \\ \frac{\partial F_2}{\partial x_1} & \frac{\partial F_2}{\partial x_2} & \dots \\ \vdots & \vdots & \dots \end{pmatrix}.\tag{5.8}$$

The matrix A is evaluated from Eq. (5.8) at X and μ . Before proceeding further, it should be noted that the stability analysis here is local, meaning it is valid for a close neighborhood to the equilibrium points, since the disturbance is assumed small and because the original nonlinear system has been linearized.

Equation (5.6) represents a linear system of first-order constant-coefficient differential equations. This system can be assumed to have a solution in the form

$$\eta = ce^{\lambda t}\tag{5.9}$$

where c is a vector of constants, and λ is a characteristic exponent. Substituting Eq. (5.9) into Eq. (5.6) yields

$$c\lambda e^{\lambda t} = Ace^{\lambda t} \Rightarrow Ac = \lambda c.\tag{5.10}$$

Equation (5.10) indicates an eigenvalue problem with λ is the eigenvalue and c is the eigenvector. To solve for the eigenvalue, the below determinant needs to be evaluated

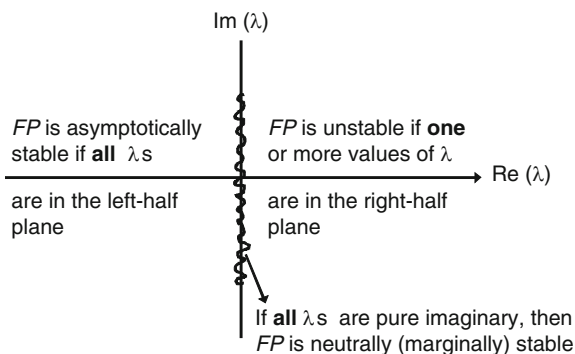
$$|A - \lambda I| = 0\tag{5.11}$$

where I is the diagonal identity matrix. Equation (5.11) yields a characteristic algebraic equation for λ , which is solved to yield the eigenvalues of the system $\lambda_1, \lambda_2, \dots, \lambda_n$. For each λ , a corresponding eigenvector c is evaluated from Eq. (5.10), which gives c_1, c_2, \dots, c_n . Therefore, according to Eq. (5.9), assuming distinct eigenvalues, and using the superposition principle, the total solution for Eq. (5.6) can be expressed as

$$\eta = c_1 e^{\lambda_1 t} + c_2 e^{\lambda_2 t} + \dots + c_n e^{\lambda_n t}.\tag{5.12}$$

In general, λ is a complex number. One can note based on Eq. (5.12) that if the real part of one of the eigenvalues is positive, then as time goes on, the exponential term containing this eigenvalue will go to infinity, meaning that the disturbance η keeps growing and never dies out. This gives the conclusion that in order to have a stable

Fig. 5.5 Schematic illustrating the various conclusions about the stability of a fixed point FP based on the real parts Re and imaginary parts Im of the eigenvalues λs



equilibrium point, the real part of all the eigenvalues needs to be negative so that the disturbance η eventually dies out, and the system converges to the equilibrium point. If the real part of one or more eigenvalue is positive, then the equilibrium point is unstable. If all the eigenvalues have zero real part, then η will neither grow nor diminish with time. In this case, the equilibrium point is said to be marginally or neutrally stable and is also called “center.” In such case, the linearization approach generally is not sufficient to indicate whether the fixed point is stable or not, and hence, other approaches need to be utilized. A summary of these conclusions is presented in Fig. 5.5.

In addition, if all λs are on left half of the complex plane then the fixed point is called sink. If all λs are on right half of the complex plane, then the fixed point is called source. If λs are distributed between the left and right half planes, then the fixed point is called saddle, which is unstable. Moreover, if all λs are real, the fixed point is called node. If at least some λs are complex, the fixed point is called focus. Next, several examples are solved to illustrate the application of the theory presented so far.

Example 5.3: Find the equilibrium solution of a linear spring–mass–damper oscillator and analyze its stability assuming the control parameter to be the damping ratio ζ .

Solution: The equation of motion of the oscillator is written according to Eq. (2.17) as

$$\ddot{x} + 2\zeta\omega_n\dot{x} + \omega_n^2x = 0. \quad (a)$$

The first step in the analysis is to write the equation of motion in a state-space representation. Toward this, we let $x_1 = x$ and $x_2 = \dot{x}$. Then Eq. (a) is written in terms of two first-order differential equations as

$$\dot{x}_1 = x_2 \quad (b)$$

$$\dot{x}_2 = -2\zeta\omega_nx_2 - \omega_n^2x_1. \quad (c)$$

The equilibrium point(s) can be found according to Eq. (5.2) by setting the right hand side of Eqs. (b) and (c) equal to zero. This gives $x_2 = x_1 = 0$ or $(0,0)$ is an equilibrium point. To analyze its stability, the Jacobian of Eqs. (b) and (c) is calculated from Eq. (5.8) at the equilibrium point as

$$A = \nabla_x F[(0,0); \zeta] = \begin{bmatrix} 0 & 1 \\ -\omega_n^2 & -2\zeta\omega_n \end{bmatrix}. \quad (d)$$

Next, we apply Eq. (5.11) and obtain

$$|A - \lambda I| = \begin{vmatrix} -\lambda & 1 \\ -\omega_n^2 & -2\zeta\omega_n - \lambda \end{vmatrix} = 0. \quad (e)$$

From which, the below characteristic equation is obtained:

$$\lambda^2 + 2\zeta\omega_n\lambda + \omega_n^2 = 0. \quad (f)$$

Equation (f) has the below solutions

$$\lambda_{1,2} = -\zeta\omega_n \pm \omega_n\sqrt{\zeta^2 - 1}. \quad (g)$$

Based on Eq. (g), the following notes on stability can be deduced

- For $\zeta > 0$ (positive damping), both λ_1 and λ_2 are in the left-half plane indicating that the fixed point (FP) is stable. If $\zeta > 1$, the FP is a stable node (overdamped). If $1 > \zeta > 0$, it is a stable focus (underdamped).
- For $\zeta < 0$ (negative damping), both λ_1 and λ_2 are in the right-half plane indicating that the FP is unstable.
- If $\zeta = 0$, then $\lambda_{1,2} = \pm i\omega_n\sqrt{-1} = \pm i\omega_n$, which are on the imaginary axis. Thus, the FP is marginally stable and it is a center. For the considered example, this is the case of undamped oscillation.

Figure 5.6 shows phase plots (displacement versus velocity) for the stable equilibrium points. More on phase plane and plots are presented in Sect. 5.5.

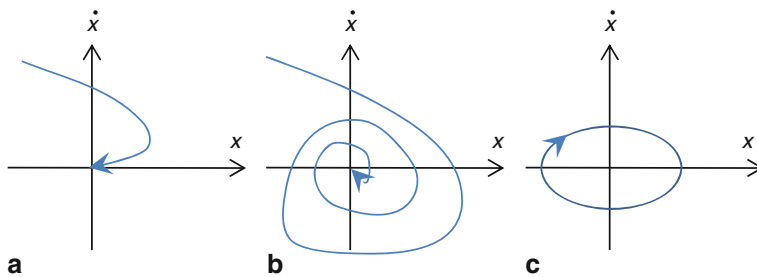
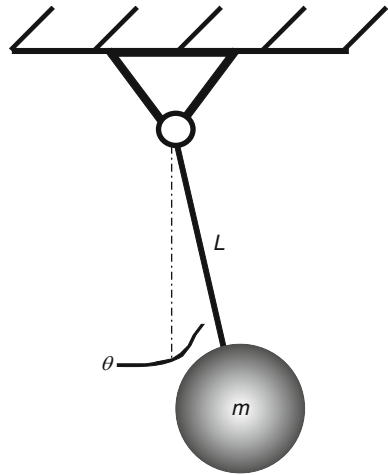


Fig. 5.6 The stable equilibrium points of a linear damped oscillator in the phase space: **a** is a stable node, **b** is a stable focus, and **c** is a center

Fig. 5.7 A swinging pendulum



Example 5.4: Find the equilibrium points of the pendulum of Fig. 5.7 and analyze their stability. Consider the undamped equation of motion of the pendulum as

$$\ddot{\theta} + \frac{g}{L} \sin(\theta) = 0. \quad (\text{a})$$

Solution: First, assume $x_1 = \theta$ and $x_2 = \dot{\theta}$. Then Eq. (a) is written in a state-space form as

$$\dot{x}_1 = x_2 \quad (\text{b})$$

$$\dot{x}_2 = -\omega_n^2 \sin(x_1) \quad (\text{c})$$

where $\omega_n^2 = g/L$. The equilibrium points are obtained by setting the right-hand side of Eqs. (b) and (c) equal to zero, which yields

$$\begin{aligned} x_2 &= 0; \\ \sin(x_1) &= 0 \Rightarrow x_1 = 0, \pi, \dots \end{aligned} \quad (\text{d})$$

Hence, there are at least two fixed points $(0, 0)$ and $(\pi, 0)$. The rest are just repetitions of these two (corresponding to repeated cycles). The Jacobian of Eqs. (b) and (c) is written as

$$\nabla_x F = \begin{bmatrix} 0 & 1 \\ -\omega_n^2 \cos(x_1) & 0 \end{bmatrix}. \quad (\text{e})$$

The characteristic equation at a given FP can be calculated from

$$|\nabla_x F - \lambda I| = \begin{vmatrix} -\lambda & 1 \\ -\omega_n^2 \cos(x_1) & -\lambda \end{vmatrix} = \lambda^2 + \omega_n^2 \cos(x_1) = 0. \quad (\text{f})$$

Solving Eq. (f) gives

$$\lambda_{1,2} = \pm i\omega_n \sqrt{\cos(x_1)}. \quad (g)$$

For the FP (0,0), based on Eq. (g), $\lambda_{1,2} = \pm i\omega_n$, which means that (0, 0) is marginally stable, and it is a center. This corresponds to undamped oscillation. For the FP $(\pi, 0)$, $\lambda_{1,2} = \pm\omega_n$, which means the FP is an unstable saddle. Physically this is expected, as explained in Fig. 5.4c, since the system diverges from this equilibrium point under any small perturbation.

Example 5.5: Find the equilibrium points of the parallel-plate electrostatic actuator of Fig. 5.8 and analyze their stability.

Solution: The equation of motion of the upper electrode can be written as (see Sect. 3.5)

$$m\ddot{x} + kx + c\dot{x} = \frac{\varepsilon A V_{DC}^2}{2(d-x)^2}. \quad (a)$$

Next, we let $x_1 = x$ and $x_2 = \dot{x}$. Then Eq. (a) is written in a state-space form as

$$\dot{x}_1 = x_2 \quad (b)$$

$$\dot{x}_2 = \frac{\varepsilon A V_{DC}^2}{2m(d-x_1)^2} - \frac{c}{m}x_2 - \frac{k}{m}x_1. \quad (c)$$

The equilibrium points are found by setting the right-hand side of Eqs. (b) and (c) equal to zero. This gives

$$x_2 = 0 \quad (d)$$

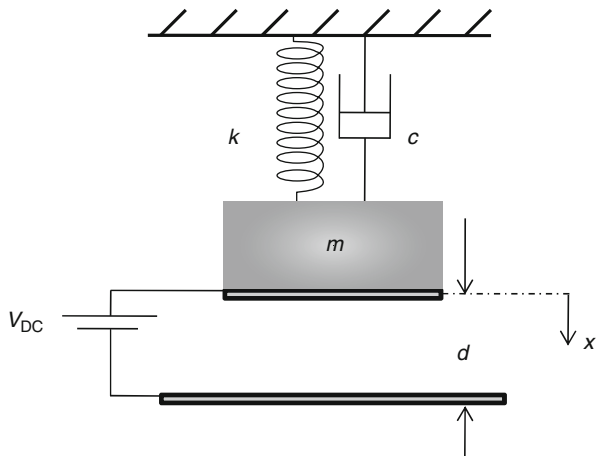


Fig. 5.8 Parallel-plate electrostatic actuator

$$\frac{\varepsilon A V_{DC}^2}{2m(d-x_1)^2} - \frac{c}{m}x_2 - \frac{k}{m}x_1 = 0 \Rightarrow x_1^3 - 2x_1^2d + x_1d^2 - \frac{\varepsilon A V_{DC}^2}{2k} = 0. \quad (e)$$

Solving Eq. (e) yields three solutions for x_1 (x_{11} , x_{12} , and x_{13}). These solutions are then normalized with respect to d to enable distinguishing whether they are physically possible solutions (less than the gap width d) or nonphysical (larger than d). It turns out that the magnitudes of the three solutions come as below

$$\frac{x_{11}}{d} < 1; \quad \frac{x_{12}}{d} < 1; \quad \frac{x_{13}}{d} > 1. \quad (f)$$

Hence, x_{13} is dropped as a nonphysically possible solution. To analyze the stability of the other two solutions, the Jacobian of Eqs. (b) and (c) need to be determined and then Eq. (5.11) is applied:

$$|A - \lambda I| = 0 \Rightarrow \begin{vmatrix} -\lambda & 1 \\ \frac{\varepsilon A V_{DC}^2}{m(d-x_1)^3} - \frac{k}{m} & -\frac{c}{m} - \lambda \end{vmatrix} = 0. \quad (g)$$

Equation (g) yields a characteristic equation for λ , the solution of which at each fixed point indicates the stability of that point. In the case of no damping, $c = 0$, the solution of the characteristic equation yields

$$\lambda_{1,2} = \pm \sqrt{\frac{\varepsilon A V_{DC}^2}{m(d-x_1)^3} - \frac{k}{m}}. \quad (h)$$

When substituting the numbers for a specific capacitor, it turns out that for the smaller solution x_{11} , λ_1 and λ_2 are both pure imaginary indicating neutrally stable FP. On the other hand, for the larger solution x_{12} , it is found that the real part of one of the eigenvalues is located on the right-half complex plane, and the other is located on the left-half plane. This indicates that this FP is an unstable saddle. All these remarks are under the assumption that V_{DC} is less than the pull-in voltage. Estimating the pull-in voltage is illustrated next when discussing bifurcations.

5.4 Bifurcations of Fixed Points

It is quite common in MEMS to note that the static and dynamic behavior of a system undergoes dramatic qualitative change when adjusting one of its control parameter, such as a biasing voltage or a damping coefficient. In nonlinear dynamics, this phenomenon is called bifurcation. Bifurcation is a French word introduced by Poincaré to indicate a qualitative change in the feature of the system, such as the number and type of solutions/states, under the variation of one or more of its control parameter [2]. In this section, we study local bifurcations, where a qualitative change occurs in the neighborhood of a fixed point, of autonomous systems.

Local bifurcations of fixed points can be classified into static and dynamic. The static includes saddle-node, transcritical, and pitchfork bifurcations. These lead to static or fixed points of another kind or number while changing the control parameter. The dynamic bifurcation of fixed points is called Hopf bifurcation. In this bifurcation, periodic (dynamic) solutions are born from the fixed points. All these bifurcations have been reported in various applications in MEMS.

For the system of Eq. (5.1), the below conditions are necessary, but not sufficient, for the point (X_0, μ_0) to undergo a static bifurcation [2]:

- $F(X_0, \mu_0) = 0$, meaning that the point is actually a fixed point.
- $\nabla_x F(X_0, \mu_0)$ (the Jacobian at the fixed point) has a zero eigenvalue while all of its other eigenvalues have nonzero real parts.

In addition to these conditions, an actual qualitative change in the nature of the fixed points before and after (X_0, μ_0) needs to occur to confirm that this point is a bifurcation point. Next, the various types of bifurcations are discussed.

5.4.1 Saddle-Node Bifurcation

Saddle-node, also called tangent or fold, bifurcation is considered the most common bifurcation. In this case, a stable solution meets another unstable solution in the bifurcation diagram, where both destroy each other. Beyond the bifurcation point there is no solution for the system. Hence, this kind is classified as a “dangerous bifurcation” because the system is forced to escape the local bifurcation point to a remote, potentially unsafe, state or solution.

Example 5.6: Find the equilibrium solution of the system governed by Eq. (a) below and analyze its stability and bifurcation type as the control parameter μ is changed.

$$\dot{x} = \mu - x^2. \quad (a)$$

Solution: The fixed points of Eq. (a) are found by setting its right-hand side equal to zero:

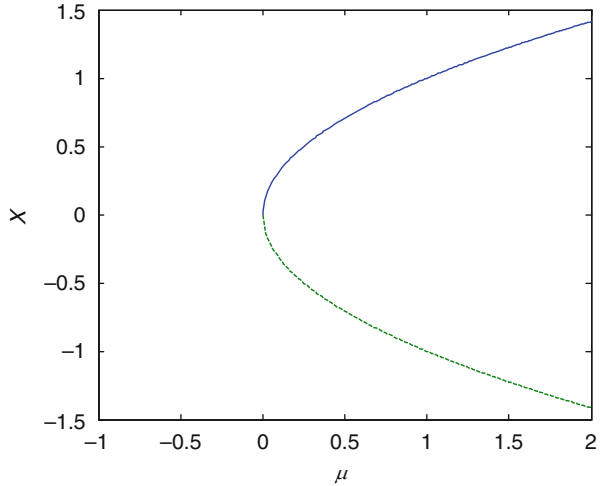
$$\mu - x^2 = 0 \Rightarrow x = X = \pm\sqrt{\mu}. \quad (b)$$

Next, we calculate $|A - \lambda I|$ for Eq. (a) as

$$\begin{aligned} -2X - \lambda &= 0 \Rightarrow \lambda(X = +\sqrt{\mu}) = -2\sqrt{\mu}; \\ \lambda(X = -\sqrt{\mu}) &= +2\sqrt{\mu}. \end{aligned} \quad (c)$$

It is concluded based on Eqs. (b) and (c) that for $\mu > 0$, $X = +\sqrt{\mu}$ is a stable FP (since $\lambda < 0$) and $X = -\sqrt{\mu}$ is an unstable FP (since $\lambda > 0$). For $\mu < 0$, there are no fixed points for the system (fixed points cannot be imaginary). At $\mu = 0$, the FP $X = 0$ has a zero eigenvalue, $\lambda = 0$. To better describe these results, a diagram

Fig. 5.9 A bifurcation diagram showing a saddle-node bifurcation



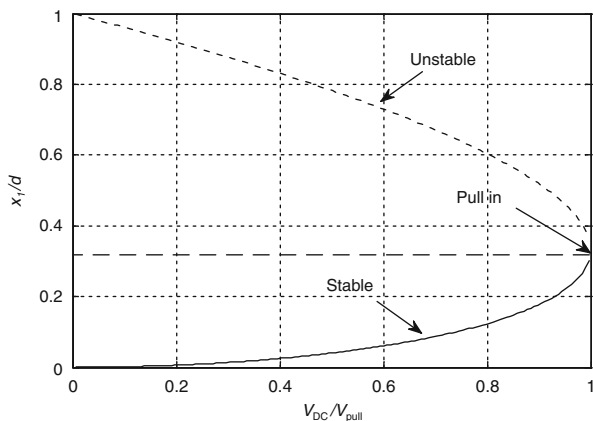
is plotted showing the fixed points versus μ , Fig. 5.9. Such a diagram is called bifurcation diagram. In the diagram, the stable equilibrium solution is plotted as a solid line and the unstable solution as a dashed line. As noted, there is qualitative change of the fixed points of the system at the point ($\mu = 0, X = 0$); the number of solutions is changed from two to zero before and after this point. Also, at ($\mu = 0, X = 0$) the two necessary conditions for a static bifurcation are satisfied, which are being an equilibrium point of zero eigenvalue. Hence, the point ($\mu = 0, X = 0$) is a static bifurcation point. More specifically, since at this point a stable branch meets an unstable branch, both have the same slope, and both destroy each other; the bifurcation is a saddle-node. Next, examples of saddle-node bifurcations in MEMS are discussed.

5.4.1.1 Parallel-Plate Capacitor and the Pull-in Voltage

Example 5.7: A classic example of a saddle-node bifurcation in MEMS is the pull-in instability of parallel-plate capacitors. Investigate pull-in by analyzing the bifurcation of the case of Example 5.5.

Solution: We found in Example 5.5 that the capacitor has two solutions, a smaller stable one, x_{11} , and a larger unstable one, x_{12} . A plot of these two solutions as a function of V_{DC} is shown in Fig. 5.10. It is noted that the two solutions coalesce at a certain x_1 and specific voltage. At this voltage load, it turns out that one eigenvalue of each solution reaches zero value. Because of this, the fact that this point is an equilibrium solution of the system, and that there is qualitative change in the solutions of the system at this point indicate that this is a static bifurcation point. Because the two solutions meet tangentially destroying each other, this is a saddle-node bifurcation. This bifurcation is nothing but the pull-in instability.

Fig. 5.10 A bifurcation diagram of a parallel-plate capacitor



To find the pull-in voltage, we need first to determine the location of the bifurcation point. This can be found by observing the point of the coalescence of the two solutions, which as seen from Fig. 5.10 turns out to be at $x_1/d = 1/3$. Analytically, this point can be found by recalling that this point is an equilibrium solution, thus it satisfies Eq. (e) of Example 5.5 or

$$\frac{\varepsilon A V_{\text{DC}}^2}{2m(d - x_1)^2} = \frac{k}{m} x_1. \quad (\text{a})$$

Also, by noting that at this point, $\lambda_{1,2} = 0$, hence from Eq. (h) of Example 5.5

$$\frac{\varepsilon A V_{\text{DC}}^2}{m(d - x_1)^3} = \frac{k}{m}. \quad (\text{b})$$

Substituting for k from Eq. (a) into Eq. (b) and solving for x_1 gives that $x_1 = d/3$.

To find the pull-in voltage V_{pull} , the expression for the eigenvalue, Eq. (h) of Example 5.5, is set equal to zero then $x_1 = d/3$ is plugged in, which gives

$$\lambda_{1,2} = \pm \sqrt{\frac{\varepsilon A V_{\text{pull}}^2}{m(d - \frac{d}{3})^3} - \frac{k}{m}} = 0. \quad (\text{c})$$

Solving for V_{pull} yields the below expression for the pull-in voltage

$$V_{\text{pull}} = \sqrt{\frac{8kd^3}{27\varepsilon A}} \quad (\text{d})$$

which is the same expression of Eq. (3.27).

5.4.1.2 Capacitor with a Dielectric Layer and the Release Voltage

It is worth to discuss at this juncture the effect of having an insulating layer on top of the lower electrode of a parallel-plate capacitor. As a by-product of this discussion, the physical meaning of the unstable solution of the capacitor is explained. Using insulating layers is common in RF switches, where a microstructure is actuated beyond pull-in and collapses to the lower electrode. With no insulation layer on the lower electrode, the microstructure can get stuck hardily and permanently to the lower electrode making it difficult to actuate it again. Hence, an insulation layer of dielectric material is used to reduce the stiction effect of the electrostatic forces on the microstructure. Also, landing pads and contact stops are deposited on the lower electrode to perform a similar function as the insulation layer. We refer to any of these as the insulation layer for brevity.

Example 5.8: Consider the parallel-plate capacitor of Fig. 5.11a, which has an insulation layer of thickness s deposited on its lower electrode. Derive an expression for the release voltage V_{release} as a function of s . Neglect the change of the dielectric constant due to the insulation layer. Plot the bifurcation diagram assuming $k = 16 \text{ N/m}$, $A = 800 \mu\text{m}^2$, $s = 0.1 \mu\text{m}$, and $d = 0.7 \mu\text{m}$, which is the case study investigated theoretically and experimentally in [3], and determine V_{release} of this case.

Solution: When the upper electrode is brought down by a voltage load beyond pull-in, it collapses and lands on the insulating layer. The balance of the equilibrium forces on the upper electrode, depicted in Fig. 5.11b, can be expressed as

$$R + k(d - s) = \frac{\epsilon A V_{\text{DC}}^2}{2s^2} \quad (\text{a})$$

where R is the reaction force exerted from the insulation layer on the upper electrode. Here, all other possible stiction forces are assumed negligible. When the actuation

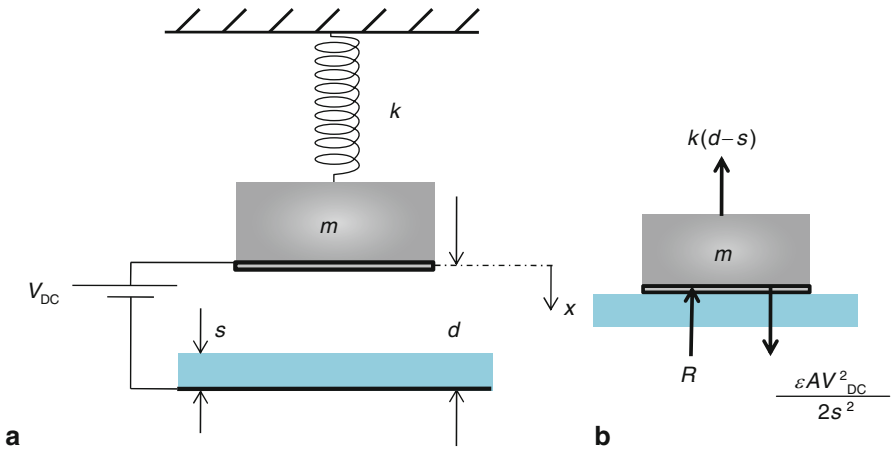


Fig. 5.11 **a** A parallel-plate capacitor with an insulating layer. **b** A force diagram of the upper electrode when it is in contact with the insulating layer

voltage V_{DC} at this position is lowered, R decreases. Continuing to decrease V_{DC} lowers R further until it reaches eventually zero. At this moment, both the electrostatic force and the restoring force balance each other. This represents the second (larger) equilibrium point of the parallel-plate capacitor. As found from Example 5.5, this equilibrium point is unstable; the upper electrode cannot hold on this position, and it is kicked back to the other stable equilibrium position (switch is released). The value of voltage at which this occurs ($R = 0$) is called the release voltage V_{release} . The difference between the actuation voltage of the switch and the release voltage results in a hysteresis phenomenon that needs to be accounted for carefully when designing RF switches. Substituting $R = 0$ in Eq. (a) and solving for the voltage yields the following expression for the release voltage:

$$V_{\text{release}} = \sqrt{\frac{2ks^2}{\epsilon A}}(d - s). \quad (b)$$

Substituting the numbers for this considered example yields $V_{\text{release}} = 5.2$ V. Also, it turns out that $V_{\text{pull}} = 15$ V. Hence, when actuating the switch, V_{DC} must be larger than 15 V and to release the switch to its original position, V_{DC} needs to be lowered below 5.2 V. The bifurcation diagram of this capacitor remains the same as the case of no insulating layer, Fig. 5.12. From the figure however, one can read directly the release voltage for a given s . To do this, a horizontal line is drawn on the figure a distance

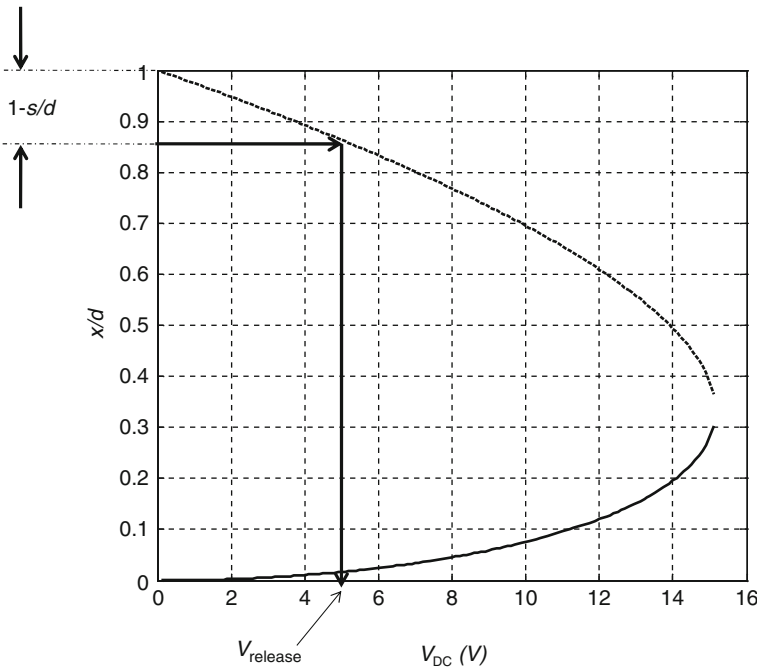


Fig. 5.12 A bifurcation diagram for a parallel-plate capacitor showing how to extract the release voltage V_{release} for a given insulation layer thickness s

$1 - s/d$ below 1. The value of V_{DC} where this line intersects the upper unstable solution represents V_{release} , as illustrated in Fig. 5.12. This again is under the assumption that the insulation layer has a dielectric constant, which is the same as the airgap.

5.4.1.3 Collapse Due to Capillary Forces and the Elastocapillary Number

The fabrication of many microstructures involves wet etching of a sacrificial layer underneath them for their release. Following this are cleaning and drying processes, during which droplet of liquids may be trapped underneath the microstructures. In addition, operating already released structures under certain humidity levels can create such droplet of liquids. These create strong capillary forces pulling the microstructures toward the substrate. If the resorting force of the microstructures cannot resist the capillary force, they collapse hitting the substrate, where they can get permanently stuck. This is similar to the pull-in instability due to electrostatic forces. A simplified model of this phenomenon is depicted in Fig. 5.13. The capillary force F_{cap} that acts on the microstructure can be expressed as

$$F_{\text{cap}} = \frac{2\gamma A \cos(\theta)}{(d - x)} \quad (5.13)$$

where γ is the surface tension of the liquid ($\gamma = 73 \times 10^{-3}$ N/m for water), θ is angle that the liquid makes with the microstructure and the substrate, which can be taken to be zero assuming perfect wetting condition, and A is the surface area of the microstructure in contact with the liquid.

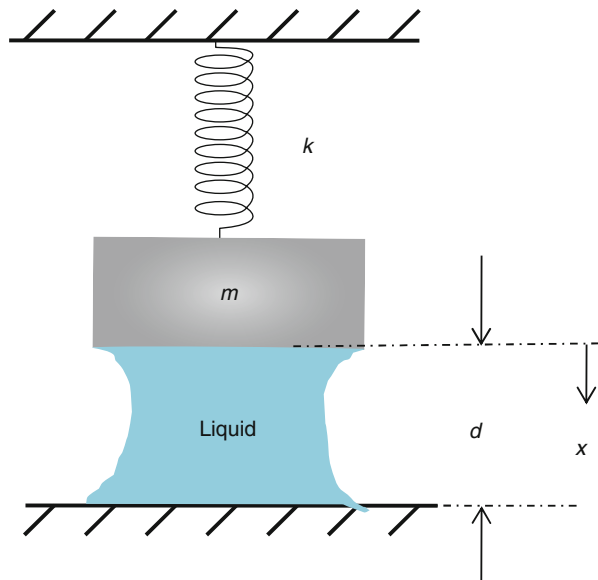


Fig. 5.13 A simplified model for the capillary force effect on microstructures

Example 5.9: Use the model of Fig. 5.13 to analyze the stability of a microstructure with a volume of liquid trapped underneath it and derive an analytical expression that determines whether a microstructure collapses or not due to the fluid.

Solution: The undamped equation of motion of the microstructure can be written as

$$m\ddot{x} + kx = \frac{2\gamma A \cos(\theta)}{(d - x)}. \quad (a)$$

First, let $x_1 = x$ and $x_2 = \dot{x}$. Also, θ is set equal to zero assuming complete wetting conditions. Then Eq. (a) is written in a state-space form as

$$\dot{x}_1 = x_2 \quad (b)$$

$$\dot{x}_2 = \frac{2\gamma A}{m(d - x_1)} - \frac{k}{m}x_1. \quad (c)$$

The equilibrium points can be found by setting the right-hand side of Eqs. (b) and (c) equal to zero. This yields

$$x_2 = 0 \quad (d)$$

$$\frac{2\gamma A}{m(d - x_1)} - \frac{k}{m}x_1 = 0 \Rightarrow x_1 = \frac{d}{2} \pm \frac{1}{2}\sqrt{d^2 - \frac{8\gamma A}{k}}. \quad (e)$$

Equation (e) gives two real equilibrium solutions provided that $d^2 - 8\gamma A/k > 0$, or

$$A \leq \frac{d^2 k}{8\gamma} = A_{\text{crt}} \quad (f)$$

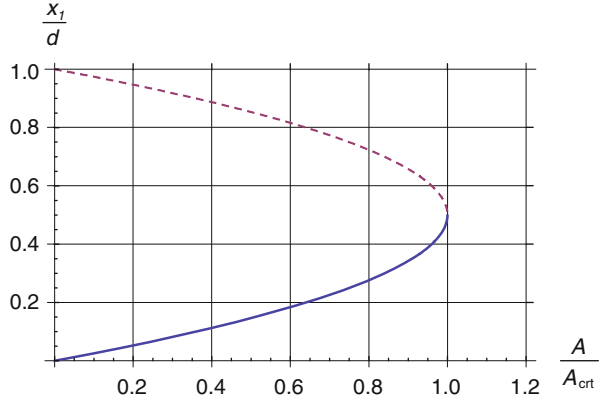
where A_{crt} refers to a critical area of the surface of the microstructure in contact with the liquid. For convenience, x_1 in Eq. (e) is normalized with respect to d and A is normalized with respect to A_{crt} , hence

$$\frac{x_1}{d} = \frac{1}{2} \left[1 \pm \sqrt{1 - \frac{8\gamma A}{kd^2}} \right] = \frac{1}{2} \left[1 \pm \sqrt{1 - R} \right] \quad (g)$$

where $R = A/A_{\text{crt}}$. One can also note that $x_1/d = 0.5$ represents the maximum value of one of the solutions and the minimum of the other. A plot of x_1/d versus A/A_{crt} is depicted in Fig. 5.14. To analyze the stability of the equilibrium solutions, the Jacobian of Eqs. (b) and (c) needs to be determined and then Eq. (5.11) is applied. Thus,

$$\begin{vmatrix} -\lambda & 1 \\ \frac{2A\gamma}{m(d - x_1)^2} - \frac{k}{m} & -\lambda \end{vmatrix} = 0. \quad (h)$$

Fig. 5.14 The equilibrium solutions and the bifurcation diagram of a microstructure affected by capillary forces



From Eq. (h), the following expressions for the eigenvalues are obtained:

$$\lambda_{1,2} = \pm \sqrt{\frac{2\gamma A}{m(d - x_1)^2} - \frac{k}{m}} \quad (i)$$

which can be rewritten as

$$\frac{\lambda_{1,2}}{\sqrt{\frac{k}{m}}} = \pm \sqrt{\frac{4R}{(1 - x_1)^2} - 1}. \quad (j)$$

Substituting Eq. (g) into Eq. (j), the stability of each equilibrium solution is determined for a given R . It turns out that the upper solution (dashed curve in Fig. 5.14) has two real λ s, with one of them is positive; hence it is unstable. On the other hand, the lower equilibrium solution (the solid curve in Fig. 5.14) has two imaginary λ s; hence it is marginally stable. Both solutions have zero λ s when $A = A_{\text{crit}}$ corresponding to $x_1/d = 0.5$. Note that $x_1/d = 0.5$ can be confirmed analytically by setting Eq. (i) equal to zero, solving for an analytical expression for k , and then substituting it in Eq. (e). Note also that by setting Eq. (i) equal to zero and solving for A at $x_1/d = 0.5$, the same A_{crit} as Eq. (f) is obtained. The zero eigenvalue, the qualitative change in the equilibrium solutions, and the turning point of the equilibrium curves at $A = A_{\text{crit}}$ indicate that this point is a saddle-node bifurcation. Figure 5.15a shows the variation of the eigenvalues of the upper solution with R . Figure 5.15b depicts the real coefficient of the imaginary eigenvalues of the lower solution versus R . As seen in both figures, the eigenvalues reach zero value at $R = 1$.

The conclusion of this example is that a microstructure under capillary forces can stay in a stable equilibrium position if Eq. (f) is satisfied, or by dividing both sides of Eq. (f) by A , this can be restated as

$$1 \leq \frac{d^2 k}{8A\gamma} = \frac{1}{R} = N_{\text{EC}} \quad (k)$$

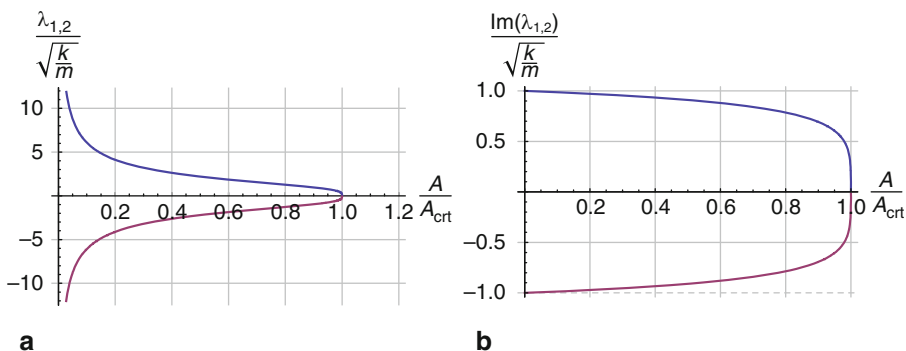


Fig. 5.15 The variation of the eigenvalues with the area of the liquid underneath a microstructure. Figure part **a** is for the upper branch solution and figure part **b** is for the lower branch

where N_{EC} is known in the literature as the elastocapillary number [4]. If $N_{\text{EC}} > 1$, the microstructure is “free” or in stable position and if $N_{\text{EC}} < 1$, the microstructure is “pinned” or in an unstable position.

5.4.2 Transcritical Bifurcation

If two equilibrium branches of solutions exchange stability across a point, i.e., the stable one becomes unstable and the unstable becomes stable, a transcritical bifurcation is said to occur. An example in MEMS of this kind has been cited in [4] when investigating stiction of clamped–clamped microbeams.

Example 5.10: Find the equilibrium solutions of the system governed by Eq. (a) below and analyze their stability and bifurcation type as the control parameter μ is varied.

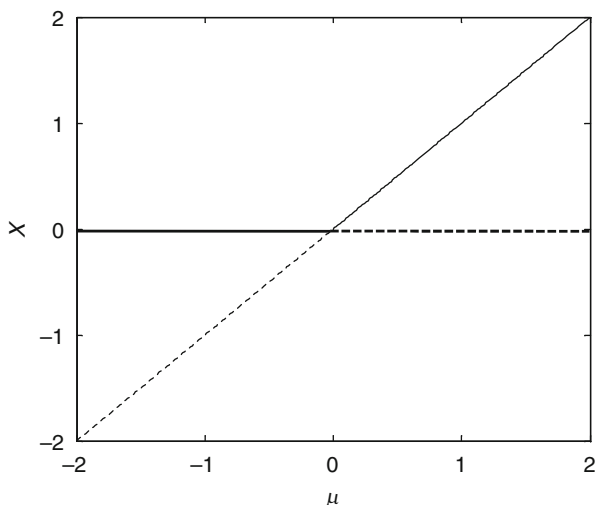
$$\dot{x} = \mu x - x^2 \quad (\text{a})$$

Solution: The fixed points of Eq. (a) are found by setting its right-hand side equal to zero, which gives $X = 0$ and $X = \mu$. The eigenvalues of the system are expressed as

$$\lambda = \mu - 2X. \quad (\text{b})$$

Hence, for $X = 0$, $\lambda = \mu$, which means a stable solution for $\mu < 0$ and an unstable solution for $\mu > 0$. For $X = \mu$, $\lambda = -\mu$, which gives an opposite stability result to the other solution, that is, a stable solution for $\mu > 0$ and an unstable solution for $\mu < 0$. At the point $(\mu = 0, X = 0)$, the eigenvalue is equal to zero. This, in addition to the fact that there is a qualitative change in the type of solutions before and after this point, means that the point is a static bifurcation point. The exchange of stability at the

Fig. 5.16 A bifurcation diagram showing a transcritical bifurcation



point indicates a transcritical bifurcation. The bifurcation diagram of this example is depicted in Fig. 5.16.

5.4.3 Pitchfork Bifurcation

The layout of equilibrium solutions of this kind of bifurcation in a bifurcation diagram looks like a pitchfork. This bifurcation can take one of two forms: supercritical and subcritical. The latter is considered a dangerous bifurcation with the possibility of the system to jump to a remote unsafe state (from a stability point of view). In MEMS, pitchfork bifurcation has been reported for resonators excited nonlinearly by subharmonic excitations [5, 6] and in the case of a moveable electrode sandwiched between two stationary electrodes [7, 8], in which pitchfork bifurcation is responsible for the side-sticking phenomenon of comb-drive actuators. Also, buckling of microbeams under compressive axial load is another example of pitchfork bifurcation (see Problem 3). The below example illustrates this bifurcation with its two kinds.

Example 5.11: Find the equilibrium solutions of the system governed by Eq. (a) below and analyze their stability and bifurcation type as the control parameter μ is changed for the two cases: $\alpha = 1$ and $\alpha = -1$.

$$\dot{x} = \mu x + \alpha x^3. \quad (a)$$

Solution: The fixed points of Eq. (a) are found by setting its right-hand side to zero, which yield $X = 0$, $X = \pm\sqrt{-\mu/\alpha}$. Note that the nontrivial solutions exist only when the term under the square root is positive. Hence, for $\mu < 0$, the solutions exist

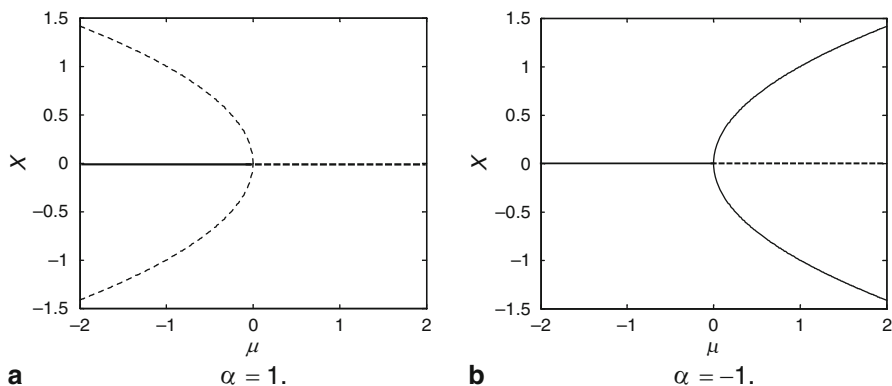


Fig. 5.17 A bifurcation diagram showing two kinds of pitchfork bifurcations: **a** subcritical and **b** supercritical

when $\alpha > 0$. For $\mu > 0$, they exist when $\alpha < 0$. The eigenvalues of the system at the equilibrium points are expressed as

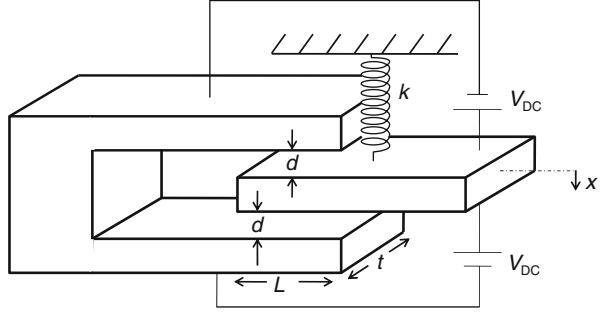
$$\lambda = \mu + 3\alpha X^2. \quad (\text{b})$$

For $X = 0$, $\lambda = \mu$, which indicates stable solutions for $\mu < 0$ and unstable solutions for $\mu > 0$. For the other two solutions, $\lambda = -2\mu$, which indicates stable solutions for $\mu > 0$ and unstable solutions for $\mu < 0$. Figure 5.17 shows bifurcations diagrams for the two values of α . Note that at the point $(\mu = 0, X = 0)$, a qualitative change in the number and type of the equilibrium solutions of the system occurs. Also, the eigenvalue at this point is equal to zero. Hence, this is a static bifurcation point. Because of the pitchfork layout in the bifurcation diagram, it is called pitchfork bifurcation. Note from Fig. 5.17a that as the value of μ is swept from small to large passing $(\mu = 0, X = 0)$, the trivial stable equilibrium solution loses stability, and then the system is left with no nearby stable state. This causes the system to jump to any remote state/solution, which can be unsafe. Hence, this bifurcation is considered dangerous from a stability point of view. Such a bifurcation scenario is called subcritical pitchfork. Note on the other hand the case of Fig. 5.17b. Sweeping μ from small to large values passing $(\mu = 0, X = 0)$ causes the trivial stable equilibrium solution to lose stability. However, in this case the system can land on any of the other stable nontrivial solutions, which exist nearby. This typically does not cause significant change in the dynamics of the system or a big jump, and hence, this bifurcation is considered safe. This kind is called supercritical pitchfork bifurcation.

5.4.3.1 Side-Instability of Comb-Drive Fingers

In Sect. 3.5 of Chap. 3, the so-called side instability of comb-drive fingers of electrostatic actuators is discussed briefly. Here, a quantitative analysis of this phenomenon is presented.

Fig. 5.18 A moveable electrode sandwiched between two stationary electrodes



Example 5.12: Consider the moveable finger of Fig. 5.18, which is sandwiched between two stationary electrodes. The moveable electrode is biased from the upper and lower sides with two voltage sources, each of V_{DC} load. Analyze the stability of the moveable electrode and the bifurcation involved. How these differ if the moveable finger is shifted from the center location between the two stationary electrodes a distance of $u = 0.1 \mu\text{m}$? Plot bifurcation diagrams assuming the moveable electrode has a mass $m = 9.33 \times 10^{-11} \text{ kg}$, stiffness $k = 5 \text{ N/m}$, $d = 1 \mu\text{m}$, $t = 100 \mu\text{m}$, and $L = 200 \mu\text{m}$. Neglect damping from all calculations.

Solution: The undamped equation of motion of the moveable electrode can be written from the forces balance as

$$m\ddot{x} + kx = \frac{\varepsilon(Lt)V_{DC}^2}{2} \left[\frac{1}{(d-x)^2} - \frac{1}{(d+x)^2} \right]. \quad (\text{a})$$

Next, we let $x_1 = x$ and $x_2 = \dot{x}$. Then Eq. (a) is written in a state-space form as

$$\dot{x}_1 = x_2 \quad (\text{b})$$

$$\dot{x}_2 = \frac{\varepsilon(Lt)V_{DC}^2}{2m} \left[\frac{1}{(d-x_1)^2} - \frac{1}{(d+x_1)^2} \right] - \frac{k}{m}x_1. \quad (\text{c})$$

The equilibrium points are found by setting the right-hand side of Eqs. (b) and (c) equal to zero, that is

$$x_2 = 0 \quad (\text{d})$$

$$\frac{\varepsilon(Lt)V_{DC}^2}{2m} \left[\frac{1}{(d-x_1)^2} - \frac{1}{(d+x_1)^2} \right] - \frac{k}{m}x_1 = 0. \quad (\text{e})$$

Solving Eq. (e) yields five solutions for x_1 . Of these, two are physically impossible since they predict displacement greater than the gap width d . Of the other three, one is a trivial solution, $x_{11} = 0$. The other two, x_{12} and x_{13} , have the same magnitude

but with different sign. To analyze the stability of the solutions, the Jacobian of Eqs. (b) and (c) needs to be determined and then Eq. (5.11) is applied:

$$\begin{vmatrix} -\lambda & 1 \\ \frac{\varepsilon(Lt)V_{DC}^2}{m} \left[\frac{1}{(d-x_1)^3} + \frac{1}{(d+x_1)^3} \right] - \frac{k}{m} & -\lambda \end{vmatrix} = 0. \quad (f)$$

Equation (f) yields a characteristic equation for λ at a given x_1 , which has the solution

$$\lambda_{1,2} = \pm \sqrt{\frac{\varepsilon(Lt)V_{DC}^2}{m} \left[\frac{1}{(d-x_1)^3} + \frac{1}{(d+x_1)^3} \right] - \frac{k}{m}}. \quad (g)$$

When substituting the numbers for a specific capacitor, it turns out that the trivial solution $x_{11} = 0$ has both λ_1 and λ_2 to be pure imaginary indicating neutrally stable FP up to a specific V_{DC} , after which the solution loses stability. The other two solutions are found to be unstable and are terminated at the same specific V_{DC} , where the trivial solution loses stability. Also, at this point, it turns out that the eigenvalues of the three solutions are equal to zero. Figure 5.19a shows the bifurcation diagram for the given parameters of the example. Clearly, the diagram shows a pitchfork bifurcation, particularly a subcritical bifurcation. Physically, when exceeding the specific V_{DC} at the bifurcation point, the moveable electrode gets stuck to one of the other stationary electrodes. This phenomenon is known in the comb-drive literature as the side instability. Also it is known as pull-in of double-sided capacitors. To find V_{DC} where side instability occurs, V_{side} , the expression of $\lambda_{1,2}$ of Eq. (g) is set equal to zero at $x_1 = 0$. This yields

$$V_{side} = \sqrt{\frac{kd^3}{2\varepsilon(Lt)}}. \quad (h)$$

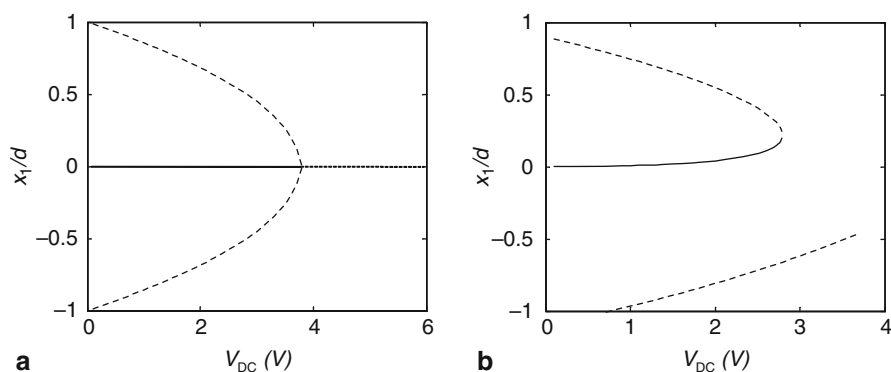


Fig. 5.19 Bifurcation diagrams for a moveable finger sandwiched between two electrodes. Figure part **a** shows a pitchfork bifurcation for $u = 0$ and figure part **b** shows a saddle-node bifurcation for $u = 0.1 \mu\text{m}$

The above expression is the same as that reported by Hirano et al. [9].

Due to fabrication tolerances, the moveable finger might be shifted from the center a distance u . In this case, Eq. (a) becomes

$$m\ddot{x} + kx = \frac{\varepsilon(Lt)V_{DC}^2}{2} \left[\frac{1}{(d-x-u)^2} - \frac{1}{(d+x+u)^2} \right]. \quad (i)$$

The details of the bifurcation and stability analysis of this case will be left as an exercise. However, when following similar procedure, it turns out that the pitchfork bifurcation is replaced by a saddle-node bifurcation, Fig. 5.19b. In this case, a pull-in instability in the finger is induced, which is triggered at a voltage V_{pull} , lower than V_{side} . In fact, the larger u is the lower V_{pull} . Hence, it is desirable for comb-drive actuators to have the moveable fingers as close to the center distance between the stationary electrodes as possible to extend their operating range without instability problems.

5.4.4 Hopf Bifurcation

Unlike the previously discussed static bifurcations, which lead to the creation, disappearance, or change in the stability of fixed points, Hopf is dynamic bifurcation that leads to the creation of periodic solution from fixed points as a control parameter is varied. Hence, in the bifurcation diagram, instead of having equilibrium solutions meeting each other at the bifurcation point, in Hopf, equilibrium solutions meet periodic solutions. A typical example of a Hopf bifurcation is the flutter phenomenon in aeroelasticity, such as in airplane wings and bridges, in which structures undergo violent vibrations because of the excitation from air flow. The collapse of the Tacoma Bridge in 1940 is a classic example of this. In MEMS, the Hopf bifurcation has been observed in a thin disk-shaped resonator when it is illuminated by a DC laser of sufficient amplitude [10]. The resonator was shown to be self-excited into periodic motion due to this illumination without the need for any external forcing (hence, it transits from being in equilibrium state to periodic state).

For the system of Eq. (5.1) to undergo a Hopf bifurcation at the point (X_0, μ_0) , the below conditions need to be satisfied [2]:

- $F(X_0, \mu_0) = 0$, meaning that the point is a fixed point.
- $\nabla_x F(X_0, \mu_0)$ (the Jacobian at the fixed point) has a pair of purely imaginary eigenvalues ($\pm i\omega$) while all of its other eigenvalues have nonzero real parts.
- Let the eigenvalues just before (X_0, μ_0) be in the form $\hat{\lambda} \pm i\omega$, then $\frac{d\hat{\lambda}}{d\mu}$ must have a nonzero value at μ_0 .

In addition to these conditions, an actual change of the fixed points into periodic solutions needs to be confirmed before and after (X_0, μ_0) . If all these conditions are satisfied, then a periodic motion of period $2\pi/\omega$ is born at (X_0, μ_0) . Hopf bifurcation can be of supercritical type, in which case the equilibrium solution loses stability

to two newly born stable periodic solutions, or subcritical, in which case the stable equilibrium solution coexists with two unstable periodic solutions. Then, the stable equilibrium solution loses stability at the bifurcation point, and at the same time both unstable periodic solutions vanish. The bifurcation diagrams of these look similar to the pitchfork bifurcation types of Fig. 5.17, except that the two nontrivial solutions are periodic and not fixed points.

Example 5.13: The system governed by Eq. (a) below, called the van der Pol oscillator equation, is a model of the so-called self-excited systems. These essentially get excited into vibrations without external forces typically through a Hopf bifurcation. Analyze the stability and bifurcation of this system assuming $\mu > 0$.

$$\ddot{x} + 2\mu(x^2 - 1)\dot{x} + x = 0. \quad (\text{a})$$

Solution: First, we let $x_1 = x$ and $x_2 = \dot{x}$. Then Eq. (a) is written in a state-space form as

$$\dot{x}_1 = x_2 \quad (\text{b})$$

$$\dot{x}_2 = -2\mu(x_1^2 - 1)x_2 - x_1. \quad (\text{c})$$

The equilibrium points can be found by setting the right-hand side of Eqs. (b) and (c) equal to zero, which yields

$$x_1 = 0; \quad x_2 = 0. \quad (\text{d})$$

To analyze the stability of the equilibrium solutions, first the Jacobian of Eqs. (b) and (c) are calculated:

$$\nabla_x F(\mathbf{X}; \mu) = \begin{bmatrix} 0 & 1 \\ -4\mu x_1 x_2 - 1 & -2\mu(x_1^2 - 1) \end{bmatrix}. \quad (\text{e})$$

Then, Eq. (5.11) is applied:

$$|A - \lambda I|_{(0,0)} = \begin{vmatrix} -\lambda & 1 \\ -1 & 2\mu - \lambda \end{vmatrix} = 0. \quad (\text{f})$$

From Eq. (f), the following expressions for the eigenvalues are obtained:

$$\lambda_1 = \mu + \sqrt{\mu^2 - 1}; \quad \lambda_2 = \mu - \sqrt{\mu^2 - 1}. \quad (\text{g})$$

Hence, according to Eq. (g), λ_1 and λ_2 or their real parts are always positive for $\mu > 0$ indicating unstable fixed points, and are always negative for $\mu < 0$ indicating stable fixed points. At $\mu = 0$, $\lambda_1 = i$ and $\lambda_2 = -i$, which indicates neutral stability. Further, $d\mu/d\mu = 1 \neq 0$. Therefore, at $x_1 = x_2 = \mu = 0$, there is a Hopf bifurcation, where a new periodic solution of period 2 is born. This result is further confirmed by numerical integration of Eq. (a), as discussed in Sect. 2.8. The results are depicted in

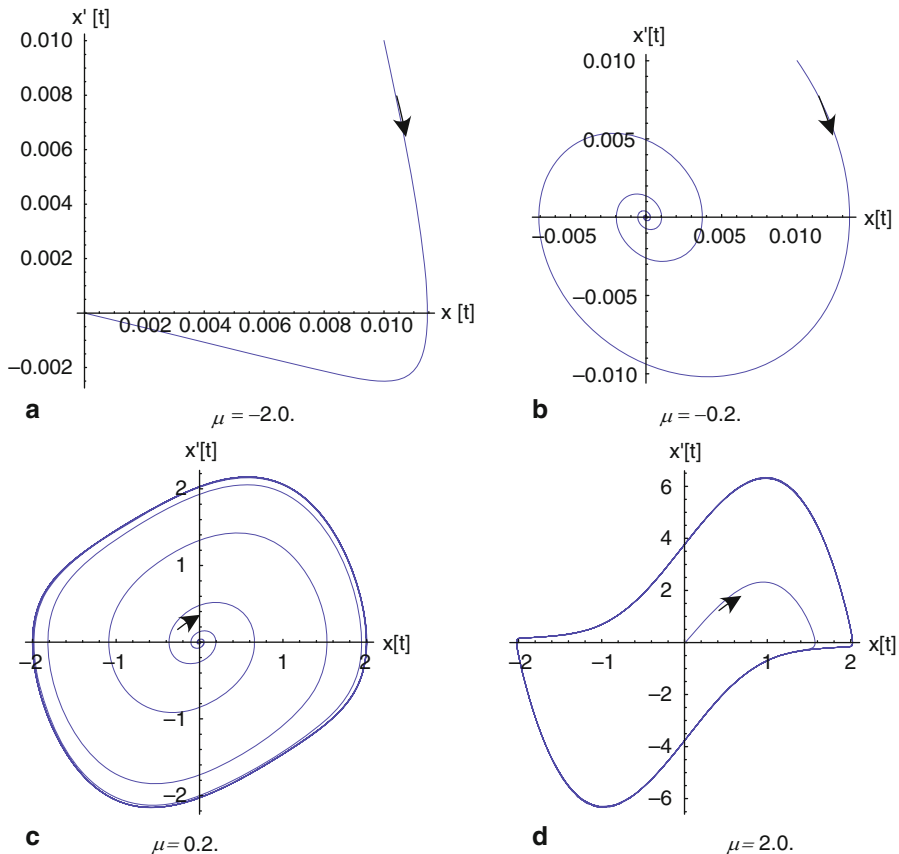


Fig. 5.20 Phase space responses (*trajectories*) of the van der Pol oscillator for various values of damping coefficient

Fig. 5.20 in the form of phase space plots. Note that for $\mu < 0$, the trivial fixed point is a stable node, Fig. 5.20a, and a stable focus, Fig. 5.20b. As μ is raised past $\mu = 0$, the trivial fixed point loses stability to the new stable periodic motion and becomes an unstable focus, Fig. 5.20c, and an unstable node Fig. 5.20d. Since the created periodic solution is stable, the Hopf bifurcation is of a supercritical type.

5.5 Phase Portraits

A powerful method to understand the behavior and stability of a dynamical system is through the so-called phase portrait method. This technique is used to give a qualitative picture of the dynamics of a system in a local and global perspective, i.e., even when the motion is large and the nonlinearity is strong. The origin of this technique is credited to Henry Poincaré. It is best suited for conservative (undamped)

1-DOF systems. Nevertheless, valuable information can be also inferred about the dynamics and stability of other systems. Next, several examples are presented to illustrate how to sketch a phase portrait along with the introduction of various key-related terminologies.

Example 5.14: Sketch a phase portrait of a spring–mass system, similar to that of Fig. 2.2.

Solution: Before illustrating the sketching method, it is worth to introduce some basic concepts. First, we recall the system equation in this case, which is Eq. (2.5):

$$\ddot{x} + \omega_n^2 x = 0. \quad (a)$$

The solution of this equation is given in Eq. (2.9):

$$x(t) = A \sin(\omega_n t + \phi) \quad (b)$$

where A and ϕ depend on the initial conditions, as shown in Eq. (2.11). The velocity of the mass is obtained by taking a time derivative of Eq. (b), which yields

$$\dot{x}(t) = \omega_n A \cos(\omega_n t + \phi). \quad (c)$$

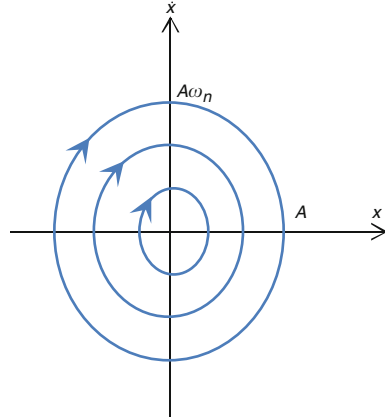
One way to view the dynamic of the system is by plotting $x(t)$ and $\dot{x}(t)$ versus time, which are called **time history responses**. An example of such is depicted in Fig. 2.3. These plots however may not reveal much information about the dynamics, especially for complicated systems, such as the attraction of initial conditions in the presence of multiple fixed points or other possible dynamical “attractors” (an **attractor** represents a set of points in the phase space toward which a time history approaches after transients die out.) A more convenient method is through plotting $x(t)$ versus $\dot{x}(t)$. The space that is formed by $x(t)$ and $\dot{x}(t)$ is called the **phase space** or the **phase plane**. A single curve in the phase space shows how a specific set of initial conditions ($x(0)$, $\dot{x}(0)$) evolves with time, which may end up in a fixed point or other dynamical state. This curve is called **trajectory**. Examples of trajectories have been already shown in Fig. 5.20. The ensemble of many trajectories in the phase plane that shows the evolution of various initial conditions as time goes on is called the **phase portrait**. The trajectories can, for example, converge to a single point in the case of a stable fixed point, deviate to infinity in the case of an unstable attractor, or roam around in a strange fashion with no place to settle-in, such as the case of a chaotic attractor. Mathematically, these trajectories represent the possible solutions of the differential equation governing the dynamical system for a given set of initial conditions.

It turns out that for this particular example, the phase portrait can be easily sketched based on the known solutions. One can note from Eqs. (b) and (c) that

$$x^2 + \left(\frac{\dot{x}}{\omega_n} \right)^2 = A^2. \quad (d)$$

Equation (d) is an equation of an ellipse of a major axis $A\omega_n$ and a minor axis A . Plotting Eq. (d) for various set of initial conditions, and hence various values of A ,

Fig. 5.21 Phase portrait of an undamped spring–mass system



yields ellipses of different sizes, as depicted in Fig. 5.21. Each ellipse represents a trajectory. The evolution of the motion from a set of initial conditions on a trajectory takes a specific direction, shown as an arrowhead in Fig. 5.21. This direction is set such that an increase in the value of \dot{x} leads to an increase also in x . The ensemble of the various trajectories in the phase space composes the phase portrait. The ellipse, as well as any other closed loop in the phase plane, indicates a motion that repeats itself or periodic motion. The size of the orbit of the periodic motion depends on A or the initial conditions. The trajectories indicate undamped motion since they do not converge to any fixed point or other attractors of the system. They indicate the presence of a center fixed point, which is located at the center of the trajectory loops.

The phase portrait of Fig. 5.21 has been sketched based on the already known analytical solutions of the system. This seems of not much advantage. Fortunately, phase portraits can be also sketched based on the differential equation of motion without actually solving it, which is significant for systems of complicated equations of motion with no explicit analytical solutions. To this end, the equation of motion, Eq. (a), is integrated with respect to x as below

$$\int (\ddot{x} + \omega_n^2 x = 0) dx. \quad (e)$$

Note that

$$\ddot{x} dx = \left(\frac{d\dot{x}}{dt} \right) dx = \left(\frac{dx}{dt} \right) d\dot{x} = \dot{x} d\dot{x}. \quad (f)$$

Hence, carrying out the integrations, Eq. (e) becomes

$$\frac{\dot{x}^2}{2} + \frac{\omega_n^2 x^2}{2} = H \quad (g)$$

where H is a constant of integration that depends on the initial conditions. One can note that the first term of Eq. (g) is the kinetic energy of the system per unit mass,

and the second term is the potential energy of the system per unit mass. Thus, H represents the total energy of the system per unit mass for a specific set of initial conditions (more generally, it represents the Hamiltonian of the system). From Eq. (g), \dot{x} can be expressed explicitly as

$$\dot{x} = \pm \sqrt{2H - \omega_n^2 x^2} = \pm \sqrt{2(H - V)}; \quad H > V \quad (\text{h})$$

where $V(x)$ is the potential energy of the system per unit mass. Next, Eq. (h) is used to plot \dot{x} versus x for several values of initial conditions, and hence levels of H . This can be done numerically using software, such as Matlab or Mathematica. For simple systems, a sketch can also be made manually. For this, $V(x)$ is plotted versus x (this plot in itself can give insight into the behavior of the system). For the considered example $V(x)$ is just a parabola as depicted in Fig. 5.22. Then several levels of the constant energy H are plotted on the same plot with $V(x)$. After that, one can visually draw the difference curve $H - V$ on the $x - \dot{x}$ plane, which starts from zero values at the intersections of $V(x)$ and H and then grows to a maximum value when $V(x)$ is minimum. No plot is made for the portion when $H < V$ (\dot{x} cannot be complex). The outcome of this is an upper half of a trajectory above the x axis. The second lower half can be plotted by mirror-imaging the upper half below the x axis. Figure 5.22 further illustrates the procedure. The fact that the phase portrait predicts a neutrally stable equilibrium point, a center, is confirmed by a role by Lagrange, which says that

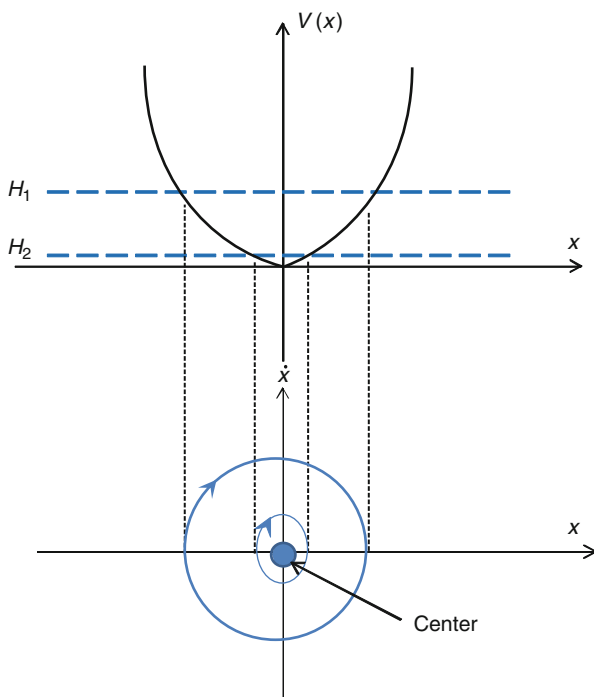


Fig. 5.22 A plot of the potential energy $V(x) = \omega_n^2 x^2 / 2$ versus x (up) with two energy levels H_1 , H_2 , and their corresponding trajectories on the phase plane (bottom)

an isolated equilibrium point corresponding to a minimum of the potential energy is stable. Clearly at $x = 0$, $V(x)$ is minimum.

Adding a positive light damping to the system makes the center fixed point a stable focus and the trajectories become of spiral shapes, as illustrated in Example 5.3 and Fig. 5.6b. Adding heavy damping makes the center a stable node and the trajectory look likes that of Fig. 5.6a.

Example 5.15: Sketch a phase portrait of an undamped spring–mass system with a negative stiffness coefficient.

Solution: The equation of motion in this case is written as

$$m\ddot{x} - kx = 0 \Rightarrow \ddot{x} - \omega_n^2 x = 0. \quad (\text{a})$$

Integrating Eq. (a) with respect to x yields

$$\frac{\dot{x}^2}{2} - \frac{\omega_n^2 x^2}{2} = H. \quad (\text{b})$$

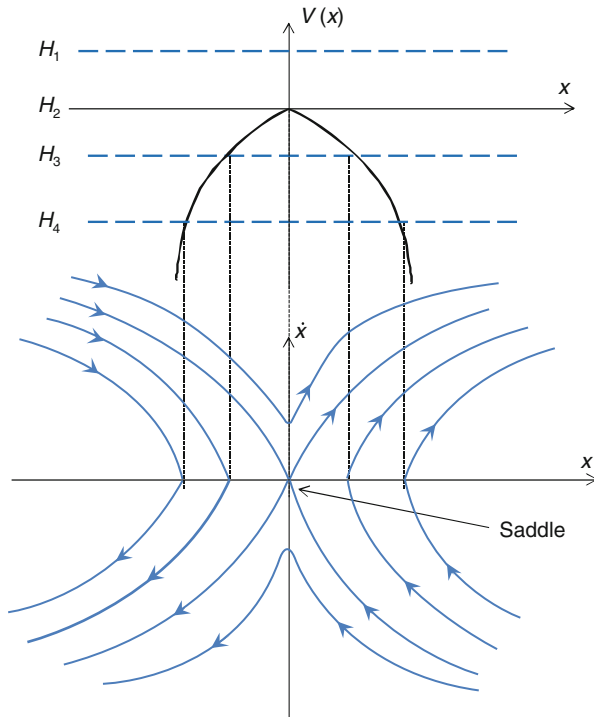


Fig. 5.23 A plot of the potential energy $V(x) = -\omega_n^2 x^2 / 2$ versus x (*up*) for various energy levels H_i and their corresponding trajectories (*bottom*)

Hence in this case, the potential function is $V(x) = -\omega_n^2 x^2/2$. A plot of $V(x)$ is shown in Fig. 5.23 with several levels of constant energy H . Also shown below the $V(x)$ plot are the corresponding trajectories in the phase space. As noted from the phase portrait, the fixed point of the system is unstable saddle; thus, there is no possibility of an oscillatory stable motion. For all initial conditions, the motion diverges to infinity. This conclusion about the fixed point can be also read from the potential energy plot. According to a role by Lyapunov, if the potential energy has no minimum at an equilibrium point, the equilibrium point is unstable.

Example 5.16: Sketch a phase portrait of the pendulum of Example 5.4.

Solution: We recall the equation of motion of the pendulum is written as

$$\ddot{\theta} + \frac{g}{L} \sin(\theta) = 0. \quad (a)$$

Integrating Eq. (a) with respect to θ yields

$$\frac{\dot{\theta}^2}{2} - \frac{g}{L} \cos(\theta) = H. \quad (b)$$

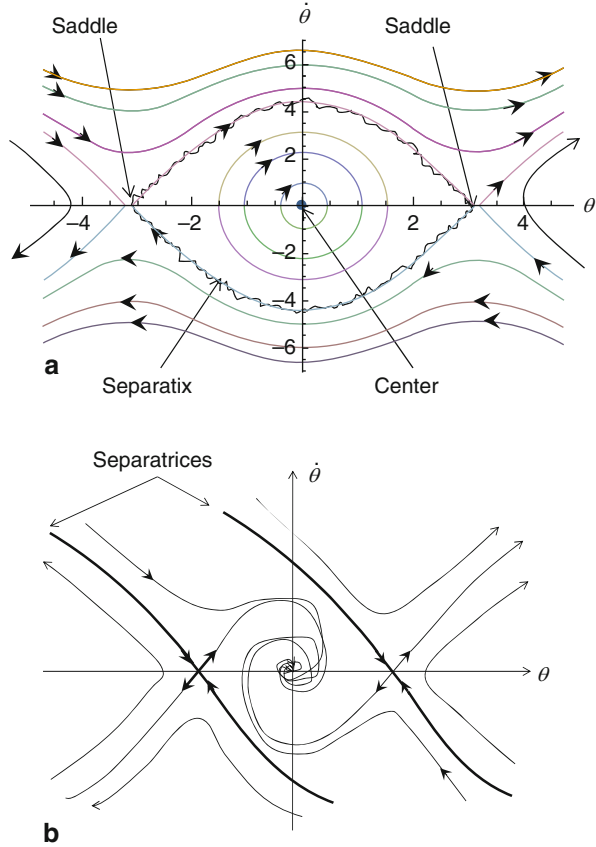
In this case, we choose to sketch the phase portrait directly without referring to the potential energy. To this end, an explicit expression for the velocity $\dot{\theta}$ is obtained from Eq. (b), which yields

$$\dot{\theta} = \pm \sqrt{2 \left(H + \frac{g}{L} \cos(\theta) \right)}. \quad (c)$$

Next, several initial conditions are used to calculate various levels of the constant H from Eq. (b). Then, these constants are plugged into Eq. (c), which is then plotted as a function of θ to yield the trajectories corresponding to the initial conditions. The results are depicted in Fig. 5.24a for $L = 1$. Because $\sin(\theta)$ in Eq. (a) yields infinite fixed points, which are just repeated cycles of the zero and $\pm\pi$, the sketch is made on a small representative range from $-\pi$ to π . Figure 5.24a reveals that there are two unstable saddles and one stable center. Note the various trajectories, which indicate various dynamical scenarios. Of particular importance are the curves that run between the two saddles, which form an elliptic-like shape labeled **separatix** in the figure and highlighted with a wiggly curve. Note that if the initial conditions of the system lie inside the separatix, the result is periodic motion as indicated by the closed trajectory. Otherwise, the motion is not periodic. Hence, the separatix separates regions in the phase space corresponding to qualitatively different dynamical behavior. This particular separatix that runs between two saddles is called **heteroclinic orbit**. It plays significant role in the complexity of the dynamics of the system.

The addition of light damping to the system destroys the heteroclinic orbit. Also, the center becomes a focus while the saddles remain saddles. The phase portrait in this case can be sketched directly based on these clues and Fig. 5.24a as shown in Fig. 5.24b. Note the new separatrices (plural of a separatix) of the system, which are shown as bold lines.

Fig. 5.24 Phase portraits of a swinging pendulum in the case of no damping (a) and in the case of light damping (b)



5.5.1 Phase Diagram of a Parallel-Plate Capacitor and the Dynamic Pull-in Concept

So far, several MEMS instabilities have been introduced as bifurcation points, such as pull-in of parallel-plate capacitors, side-instability in comb-drive fingers, and collapse instability due to capillary forces. The discussion has been under the assumption of static or quasi-static conditions with no account for any transient or dynamic behavior of the systems. For example, the voltage load is assumed to be increased in a very small step, and not ramped suddenly from zero to a specific value. Also, the effect of the inertia of the system during loading has not been accounted for. These transient effects cause the various systems instabilities to be triggered at lower thresholds compared to the predictions assuming static conditions. This dynamic effect has been cited for example in [11, 12] in the case of parallel-plate capacitors through the so-called dynamic pull-in phenomenon. Also, in the case of the collapse due to capillary forces, Mastrangelo and Hsu [4] stated that the transition between a

collapsed and noncollapsed structure based on the derived elastocapillary number is not sharp due to the kinetic energy that a microstructure may have.

One way to understand the transient effect in triggering instabilities is through phase portraits. Next, the concept is explained through an example of a single-sided parallel-plate capacitor. The case of a double-sided parallel-plate capacitor is discussed in the next section. Consider a parallel-plate capacitor similar to that of Example 5.5. We would like to sketch a phase portrait of the capacitor for two cases, assuming no damping and assuming light damping. The undamped equation of motion of the capacitor is written as

$$m\ddot{x} + kx = \frac{\varepsilon A V_{\text{DC}}^2}{2(d-x)^2}. \quad (5.14)$$

Integrating Eq. (5.14) with respect to x yields

$$\frac{m\dot{x}^2}{2} + \frac{kx^2}{2} - \frac{\varepsilon A V_{\text{DC}}^2}{2(d-x)} = H. \quad (5.15)$$

Thus, the total energy H is composed of the kinetic energy $m\dot{x}^2/2$ and potential energy, which is according to Eq. (5.15) is expressed as

$$V(x) = \frac{kx^2}{2} - \frac{\varepsilon A V_{\text{DC}}^2}{2(d-x)}. \quad (5.16)$$

Note that $V(x)$ varies with the voltage load V_{DC} . Figure 5.25 shows $V(x)$ and the corresponding phase portraits for various values of V_{DC} . As noted from Fig. 5.25a, for V_{DC} much lower than the pull-in voltage, the potential well $V(x)$ is deep. The phase portrait in this case reveals a center, a saddle, and a separatrix running through the saddle and encircling the center (such a separatrix is called a **homoclinic orbit**). If the initial conditions of the system lie inside the separatrix, the result is stable oscillation around the deflected position (the center). If the initial conditions lie outside the separatrix, the result is a nonoscillating motion that escapes to “infinity,” which in this case means pull-in. An explicit expression for the separatrix can be found analytically as follows. First, the saddle point ($x = X_{\text{un}}, \dot{x} = 0$), where X_{un} is the unstable equilibrium solution for a given V_{DC} , is substituted into Eq. (5.15) to estimate the energy level corresponding to the separatrix H_s :

$$H_s = \frac{kX_{\text{un}}^2}{2} - \frac{\varepsilon A V_{\text{DC}}^2}{2(d-X_{\text{un}})}. \quad (5.17)$$

Then, H_s is substituted into Eq. (5.15) and an expression for \dot{x} , and hence the separatrix curve, in terms of x is obtained as below

$$\dot{x} = \pm \sqrt{\frac{2H_s}{m} - \frac{kx^2}{m} + \frac{\varepsilon A V_{\text{DC}}^2}{m(d-x)}}. \quad (5.18)$$

The difference in initial conditions practically is most likely to occur through changing the initial velocity \dot{x} , which can be due to dynamic disturbances and transient

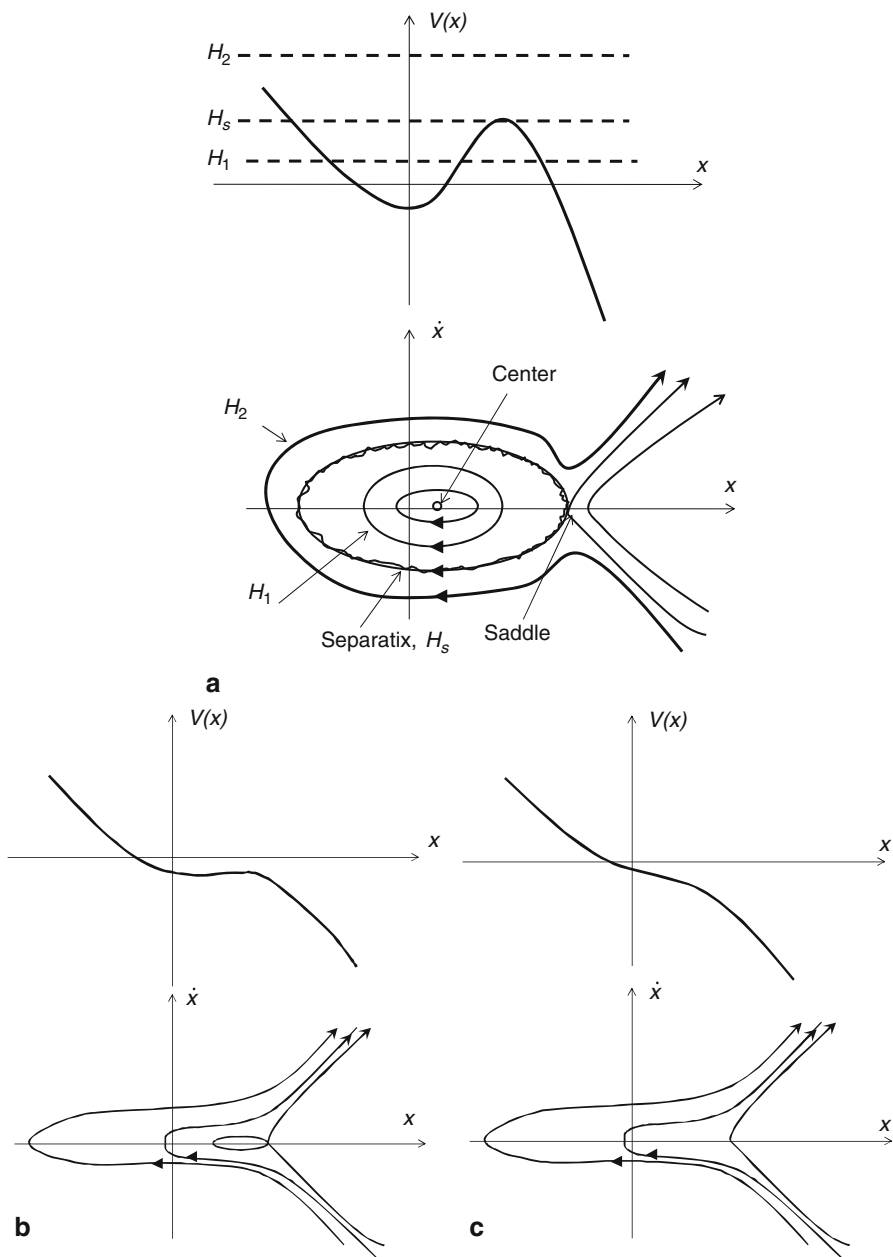


Fig. 5.25 The potential functions of a parallel-plate capacitor and the corresponding phase portraits for values of voltage load much lower than pull-in (a), just below pull-in (b), and beyond pull-in (c)

effects, for instance due to a sudden step voltage actuation. These raise the kinetic energy of the system, and hence its initial velocity. As an example, consider the energy level H_1 shown on the $V(x)$ plot of Fig. 5.25a. According to Eq. (5.15), the sources of the energy level are through the system stiffness, the electrostatic potential, and the kinetic energy. The corresponding trajectory of H_1 is a periodic motion, as depicted on the phase portrait. Assume now that the system has gained some additional energy and reached the H_2 level. According to Eq. (5.15), for the same system and V_{DC} , this can be only achieved through an increase in its kinetic energy. The corresponding trajectory of H_2 is a nonperiodic motion leading to escape to pull-in. Because pull-in occurs in this case due to the kinetic energy or the dynamic effects it is called **dynamic pull-in**. One definition of dynamic pull-in can be the collapse of a moveable electrode to a stationary electrode of a capacitor due to the combined action of its kinetic and potential energies. Sources of kinetic energy can be due to transient effects, for example due to a sudden step actuation of the microstructure, or due to dynamic loading, for example due to an AC harmonic voltage. Generally, dynamic pull-in requires lower values of DC voltage to be triggered compared to the static pull-in threshold.

Figure 5.25b shows the potential function $V(x)$ and the corresponding phase portrait for V_{DC} just below pull-in. As indicated in the figure, $V(x)$ here is shallow resulting in a slight possibility of stable oscillation around the equilibrium position. Increasing V_{DC} past pull-in makes $V(x)$ with no local minimum. This leads to the disappearance of both the saddle and the center. The trajectories on the phase portrait indicate the impossibility to achieve any stable oscillation for all initial conditions. This is an indication of the “traditional” pull-in phenomenon from static and dynamic perspectives.

The addition of light damping for the case of Fig. 5.25a transforms the center into a focus while the saddle remains saddle. A sketch of the phase portrait in this case is depicted in Fig. 5.26.

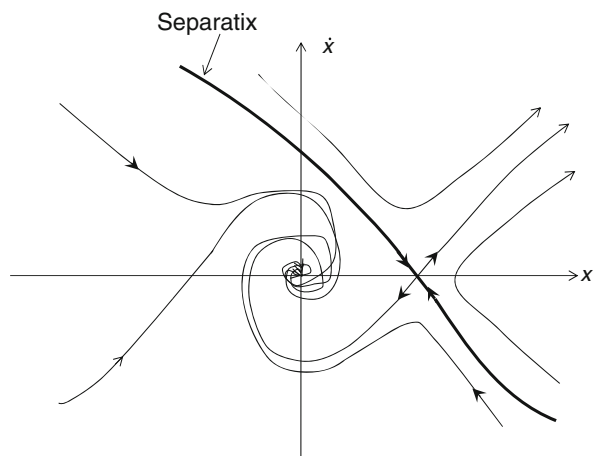


Fig. 5.26 The phase portrait of a parallel-plate capacitor in the presence of light damping

5.5.2 Phase Diagram of a Double-Sided Capacitor

Double-sided capacitors represent an essential component for several applications in MEMS actuation and detection. For example, they have been used for capacitive accelerometers because they provide better stability of the proof masses against mechanical shock and accidental dynamic disturbances. However, they have the disadvantage of being more complicated to fabricate compared to single-side capacitors. Also, they are used for positioning the tip of Nanoindentation transducers since they provide enhanced controllability [8]. In addition, they form the backbone of the interdigitated comb-drives. Next, an example is solved demonstrating their dynamical characteristics through phase portrait drawings.

Example 5.17: Consider the model of a double-sided parallel-plate capacitor of Fig. 5.27. The capacitor is composed of a proof mass attached to two springs. The springs can be linear or nonlinear, such as the case of a clamped–clamped microbeam sandwiched between two electrodes [13]. To consider the most generic case, assume the resultant restoring force F_s of the two springs expressed as

$$F_s = k_1 x + k_3 x^3 \quad (a)$$

where k_1 and k_3 are the linear and nonlinear coefficients of the springs, respectively. Assume the following parameters for the system: $m = 9.33 \times 10^{-11}$ kg, $k_1 = 5$ N/m, $d = 5$ μm , and the electrode area $A = 100 \times 200$ μm^2 .

Sketch the potential energy and the corresponding phase portraits of the system for the below cases:

- (a) $k_3 = 0$ and $V_{\text{DC}} = 12$ V
- (b) $k_3 = 0$ and $V_{\text{DC}} = 20$ V
- (c) $k_3 = 2 \times 10^{11}$ N/m³ and $V_{\text{DC}} = 12$ V
- (d) $k_3 = 2 \times 10^{11}$ N/m³ and $V_{\text{DC}} = 20$ V

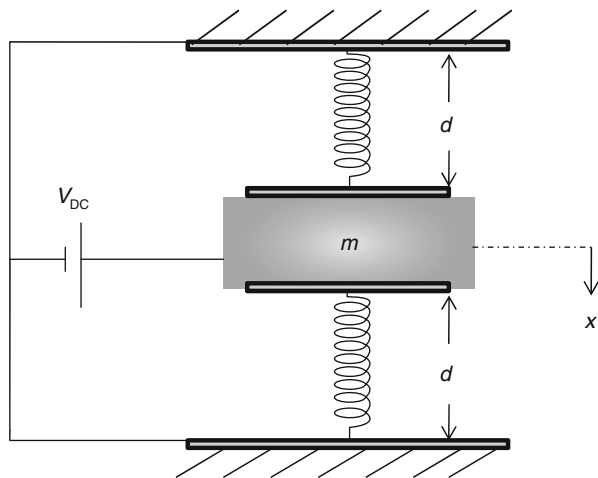


Fig. 5.27 A model of a double-sided capacitor

Solution: The equation of motion governing the behavior of the proof mass can be written as

$$m\ddot{x} + k_1x + k_3x^3 = \frac{\varepsilon AV_{\text{DC}}^2}{2} \left[\frac{1}{(d-x)^2} - \frac{1}{(d+x)^2} \right]. \quad (\text{b})$$

For convenience, and to better understand the contribution of the nonlinear restoring force, Eq. (a) is nondimensionalized by letting

$$\hat{x} = \frac{x}{d}; \quad \hat{t} = \frac{t}{T}. \quad (\text{c})$$

Then, substituting Eq. (c) into Eq. (a) and following the procedure of Sect. 5.2 yields the below nondimensional equation

$$\ddot{x} + x + \alpha x^3 = \beta V_{\text{DC}}^2 \left[\frac{1}{(1-x)^2} - \frac{1}{(1+x)^2} \right] \quad (\text{d})$$

where

$$\alpha = \frac{k_3 d^2}{k_1}; \quad \beta = \frac{\varepsilon A}{2k_1 d^3}. \quad (\text{e})$$

In Eq. (d), the “dot” denotes derivative with respect to \hat{t} and the hats are omitted from all the variables of the equation for convenience. Integrating Eq. (d) over x yields the total energy or the Hamiltonian H :

$$\frac{\dot{x}^2}{2} + \frac{x^2}{2} + \frac{\alpha x^4}{4} + \beta V_{\text{DC}}^2 \left[\frac{1}{x-1} - \frac{1}{x+1} \right] = H. \quad (\text{f})$$

To draw phase portraits, H is calculated for various values of (x, \dot{x}) . Then, the curves of \dot{x} as a function of x are plotted according to

$$\dot{x} = \pm \sqrt{2(H - V)}; \quad H > V \quad (\text{g})$$

where

$$V(x) = \frac{x^2}{2} + \frac{\alpha x^4}{4} + \beta V_{\text{DC}}^2 \left[\frac{1}{x-1} - \frac{1}{x+1} \right]. \quad (\text{h})$$

- (a) As a first step for the given parameters, it is good to check the pull-in voltage of the capacitor. This is the same as the side instability threshold discussed in Example 5.12, which predicts the pull-in to be

$$V_{\text{pull}} = \sqrt{\frac{k_1 d^3}{2\varepsilon A}}. \quad (\text{i})$$

Using Eq. (i) and the given parameters yield $V_{\text{pull}} = 18.8$ V. Hence, for part (a), the voltage load is below pull-in. Figure 5.28a depicts the potential energy

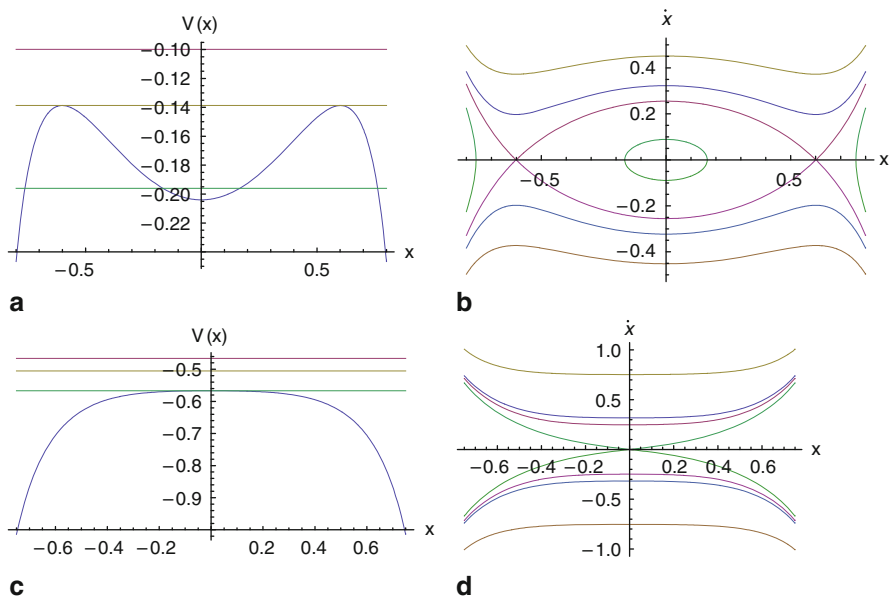


Fig. 5.28 The potential energy and the corresponding phase portrait for a double-sided capacitor with linear springs. For **a** and **b**, $V_{DC} = 12$ V, and for **c** and **d** $V_{DC} = 20$ V

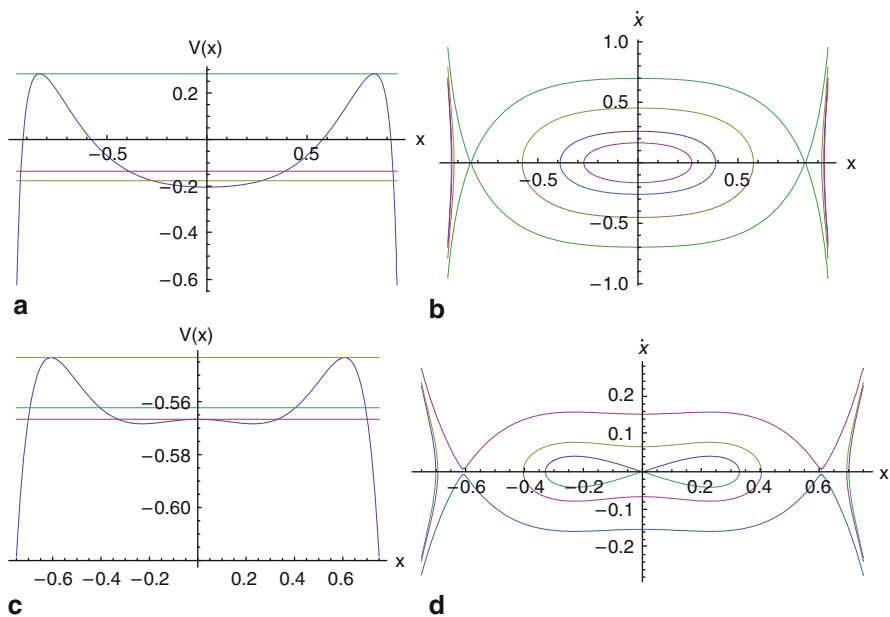


Fig. 5.29 The potential energy and the corresponding phase portrait for a double-sided capacitor with cubic nonlinear springs. For **a** and **b**, $V_{DC} = 12$ V, and for **c** and **d** $V_{DC} = 20$ V

of the system along with several lines of H . The figure indicates a single-well potential. Figure 5.28b shows the corresponding phase portrait. The figure shows a heteroclinic orbit passing through two saddles and encircling a center. This is expected based on the analysis of Example 5.12.

- (b) Increasing the voltage beyond pull-in to $V_{DC} = 20$ V leads to a potential function with no well (or minimum), Fig. 5.28c. The corresponding phase portrait, Fig. 5.28b, indicates an unstable saddle.
- (c) The addition of nonlinear springs may or may not change the phase portrait and the nature of solutions. For case (c), there is no qualitative change in the potential function nor the corresponding phase portrait, as demonstrated in Fig. 5.29a, b.
- (d) In this case, the nonlinear springs create a two-well potential function, Fig. 5.29c. Also, the center fixed point, which used to be stable below pull-in, is an unstable saddle similar to the linear case of part (b). However, there are two other stable centers that are created. These are shown in Fig. 5.29d surrounded by two homoclinic orbits.

5.6 Step-Input Actuation of Capacitive RF Switches

A switch is a device for making or breaking an electric circuit [14]. Switches can be made by various technologies, for example using semiconductors, transistors, and diodes. They can be purely mechanical, electrical, or a combination. A special category of switches that have gained a great deal of attention in recent years is RF (radio frequency) MEMS switches. MEMS switches can be defined as miniature devices that use a mechanical movement to achieve a short circuit or an open circuit in a transmissions line [15]. Most MEMS switches rely on electrostatic forces to actuate a moveable electrode or a microstructure with a voltage load beyond pull-in to achieve large stroke in a short time. The actuation mainly is achieved by a step-input voltage that is applied repeatedly at a certain frequency (a periodic square signal). The duration of time a microstructure takes to travel from the unactuated state (the “off” state) to pull-in (the “on” state) is called the pull-in time. It plays a vital role in determining the capability and range of applications of the switch. The shorter the pull-in time the better the switch is.

Besides the common known advantages of MEMS and electrostatic actuation, especially the low-power consumption and the batch-fabrication, capacitive switches feature many other advantages. These include high isolation (isolation is the amount of output signal when the switch is off), low insertion loss (insertion is characterized by the amount of losses in the signal output line when the switch is on), high on-off capacitance ratio, and a much broader operating temperature range than silicon electronic devices. Their major disadvantages however are their relatively high driving voltage and low switching speed. Applications of capacitive microswitches are in the domain of wireless communications and radar systems. Transmit/receive switches in a cellular phone are one example of such uses. Also, these devices are

excellent candidates to be used in phase shifting and time-delay circuits, such as in phased-array radars and communications antennas.

A simple model to characterize the dynamics of a MEMS switch is the simple parallel-plate capacitor of Fig. 5.8 or Fig. 5.11, in the case of an insulation layer. Thus, the analysis of Examples 5.5, 5.7, 5.8, and Sect. 5.5.1 all apply. In addition to predicting the pull-in and release voltages, there are other essential issues related to the response of a switch to a step input voltage. One parameter is the minimum step voltage required to actuate a switch in the “off” position, V_{step} . Note that V_{step} is different from the pull-in voltage V_{pull} since the former refers to a sudden dynamic actuation. Thus it is affected by the inertia and damping of the system. On the other hand, V_{pull} is a static concept, in which the voltage load is assumed to be applied slowly or quasi-statically such that any transient or inertia effects are negligible. In the literature, V_{step} sometimes is referred to as the dynamic pull-in voltage [2, 11, 16–18].

To understand the dynamical impact of V_{step} , let us refer to the analysis of Sect. 5.5.1. The definition of V_{step} implies that the initial conditions of the switch are zero velocity and zero displacement at the time of actuation (note that this may not be the actual case in an active switch, which may experience some oscillations when returning back to the off position before it is actuated again to the on position). On a phase portrait, V_{step} represents the minimum voltage, below which the initial conditions pair (0,0) leads to a stable oscillation and above which, (0,0) leads to pull-in. Hence, at V_{step} , the homoclinic orbit or the separatrix passes through the point (0,0). These scenarios are illustrated in Fig. 5.30.

To determine V_{step} , we recall the fact that at the moment of actuation when the switch is in the off position at (0,0), its energy level according to Eq. (5.15) is given by

$$H_{(0,0)} = \frac{-\varepsilon A V_{\text{step}}^2}{2d}. \quad (5.19)$$

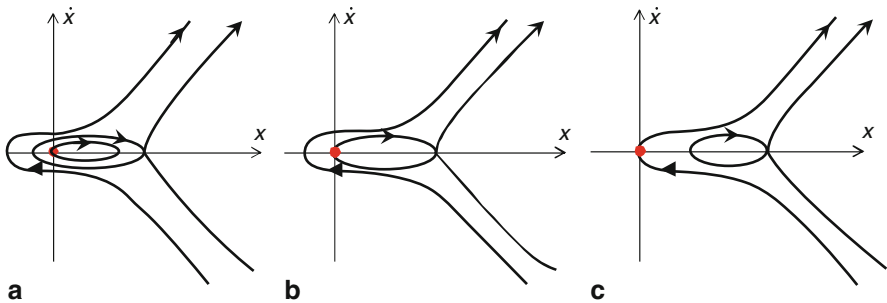


Fig. 5.30 Phase plots of a parallel-plate capacitor illustrating the dynamical outcome of the initial conditions (0,0) when the actuation voltage is below V_{step} (a), at V_{step} (b), and greater than V_{step} (c)

During the motion of the switch after applying V_{step} , in the absence of damping, its energy level must be conserved all the time at $H_{(0,0)}$. This same energy level corresponds to the separatix that passes through (0,0). The separatix also passes through the unstable saddle (see Fig. 5.30b), which is expressed in Eq. (5.17). Equating both Eq. (5.17) and Eq. (5.19) yields

$$\frac{-\varepsilon A V_{\text{step}}^2}{2d} = \frac{k X_{\text{un}}^2}{2} - \frac{\varepsilon A V_{\text{step}}^2}{2(d - X_{\text{un}})}. \quad (5.20)$$

We recall here that X_{un} is actually an equilibrium point satisfying

$$k X_{\text{un}} = \frac{\varepsilon A V_{\text{step}}^2}{2(d - X_{\text{un}})^2}. \quad (5.21)$$

Substituting for $k X_{\text{un}}$ from Eq. (5.21) into Eq.(5.20) yields

$$\frac{-\varepsilon A V_{\text{step}}^2}{2d} = \frac{\varepsilon A V_{\text{step}}^2 X_{\text{un}}}{4(d - X_{\text{un}})^2} - \frac{\varepsilon A V_{\text{step}}^2}{2(d - X_{\text{un}})}. \quad (5.22)$$

Dividing Eq. (5.22) by $\varepsilon A V_{\text{step}}^2$ and simplifying the outcome further yield

$$X_{\text{un}}^2 - \frac{d X_{\text{un}}}{2} = 0. \quad (5.23)$$

The nontrivial solution of Eq. (5.23) is $X_{\text{un}} = d/2$. Substituting this value into Eq. (5.20) yields the below expression for V_{step}

$$V_{\text{step}} = \sqrt{\frac{k d^3}{4 \varepsilon A}}. \quad (5.24)$$

Dividing V_{step} by V_{pull} of Eq. (3.27), or Eq. (d) of Example 5.7, gives

$$V_{\text{step}} = \sqrt{\frac{27}{32}} V_{\text{pull}} \approx 0.919 V_{\text{pull}}. \quad (5.25)$$

This result assumes no damping. Adding damping makes V_{step} approaches V_{pull} until both become equal under heavy damping. Similar analysis can be also conducted for **torsional actuators**, which reveals that [18]

$$V_{\text{torsional, step}} \approx 0.911 V_{\text{pull}}. \quad (5.26)$$

The other important parameter of MEMS switches is the pull-in time, which is the time the switch takes to travel from $x = 0$ to $x = d$ when actuated by $V_{\text{DC}} \geq V_{\text{step}}$. Again, at the moment of actuation when the switch is in the off position at (0,0), its energy level can be expressed according to Eq. (5.19) with V_{step} replaced by V_{DC} . Substituting $H_{(0,0)}$ into Eq. (5.18), the below expression is obtained for the velocity of the switch at a given position and voltage:

$$\dot{x} = \frac{dx}{dt} = \sqrt{\frac{\varepsilon A V_{\text{DC}}^2}{m} \left[\frac{x}{d(d-x)} \right] - \frac{k x^2}{m}}. \quad (5.27)$$

Solving for t from Eq. (5.27) and integrating the outcome from $x = 0$ to $x = d$ yield an integral expression of the pull-in time t_{pull} :

$$t_{\text{pull}} = \int_0^d \frac{1}{\sqrt{\frac{\varepsilon A V_{\text{DC}}^2}{m} \left[\frac{x}{d(d-x)} \right] - \frac{kx^2}{m}}} dx. \quad (5.28)$$

Unfortunately, there is no close-form analytical expression of the integral of Eq. (5.28) (a solution in the form of elliptic functions has been proposed in [19]). Hence, a numerical integration scheme, such as the Trapezoidal method, should be used, which most computational software, such as Mathematica and Matlab, can carryout easily. An alternative method to determine t_{pull} is through direct numerical integration of the equation of motion and then monitoring the time history response to catch the instant of reaching the other electrode. This method applies also in the presence of damping and other nonlinearities of the system. However, since $x = d$ represents a singularity of the electrostatic force term, one may need to measure the time up to $x = 0.99d$ as an approximation. In the presence of an insulator of thickness s , the time is monitored up to $x = d - s$. The below example illustrates the procedure.

Example 5.18: Consider the single-sided capacitor of Fig. 5.8 as a model of an RF MEMS switch. Assume $m = 2.332 \times 10^{-10}$ kg, $k = 37.35$ N/m, $d = 1.0$ μm , and the electrode area $A = 500 \times 100$ μm^2 .

1. Assume ζ (damping ratio) = 0.1 and calculate the pull-in time using direct integration of the equation of motion when the switch is actuated by (a) $V_{\text{DC}} = 1.2 V_{\text{pull}}$, (b) $V_{\text{DC}} = 1.5 V_{\text{pull}}$, and (c) $V_{\text{DC}} = 1.8 V_{\text{pull}}$.
2. Repeat (1) assuming no damping and compare to the results of Eq. (5.28).

Solution:

1. Because we will use numerical integration of the equation of motion, it is recommended to deal with normalized quantities and a nondimensional equation to avoid any numerical problems and convergence issues. Hence, we refer to Examples 5.2 and 5.3 and write the equation of motion in a nondimensional form as

$$\frac{d^2 \hat{x}}{d\hat{t}^2} + \mu \frac{d\hat{x}}{d\hat{t}} + \hat{x} = \frac{\beta V_{\text{DC}}^2}{(1 - \hat{x})^2} \quad (a)$$

where

$$\hat{x} = \frac{x}{d}; \quad \hat{t} = \frac{t}{T} \quad (b)$$

and the parameters of Eq. (a) are calculated as

$$\beta = \frac{\varepsilon A}{2kd^3} \approx 0.0059 \text{ V}^{-2}; \quad \mu = \frac{c}{\sqrt{mk_1}} = 0.2; \quad T = \sqrt{\frac{m}{k}} \approx 2.5 \text{ } \mu\text{s}. \quad (c)$$

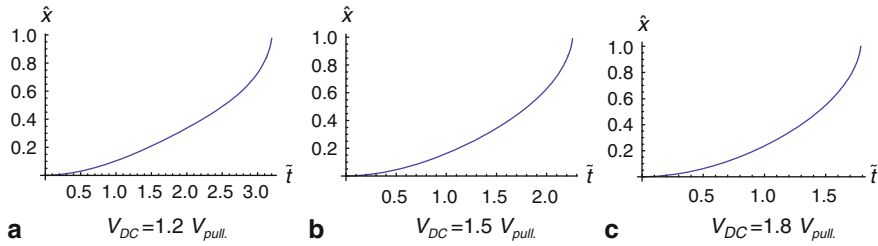


Fig. 5.31 A plot showing the time response of a switch actuated beyond pull-in

Using Eq. (3.27), the pull-in voltage is found to be $V_{\text{pull}} = 5$ V. Integrating Eq. (a) numerically in time gives the plots of Fig. 5.31. The results in the plot are shown for \hat{x} just below 1 since beyond this value the results diverge due to the singularity at pull-in.

- (a) The nondimensional time of pull-in is $\hat{t}_{\text{pull}} = 3.20$, which means $t_{\text{pull}} \approx 8 \mu\text{s}$
- (b) $\hat{t}_{\text{pull}} = 2.258$ and $t_{\text{pull}} \approx 5.64 \mu\text{s}$
- (c) $\hat{t}_{\text{pull}} = 1.786$ and $t_{\text{pull}} \approx 4.46 \mu\text{s}$

Note from the results of (a)–(c), as V_{DC} increases, t_{pull} decreases. Practically, there is a trade-off on how much one can increase V_{DC} to achieve acceptable t_{pull} .

2. For this part with no damping, Eq. (5.28) applies. We use the command “NIntegrate” in Mathematica to carry out the integration. It turns out that the results of both the direct time integration of the equation of motion and Eq. (5.28) are exactly the same. The results are listed below. Note that t_{pull} here is less than part (1).

- (a) $t_{\text{pull}} \approx 7.4 \mu\text{s}$
- (b) $t_{\text{pull}} \approx 5.39 \mu\text{s}$
- (c) $t_{\text{pull}} \approx 4.31 \mu\text{s}$

5.7 Dynamics of Torsional Actuators and Micromirrors

This section presents detailed analysis of the dynamics of torsional actuators and micromirrors as a special case study to demonstrate the application of several analytical tools that have been discussed so far. The dynamic response of torsional actuators and micromirrors has drawn considerable interest in recent years [20–30]. A 1-DOF [20–26] and two-degree-of-freedom (2-DOF) models [27–30] have been presented. The dynamics of a micromirror under the effect of electrostatic [20–22, 27–30], van der Waals [23, 24], Casimir [23, 25], and capillary forces [26] have been analyzed. Next, the dynamics of an electrostatically actuated torsional actuator are discussed using first a 1-DOF model and then using a 2-DOF model.

5.7.1 Single-Degree-of-Freedom Model

Here, we follow the notations of Sect. 3.5.2 and consider the torsional actuator of Fig. 3.23, which is actuated by electrostatic forces and supported by two torsional springs. The dimensional equation of motion of the actuator can be written as

$$I_m \ddot{\alpha} + c \dot{\alpha} + K_t \alpha = \frac{\varepsilon b V_{DC}^2}{2\alpha^2} \left[\frac{d}{d - a_2 \alpha} - \frac{d}{d - a_1 \alpha} + \ln \left(\frac{d - a_2 \alpha}{d - a_1 \alpha} \right) \right] \quad (5.29)$$

where I_m is the mass moment of inertia of the top plate of the actuator, c is a viscous damping coefficient, and K_t is the effective stiffness coefficient of the two torsional springs. Next, we introduce the following nondimensional variables:

$$\theta = \frac{\alpha}{\alpha_{\max}}; \quad \hat{t} = \frac{t}{T}. \quad (5.30)$$

Also, the following normalized ratios are introduced as explained in Sect. 3.5.2:

$$\gamma = \frac{a_1}{a_3}; \quad \beta = \frac{a_2}{a_3}. \quad (5.31)$$

Substituting Eq. (5.30) and Eq. (5.31) into Eq. (5.29) results in the following nondimensional equation:

$$\ddot{\theta} + \mu \dot{\theta} + \theta = \frac{\eta}{\theta^2} \left[\frac{1}{1 - \beta \theta} - \frac{1}{1 - \gamma \theta} + \ln \left(\frac{1 - \beta \theta}{1 - \gamma \theta} \right) \right] \quad (5.32)$$

where

$$\mu = \frac{cT}{I_m}; \quad \eta = \frac{\varepsilon b V_{DC}^2}{2\alpha_{\max}^3 K_t}; \quad T = \sqrt{\frac{I_m}{K_t}}. \quad (5.33)$$

Next, stability analysis is conducted based on Eq. (5.32). Toward this, we let $x_1 = \theta$ and $x_2 = \dot{\theta}$. Then Eq. (5.32) is written in a state-space form as

$$\dot{x}_1 = x_2 \quad (5.34)$$

$$\dot{x}_2 = F_1(x_1, x_2) = \frac{\eta}{x_1^2} \left[\frac{1}{1 - \beta x_1} - \frac{1}{1 - \gamma x_1} + \ln \left(\frac{1 - \beta x_1}{1 - \gamma x_1} \right) \right] - \mu x_2 - x_1. \quad (5.35)$$

The equilibrium points are found by setting the right-hand side of Eqs. (5.34) and (5.35) equal to zero. This gives $x_2 = 0$ and

$$\frac{\eta}{x_1^2} \left[\frac{1}{1 - \beta x_1} - \frac{1}{1 - \gamma x_1} + \ln \left(\frac{1 - \beta x_1}{1 - \gamma x_1} \right) \right] - x_1 = 0. \quad (5.36)$$

Solving Eq. (5.36) yields two physical solutions: x_{11} and x_{12} , where $x_{11} < x_{12}$. To analyze their stability, the Jacobian of Eqs. (5.34) and (5.35) are determined as

$$|A - \lambda I| = 0 \Rightarrow \begin{vmatrix} -\lambda & 1 \\ \frac{\partial F_1(x_1, x_2)}{\partial x_1} & -\mu - \lambda \end{vmatrix} = 0. \quad (5.37)$$

Equation (5.37) yields a characteristic equation for λ , the solution of which at each fixed point indicates the stability of that point. In the case of **no damping**, $\mu = 0$, the solution of the characteristic equation is simplified to

$$\lambda_{1,2} = \pm \sqrt{\frac{\partial F_1(x_1, x_2)}{\partial x_1}}. \quad (5.38)$$

When substituting the numbers for a specific mirror, it turns out that for the smaller solution x_{11} , λ_1 and λ_2 are both pure imaginary indicating neutrally stable fixed point. The larger solution x_{12} is found to be unstable saddle. These results apply for V_{DC} less than the pull-in voltage. At pull-in, both solutions coalesce in a saddle-node bifurcation where $\lambda_1 = \lambda_2 = 0$. This gives an equation in terms of x_1 , which along with the equilibrium equation, Eq. (5.36), can be solved to determine the value of x_1 at pull-in. As a special case, consider a full electrode on the upper plate of the actuator, so that $a_1 = \gamma = 0$, $a_2 = a_3$ and $\beta = 1$. Substituting these values in Eq. (5.38) and setting it equal to zero yields

$$-1 + \frac{\eta}{x_1^2} \left[\left(\frac{1}{(1-x_1)^2} - \frac{1}{1-x_1} \right) \right] - \frac{2\eta}{x_1^3} \left[-1 + \frac{1}{1-x_1} + \ln(1-x_1) \right] = 0. \quad (5.39)$$

Equation (5.39) is used to eliminate η from Eq. (5.36), which results in a single equation in terms of x_1 that needs to be solved numerically. The outcome of this gives the well-known result of

$$x_1 = \theta = 0.440423. \quad (5.40)$$

Substituting for x_1 from Eq. (5.40) into Eq. (5.39) and then solving for η gives

$$\eta_{\text{pull}} = 0.4137. \quad (5.41)$$

Recalling the definition of η and solving for the voltage load yields

$$V_{\text{pull}} = \sqrt{\frac{0.8277 K_t \alpha_{\text{max}}^3}{\varepsilon b}} = 0.90967 \sqrt{\frac{K_t d^3}{\varepsilon b a_2^3}} \quad (5.42)$$

which is the same as Eq. (3.41).

Another quantity of interest is the variation of the natural frequency of the actuator with V_{DC} . This can be calculated by first solving Eq. (5.36) for x_{11} at the given V_{DC} .

Then the result is substituted into Eq. (5.38). By taking the real value of λ_1 or λ_2 the natural frequency is obtained.

The next step in analyzing the dynamic response of the device is to plot its potential energy and phase portrait. Toward this, the undamped case is first considered. Hence, μ is set equal to zero in Eq. (5.32), then the equation is multiplied by $\dot{\theta}$ and the whole equation is integrated with respect to θ , which gives the total energy equation:

$$\frac{\dot{\theta}^2}{2} + \frac{\theta^2}{2} + \frac{\eta \ln\left(\frac{1-\beta\theta}{1-\gamma\theta}\right)}{\theta} = H = \frac{\dot{\theta}^2}{2} + V(\theta). \quad (5.43)$$

Example 5.19 illustrates further these steps.

Example 5.19: Consider the torsional actuator of Example 4.3. Assume $I_m = 4.372 \times 10^{-15} \text{ kg m}^2$.

- Calculate the equilibrium solutions of the system and determine their stability for various values of V_{DC} up to pull-in. Plot the solutions versus V_{DC} .
- Calculate and plot the natural frequency of the actuator versus V_{DC} up to pull-in.
- Plot the potential energy of the system and the corresponding phase portraits for (i) $V_{DC} = 10 \text{ V}$ and (ii) $V_{DC} = 15.4 \text{ V}$.

Solution:

- Equilibrium points are found by solving numerically Eq. (5.35). The easiest way to do this is to solve for η in terms of x_1 , which gives

$$\eta = \frac{x_1^3}{\left[\frac{1}{1-\beta x_1} - \frac{1}{1-\gamma x_1} + \ln\left(\frac{1-\beta x_1}{1-\gamma x_1}\right) \right]}. \quad (a)$$

By recalling the definition of η , a direct relationship between V_{DC} and x_1 is obtained, which turns out to be the same as that of Eq. (3.38). A plot of V_{DC} versus x_1 is shown in Fig. 5.32. Based on this plot, for each value of V_{DC} , an

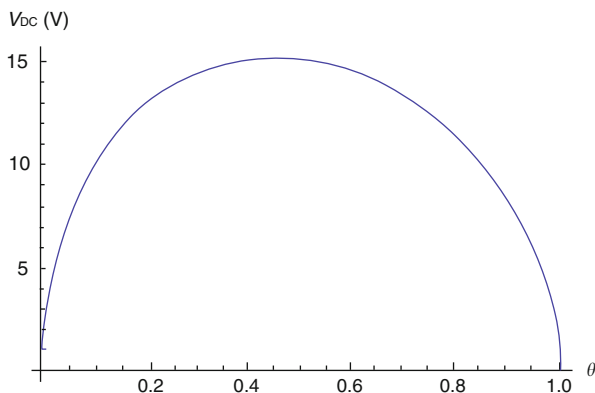


Fig. 5.32 The equilibrium solutions of a torsional actuator

appropriate initial condition is provided to numerically solve Eq. (5.35) to obtain either the lower solution x_{11} or the unstable solution x_{12} . This value is substituted into Eq. (5.37) to determine the stability of the solutions.

- (b) The nondimensional natural frequency ω_{non} of the system is calculated by taking the real value of λ of the stable solutions x_{11} , that is

$$\omega_{\text{non}} = \text{Re} \left[\sqrt{-1 + \frac{\eta}{x_{11}^2} \left[\left(\frac{1}{(1-x_{11})^2} - \frac{1}{1-x_1} \right) \right] - \frac{2\eta}{x_{11}^3} \left[-1 + \frac{1}{1-x_{11}} + \ln(1-x_{11}) \right]} \right]. \quad (\text{b})$$

The dimensional natural frequency in Hz, f_n , is related to ω_{non} as

$$f_n = \frac{\omega_{\text{non}}}{2\pi} \sqrt{\frac{K_t}{I_m}}. \quad (\text{c})$$

Figure 5.33 shows the stable and unstable equilibrium solutions. Figure 5.34a shows the eigenvalue of the upper unstable solution, which as shown is always a real number. Figure 5.34b shows the calculated natural frequency based on the eigenvalue of the lower stable solution, which as mentioned, is always pure imaginary.

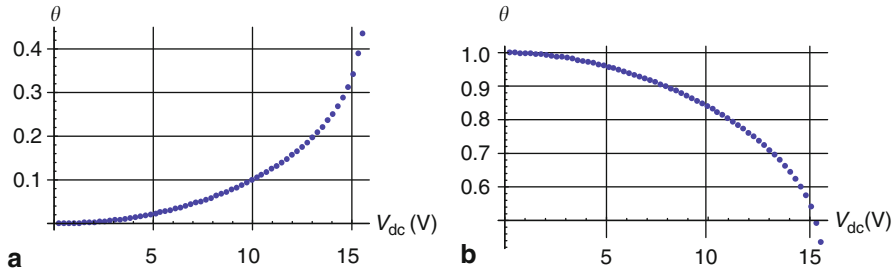


Fig. 5.33 The stable (a) and unstable (b) equilibrium solutions of the torsional actuator

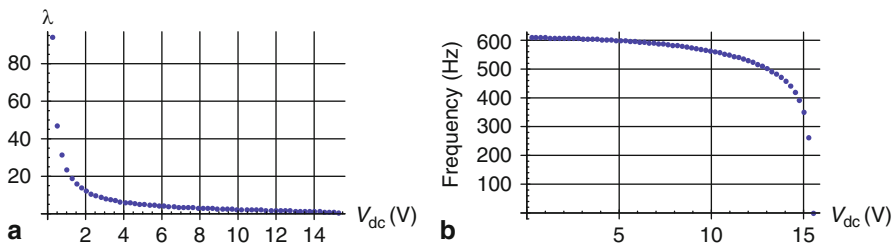


Fig. 5.34 a The eigenvalues of the unstable solution. b The natural frequency of the torsional actuator

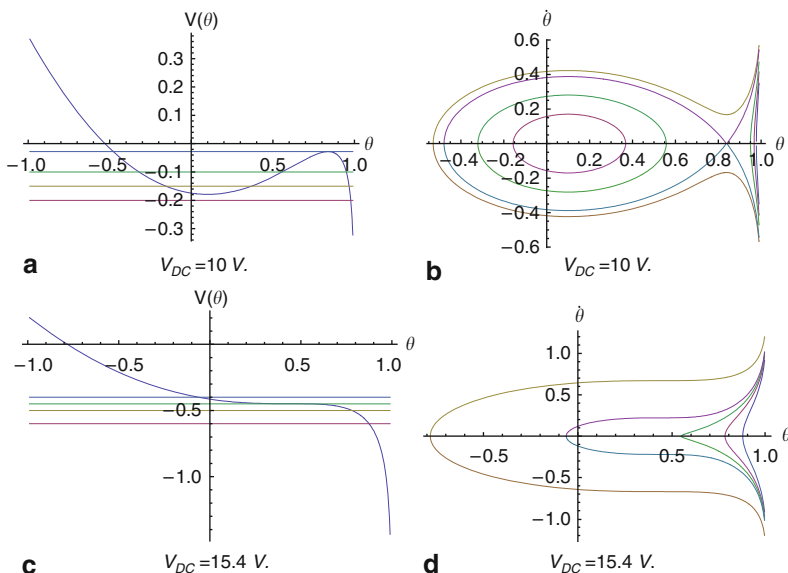


Fig. 5.35 The potential energy functions and the corresponding phase portraits

- (c) The potential energy and total energy of the system are given according to Eq. (5.43). Hence, the phase portrait is drawn according to the below equation:

$$\dot{\theta} = \pm \sqrt{2(H - V)}; \quad H > V. \quad (d)$$

Figure 5.35 shows the various potential energy plots and the corresponding phase portraits.

5.7.2 Two-Degree-of-Freedom Model

The analysis of the previous section is based on a 1-DOF model, which assumes that the only DOF of the system is through its rotational motion. This assumption can be considered accurate if the top plate of the actuator undergoes very small vertical translational motion toward the stationary electrode. However, if the vertical motion becomes comparable to the rotational motion, then a 2-DOF model becomes necessary to capture accurately the static and dynamic features of the system.

For this, consider the 2-DOF model shown in Fig. 5.36. The notations of the previous section still apply. In addition, a vertical motion of the top plate y is assumed. Also, a translational spring of coefficient k_y is assumed, which represents the effective bending resistance of the two springs attached to the top plate. Next, an expression of the electrostatic force acting on a small portion of the upper electrode of length dx is calculated. Under the assumptions of negligible fringing effect, infinitely wide

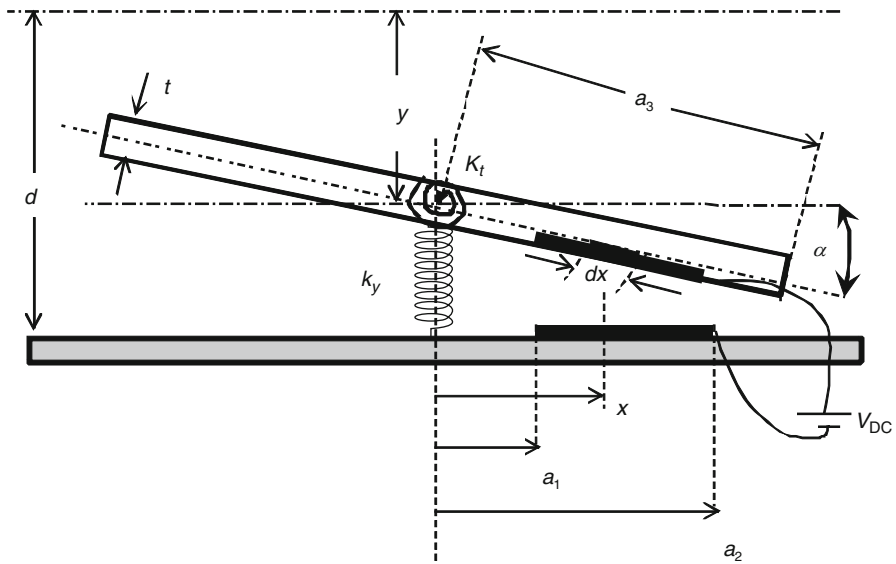


Fig. 5.36 A two-degree-of-freedom model of a torsional actuator

plates (parallel-plate approximation), and a small tilting angle α , this portion of the electrode and the one directly underneath it can be treated as two parallel plates. Assuming also a small deflection y in addition to the tilting angle α , the electrostatic force is expressed, according to Eq. (3.24), as

$$dF = \frac{\epsilon b V^2 dx}{2(d - y - x\alpha)^2}. \quad (5.44)$$

Then, the total vertical electrostatic force F_e can be calculated as

$$F_e = \int_{a_1}^{a_2} dF = \frac{\epsilon b V_{DC}^2}{2\alpha(d - y - a_2\alpha)} - \frac{\epsilon b V_{DC}^2}{2\alpha(d - y - a_1\alpha)}. \quad (5.45)$$

Also, the electrostatic moment M_e is calculated as

$$M_e = \int_{a_1}^{a_2} x dF = \frac{\epsilon b V_{DC}^2}{2\alpha^2} \left[\frac{d - y}{d - y - a_2\alpha} - \frac{d - y}{d - y - a_1\alpha} + \ln \left(\frac{d - y - a_2\alpha}{d - y - a_1\alpha} \right) \right]. \quad (5.46)$$

The dimensional equations of motion of the actuator can be written as

$$I_m \ddot{\alpha} + c \dot{\alpha} + K_t \alpha = M_e \quad (5.47)$$

$$m \ddot{y} + c_y \dot{y} + k_y y = F_e \quad (5.48)$$

where m is the effective mass of the upper plate, c_y is the translational viscous damping coefficient, and the rest of parameters are as defined in the previous section. Next, we introduce the following nondimensional variables:

$$\theta = \frac{\alpha}{\alpha_{\max}}; \quad \delta = \frac{y}{d}; \quad \hat{t} = \frac{t}{T}. \quad (5.49)$$

Substituting Eq. (5.49) and the normalized ratios of Eq. (5.31) into Eqs. (5.47) and (5.48) results in the following nondimensional equations:

$$\ddot{\theta} + \mu\dot{\theta} + \theta = \frac{\eta}{\theta^2} \left[\frac{1 - \delta}{1 - \delta - \beta\theta} - \frac{1 - \delta}{1 - \delta - \gamma\theta} + \ln\left(\frac{1 - \delta - \beta\theta}{1 - \delta - \gamma\theta}\right) \right] \quad (5.50)$$

$$\ddot{\delta} + \mu_y\dot{\delta} + \omega_0^2\delta = \frac{\eta_y}{\theta} \left[\frac{1}{1 - \delta - \beta\theta} - \frac{1}{1 - \delta - \gamma\theta} \right] \quad (5.51)$$

where

$$\begin{aligned} \mu_y &= \frac{c_y}{m} \sqrt{\frac{I_m}{K_t}}; & \eta_y &= \frac{I_m \varepsilon b V_{DC}^2}{2K_t d^2 m \alpha_{\max}}; \\ \omega_0^2 &= \frac{\omega_y^2}{\omega_t^2}; & \omega_t^2 &= \frac{K_t}{I_m}; & \omega_y^2 &= \frac{k_y}{m} \end{aligned} \quad (5.52)$$

and the rest of parameters are as defined in Eq. (5.33). Note that the nondimensional translational natural frequency ω_0 represents the ratio of the bending natural frequency ω_y to the torsional one ω_t . Equations (5.50) and (5.51) represent a coupled 2-DOF system, which forms the basis of studying more accurately the behavior of a torsional actuator. Note that the coupling of the two equations comes from the voltage load or the η and η_y terms.

Next, stability analysis is conducted. Toward this, we let $x_1 = \theta$, $x_2 = \dot{\theta}$, $x_3 = \delta$, and $x_4 = \dot{\delta}$. Then Eqs. (5.50) and (5.51) are written in a state-space form as

$$\dot{x}_1 = x_2 \quad (5.53)$$

$$\begin{aligned} \dot{x}_2 &= F_1(x_1, x_2, x_3) = -\mu x_2 - x_1 \\ &+ \frac{\eta}{x_1^2} \left[\frac{1 - x_3}{1 - x_3 - \beta x_1} - \frac{1 - x_3}{1 - x_3 - \gamma x_1} + \ln\left(\frac{1 - x_3 - \beta x_1}{1 - x_3 - \gamma x_1}\right) \right] \end{aligned} \quad (5.54)$$

$$\dot{x}_3 = x_4 \quad (5.55)$$

$$\dot{x}_4 = F_2(x_1, x_3, x_4) = -\mu_y x_4 - \omega_0^2 x_3 + \frac{\eta_y}{x_1} \left[\frac{1}{1 - x_3 - \beta x_1} - \frac{1}{1 - x_3 - \gamma x_1} \right] \quad (5.56)$$

The equilibrium points are found by setting the right-hand side of Eqs. (5.53)–(5.56) equal to zero. This gives $x_2 = x_4 = 0$ and

$$-x_1 + \frac{\eta}{x_1^2} \left[\frac{1 - x_3}{1 - x_3 - \beta x_1} - \frac{1 - x_3}{1 - x_3 - \gamma x_1} + \ln \left(\frac{1 - x_3 - \beta x_1}{1 - x_3 - \gamma x_1} \right) \right] = 0 \quad (5.57)$$

$$-\omega_0^2 x_3 + \frac{\eta_y}{x_1} \left[\frac{1}{1 - x_3 - \beta x_1} - \frac{1}{1 - x_3 - \gamma x_1} \right] = 0. \quad (5.58)$$

Solving Eqs. (5.57) and (5.58) yield four physical solutions: x_{01} , x_{02} , x_{03} , and x_{04} . To analyze their stability, the Jacobian of Eqs. (5.53)–(5.56) are evaluated at these roots to form the A matrix (see Sect. 5.3), and then the below determinant is evaluated:

$$|A - \lambda I| = 0 \Rightarrow \begin{vmatrix} -\lambda & 1 & 0 & 0 \\ \frac{\partial F_1}{\partial x_1} & -\mu - \lambda & \frac{\partial F_1}{\partial x_3} & 0 \\ 0 & 0 & -\lambda & 1 \\ \frac{\partial F_2}{\partial x_1} & 0 & \frac{\partial F_2}{\partial x_3} & -\mu_y - \lambda \end{vmatrix} = 0. \quad (5.59)$$

Equation (5.59) yields a forth-order algebraic equation for λ , which can be solved numerically to give four roots of λ . The roots come in two pairs; each pair is composed of two roots of the same magnitude but of different sign. Each pair corresponds to either the torsional or translational solution. It turns out that below pull-in, the smallest two torsional and translational solutions are stable, with eigenvalues of negative real numbers in the case of damping or pure imaginary in the case of no damping. The real value of the eigenvalue of each pair represents the nondimensional natural frequency. Note that at $V_{DC} = 0$, the nondimensional natural frequency of the torsional mode ω_t^{non} , according to Eq. (5.50), equals unity, and the nondimensional natural frequency of the translational mode, according to Eq. (5.51), equals ω_0 .

Example 5.20: In this example, we study the torsional micromirror of Huang et al. [28] and Zhao et al. [29] using the 2-DOF model. The mirror is similar to that of Fig. 5.36, in which the upper plate is connected by two bars that serve as torsional and translational springs. Consider the geometric and material prosperities of the mirror as in the below table:

a_1 (μm)	a_2 (μm)	a_3 (μm)	d (μm)	b (μm)	
3	42	50	2.75	1,000	
t (μm)	w (μm)	l (μm)	E (GPa)	G (GPa)	ρ (kg/m^3)
1.5	1.55	65	170.3	66	2,332

Zhao et al. [29] conducted a finite-element analysis to estimate the natural frequencies of the mirror at zero voltage. They found that the first translational natural frequency = 61.72 kHz and the first torsional one = 39.33 kHz. Calculate the stable equilibrium solutions, prove their stability, and calculate the translational and torsional natural

frequencies of the mirror as they vary for various values of V_{DC} starting from zero up to pull-in. Show plots of the results.

Solution: We first need to calculate K_t due to the two torsional springs as

$$K_t = 2 \times \frac{G J_p}{l} \quad (a)$$

where J_p is calculated from Eq. (4.6). The result is $K_t = 1.54 \times 10^{-9}$ N m. Also, k_y is calculated by considering the mirror with the two bars as beams connected in parallel to a rigid plate, which is case 5 of Table 4.1. Thus,

$$k_y = 2 \times \frac{12EI}{l^3} \quad (b)$$

where $I = wt^3/12$. This gives $k_y = 6.49$ N/m.

In addition, the effective mass of the mirror is calculated according to Eq. (4.9):

$$m = \frac{k_y}{\omega_y^2}. \quad (c)$$

After transforming the giving frequency to rad/s, Eq. (c) gives $m = 4.3 \times 10^{-11}$ kg. Similarly, the mass moment of inertia of the mirror is calculated according to

$$I_m = \frac{K_t}{\omega_t^2} \quad (d)$$

which yields $I_m = 2.5 \times 10^{-20}$ kgm².

Although this is a 2-DOF problem, it is good idea to simulate the response of the mirror using a single-DOF of Sect. 5.7.1. Using Eq. (3.40), the pull-in of the device is found approximately near 20 V. This should be taken only as an approximate answer to help us determine the range of voltage to be considered. The rest of the analysis will be left as an exercise. Next, the 2-DOF static problem of Eqs. (5.57) and (5.58) is numerically solved starting from a very small value of V_{DC} with initial guesses for x_1 and x_3 near zero and using the command “FindRoot” in the software Mathematica. Then, the solutions at this voltage step are used as initial guesses for the next voltage step, and the process is repeated until reaching pull-in. The results of this process should yield the stable solutions. To obtain the unstable solutions, one needs to start from higher values of initial guesses (near unity for x_3). Figure 5.37 shows the stable equilibrium solutions. Note that the new pull-in voltage based on the 2-DOF is near 18 V, which is in agreement with the experimental data of this device [28, 29].

To calculate the variation of the natural frequencies of the actuator, the characteristic equation of Eq. (5.59) needs to be solved at each V_{DC} step. Also, the corresponding stable solutions x_1 and x_3 need to be substituted into Eq. (5.59). This results in an algebraic equation with four roots of λ . Substituting the stable equilibrium solution into Eq. (5.59) gives four pure imaginary λ . Taking the real value of each imaginary pair yields the nondimensional natural frequency of each mode (ω_t^{non} and ω_0). Plots of the drop of these frequencies with V_{DC} are shown in Fig. 5.38. Note that at pull-in, the natural frequency of the torsional mode drops to zero.

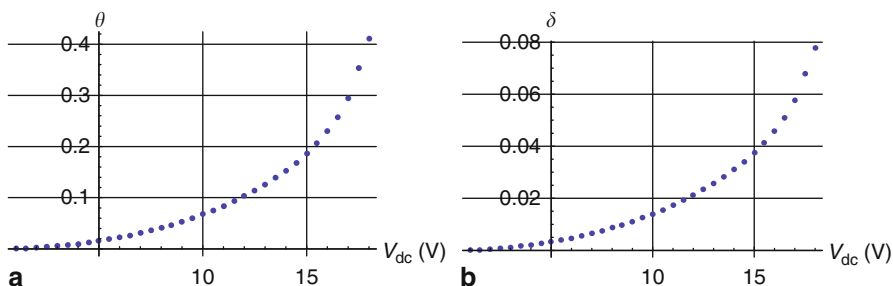


Fig. 5.37 The two stable equilibrium solutions of the mirror, **a** rotational deflection and, **b** is the translational deflection

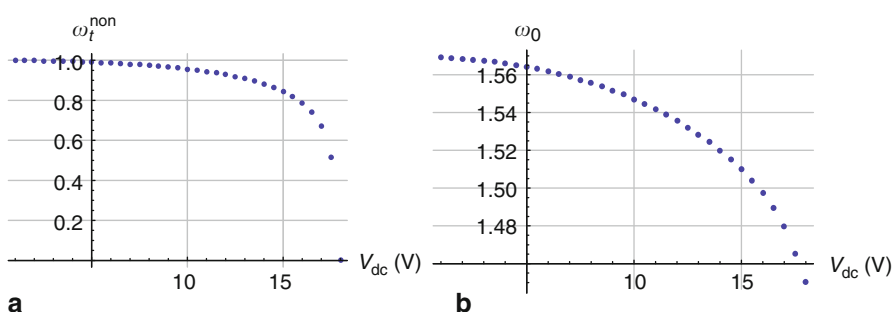


Fig. 5.38 The two nondimensional natural frequencies of the mirror. Shown are the nondimensional torsional **a** and translational **b** natural frequencies

5.8 Nonlinear Oscillations

This section discusses the vibration of nonlinear systems near equilibrium points. This kind of motion is considered local dynamics since it is concerned with the dynamical behavior in the vicinity of equilibrium points and not to that far from equilibrium points. In a phase portrait such as Fig. 5.24a or Fig. 5.25a, this corresponds to the oscillation inside the separatrix around the center. This is in contrast to global dynamics that is concerned with the all aspects of dynamics in a phase portrait, such as the motions across several potential wells or in and out separatrices. The subject of nonlinear vibration has been treated in great depth qualitatively and quantitatively in the classical book of Nayfeh and Mook [31]. Our focus here is on revealing interesting phenomena and behaviors concerning MEMS without going into much analytical details. Concepts, such as softening and hardening, hysteresis, jumps, subharmonic, superharmonic, and parametric resonances are explained and discussed. Most of the common and dominant nonlinearities in MEMS are either of quadratic type, due to electrostatic forces and piezoelectric material, or of cubic type, which are due to the geometric configuration of microstructures. Therefore, these will be the center of focus of this section.

5.8.1 The Effect of a Constant Force

We start by illustrating the effect of a constant force on changing the natural frequency and type of nonlinearities of a nonlinear system. Consider as an example the spring-mass system of Fig. 5.39, where the mass is pulled downward by a constant force F_0 . The equation of motion of the system in this case is governed by

$$m\ddot{x} + F_{\text{res}} = F_0 \quad (5.60)$$

where F_{res} is the restoring force of the spring. In the case of a linear spring, $F_{\text{res}} = kx$. The new equilibrium position due to the constant force is $x = \delta = F_0/k$. The deflection of the mass can be then expressed as the summation of δ and the dynamic deflection $u(t)$ with respect to δ , that is

$$x(t) = \delta + u(t). \quad (5.61)$$

Substituting Eq. (5.61) into Eq. (5.60) and dropping the static term ($k\delta = F_0$) yields

$$m\ddot{u} + ku = 0. \quad (5.62)$$

Equation (5.62) indicates that the constant force has no effect on the dynamic behavior of the mass since it is still governed by a differential equation similar to that obtained when neglecting F_0 ($m\ddot{x} + kx = 0$). The only difference is that the motion in terms of u is measured with respect to the new equilibrium position $x = \delta$ instead of $x = 0$. Thus, in linear vibrations, the effect of a constant force, such as the weight of the mass (mg), is usually neglected since it does not affect the dynamic response.

Next, the spring force is assumed to have a **quadratic** nonlinear component in addition to the linear component, that is $F_{\text{res}} = kx + \alpha_q x^2$, where α_q is a constant coefficient associated with the quadratic nonlinearity. The equation of motion in this case is expressed as

$$m\ddot{x} + kx + \alpha_q x^2 = F_0. \quad (5.63)$$

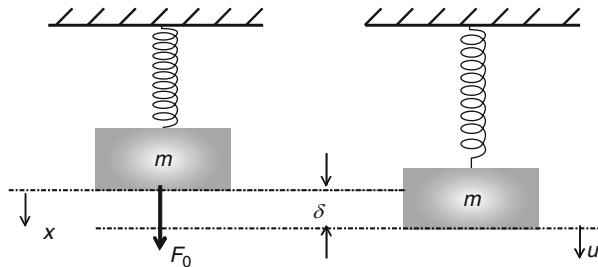


Fig. 5.39 A spring-mass system pulled by a constant force

The static equilibrium positions can be obtained by substituting the constant δ in Eq. (5.63), which gives

$$k\delta + \alpha_q\delta^2 = F_0. \quad (5.64)$$

The total deflection $x(t)$ can be then expressed as the sum of the static and dynamic components. Accordingly, substituting Eq. (5.61) into Eq. (5.63) yields

$$m\ddot{u} + k\delta + ku + \alpha_q(\delta + u)^2 = F_0. \quad (5.65)$$

Dropping the static terms, Eq. (5.64), from Eq. (5.65) yields

$$m\ddot{u} + (k + 2\alpha_q\delta)u + \alpha_q u^2 = 0. \quad (5.66)$$

Note that neglecting F_0 from the beginning in Eq. (5.63) does not result in a similar differential equation as that of Eq. (5.66). In particular, the linear stiffness coefficient $(k + 2\alpha_q\delta)$, and hence the linear natural frequency of the system, is different in both cases. For $\delta > 0$, a positive α_q increases the stiffness of the system whereas a negative α_q decreases it. Therefore, the linear natural frequency $\omega_n = \sqrt{(k + 2\alpha_q\delta)/m}$ has been changed because of the constant force and the presence of nonlinearity. Subjecting this system to a frequency-sweep test will reveal resonance at the shifted natural frequency even if the amplitude of the excitation force is very small. Figure 5.40a shows a simulation example of this case. Note from the figure that resonance is not triggered at the original natural frequency of the system $\omega_n = 1$ rad/s but rather at the shifted natural frequency $\omega_n = 1.3$ rad/s.

Next, the spring force is assumed to have a **cubic** component in addition to the linear component, $F_{\text{res}} = kx + \alpha_c x^3$, where α_c is a constant coefficient associated with the cubic nonlinearity. The equation of motion in this case is expressed as

$$m\ddot{x} + kx + \alpha_c x^3 = F_0. \quad (5.67)$$

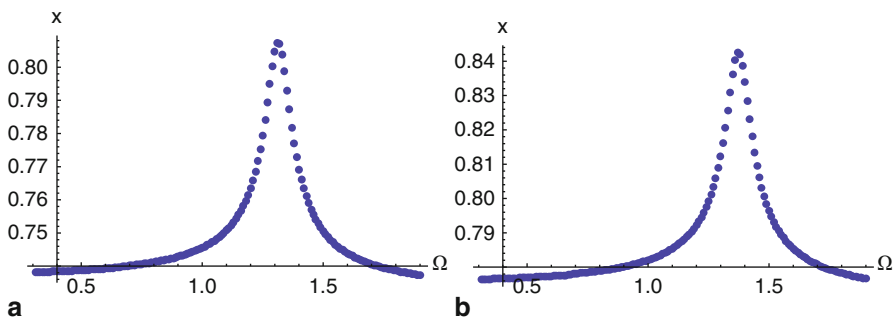


Fig. 5.40 The frequency-response of a nonlinear spring-mass-damper system of $m = 1$ kg, $k = 1$ N/m, and $c = 0.1$ kg/s when subjected to a static force $F_0 = 1$ N and a small harmonic force of amplitude $f = 0.01$ N/m for the cases of **a** $\alpha_q = 0.5$ N/m² and **b** $\alpha_c = 0.5$ N/m³

The static equilibrium positions are obtained by substituting the constant δ in Eq. (5.63), which gives

$$k\delta + \alpha_c \delta^3 = F_0. \quad (5.68)$$

Then, substituting Eq. (5.61) into Eq. (5.67) yields

$$m\ddot{u} + k\delta + ku + \alpha_c(\delta + u)^3 = F_0. \quad (5.69)$$

Dropping the static terms, Eq. (5.68), from Eq. (5.69) yields

$$m\ddot{u} + (k + 3\alpha_c \delta^2)u + 3\alpha_c \delta u^2 + \alpha_c u^3 = 0. \quad (5.70)$$

Here once again it is noted that the linear stiffness coefficient $(k + 3\alpha_c \delta^2)$ of Eq. (5.70) differs from what would be obtained from Eq. (5.67) when setting $F_0 = 0$. The linear natural frequency of the system $\omega_n = \sqrt{(k + 3\alpha_c \delta^2)/m}$ is shifted because of the new equilibrium position and the presence of nonlinearity. It increases for $\alpha_c > 0$ and decreases for $\alpha_c < 0$. Figure 5.40b shows an example of a simulated frequency-sweep for the system of Eq. (5.67) when subjected to harmonic excitation of very small amplitude. As seen in the figure, resonance is triggered at the new shifted natural frequency $\omega_n = 1.33$ rad/s. In addition, one can note that the perturbed system of Eq. (5.70) has acquired a new quadratic nonlinearity $3\alpha_c \delta u^2$ in addition to the original cubic nonlinearity. This is very important result that should be taken into consideration when studying systems with cubic nonlinearities if their equilibrium positions are changed because of a constant force.

5.8.1.1 The Effect of DC Load on a Parallel-Plate Capacitor

A common constant non time-varying force in MEMS is the electrostatic force due to a DC load V_{DC} in parallel-plate capacitors such as that of Fig. 5.8. Next, the effects of V_{DC} on the natural frequency and the nonlinearities of the capacitor are illustrated. For this, we refer back to the equation of motion, Eq. (a) of Example 5.5, and set $c = 0$ to simplify the analysis. Hence, the equation becomes

$$m\ddot{x} + kx = \frac{\varepsilon A V_{DC}^2}{2(d - x)^2}. \quad (5.71)$$

The static equilibrium positions are obtained by substituting the constant δ in Eq. (5.71), which gives

$$k\delta = \frac{\varepsilon A V_{DC}^2}{2(d - \delta)^2}. \quad (5.72)$$

Next, $x(t)$ is expressed in terms of δ and the dynamic deflection $u(t)$. Substituting Eq. (5.61) into Eq. (5.71) yields

$$m\ddot{u} + k(u + \delta) = \frac{\varepsilon A V_{DC}^2}{2(d - \delta - u)^2}. \quad (5.73)$$

The electrostatic force term can be expanded in Taylor series as

$$\begin{aligned} \frac{\varepsilon A V_{\text{DC}}^2}{2(d - \delta - u)^2} &= \frac{\varepsilon A V_{\text{DC}}^2}{2} \left(\frac{1}{(d - \delta)^2} + \frac{2u}{(d - \delta)^3} + \frac{3u^2}{(d - \delta)^4} \right. \\ &\quad \left. + \frac{4u^3}{(d - \delta)^5} + \frac{5u^4}{(d - \delta)^6} + \frac{6u^5}{(d - \delta)^7} + \dots \right). \end{aligned} \quad (5.74)$$

It is clear from Eq. (5.74) that the electrostatic force is an inherent source of nonlinearities producing infinite of them. However, the strongest and most important ones are the quadratic and cubic. Hence, we shall consider up to cubic terms in Eq. (5.74). Substituting Eq. (5.74) into Eq. (5.73) and dropping the static terms of Eq. (5.72) and the higher order nonlinearities yield

$$m\ddot{u} + ku = \frac{\varepsilon A V_{\text{DC}}^2}{2} \left(\frac{2u}{(d - \delta)^3} + \frac{3u^2}{(d - \delta)^4} + \frac{4u^3}{(d - \delta)^5} \right). \quad (5.75)$$

Equation (5.75) can be rewritten as

$$m\ddot{u} + k_{\text{eff}}u + \alpha_q u^2 + \alpha_c u^3 = 0 \quad (5.76)$$

where

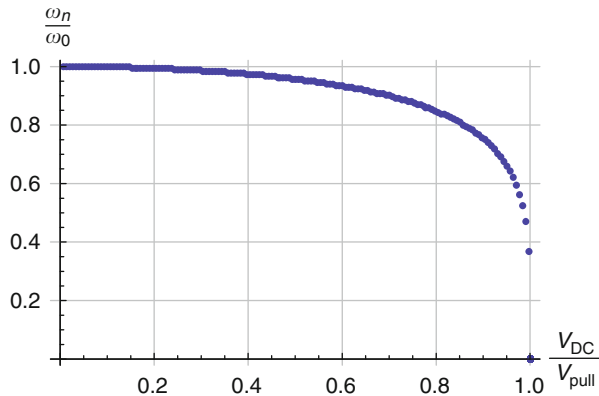
$$k_{\text{eff}} = k - \frac{\varepsilon A V_{\text{DC}}^2}{(d - \delta)^3}; \quad \alpha_q = \frac{-3\varepsilon A V_{\text{DC}}^2}{2(d - \delta)^4}; \quad \alpha_c = \frac{-2\varepsilon A V_{\text{DC}}^2}{(d - \delta)^5}. \quad (5.77)$$

One can see from k_{eff} above that V_{DC} decreases the stiffness of the structure and makes it softer (softening effect). This effect is amplified with the increase of δ , which also depends on V_{DC} . Another observation is that V_{DC} produces negative nonlinearities with the strongest are the quadratic and cubic nonlinearities as indicated through α_q and α_c . These nonlinearities are strengthened directly with V_{DC} and indirectly through δ , which also depends on V_{DC} . The linear natural frequency of the system is expressed as

$$\omega_n = \sqrt{\frac{k}{m} - \frac{\varepsilon A V_{\text{DC}}^2}{m(d - \delta)^3}}. \quad (5.78)$$

Equation (5.78) is the same as that of Eq. (h) of Example 5.5, which is an expression of the eigenvalues of the linearized system, except that here it is a real number. This indicates two possible techniques to estimate the natural frequencies of the system, either through direct linearization and estimating an effective stiffness or through evaluating the eigenvalues of the linearized system, similar to Examples 5.19 and 5.20. An example of a plot for ω_n normalized to its value at zero voltage ω_0 versus V_{DC} normalized to the pull-in voltage V_{pull} is depicted in Fig. 5.41. As expected, at pull-in the natural frequency drops to zero.

Fig. 5.41 The normalized natural frequency versus the normalized DC voltage



5.8.2 Free Vibration in the Presence of Nonlinearities

Unlike linear systems, nonlinear systems may vibrate in a frequency other than their natural frequencies when perturbed from their equilibrium position or vibrate freely due to some initial conditions. For example, consider a system with quadratic and cubic nonlinearities with the equation of motion:

$$\ddot{u} + \omega_n^2 u + \alpha_q u^2 + \alpha_c u^3 = 0. \quad (5.79)$$

Equation (5.79) does not have an analytical solution. However, an approximate solution using perturbation techniques [31] can be obtained if the nonlinearities are assumed weak, which can shed light on the expected behavior in general. In this case, the solution of Eq. (5.79) is expressed as [31]

$$u = a_0 \cos(\omega t + \beta_0) + \frac{a_0^2 \alpha_q}{6\omega_n^2} [\cos(2\omega t + 2\beta_0) - 3] \quad (5.80)$$

where a_0 and β_0 are the constants representing the amplitude and phase of oscillation, which depend on the initial conditions of the system, and ω is the frequency of free vibration given by

$$\omega = \omega_n \left[1 + \left(\frac{9\omega_n^2 \alpha_c - 10\alpha_q^2}{24\omega_n^4} \right) a_0^2 \right]. \quad (5.81)$$

It is noted from Eq. (5.81) that the frequency of oscillation is shifted from the linear natural frequency ω_n by a correction factor that depends on the amplitude of oscillation and the nonlinearity coefficients. This frequency–amplitude interaction is a unique property of nonlinear systems. One can see that the frequency of vibration always decreases (softening effect) in the presence of quadratic nonlinearity regardless of the sign of α_q . The effect of cubic nonlinearity on the other hand depends on its sign; for $\alpha_c > 0$ the frequency of vibration increases (hardening effect) and

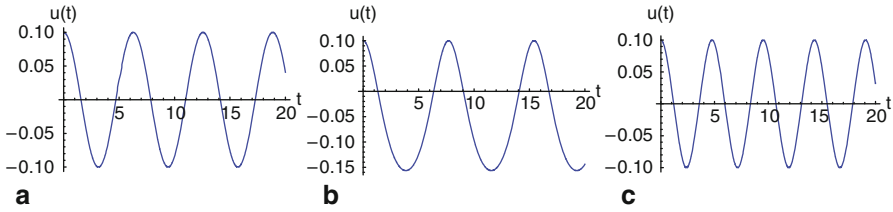


Fig. 5.42 The time history response obtained by numerically integrating Eq. (5.79) in time for **a** $\alpha_c = 0; \alpha_q = 0$, **b** $\alpha_c = 0; \alpha_q = 4.5 \text{ N/m}^2$, and **c** $\alpha_c = 100 \text{ N/m}^3; \alpha_q = 0$

for $\alpha_c < 0$ it decreases (softening effect). Figure 5.42 demonstrates these effects for $\omega_n = 1 \text{ rad/s}$, as obtained from direct time integration of Eq. (5.79). Note that the frequency of oscillation is the smallest for the case of quadratic nonlinearity and is the largest for the case of a positive cubic nonlinearity.

5.8.3 Forced Harmonic Vibration

The influence of nonlinearities on the response of microstructures when excited by external harmonic forces is a major topic in MEMS. As discussed in Sect. 3.6, resonating structures or resonators can be implemented in variety of sensing applications including pressure, mass, and temperature sensors, in addition to their potential as RF filters. Some resonating structures may have intrinsic nonlinearities due to their geometry, such as clamped–clamped beams. Also, the actuation technique that drives the resonators may introduce nonlinearities, such as electrostatic actuation. In any of such scenarios, there is interest to determine the impact of the nonlinearities on the resonance frequency of the resonator, its stability, accuracy, and calibration. Thus, numerous investigations in recent years have been conducted to address these issues in MEMS [5–7, 32–57].

The dynamic response of structures when excited by a harmonic force can be classified based on the frequency of excitation into two types: primary and secondary resonances. Primary resonance refers to the case of exciting a structure near one of its natural frequencies. Secondary resonance refers to exciting the structure into large motion at frequencies other than and way from its natural frequencies. Next, both kinds are discussed.

5.8.3.1 Primary Resonance

Let us first consider a system with a cubic nonlinearity with an equation of motion

$$\ddot{u} + 2\mu\dot{u} + \omega_n^2 u + \alpha_c u^3 = f \cos(\Omega t) \quad (5.82)$$

where f is the amplitude of the excitation force, Ω is its frequency, and μ is a linear damping coefficient. Equation (5.82) is known as the forced Duffing equation. This equation does not have an analytical solution, except for the case of weak

nonlinearity and small excitation force, in which case it can be solved analytically using perturbation techniques [31, 58]. Also, the equation can be solved numerically by integrating it with respect to time at each value of Ω and then allowing the system to settle down to a steady-state solution. However, this technique does not capture accurately the response near bifurcation and turning points and may suffer convergence problems. Also, it cannot capture unstable solutions, which as will be seen can provide useful information about the behavior of the system. A third and more accurate technique to solve this equation is called the shooting method [2]. This method can capture the periodic solutions of the equation, both stable and unstable, and enables stability analysis through the so-called Floquet theory [2]. It is also applicable for strong forcing and nonlinearities. This method is illustrated in Chap. 7.

For now, let us assume that we are able to simulate Eq. (5.82) accurately and focus on the interpretation and meaning of the results. Figure 5.43 shows simulated frequency–response curves for $\alpha_c > 0$ and $\alpha_c < 0$, where A is the steady-state response amplitude. The following observations can be read from the figure:

- The frequency–response curve is tilted, unlike the linear case where it is straightened up. It is tilted to the left in the case of $\alpha_c < 0$, which is called softening behavior, and to the right in the case of $\alpha_c > 0$, which is called hardening behavior. This is true even in the case of no damping. In comparison with the linear case, where the undamped response goes to infinity at resonance, the nonlinear undamped response is capped by the nonlinearity (titled to left or right) and does not go to infinity.
- The maximum amplitude response does not occur near the natural frequency ω_n but rather near a frequency Ω_r , which is called the nonlinear resonance frequency. Using a perturbation technique, the method of multiple scales, and assuming weak nonlinearity and forcing, Ω_r can be approximated as [31]

$$\Omega_r = \omega_n + \frac{3\alpha_c}{8\omega_n} A_{\max}^2 \quad (5.83)$$

where $A_{\max} = f/(2\mu\omega_n)$ is the maximum amplitude response at Ω_r . Thus, Ω_r increases for $\alpha_c > 0$ and decreases for $\alpha_c < 0$. Equation (5.83) applies for the special

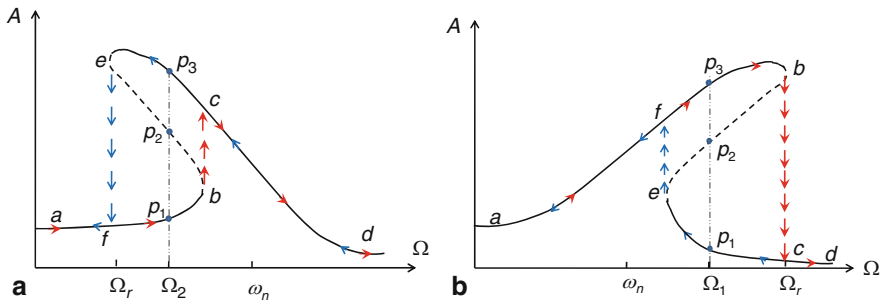


Fig. 5.43 Frequency–response curves of the forced Duffing equation near primary resonance for the case of **a** negative and **b** positive cubic nonlinearity

cases of small damping and force; hence, care should be taken when using it for quantitative results.

- The response at a single excitation frequency Ω may not be unique. For some values of Ω , for example Ω_1 and Ω_2 in the figure, there appear to be three possible corresponding values of A (points p_1 , p_2 , and p_3). This nonuniqueness of solution is one of the significant characteristics of a nonlinear system. It turns out, based on stability analysis of the solutions, that one of the solutions is unstable, which is shown as a dashed line in the figures. Hence, at Ω_1 or Ω_2 , the system can settle on either point p_1 or p_3 . This depends on many factors, such as the initial conditions of the system.
- The multivaluedness of the frequency–response curve has far-reaching consequences on the complexity of the dynamics leading to the phenomena of hysteresis and jumps. To illustrate this, consider first $\alpha_c < 0$ and Fig. 5.43a. Let us assume a frequency-sweep test is being conducted on the system, in which the force is kept constant while the frequency of excitation is swept from low values to high values (forward sweep). Starting from point a , increasing Ω leads to an increase of A up to point b , where a sudden jump in the response leads to a higher value, point c . Increasing Ω further leads to a decrease in A all the way up to point d . When a jump occurs, one should suspect a nonlinear response. Hence, whether in an experiment or in simulations, one needs to conduct another test/simulation in which Ω is decreased all the way from high values to low values (backward sweep). Decreasing Ω from point d leads to an increase in A up to point e , where a second jump in the response occurs leading to a lower value of A at point f . Decreasing Ω further up to point a decreases A even more. Note the hysteresis loop in the response b – c – e – f . Similar phenomena occur in the case of $\alpha_c > 0$ of Fig. 5.43b. Sweeping Ω from small values at a all the way to b leads to a jump in the response to a lower value at c . Continuing the sweep leads to a further decrease of A to d . Sweeping back Ω from large values at d leads to a jump in the response from e to a higher amplitude at f . Continuing the backward sweep toward a leads to a monotonic decrease in A . The conclusion of these observations is that jumps and hysteresis can lead to serious consequences on the stability and reliability of oscillators and resonators.
- The points of jumps, e and b , are tangent bifurcation points, which are similar to the saddle-node bifurcation of fixed points.

Equation (5.82) can be also simulated for various values of damping coefficient μ and forcing f . Examples of the results are depicted in Fig. 5.44. As noted, decreasing the damping or increasing the forcing leads to an amplified response, which can trigger nonlinear phenomena, such as jumps and hysteresis.

Next, consider a system with a quadratic nonlinearity of the equation

$$\ddot{u} + 2\mu\dot{u} + \omega_n^2 u + \alpha_q u^2 = f \cos(\Omega t). \quad (5.84)$$

It turns out that the response of this system is qualitatively similar to that of Fig. 5.43. This is true regardless of the sign of α_q , i.e., the quadratic nonlinearity always results in a softening behavior. Using the method of multiple scales, the nonlinear resonance

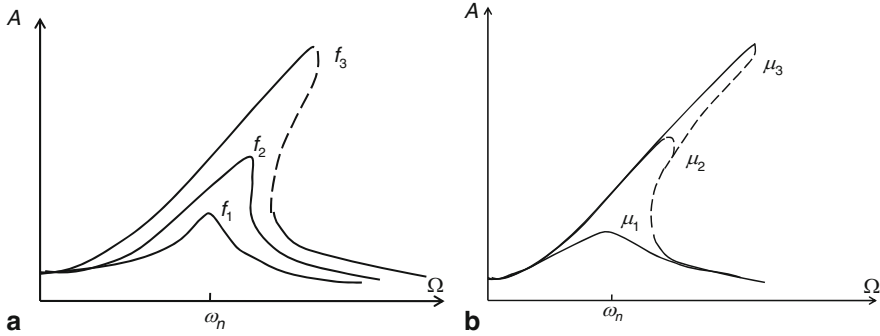


Fig. 5.44 Frequency–response curves of the forced Duffing equation showing the effect of **a** forcing for $f_1 < f_2 < f_3$ and **b** damping for $\mu_1 > \mu_2 > \mu_3$

frequency in this case can be approximated for small α_q and f as

$$\Omega_r = \omega_n - \frac{5\alpha_q^2}{12\omega_n^2} \left(\frac{f}{2\mu\omega_n} \right)^2. \quad (5.85)$$

Hence, once again one can see that Ω_r decreases regardless of the sign of α_q . Since this formula applies for small damping and force, care should be taken to use it for quantitative results.

Example 5.21: Use numerical integration of the equation of motion over a long period of time to simulate the steady-state response of the Duffing equation, Eq. (5.82), for $\mu = 0.02$ and $\alpha_c = 0.5$ and assuming (a) $f = 0.03$ and (b) $f = 0.2$. Plot frequency–response curves. Evaluate the nonlinear resonance frequency Ω_r in both cases and compare to the prediction of Eq. (5.83).

Solution: Here, we can generate the stable solutions only using the time integration approach. Some level of knowledge of what to expect of the response can be very helpful to simulate the response of nonlinear systems. In this example, since the nonlinearity is positive and cubic, it is anticipated that the frequency–response curve might be of hardening behavior with hysteresis possibility and jumps. Hence, a forward sweep of the response is our best bid to capture the upper branch of the frequency–response curve, if the system is provided with the proper initial conditions. Because of the hysteresis in the response, for some frequency range, the upper and lower branches of the frequency–response curve can coexist for some range of frequency. If initial conditions of small values are provided to the numerical integrator, such as trivial initial conditions, then the integrator will converge to the lower solution if it coexists with the upper, since it is closer to the provided initial conditions. If the interest is to catch what is the maximum response and at what frequency it occurs, another method of loading the initial conditions needs to be used. The numerical scheme needs to be set such that for a value of Ω during the frequency sweep, the initial conditions are loaded to be points from the solution of

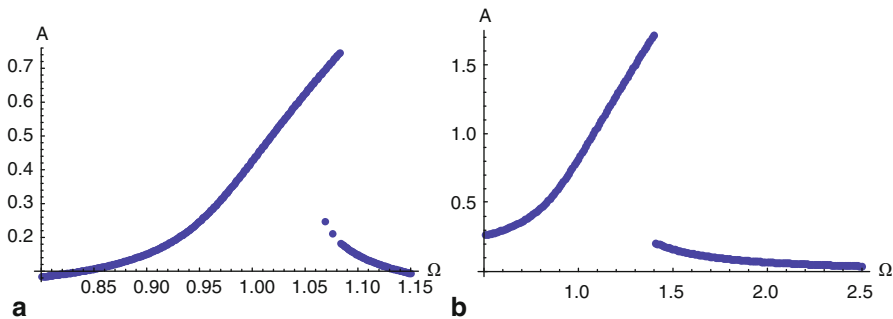


Fig. 5.45 Forward sweep-response curves using time integration of the forced Duffing equation for $\mu = 0.02$, $\alpha_c = 0.5$, and **a** $f = 0.03$ and **b** $f = 0.2$

the previous frequency value at $\Omega - \Delta\Omega$, where $\Delta\Omega$ is the frequency step of the sweep. This is called the **continuation approach**, since it seeks continuity on the initial conditions of the frequency-response branch. Once the integration is carried over a long period of time at each Ω , to guarantee reaching a steady-state solution, the maximum response of the last period of oscillation is recorded. Following this approach and using a forward sweep, the results for cases (a) and (b) are depicted in Fig. 5.45. If the interest is to catch closely the location of the other jump, where the lower branch solution starts exactly, then a backward sweep simulation needs to be carried out.

We note from Fig. 5.45 that the maximum amplitude response is $A_{\max} \approx 0.7$ at $\Omega_r \approx 1.1$ and $A_{\max} \approx 1.8$ at $\Omega_r \approx 1.5$ for cases (a) and (b), respectively. Using Eq. (5.83), the maximum amplitudes and nonlinear resonance frequencies are $A_{\max} = 0.75$, $\Omega_r = 1.106$ and $A_{\max} = 5.7$, $\Omega_r = 5$ for cases (a) and (b), respectively. Thus, one can see that Eq. (5.83) is accurate for small forcing, but inaccurate for large force and response.

5.8.3.2 Secondary Resonances

Secondary resonance refers to the large response of a nonlinear system when excited by a harmonic force of a frequency that is far from one of its natural frequencies. For a system with quadratic nonlinearity, secondary resonances can be triggered when the excitation frequency gets close to twice or half one of its natural frequencies. For a system with cubic nonlinearity, they can be triggered near triple and one-third one of the system's natural frequencies. For a system with both quadratic and cubic nonlinearities, all the previous resonances can be triggered.

For a system with a cubic nonlinearity, such as Eq. (5.82), if the excitation frequency Ω is near $\omega_n/3$ then using the method of multiple scales, assuming weak nonlinearity and forcing, the response of the system can be approximated as [31]

$$u = a \cos(3\Omega t - \gamma) + \frac{f}{\omega_n^2 - \Omega^2} \cos(\Omega t) \quad (5.86)$$

where a and γ are constants that depend on f, μ, α_c , and Ω . Note here that the response is composed of two components, one of frequency Ω , similar to a linear system, and the other of frequency 3Ω . In other words, the nonlinearity introduces a new component in the response of frequency 3Ω , such that it gets close to ω_n , thereby creating a primary-resonance-like response. This new component yields unexpectedly large response compared to what one would expect for an excitation that is away from the natural frequency (it is much larger than that with the $\cos(\Omega t)$ term). Since the new component has a frequency that is three times the excitation frequency, it is called **superharmonic resonance of order three**. For a system with quadratic nonlinearity, such as that of Eq. (5.84), if the system is excited near $\omega_n/2$, then its response can be approximated by perturbation theory as

$$u = a \cos(2\Omega t - \gamma) + \frac{f}{\omega_n^2 - \Omega^2} \cos(\Omega t). \quad (5.87)$$

Here, a new response component of frequency 2Ω is created because of the quadratic nonlinearity, and it is large compared to the other component at Ω . The system in this case is said to be excited by **superharmonic resonance of order two**, since it responds at twice the excitation frequency.

Superharmonic resonance produces large response; however, it remains below that due to primary resonance for the same magnitude of force. Qualitatively, it behaves like primary resonance. Hence, the response due to superharmonic resonance can look like a linear resonance for a very weak force, a nonlinear resonance of softening type in the case of α_c or $\alpha_c < 0$, and a nonlinear resonance of hardening type in the case of $\alpha_c > 0$. Figure 5.46 illustrates these scenarios.

If the excitation frequency Ω is near $3\omega_n$ then using the method of multiple scales, assuming weak nonlinearity and forcing, the response can be approximated as [31]

$$u = a \cos\left(\frac{\Omega t}{3} - \frac{\gamma}{3}\right) + \frac{f}{\omega_n^2 - \Omega^2} \cos(\Omega t). \quad (5.88)$$

Also here the response is composed of two components, one of frequency Ω and another unexpected one of frequency $\Omega/3$. This means that the nonlinearity introduces

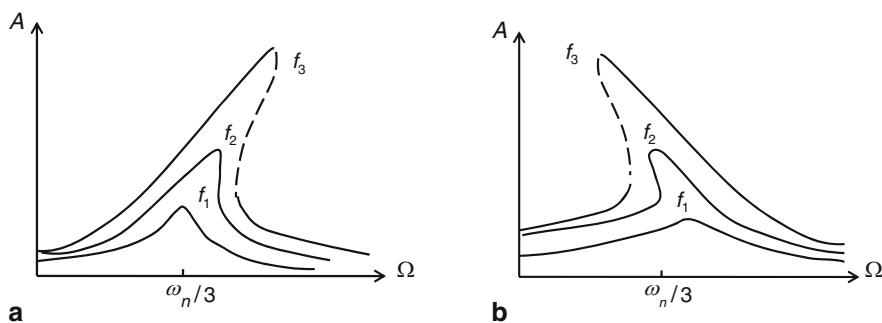


Fig. 5.46 Frequency–response curves of the Duffing equation showing superharmonic resonance of order three for $f_1 < f_2 < f_3$ and **a** $\alpha_c > 0$ and **b** $\alpha_c < 0$

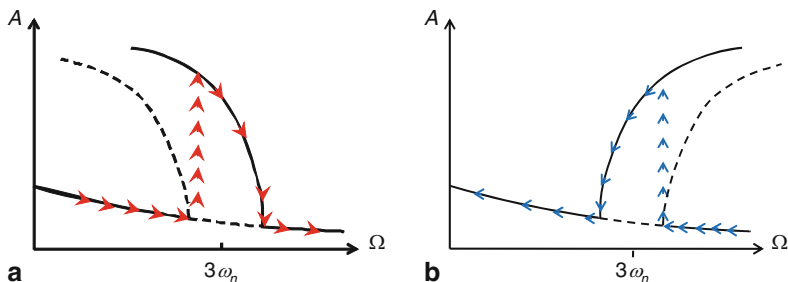


Fig. 5.47 Frequency–response curves of the Duffing equation showing subharmonic resonance of order one-third for **a** $\alpha_c > 0$ and **b** $\alpha_c < 0$

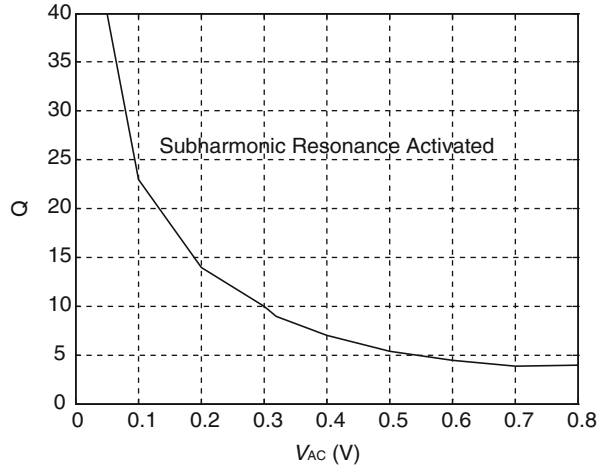
a new component in the response of frequency $\Omega/3$, which is close to ω_n , thereby creating a primary-resonance-like response of large amplitude compared to what is expected for Ω close to $3\omega_n$. Since the new component has a frequency that is one-third the excitation frequency, the response in this case is called **subharmonic resonance of order one third**. Quadratic nonlinearity produces **subharmonic resonance of order one half** if the system is excited near $2\omega_n$. The response in this case can be approximated using the method of multiple scales as [31]

$$u = a \cos\left(\frac{\Omega t}{2} - \frac{\gamma}{2}\right) + \frac{f}{\omega_n^2 - \Omega^2} \cos(\Omega t). \quad (5.89)$$

Subharmonic resonance produces large response that is typically below that of primary resonance for the same magnitude of force. However, it is larger than that of superharmonic resonance. This is one reason why it is considered more dangerous, from a stability point of view, than superharmonic resonance. Another reason is that it occurs at a frequency much larger than the natural frequency, which is typically considered of safely low amplitude (and might be completely overlooked in the design of devices and resonators). Another distinctive feature of subharmonic resonance is that the jump in the response is dramatic and distinctive, unlike the case of the other resonances. The bifurcation involved in this jump is of a pitchfork type. Figure 5.47 shows examples of subharmonic resonances of the Duffing equation. Note the possible jump in a forward sweep of Fig. 5.47 and in a backward sweep in Fig. 5.47. It is worth mentioning here that subharmonic resonance is not always activated under all excitation forces and damping conditions. In fact, there is a forcing–damping zone of large force and low damping, wherein subharmonic resonance is activated and outside the zone it is not activated. Figure 5.48 shows an example of such zone. This zone can be found numerically by running several simulations of the equation of motion using long-time integration for several values of forcing and damping [59].

Example 5.22: Use numerical integration of the equation of motion over a long period of time to simulate the steady-state response of the Duffing equation, Eq. (5.82), near subharmonic resonance for $\mu = 0.005$ and $f = 1.5$ assuming (a) $\alpha_c = 0.2$ and (b) $\alpha_c = -0.2$. Plot the frequency–response curves.

Fig. 5.48 A plot of the quality factor Q versus the amplitude of a harmonic force f showing the activation zone for subharmonic resonance in a nonlinear oscillator. (Reprinted with permission. Copyright 2009, ASME [59])



Solution: In case (a), since the nonlinearity is positive and cubic, we know in advance that the frequency–response curve is of hardening type. Hence, a forward sweep of the response should be used to capture the upper branch of the frequency–response curve combined with the continuation approach of loading the initial conditions, as explained in Example 5.21. In addition, one should note that the response due to subharmonic excitation has a period $T = 2\pi/(\Omega/3)$ or $T = 3(2\pi/\Omega)$. Thus, to generate the frequency–response curve, the maximum response needs to be estimated from the last runs at a period of $T = 3(2\pi/\Omega)$. In case (b), a softening behavior is expected. Therefore, a backward sweep of the response should be used to capture the upper branch of the frequency–response curve combined with the continuation approach of loading the initial conditions. Figure 5.49 shows the obtained results of both cases.

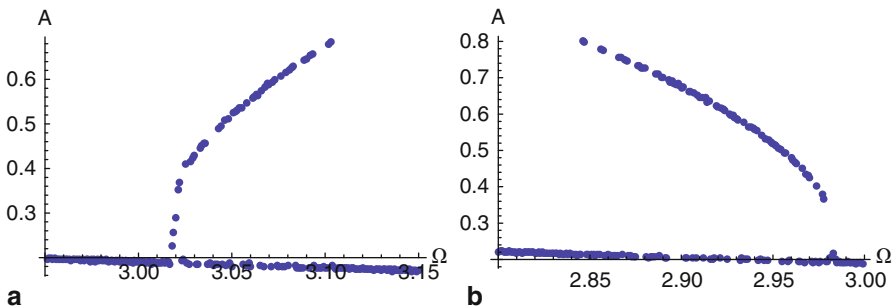


Fig. 5.49 Simulated response curves using time integration of the forced Duffing equation near subharmonic resonance for **a** $\alpha_c = 0.2$ and **b** $\alpha_c = -0.2$

5.8.3.3 Primary and Secondary Resonances of Electrostatic MEMS

Nonlinear behaviors of microstructures when excited by harmonic forces have been reported numerous in the literature through experimental and modeling works [5–8, 10–13, 32–57, 59–61]. While most of the research has been on electrostatic MEMS because of the inherent nature of electrostatic forces, other works have been also reported of resonators behaving nonlinearly due to actuation and geometry. For example, a softening behavior was reported experimentally when cantilever microbeams excited by piezoelectric forces due to the quadratic nonlinearity of the piezoelectric material [61]. A hardening behavior has also been noted of clamped–clamped microbeam when excited by piezoelectric forces [44]. This was attributed to the dominant effect of the cubic nonlinearity of mid-plane stretching, which is of hardening effect, over the softening effect of the quadratic nonlinearity of the piezoelectric layer. Next, primary and secondary resonances of electrically actuated resonators are discussed.

To understand the influence of the electrostatic forces, we refer to the model of Sect. 5.6.1 of a capacitive structure under a DC load actuation. In addition, the structure is assumed to be excited by an AC harmonic load and subjected to light viscous damping. Hence, Eq. (5.71) is modified to become

$$m\ddot{x} + c\dot{x} + kx = \frac{\varepsilon A [V_{DC} + V_{AC} \cos(\Omega t)]^2}{2(d-x)^2}. \quad (5.90)$$

Equation (5.90) can be integrated directly in time to simulate the response of a resonating structure. Note here that the voltage load term can be expanded as

$$\begin{aligned} [V_{DC} + V_{AC} \cos(\Omega t)]^2 &= V_{DC}^2 + 2V_{DC}V_{AC} \cos(\Omega t) + V_{AC}^2 \cos^2(\Omega t) \\ &= \left(V_{DC}^2 + \frac{V_{AC}^2}{2} \right) + 2V_{DC}V_{AC} \cos(\Omega t) - \frac{V_{AC}^2 \cos(2\Omega t)}{2}. \end{aligned} \quad (5.91)$$

Next, we simplify the equation further assuming small motion to gain some analytical insight into the behavior. Because in many resonators applications $V_{AC} \ll V_{DC}$, the voltage load can be expressed as

$$[V_{DC} + V_{AC} \cos(\Omega t)]^2 \approx V_{DC}^2 + 2V_{DC}V_{AC} \cos(\Omega t) \quad (5.92)$$

where V_{AC}^2 is dropped. Next, $x(t)$ is assumed to be composed of a static component δ and a dynamic component $u(t)$. Substituting Eq. (5.92) into Eq. (5.90) and substituting $x = u + \delta$ gives

$$m\ddot{u} + c\dot{u} + k(u + \delta) = \frac{\varepsilon A [V_{DC}^2 + 2V_{DC}V_{AC} \cos(\Omega t)]}{2(d - \delta - u)^2}. \quad (5.93)$$

Expanding the electrostatic force term in Taylor series, dropping the higher order terms, and dropping the static equilibrium equation of the outcome yields

$$m\ddot{u} + c\dot{u} + k_{\text{eff}}u + \alpha_q u^2 + \alpha_c u^3 = F \cos(\Omega t) + F_p u \cos(\Omega t) \quad (5.94)$$

where

$$k_{\text{eff}} = k - \frac{\varepsilon A V_{\text{DC}}^2}{(d - \delta)^3}; \quad \alpha_q = \frac{-3\varepsilon A V_{\text{DC}}^2}{2(d - \delta)^4}; \quad \alpha_c = \frac{-2\varepsilon A V_{\text{DC}}^2}{(d - \delta)^5};$$

$$F = \frac{V_{\text{DC}} V_{\text{AC}}}{(d - \delta)^2}; \quad F_p = \frac{2V_{\text{DC}} V_{\text{AC}}}{(d - \delta)^3}. \quad (5.95)$$

One can note from Eq. (5.94) that there are two harmonic forces affecting the resonator, of which one is multiplied by the dynamic response $u(t)$. This kind of excitation is called parametric excitation, which is discussed in the next section. Because Eq. (5.94) is derived under the assumption of small motion u around δ , and in the presence of damping, the parametric excitation force can be considered of small effect compared to the other direct forcing component. Equation (5.94) indicates a quadratic nonlinearity and a cubic nonlinearity of negative sign. Hence both have softening effect on the frequency response of the resonator. Also, for small values of u , the quadratic nonlinearity dominates the cubic one. Thus, superharmonic resonance of order two and subharmonic resonance of order one half are the strongest secondary resonances. Next, these phenomena are demonstrated through experimental data.

Figure 5.50 shows pictures of cantilever and clamped microbeams [60] made of gold of length 50 μm and 300 μm , respectively. Each microbeam forms the upper side of a parallel-plate capacitor. The microbeams have a thickness 1.2 μm and a gap width separating them from the substrate near 0.8 μm . The microbeams are wire-bonded to enable exciting them electrically. They are placed inside a vacuum chamber under reduced pressure. Their motion is detected using a Polytec MSA-400 motion analyzer, which is a high-frequency laser Doppler vibrometer, Fig. 5.51. Figures 5.52a and 5.52b show the measured response of the cantilever and clamped–clamped microbeams, respectively, near their fundamental natural frequencies. The figures show

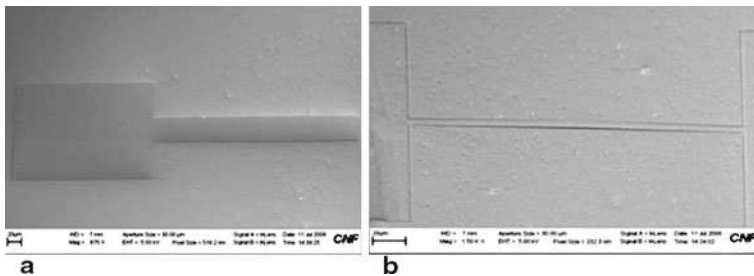


Fig. 5.50 A SEM picture of **a** cantilever and **b** clamped-clamped microbeams forming one side of parallel-plates capacitors. (Reprinted with Permission. Copyright 2010, IEEE [60])

Fig. 5.51 The experimental set-up for testing the microbeams. (Reprinted with permission. Copyright 2010, IEEE [60])

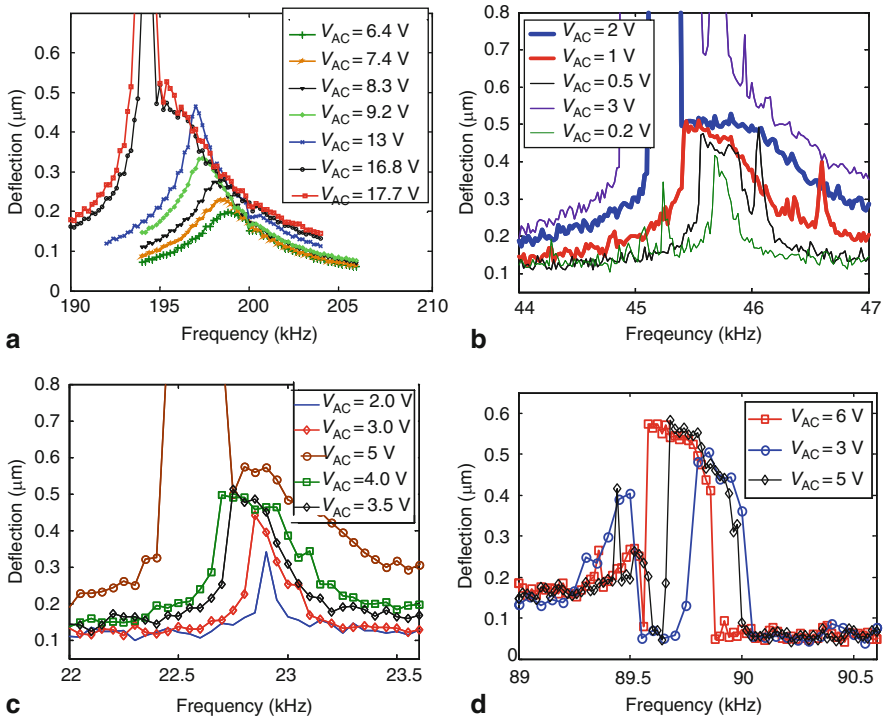
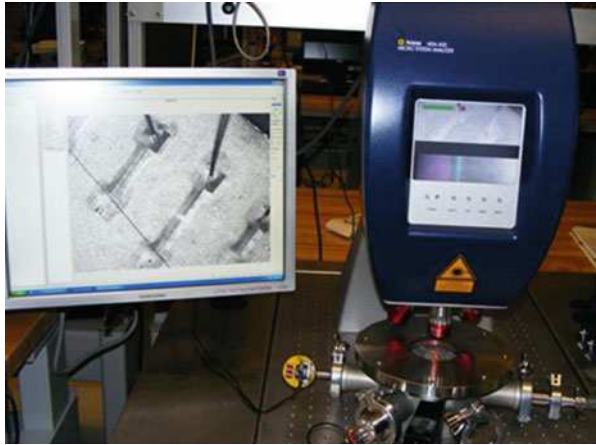
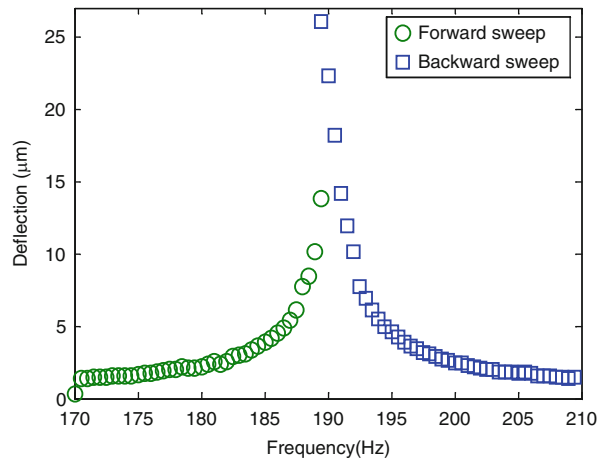


Fig. 5.52 Experimentally measured frequency response showing **a** primary resonance of a cantilever microbeam, **b** a primary resonance of a clamped-clamped microbeam, **c** superharmonic resonance of the clamped-clamped beam, and **d** subharmonic resonance of the clamped-clamped beam. For **a** $V_{DC} = 10$ V and the pressure = 176 mtorr. For **b–d**, $V_{DC} = 2$ V and the pressure = 155 mtorr. (Reprinted with permission. Copyright 2010, IEEE [60])

Fig. 5.53 Measured frequency response of a capacitive sensor near its fundamental natural frequency showing softening behavior for $V_{DC} = 19.4$ V and $V_{AC} \approx 16$ V. (Reprinted with permission. Copyright 2009, IOP Publishing Ltd [57])

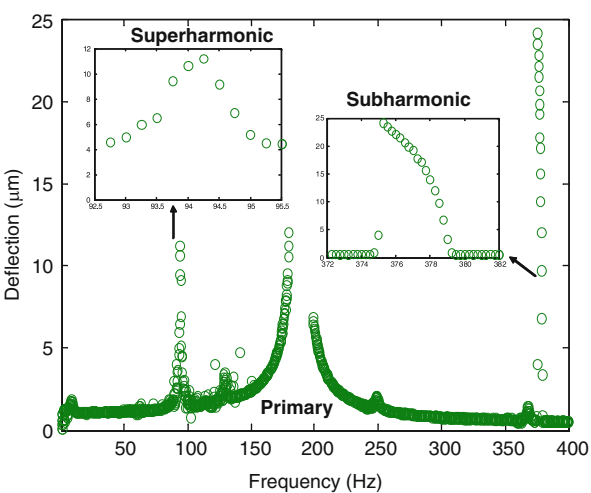


softening behavior for small values of voltage and dynamic pull-in for larger values of voltage, where the frequency–response curves open up. Figure 5.52c shows the measured response of the clamped–clamped microbeam near half its fundamental natural frequency indicating superharmonic resonance, and Fig. 5.52d depicts the response near twice the fundamental natural frequency indicating subharmonic resonance.

In another case study, the capacitive sensor of Fig. 3.17 was tested experimentally for harmonic electric excitation [57]. The device consists of a proof mass suspended by two long cantilever beams. The proof mass forms the upper electrode of a capacitor, and the lower electrode is placed directly underneath it on a silicon substrate. When excited electrostatically the proof mass oscillates in the out of plane direction. The proof mass is approximately of length 9 mm, width 5.32 mm (the electrode width 4.4 mm), and thickness 150 μm and separated from the substrate a distance 42 μm . The pull-in voltage of the device was measured and found to be ≈ 116 V. The response of the device when excited near primary resonance is depicted in Fig. 5.53. This figure was obtained by conducting both backward and forward frequency sweeps. The figure shows clearly a softening behavior. In Fig. 5.54, V_{DC} was raised and then forward sweep test was conducted over a wide range of frequency. The figure shows the activation of superharmonic, subharmonic, and primary resonances. The primary resonance response was so large that it triggered dynamic pull-in near some frequency range, where the curve opens up. Dynamic pull-in due to AC excitation is discussed in Chap. 7. Note that the response of the subharmonic resonance is larger than that of the superharmonic resonance, and it shows softening behavior.

Example 5.23: Use numerical integration of the equation of motion over a long period of time to simulate the steady-state response of the capacitive sensor for the loading conditions of Fig. 5.53. Compare the simulation results to the experimental data of the figure. Consider the measured linear natural frequency to be 192.5 Hz and the pressure value inside the vacuum chamber ≈ 140 mtorr.

Fig. 5.54 Experimentally measured forward frequency-sweep response showing the response of a capacitive sensor for $V_{DC} = 40.1\text{ V}$ and $V_{AC} = 18.4\text{ V}$. (Reprinted with permission. Copyright 2009, IOP Publishing Ltd [57])



Solution: Here, Eq. (5.90) is used directly. The stiffness coefficient k can be estimated based on the measured pull-in voltage from Eq. (4.2), which is found to be 215.6 N/m. The effective mass can be found from Eq. (4.9). The damping coefficient c is found from Eq. (4.48). However, an effective viscosity coefficient μ_{eff} needs to be used, which can be calculated from Table 4.5 using the model of Veijola et al. [62] after calculating the Knudsen number K from Eqs. (4.20) and (4.21) at the given pressure value. The result of these calculations gives $c \approx 0.00297\text{ kg/s}$. Based on these parameters, a backward sweep simulation is conducted using continuation of the initial conditions. The results are shown in Fig. 5.55. These are close to Fig. 5.53. In general, a forward sweep needs also to be conducted to capture accurately both sides of the frequency–response curve. However, in this case it turns out that the backward sweep gives close results to those of the forward sweep for the lower left branch.

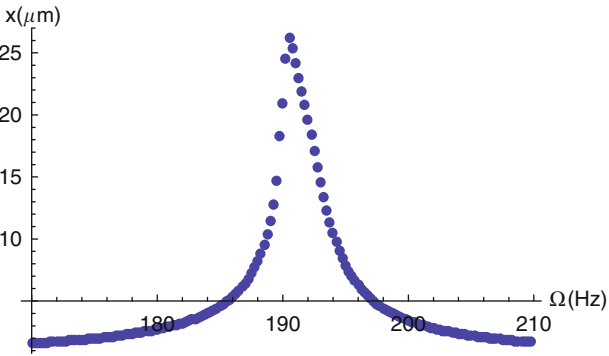


Fig. 5.55 Simulated backward frequency-sweep response of Example 5.23

5.8.4 *Parametric Excitation*

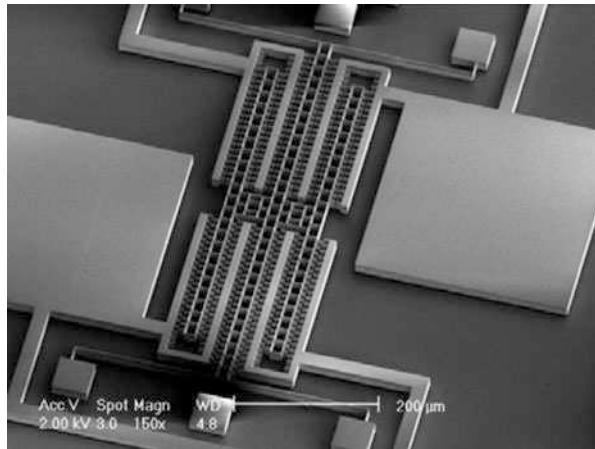
This section discusses another form of excitation of microstructures, which have drawn major interest in the MEMS community in recent years. Unlike the excitation forces of the previous section, which appear as inhomogeneous terms in the differential equation governing the dynamics of a system, the forces here appear as time-varying coefficients or parameters in the differential equation [31]. Hence, they are called parametric forces as opposed to external forces. Whether the differential equation of a system is linear or nonlinear, parametric excitation has far reaching consequences on the stability and behavior of the system. One distinction is that resonance is triggered whenever the excitation frequency $\hat{\Omega}$ gets close to $2\hat{\omega}_n/n$; where $\hat{\omega}_n$ is the natural frequency of the system, and n is an integer greater than or equal to one. Unlike external excitation, the most significant resonance occurs when $\hat{\Omega} \rightarrow 2\hat{\omega}_n$, which is called the principal parametric resonance.

Parametric excitation has fascinated scientist since the early 1800s when Faraday observed that the surface waves of fluid-filled cylinders exhibit periodic motion that is twice the vertical excitation frequency. Since then, many researchers have observed parametric excitation in structural systems, such as strings and columns. They noted that, when excited by periodic axial loads, these structures may experience large motion in a direction perpendicular to the axial loads for some range of excitation frequency. In addition, several investigations have been conducted on the use of parametric excitation to stabilize systems that are statically unstable, such as columns under axial force beyond the buckling threshold. A thorough review on the topic can be found in [31].

Parametric excitation has been investigated extensively for MEMS applications over the past two decades. One reason for this is the fact that many excitation methods can induce naturally parametric excitation, such as electrostatic actuation. In addition, the low-damping environment that many microstructures are driven at stimulates and further amplifies the influence of this excitation. This means that it is easy to drive a microstructure parametrically into large distinctive response, which is desirable for many sensing, filtering, and actuation applications in MEMS. Of the early effort in this domain, Rugar and Grutter [63] demonstrated experimentally a mechanical amplifier based on exciting a cantilever beam by pure harmonic capacitive load. They stated that such amplification can be used to improve the sensitivity of sensors, especially against noise. Turner et al. [64] reported experimentally, and verified theoretically, parametric resonances in electrically actuated torsional oscillator. Under reduced pressure and low damping, five parametric resonances regimes have been identified and measured.

Since then, many other groups have conducted research in this field. Among them, Zhang et al. [65] and Zhang and Turner [66] demonstrated the use of parametric excitation to realize a mass sensor of amplified response. They investigated the response of a comb-drive shuttle, composed of noninterdigitated fingers, excited electrically by a square-rooted harmonic signal. They demonstrated experimentally and analyzed analytically, using a perturbation technique, the principal parametric resonance including the effect of damping, and cubic nonlinearity of the mechanical

Fig. 5.56 A picture of a noninterdigitated comb-drive actuator. (Courtesy of Prof. Jeffrey Rhoads, Purdue University)



springs. Based on a similar device of [65, 66], Rhoads et al. [67] proposed an improved bandpass filter composed of a pair of tunable comb-drive electrostatically driven oscillators. DeMartini et al. [68] investigated the tuning of the comb-drive actuators using a DC voltage. They demonstrated the tuning of the effective linear and nonlinear stiffness of the oscillator showing several scenarios of softening, near linear, and hardening behavior. Figure 5.56 shows a picture of the noninterdigitated comb-drive actuator studied by Rhoads et al. [67] and DeMartini et al. [68].

Parametric excitation has been also demonstrated on microbeams. For example, Requa and Turner [69] demonstrated parametric resonance of electromagnetically driven and sensed silicon microcantilevers. The cantilevers are excited axially by Lorentz forces with the help of a permanent magnet, Fig. 5.57a. Krylov et al. [7] demonstrated experimentally and theoretically parametric stabilization of a cantilever beam actuated by a voltage load beyond pull-in using an AC harmonic load applied from two electrodes located symmetrically at both sides of the beam, Fig. 5.57b, Fig. 5.57c. They applied the Galerkin decomposition on string and beam models and conducted theoretical investigation that verified the experimental results. Krylov [13] also conducted theoretical investigation on the stabilization of a clamped–clamped microbeam including the effect of mid-plane stretching. Rhoads et al. [70] presented a theoretical analysis of a clamped–clamped microbeam excited purely by parametric excitation. The excitation is also achieved electrically through sandwiching the beam between double symmetrical electrodes.

In addition, parametric excitation has been demonstrated in other microstructures. Zhalutdinov et al. [71] demonstrated experimentally parametric resonance of a micromechanical disc oscillator made of silicon. This was achieved through a double frequency modulation of the intensity of a laser power beam applied at the periphery of the disk, which causes a periodic change of the stiffness of the oscillator. Carr et al. [72] reported experimentally parametric amplification in a torsional micron-scale mechanical resonator when excited by an electric load at twice the resonant frequency.

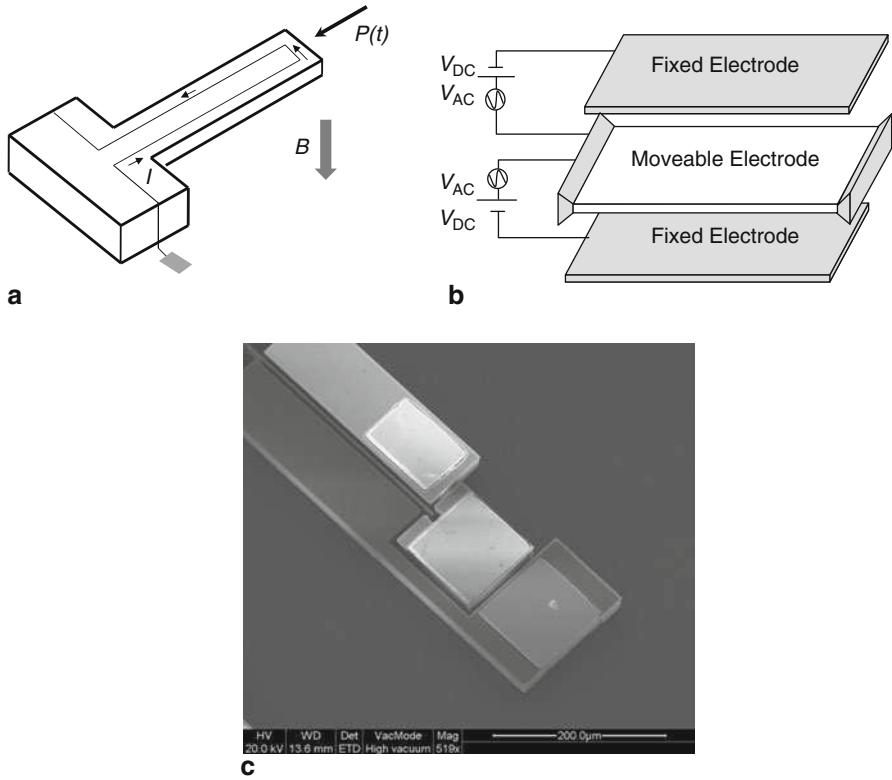


Fig. 5.57 Methods to induce parametric excitation in microstructures: **a** electromagnetic actuation, **b** double-electrodes electric actuation, **c** a picture of a cantilever beam sandwiched between two electrodes. (Courtesy of Prof. Slava Krylov, Tel Aviv University)

To clarify the mechanism of parametric excitation, consider as an example the double-electrodes actuation of Fig. 5.57. Assume that the two electrodes are symmetric and placed the same distance d from the microbeam. Also, assume that the same voltage load is applied between the beam and each electrode, labeled as $V(t)$, which can be either a pure AC harmonic load or a combination of a DC and AC harmonic load. The equation of motion of the microbeam in this case, assuming lumped parameters and neglecting the geometric nonlinearity, can be written as

$$m\ddot{x} + c\dot{x} + kx = \frac{\varepsilon AV^2(t)}{2} \left[\frac{1}{(d-x)^2} - \frac{1}{(d+x)^2} \right]. \quad (5.96)$$

Under the assumption of small motion, the electrostatic force terms are expanded in Taylor series up to third order, which yields

$$m\ddot{x} + c\dot{x} + kx = \frac{\varepsilon AV^2(t)}{2} \left[\frac{4x}{d^3} + \frac{8x^3}{d^5} \right]. \quad (5.97)$$

After regrouping, the equation becomes

$$m\ddot{x} + c\dot{x} + \left(k - \frac{2\varepsilon AV^2(t)}{d^3}\right)x - \left(\frac{4\varepsilon AV^2(t)}{d^5}\right)x^3 = 0. \quad (5.98)$$

We can see that the coefficient of x in Eq. (5.98) is time varying. Without any loss of generality, and for simplicity, we assume a pure square-rooted AC load, for example $V(t) = V_{AC}\sqrt{\cos \hat{\Omega}t}$. Thus, the equation becomes

$$m\ddot{x} + c\dot{x} + \left(k - \frac{2\varepsilon AV_{AC}^2 \cos \hat{\Omega}t}{d^3}\right)x + \left(\frac{-4\varepsilon AV_{AC}^2 \cos \hat{\Omega}t}{d^5}\right)x^3 = 0. \quad (5.99)$$

Equation (5.99) shows explicitly a periodic dependence of the stiffness on the AC load. It belongs to a more generic class of equations called Hill's equation. A special case of this class is the Mathieu equation, which has been analyzed thoroughly in the literature and is considered the base of studying parametric excitation. Next, we discuss the Mathieu equation.

First consider a dimensional form of the Mathieu equation

$$\frac{d^2\hat{u}}{d\hat{t}} + [\hat{\omega}_n^2 + \hat{f} \cos(\hat{\Omega}\hat{t})]\hat{u} = 0 \quad (5.100)$$

where the superscript \wedge has been added to denote dimensional parameters, $\hat{\omega}_n$, $\hat{\Omega}$, and \hat{f} are the natural frequency, excitation frequency, and forcing amplitude, respectively. Next, nondimensional variables are introduced as [58]

$$u = \frac{\hat{u}}{u_0}; \quad t = \frac{\hat{t}\hat{\Omega}}{2} \quad (5.101)$$

where u_0 is a dimensional constant of interest. Substituting Eq. (5.101) into Eq. (5.100) yields the nondimensional Mathieu equation

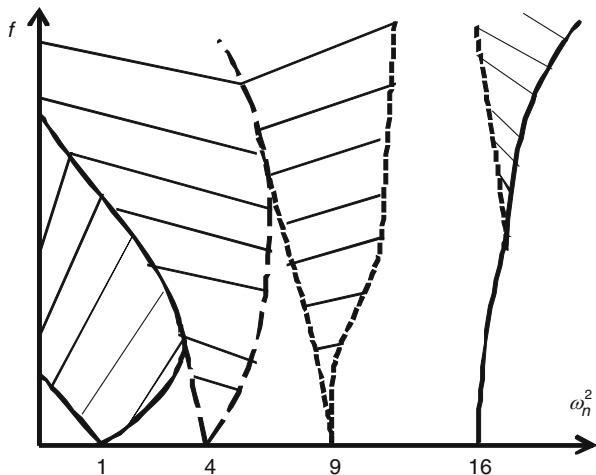
$$\ddot{u} + [\omega_n^2 + 2f \cos(2t)]u = 0 \quad (5.102)$$

where ω_n^2 and f are nondimensional frequency and forcing defined as

$$\omega_n^2 = \frac{4\hat{\omega}_n^2}{\hat{\Omega}^2}; \quad f = \frac{4\hat{f}}{\hat{\Omega}^2}. \quad (5.103)$$

Note that changing the excitation frequency $\hat{\Omega}$ in Eq. (5.100) is equivalent to changing ω_n^2 in Eq. (5.102). Although Eq. (5.102) is linear, its response is more complicated than other linear equations with constant coefficients. The solution of Eq. (5.102), and its stability can be determined using the Floquet theory [31, 58]. This solution is not explicit and of complicated form. Based on the Floquet analysis, a diagram has been established that indicates the stability of the solution in terms of the parameters ω_n^2 and f . The diagram, called the Strutt diagram, is depicted in Fig. 5.58. The figure

Fig. 5.58 The instability tongues (dashed) of the Mathieu equation (the *Strutt diagram*)



shows shaded zones, called instability tongues, wherein any pair of (ω_n^2, f) inside the tongues results in unstable solution (or motion). In theory, there are infinite number of these instability tongues located at the ω_n^2 axis at $\omega_n^2 = n^2$, or as stated earlier when $\hat{\Omega} = 2\hat{\omega}_n/n$, where n is an integer greater than or equal to one. The biggest of these tongues is located at $\omega_n^2 = 1$ or at $\hat{\Omega} = 2\hat{\omega}_n$, which is the principal parametric resonance. As n^2 gets larger, the instability tongue shrinks in size.

Simplified approaches have been proposed to predict the boundaries of the instability tongues, called transition curves, based on perturbation methods and the so-called Hill's determinant [31]. These yield analytical expressions assuming small forcing. Before presenting these results, let us consider a more generic case and add a damping coefficient μ to the Mathieu equation. Hence, Eq. (5.102) is modified as

$$\ddot{u} + 2\mu\dot{u} + [\omega_n^2 + 2f \cos(2t)]u = 0. \quad (5.104)$$

Using the method of strained parameters and under the assumption of small μ and f , the transition curves of the first instability tongue at $n^2 = 1$ are given by [31, 58]

$$\omega_n^2 = 1 \pm \sqrt{f^2 - 4\mu^2} - \frac{f^2}{8}. \quad (5.105)$$

Also, for the case of $n^2 = 4$, the expressions are

$$\omega_n^2 = 4 + \frac{f^2}{6} \pm \sqrt{\frac{f^4}{16} - 16\mu^2}. \quad (5.106)$$

Equations (5.105) and (5.106) are plotted for $\mu = 0$ and $\mu = 0.1$, Fig. 5.59. Note that damping raises the instability tongues, so a nonzero force is needed to trigger instability. The larger the value of μ is the higher the instability tongues are raised. Figure 5.60 shows examples of the time history response obtained by integrating

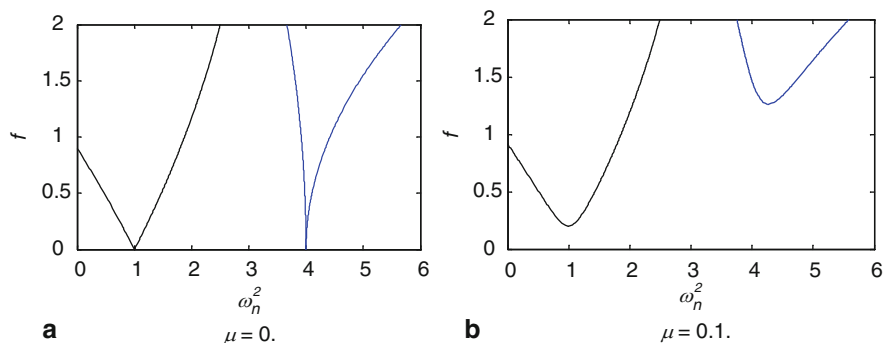


Fig. 5.59 The first two instability tongues of the Mathieu equation

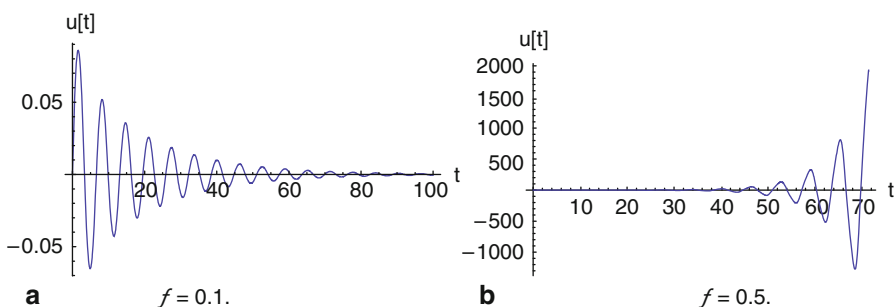


Fig. 5.60 Time history responses of the Mathieu equation for $\mu = 0.1$ and $n = 1$, **a** $f = 0.1$, **b** $f = 0.5$

Eq. (5.104) numerically in time for a pair of (ω_n^2, f) inside the first instability tongue, showing unstable oscillation, and another pair outside the tongue showing stable oscillation. Note that damping does not cap the response in the case of parametric resonance.

As in the case of external excitation, nonlinearity of the system caps the response in the instability tongue and makes it finite instead of infinite. The instability tongue itself however is not affected by the presence of nonlinearity. As an example, consider a damped Mathieu equation with an added cubic nonlinearity of coefficient α as below

$$\ddot{u} + 2\mu\dot{u} + \alpha u^3 + [\omega_n^2 + 2f \cos(2t)]u = 0. \quad (5.107)$$

Figure 5.61 shows the principal parametric instability tongue with several time history responses obtained from the numerical integration of Eq. (5.107) for various pairs of (ω_n^2, f) inside and outside the tongue. As seen in the figure, the response inside the tongue is significantly higher than that outside the tongue. This feature is what draws attention to parametric excitation in MEMS as a possible method for amplifying the response and improving the signal-to-noise ratio of sensors. To better understand this feature, we show in Fig. 5.62 a schematic of an instability tongue. On top of it is a frequency–response curve obtained from simulating Eq. (5.107) for a constant value

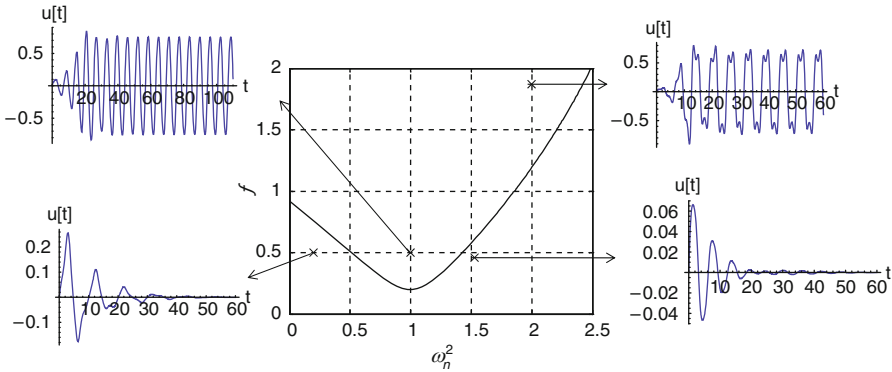
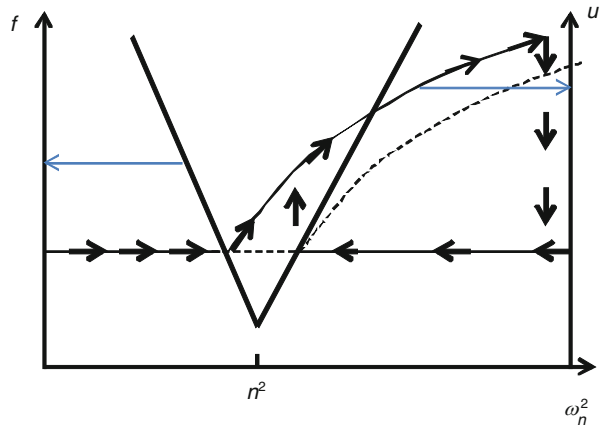


Fig. 5.61 The principal parametric instability tongue showing several time history responses of the nonlinear damped Mathieu equation with cubic nonlinearity for $\mu = 0.1$ and $\alpha = 1.0$

Fig. 5.62 An instability tongue with a frequency–response curve on top of it



of force f . As indicated in the figure, if the frequency of excitation is swept from small to large values to the left of the tongue, the response of the system remains trivial since parametric resonance is not activated. Once the frequency crosses into the tongue, parametric resonance is activated, and a new nontrivial solution is born while the trivial solution loses stability, as indicated by the dashed curve. If the sweeping continues and the tongue is crossed from the other side, the trivial solution regains stability, at the same time, the larger solution remains stable. Also another unstable solution is born at this point. Note that the trivial solution experiences two pitchfork bifurcations while crossing the tongue. This coexistence of the two stable solutions to the right of the tongue means that depending on the initial conditions, the system may land on either one. Also, this indicates hysteresis in the frequency–response curve when sweeping the frequency forward and backward passing the instability tongue. This sweeping is indicated in the figure by the arrows. Figure 5.63 shows simulated forward and backward frequency-sweep responses obtained by integrating

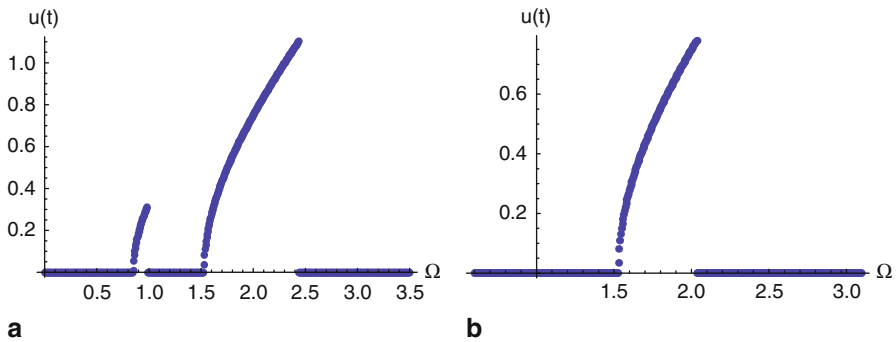


Fig. 5.63 Frequency–response curves of a nonlinear damped Mathieu equation showing **a** forward sweep and **b** backward sweep for $\mu = 0.1$, $f = 0.5$, and $\alpha = 1.0$

Eq. (5.107) numerically in time for a selected case of loading. Note the hysteresis as observed from the difference of the response between the backward and forward sweeps.

5.8.5 Self-Excited Oscillators

Self-excited oscillators are systems that can sustain steady-state oscillation without an external harmonic forcing. Usually, a self-excited oscillator has a mechanism to pump energy into the system, which can be considered as negative damping as opposed to positive damping that dissipates energy. For example, in the works of Zook et al. [73], Pandey et al. [10, 74], Zalalutdinov et al. [71], and Aubin et al. [75], the energy source is a laser power. When applying the laser beam on a thin microbeam [72] or planar NEMS disk [10, 71, 73, 74], the structure heats up and then self-oscillates into harmonic motion, despite the absence of any external harmonic forcing. Albrecht et al. [76], Yabuno et al. [77], and Ouakad et al. [78] used active feedback control, in which the velocity of the vibrating structure is fed back to provide a negative damping. Negative damping itself does not yield self-excitation; it must be balanced by another mechanism of energy dissipation.

The most studied equations to model self-excited oscillators are the **van der Pol oscillator**, discussed in Example 5.13, and the **Rayleigh's oscillator**. The equation of the van der Pol oscillator can be written as

$$\ddot{x} + \mu(x^2 - 1)\dot{x} + x = 0. \quad (5.108)$$

Pandey et al. [74], Yabuno et al. [77], and Ouakad et al. [78] used the van der Pol equation to model self-excited NEMS disk resonator, atomic force microscope (AFM), and clamped–clamped microbeam band-pass filter, respectively.

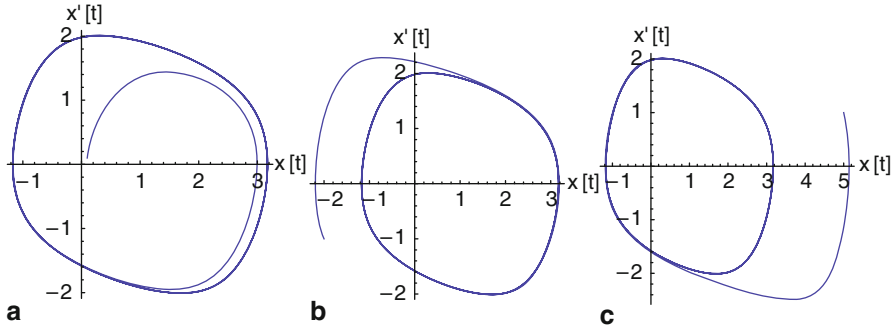


Fig. 5.64 A limit cycle of the Rayleigh's oscillator for various initial conditions for $\mu = 1.0$

The equation of the Rayleigh's oscillator can be written as

$$\ddot{x} - \mu(\dot{x} - \dot{x}^3/3) + x = 0. \quad (5.109)$$

Note that in either oscillator, there is a negative linear damping that is balanced by a positive nonlinear damping. For small oscillation, the negative linear damping dominates causing pumping of energy into the system. This leads to the growth of motion, in which case, the nonlinear positive damping dominates causing dissipation of the energy. When this process of energy pumping and dissipation balances each other over one cycle of vibration, the outcome becomes steady-state oscillation that is independent of initial conditions or the so-called **limit cycle**. A limit cycle is defined as an isolated periodic solution corresponding to an isolated closed orbit in the state space [2]. The isolation means that all the initial conditions near the limit cycle converge to it as time grows. Figure 5.64 shows a limit cycle obtained by numerically integrating Eq. (5.109) in time for various initial conditions. Note that all the initial conditions lead to the same periodic motion in the phase plane. Using the method of multiple scales and assuming weak damping, Eqs. (5.108) and (5.109) can be shown to have a solution of the form [58]:

$$x = 2 \left[1 + \left(\frac{4}{a_0^2} - 1 \right) e^{-\mu t} \right]^{-1/2} \cos t \quad (5.110)$$

where a_0 is the assumed initial displacement and the initial velocity is assumed to be zero. Equation (5.110) clearly indicates that for all initial conditions, as $t \rightarrow \infty$, or when the system reaches steady state, all trajectories converge to a periodic motion of frequency equal to the natural frequency of the system.

When actuating a self-excited oscillator with a force, external or parametric, of magnitude F and frequency Ω , then the response of the oscillator in general contains two frequency components: Ω and the frequency of free oscillation ω_n , which comes from the self-excitation. If the ratio between Ω and ω_n is an incommensurate (irrational) number, such as π , then the ensuing motion is a semi-periodic or **quasi-periodic motion** [2]. If Ω approaches ω_n and F is sufficiently strong, then the system

responds at only the excitation frequency Ω . In this case, the forced oscillation is said to **entrain** or enslave the unforced oscillation or the unforced oscillation to be locked onto the forced one [13, 79, 80]. The phenomenon of **entrainment** has been investigated theoretically and experimentally for the case of a NEMS disk resonator heated by a laser beam to activate the self-excitation and then actuated externally and harmonically by a piezo drive [10, 73].

5.9 Modal Interaction, Chaos, and Fractal Behavior

So far, several common nonlinear phenomena in MEMS have been discussed. In addition to these, recent researches have revealed other interesting phenomena in MEMS that are of great significance and potential. These include internal resonance or modal interaction, chaos, and the fractal behavior due to the phenomenon of escape.

Internal resonance [81], also called autoparametric resonance, refers to the transfer of energy from one mode of vibration into another mode due to the presence of nonlinearity and the fact that the natural frequencies of the two modes are related by a constant (for example, one natural frequency is twice or triple the other). The most significant impact of this resonance is when the energy transfers from an excited higher order mode of low amplitude of vibration into a nonexcited lower order mode. This yields large amplitude of oscillation of the lower mode that might be order-of-magnitude higher than that anticipated from the directly excited higher order mode. Such an event can be dangerous on the stability and reliability of MEMS devices. The possibility of an internal resonance in electrostatically actuated microbeams has been investigated for the case when the second natural frequency of a microbeam gets close to three times its first natural frequency (three-to-one internal resonance) [36]. The possibility of two-to-one internal resonance between the second and third modes of an AFM has been studied [36]. Also, the possibility of two-to-one internal resonance between the first and second mode of a microscanner mirror has been investigated [82]. In addition, modal interaction has been investigated recently to realize a novel mass sensor and a filter [84]. This is achieved by activating two-to-one internal resonance of an electrostatically actuated “T” pedal resonator composed of a clamped–clamped microbeam attached in the middle with another cantilever microbeam. In this resonator, the energy of the flexure in-plane vibration of the directly excited clamped–clamped microbeam is transferred into an out-of-plane torsional vibration mode of the cantilever microbeam of lower frequency and larger amplitude.

Chaos in MEMS represents a new exotic area of research that has seen increasing interest in recent years. Chaos can be defined as a bounded steady-state behavior that is not an equilibrium solution, a periodic solution, or a quasi-periodic solution [2]. Also, it can be defined as aperiodic long-term behavior in a deterministic (not random) system that exhibits a sensitive dependence on initial conditions [85, 86]. Chaotic systems are generally characterized by sensitivity to initial conditions, that is, tiny

differences in input can be quickly amplified to create overwhelming differences in the output. The attractor associated with a chaotic motion is not a simple geometrical object, like a finite number of points or a closed curve (it is called strange attractor). It is not even a smooth surface or curve. The most common signs of chaos, which usually are sought after as evidences of its presence, are

- A continuous broadband frequency spectrum
- A strange attractor of fractal nonsmooth dimensions as seen through Poincaré sections
- Positive Lyapunov exponent (sensitivity to initial conditions)
- Tangling (Homoclinic or Heteroclinic bifurcations), which is characterized by the Melnikov theory

There are a number of possible routes to chaos. The most famous in MEMS are tangling (Homoclinic or Heteroclinic bifurcations) or through cascade of period doubling bifurcations.

Chaos has been the center of focus of several studies in the MEMS community to predict it theoretically and show its presence experimentally [87–98]. Also, controlling chaos in MEMS has been recently an active research area [89, 92, 93, 95]. Chaos is desirable for microfluidic mixer and for communications to encrypt signals. It is undesirable for sensors since it caps the amount of signal strength and output energy that can be measured. Also it can be harmful for actuators since it limits their stable operating range. For devices, such as an AFM, chaotic behavior can lead to distorted and unreliable images of the surface profiles of samples.

Most of the works on chaos in MEMS have been based on systems with two-well potential or the so-called bistable systems [87–89, 92, 95]. For example, Wang et al. [87] presented theoretical and experimental investigation of the chaotic behavior of bistable MEMS oscillator based on noninterdigitated comb-drive actuator. The shuttle of the actuator is connected to clamped–clamped microbeams, which provide a cubic stiffness component. DeMartini et al. [88] conducted a theoretical investigation on the chaotic behavior of a device similar to that of Wang et al. [87] for the case of parametric excitation. Haghighi et al. [89] studied the chaotic dynamics of a micromechanical resonator actuated by double electrodes on its both sides. They also proposed an adaptive fuzzy control algorithm to control the chaotic motion.

Others work have been presented on the investigation of chaos in parallel-plate capacitors, such as the works of Luo and Wang [19], De and Aluru [90], Park et al. [91], Liu et al. [91], Chavarette et al. [91], and Stulemeijer et al. [92]. De and Aluru [90] studied chaos in the case of superharmonic excitation of the capacitor. Chavarette et al. [93] used a technique of the optimal linear control for reducing the chaotic oscillatory movement of the nonlinear systems to a periodic orbit. Park et al. [91] investigated chaos in electrostatically actuated resonant microbeams and proposed a method to control the chaotic behavior of the microbeams while keeping their amplitude high under large excitation loads. Liu et al. [92] investigated the chaotic behavior of an electrostatically actuated cantilever beam with a closed loop controller, which turns out to be similar to a double-well potential case.

Chaos in AFM has been also investigated thoroughly. Ashhab et al. [95] studied chaos in an AFM based on a spring–mass model of a cantilever beam that interacts

at the tip with a sample through the Lennard–Jones potential forces. They found that the system has two-well potential, which results in two homoclinic orbits. They used the Melnikov analysis to predict chaos. They also proposed a feedback controller to eliminate chaos. Hu and Raman [96] characterized the chaotic oscillations of an AFM microcantilever. They showed distorted AFM images due to the chaotic behavior. Jamitzky et al. [97] analyzed experimental time series data of an AFM and demonstrated period doubling bifurcations and a weakly chaotic regime. Liu and Chelidze [98] proposed to exploit chaos to realize a new chaotic motion-based AFM.

Another significant nonlinear MEMS phenomenon is the **escape from potential well** and the associated **fractal behavior**. Fractal behavior is a chaotic-like behavior, which makes a system characterized by sensitivity to initial conditions. However, in the presence of the escape phenomenon, the system does not enjoy steady-state chaotic behavior for an extended-range of operating conditions, such as the aforementioned examples of chaotic systems, but rather the system escapes the potential well to a remote state. The most common forms of this phenomenon in MEMS are the escape to pull-in in electrostatic MEMS and the jump-to-contact escape in AFM. Due to the importance of this topic, it is further discussed in Chap. 7.

Problems

1. Write a nondimensional equation for a microstructure under the effect of capillary force as shown in Fig. 5.13.
2. The dynamics of an AFM including the interaction of its tip with a sample surface can be modeled using a lumped-parameter model as [95]

$$m\ddot{x} + kx = \frac{Dk\sigma^6}{30(Z+x)^8} - \frac{Dk}{(Z+x)^2} \quad (a)$$

where m and k are the effective stiffness and mass of the AFM cantilever, respectively, Z is the distance from the cantilever tip to the sample, $D = AR/6k$ where A is the Hamacker constant, R is the radius of the sphere at the tip of the cantilever beam, and σ is the molecular diameter (approximately 0.3 Å).

- (a) Derive a nondimensional equation for Eq. (a) and identify the two new nondimensional parameters associated with the tip forces.
 - (b) Find the equilibrium solution of the nondimensional equation. Assume several values of the nondimensional parameters and determine the stability and type of the solutions. Analyze any possible bifurcations.
 - (c) Plot the potential energy of the system for several values of the nondimensional parameters and sketch the corresponding phase portraits.
3. The equation of motion of a buckled microbeam assuming a lumped-parameter model can be written in a nondimensional form as

$$\ddot{x} - x + \alpha x^3 + \mu \dot{x} = 0 \quad (a)$$

where α is a positive constant, and μ is a viscous damping coefficient.

- (a) Assume $\mu = 0$, find the equilibrium solutions of the system and identify their stability and type. Analyze any possible bifurcations.
 - (b) Assume $\mu = 0$, plot the potential energy of the system and sketch the corresponding phase portrait.
 - (c) Find the equilibrium solutions of the system and identify their stability and type for small and large values of μ .
 - (d) Sketch phase portraits corresponding to the cases of (c).
 - (e) Using long-time integration for the equation of motion, determine the response and plot the frequency–response curves of the system near primary resonance assuming $\mu = 0.1$, $\alpha = 1$, and an external force $f = 2 \cos(\Omega t)$.
4. Consider the single-sided capacitor of Fig. 5.8. Assume $m = 1.784 \times 10^{-10}$ kg, $k = 17.96$ N/m, $c = 0$, $d = 1.18$ μm , and the electrode area $A = 510 \times 100$ μm^2 .
- (a) Find the equilibrium solutions of the system and analyze their stability for values of voltage ranging from zero to pull-in with an increment of 0.2 V.
 - (b) Show a plot for the equilibrium (physical) solutions, normalized by d , versus V_{DC} .
 - (c) Show a plot for the eigenvalues of the largest physical solution versus V_{DC} .
 - (d) Plot the release voltage for a range of insulation layer thickness of 0.1–0.5 μm .
 - (e) Plot the potential energy of the system and the corresponding phase portrait for $V_{\text{DC}} = 1, 3$, and 4.3 V.
 - (f) Use direct-time integration of the equations of motion to plot the time history of the displacement for $V_{\text{DC}} = 4$ V. Model the voltage load as a step load starting at zero time. Take the initial conditions of the system to be zero velocity and displacement.
 - (g) Repeat (f), but with initial conditions of zero displacement and velocity equal to 0.055 m/s.
 - (h) Plot the potential energy of the system for $V_{\text{DC}} = 4$ V and the total energy H for cases (f) and (g) and show the corresponding time trajectories on a phase portrait.
 - (i) Draw conclusions from (f) to (h).
5. Consider the device of Problem 4 as a model of an RF MEMS switch.
- (a) Plot the potential energy of the system and the corresponding phase portrait for $V_{\text{DC}} = V_{\text{step}}$.
 - (b) Assume ζ (damping ratio) = 0.2 and calculate the pull-in time using direct integration of the equation of motion when the switch is actuated by (i) $V_{\text{DC}} = 1.3V_{\text{pull}}$, (ii) $V_{\text{DC}} = 1.7V_{\text{pull}}$, and (iii) $V_{\text{DC}} = 2V_{\text{pull}}$.
 - (c) Repeat (b) assuming no damping and compare to the results of Eq. (5.68).
6. Resolve Example 5.12 of the double-sided capacitor for the cases of (a) $u = 0.05$ μm and (b) $u = 0.2$ μm .
7. For the torsional actuator of Fig. 3.23, prove the analytical expression of the step pull-in voltage of Eq. (5.67).

8. Consider the torsional actuator of the parameters in the table below.

a_1 (μm)	a_2 (μm)	a_3 (μm)	d (μm)	b (μm)
0	700	700	21.2	700

The actuator is supported by two torsional springs of $K_t \approx 3 \times 10^{-8}$ N m. Assume $I_m = 4.372 \times 10^{-15}$ kg m². Using a 1-DOF model:

- Calculate the equilibrium solutions of the system and determine their stability for various values of V_{DC} up to pull-in. Plot the solutions versus V_{DC} .
 - Calculate and plot the natural frequency of the actuator versus V_{DC} up to pull-in.
 - Plot the potential energy of the system and the corresponding phase portraits for (i) $V_{\text{DC}} = 0.5 V_{\text{pull}}$ and (ii) $V_{\text{DC}} = 0.8 V_{\text{pull}}$.
9. Consider the torsional actuator of Example 5.20.
- Use a 1-DOF model for the mirror and solve for the equilibrium positions and natural frequencies of the mirror and compare to the results of the 2-DOF model.
 - Plot the time history response of the mirror to a step input actuation of $V_{\text{DC}} = 10$ V and assuming a damping ratio of both the translational and torsional modes of 0.01.
10. We want to investigate the effect of the van der Waals forces on the electrostatically actuated torsional actuator of Fig. 3.23 [24]. These forces are usually significant when the upper electrode of the micromirror is very close to the lower electrode. The nondimensional equation of motion of the mirror can be written as [24]

$$\ddot{\theta} + \mu \dot{\theta} + \theta = \frac{\eta}{\theta^2} \left[\frac{1}{1 - \beta\theta} - \frac{1}{1 - \gamma\theta} + \ln \left(\frac{1 - \beta\theta}{1 - \gamma\theta} \right) \right] + \frac{\delta_{\text{vdW}}\theta}{(1 - \theta^2)^2}. \quad (\text{a})$$

where $\delta_{\text{vdW}} = A_h b a_3^3 / 3\pi K_t d^4$, A_h is the Hamacker constant $= 4 \times 10^{-19}$ J, and the rest of parameters are as defined in Sect. 5.7.1. Assume the below geometric properties of the mirror:

a_1 (μm)	a_2 (μm)	a_3 (μm)	b (μm)	l (μm)	w (μm)	t (μm)
0	100	100	100	65	1.55	1.5

Also, assume $G = 66$ GPa and $\rho = 2,332$ kg/m³. For parts (a)–(c), assume no electrostatic force.

- For a range of $\alpha_{\text{max}} = (0 - 0.03)$, calculate the equilibrium solutions of the system and identify a critical gap d_c , below which the mirror experiences a collapse instability similar to the pull-in instability.
- Plot a phase portrait for the system $d < d_c$.

- (c) Plot a phase portrait for the system $d > d_c$.
 - (d) Plot a phase portrait for the system for $d < d_c$ and assuming $V_{DC} = 5.5$ V.
11. Assume the device of Problem 4 is excited by $V(t) = V_{DC} + V_{AC} \cos(\Omega t)$. Using long-time integration for the equation of motion, determine the response and plot the frequency–response curves of the system for
- (a) $V_{DC} = 2$ V, $V_{AC} = 0.1$ V, the damping ratio $\zeta = 0.01$, and $\Omega \rightarrow \omega_n$
 - (b) $V_{DC} = 2$ V, $V_{AC} = 1$ V, the damping ratio $\zeta = 0.01$, and $\Omega \rightarrow \omega_n$
 - (c) $V_{DC} = 2$ V, $V_{AC} = 1$ V, the damping ratio $\zeta = 0.1$, and $\Omega \rightarrow \omega_n$
 - (d) $V_{DC} = 2$ V, $V_{AC} = 2$ V, the damping ratio $\zeta = 0.01$, and $\Omega \rightarrow \omega_n$
 - (e) $V_{DC} = 2$ V, $V_{AC} = 2$ V, the damping ratio $\zeta = 0.01$, and $\Omega \rightarrow 0.5\omega_n$
 - (f) $V_{DC} = 2$ V, $V_{AC} = 2$ V, the damping ratio $\zeta = 0.01$, and $\Omega \rightarrow 2\omega_n$
 - (g) $V_{DC} = 2$ V, $V_{AC} = 2$ V, the damping ratio $\zeta = 0.1$, and $\Omega \rightarrow 2\omega_n$
12. Use numerical integration of the equation of motion over a long period of time to simulate the steady-state response of a capacitive sensor of a proof mass approximately of length 9 mm, width 5.32 mm (the electrode width 4.4 mm), and thickness 150 μm and separated from the substrate a distance 42 μm . Consider the measured pull-in voltage of the device to be 116 V and the measured linear natural frequency to be 192.5 Hz. Assume the device is operated under pressure of 140 mtorr. Show results for the following loading conditions:
- (a) $V_{DC} = 19.4$ V and $V_{AC} = 5$ V
 - (b) $V_{DC} = 19.4$ V and $V_{AC} = 13$ V
 - (c) $V_{DC} = 19.4$ V and $V_{AC} = 17$ V
13. Consider the double-sided capacitor with a cubic nonlinear stiffness of Example 5.17.
- (a) For case (d) in the example, find the equilibrium solutions of the system and identify their stability and type.
 - (b) Sketch the potential energy and the corresponding phase portraits for $V_{DC} = 21$ V and $V_{DC} = 22$ V.
14. Consider the double-sided capacitor of Example 5.17.
- (a) Assuming only the linear stiffness part, determine an expression for the effective stiffness of the system and its linearized natural frequency as a function of V_{DC} . Plot the natural frequency versus V_{DC} .
 - (b) Assume only the linear stiffness part and a slight damping (estimate a reasonable value to keep the system underdamped). Also, assume the system actuated by a voltage load of the form $V(t) = V_{DC} + V_{AC} \cos(\Omega t)$, determine the response and plot the frequency–response curves of the system for $V_{DC} = 12$ V and $V_{AC} = 5$ V.
 - (c) Repeat (b) assuming $V(t) = V_{AC} \sqrt{\cos \Omega t}$.
 - (d) Repeat (b) assuming the full nonlinear spring force and $V_{DC} = 20$ V and $V_{AC} = 1$ V.

15. Use numerical integration of the equation of motion over a long period of time to simulate the steady-state response of the system with quadratic nonlinearity of Eq. (5.74) near primary resonance for $\mu = 0.02$ and $\alpha_q = 0.2$ and assuming (a) $f = 0.03$ and (b) $f = 0.2$. Plot frequency–response curves. Evaluate the nonlinear resonance frequency Ω_r in both cases and compare to the prediction of Eq. (5.75).
16. Rework Problem 13 near superharmonic and subharmonic resonances assuming $\mu = 0.002$. Plot frequency–response curves.
17. Rework Example 5.23 for the capacitive sensor assuming the below excitations
 - (a) $V_{DC} = 40.1$ V, $V_{AC} = 18.4$ V, and $\Omega \rightarrow \omega_n$
 - (b) $V_{DC} = 40.1$ V, $V_{AC} = 18.4$ V, and $\Omega \rightarrow 0.5\omega_n$
 - (c) $V_{DC} = 40.1$ V, $V_{AC} = 18.4$ V, and $\Omega \rightarrow 2\omega_n$
18. Use numerical integration of the equation of motion over a long period of time to simulate the response of the van der Pol oscillator, Eq. (5.107), for
 - (a) $\mu = 0.01$
 - (b) $\mu = 0.1$
 - (c) $\mu = 1.0$

References

- [1] Thompson J, Stewart H (2001) Nonlinear dynamics and chaos, Wiley, New York
- [2] Nayfeh A, Balachandran B (1995) Applied nonlinear dynamics, New York, Wiley
- [3] Gilbert J R, Ananthasuresh G K, Senturia S D (1996) 3D Modeling of contact problems and hysteresis in coupled electro-mechanics, In Proceeding of the IEEE Annual International Conference on Microelectromechanical Systems (MEMS), 127–132
- [4] Mastrangelo C H, Hsu C H (1993) Mechanical stability and adhesion of microstructures undercapillary forces. I. Basic theory. Journal of Microelectromechanical Systems, 2:33–43
- [5] Abdel-Rahman E M, Younis M I, Nayfeh A H (2004) Finite-amplitude motions of resonators and their stability. Journal of Computational and Theoretical Nanoscience, 4:385–391
- [6] Nayfeh A H, Younis M I (2005) Dynamics of MEMS resonators under superharmonic and subharmonic excitations. Journal of Micromechanics and Microengineering, 15:1840–1847
- [7] Krylov S, Harari I, Yaron C (2005) Stabilization of electrostatically actuated microstructures using parametric excitation. Journal of Micromechanics and Microengineering, 15:1188–1204.
- [8] Mann B, Liu J, Hazra S (2006) Correcting measurement nonlinearity in dynamic nanoindentation, In Proceedings of 2006 ASME International Mechanical Engineering Congress and Exposition, IMECE2006, Chicago, Illinois, IMECE2006–15070.
- [9] Hirano T, Furuhashi T, Gabriel K J, Fujita H (1992) Design, fabrication, and operation of submicron gap comb-drive microactuators. Journal of Microelectromechanical Systems, 1(1):52–59.
- [10] Pandey M, Aubin M, Zalalutdinov R B, Reichenbach A T, Zehnder, R H, Rand K, Craighead H G, Analysis of Frequency Locking in Optically Driven MEMS Resonators. Journal of Microelectromechanical systems, 15(6):1546–1554
- [11] Ananthasuresh G K, Gupta R K, Senturia S D (1996) An approach to macromodeling of MEMS for nonlinear dynamic simulation, In Proceeding of ASME International Conference of Mechanical Engineering Congress and Exposition (MEMS), Atlanta, GA, pp. 401–407
- [12] Krylov S, Maimon R (2004) Pull-in dynamics of an elastic beam actuated by continuously distributed electrostatic force,” ASME Journal of Vibrations and Acoustics, 126(3):332–342

- [13] Krylov S (2008) Parametric excitation and stabilization of electrostatically actuated microstructures. *International Journal of Multiscale Computational Engineering*, 6(6):563–584
- [14] Rebeiz G M (2003) RF MEMS: theory, design, and technology, Wiley, New York
- [15] Varadan V M, Vinoy K J, Jose K A (2003) RF MEMS and their applications, Wiley New York
- [16] Krylov S, Maimon R (2004) Pull-in dynamics of an elastic beam actuated by continuously distributed electrostatic force. *ASME Journal of Vibrations and Acoustics*, 126(3):332–342
- [17] Elata D, Bamberger H (2006) On the dynamic pull-in of electrostatic actuators with multiple degrees of freedom and multiple voltage sources, *Journal of Microelectromechanical Systems*, 15:131–140
- [18] Nielson G N, Barbastathis G (2006) Dynamic Pull-in of Parallel-Plate and Torsional MEMS Actuators, *Journal of Microelectromechanical Systems*, 15:811–821
- [19] Luo A C, Wang F Y (2004) Nonlinear dynamics of a Micro-electro-mechanical system with time-varying capacitors. *Journal of Vibration and Acoustics*, 126:77–83
- [20] Sattler R, Plotz F, Fattinger G, Wachutka G (2002) Modeling of an electrostatic torsional actuator demonstrated with an RF MEMS switch. *Sensors and Actuators A*, 97–98:337–346
- [21] Xiao Z, Sun Y, Li B, Lee S, Sidhu K S, Chin K K, Farmer K R (2004) Natural Frequency Shift of Rectangular Torsion Actuators due to Electrostatic Force, In *Proceeding of NSTI-Nanotech 2004*, pp. 1:9728422-7-6
- [22] Krylov S, Barnea D I (2005) Bouncing mode electrostatically actuated scanning micromirror for video applications,” *Smart Material Structures*, 14:1281–1296
- [23] Guo J G, Zhao Y P (2004) Influence of van der Waals and Casimir Forces on Electrostatic Torsional Actuators, *Journal of Microelectromechanical Systems*, 13(6):1027–1035
- [24] Guo J G, Zhao Y P (2006) Dynamic stability of electrostatic torsional actuators with van der Waals effect. *International Journal of Solids and Structures*, 43:675–685
- [25] Gusso A, Delben G J (2007) Influence of the Casimir force on the pull-in parameters of silicon based electrostatic torsional actuators. *Sensors and Actuators A*, 135:792–800
- [26] Guo J G, Zhao Y P, Zhao Y P (2009) Instability analysis of torsional MEMS/NEMS actuators under capillary force. *Journal of Colloid and Interface Science*, 331:458–462
- [27] Degani O, Nemirovsky Y (2002) Modeling the pull-in parameters of electrostatic actuators with a novel lumped two degrees of freedom pull-in model. *Sensors and Actuators A*, 97–98:569–578
- [28] Huang J M, Liu A Q, Deng Z, Zhang Q X, Ahn J, Asundi A (2004) An approach to the coupling effect between torsion and bending for electrostatic torsional micromirrors. *Sensors and Actuators A*, 115:159–167
- [29] Zhao J P, Chen H L, Huang J M, Liu A Q (2005) A study of dynamic characteristics and simulation of MEMS torsional micromirrors. *Sensors and Actuators A*, 120:199–210
- [30] Lee K B (2007) Closed-form expressions for pull-in parameters of two-degree-of-freedom torsional microactuators. *Journal of Micromechanics and Microengineering*, 17:1853–1862.
- [31] Nayfeh A, Mook D (1979) *Nonlinear oscillations*, Wiley, New York
- [32] Ayala F, Fournier T (1998) An experimental study of anharmonic micromachined silicon resonators. *Measurement, Science and Technology*, 9:1821–1830
- [33] Gui C, Legtenberg R, Tilmans H A C, Fluitman J H J, Elwenspoek M (1998) Nonlinearity and hysteresis of resonant strain gauges. *Journal of Microelectromechanical Systems*, 7:122–127
- [34] Wang Y C, Adams S G, Thorp J S, MacDonald N C, Hartwell P, Bertsch F (1998) Chaos in MEMS, parameter estimation and its potential application. *IEEE Transactions on Circuits and Systems-I: Fundamental Theory and Applications*, 45:1013–1020
- [35] Veijola T, Mattila T, Jaakkola O, Kihamäki J, Lamminmäki T, Oja A, Ruokonen K, Seppä A H, Seppälä P, Tittonen I (2000) Large-displacement modeling and simulation of micromechanical electrostatically driven resonators using the harmonic balance method, In *Proceedings of the International Microwave Symposium*, 99–102
- [36] Younis M I, Nayfeh A H (2003) A study of the nonlinear response of a resonant microbeam to an electric actuation. *Nonlinear Dynamics*, 31:91–117
- [37] Abdel-Rahman E M, Nayfeh A H (2003) Secondary resonances of electrically actuated resonant microsensors. *Journal of Micromechanics and Microengineering*, 13:1–11

- [38] Najar F, Choura S, Abdel-Rahman E M, El-Borgi S, Nayfeh A (2006) Dynamic analysis of variable-geometry electrostatic microactuators. *Journal of Micromechanics and Microengineering*, 16:2449–2457
- [39] Liu S, Davidson A, Lin Q (2004) Simulation studies on nonlinear dynamics and chaos in a MEMS cantilever control system. *Journal of Micromechanics and Microengineering*, 14:1064–1073
- [40] De S K, Aluru N R (2004) Full-lagrangian schemes for dynamic analysis of electrostatic MEMS. *Journal of Microelectromechanical Systems*, 13:737–758
- [41] Lenci S, Rega G (2006) Control of pull-In dynamics in a nonlinear thermoelasticelectrically actuated microbeam. *Journal of Micromechanics and Microengineering*, 16:390–401
- [42] Liqin L, Gang T Y, Zhiqiang W (2006) Nonlinear dynamics of microelectromechanical systems. *Journal of Vibration and Control*, 12:57–65
- [43] Elata D, Bamberger H (2006) On the dynamic pull-in of electrostatic actuators with multiple degrees of freedom and multiple voltage sources. *Journal of Microelectromechanical Systems*, 15:131–140
- [44] Li H, Preidikman S, Balachandran B, Mote Jr C D (2006) Nonlinear free and forced oscillations of piezoelectric microresonators. *Journal of Micromechanics and Microengineering*, 16:356–367
- [45] De S K, Aluru N R (2006) Complex Nonlinear oscillations in electrostatically actuated microstructures. *Journal of Microelectromechanical Systems*, 15:355–369
- [46] Tadayon M A, Rajaei M, Sayyaadi H, Nakhaie, Jazar G, Alasty A (2006) Nonlinear dynamics of microresonators. *International MEMS Conference*, 34:961–966
- [47] Jazar G N (2006) Mathematical modeling and simulation of thermal effects in flexural microcantilever. *Journal of Vibration and Control*, 12(2):139–163
- [48] Zhao J H, Bridges G E, Thomson D J (2006) Direct evidence of spring softening nonlinearity in micromachined mechanical resonator using optical beam deflection technique. *Journal of Vacuum Science & Technology A*, 24(3):732–736
- [49] Zhang W-M, Meng G (2007) Nonlinear dynamic analysis of electrostatically actuated resonant MEMS sensors under parametric excitation. 7(3):370–380
- [50] Zhou J, Wang Z, Grots A, He X (2007) Electric field drives the nonlinear resonance of a piezoelectric nanowire. *Solid State Communications, Elsevier, Solid State Communications*. 144(3–4):118–123
- [51] Sahaia T, Rustom B, Bhiladvalab C, Zehnder A T (2007) Thermomechanical transitions in doubly-clamped micro-oscillators. *International Journal of Non-Linear Mechanics*, 42(4):596–607
- [52] Ai S, Pelesko J A (2007) Dynamics of a canonical electrostatic MEMS/NEMS system. *Journal of Dynamics and Differential Equation*, 20:609–641
- [53] Trusov A A, Shkel A M (2007) The effect of high order non-linearities on sub-harmonics excitation with parallel plate capacitive actuators. In *Proceedings of the ASME 2007 International Design Engineering Technical Conferences & Computers and Information in Engineering Conference IDETC/CIE 2007, Las Vegas*
- [54] Mestrom R M, Fey R H, Phan K L, van Beek J T, Nijmeijer H (2008) Modeling the dynamics of a MEMS resonator: simulations and experiments. *Sensors & Actuators A*, 142:306–315
- [55] Batra R C, Porfiri M, Spinello D (2008) Vibrations of narrow microbeams predeformed by an electric field. *Journal of Sound and Vibration*, 309(3–5): 600–612
- [56] Zamanian M, Khadem S E, Mahmoodi S N (2008) The effect of a piezoelectric layer on the mechanical behavior of an electrostatic actuated microbeam. *Smart Materials and Structures*, 17:065024(15pp)
- [57] Alsaleem F, Younis M I, Ouakad H (2009) On the nonlinear resonances and dynamic pull-in of electrostatically actuated resonators. *Journal of Micromechanics and Microengineering*, 19:045013(1–14)
- [58] Nayfeh A (1981) *Introduction to perturbation techniques*, Wiley, New York
- [59] Younis M I, Alsaleem F M (2009) Exploration of new concepts for mass detection in electrostatically-actuated structures based on nonlinear phenomena. *Journal of Computational and Nonlinear Dynamics*, 4(2):1–15

- [60] Alsaleem F M, Younis M I, Ruzziconi L (2010) An experimental and theoretical investigation of dynamic pull-in in MEMS resonators actuated electrostatically. *Journal of Microelectromechanical Systems*, 19(4):794–806
- [61] Mahmoodi S N, Jalili N, Daqaq M F (2008) Modeling, nonlinear dynamics, and identification of a piezoelectrically actuated micro-cantilever sensor. *IEEE/ASME Transactions on Mechatronics*, 13(1):58–65
- [62] Veijola T, Kuisma H, Lahdenpera J, Ryhanen T (1995) Equivalent-circuit model of the squeezed gas film in a silicon accelerometer. *Sensors and Actuators A*, 48:239–248
- [63] Rugar D, Grutter P (1991) Mechanical parametric amplification and thermomechanical noise squeezing. *Physical Review Letters*, 67(6):699–702.
- [64] Turner K L, Miller S A, Hartwell P G, MacDonald N C, Strogatz S H and Adams S G (1998) Five parametric resonances in a micromechanical system *Nature*, 36:149–152.
- [65] Zhang W, Baskaran R and Turner K L (2002) Effect of cubic nonlinearity on auto-parametrically amplified resonant MEMS mass sensor. *Sensors Actuators A*, 102:139–150
- [66] Zhang W, Turner K L (2005) Application of parametric resonance amplification in a single-crystal silicon micro-oscillator based mass sensor. *Sensors and Actuators A*, 122:23–30
- [67] Rhoads J, Shaw S, Turner K L, Baskaran R (2005) Tunable microelectromechanical filters that exploit parametric resonance. *Journal of Sound and Acoustics*, 127:423–430
- [68] DeMartini B E, Rhoads J F, Turner K L, Shaw S W, Moehlis J (2007) Linear and nonlinear tuning of parametrically excited MEMS oscillators. *Journal of Microelectromechanical Systems*, 16(2): 310–318
- [69] Requa M, Turner K (2006) Electromechanically driven and sensed parametric resonance in silicon microcantilevers. *Applied Physics Letters*, 88:263508(1–3)
- [70] Rhoads J F, Shaw S W, Turner K L (2006) The nonlinear response of resonant microbeam systems with purely-parametric electrostatic actuation. *Journal of Micromechanics and Microengineering*, 16:890–899.
- [71] Zalalutdinov M, Olkhovets A, Zehnder A T, Ilic B, Czaplowski D, Craighead H G, Parpia J M (2001) Optically pumped parametric amplification for micromechanical oscillators. *Applied Physical Letters*, 78:3142–3144
- [72] Carr D W, Evoy S, Sekaric L, Craighead H G, Parpia J M (2000) Parametric amplification in a torsional microresonator. *Applied Physics Letters*, 77(10)
- [73] Zook D J, Burns D W, Herb W R, Guckel H, Kang J W, and Ahn Y (1996) Optically excited self-resonant microbeams. *Sensors and Actuators A*, 52:92–98
- [74] Pandey M, Rand R H, Zehnder A T (2008) Frequency locking in a forced Mathieu–van der Pol–Duffing system. *Nonlinear Dynamics*, 54:3–12
- [75] Aubin K, Zalalutdinov M, Alan T, Reichenbach R B, Rand R, Zehnder A, Parpia J, Craighead H (2004) Limit cycle oscillations in CW laser-driven NEMS. *Journal of Microelectromechanical Systems*, 13(6):1018–1026
- [76] Albrecht T R, Grütter P, Horne D, Rugar D (1991) Frequency modulation detection using high Q cantilevers for enhanced force microscope sensitivity. *Applied Physical Letters*, 69(2):668–673
- [77] Yabuno H, Kaneko H, Kuroda M, Kobayashi T (2008) Van der Pol type self-excited micro-cantilever probe of atomic force microscopy. *Nonlinear Dynamics*. 54:137–149
- [78] Ouakad H, Nayfeh A H, Choura S, Abdel-Rahman E M, Najar F, Hamad B (2008) Nonlinear feedback control and dynamics of an electrostatically actuated microbeam filter. In *Proceeding of the 2008 ASME International Mechanical Engineering Congress and Exposition, IMECE2008, Boston, MA*
- [79] Rand R H (2005) *Lecture Notes on Nonlinear Vibrations*. version 52, 2005, <http://audiophile.tam.cornell.edu/randdocs/nlvibe52.pdf>
- [80] Hayashi C (1964) *Nonlinear Oscillations in Physical Systems*, McGraw Hill, New York
- [81] Nayfeh A (2000) *Nonlinear Interactions: Analytical, Computational, and Experimental Methods*, Wiley Interscience, New York
- [82] Arafat H N, Nayfeh A H, Abdel-Rahman E M (2008) Modal interactions in contact-mode atomic force microscopes. 54(1–2):151–166

- [83] Daqaq M F, Abdel-Rahman E M, Nayfeh A H (2009) Two-to-one internal resonance in microscanners. 57(1–2):231–251
- [84] Vyas A, Peroulis D, Bajaj A K (2008) Dynamics of a nonlinear microresonator based on resonantly interacting flexural-torsional modes. *Nonlinear Dynamics* 54(1–2):31–52
- [85] Strogatz S H (1994) *Nonlinear dynamics and chaos*, Westview Press, Cambridge, MA
- [86] Moon F C (2004) *Chaotic Vibrations: An Introduction for Applied Scientists and Engineers*, Wiley Interscience, New Jersey
- [87] Wang Y, Adams S, Thorp J, MacDonald N, Hartwell P, Bertsch F (1998) Chaos in MEMS, parameter estimation and its potential application. *IEEE Trans. Circuits Syst. I, Fundamental Theory Application*, 45(10):1013–1020
- [88] DeMartini B E, Butterfield H, Moehlis J, Turner K L (2007) Chaos for a Microelectromechanical oscillator governed by the nonlinear Mathieu equation. *Journal of Microelectromechanical Systems*, 16(6):1314–1323
- [89] Haghighi H S, Markazi A H D (2009) Chaos prediction and control in MEMS resonators. *Communication Nonlinear Sciences Numerical Simulation*, doi:10.1016/j.cnsns.2009.10.002
- [90] De S K, Aluru N (2005) Complex oscillations and chaos in electrostatic microelectromechanical systems under superharmonic excitations. *Physical Review Letters*, 94(20):204 101.1–204 101.4
- [91] Park K, Chen Q, Lai Y C (2008) Energy enhancement and chaos control in microelectromechanical systems. *Physical Review E*, 77:026210
- [92] Liu S, Davidson A, Lin Q (2004) Simulation studies on nonlinear dynamics and chaos in a MEMS cantilever control system. *Journal of Micromechanics and Microengineering*, 14(7):1064–1073
- [93] Chavarette F R, Balthazar J M, Felix J L P, Rafikov M (2009) A reducing of a chaotic movement to a periodic orbit, of a micro-electro-mechanical system, by using an optimal linear control design. *Communication Nonlinear Sciences Numerical Simulation*, 14:1844–1853
- [94] Stulemeijer J, Herfst R W, Bielen J A (2009) Chaos in electrostatically actuated RF-MEMS measured and modeled. *Proceeding of 22nd International Conference on Micro Electro Mechanical Systems MEMS 2009, Sorrento, Italy*, pp. 920–922
- [95] Ashhab M, Salapaka M, Dahleh M, Mezi/c I (1999) Melnikov-based dynamical analysis of microcantilevers in scanning probe microscopy. *Nonlinear Dynamics*, 20(3):197–220
- [96] Hu S, Raman A (2006) Chaos in atomic force microscopy. *Physical Review Letters*, 96(3):036–107
- [97] Jamitzky F, Stark M, Bunk W, Heckl W, Stark R (2006) Chaos in dynamic atomic force microscopy. *Nanotechnology*, 17(7):S213–S220
- [98] Liu M, Chelidze D (2008) A new type of atomic force microscope based on chaotic motions. *International Journal of Non-Linear Mechanics*, 43:521–526

Chapter 6

Microbeams

Microbeams are perhaps the most commonly used structural component in MEMS. Microbeams form the backbone of a wide range of devices including resonators, resonant sensors, actuators, filters, atomic force microscope probes, and RF switches. They are also used as spring elements with other microstructures and MEMS components, such as comb-drive actuators. Because of their special place in MEMS, this chapter deals with the static and dynamic behavior and phenomena of microbeams in some depth.

Unlike the previous chapters, where systems are modeled as discrete elements of lumped parameters, microbeams here are modeled more accurately as continuous or distributed-parameter systems of distributed mass, stiffness, damping, and forcing. As such, they are considered systems of infinite degrees of freedom. Their dynamical behavior is governed by partial differential equations that vary in space and time as opposed to ordinary differential equations in time in the case of lumped-parameter systems.

The static behavior, natural frequencies and modeshapes, and forced vibrations of microbeams are discussed for both linear and nonlinear cases. Their response under electrostatic forces is treated in details. Methods to tackle the nonlinear beam equations, such as reduced-order modeling, are also presented. The static and dynamic behaviors of AFM cantilevers are discussed. Other topics that are covered include the effect of residual stresses, nonideal boundary conditions, midplane stretching, and damping mechanisms.

6.1 The Linear Equation of Motion

In this section, the linear equation of motion of a beam in bending and under axial loading is derived. The derivation here follows Newtonian dynamics or vector-based approaches [1, 2]. An alternative analytical or energy-based approach is the Hamilton's principle, which is particularly powerful when dealing with complicated dynamics and boundary conditions. Since these are rare in most MEMS applications and because this method requires advanced knowledge in dynamics, the derivations using this technique will not be discussed here but will be presented in Appendix A.

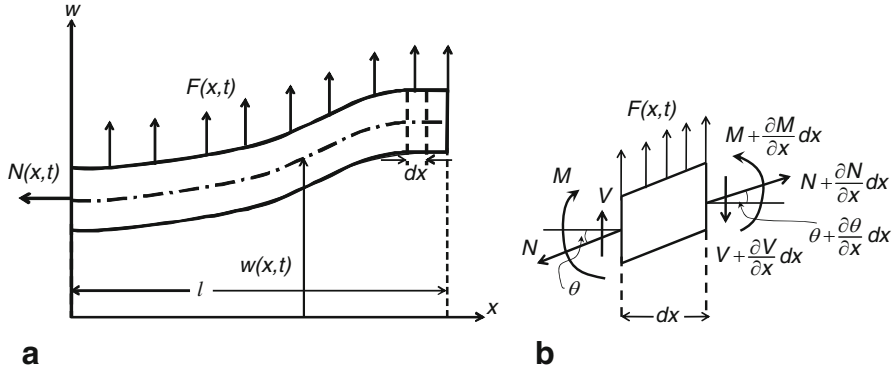


Fig. 6.1 **a** Schematic of a beam in bending. **b** A free-body diagram of an element on the beam

Next, we consider the beam in bending of Fig. 6.1a. The transverse deflection of the beam at a position x and time t is labeled $w(x,t)$. The beam has a length l , a uniform density ρ , a cross-sectional area A , and a flexural rigidity $EI(x)$, where I is the moment of inertia of the cross section and E is Young's modulus. The beam is subjected to a tensile axial force $N(x,t)$ and a distributed force per unit length $F(x,t)$. To proceed with the Newtonian approach, the internal forces and moments of a small element, of length dx , on the beam are analyzed, Fig. 6.1. In the figure, M refers to the bending moment, V is the shear force, and θ is the slope angle of the beam deflection curve with the horizontal line ($\theta = \partial w / \partial x$). A positive sign convention is adapted for the directions of M , V , N , and F as shown in Fig. 6.1b. It is assumed that all the variables on the left side of the beam element undergo small variation while moving to the other side of the element at a distance dx . Hence, all the variables are expanded in Taylor series, up to the first order in dx , to represent this small change as shown on the right side of the beam element.

Applying Newton's second law in the vertical direction gives

$$V - \left(V + \frac{\partial V}{\partial x} dx \right) + F dx - N \frac{\partial w}{\partial x} + \left(N + \frac{\partial N}{\partial x} dx \right) \left(\frac{\partial w}{\partial x} + \frac{\partial^2 w}{\partial x^2} dx \right) = \rho A dx \frac{\partial^2 w}{\partial t^2}. \quad (6.1)$$

Dropping the higher order terms in dx and simplifying the equation yield

$$-\frac{\partial V}{\partial x} + F + \frac{\partial}{\partial x} \left(N \frac{\partial w}{\partial x} \right) = \rho A \frac{\partial^2 w}{\partial t^2}. \quad (6.2)$$

Applying Newton's second law in the horizontal direction, while neglecting the axial inertia, and assuming small slope angle give

$$N + \frac{\partial N}{\partial x} dx - N = 0 \Rightarrow \frac{\partial N}{\partial x} = 0. \quad (6.3)$$

This means N can be assumed constant. Also, summing the moments on the left-hand side of the element and ignoring the rotary inertia (typically of negligible effect) give

$$M + \frac{\partial M}{\partial x} dx - M - \left(V + \frac{\partial V}{\partial x} dx \right) dx + (F dx) \frac{dx}{2} = 0. \quad (6.4)$$

Dropping the higher order terms and simplifying yield

$$V = \frac{\partial M}{\partial x}. \quad (6.5)$$

The next step in the derivation is to recall the relationship between the bending moment and the beam radius of curvature due to bending R , which is [3]

$$M = \frac{EI}{R}. \quad (6.6)$$

Mathematically, the radius of curvature of a curve is expressed as

$$R = \frac{\left[1 + \left(\frac{\partial w}{\partial x} \right)^2 \right]^{3/2}}{\frac{\partial^2 w}{\partial x^2}}. \quad (6.7)$$

Under the assumption of a small slope, $\frac{\partial w}{\partial x} \ll 1$, Eq. (6.7) is simplified to

$$R = \frac{1}{\frac{\partial^2 w}{\partial x^2}}. \quad (6.8)$$

Substituting Eq. (6.8) into Eq. (6.6) yields the basic form of the Euler–Bernoulli or thin-beam theory:

$$M = EI \frac{\partial^2 w}{\partial x^2}. \quad (6.9)$$

Substituting Eq. (6.9) into Eq. (6.5) and then the outcome along with Eq. (6.3) into Eq. (6.2) yield

$$\frac{\partial^2}{\partial x^2} \left(EI \frac{\partial^2 w}{\partial x^2} \right) + \rho A \frac{\partial^2 w}{\partial t^2} - N \frac{\partial^2 w}{\partial x^2} = F. \quad (6.10)$$

A more general equation of motion of the beam is obtained by adding a distributed damping force in the form of $F_d = -c \frac{\partial w}{\partial t}$, where c is the viscous damping coefficient and the minus sign indicates that the force is a resistance force acting in direction opposite to the motion. Thus, the final form of the linear equation of motion becomes

$$\frac{\partial^2}{\partial x^2} \left(EI \frac{\partial^2 w}{\partial x^2} \right) + \rho A \frac{\partial^2 w}{\partial t^2} + c \frac{\partial w}{\partial t} - N \frac{\partial^2 w}{\partial x^2} = F. \quad (6.11)$$

Frequently, microbeams are fabricated too wide that they become more of plates than beams. For wide beams ($b > 5h$), E is replaced by $E/(1 - \nu^2)$, where ν is the Poisson's ratio.

6.1.1 Boundary Conditions

Equation (6.11) is a partial differential equation of order four in x , which requires four boundary conditions. These can be determined from the geometrical features of the deflection and slope and also from the forces and moments balance at the beam ends. Figure 6.2 shows several examples of common boundary conditions.

Next, we discuss the boundary conditions of Fig. 6.2. In the following, for all the boundary conditions, point a refers to either the left edge of the beam, $x = 0$, or to the right edge, $x = l$.

- (a) **Simply supported (hinged, pinned):** This boundary constraints the translational motion of the beam edge while allows it to rotate freely ($M = 0$). This means

$$w(a, t) = 0; \quad EI \frac{\partial^2 w(a, t)}{\partial x^2} = 0. \quad (6.12)$$

- (b) **Clamped support (fixed, built-in):** This boundary constraints the translational and rotational motion of the beam edge, hence

$$w(a, t) = 0; \quad \frac{\partial w(a, t)}{\partial x} = 0. \quad (6.13)$$

- (c) **Free end:** As the name implies, this boundary means that the edge is free to move in translational ($V = 0$) and rotational ($M = 0$) motion. Hence,

$$\frac{\partial}{\partial x} \left(EI \frac{\partial^2 w(a, t)}{\partial x^2} \right) = 0; \quad EI \frac{\partial^2 w(a, t)}{\partial x^2} = 0. \quad (6.14)$$

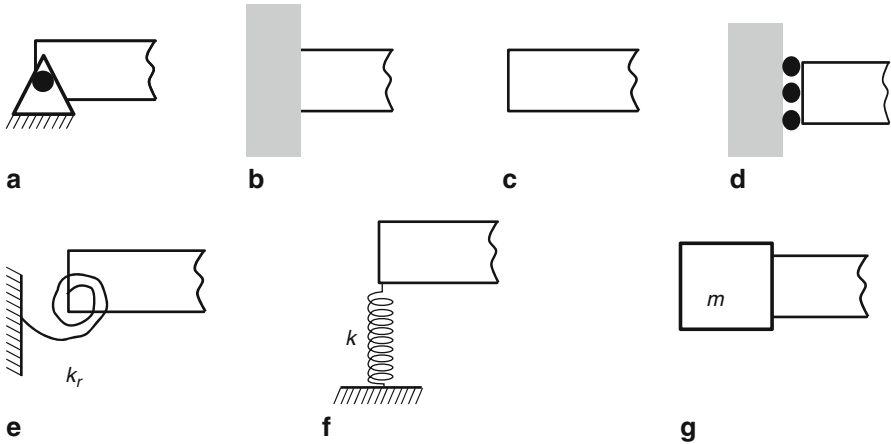


Fig. 6.2 Common beam boundary conditions: **a** pinned, **b** clamped, **c** free, **d** guided, **e** with rotational spring, **f** with translational spring, and **g** with a lumped mass

- (d) **Guided (sliding) end:** In this case, the edge is free to translate ($V = 0$) but is not free to rotate, thus

$$\frac{\partial w(a, t)}{\partial x} = 0; \quad \frac{\partial}{\partial x} \left(EI \frac{\partial^2 w(a, t)}{\partial x^2} \right) = 0. \quad (6.15)$$

The next category of boundary conditions (the second row of Fig. 6.2) requires drawing a free-body diagram for the small portion of the beam near the boundary or edge of interest. In addition, such boundaries are location-dependent; they differ depending if they are on the left or right end of the beam, as explained next. In the following, the internal axial load N will not be included in the free-body diagram since it is always equal zero in the considered boundaries.

- (e) **An edge with a rotational spring:** First, consider the spring is located at the left end of the beam at $x = 0$. The free-body diagram of this case is depicted in Fig. 6.3a. Note that the internal moments and forces (in the right side of the element) follow the sign convention of Fig. 6.1b. Note also that the small portion of the beam is assumed to undergo a positive rotational motion (positive slope angle) and that the spring is assumed to exert a moment of opposing direction to motion. Thus, applying moments and forces balance on this beam portion yields, respectively,

$$M - M_{\text{ext}} = 0 \Rightarrow EI \frac{\partial^2 w(0, t)}{\partial x^2} = k_r \frac{\partial w(0, t)}{\partial x} \quad (6.16a)$$

$$V = \frac{\partial}{\partial x} \left(EI \frac{\partial^2 w(0, t)}{\partial x^2} \right) = 0. \quad (6.16b)$$

Similarly, the boundary conditions on the right side at $x = l$, Fig. 6.3b are

$$-M - M_{\text{ext}} = 0 \Rightarrow EI \frac{\partial^2 w(l, t)}{\partial x^2} = -k_r \frac{\partial w(l, t)}{\partial x} \quad (6.17a)$$

$$V = \frac{\partial}{\partial x} \left(EI \frac{\partial^2 w(l, t)}{\partial x^2} \right) = 0. \quad (6.17b)$$

- (f) **An edge with a translational spring:** In this case, a positive transverse displacement and an opposing spring force are assumed at the considered end. Hence, the boundary conditions for the left edge, according to Fig. 6.3c, are written as

$$M = 0 \Rightarrow EI \frac{\partial^2 w(0, t)}{\partial x^2} = 0 \quad (6.18a)$$

$$-F_{\text{ext}} - V = 0 \Rightarrow \frac{\partial}{\partial x} \left(EI \frac{\partial^2 w(0, t)}{\partial x^2} \right) = -k w(0, t). \quad (6.18b)$$

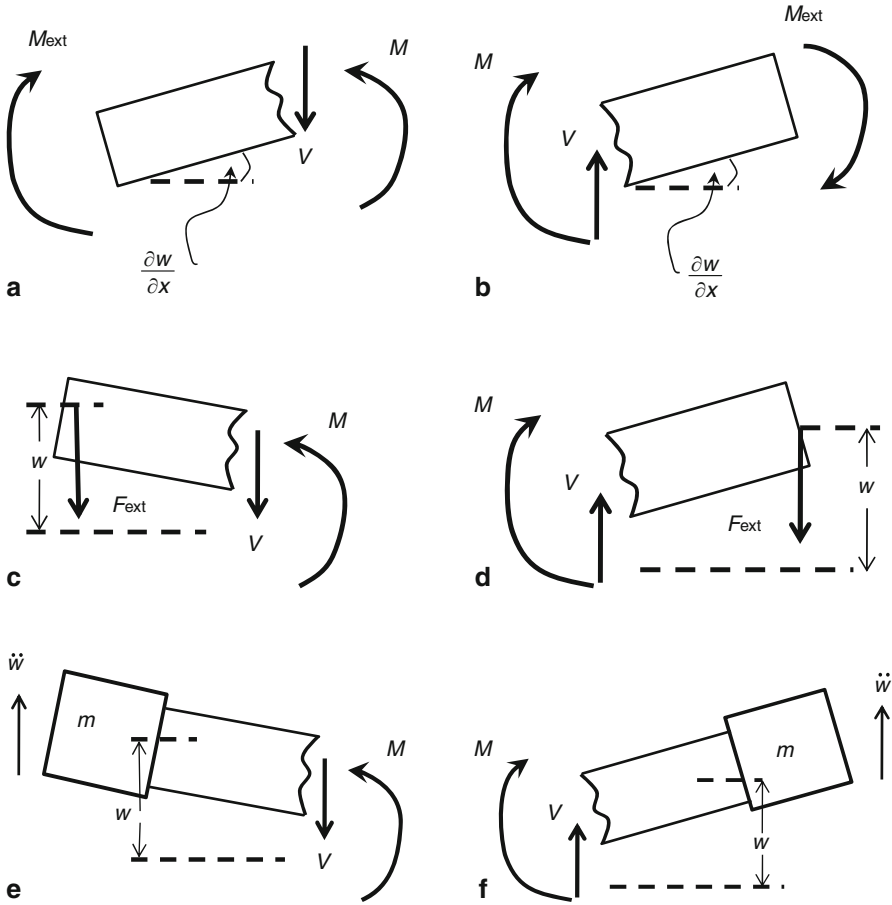


Fig. 6.3 Free body diagrams for a small portion of a beam near boundary conditions of **a** a rotational spring at $x = 0$, **b** a rotational spring at $x = l$, **c** a translational spring at $x = 0$, **d** a translational spring at $x = l$, **e** a lumped mass at $x = 0$, **f** a lumped mass at $x = l$. The subscript *ext* means “external” due to the springs

At the right end, Fig. 6.3d, the boundary conditions are

$$-M = 0 \Rightarrow EI \frac{\partial^2 w(l, t)}{\partial x^2} = 0 \quad (6.19a)$$

$$-F_{\text{ext}} + V = 0 \Rightarrow \frac{\partial}{\partial x} \left(EI \frac{\partial^2 w(l, t)}{\partial x^2} \right) = kw(l, t). \quad (6.19b)$$

(g) **An edge with a tip mass:** Here, the transversal inertia of the mass should be accounted for. For the case of $x = 0$, Fig. 6.3e, applying Newton’s second law

on the portion of the beam with the lump mass yields

$$-V = m \frac{\partial^2 w(0, t)}{\partial t^2} \Rightarrow \frac{\partial}{\partial x} \left(EI \frac{\partial^2 w(0, t)}{\partial x^2} \right) = -m \frac{\partial^2 w(0, t)}{\partial t^2}. \quad (6.20a)$$

The moment balance at this end, ignoring the rotary inertia of the mass, yields

$$M = 0 \Rightarrow EI \frac{\partial^2 w(0, t)}{\partial x^2} = 0. \quad (6.20b)$$

Similarly, for the case of $x = l$, Fig. 6.3f, the boundary conditions are

$$V = m \frac{\partial^2 w(l, t)}{\partial t^2} \Rightarrow \frac{\partial}{\partial x} \left(EI \frac{\partial^2 w(l, t)}{\partial x^2} \right) = m \frac{\partial^2 w(l, t)}{\partial t^2} \quad (6.21a)$$

$$-M = 0 \Rightarrow EI \frac{\partial^2 w(l, t)}{\partial x^2} = 0. \quad (6.21b)$$

In general, the boundary conditions can be more complicated and can have any combination of the above. However, the procedure is the same; it starts with drawing a free-body diagram of the beam end of consideration and writing Newton's second law and moments balance equation. One can note that with the Newtonian method, extra care should be taken to avoid sign mistakes with the direction of forces and moments.

Example 6.1: Derive the boundary conditions of a beam attached to a rigid paddle of a mass m at the tip, as shown in Fig. 6.4a.

Solution: Beams with paddles or almost rigid plates are common in MEMS. Paddles provide large mass, which increases the sensitivity of the beam to motion and inertia effects, and big surface area that enhances sensitivity for mass detection. To derive the boundary conditions at the beam's tip, a small portion of the beam with the

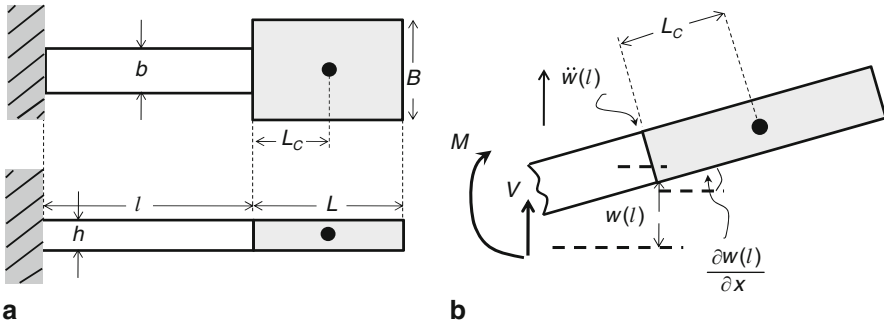


Fig. 6.4 **a** A beam with a paddle. **b** A free body diagram for a small portion of the beam near the attachment point with the paddle

paddle is separated from the rest of the beam. Then, a free body diagram of this portion is drawn, Fig. 6.4b. Since the paddle's center of mass does not coincide with the beam tip, the assumption of a point mass of Fig. 6.3f is not accurate. Hence, the rotation of the paddle and its rotary inertia need to be accounted for. Accordingly, the acceleration of the center of the paddle a_{paddle} differs from that of the beam tip $a_{\text{beam tip}}$, but are related from the kinematics according to

$$a_{\text{paddle}} = a_{\text{beam tip}} + \alpha \times L_c + \omega \times \omega \times L_c \quad (\text{a})$$

where ω and α are the rotational speed and acceleration of the paddle, respectively (assumed to be the same as that of the beam tip), which are expressed as:

$$\omega = \frac{\partial^2 w(l, t)}{\partial x \partial t}; \quad \alpha = \frac{\partial^3 w(l, t)}{\partial x \partial t^2}. \quad (\text{b})$$

Assuming small angle deformation at the beam's tip and neglecting the nonlinear term with ω of Eq. (a), the acceleration of the paddle's center of mass becomes

$$a_{\text{paddle}} = \frac{\partial^2 w(l, t)}{\partial t^2} + \frac{\partial^3 w(l, t)}{\partial t^2 \partial x} L_c. \quad (\text{c})$$

Applying Newton's second law gives

$$V = m a_{\text{paddle}} \Rightarrow \quad (\text{d})$$

$$\frac{\partial}{\partial x} \left(EI \frac{\partial^2 w(l, t)}{\partial x^2} \right) = m \left(\frac{\partial^2 w(l, t)}{\partial t^2} + \frac{\partial^3 w(l, t)}{\partial t^2 \partial x} L_c \right). \quad (\text{e})$$

To obtain the other boundary condition, the moment equation is applied around the paddle's center of mass:

$$\sum \text{Moments} = J \alpha \quad (\text{f})$$

where $J = mL^2/12$ is the mass moment of inertia of the paddle around a line parallel to its width and passing through its center of mass. Hence, according to Fig. 6.4b

$$-M - VL_c = J \alpha \Rightarrow M + (m a_{\text{paddle}}) L_c + J \alpha = 0 \quad (\text{g})$$

which can be written as

$$EI \frac{\partial^2 w(l, t)}{\partial x^2} + mL_c \frac{\partial^2 w(l, t)}{\partial t^2} + \left(mL_c^2 + \frac{mL^2}{12} \right) \frac{\partial^3 w(l, t)}{\partial x \partial t^2} = 0. \quad (\text{h})$$

Equations (e) and (h) are the same used by Krylov and Maimon [4].

6.1.2 Beams Made of Different Material Layers

In many cases, a microbeam is made by depositing more than one layer of material, such as silicon and silicon oxides, each of different modulus of elasticity. In such cases, an effective flexural of rigidity (EI_{eff}) should be used in Eq. (6.11) and the associated boundary conditions. Example 6.2 below illustrates the procedure for the special case of a beam made of two layers. The same procedure applies for beams made of more than two layers.

Example 6.2: Derive an expression of the effective flexural of rigidity of a beam in bending made of two different material layers, Fig. 6.5a.

Solution: One possible approach is to use the method of transformed or equivalent cross section [3, 5, 6]. In this method, the original cross section of the beam of the different materials is transformed into an equivalent one, which is made of one homogeneous material. This material is called material number one with a modulus of elasticity E_1 and thickness t_1 . The following steps are then followed:

- Define the ratio $n = E_2/E_1$.
- Transform the actual cross section of the beam, which is made of the two different material layers, into an equivalent one made of one material. This is done by modifying the width of the layer made of the other material, material #2, to become nb while keeping the width of the layer made of material #1 unchanged as b . Figure 6.5b illustrates this step.
- Find the centroid of the new cross section. This defines the location of the neutral axis Y_n , where the stresses due to bending are zero. This can be done according to the below formula

$$Y_n \sum_i A_i = \sum_i Y_i A_i \quad (\text{a})$$

- where A_i and Y_i are the area and the local centroid location of each individual layer in the transformed cross section, respectively. For this particular example

$$Y_n (t_1 b + t_2 nb) = (t_1/2 + t_2) t_1 b + (t_2/2) t_2 nb \Rightarrow \quad (\text{b})$$

$$Y_n = \frac{(t_1/2 + t_2) t_1 + (t_2/2) t_2 n}{(t_1 + t_2 n)}. \quad (\text{c})$$

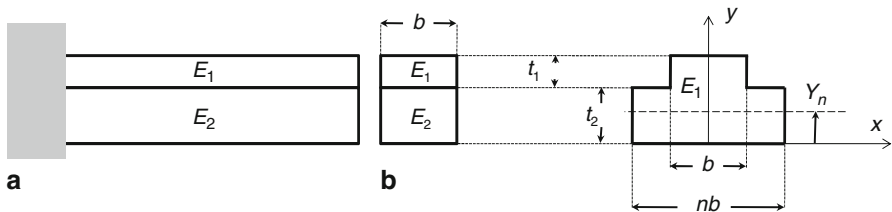


Fig. 6.5 **a** Beam made with two different materials. **b** The original cross section of the beam and the equivalent one, where $n = E_2/E_1$

- Evaluate the total or effective moment of inertia I_{eff} of the new transformed cross section around Y_n . This step involves the use of parallel axes theorem to transform the moment of inertia of each layer around its local centroid location Y_i to that around the neutral axis at Y_n . For this example,

$$I_{\text{eff}} = I_1 + I_2 \Rightarrow \quad (d)$$

$$I_{\text{eff}} = \left(\frac{bt_1^3}{12} + t_1b[t_2 + t_1/2 - Y_n]^2 \right) + \left(\frac{nbt_2^3}{12} + t_2nb[t_2/2 - Y_n]^2 \right). \quad (e)$$

Therefore, when modeling the behavior of this beam, an effective flexural of rigidity E_1I_{eff} should be used in place of EI in Eq. (6.11) and any associated boundary conditions involving EI .

Finally, the term ρA in Eq. (6.11) is calculated by summing the mass per unit length of each individual layer, based on the original cross section. In this example

$$\rho A = \rho_1 A_1 + \rho_1 A_2 \Rightarrow \quad (f)$$

$$\rho A = b(\rho_1 t_1 + \rho_2 t_2) \quad (g)$$

where ρ_1, ρ_2 are the material density of material one and material two, respectively.

6.2 The Static Response

The equation governing the static response of a beam can be generally found from its equation of motion by setting the displacement to be time independent. Hence, substituting $w = w(x)$ in Eq. (6.11) and setting all the time-dependent and time derivative terms equal to zero, the static equation is obtained

$$\frac{d^2}{dx^2} \left(EI \frac{d^2 w}{dx^2} \right) - N \frac{d^2 w}{dx^2} = F(x). \quad (6.22)$$

Equation (6.22) is a differential equation in space, which with its boundary conditions form a boundary-value problem. This problem can be solved analytically for simple cases and numerically otherwise.

Example 6.3: Determine the deflection profile of a cantilever beam subjected to a constant distributed force per unit length F_0 , Fig. 6.6a. Assume EI constant.

Solution: The differential equation of the static deflection in this case is written as

$$EI \frac{d^4 w}{dx^4} = F_0. \quad (a)$$

The boundary conditions of the cantilever are clamped-free, or

$$w(0) = 0; \quad \frac{dw(0)}{dx} = 0 \quad (b)$$

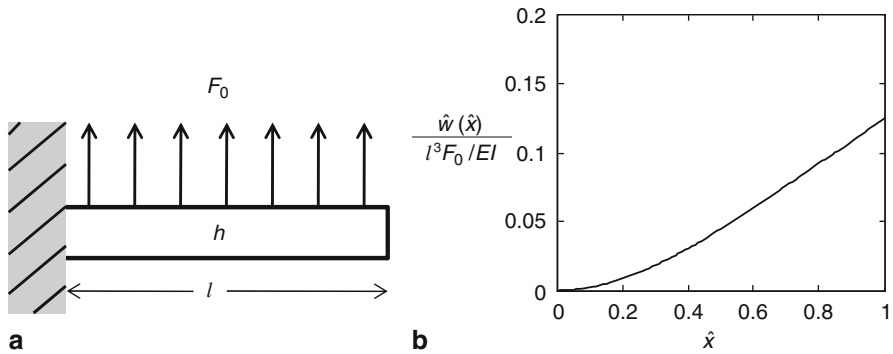


Fig. 6.6 **a** A cantilever beam subjected to a constant force. **b** The static deflection of the beam due to the force

$$EI \frac{d^3 w(l)}{dx^3} = 0; \quad EI \frac{d^2 w(l)}{dx^2} = 0. \quad (c)$$

Integrating Eq. (a) four times successively with respect to x yields

$$\frac{d^3 w}{dx^3} = \frac{F_0}{EI} x + c_1 \quad (d)$$

$$\frac{d^2 w}{dx^2} = \frac{F_0}{2EI} x^2 + c_1 x + c_2 \quad (e)$$

$$\frac{dw}{dx} = \frac{F_0}{6EI} x^3 + \frac{c_1}{2} x^2 + c_2 x + c_3 \quad (f)$$

$$w = \frac{F_0}{24EI} x^4 + \frac{c_1}{6} x^3 + \frac{c_2}{2} x^2 + c_3 x + c_4 \quad (g)$$

where c_1 – c_4 are the constants of integrations. Using Eqs. (b)–(c) in Eqs. (d)–(g) gives

$$c_1 = \frac{-F_0 l}{EI}; \quad c_2 = \frac{F_0 l^2}{2EI}; \quad c_3 = 0; \quad c_4 = 0. \quad (h)$$

Substituting Eq. (h) into Eq. (g) yields the analytical expression of the beam profile:

$$w = \frac{F_0}{24EI} x^4 - \frac{F_0 l}{6EI} x^3 + \frac{F_0 l^2}{4EI} x^2. \quad (i)$$

The maximum deflection of the beam at $x=l$ is calculated according to Eq. (i) as

$$w_{\max} = \frac{F_0 l^4}{8EI}. \quad (j)$$

It is worth to note here that the effective stiffness of the beam can be calculated, as discussed in Sect. 4.1.3, as

$$k = \frac{F}{\delta} = \frac{(F_0 l)}{w_{\max}} = \frac{8EI}{l^3}. \quad (\text{k})$$

This is the same result of case 4 of Table 4.1. For convenience, Eq. (i) can be written in normalized form by defining $\hat{x} = x/l$ and $\hat{w} = w/l$, which gives

$$\hat{w} = \frac{F_0 l^3}{EI} \left(\frac{\hat{x}^4}{24} - \frac{\hat{x}^3}{6} + \frac{\hat{x}^2}{4} \right). \quad (\text{l})$$

Equation (l) is plotted in Fig. 6.6b showing the static profile of the beam.

6.3 Residual Stresses and Nonideal Supports of Cantilever Microbeams

Residual stress or stress gradient in thin films and microstructures is an important topic in MEMS. Residual stress in microstructures with a support-free edge, such as cantilever beams, can cause deformation in their geometry. This deformation affects their functionality, for example by altering their pull-in threshold, and may also lead to their failure through curling them downward and sticking them to the substrate. Residual stress in microstructures of immovable edges, such as clamped-clamped beams, introduces axial stresses or forces (the N term in Eq. (6.11)). This alters their stiffness and natural frequency and may cause deformation in the form of buckling or imperfections. Stress gradient across the thickness of a beam can be induced due to a thermal mismatch between the beam material and the substrate or among the various layers of the beam itself, in the case of a composite beam, during material deposition. This causes curling in cantilever microbeams.

To understand the basic mechanism of curling, consider a cantilever microbeam made of a single thin film just before its release from the substrate with compressive type residual stresses, Fig. 6.7a [7, 8]. The thin film of the beam at this stage is under the induced residual stresses, which in general are composed of an average stress component and a stress gradient component across its thickness as illustrated in the top of Fig. 6.7a, b. Immediately after its release, Fig. 6.7b, the beam finds itself still under the same residual stresses. Since at this instant the beam's end is free, it deforms to relieve the residual stresses. Hence, internal stresses are induced, which are equal in magnitude and opposite in direction to the external stresses from fabrication. The internal stresses, while relieving the beam from stresses, deform the beam into a new equilibrium configuration. Figure 6.7c shows the axial deformation of the beam due to the tensile internal average stresses, which oppose the compressive residual stresses. This axial deformation is in general of negligible effect on the beam's geometry. Also, Fig. 6.7d shows the reaction of the beam to oppose the stress gradient from the residual stresses by inducing an equal internal stress gradient of opposite direction, which curls the beam as shown. Unlike the axial deformation, the curling of the beam

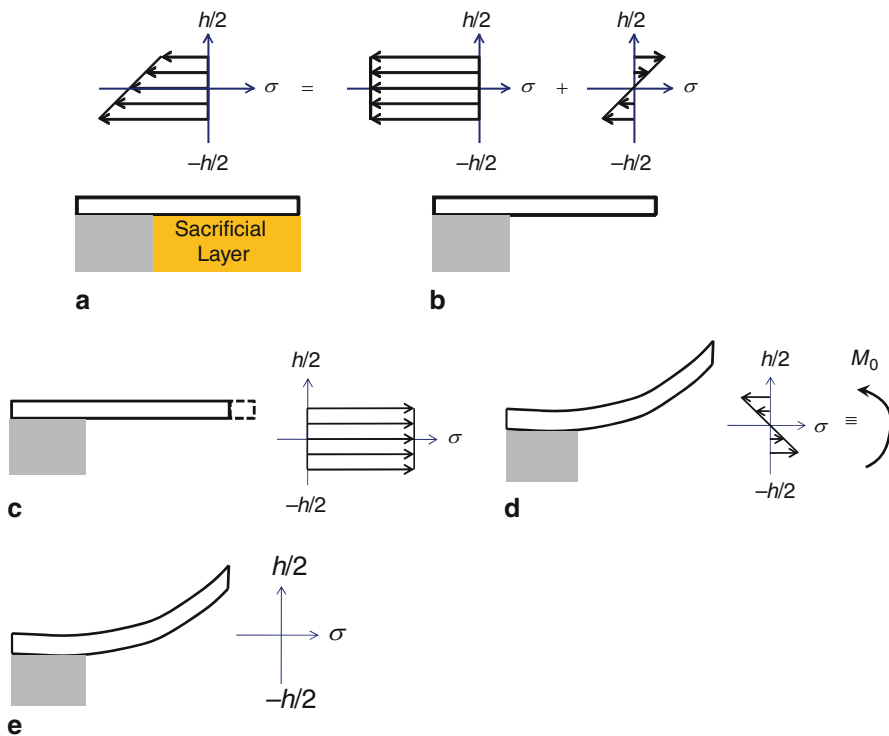


Fig. 6.7 The various stages for the deformation of a cantilever beam due to residual stresses. Figure **a** shows a cantilever microbeam just before its release, **b** immediately after its release, **c** the microbeam deformed axially, **d** a curled beam with the induced internal stress gradient, and **e** a curled beam with zero internal stresses

can be very significant. Finally, the curled beam becomes in equilibrium with a net of zero stresses, Fig. 6.7e.

The conclusion of this discussion is that a curled microbeam is a stress-free structure that is brought to its deformed shape by a stress gradient, which is equivalent to a constant applied moment on the beam. Hence, from a modeling stand, the problem is casted into finding the stress gradient, or an equivalent constant moment, that causes a straight cantilever microbeam to deform to some curled configuration. One practical application of this is the use of cantilever microbeams as test structures. They can be fabricated on the same chip with other more complicated devices that share the same material composition. Then, by measuring the deformed configuration of the cantilever microbeams, using an interferometer or optical profiler, the stress gradient that affects the thin films of the beams can be calculated [9]. This can be assumed the same stress gradient affecting the other complicated microstructures since they share the same fabrication processes.

Another common case of interest is the composite microbeam, which is made of a thin film of thickness h under a uniform average stress σ_0 placed on top of a stress-free film of thickness H , which is much thicker than the thin film, Fig. 6.8. It

Fig. 6.8 A composite cantilever beam deforms due to residual stresses

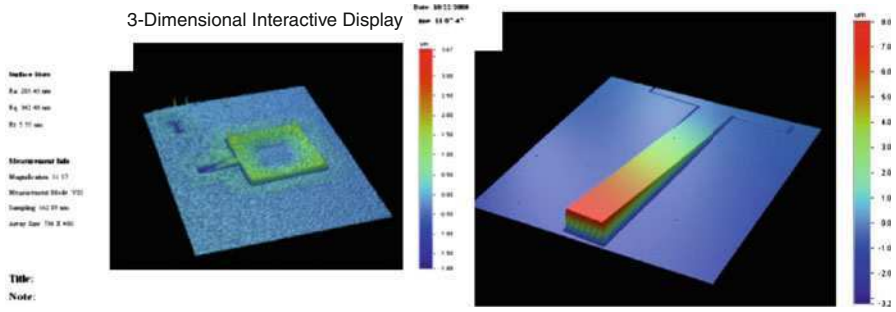
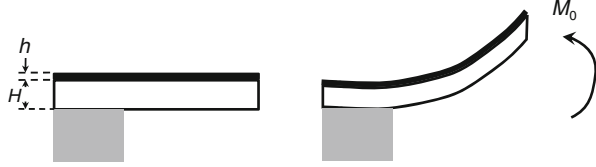


Fig. 6.9 Images of profiled cantilever microbeams showing their deformation due to stress gradient and nonideal supports

can be shown that the induced bending moment in this case is approximated as [7]

$$M_0 = \frac{1}{2} \sigma_0 H h. \quad (6.23)$$

The thin film stress can be estimated by measuring the radius of curvature of the microbeam R and using the so-called Stoney's formula [10], which is

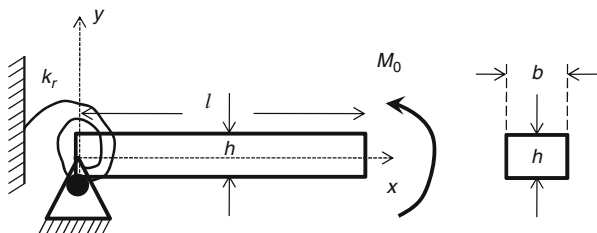
$$\sigma_0 = \frac{E_H H^2}{6hR} \quad (6.24)$$

where E_H is the modulus of elasticity of the thick film. Equation (6.24) is used in general to estimate the induced stress in thin films when deposited on disk substrates by measuring the radius of curvature of the substrate after the deposited material cools down.

In addition to curling, cantilever microbeams can tilt upward or downward due to the deformation of their support. In another words, the ideal assumption of perfectly clamped edge with zero slope may not be true. Hence, the total deformation of a cantilever microbeam in general can be due to nonideal support plus curling due to stress gradient [8]. By measuring the static profile of the microbeam one can determine if both factors are influential. Modeling a nonideal support can be done analytically by assuming torsional and translational springs at the beam edge. Then, by measuring the natural frequency of the microbeam and comparing it to the analytically obtained with the two springs, the values of the spring's constants at the beam edge can be estimated. More on this is discussed in Sect. 6.4.2. Figure 6.9 shows examples of profiler images of deformed microbeams using a Wyko interferometer.

Example 6.4: Figure 6.10 shows a model of a cantilever microbeam with a hinged edge and a torsional spring subjected to a constant bending moment. This can be a

Fig. 6.10 A cantilever beam with nonideal support subjected to a constant moment



possible model to study the deformation of a cantilever of flexible support due to residual stresses. For the numerical calculations, consider the beam has a length $l = 510 \mu\text{m}$, thickness $h = 1.5 \mu\text{m}$, width $b = 100 \mu\text{m}$, and a Young's modulus $E = 166 \text{ GPa}$. Assume that the deflection of the beam tip has been measured and found to be $6 \mu\text{m}$ upward.

- Derive analytical expressions of the beam deflection and the beam maximum tip deflection.
- Assume the edge of the cantilever to be perfectly clamped ($k_r = \infty$), calculate the internal moment that can cause this tip deflection.
- For part (b), estimate the corresponding stress gradient.
- Assume that, based on measuring the natural frequency of the beam, it is determined that the edge of the beam is flexible and cannot be considered perfectly clamped. Consider that the rotational spring coefficient is estimated to be $k_r = 1.3 \times 10^{-9} \text{ Nm}$. Calculate the internal moment assuming the deflection of the beam to be completely due to tilting caused by the flexibility of the edge (ignore the bending contribution).
- Now calculate the internal moment considering both the bending effect and the nonideal support.
- Plot and compare the beam profiles of cases (b), (d), and (e).

Solution:

- The differential equation of the static deflection in this case is expressed as

$$EI \frac{d^4 w}{dx^4} = 0. \quad (\text{a})$$

The boundary conditions of the cantilever are hinged with a rotational spring at $x = 0$ and shear-free with an applied constant moment at $x = l$, that is

$$EI \frac{d^2 w(0)}{dx^2} = k_r \frac{dw(0)}{dx}; \quad w(0) = 0. \quad (\text{b})$$

$$EI \frac{d^3 w(l)}{dx^3} = 0; \quad EI \frac{d^2 w(l)}{dx^2} = M_0. \quad (\text{c})$$

Integrating Eq. (a) four times successively with respect to x yields an algebraic equation with four constant coefficients, which generally can be written as

$$w = c_1 x^3 + c_2 x^2 + c_3 x + c_4 \quad (\text{d})$$

where c_1 – c_4 are the constants of integrations. Using Eqs. (b) and (c) in Eq. (d) gives

$$c_1 = 0; \quad c_2 = \frac{M_0}{2EI}; \quad c_3 = \frac{M_0}{k_r}; \quad c_4 = 0. \quad (e)$$

Substituting Eq. (e) into Eq. (d) yields the analytical expression of the beam profile

$$w = \frac{M_0}{2EI}x^2 + \frac{M_0}{k_r}x. \quad (f)$$

The maximum deflection of the beam at $x=l$ is calculated according to Eq. (f) as

$$w_{\max} = \frac{M_0}{2EI}l^2 + \frac{M_0}{k_r}l. \quad (g)$$

From Eq. (g), the below expression for the moment is derived:

$$M_0 = \frac{w_{\max}}{\frac{l^2}{2EI} + \frac{l}{k_r}}. \quad (h)$$

For convenience, Eq. (f) can be written in a normalized form by defining $\hat{x} = x/l$ and $\hat{w} = w/l$, which gives

$$\hat{w} = \frac{M_0 l}{2EI}\hat{x}^2 + \frac{M_0}{k_r}\hat{x}. \quad (i)$$

(b) Setting $k_r = \infty$ (perfectly clamped) in Eq. (h) yields

$$M_0 = \frac{2EIw_{\max}}{l^2}. \quad (j)$$

Substituting the numbers with $I = bh^3/12$ in Eq. (j) gives $M_0 = 1.66 \times 10^{-10}$ Nm.

(c) The absolute value of the stress at any point on the transversal cross section of the beam of area $b \times h$ above the neutral axis (the centroid of the cross section at $y=0$) is given by

$$\sigma(y) = \frac{M_0 y}{I}. \quad (k)$$

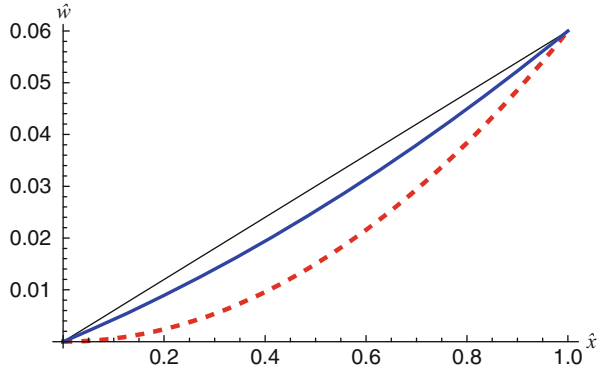
The stress gradient Γ is defined as

$$\Gamma = \frac{\partial \sigma}{\partial y} = \frac{M_0}{I}. \quad (l)$$

In the case of pure bending, substituting Eq. (j) into (l) yields

$$\Gamma = \frac{\partial \sigma}{\partial y} = \frac{2Ew_{\max}}{l^2}. \quad (m)$$

Fig. 6.11 The profile of a deflected cantilever beam: *solid thin* assuming pure tilting, *dashed* assuming pure bending, and *solid thick* assuming both tilting and bending



Plugging the numbers into Eq. (m) yields $\Gamma = 199.2 \text{ MPa}/\mu\text{m}$. Hence, the maximum stress occurs at $y = h/2$, which is equal to $h/2 \times \Gamma = 99.6 \text{ MPa}$.

- (d) Substituting $k_r = 1.3 \times 10^{-9}$ in Eq. (h), while setting the bending component (coefficient of x^2) equal to zero, and carrying out the calculations yield $M_0 = 7.8 \times 10^{-11} \text{ Nm}$.
- (e) Substituting $k_r = 1.3 \times 10^{-9}$ in Eq. (h) and carrying out the calculations yield $M_0 = 5.31 \times 10^{-11} \text{ Nm}$.
- (f) Figure 6.11 shows the plots of the beam profiles of cases (b), (d), and (e). As noted in the figure, while the maximum deflection is the same in the three cases, there is significant difference among the various profiles, especially near the support. Thus, measuring the complete profile and the natural frequency of the microbeam can help determine which model should be used.

6.4 Natural Frequencies and Modeshapes

Determining accurately the natural frequencies of microbeams is crucial for characterizing their actual geometry and boundary conditions after fabrication, revealing their operating range and restrictions, and enabling accurate calibration of resonator-based devices, such as resonant sensors, RF filters, and atomic force microscopes. This section details the fundamental procedure for estimating exactly the natural frequencies of linearly-behaving microbeams and their corresponding modeshapes through solving the so-called eigenvalue problems.

Toward this, we refer back to Eq. (6.11) and set the forcing and damping terms equal to zero. In addition, to simplify the analysis, the axial force N is set equal to zero (discussion on this term is in Sect. 6.5) and EI is assumed constant. Therefore, the equation of motion is reduced to

$$EI \frac{\partial^4 w}{\partial x^4} + \rho A \frac{\partial^2 w}{\partial t^2} = 0. \quad (6.25)$$

Next, a separation-of-variables approach is followed to solve Eq. (6.25). For this, a solution is assumed to be composed of a spatial function $\phi(x)$ multiplying a function in time, which can be proven to be harmonic of the form $e^{i\omega t}$, where ω is a real-number constant. As will be seen later, ω represents the natural frequency of the beam and ϕ is the corresponding modeshape or eigenfunction. At this level, both ϕ and ω are unknowns and will be determined through the course of the solution. Thus, $w(x,t)$ is expressed as

$$w(x,t) = \phi(x)e^{i\omega t}. \quad (6.26)$$

Substituting Eq. (6.26) into Eq. (6.25), dividing by $e^{i\omega t}$, and simplifying give

$$\phi'''' - \beta^4 \phi = 0 \quad (6.27)$$

where the superscript prime refers to a derivative with respect to x (four primes means four time derivatives with respect to x) and β is defined according to

$$\beta^4 = \frac{\rho A \omega^2}{EI}. \quad (6.28)$$

The expression of Eq. (6.28) can be rewritten to express ω explicitly in terms of β as

$$\omega = \sqrt{\frac{EI}{\rho A}} \beta^2. \quad (6.29)$$

By introducing the nondimensional number $\omega_{\text{non}} = \beta^2 l^2$, Eq. (6.29) is written as

$$\omega = \sqrt{\frac{EI}{\rho A l^4}} \omega_{\text{non}}. \quad (6.30)$$

As will be explained latter, ω_{non} turns out to be a universal nondimensional number of the natural frequency of a beam that depends on its boundary conditions. To obtain the dimensional natural frequency ω of a beam of specific material and geometry, the term under the square root in Eq. (6.30) is calculated and then multiplied by ω_{non} .

Equation (6.27) represents, with an appropriate set of boundary-conditions, a boundary-value problem that can be solved analytically. Toward this, a solution of Eq. (6.27) is assumed in the form of

$$\phi(x) = A_0 e^{sx} \quad (6.31)$$

where A_0 and s are unknown constants. Substituting Eq. (6.31) into Eq. (6.27) and simplifying yield the below algebraic equation for s :

$$s^4 - \beta^4 = 0. \quad (6.32)$$

Solving Eq. (6.32) gives

$$s = \pm\beta; \quad s = \pm i\beta. \quad (6.33)$$

From Eq. (6.31) and Eq. (6.33) and using the principle of superposition, the total solution of ϕ becomes

$$\phi(x) = A_1 e^{\beta x} + A_2 e^{-\beta x} + A_3 e^{i\beta x} + A_4 e^{-i\beta x} \quad (6.34)$$

where A_1 – A_4 are constants of integration, which are determined from the boundary conditions of the beam. A more convenient form of Eq. (6.34) can be written as

$$\phi(x) = A \cos(\beta x) + B \sin(\beta x) + C \cosh(\beta x) + D \sinh(\beta x) \quad (6.35)$$

where also A , B , C , and D are determined from the boundary conditions of the beam.

To illustrate the procedure and some basic concepts, we consider next the case of a hinged–hinged beam. The boundary conditions in this case are given in Eq. (6.12) at $x = 0$ and $x = l$. Using Eq. (6.26) with the hinged–hinged boundary conditions yields the boundary conditions in terms of ϕ :

$$\phi(0) = 0; \quad \phi''(0) = 0 \quad (6.36a)$$

$$\phi(l) = 0; \quad \phi''(l) = 0. \quad (6.36b)$$

Applying Eq. (6.36a) and Eq. (6.36b) in Eq. (6.35) yields four algebraic equations, which can be casted in a matrix format as below

$$\underbrace{\begin{bmatrix} 1 & 0 & 1 & 0 \\ -1 & 0 & 1 & 0 \\ \cos(\beta l) & \sin(\beta l) & \cosh(\beta l) & \sinh(\beta l) \\ -\cos(\beta l) & -\sin(\beta l) & \cosh(\beta l) & \sinh(\beta l) \end{bmatrix}}_{[\tilde{A}]} \begin{Bmatrix} A \\ B \\ C \\ D \end{Bmatrix} = \{0\}. \quad (6.37)$$

A first look at the system of Eq. (6.37) suggests a trivial solution with $A = B = C = D = 0$. This indicates that $\phi(x)$, and thus $w(x, t)$, is also trivial meaning no vibration. To avoid this possibility of a trivial solution, $[\tilde{A}]$ is assumed to have no inverse, meaning its determinant must be equal to zero. Hence, the problem is translated to what is called an **eigenvalue problem**. Setting the determinant equal to zero yields an algebraic equation, called **characteristic equation**, in βl , which is called the **eigenvalue**. Solving this equation gives infinite possible solutions. The next step is to substitute a given value of βl into Eq. (6.37) and then selecting as maximum three independent equations out of the possible four to solve for three constants of integrations in terms of the forth one. This represents a feature of all eigenvalue problems, which is for an $n \times n$ algebraic system of equations, only $n - 1$ independent equations can be used.

Proceeding with the example, it turns out that the system of Eq. (6.37) can be further simplified by noting that the first two rows give $A = C = 0$. Hence, the system is reduced to

$$\begin{bmatrix} \sin(\beta l) & \sinh(\beta l) \\ -\sin(\beta l) & \sinh(\beta l) \end{bmatrix} \begin{Bmatrix} B \\ D \end{Bmatrix} = \{0\}. \quad (6.38)$$

Setting the determinant equal to zero gives the characteristic equation in terms of the eigenvalue βl :

$$2 \sinh(\beta l) \sin(\beta l) = 0 \Rightarrow \sin(\beta l) = 0. \quad (6.39)$$

As pointed previously, this characteristic equation has infinite solutions, which are

$$\beta_n l = n\pi; \quad n = 1, 2, \dots \quad (6.40)$$

where the subscript n is introduced to refer to the various possible n eigenvalues. Hence, the nondimensional natural frequency of the n mode is given by

$$\omega_{\text{non},n} = n^2 \pi^2; \quad n = 1, 2, \dots \quad (6.41)$$

Next, an expression for the eigenfunction ϕ is derived by substituting Eq. (6.40) into Eq. (6.37) or in its reduced version Eq. (6.38). For the latter case, one algebraic equation only can be used since the system has only two equations. The choice of which equation to use should not affect the results. Here we select the equation of the second row, that is

$$-\sin(n\pi) B + \sinh(n\pi) D = 0. \quad (6.42)$$

The first term is clearly always zero leaving only the term with the D coefficient, which means $D = 0$. Therefore, with $A = C = D = 0$, Eq. (6.35) is reduced to

$$\phi_n(x) = B_n \sin(\beta_n x) \quad (6.43)$$

where also the subscript n is introduced to associate the modeshape to the n eigenvalue. Equation (6.43) indicates infinite number of modeshapes corresponding to the infinite natural frequencies. However, usually only the first few modeshapes participate considerably in the dynamic response with the strongest contributions comes from the modes of the lowest number. Figure 6.12 shows the first four modeshapes corresponding to the first four natural frequencies with $B_n = 1$. As seen in the figure, the odd modeshapes are symmetric and the even are antisymmetric. This trend continues for the rest of the modeshapes. It is worth mentioning that the value of the coefficient B_n in Eq. (6.43) is arbitrary. This coefficient can take any real value number without affecting the “shape” or the profile of the eigenfunction. This arbitrariness is the price we paid for rescuing the solution from being nontrivial. Mathematically, this is a feature of all eigenfunctions. Next, several examples are discussed for beams with other boundary conditions.

Example 6.5: Determine the natural frequencies and modeshapes of a clamped–clamped beam.

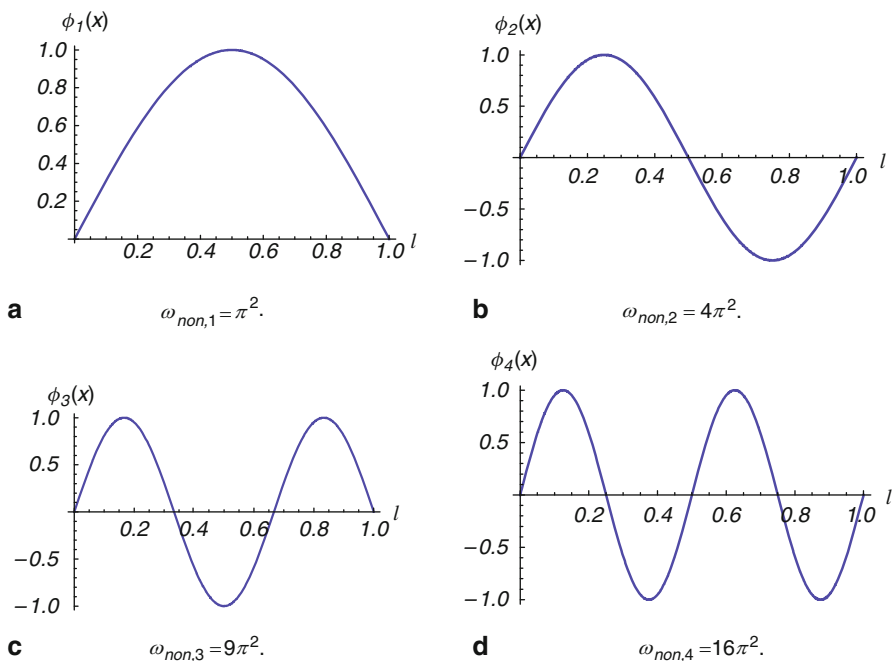


Fig. 6.12 The first four modeshapes of a hinged-hinged beam. **a** first modeshape, **b** second modeshape, **c** third modeshape, **d** fourth modeshape

Solution: The modeshape is governed by Eq. (6.35) with the boundary conditions:

$$\phi(0) = 0; \quad \phi'(0) = 0 \quad (a)$$

$$\phi(l) = 0; \quad \phi'(l) = 0. \quad (b)$$

Using Eq. (a) and Eq. (b) in Eq. (6.35) yields four algebraic equations, which can be casted in a matrix format as below

$$\underbrace{\begin{bmatrix} 1 & 0 & 1 & 0 \\ 0 & 1 & 0 & 1 \\ \cos(\beta l) & \sin(\beta l) & \cosh(\beta l) & \sinh(\beta l) \\ -\sin(\beta l) & \cos(\beta l) & \sinh(\beta l) & \cosh(\beta l) \end{bmatrix}}_{[\tilde{A}]} \begin{Bmatrix} A \\ B \\ C \\ D \end{Bmatrix} = \{0\}. \quad (c)$$

Setting the determinant above equal to zero gives the characteristic equation

$$\cos^2(\beta l) - 2 \cos(\beta l) \cosh(\beta l) + \cosh^2(\beta l) + \sin^2(\beta l) - \sinh^2(\beta l) = 0. \quad (d)$$

Equation (d) can be solved numerically, for example using the command “FindRoot” in the software Mathematica, which requires providing an initial guess for every

eigenvalue. One way to provide an initial guess is to plot Eq. (d) versus βl and watch for the crossing with the zero axes. Solving Eq. (d) for the first four roots gives

$$\beta_1 l = 4.73; \quad \beta_2 l = 7.85; \quad \beta_3 l = 10.996; \quad \beta_4 l = 14.14. \quad (e)$$

Hence, the first four nondimensional natural frequencies are

$$\omega_{\text{non},1} = 22.373; \quad \omega_{\text{non},2} = 61.673; \quad \omega_{\text{non},3} = 120.90; \quad \omega_{\text{non},4} = 199.859. \quad (f)$$

By substituting a value of βl into Eq. (c), and making use of three of the four algebraic equations, the blow expressions of the modeshapes are obtained:

$$\begin{aligned} \phi_1 &= 1.01781 \cos[4.73004 x] - 1.01781 \cosh[4.73004 x] \\ &\quad - \sin[4.73004 x] + \sinh[4.73004 x] \\ \phi_2 &= 0.999223 \cos[7.8532 x] - 0.999223 \cosh[7.8532 x] \\ &\quad - \sin[7.8532 x] + \sinh[7.8532 x] \\ \phi_3 &= 1.00003 \cos[10.9956 x] - 1.00003 \cosh[10.9956 x] \\ &\quad - \sin[10.9956 x] + \sinh[10.9956 x] \\ \phi_4 &= 0.999999 \cos[14.1372 x] - 0.999999 \cosh[14.1372 x] \\ &\quad - \sin[14.1372 x] + \sinh[14.1372 x]. \end{aligned} \quad (g)$$

Note that the expressions of Eq. (g) are not unique (arbitrary within a constant). Figure 6.13 depicts the first four natural frequencies and the corresponding modeshapes.

6.4.1 Nondimensionalization

As discussed in Sect. 5.2, normalization or nondimensionalization offers several advantages in MEMS. For estimating the natural frequency of a microbeam, nondimensionalization simplifies the analysis of the eigenvalue problem by dealing directly with ω_{non} . To illustrate this, we consider Eq. (6.25) and introduce the below nondimensional variables (denoted by hats)

$$\hat{w} = \frac{w}{l}, \quad \hat{x} = \frac{x}{l}, \quad \hat{t} = \frac{t}{T} \quad (6.44)$$

where T is a time scale that will be defined below. Note that

$$\frac{\partial^4 w}{\partial x^4} = \frac{\partial^4 (\hat{w}l)}{\partial (\hat{x}l)^4} = \frac{1}{l^3} \frac{\partial^4 \hat{w}}{\partial \hat{x}^4}; \quad \frac{\partial^2 w}{\partial t^2} = \frac{\partial^2 (\hat{w}l)}{\partial (\hat{t}T)^2} = \frac{l}{T^2} \frac{\partial^2 \hat{w}}{\partial \hat{t}^2}.$$

Substituting Eq. (6.44) into Eq. (6.25) gives

$$\frac{\partial^4 \hat{w}}{\partial \hat{x}^4} + \frac{\rho A l^4}{E I T^2} \frac{\partial^2 \hat{w}}{\partial \hat{t}^2} = 0. \quad (6.45)$$

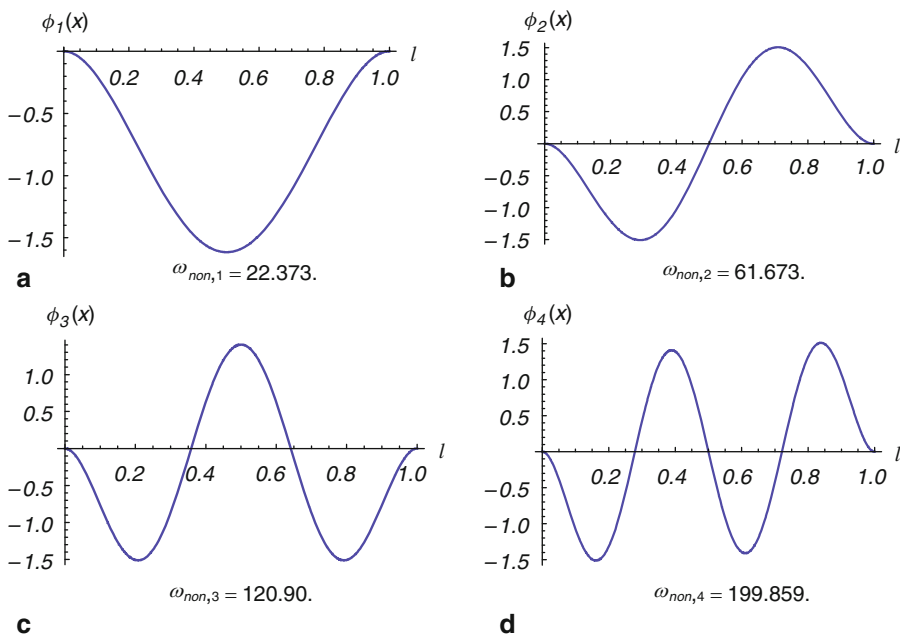


Fig. 6.13 The first four modeshapes of a clamped-clamped beam. **a** first modeshape, **b** second modeshape, **c** third modeshape, **d** fourth modeshape

Next, T is defined by setting the coefficient of the inertia term equal to unity:

$$\frac{\rho A l^4}{E I T^2} = 1 \Rightarrow T = \sqrt{\frac{\rho A l^4}{E I}}. \quad (6.46)$$

Hence, Eq. (6.45) is simplified to

$$\frac{\partial^4 \hat{w}}{\partial \hat{x}^4} + \frac{\partial^2 \hat{w}}{\partial \hat{t}^2} = 0. \quad (6.47)$$

As before, to derive the eigenvalue problem, we define $\hat{w}(\hat{x}, \hat{t})$ as

$$\hat{w}(\hat{x}, \hat{t}) = \hat{\phi}(\hat{x}) e^{i \hat{\omega} \hat{t}} \quad (6.48)$$

where $\hat{\omega}$ denotes a nondimensional natural frequency. Substituting Eq. (6.48) into Eq. (6.47), dividing by $e^{i \hat{\omega} \hat{t}}$, and simplifying give

$$\frac{d^4 \hat{\phi}}{d \hat{x}^4} - \hat{\beta}^4 \hat{\phi} = 0 \quad (6.49)$$

where $\hat{\beta}$ is defined as

$$\hat{\beta}^4 = \hat{\omega}^2. \quad (6.50)$$

Once Eq. (6.49) is solved with the appropriate boundary conditions, the dimensional natural frequency ω can be obtained by multiplying $\hat{\omega}$ by $1/T$ from Eq. (6.46). Hence

$$\omega = \sqrt{\frac{EI}{\rho Al^4}} \hat{\omega}. \quad (6.51)$$

One can see from Eq. (6.30) and Eq. (6.51) that $\hat{\omega} = \omega_{\text{non}}$. Hence, solving the eigenvalue problem based on a nondimensional beam equation yields directly the nondimensional natural frequency ω_{non} .

Following a procedure similar to Eqs. (6.31)–(6.35), the nondimensional modeshape can be expressed as

$$\hat{\phi}(\hat{x}) = \hat{A} \cos(\hat{\beta}\hat{x}) + \hat{B} \sin(\hat{\beta}\hat{x}) + \hat{C} \cosh(\hat{\beta}\hat{x}) + \hat{D} \sinh(\hat{\beta}\hat{x}) \quad (6.52)$$

where \hat{A} , \hat{B} , \hat{C} , and \hat{D} are determined from the normalized boundary conditions of the beam. In the following, we will utilize Eq. (6.51) and Eq. (6.52). However the superscript “ $\hat{}$ ” will be dropped for convenience.

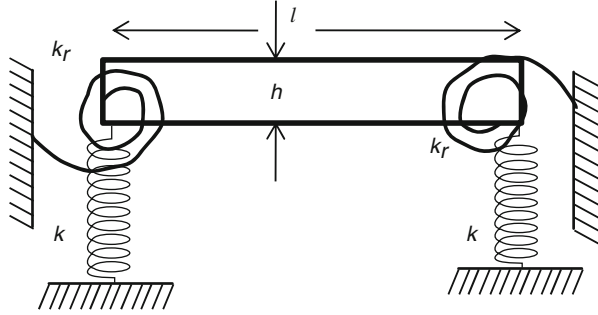
6.4.2 Flexible (Nonideal) Supports

As discussed in Sect. 6.3, the anchors or supports of microbeams can have some flexibility making the assumption of perfect clamping inaccurate. Several studies have been presented to address this issue [8, 11–16]. Some have used finite-element analysis to model the exact geometry of the supports, and hence account for its deformation under actuation or during motion. Others have used analytical approaches, in which the flexibility of the supports are accounted for by assuming springs at the beams boundaries, which can be transversal, rotational, axial, or any combination of these. By measuring the natural frequencies of the microbeams and comparing them to the analytical predictions with the assumed springs, values of the spring stiffness coefficients can be estimated. Also, images of the measured microbeams profiles can give indications on the role of rotational springs based on the slope of the profiles near the supports. Next, we discuss estimating the natural frequencies of beams with springs at the boundaries and how these frequencies can be tuned by adjusting the spring stiffness coefficients.

Example 6.6: Consider a beam with rotational and transversal springs attached at its both ends, Fig. 6.14. Investigate the effect of reducing the spring stiffness coefficients on one side of the beam from very large to very small values on the first four natural frequencies.

Solution: The boundary conditions of the beam in this case can be read from Eqs. (6.16a) and (6.18b) at $x = 0$ and Eqs. (6.17a) and (6.19b) at $x = l$. Using

Fig. 6.14 A beam with springs at the boundaries



Eqs. (6.44) and (6.48), and after omitting the superscript “ \wedge ” for convenience, the nondimensional boundary conditions can be written as

$$\phi'' - \frac{lk_r}{EI}\phi' = 0; \quad \phi''' + \frac{l^3k}{EI}\phi = 0; \quad \text{at } x = 0 \quad (\text{a})$$

$$\phi'' + \frac{lk_r}{EI}\phi' = 0; \quad \phi''' - \frac{l^3k}{EI}\phi = 0; \quad \text{at } x = 1. \quad (\text{b})$$

To describe the change in the stiffness coefficients at the boundaries, the following stiffness ratios of the translational R_t and rotational R_r spring coefficients are introduced:

$$R_t = \frac{k}{EI/l^3}; \quad R_r = \frac{k_r}{EI/l}. \quad (\text{c})$$

Hence, substituting Eq. (c) into Eq. (a) and Eq. (b), the boundary conditions become

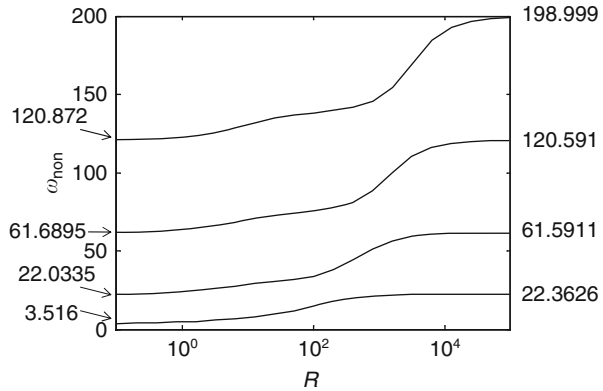
$$\phi'' - R_r\phi' = 0; \quad \phi''' + R_t\phi = 0; \quad \text{at } x = 0 \quad (\text{d})$$

$$\phi'' + R_r\phi' = 0; \quad \phi''' - R_t\phi = 0; \quad \text{at } x = 1. \quad (\text{e})$$

By adjusting the ratios R_t and R_r , ω_{non} can be tuned to a wide range of values. For simplicity, in this example we adjust both R_t and R_r by the same magnitude. Hence, we assume $R_t = R_r = R$ and solve the eigenvalue problem of the beam while varying R from very small to very large values. Of course, this is only one possibility of tuning the natural frequency. Other possibilities may involve changing either R_t or R_r or changing both but by different magnitudes, which depend on the available experimental data on the case of interest.

Applying Eqs. (d) and (e) on Eq. (6.52) yields a 4×4 matrix for the constant of integrations. Setting the determinant of this matrix equal to zero yields the characteristic equation, which is then solved for β , and hence for ω_{non} for a given value of R . Next, the values of R_t and R_r at $x = 0$ are fixed at very large numbers ($R_t = R_r = R \rightarrow \infty$), which is equivalent to assuming perfect clamping. Then, we investigate changing R_t and R_r at $x = l$ from small to large values. The results are depicted in Fig. 6.15 for the first four natural frequencies. When $R_t = R_r = R \rightarrow 0$ at $x = l$, the beam

Fig. 6.15 The first four natural frequencies of a beam clamped from one end and with springs at the other end versus the stiffness coefficient ratio R



approaches that of a clamped-free beam or a cantilever. Hence, the values of ω_{non} for the small values of R are actually the same as that of a cantilever beam. As R is raised, the four natural frequencies start to increase at various rates. Eventually, when $R_t = R_r = R \rightarrow \infty$ at $x = l$, the beam becomes very much like a clamped-clamped beam. Hence, its natural frequencies approach those of a clamped-clamped beam (see Example 6.5). Figure 6.16 shows a zoomed view of the first natural frequency of Fig. 6.15.

Another interesting case is to tune the natural frequency of a cantilever beam of a flexible support. For this, the springs at $x = l$ are set equal to zero to realize a free end, $R_t = R_r = R \rightarrow 0$, while adjusting R_t and R_r at the other end at $x = 0$ to tune the frequency to the desired range. Examples of the results are depicted in Figs. 6.17 and 6.18. One can see the significant drop of ω_{non} . In principle, as $R_t = R_r = R \rightarrow 0$ at $x = 0$, the case approaches that of a free-free beam, for which $\omega_{\text{non},1} \rightarrow 0$. This case demonstrates how one can tune the stiffness coefficients of a cantilever beam to match the experimental measurements, and hence attain an accurate model of the

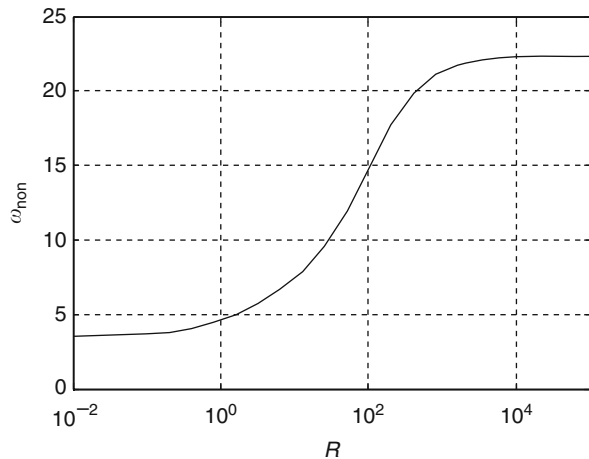


Fig. 6.16 A zoomed view of the first natural frequency of the beam of Fig. 6.15

Fig. 6.17 The first four natural frequencies of a cantilever beam with springs at its support versus the stiffness coefficient ratio R

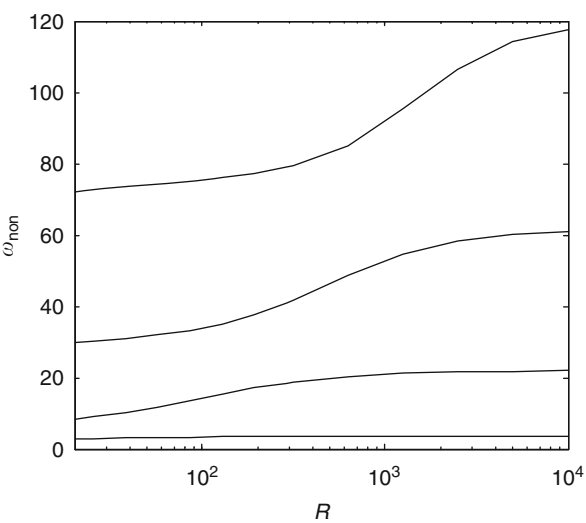
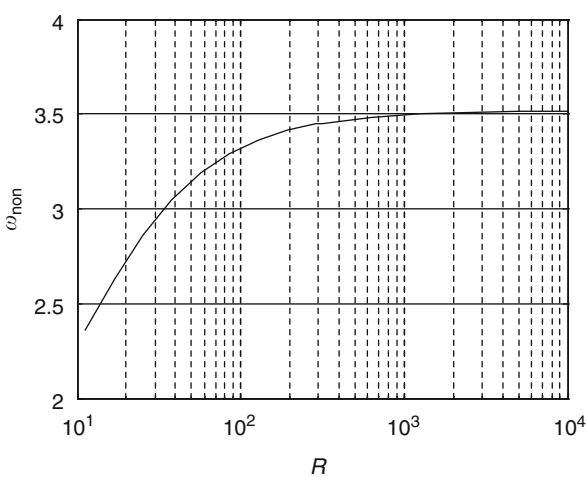


Fig. 6.18 The first natural frequency of the beam of Fig. 6.17

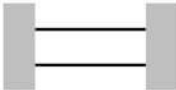
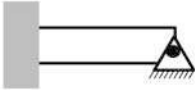
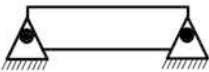
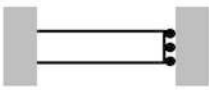
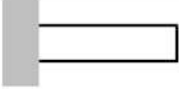



beam supports. Similar tuning can be conducted for clamped–clamped beams by adjusting R_l and R_r at both ends of the beam. This case will be left as an exercise. Values of ω_{non} of several interesting cases related to this example and other cases are tabulated in Table 6.1.

6.4.3 Cantilever Beam with a Lumped Mass at the Tip

Cantilever beams with proof masses at their tips represent a model of several MEMS devices, especially inertia sensors, such as accelerometers and gyroscopes. Next, we discuss determining the natural frequencies of such systems.

Table 6.1 The first four natural frequencies and modeshapes of common beams [17]

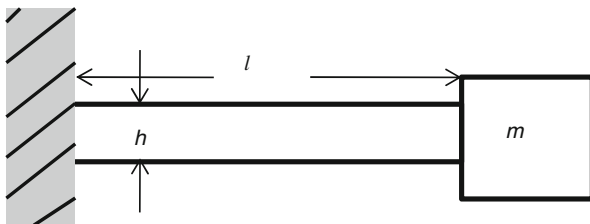
Beam Configuration	n	$\omega_{non,n}$	σ_n	$\phi_n(x)$
 Clamped-clamped	1	22.3733	0.982502	$\cosh(\sqrt{\omega_{non}} x) - \cos(\sqrt{\omega_{non}} x)$ $-\sigma_n [\sinh(\sqrt{\omega_{non}} x) - \sin(\sqrt{\omega_{non}} x)]$
	2	61.6728	1.00078	
	3	120.903	0.999966	
	4	199.859	1.0	
 Clamped-pinned	1	15.4182	1.0008	$\cosh(\sqrt{\omega_{non}} x) - \cos(\sqrt{\omega_{non}} x)$ $-\sigma_n [\sinh(\sqrt{\omega_{non}} x) - \sin(\sqrt{\omega_{non}} x)]$
	2	49.9649	1.0	
	3	104.248	1.0	
	4	178.27	1.0	
 Pinned-pinned	1	9.8696	-----	$\sin(\sqrt{\omega_{non}} x)$
	2	39.4784	-----	
	3	88.8264	-----	
	4	157.9137	-----	
 Clamped-guided	1	5.59332	0.9825	$\cosh(\sqrt{\omega_{non}} x) - \cos(\sqrt{\omega_{non}} x)$ $-\sigma_n [\sinh(\sqrt{\omega_{non}} x) - \sin(\sqrt{\omega_{non}} x)]$
	2	30.2258	1.0	
	3	74.6389	1.0	
	4	138.791	1.0	
 Clamped-free	1	3.51602	0.7341	$\cosh(\sqrt{\omega_{non}} x) - \cos(\sqrt{\omega_{non}} x)$ $-\sigma_n [\sinh(\sqrt{\omega_{non}} x) - \sin(\sqrt{\omega_{non}} x)]$
	2	22.0345	1.0185	
	3	61.6972	0.9992	
	4	120.902	1.0	
 Free-free	1	0	-----	$\cosh(\sqrt{\omega_{non}} x) + \cos(\sqrt{\omega_{non}} x)$ $-\sigma_n [\sinh(\sqrt{\omega_{non}} x) + \sin(\sqrt{\omega_{non}} x)]$
	2	22.3729	0.9825	
	3	61.6728	1.0008	
	4	120.9034	0.9999	

Example 6.7: Consider a cantilever beam with a lumped mass of mass m at its tip, Fig. 6.19. Determine the first four natural frequencies and show their variations with the mass m . Plot the modeshapes of the beam for the cases when m is equal to (a) 0.01 of the beam's mass, (b) the beam's mass, and (c) 100 times that of the beam's mass.

Solution: The boundary conditions of the beam in this case can be read from Eq. (6.13) at $x = 0$ and from Eq. (6.21a) and Eq. (6.21b) at $x = l$. Using Eq. (6.44) and Eq. (6.48), and after omitting the superscript “ \wedge ” for convenience, the nondimensional boundary conditions can be written as

$$\phi = 0; \quad \phi' = 0; \quad \text{at } x = 0 \quad (\text{a})$$

Fig. 6.19 A cantilever beam with a lumped mass at the tip



$$\phi'' = 0; \quad \phi''' + R_m \omega_{\text{non}}^2 \phi = 0; \quad \text{at } x = 1 \quad (\text{b})$$

where R_m is the ratio of the mass of the lumped mass to that of the cantilever beam, that is

$$R_m = \frac{m}{\rho A l}. \quad (\text{c})$$

Recalling Eq. (6.50), after omitting “ \wedge ”, Eq. (b) can be rewritten as

$$\phi'' = 0; \quad \phi''' + R_m \beta^4 \phi = 0; \quad \text{at } x = 1. \quad (\text{d})$$

Applying Eqs. (a) and (d) to Eq. (6.52) yields a 4×4 matrix for the constants of integration. Setting the determinant of this matrix equal to zero yields the characteristic equation, which is then solved numerically for β , and hence for ω_{non} for a given value of R_m . Figures 6.20 and 6.21 show the results. As seen from the figures, the first natural frequency drops from near 3.5, which is that of a cantilever beam with no mass, to zero for very large mass. Table 6.2 shows the first four modeshapes for the selected mass ratios R_m .

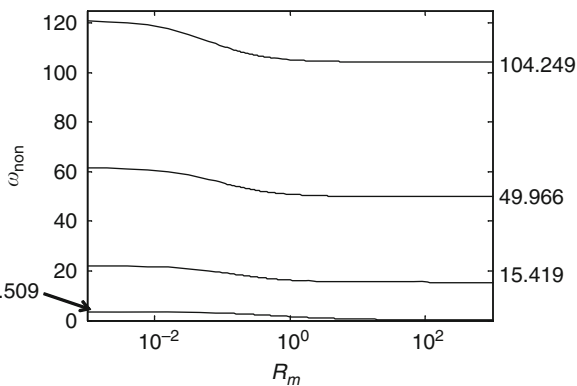


Fig. 6.20 The variation of the first four natural frequencies of the cantilever beam with a lumped mass at the tip versus the mass ratio $R_m = m/\rho A l$

Fig. 6.21 The variation of the first natural frequency of the cantilever beam with a lumped mass at the tip versus the mass ratio $R_m = m/\rho Al$

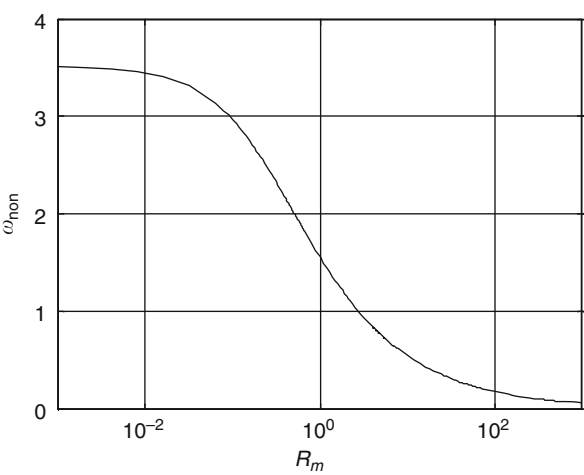


Table 6.2 The first four modeshapes of the beam for selected values of R_m

R_m	$n=1$	$n=2$	$n=3$	$n=4$
0.01				
1				
100				

6.5 The Effect of Axial Load on the Natural Frequency and the Buckling Limit

Axial force can be induced on microbeams with anchors or supports at both ends through actuation, such as electrothermal [18] and electrostatic [19], or due to induced residual stresses [14, 20]. Axial force changes the stiffness of the microbeam by increasing it in the case of a tensile force and decreasing it in the case of a compressive load. A compressive axial force can also induce buckling when it exceeds a certain instability threshold.

The nondimensional unforced and undamped equation of motion of a microbeam with an axial force is obtained by dropping the external forcing and damping terms in Eq. (6.11), substituting Eq. (6.44) into the outcome, and dropping the superscript

“^” for convenience, which yield

$$\frac{\partial^4 w}{\partial x^4} + \frac{\partial^2 w}{\partial t^2} - N_{\text{non}} \frac{\partial^2 w}{\partial x^2} = 0 \quad (6.53)$$

where $N_{\text{non}} = l^2 N / (EI)$ is the nondimensional axial load, which is positive for a tensile force and negative for a compressive force. The beam boundary conditions remain unchanged in the presence of an axial force for any combination of pinned and clamped supports. Other boundary conditions of nonzero displacement, such as free and guided ends, can be affected [21]. Example 6.8 demonstrates extracting the boundary conditions for a beam under an externally applied axial force with nonideal supports.

Next, we discuss the effect of the axial force on the natural frequency of microbeams. To derive the nondimensional eigenvalue problem, Eq. (6.48) is substituted into Eq. (6.53), which gives

$$\phi'''' - N_{\text{non}} \phi'' - \omega_{\text{non}}^2 \phi = 0. \quad (6.54)$$

Substituting Eq. (6.31) into Eq. (6.54) yields the below algebraic equation for the characteristic exponent s :

$$s^4 - N_{\text{non}} s^2 - \omega_{\text{non}}^2 = 0. \quad (6.55)$$

Solving Eq. (6.55) gives two roots, a positive root s_1^2 and a negative root s_2^2 :

$$s_1^2 = \frac{N_{\text{non}} + \sqrt{N_{\text{non}}^2 + 4\omega_{\text{non}}^2}}{2}; \quad s_2^2 = \frac{N_{\text{non}} - \sqrt{N_{\text{non}}^2 + 4\omega_{\text{non}}^2}}{2}. \quad (6.56)$$

From Eq. (6.31) and Eq. (6.56) and using the principle of superposition, the total solution of ϕ becomes

$$\phi(x) = A \cosh(s_1 x) + B \sinh(s_1 x) + C \cos(\sigma x) + D \sin(\sigma x) \quad (6.57)$$

where σ is the real part of s_2 ($s_2 = i\sigma$) and A , B , C , and D are determined from the boundary conditions of the beam. As an example, applying the boundary conditions of a pinned–pinned beam on Eq. (6.57) yields the following four algebraic equations:

$$\phi(0) = A + C = 0 \quad (6.58a)$$

$$\phi''(0) = s_1^2 A - \sigma^2 C = 0 \quad (6.58b)$$

$$\phi(1) = A \cosh(s_1) + B \sinh(s_1) + C \cos(\sigma) + D \sin(\sigma) = 0 \quad (6.58c)$$

$$\phi''(1) = s_1^2 A \cosh(s_1) + s_1^2 B \sinh(s_1) - \sigma^2 C \cos(\sigma) + \sigma^2 D \sin(\sigma) = 0. \quad (6.58d)$$

Casting Eq. (6.58a)–Eq. (6.58d) into a matrix format and setting the determinant of the matrix equal to zero, to preclude the possibility of a trivial solution, yields

$$\sin \sigma = 0 \Rightarrow \sigma = n\pi. \quad (6.59)$$

Recalling $s_2 = i\sigma$ and using Eq. (6.56) give the dependence of the natural frequency on the axial force:

$$\omega_{\text{non}} = n\pi\sqrt{N_{\text{non}} + n^2\pi^2}. \quad (6.60)$$

Note that setting N_{non} equal to zero reduces ω_{non} to the familiar result of a hinged–hinged beam with no axial load $\omega_{\text{non}} = n^2\pi^2$. Note also that a positive (tensile) N_{non} leads to an increase in ω_{non} and a negative (compressive) N_{non} leads to a decrease in ω_{non} . At a critical compressive load, the natural frequency is reduced to zero, at which the beam is forced to buckle. This is similar to the pull-in instability since in both phenomena the stiffness and the natural frequency of the structure reach zero. Setting Eq. (6.60) equal to zero and solving for the critical force yield

$$(N_{\text{non}})_{\text{critical}} = -n^2\pi^2. \quad (6.61)$$

Recalling the definition of N_{non} and solving for the dimensional critical axial force give

$$P_{\text{cr}} = \frac{n^2\pi^2 EI}{l^2} \quad (6.62a)$$

where P_{cr} is the absolute value of the dimensional compressive axial load. Setting $n = 1$ yields the critical axial force of the first mode (the first buckling limit)

$$P_{\text{cr}} = \frac{\pi^2 EI}{l^2}. \quad (6.62b)$$

The expression of Eq. (6.62b) is the same as the so-called the Euler-buckling limit of a pinned–pinned beam. Figure 6.22 shows the variation of the first three natural frequencies of the beam versus the axial force plotted based on Eq. (6.60). Following a similar procedure as the above, the Euler-buckling limit for beams of other boundary conditions is obtained. The results of some cases are presented in Table 6.3.

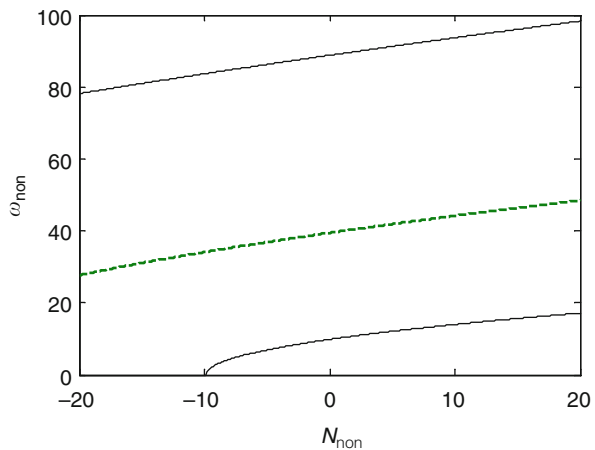


Fig. 6.22 The variation of the first three natural frequencies of a pinned–pinned beam under an axial force

Table 6.3 The buckling limits of some common beams [21, 22]

Boundary conditions	σ	First critical load
Pinned–pinned	$n\pi$	$\frac{\pi^2 EI}{l^2}$
Guided–guided	$n\pi$	$\frac{\pi^2 EI}{l^2}$
Guided–pinned	$\frac{(2n - 1) \pi}{2}$	$\frac{\pi^2 EI}{4l^2}$
Clamped–clamped	$2n\pi$	$\frac{4\pi^2 EI}{l^2}$
Clamped–guided	$n\pi$	$\frac{\pi^2 EI}{l^2}$
Clamped–pinned	4.493, 7.72, 10.9, ...	$\frac{\pi^2 EI}{(0.699l)^2}$
Clamped–free	$\frac{(2n - 1) \pi}{2}$	$\frac{\pi^2 EI}{4l^2}$

Example 6.8: A clamped–clamped beam with nonideal supports and induced residual stresses can be modeled using the model of Fig. 6.23a with rotational and translational springs and an applied axial force. Derive the dimensional expressions of the boundary conditions of the beam in this case.

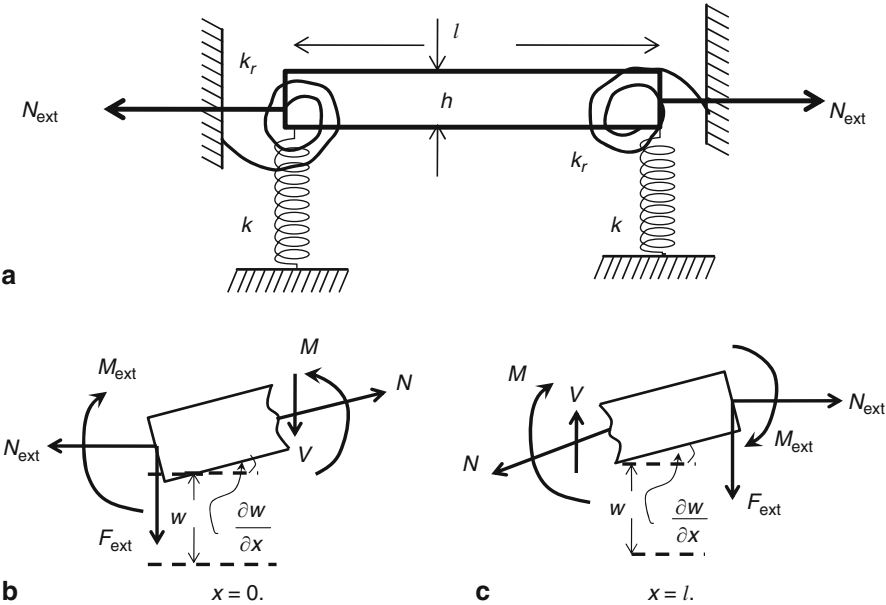


Fig. 6.23 **a** A beam with rotational and translational springs under an applied axial force. **b** and **c** Free-body diagrams near the edges of the beam

Solution: A free-body diagram near each edge is sketched, Figs. 6.23b and 6.23c, to indicate both the external forces and moments, due to the springs and the axial force, and the internal reaction forces and moments in accordance with Fig. 6.1b. Applying moments and forces balance, on the vertical direction, on the beam portion near $x=0$ yields

$$M - M_{\text{ext}} = 0 \Rightarrow EI \frac{\partial^2 w(0, t)}{\partial x^2} = k_r \frac{\partial w(0, t)}{\partial x} \quad (\text{a})$$

$$-F_{\text{ext}} - V + N \frac{\partial w(0, t)}{\partial x} = 0 \Rightarrow \frac{\partial}{\partial x} \left(EI \frac{\partial^2 w(0, t)}{\partial x^2} \right) = N \frac{\partial w(0, t)}{\partial x} - k w(0, t). \quad (\text{b})$$

Similarly, the boundary conditions at $x=l$ are

$$-M - M_{\text{ext}} = 0 \Rightarrow EI \frac{\partial^2 w(l, t)}{\partial x^2} = -k_r \frac{\partial w(l, t)}{\partial x} \quad (\text{c})$$

$$-F_{\text{ext}} + V - N \frac{\partial w(l, t)}{\partial x} = 0 \Rightarrow \frac{\partial}{\partial x} \left(EI \frac{\partial^2 w(l, t)}{\partial x^2} \right) = N \frac{\partial w(l, t)}{\partial x} + k w(l, t). \quad (\text{d})$$

Note that $N = N_{\text{ext}}$ based on the force balance in the horizontal direction.

6.6 The Orthogonality of Modeshapes

An important feature of the modeshapes of beams is their orthogonality to each other. To explain this concept, without any loss of generality, consider the simple case of the undamped-free vibrations of a beam with no axial force. According to Eq. (6.49), the nondimensional equation governing the i th natural frequency and modeshape can be written as

$$\phi_i'''' - \omega_{\text{non},i}^2 \phi_i = 0. \quad (6.63\text{a})$$

Consider now the equation of the j th modeshape and natural frequency

$$\phi_j'''' - \omega_{\text{non},j}^2 \phi_j = 0. \quad (6.63\text{b})$$

Next, multiply Eq. (6.63a) with ϕ_j , Eq. (6.63b) with ϕ_i , and integrate both equations over the domain of the beam, which is from 0 to 1:

$$\int_0^1 \phi_j (\phi_i'''' - \omega_{\text{non},i}^2 \phi_i) dx = 0 \quad (6.64\text{a})$$

$$\int_0^1 \phi_i (\phi_j'''' - \omega_{\text{non},j}^2 \phi_j) dx = 0. \quad (6.64\text{b})$$

Distributing the integrals on the brackets then subtracting Eq. (6.64a) from Eq. (6.64b) yield

$$\int_0^1 \phi_j \phi_i'''' dx - \int_0^1 \phi_i \phi_j'''' dx = (\omega_{\text{non},i}^2 - \omega_{\text{non},j}^2) \int_0^1 \phi_i \phi_j dx. \quad (6.65)$$

To simplify Eq. (6.65), the first integral of Eq. (6.65) is integrated by parts for four consecutive times:

$$\int_0^1 \phi_j \phi_i'''' dx = \int_0^1 \phi_i \phi_j'''' dx + [\phi_j \phi_i''' - \phi_j' \phi_i'' + \phi_j'' \phi_i' - \phi_j''' \phi_i]_0^1. \quad (6.66)$$

Substituting Eq. (6.66) into Eq. (6.65) yields

$$(\omega_{\text{non},i}^2 - \omega_{\text{non},j}^2) \int_0^1 \phi_i \phi_j dx = [\phi_j \phi_i''' - \phi_j' \phi_i'' + \phi_j'' \phi_i' - \phi_j''' \phi_i]_0^1. \quad (6.67)$$

It can be shown that the right-hand side of Eq. (6.67) vanishes for beams of any combination of hinged, clamped, and free boundary conditions. In this case, Eq. (6.67) is reduced to

$$(\omega_{\text{non},i}^2 - \omega_{\text{non},j}^2) \int_0^1 \phi_i \phi_j dx = 0. \quad (6.68)$$

For distinct eigenvalues ($\omega_{\text{non},i} \neq \omega_{\text{non},j}$), Eq. (6.68) is satisfied if and only if

$$\int_0^1 \phi_i \phi_j dx = 0. \quad (6.69a)$$

Equation (6.69a) represents a statement of the orthogonality of modeshapes. A similar conclusion can be proven for beams with “self-adjoint” stiffness and mass operators [1], which encompass most of the known boundary conditions in MEMS. The statement of orthogonality for the case of a beam attached to a tip mass takes a slightly different form [1]. In the case of $i=j$, Eq. (6.68) is readily satisfied, i.e., the integral of Eq. (6.69a) can yield any nonzero value. For convenience, when $i=j$, it is customary to normalize the modeshapes such that

$$\int_0^1 \phi_j^2 dx = 1. \quad (6.69b)$$

Hence, a modeshape that satisfies Eq. (6.69a) and Eq. (6.69b) is called orthonormal. The orthonormality condition can be summarized in the below equation:

$$\int_0^1 \phi_i \phi_j dx = \delta_{ij} = \begin{cases} 1, & i = j \\ 0, & i \neq j \end{cases} \quad (6.70)$$

where δ_{ij} is the Kronecker delta. Note from Eq. (6.64a) or Eq. (6.64b) that when $i=j$,

$$\int_0^1 \phi_j \phi_j'''' dx = \omega_{\text{non},j}^2 \int_0^1 \phi_j^2 dx = \omega_{\text{non},j}^2. \quad (6.71)$$

This important feature of the orthogonality or the orthonormality of the modeshapes forms the basis of solving the free and forced vibration problems of beams both exactly, in the case of simple linear problems, and approximately, in the case of more complicated problems using the Galerkin method.

6.7 Forced Vibrations and Modal Analysis

Thus far, we have analyzed the static and eigenvalue problems of microbeams. The next step in studying dynamics is to investigate the response of microbeams to initial conditions and forced vibration. In the case of a beam with simple geometry, uniform properties, and a linear equation and boundary conditions, the problem can be solved exactly by expanding the response in terms of the beam modeshapes and unknown coefficients called modal coordinates. This transforms the partial differential equation of the beam into a system of ordinary differential equations in time in terms of the modal coordinates. The differential equations can be then solved exactly for simple cases or integrated in time for complicated geometries or material properties to simulate the dynamic response. This procedure is called modal analysis.

To facilitate the procedure of modal analysis of beams, Eq. (6.11) is normalized by substituting Eq. (6.44) into it, which yields after dropping the superscript “ \wedge ”

$$\frac{\partial^4 w}{\partial x^4} - N_{\text{non}} \frac{\partial^2 w}{\partial x^2} + \frac{\partial^2 w}{\partial t^2} + c_{\text{non}} \frac{\partial w}{\partial t} = F_{\text{non}} \quad (6.72)$$

where the nondimensional parameters of Eq. (6.72) are defined as below:

$$c_{\text{non}} = \frac{cl^4}{EIT}; \quad N_{\text{non}} = \frac{l^2 N}{EI}; \quad F_{\text{non}} = \frac{l^3 F}{EI}. \quad (6.73)$$

6.7.1 Undamped Response with no Axial Load

We start by considering the simple case of the undamped vibration of beams with no axial load. The nondimensional equation of motion after setting N_{non} and c_{non} equal to zero in Eq. (6.72) is written as

$$\frac{\partial^4 w}{\partial x^4} + \frac{\partial^2 w}{\partial t^2} = F_{\text{non}}. \quad (6.74)$$

Next, using the expansion theorem [1], the displacement of the beam is expanded in terms of its modeshapes and modal coordinates $u_i(t)$ as

$$w(x, t) = \sum_{i=1}^n u_i(t) \phi_i(x) \quad (6.75)$$

where n is the number of modes. Note here that $\phi_i(x)$ satisfies the eigenvalue problem, Eq. (6.27) or Eq. (6.63a). Usually n is not known upfront. A convergence study needs to be conducted to determine the minimum number of modes that is needed to capture the dynamic behavior accurately. Generally, the first few modes (1–6) are the most important with a weaker effect of the modes of higher order number. Also, some modes may not be activated at all, such as antisymmetric modes in the case of beams with symmetric forces and properties. To proceed, Eq. (6.75) is substituted into Eq. (6.74):

$$\sum_{i=1}^n u_i(t) \phi_i''''(x) + \sum_{i=1}^n \ddot{u}_i(t) \phi_i(x) = F_{\text{non}} \quad (6.76a)$$

where the superscript “prime” indicates spatial derivative and the “dot” indicates temporal derivative. Then Eq. (6.76a) is multiplied by the modeshape ϕ_j and is integrated over the beam domain from 0 to 1:

$$\int_0^1 \left\{ \phi_j(x) \left(\sum_{i=1}^n u_i(t) \phi_i''''(x) + \sum_{i=1}^n \ddot{u}_i(t) \phi_i(x) \right) = F_{\text{non}} \right\} dx. \quad (6.76b)$$

Next, $\phi_i''''(x)$ in Eq. (6.76b) is replaced with $\omega_{\text{non},i}^2 \phi_i$ according to Eq. (6.63a). Then, distributing the integral over each term of the equation gives

$$\sum_{i=1}^n u_i(t) \int_0^1 \phi_j(x) \omega_{\text{non},i}^2 \phi_i dx + \sum_{i=1}^n \ddot{u}_i(t) \int_0^1 \phi_i(x) \phi_j(x) dx = \int_0^1 \phi_j(x) F_{\text{non}} dx. \quad (6.76c)$$

The two summation terms of Eq. (6.76c) can be simplified by making use of the orthonormality of the modeshapes, Eq. (6.70) and Eq. (6.71), which reduces Eq. (6.76c) to

$$\ddot{u}_j(t) + \omega_{\text{non},j}^2 u_j(t) = f_j; \quad j = 1, \dots, n \quad (6.77)$$

where $f_j = \int_0^1 \phi_j F_{\text{non}} dx$ is the modal force (the projected force with respect to the modeshape). Equation (6.77) represents a system of linear uncoupled second-order ordinary differential equations. Each equation looks similar to a single-degree-of-freedom model. Hence, the method of solution for the steady-state response follows the procedure of Chap. 2, which depends on the forcing type whether it is harmonic or arbitrary. Once the equations are solved for the modal coordinates, the results are substituted into Eq. (6.75) to yield the final results of the dynamic behavior of the beam.

To determine the transient response of the beam, the **initial conditions** (initial displacement and velocity) need to be utilized. Toward this, consider the below generic form of the initial conditions of the beam:

$$w(x, 0) = w_0(x) \quad (6.78a)$$

$$\dot{w}(x, 0) = v_0(x) \quad (6.78b)$$

where $w_0(x)$ and $v_0(x)$ are initial shape and velocity profile of the beam, respectively. Next, the initial conditions are transformed in terms of the modal coordinates. For this, Eq. (6.75) is substituted into Eq. (6.78a) and Eq. (6.78b)

$$\sum_{i=1}^n u_i(0)\phi_i(x) = w_0(x) \quad (6.79a)$$

$$\sum_{i=1}^n \dot{u}_i(0)\phi_i(x) = v_0(x). \quad (6.79b)$$

Next, Eq. (6.79a) and Eq. (6.79b) are multiplied by the modeshape ϕ_j . The outcome are then integrated over the beam domain from 0 to 1 and the orthonormality condition is imposed, which yield

$$u_j(0) = \int_0^1 \phi_j(x)w_0(x)dx \quad (6.80a)$$

$$\dot{u}_j(0) = \int_0^1 \phi_j(x)v_0(x)dx. \quad (6.80b)$$

To obtain the transient response, Eq. (6.77) is solved for the j th mode with $f_j = 0$ according to the method of Sect. 2.2 and using the initial conditions of Eq. (6.80a) and Eq. (6.80b). The results are then substituted into Eq. (6.75) to yield the physical response, in the case of no external forcing, or are added to the steady-state forced modal response and then are substituted into Eq. (6.75) for the total physical response in the case of external forcing.

Example 6.9: Determine the steady-state response of a hinged–hinged beam subjected to a fully distributed harmonic force over the length of the beam of amplitude F_0 . Evaluate the response of the beam at its midpoint when driven at a frequency equal half its fundamental natural frequency. Discuss the convergence of the solution and how many modes are needed.

Solution: We recall the nondimensional modeshape and natural frequency of a pinned–pinned beam:

$$\omega_{\text{non},j} = j\pi; \quad \phi_j = A_j \sin(j\pi x) \quad (a)$$

where A_j is an arbitrary constant. The first step is to fix the value of A_j by imposing the normality condition, Eq. (6.69b), which gives

$$A_j = 1/\sqrt{\int_0^1 \phi_j^2 dx} = \sqrt{2}. \quad (b)$$

Next, the modal force f_j is calculated. The nondimensional form of the external force is written, based on Eq. (6.73), as

$$F_{\text{non}} = \frac{l^3 F_0 \cos(\Omega t)}{EI} \quad (c)$$

where Ω is a nondimensional frequency. Hence, the modal force is calculated as

$$f_j = \int_0^1 \phi_j F_{\text{non}} = F_{\text{non}} \int_0^1 \sqrt{2} \sin(j\pi x) dx = \sqrt{2} F_{\text{non}} \left[\frac{1 - \cos(j\pi)}{j\pi} \right]. \quad (\text{d})$$

Note from Eq. (d) that the even antisymmetric modes ($j = 2, 4, \dots$) are orthogonal to the symmetric force, and hence they result in zero f_j . The modal differential equations, Eq. (6.77), can be written as

$$\ddot{u}_j(t) + (j\pi)^2 u_j(t) = \frac{\sqrt{2} l^3 F_0}{EI} \left[\frac{1 - \cos(j\pi)}{j\pi} \right] \cos(\Omega t); \quad j = 1, \dots, n. \quad (\text{e})$$

The convolution integral approach of Sect. 2.6 can be generally used for any form of excitation to yield the steady-state response in addition to the transient response assuming trivial initial conditions. Alternatively, in the case of Eq. (e) with the harmonic excitation, the method of Sect. 2.3 can be also used for the steady-state response (or even an easier method is to substitute $u_j = B e^{i\Omega t}$ and then solve for B). Using the second approach gives

$$u_j(t) = \frac{\sqrt{2} l^3 F_0}{EI} \left[\frac{1 - \cos(j\pi)}{j\pi} \right] \frac{\cos(\Omega t)}{(j\pi)^2 - \Omega^2}. \quad (\text{f})$$

Therefore, based on Eq. (6.75), the beam deflection becomes

$$w(x, t) = \sum_{j=1}^n \frac{2l^3 F_0}{EI} \left[\frac{1 - \cos(j\pi)}{j\pi} \right] \frac{\sin(j\pi x)}{(j\pi)^2 - \Omega^2} \cos(\Omega t). \quad (\text{g})$$

One can note that the expression of Eq. (g) is singular when $\Omega = j\pi$, i.e., whenever the system is driven at a frequency equal to one of the beam's natural frequencies. These are, as expected, the **resonance frequencies**. Hence, beams, as well as all distributed-parameter systems, possess infinite resonance frequencies corresponding to their infinite natural frequencies.

As mentioned before, the even antisymmetric modes ($j = 2, 4, \dots$) do not participate in the response (yield zero components in the solution series). Hence, Equation (g) can be further simplified by excluding the even modes, which is done by replacing the index j with $2j - 1$ and replacing $1 - \cos(j\pi)$ by 2:

$$w(x, t) = \sum_{j=1}^n \frac{4l^3 F_0}{EI(2j - 1)\pi} \left(\frac{\sin[(2j - 1)\pi x]}{(2j - 1)^2 \pi^2 - \Omega^2} \right) \cos(\Omega t). \quad (\text{h})$$

To simulate the dynamic response of the beam at $x = 1/2$ and $\Omega = \pi^2/2$, these values are substituted into Eq. (h)

$$w(0.5, t) = \sum_{j=1}^n \beta_j \cos\left(\frac{\pi^2}{2} t\right) \quad (\text{i})$$

Table 6.4 The modal coefficients β_j of the beam of Example 6.9

j : odd mode number	$\beta_j / \left(\frac{8l^3 F_0}{EI\pi^3} \right)$
1	1.0
2	-0.02
3	0.0041
4	-0.0015
5	0.0007
6	-0.00038

where

$$\beta_j = \frac{4l^3 F_0}{EI(2j-1)\pi} \left(\frac{\sin[(2j-1)\pi/2]}{(2j-1)^2 \pi^2 - \frac{\pi^2}{2}} \right). \quad (j)$$

Table 6.4 shows the calculated values of β_j for the first six odd modes. As noted, accurate dynamic response is obtained in this case using the first two odd modes. Even using a single mode yields sufficient accuracy. Care however should be taken whenever truncating the series solution to a single mode since this does not allow the detection of the higher order mode resonances nor any other possible interaction among the various modes, which is especially important for nonlinear systems. The final expression of the beam dynamical response at $x = l/2$ and $\Omega = \pi^2/2$ using two modes are expressed as below:

$$w(0.5, t) = \frac{1}{\left(\frac{8l^3 F_0}{EI\pi^3} \right)} \left[\cos\left(\frac{\pi^2}{2}t\right) - 0.02 \cos\left(\frac{\pi^2}{2}t\right) \right]. \quad (k)$$

6.7.2 Adding Axial Force

The nondimensional equation of motion with an axial load is obtained by setting c_{non} equal to zero in Eq. (6.72):

$$\frac{\partial^4 w}{\partial x^4} - N_{\text{non}} \frac{\partial^2 w}{\partial x^2} + \frac{\partial^2 w}{\partial t^2} = F_{\text{non}}. \quad (6.81)$$

In this case, the displacement of the beam can be expanded in terms of the modeshapes of Eq. (6.54), which accounts for the effect of the axial load. The equation of the i th mode is written as

$$\phi_i'''' - N_{\text{non}} \phi_i'' - \omega_{\text{non},i}^2 \phi_i = 0. \quad (6.82a)$$

From which,

$$\phi_i''''(x) = N_{\text{non}} \phi_i'' + \omega_{\text{non},i}^2 \phi_i. \quad (6.82b)$$

Next, Eq. (6.75) is substituted into Eq. (6.81):

$$\sum_{i=1}^n u_i(t) \phi_i'''(x) - N_{\text{non}} \sum_{i=1}^n u_i(t) \phi_i''(x) + \sum_{i=1}^n \ddot{u}_i(t) \phi_i(x) = F_{\text{non}}. \quad (6.83a)$$

Then, Eq. (6.82b) is substituted into Eq. (6.83a):

$$\begin{aligned} \sum_{i=1}^n u_i(t) [N_{\text{non}} \phi_i'' + \omega_{\text{non},i}^2 \phi_i] - N_{\text{non}} \sum_{i=1}^n u_i(t) \phi_i''(x) + \sum_{i=1}^n \ddot{u}_i(t) \phi_i(x) &= F_{\text{non}} \\ \Rightarrow \sum_{i=1}^n u_i(t) \omega_{\text{non},i}^2 \phi_i + \sum_{i=1}^n \ddot{u}_i(t) \phi_i(x) &= F_{\text{non}}. \end{aligned} \quad (6.83b)$$

Equation (6.83b) is then multiplied by the modeshape ϕ_j , the outcome is integrated over the beam domain from 0 to 1, and the orthonormality of the modeshapes is imposed, which yield

$$\ddot{u}_j(t) + \omega_{\text{non},j}^2 u_j(t) = f_j; \quad j = 1, \dots, n. \quad (6.84)$$

Equation (6.84) looks similar to Eq. (6.77). The difference however is that $\omega_{\text{non},j}^2$ in Eq. (6.84) is governed by Eq. (6.82a) with the effect of axial force embedded in the frequency term $\omega_{\text{non},j}^2$. Also, the modeshape ϕ_j to be used in Eq. (6.54) is different and is governed by Eq. (6.82a) in the case of axial force. The method of solving Eq. (6.84) follows the same procedure of Sect. 6.7.1.

6.7.3 Adding Damping

Modeling damping is generally a challenging task for microstructures. However, for beams operating in air or gases, if squeeze-film damping is not dominant, damping can be reasonably assumed to be viscous and linearly proportional to the velocity of the beam through a constant coefficient. In this case, the damping force can be expressed as

$$F_d = -c_{\text{non}} \frac{\partial w}{\partial t}. \quad (6.85)$$

The equation of motion of the beam including damping is as given in Eq. (6.72). To include damping in the modal equations, the viscous damping term of Eq. (6.85) is multiplied by $\phi_j(x)$, then the outcome is integrated over the beam domain and the

orthonormality condition is imposed as below:

$$\begin{aligned} \int_0^1 \phi_j(x) \left(-c_{\text{non}} \sum_{i=1}^n \dot{u}_i(t) \phi_i(x) \right) dx \\ = -c_{\text{non}} \sum_{i=1}^n \dot{u}_i(t) \int_0^1 \phi_j(x) \phi_i(x) dx = -c_{\text{non}} \dot{u}_j(t). \end{aligned} \quad (6.86)$$

Adding Eq. (6.86) to either Eq. (6.77) or Eq. (6.84) gives the damped modal equations:

$$\ddot{u}_j(t) + 2\zeta_j \omega_{\text{non},j} \dot{u}_j(t) + \omega_{\text{non},j}^2 u_j(t) = f_j; \quad j = 1, \dots, n \quad (6.87)$$

where ζ_j is the modal damping ratio defined as

$$\zeta_j = \frac{c_{\text{non}}}{2\omega_{\text{non},j}}. \quad (6.88)$$

Another approach to include damping in the model is to assign ζ_j directly to Eq. (6.87) for each mode based on experimental measurements or experience [23]. Each equation of Eq. (6.87) looks similar to an equation of a single-degree-of-freedom system. Hence, it is solved using the same methods of Chap. 2 depending on the nature of f_j .

6.8 A Nonlinear Model of Beams with Midplane Stretching

In this section, we discuss the derivation of the nonlinear equation of motion of beams with immovable edges, which induce the so-called midplane stretching. Midplane stretching is by far the most significant source of geometric nonlinearity in MEMS. It is induced when a beam undergoes moderately large deflection compared to its thickness. In this case, the beam tends to stretch and undergo large deformation in response to large forcing. This induces tensile axial stress, thereby changing the stiffness of the beam in a nonlinear way that resembles a cubic effect. The induced axial stress couples the in-plane and out-of-plane motions of the beam. Midplane stretching affects microstructures, beams, plates, and diaphragms of clamped or near fixed edge conditions.

Here, we assume planar motion, linear stress–strain law, and initially straight beam. For simplicity, the beam properties E , I , A , and ρ are assumed uniform and constant. The effects of rotary inertia and transverse shear are neglected. Also, nonlinearities due to inertia and curvature are neglected since they are much weaker than the midplane stretching nonlinearity. A Newtonian dynamics approach is followed [24]. An alternative derivation based on Hamilton’s principle is presented in Appendix A.

First, geometrical relationships are derived. For this, consider Fig. 6.24, which shows a schematic of a segment of the beam centerline before deformation, with

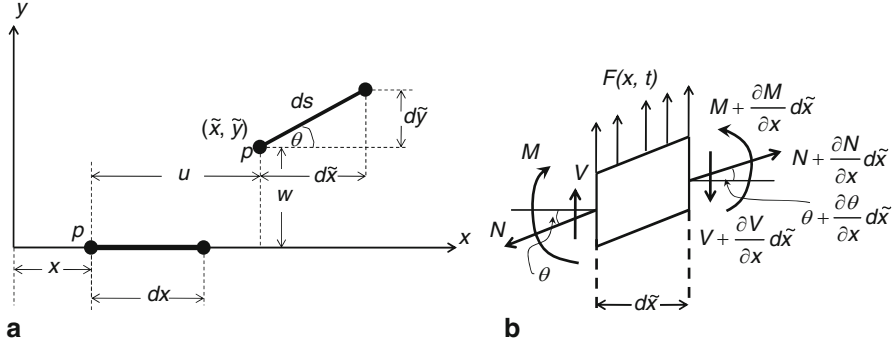


Fig. 6.24 **a** A segment on the beam before and after deformation. **b** A free-body diagram of an element on the beam

length dx , and after deformation with a new length ds . The deformed element undergoes an axial displacement $u(x, t)$ and a vertical displacement $w(x, t)$ (note that in linear theory, u is neglected). The position of point p on the element after deformation is expressed as

$$\tilde{x} = x + u; \quad \tilde{y} = w. \quad (6.89)$$

The variation of the position on the deformed element is expressed by taking derivative of Eq. (6.89) as

$$d\tilde{x} = dx + \frac{\partial u}{\partial x} dx = dx (1 + u'); \quad d\tilde{y} = \frac{\partial w}{\partial x} dx = w' dx \quad (6.90)$$

where the prime denotes derivative with respect to x . Hence, using Eq. (6.90), the length of the deformed element can be expressed as

$$ds = \sqrt{d\tilde{x}^2 + d\tilde{y}^2} = \sqrt{(1 + u')^2 + w'^2} dx. \quad (6.91)$$

The axial strain ε is defined as the normalized change of length of the beam element, that is

$$\varepsilon = \frac{ds - dx}{dx} = \sqrt{(1 + u')^2 + w'^2} - 1. \quad (6.92a)$$

Next, ε is expanded in Taylor series and terms up to cubic order in w' are retained (the axial displacement and its derivative are assumed smaller than those due to bending and of the same order as the quadratic bending terms)

$$\varepsilon \approx u' + \frac{w'^2}{2} + \dots \quad (6.92b)$$

From Fig. 6.24a, the following relationships for the deformation angle are derived:

$$\sin \theta = \frac{d\tilde{y}}{ds}; \quad \cos \theta = \frac{d\tilde{x}}{ds}. \quad (6.93a)$$

Substituting Eq. (6.90) and Eq. (6.91) into Eq. (6.93a) gives

$$\sin \theta = \frac{w'}{\sqrt{(1+u')^2 + w'^2}}; \quad \cos \theta = \frac{1+u'}{\sqrt{(1+u')^2 + w'^2}}. \quad (6.93b)$$

Expanding in Taylor series and keeping terms up to cubic order in w' gives

$$\sin \theta \approx w' - u'w' - \frac{w'^3}{3} + \dots; \quad \cos \theta \approx 1 - \frac{w'^2}{2} + \dots. \quad (6.93c)$$

To analyze the axial load on the other end of the deformed element, where the deformed angle is $\theta + \theta' d\tilde{x}$ as shown in Fig. 6.24b, the below trigonometric relationships are expanded in Taylor series to the first order:

$$\cos(\theta + \theta' d\tilde{x}) \approx \cos \theta + (\cos \theta)' d\tilde{x} + \dots \quad (6.94a)$$

$$\sin(\theta + \theta' d\tilde{x}) \approx \sin \theta + (\sin \theta)' d\tilde{x} + \dots. \quad (6.94b)$$

Now consider the free-body diagram of the deformed beam element of Fig. 6.24a. Applying Newton's second law in the horizontal direction gives

$$(N + N' d\tilde{x}) \cos(\theta + \theta' d\tilde{x}) - N \cos \theta = \rho A d\tilde{x} \ddot{u} \quad (6.95a)$$

where the double dots refer to two consecutive time derivatives. Substituting Eq. (6.94a) into Eq. (6.95a) and dropping the higher order terms in $d\tilde{x}$ yield

$$(N \cos \theta)' = \rho A \ddot{u}. \quad (6.95b)$$

Applying Newton's second law in the vertical direction gives

$$V - (V + V' d\tilde{x}) + F d\tilde{x} - N \sin \theta + (N + N' d\tilde{x}) \sin(\theta + \theta' d\tilde{x}) = \rho A d\tilde{x} \ddot{w}. \quad (6.96a)$$

Substituting Eq. (6.94b) into Eq. (6.96a) and dropping the higher order terms in $d\tilde{x}$ yield

$$-V' + F + (N \sin \theta)' = \rho A \ddot{w}. \quad (6.96b)$$

The moment balance and the relationships between the moment and shear and the moment and curvature remain unchanged from Sect. 6.1. Hence, Eqs. (6.4)–(6.9) still apply here. Next, the axial force is related to the axial strain using Eq. (6.92b) as

$$N = EA\varepsilon = EA \left(u' + \frac{w'^2}{2} + \dots \right). \quad (6.97)$$

Substituting Eq. (6.97) into Eq. (6.95b) and Eq. (6.95b), and Eq. (6.9) and Eq. (6.97) into Eq. (6.96b), and dropping the higher order terms yield, respectively

$$\rho A \ddot{u} - E A u'' = E A \left(\frac{w'^2}{2} \right)' \quad (6.98a)$$

$$\rho A \ddot{w} + E I w'''' = E A \left(u' w' + \frac{w'^3}{2} \right)' + F. \quad (6.98b)$$

Equations (6.98a) and (6.98b) represent two coupled nonlinear partial differential equations governing the dynamics of beams with midplane stretching in both axial and transversal directions. A simplification can be made in the case of slender beams of small radius of gyration $r = \sqrt{I/A}$. In this case, the axial natural frequency is much higher than the transversal natural frequency. Hence, the inertia term $\rho A \ddot{u}$ in Eq. (6.98a) can be neglected indicating that the axial deformation is mainly induced due to the transversal deformation only. Thus, Eq. (6.98a) is reduced to

$$u'' = - \left(\frac{w'^2}{2} \right)' \quad (6.99)$$

Equation (6.99) shows clearly that the axial deformation is of the same order as of the quadratic transversal deformation. Next, Eq. (6.99) is integrated twice with respect to x :

$$u' = - \frac{w'^2}{2} + c_1(t) \quad (6.100a)$$

$$u = - \frac{1}{2} \int_0^x w'^2 dx + c_1(t)x + c_2(t) \quad (6.100b)$$

where $c_1(t)$ and $c_2(t)$ are constants of integration (constants in space and can be variable in time). To solve for these constants, boundary conditions for the axial motion are needed. As an example, we assume the beam is fixed axially from one end while an axial force $N_1(t)$ is applied at its other end, which causes axial deformation. Accordingly, the axial boundary conditions can be assumed as

$$u(0, t) = 0; \quad u(l, t) = \frac{N_1 l}{EA}. \quad (6.101)$$

Substituting Eq. (6.101) into Eq. (6.100a) and Eq. (6.100b) gives

$$c_1(t) = \frac{N_1(t)}{EA} + \frac{1}{2l} \int_0^l w'^2 dx; \quad c_2(t) = 0. \quad (6.102)$$

Substituting Eq. (6.102) into Eq. (6.100a) and then the outcome into Eq. (6.98b) yield

$$\rho A \ddot{w} + E I w'''' = w'' \left(N_1(t) + \frac{EA}{2l} \int_0^l w'^2 dx \right) + F. \quad (6.103)$$

Equation (6.103) is a simplified nonlinear equation that is commonly used to model beams with midplane stretching. Equation (6.103) requires four boundary conditions for the transversal displacement, which are similar to those discussed in previous sections. Note that the midplane stretching term, the integral term, shows up in Eq. (6.103) in the form of a cubic nonlinearity.

6.9 Other Nonlinear Models of Beams

In addition to midplane stretching, there are the rotary inertia effect and the curvature nonlinearities, which can contribute to the response of a beam if it undergoes significant large displacement. These are weaker than midplane stretching, in the case of beams with immovable boundary conditions. Using a full nonlinear Euler–Bernoulli beam model, the following generic equations including rotary inertia, curvature nonlinearities, and midplane stretching can be derived [24]

$$\begin{aligned} \rho A \ddot{u} - (EA u')' &= \left[EA \left(\frac{w'^2}{2} - u' w'^2 \right) \right]' \\ &+ \left\{ w' \left[EI (w' - u' w')' \right]' - 2u' w' (EI w'')' \right\}' \end{aligned} \quad (6.104)$$

$$\begin{aligned} \rho A \ddot{w} + (EI w'')'' - j_r \ddot{w}'' &= \left[EA \left(u' w' + \frac{w'^3}{2} - u'^2 w' \right) \right]' \\ &+ \left\{ \left[EI (u' w')' \right]' (1 - u') + (EI w'')' (u' - u'^2 + w'^2) \right. \\ &\quad \left. - \left[EI \left(u'^2 w' - \frac{w'^3}{3} \right) \right]' \right\}' + F \end{aligned} \quad (6.105)$$

where u and w are the axial and transversal deflections, respectively, and j_r is the mass moment of inertia of the beam with respect to the z -axis (see Fig. 6.24a). Note that Eq. (6.98a) and Eq. (6.98b) are special cases of Eq. (6.104) and Eq. (6.105) when neglecting the rotary inertia and the curvature nonlinearities involving the coefficient EI (note that when dividing the nonlinear terms of coefficient EI by EA , these terms become too small of order $r^2 = I/A$).

Another interesting special case is for beams with one end fixed or hinged while the other is free or guided. In this case, the beam can be assumed inextensional [24] with zero axial strain ($\varepsilon = 0$). Hence, according to Eq. (6.92a),

$$u' = \sqrt{1 - w'^2} - 1. \quad (6.106)$$

Using Eq. (6.106) with some other steps and assuming constant beam properties, Eq. (6.104) and Eq. (6.105) are reduced to the below equation [24]:

$$\begin{aligned} \rho A \ddot{w} = & -EI \left(w'''' + w'w''^2 + w''w'^2 \right) + j\ddot{w}'' \\ & - \frac{1}{2} \left[w' \int_l^x m \frac{\partial}{\partial t^2} \left(\int_0^x w'^2 dx \right) \right]' + F. \end{aligned} \quad (6.107)$$

It is noted from Eq. (6.107) the presence of geometric curvature nonlinearities of the coefficient EI and inertia nonlinearities with the integral term, both of cubic order. These nonlinearities exist in microcantilever beams. However, they have weak effect for most micro applications of small to moderate motion. They can be significant in applications involving large motion.

6.10 The Galerkin Discretization and Reduced-Order Modeling

If the equation characterizing the static or dynamic behavior of a beam is nonlinear or if the beam has irregular geometrical and material properties, analytical solutions may not be available. In fact, closed-form solutions are rare for systems governed by nonlinear equations. In such cases, approximate methods of solutions need to be utilized to simulate the static and dynamic behavior of the beams. These include the Rayleigh–Ritz, finite-element, and the weighted-residual methods. The Rayleigh–Ritz method is a variational approach commonly used to obtain the natural frequencies of beams. However, it does not suit nonconservative systems [1]. In addition, it is restricted to systems of equations of motion that can be casted in energy or weak forms [24, 25]. The finite-element method in principle has no such restrictions. Nevertheless, it can be computationally very expensive, especially for multiphysics, nonlinear, and time-dependent problems, such as those commonly encountered in MEMS. Next, we discuss a powerful weighted-residual method, the Galerkin method, which is computationally efficient, capable of handling nonconservative and nonlinear systems, and suits static and dynamic problems.

6.10.1 The Galerkin Method

To illustrate the method, consider a system with an equation and boundary conditions expressed, respectively, as

$$A(w) = f \quad (6.108a)$$

$$B_1(w) = w_{10}; \quad B_2(w) = w_{20} \quad (6.108b)$$

where $w(x,t)$ is the dependent variable in space x and time t , A is a differential operator in space and time, which can be linear or nonlinear, f is forcing, B_1 and B_2 are boundary operators and w_{10} and w_{20} are the boundary conditions, which here are assumed to be nontime varying. We seek an approximate solution of the above system in the form of

$$w(x,t) = \phi_0(x) + \sum_{i=1}^n u_i(t)\phi_i(x) \quad (6.109)$$

where $\phi_0(x)$ is the particular static solution of the system that satisfies the inhomogeneous boundary conditions of Eq. (6.108b). If the boundary conditions are homogeneous ($w_{10} = w_{20} = 0$) then $\phi_0(x) = 0$. In the case of time-varying w_{10} and w_{20} , the particular solution becomes $\phi_0(x,t)$, this case however will not be treated here. The parameter $u_i(t)$ is an unknown time-varying coefficient, which is determined in the course of the solution. It is very much similar to the modal coordinate of Sect. 6.7. The function $\phi_i(x)$ is an approximate or trial function, which belongs to the family of the so-called comparison functions. Each function $\phi_i(x)$ should satisfy the following conditions [25]:

- It should satisfy the homogenous form of all the boundary conditions of the problem. For Eq. (6.108b), these are $B_1(w) = 0$ and $B_2(w) = 0$.
- It should be as many times differentiable as the order of the differential equation of the system. For a beam equation, this means that $\phi_i(x)$ should be at least four times differentiable. Hence, $\phi_1 = x^2$ cannot be chosen as a comparison function for a beam equation since it is only two times differentiable (all derivatives higher than two yield zero).
- It should form and belong to a complete set of linearly independent functions. For example, $\phi_1 = x^3$ and $\phi_2 = 4x^3$ are not linearly independent functions. A complete set of such a family of functions should contain all the powers of x , i.e., $\phi_1 = x_0$; $\phi_2 = x$; $\phi_3 = x^2$; $\phi_4 = x^3$; \dots . This condition guarantees the convergence of the series of Eq. (6.109) to the exact solution as $n \rightarrow \infty$.

For structural mechanics problems, the linear undamped modeshapes of a structure are considered an excellent choice for comparison functions. They satisfy the homogenous boundary conditions and lead to quick convergence in the series of Eq. (6.109). These modeshapes can be extracted analytically for structures of simple geometries or numerically using finite-element methods for structures of complicated geometries.

To proceed, Eq. (6.109) is substituted into Eq. (6.108a). Because Eq. (6.109) represents an approximate and not an exact solution, Eq. (6.108a) is not satisfied exactly. Hence, there is an error or a residue R as an outcome of this substitution as indicated below:

$$A \left[\phi_0(x) + \sum_{i=1}^n u_i(t)\phi_i(x) \right] - f = R. \quad (6.110)$$

In weighted residual methods, including the Galerkin method, the error is minimized by requiring it to be orthogonal to every weighting function ψ_j . In the Galerkin method, ψ_j is chosen to be the same as ϕ_j . Hence, multiplying Eq. (6.110) by ϕ_j , integrating the equation over the domain of the problem Γ , and setting the minimized weighed error equal to zero yield

$$\int_{\Gamma} \phi_j(x) \left\{ A \left[\phi_0(x) + \sum_{i=1}^n u_i(t) \phi_i(x) \right] - f \right\} dx = \int_{\Gamma} \phi_j(x) R dx = 0 \quad (6.111a)$$

which can be rewritten as

$$\int_{\Gamma} \phi_j(x) (A [\phi_0(x)] - f) dx + \sum_{i=1}^n \int_{\Gamma} \phi_j(x) A [u_i(t) \phi_i(x)] dx = 0. \quad (6.111b)$$

Upon the execution of the integrals of Eq. (6.111b), the outcome would be n differential equations in time in $u_i(t)$, which can be integrated numerically using Runge–Kutta techniques. Then the results are substituted back into Eq. (6.109) to yield the total response. The number of required modes n needs to be investigated to ensure convergence and accurate results for each problem.

The reduction of a distributed-parameter system of infinite degree of freedom or a partial differential equation in space and time into a number of ordinary differential equations in time (a finite-degree of freedom system) is considered significant advantage from a computational point of view. Indeed, this is one of the major benefits of using the Galerkin method over finite-element approaches. Thus, the Galerkin method is considered a powerful technique to generate **reduced-order models**. For static problems, the Galerkin discretization yields a system of algebraic equations of unknown constant coefficients, which can be solved using Newton's Raphson methods.

6.10.2 Beams with Midplane Stretching

Next, the Galerkin procedure is demonstrated on beams. As an example, consider a clamped–clamped beam with midplane stretching of the equation of motion Eq. (6.103). For simplicity, the axial load is taken to be zero. We derive a reduced-order model of the beam using its linear orthonormal modeshapes, which satisfy the condition of Eq. (6.70). For convenience, Eq. (6.103) is nondimensionalized by substituting Eq. (6.44) and dropping the superscript “ \wedge ”, which yield

$$w'''' + \ddot{w} - \alpha w'' \int_0^1 w'^2 dx = F_{\text{non}} \quad (6.112)$$

where

$$\alpha = \frac{l^2 A}{2I}; \quad F_{\text{non}} = \frac{l^3 F}{EI}. \quad (6.113)$$

We recall the boundary conditions of the fixed–fixed beam, which are expressed as

$$w(0, t) = w'(0, t) = 0; \quad w(1, t) = w'(1, t) = 0. \quad (6.114)$$

Because the boundary conditions of the beam are homogenous, $\phi_0(x) = 0$, and hence Eq. (6.109) is reduced to

$$w(x, t) = \sum_{i=1}^n u_i(t) \phi_i(x). \quad (6.115)$$

We choose $\phi_i(x)$, $i = 1, 2, \dots$ to be the linear undamped and normalized modeshapes of the beam. This choice brings many similarities with the modal analysis procedure of Sect. 6.7. The modeshapes of a clamped–clamped beam can be read from Table 6.1. One should always check if the modeshapes are properly normalized to satisfy the condition of Eq. (6.70). Otherwise, each modeshape needs to be normalized by multiplying it by the constant $A_i = 1/\sqrt{\int_0^1 \phi_i^2 dx}$. In this case, the modeshapes of the clamped–clamped beam of Table 6.1 are already normalized with $A_i = 1$.

To proceed, Eq. (6.115) is substituted into Eq. (6.112). The outcome is then multiplied by the modeshape ϕ_j and is integrated over the beam domain from 0 to 1:

$$\begin{aligned} & \int_0^1 \phi_j \left(\sum_{i=1}^n u_i \phi_i'''' + \sum_{i=1}^n \ddot{u}_i \phi_i \right) dx \\ & + \int_0^1 \phi_j \left\{ -\alpha \sum_{i=1}^n u_i \phi_i'' \int_0^1 \left(\sum_{k=1}^n u_k \phi_k' \right)^2 = F_{\text{non}} \right\} dx. \end{aligned} \quad (6.116a)$$

Next, ϕ_i'''' in Eq. (6.116a) is replaced with $\omega_{\text{non},i}^2 \phi_i$ according to Eq. (6.63a). Then, distributing the integral over each term of the equation gives

$$\begin{aligned} & \sum_{i=1}^n u_i \int_0^1 \phi_j \omega_{\text{non},i}^2 \phi_i dx + \sum_{i=1}^n \ddot{u}_i \int_0^1 \phi_j \phi_i dx \\ & - \alpha_{j i k l} \sum_{i,k,l=1}^n u_i u_k u_l \int_0^1 \phi_j \phi_i'' dx \int_0^1 \phi_k' \phi_l' dx = \int_0^1 \phi_j F_{\text{non}} dx \end{aligned} \quad (6.116b)$$

where

$$\alpha_{j i k l} = -\alpha \int_0^1 \phi_j \phi_i'' dx \int_0^1 \phi_k' \phi_l' dx.$$

The first two summation terms of Eq. (6.116b) can be simplified by making use of the orthonormality of the modeshapes, Eq. (6.70) and Eq. (6.71), which reduces Eq. (6.116b) to

$$\ddot{u}_j + \omega_{\text{non},j}^2 u_j + \alpha_{j i k l} \sum_{i,k,l=1}^n u_i u_k u_l = f_j; \quad j = 1, \dots, n \quad (6.117)$$

where

$$f_j = \int_0^1 \phi_j F_{\text{non}} dx. \quad (6.118)$$

As an example, using a single-mode approximation ($n = 1$) reduces Eq. (6.117) to

$$\ddot{u}_1 + \omega_{\text{non},1}^2 u_1 + \alpha_{1111} u_1^3 = f_1 \quad (6.119)$$

where

$$\omega_{\text{non},1}^2 = 22.37^2 = 500.564; \quad \alpha_{1111} = -\alpha \int_0^1 \phi_1 \phi_1'' dx \int_0^1 \phi_1'^2 dx = 151.335\alpha.$$

Note that Eq. (6.119) takes the exact form of the Duffing equation. Hence, it can be integrated numerically in time or solved using perturbation techniques, as illustrated in Chap. 5. Once u_1 is determined, the results are substituted back into Eq. (6.115) to obtain the complete response.

We should emphasize again that the number of modes in the assumed solution needs to be investigated for accurate and converged results. In addition, it should be noted that using a single-mode approximation, while easy, is not capable of revealing many important dynamical features, such as multi-resonances, nonlinear interactions, and complex nonlinear phenomena, such as Hopf bifurcations and some chaotic behaviors. Also, it can lead to erroneous qualitative results related to the effective nonlinearity of the system [24]. For more than one mode, it is recommended to execute the integrals of Eq. (6.119) using a software, such as Mathematica, Matlab, or Maple.

Example 6.10: Consider a clamped–clamped microbeam made of silicon with $\rho = 2,332 \text{ kg/m}^3$ and $E = 169.0 \text{ GPa}$. The dimensions of the microbeam are $l = 1,000 \text{ }\mu\text{m}$, $h = 1.5 \text{ }\mu\text{m}$, and $b = 100 \text{ }\mu\text{m}$. Assume the microbeam free from axial stresses and undamped. Using a one mode in the Galerkin expansion, determine the maximum transient dynamic response of the microbeam at its midpoint when subjected to a spatially distributed shock force $F_0 = a\rho b h \tilde{g}(t)$, where a is an acceleration magnitude and $\tilde{g}(t)$ is a half-sine pulse expressed as

$$\tilde{g}(t) = \sin\left(\frac{\pi}{T}t\right) u(t) + \sin\left[\frac{\pi}{T}(t - T)\right] u(t - T).$$

Above, T is the pulse duration, and $u(t)$ is the unit step function. Consider $T = 0.1 \text{ ms}$ and $a = 1,000g$, where g is the constant of gravity. Compare the result to that of a linear beam model.

Solution: First, f_1 is calculated according to Eq. (6.118). Then, the result is substituted into Eq. (6.119) and the outcome is integrated numerically in time using the Runge–Kutta technique. The results of the simulations are shown in Fig. 6.25. Figure 6.25a shows the result when α_{1111} is set equal to zero (linear beam model).

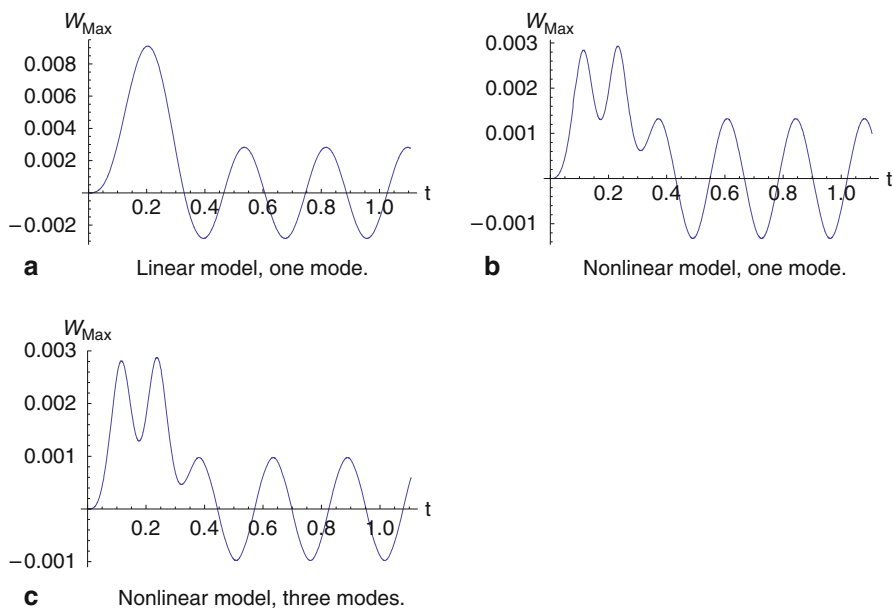


Fig. 6.25 The transient response of a clamped–clamped beam to a half-sine acceleration pulse. The figure parts **a–c** show the nondimensional midpoint deflection of the beam versus the nondimensional time.

Figure 6.25b shows the nonlinear model result. Note that there is significant difference between the linear and nonlinear model results. For the sake of verification, Fig. 6.25c shows the nonlinear beam model results using three symmetric (odd) modes. It is clear for the considered case that a one-mode approximation yields converged results.

6.11 Reduced-Order Model of Beams Under Electrostatic Force

In this section, we discuss the development of a reduced-order model ROM for the common case of beams actuated by the nonlinear electrostatic force. A review on relevant literature work of ROMs in MEMS can be found in [26]. The development here is restricted to beams of uniform and constant geometrical and material properties. The derivation is made generic for beams with midplane stretching. For other beams, such as cantilever beams, the same derivation and results apply by setting the coefficient of midplane stretching equal to zero. Note that for cantilever beams, the geometric and inertia nonlinearities of Eq. (6.107) are considered negligible since they are too weak to be activated under the small deflection that these beams undergo

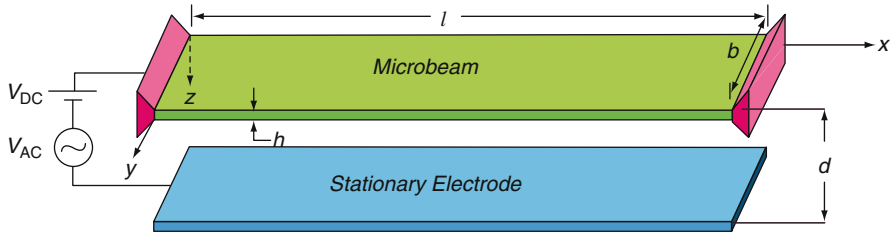


Fig. 6.26 Schematic of an electrostatically actuated microbeam with immovable edges

within the small gap separating them from the stationary electrode. Hence, under electrostatic actuation, cantilever beams can be assumed linearly behaving structures from a mechanical stand.

Next, consider a beam, Fig. 6.26, of rectangular cross section $A = bh$ with immovable edges of the equation of motion Eq. (6.103). The beam is assumed to be actuated by a parallel-plate electrostatic force per unit length of the form

$$F = \frac{\varepsilon b [V_{DC} + V_{AC} \cos(\Omega t)]^2}{2(d - w)^2} \quad (6.120)$$

where d is the width of the gap separating the beam from the substrate, V_{DC} is the DC polarization voltage, and V_{AC} and Ω are the AC harmonic voltage amplitude and frequency, respectively. Because the beam is treated as deformable, the assumption of a parallel-plate capacitive force is considered as an approximation, which for all practical purposes turns out to yield acceptable results. Also, the beam is assumed to be under a constant axial force N_1 and is subjected to a viscous damping of coefficient c . Hence, it follows that the equation of motion of the beam can be expressed as

$$EIw'''' + c\dot{w} + \rho b h \ddot{w} = \left(N_1 + \frac{EA}{2l} \int_0^l w'^2 dx \right) w'' + \frac{\varepsilon b [V_{DC} + V_{AC} \cos(\Omega t)]^2}{2(d - w)^2}. \quad (6.121)$$

For electrostatic problems, it is convenient to normalize the deflection of the beam with respect to d . Hence, the following nondimensional variables (denoted by hats) are introduced

$$\hat{w} = \frac{w}{d}, \quad \hat{x} = \frac{x}{l}, \quad \hat{t} = \frac{t}{T} \quad (6.122)$$

where T is a time scale defined as

$$T = \sqrt{\frac{\rho b h l^4}{EI}}.$$

Substituting Eq. (6.122) into Eq. (6.121) and dropping the hats from the nondimensional variables for convenience, the following nondimensional equation is

derived:

$$\begin{aligned} \frac{\partial^4 w}{\partial x^4} + \frac{\partial^2 w}{\partial t^2} + c_{\text{non}} \frac{\partial w}{\partial t} = & \left[\alpha_1 \int_0^1 \left(\frac{\partial w}{\partial x} \right)^2 dx + N_{\text{non}} \right] \frac{\partial^2 w}{\partial x^2} \\ & + \frac{\alpha_2 [V_{\text{DC}} + V_{\text{AC}} \cos(\Omega t)]^2}{(1-w)^2}. \end{aligned} \quad (6.123)$$

The parameters appearing in Eq. (6.123) are defined as

$$\alpha_1 = 6 \left(\frac{d}{h} \right)^2; \quad \alpha_2 = \frac{6\epsilon l^4}{E h^3 d^3}; \quad c_{\text{non}} = \frac{12c l^4}{E T b h^3}; \quad N_{\text{non}} = \frac{12N_1 l^2}{E b h^3}. \quad (6.124)$$

We note that the various design parameters of the system have been grouped into few nondimensional parameters, which represent midplane stretching, the electrostatic force, damping, and the axial load. This conveniently reduces the design space and facilitates studying the behavior of the system. The universality of these numbers also enables comparing the performance of various systems of different specifications.

To derive a reduced-order model, we apply the Galerkin method and use the beam's linear orthonormal modeshapes. For this, Eq. (6.115) is substituted into Eq. (6.123). The outcome is then multiplied by the modeshape ϕ_j and is integrated over the beam domain from 0 to 1:

$$\begin{aligned} & \int_0^1 \phi_j \left(\sum_{i=1}^n u_i \phi_i'''' + \sum_{i=1}^n \ddot{u}_i \phi_i \right) dx + c_{\text{non}} \int_0^1 \phi_j \left(\sum_{i=1}^n \dot{u}_i \phi_i \right) dx \\ & - \alpha_1 \int_0^1 \phi_j \left\{ \sum_{i=1}^n u_i \phi_i'' \int_0^1 \left(\sum_{k=1}^n u_k \phi_k' \right)^2 dx \right\} dx - N_{\text{non}} \int_0^1 \phi_j \left(\sum_{i=1}^n u_i \phi_i'' \right) dx \\ & = \alpha_2 [V_{\text{DC}} + V_{\text{AC}} \cos(\Omega t)]^2 \int_0^1 \left\{ \frac{\phi_j}{\left(1 - \sum_{i=1}^n u_i \phi_i \right)^2} \right\} dx. \end{aligned} \quad (6.125a)$$

Next, ϕ_i'''' above is replaced with $N_{\text{non}} \phi_i'' + \omega_{\text{non},i}^2 \phi_i$ according to Eq. (6.82b) (note that this is an optional step, we can also leave the expression as is and execute the integrals, which should lead to the same results as with the substitution). In this case, the axial force term cancels out from the equation (its effect is through $\omega_{\text{non},i}^2$). Thus, after distributing the integral over each term and using the orthonormality

condition, Eq. (6.125a) is rewritten as

$$\begin{aligned} \ddot{u}_j + \omega_{\text{non},j}^2 u_j + c_{\text{non}} \dot{u}_j - \alpha_1 \int_0^1 \phi_j \left\{ \sum_{i=1}^n u_i \phi_i'' \int_0^1 \left(\sum_{k=1}^n u_k \phi_k' \sum_{k=1}^n u_k \phi_k' \right)^2 \right\} dx \\ = \alpha_2 [V_{\text{DC}} + V_{\text{AC}} \cos(\Omega t)]^2 \int_0^1 \left\{ \frac{\phi_j}{\left(1 - \sum_{i=1}^n u_i \phi_i \right)^2} \right\} dx. \end{aligned} \quad (6.125b)$$

One can note that the electrostatic force term in Eq. (6.125b) has introduced complications due to the difficulty of executing the integral with the variables in the denominator. There are several methods that have been proposed to deal with this problem. One method is to expand the electrostatic force term in Eq. (6.123) into Taylor series expansion, which brings the terms with w from the denominator to the numerator, thereby simplifying the Galerkin expansion and the execution of the integrals. It was shown however that as the system approaches the pull-in instability, the neglected higher order terms in the Taylor series become important [27]. Hence, without retaining sufficient number of terms, this method may yield inaccurate results. One method to ascertain the convergence of the Taylor expansion is to plot the electrostatic forcing term, say $1/(1 - x^2)$, and compare it to its Taylor series expansion over the range of 0–0.999. It turns out that 20 terms and up are needed for accurate results.

The other method is to keep the summation in the denominator as shown in Eq. (6.125b) and execute the spatial integral simultaneously while integrating the modal equations in time for every time step. This method however can be computationally expensive. A third technique to resolve the above problems is to multiply the equation of motion, Eq. (6.123), by $(1 - w)^2$ and then apply the Galerkin method [27]. The disadvantage of this step is that it results in a nondiagonal mass matrix in the discretized system, which introduces some numerical complications. Nevertheless, this method has been proven to be quite efficient in simulating electrostatic MEMS problems. We will follow this method in the following analysis. Toward this, Eq. (6.123) is multiplied by $(1 - w)^2$:

$$\begin{aligned} (1 - w)^2 \frac{\partial^4 w}{\partial x^4} + (1 - w)^2 \frac{\partial^2 w}{\partial t^2} + (1 - w)^2 c_{\text{non}} \frac{\partial w}{\partial t} \\ = (1 - w)^2 \left[\alpha_1 \int_0^1 \left(\frac{\partial w}{\partial x} \right)^2 dx + N_{\text{non}} \right] \frac{\partial^2 w}{\partial x^2} + \alpha_2 [V_{\text{DC}} + V_{\text{AC}} \cos(\Omega t)]^2. \end{aligned} \quad (6.126)$$

Subsequently, Eq. (6.115) is substituted into Eq. (6.126), ϕ_i'''' is replaced with $N_{\text{non}} \phi_i'' + \omega_{\text{non},i}^2 \phi_i$, the outcome is then multiplied by the modeshape ϕ_j and is

integrated over the beam domain from 0 to 1:

$$\begin{aligned}
 & \int_0^1 \phi_j \left(1 - \sum_{l=1}^n u_l \phi_l \right)^2 \left(\sum_{i=1}^n u_i \omega_{\text{non},i}^2 \phi_i + \sum_{i=1}^n \ddot{u}_i \phi_i \right) dx \\
 & + c_{\text{non}} \int_0^1 \phi_j \left(1 - \sum_{l=1}^n u_l \phi_l \right)^2 \left(\sum_{i=1}^n \dot{u}_i \phi_i \right) dx \\
 & - \alpha_1 \int_0^1 \phi_j \left(1 - \sum_{l=1}^n u_l \phi_l \right)^2 \left\{ \sum_{i=1}^n u_i \phi_i'' \int_0^1 \left(\sum_{k=1}^n u_k \phi_k' \right)^2 dx \right\} dx \\
 & = \alpha_2 [V_{\text{DC}} + V_{\text{AC}} \cos(\Omega t)]^2 \int_0^1 \phi_j dx.
 \end{aligned} \tag{6.127}$$

Equation (6.127) represents the ROM. Executing the spatial integrals yields a system of ordinary differential equations, which can be integrated numerically in time for dynamic simulations. Using one term in the Galerkin expansion reduces the ROM to

$$\begin{aligned}
 & (\ddot{u}_1 + u_1 \omega_{\text{non},1}^2 + \dot{u}_1) \left(1 - 2u_1 \int_0^1 \phi_1^3 dx + u_1^2 \int_0^1 \phi_1^4 dx \right) \\
 & - \alpha_1 \int_0^1 \phi_1'^2 dx \left(u_1^3 \int_0^1 \phi_1 \phi_1'' dx - 2u_1^4 \int_0^1 \phi_1^2 \phi_1'' dx + u_1^5 \int_0^1 \phi_1^3 \phi_1'' dx \right) \\
 & = \alpha_2 [V_{\text{DC}} + V_{\text{AC}} \cos(\Omega t)]^2 \int_0^1 \phi_1 dx
 \end{aligned} \tag{6.128}$$

It is clear from Eq. (6.128) that the ROM contains nonlinearities up to the fifth order.

6.12 The Static Behavior of Beams Under Electrostatic Force

Next, the static behavior and universal pull-in results of cantilever and clamped-clamped microbeams are presented. For static simulations, all time-varying terms, including inertia, damping, and variable forcing, in Eq. (6.127) are set equal to zero and the time-varying modal variables are replaced with unknown constant coefficients C_i . This yields a system of nonlinear algebraic equations, which can be solved numerically using the Newton–Raphson method.

6.12.1 Cantilever Microbeams

In the case of cantilever microbeams, the midplane stretching coefficient α_1 is set equal to zero. Accordingly, the static algebraic equations of this case is reduced to

$$\int_0^1 \phi_j \left(1 - \sum_{l=1}^n C_l \phi_l \right)^2 \left(\sum_{i=1}^n C_i \omega_{\text{non},i}^2 \phi_i \right) dx = \alpha_2 V_{\text{DC}}^2 \int_0^1 \phi_j dx. \tag{6.129}$$

Note from Eq. (6.129) that the static behavior of the cantilever microbeam depends solely on the nondimensional parameter $\alpha_2 V_{DC}^2$. Using one mode, Eq. (6.129) becomes

$$\omega_{\text{non},1}^2 \int_0^1 C_1 \phi_1^2 (1 - C_1 \phi_1)^2 dx = \alpha_2 V_{DC}^2 \int_0^1 \phi_1 dx. \quad (6.130a)$$

Substituting $\omega_{\text{non},1} = 3.516$ and carrying out the integrals yield

$$-12.36C_1 + 36.54C_1^2 - 29.04C_1^3 + 0.78\alpha_2 V_{DC}^2 = 0. \quad (6.130b)$$

One can note the similarity of Eq. (6.130b) and that of a lumped-parameter model, for example Eq. (4.3). Hence, the same conclusions of a lumped-parameter model apply. Solving Eq. (6.130b), or the system of Eq. (6.129) in the case of multi modes, yields three solutions. Of these, one is nonphysical predicting a maximum normalized displacement of the cantilever beam exceeding unity. The other two are physical solutions with one stable and the other is unstable. Upon solving C_1 for a given voltage load, the displacement of the beam is expressed as $w(x) = C_1 \phi_1(x)$.

As an example, we consider $\alpha_2 = 1$ and plot the stable response of the microbeam at the tip W_{Max} using one, four, and seven modes, Fig 6.27. It is clear from the figure that a single-mode approximation is not sufficiently accurate whereas four and higher number of modes yield converged and accurate results. It is noted also that pull-in occurs near $\alpha_2 V_{DC}^2 \approx 1.72$. It turns out that this value is almost true for all cantilever microbeams regardless of their dimensions. Hence, $\alpha_2 V_{DC}^2 \approx 1.72$ can be taken as a universal number that indicates the occurrence of pull-in of any cantilever microbeam. Accordingly, the pull-in voltage V_{pull} can be estimated as

$$V_{\text{pull}} = \sqrt{1.72/\alpha_2}. \quad (6.131)$$

Figure 6.28 depicts the beam profile for selected values of $\alpha_2 V_{DC}^2$.

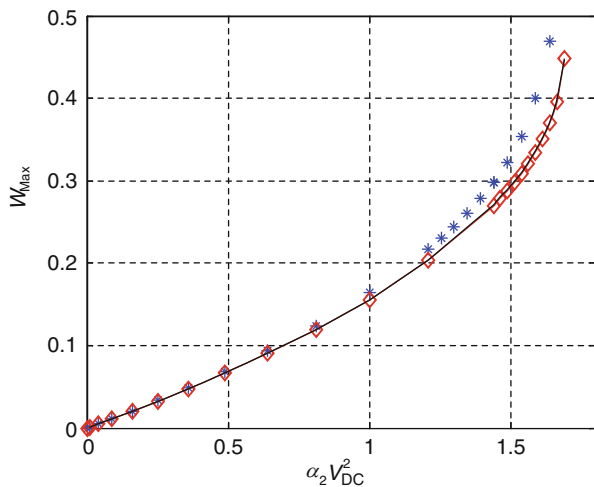
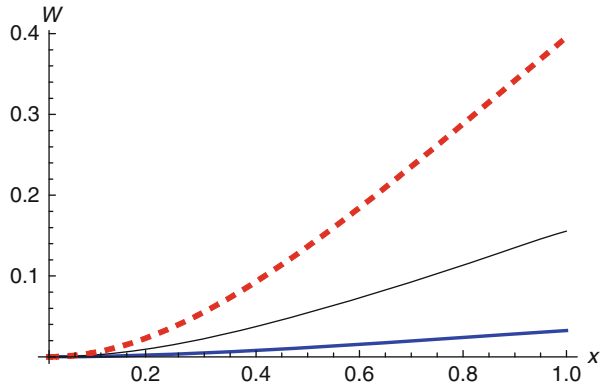


Fig. 6.27 The tip displacement of a cantilever microbeam using one (stars), four (diamonds), and seven (solid) modes for $\alpha_2 = 1$

Fig. 6.28 A cantilever microbeam displacement profile for $\alpha_2 V_{DC}^2 = 0.5$ (*thick*), $\alpha_2 V_{DC}^2 = 1$ (*thin*), and $\alpha_2 V_{DC}^2 = 1.29$ (*dashed*)



Example 6.11: Consider a cantilever microbeam made of silicon with $\rho = 2,332 \text{ kg/m}^3$ and $E = 160.0 \text{ GPa}$. The dimensions of the microbeam are $l = 100 \text{ }\mu\text{m}$, $h = 1 \text{ }\mu\text{m}$ and $b = 10 \text{ }\mu\text{m}$. The microbeam is actuated electrostatically with a gap space separating it from the stationary electrode $d = 1 \text{ }\mu\text{m}$. Assuming a complete overlap between the microbeam and the lower electrode, calculate the pull-in voltage of the microbeam?

Solution: From Eq. (6.124), α_2 is calculated and found equal $\alpha_2 = 0.0332$. Using Eq. (6.131), the pull-in voltage is found to be $V_{\text{pull}} \approx 7.2 \text{ V}$. Using four-mode approximation, the pull-in voltage is found numerically to be $V_{\text{pull}} = 7.14 \text{ V}$.

6.12.2 Clamped–Clamped Microbeams

The static algebraic equations of this case are written, based on Eq. (6.127), as

$$\begin{aligned}
 & \int_0^1 \phi_j \left(1 - \sum_{l=1}^n C_l \phi_l \right)^2 \left(\sum_{i=1}^n C_i \omega_{\text{non},i}^2 \phi_i \right) dx \\
 & - \alpha_1 \int_0^1 \phi_j \left(1 - \sum_{l=1}^n C_l \phi_l \right)^2 \left\{ \sum_{i=1}^n C_i \phi_i'' \int_0^1 \left(\sum_{k=1}^n C_k \phi_k' \right)^2 dx \right\} dx \\
 & = \alpha_2 V_{DC}^2 \int_0^1 \phi_j dx.
 \end{aligned} \tag{6.132}$$

Note that the static behavior of the clamped–clamped microbeam depends on three nondimensional parameters: α_1 , $\alpha_2 V_{DC}^2$, and N_{non} , which influences the behavior through $\omega_{\text{non},i}^2$ in Eq. (6.132). As an example, we consider the case of $N_{\text{non}} = 0$ and $\alpha_1 = 20$ and simulate the static behavior of the beam as $\alpha_2 V_{DC}^2$ is increased up to

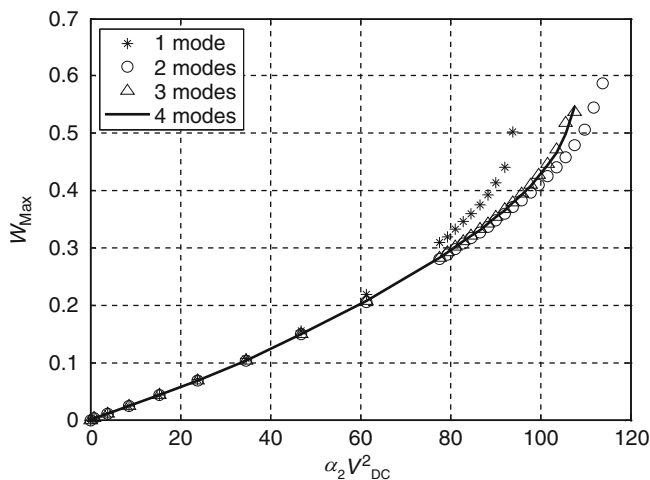


Fig. 6.29 The midbeam displacement of a clamped–clamped microbeam using one–four symmetric modeshapes for $\alpha_1 = 20$ and $N_{\text{non}} = 0$

the pull-in instability. First, the convergence of the ROM is examined. Because of the symmetric boundary conditions of the beam and the electrostatic force, only symmetric modeshapes are used. Figure 6.29 shows the maximum deflection of the beam at its midpoint using one and up to four symmetric modeshapes. It is clear that using three or higher modeshapes in the ROM yields converged results. Figure 6.30 depicts examples of the beam profile at various levels of $\alpha_2 V_{DC}^2$. Figure 6.31 depicts an example showing both the stable and unstable equilibrium solutions of the system. The unstable solution can be obtained by assuming large values of the initial guesses in the Newton–Raphson numerical scheme.

Based on plots similar to Figs. 6.29 and 6.31, the pull-in voltage of the beam can be predicted. For example, in the case of Fig. 6.29, pull-in occurs near $\alpha_2 V_{DC}^2 = 107$ V.

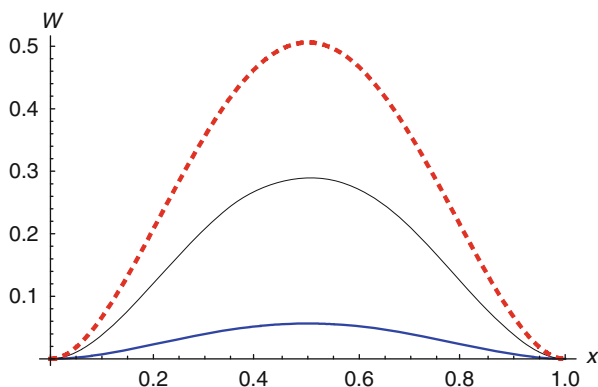
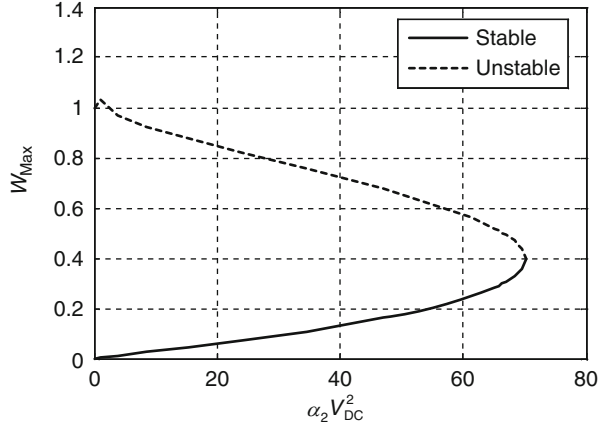


Fig. 6.30 A clamped–clamped microbeam displacement profile for $\alpha_2 V_{DC}^2 = 20$ (*thick*), $\alpha_2 V_{DC}^2 = 80$ (*thin*), and $\alpha_2 V_{DC}^2 = 106$ (*dashed*) when $\alpha_1 = 20$ and $N_{\text{non}} = 0$

Fig. 6.31 The stable and unstable midpoint equilibrium solutions of a clamped–clamped microbeam for $\alpha_1 = 0.01$ and $N_{\text{non}} = 0$



By calculating α_2 based on the dimensions of the beam, the pull-in voltage is obtained. Figures similar to Figs. 6.29 and 6.31 have been generated for various values of the nondimensional parameters α_1 and N_{non} , as depicted in Fig. 6.32. These are universal curves that can be used to predict the pull-in voltage of any clamped–clamped microbeam actuated by full electrode regardless of its dimensions. Example 6.12 illustrates the procedure. Note in Figs. 6.32b and 6.32c that the pull-in voltage reaches zero value for specific negative value of the axial force. These correspond to the buckling instability limits.

Example 6.12: Let us consider the microbeam of Example 4.1 of length $l = 510 \mu\text{m}$, thickness $h = 1.5 \mu\text{m}$, width $b = 100 \mu\text{m}$, and air-gap width $d = 1.18 \mu\text{m}$. Consider $E = 154 \text{ GPa}$ and $\rho = 2,330 \text{ kg/m}^3$. Estimate the pull-in voltage for the below cases:

- (a) Assuming zero axial strain
- (b) Assuming 10^{-5} axial strain

Solution: The parameters α_1 , α_2 , and N_{non} need to be calculated. Since this is a wide beams ($b > 5h$), E should be replaced with $E/(1 - \nu^2)$. Using Eq. (6.124), we found $\alpha_1 = 3.7$, $\alpha_2 = 3.84$, and $N_{\text{non}} = 0$ for (a) and $N_{\text{non}} = 13.9$ for (b). Graphically, using Fig. 6.32 at $\alpha_1 = 3.7$, pull-in is estimated to occur near $\alpha_2 V_{\text{DC}}^2 = 78$ for $N_{\text{non}} = 0$ and $\alpha_2 V_{\text{DC}}^2 = 98$ for $N_{\text{non}} = 13.9$. Hence, the pull-in voltage is estimated for (a) and (b), respectively, as

$$V_{\text{pull}} = \sqrt{78/\alpha_2} = 4.51 \text{ V} \quad (\text{a})$$

$$V_{\text{pull}} = \sqrt{98/\alpha_2} = 5.06 \text{ V}. \quad (\text{b})$$

The exact answers using the ROM directly are $V_{\text{pull}} = 4.45 \text{ V}$ and $V_{\text{pull}} = 5.1 \text{ V}$ for parts (a) and (b), respectively.

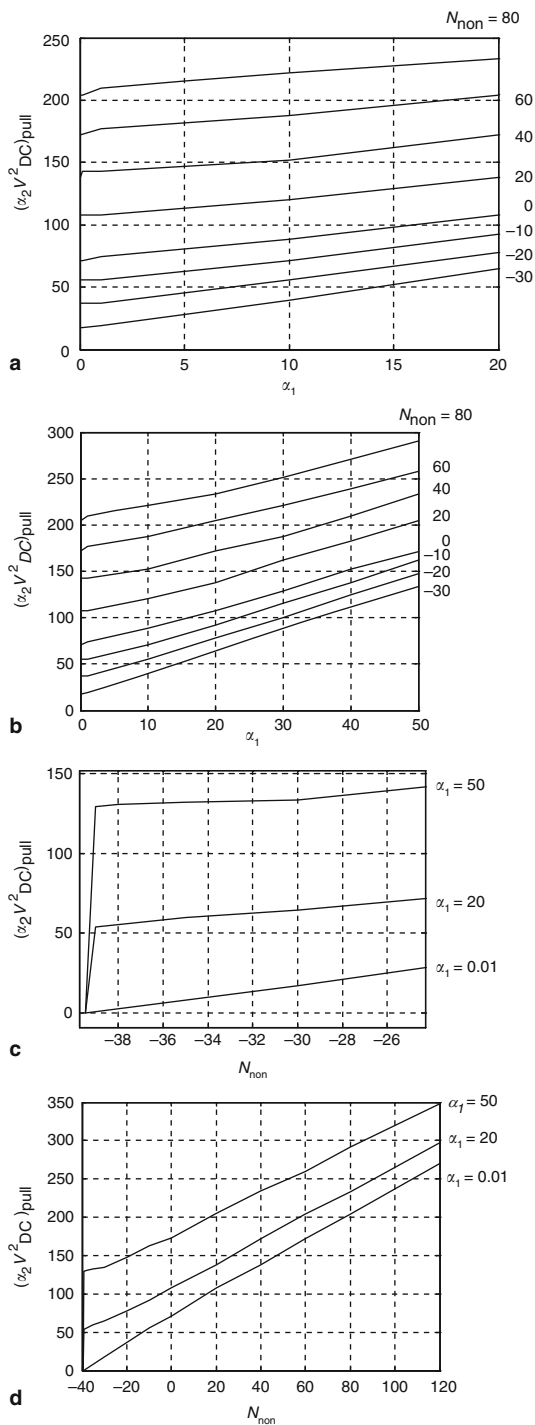


Fig. 6.32 Universal pull-in curves of a clamped-clamped microbeam for various values of $\alpha_1 = 6(d/h)^2$ and $N_{non} = 12N_1 l^2 / (Ebh^3)$. **a, b** pull-in versus α_1 and **c, d** pull-in versus N_{non}

6.12.3 Microbeams with Partial Electrodes and Initial Curvature

It is quite common for RF-MEMS switches and other devices to have the microbeams actuated by electrodes that cover partially their length or are deposited on parts of the beams. Figure 6.33 shows schematic examples of such configurations. In these cases, the electrostatic force can be represented analytically, assuming negligible fringe effect, using the unit-step functions $u(x)$. For example, the electrostatic force of Figs. 6.33a and 6.33c can be expressed, respectively, as

$$F = \frac{\varepsilon b V_{DC}^2 [u(x - x_1) - u(x - x_2)]}{2 (d - w)^2} \quad (6.133a)$$

$$F = \frac{\varepsilon b V_{DC}^2 [u(x - x_1) - u(x - x_2) + u(x - x_3) - u(x - x_4)]}{2 (d - w)^2}. \quad (6.133b)$$

As indicated in Sect. 6.3, residual stresses can cause curling or initial deformation of microbeams when released. In such cases, the initial curvature of the beams can cause significant effect on the strength and impact of the electrostatic forces. Therefore, it needs to be accounted for by modifying the electrostatic force expression to include the initial deformed shape of the beam, $g(x)$, in the effective gap separation as below for the case of full electrodes

$$F = \frac{\varepsilon b V_{DC}^2}{2 [d - w \pm g(x)]^2}. \quad (6.133c)$$

In the case of a cantilever beam, $g(x)$ can take any of the forms explained in Sect. 6.3 depending on the edge conditions and the natural frequency of the beam. The signs \pm in Eq. (6.133c) to indicate both possibilities of a beam curled up ($-$) and curling down ($+$). The rule here that the net gap distance should increase for a beam curled up away from the electrode, so the net gap becomes $[d - w + g(x)]$ and should decrease for a beam deformed toward the electrode, so the net gap becomes $[d - w - g(x)]$.

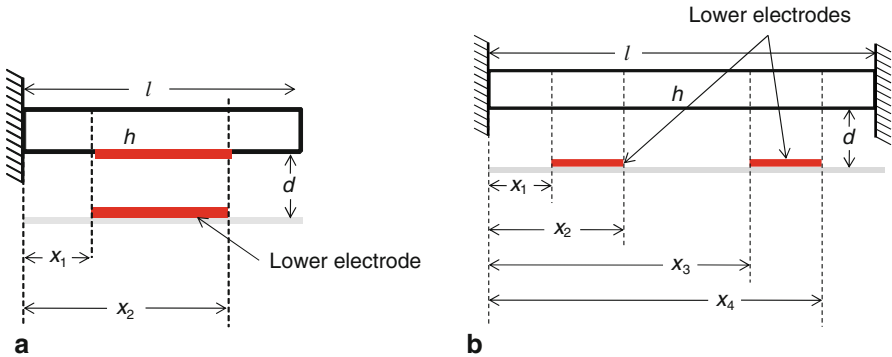


Fig. 6.33 Schematics of microbeams with partial electrodes, **a** cantilever and **b** clamped-clamped

For a clamped-clamped beam with symmetric deformation (concaved up or down), the shape can be approximated as $g(x) = b[1 - \cos(2\pi x/l)]/2$, where b is the midpoint or maximum deflection of the beam. In addition, the natural frequency of a deformed clamped-clamped beam needs to be measured and compared to theory to determine any axial load that may act on the beam due to residual stresses.

Example 6.13: Consider a microbeam of length $l = 100 \mu\text{m}$, thickness $h = 0.5 \mu\text{m}$, width $b = 10 \mu\text{m}$, and air-gap width $d = 1.0 \mu\text{m}$. Consider $E = 124 \text{ GPa}$ and $\rho = 2,332 \text{ kg/m}^3$. Calculate and plot the maximum deflection of the microbeam up to the pull-in instability for the below cases:

- Assuming a cantilever microbeam with partial electrode as in Fig. 6.33a with $x_1 = 0.25l$ and $x_2 = 0.75l$. Compare the results with that of a full electrode.
- Assuming a clamped-clamped microbeam with partial electrode as in Fig. 6.33b with $x_1 = 0.125l$, $x_2 = 0.375l$, $x_3 = 0.625l$, and $x_4 = 0.875l$. Compare the results with that of a full electrode.
- Assuming a cantilever microbeam with full electrode curled upward initially with a tip deflection equal $0.5 \mu\text{m}$.

Solution: For parts (a)–(c), we use four modes in the ROM. For parts (a) and (b), we express the electrostatic force as in Eq. (6.133a) and Eq. (6.133b). The results are depicted in Fig. 6.34a, b, and Fig. 6.35. As one would expect, the pull-in voltage has increased in the case of partial electrodes compared to full electrodes.

For part (c), according to Example 6.4 for a perfectly clamped microbeam, an assumed moment can be calculated that causes curling of the cantilever beam as

$$M_0 = \frac{2EIw_{\max}}{l^2}. \quad (\text{a})$$

Equation (a) gives $M_0 = 1.29 \times 10^{-12} \text{ Nm}$. Following also Example 6.4, the initial profile of the beam can be calculated according to

$$g(x) = \frac{M_0}{2EI}x^2 = 50x^2. \quad (\text{b})$$

Hence, the electrostatic force expression becomes

$$F = \frac{\varepsilon b V_{\text{DC}}^2}{2[d - w + 50x^2]^2}. \quad (\text{c})$$

In the case of a nondimensionalized reduced-order model, one should remember to normalize the expression of Eq. (c) including the new term. The results of this case are plotted in Fig. 6.34c. As expected, the initial curvature upward increases the pull-in voltage value.

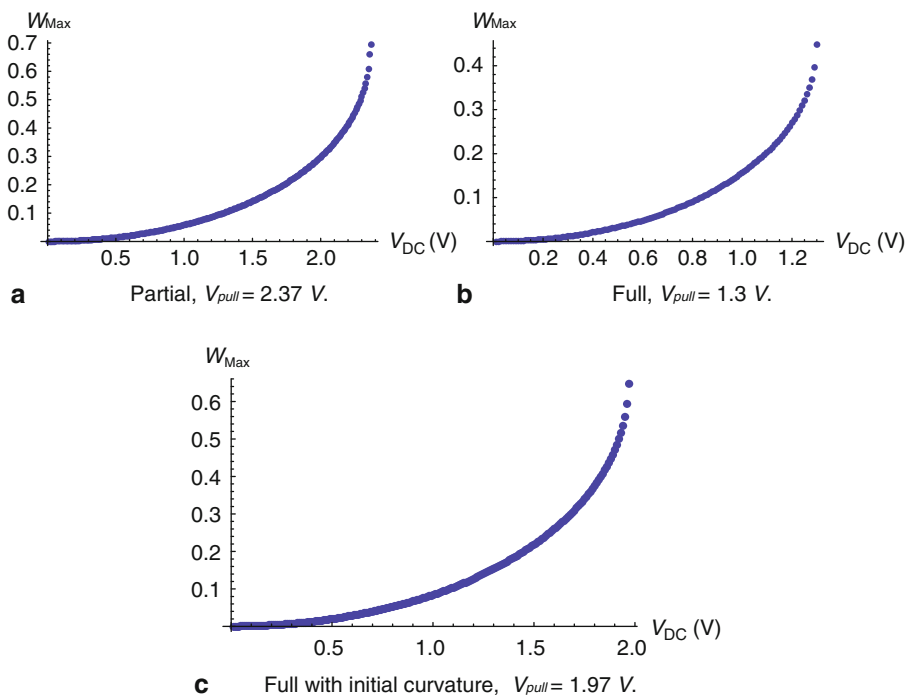


Fig. 6.34 The static responses of a cantilever beam actuated by **a** a partial electrode, **b** a full electrode, and **c** a full electrode with initial upward curling. Note that for part **c**, the deflection is measured with respect to the initial deformed configuration

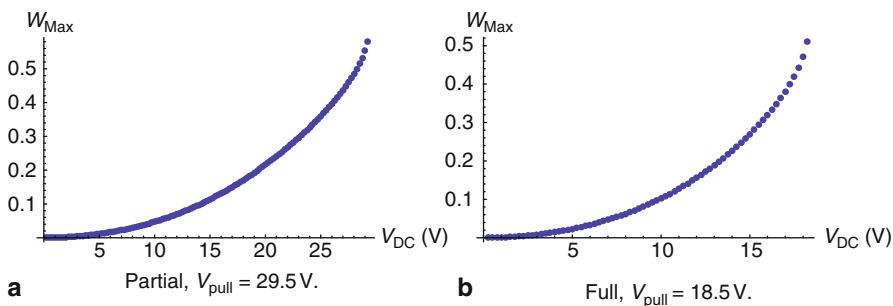


Fig. 6.35 A comparison between the static responses of a clamped-clamped beam actuated by **a** a partial electrode and **b** a full electrode

6.13 The Natural Frequencies Under Electrostatic Force

Predicting accurately the natural frequencies of microbeams is essential for several applications, such as resonators, filters, and resonant sensors. As has been demonstrated in Chap. 5, the electrostatic force tends to weaken the stiffness of

microstructures through its softening effect. Hence, the dependence of the natural frequency of microbeams on the DC bias needs to be determined.

For this, several approaches have been proposed in the literature. Among the most common are the Rayleigh's method, the Rayleigh–Ritz method, and the finite-element methods [28–32]. The Rayleigh's and Rayleigh–Ritz methods, while simple, do not provide accurate results. The finite-element methods can provide accurate results with accurate modeling of the coupling effect between the structural and electrostatic domains, which in the presence of nonlinearities can be very cumbersome.

Other analytical methods have been proposed based on solving the nonlinear Euler–Bernoulli equation. In one method [33], the nonlinear Euler–Bernoulli equation is linearized around the static equilibrium position at a given DC voltage. The resulting equation is then solved iteratively using a shooting technique combined with a collocation/finite-difference method to solve boundary-value problems. This method yields accurate results. However, the disadvantage of this method is that it suffers convergence problems near pull-in and for some stiff beams. Another method has been proposed that takes advantage of the developed ROM of Eq. (6.127). To illustrate this method, consider the ROM of Eq. (6.127). After neglecting damping, the system can be represented in a matrix form as:

$$M(\bar{u})\ddot{\bar{u}} = R(u) \quad (6.134)$$

where $\bar{u} = [u_1, u_2, u_3, \dots, u_n]$ is the modal amplitudes vector, $M(\bar{u})$ is a nonlinear matrix representing the coefficients of $\ddot{\bar{u}}$, and $R(\bar{u})$ is a right-hand side vector representing the forcing and stiffness coefficients. Both $M(\bar{u})$ and $R(\bar{u})$ are nonlinear functions of the modal coordinates $u_i(t)$. Next, \bar{u} is split into a static component X_s , representing the equilibrium position due to the DC actuation, and a dynamic component $\eta(t)$ representing the perturbation around the equilibrium position, that is

$$\bar{u} = X_s + \eta(t). \quad (6.135)$$

Then, substituting Eq. (6.135) into Eq. (6.134), using the Taylor series expansion assuming small η , eliminating the higher-order terms, and using the fact that $R(X_s) = 0$, the following equation is obtained:

$$M(X_s)\ddot{\eta} = J(X_s)\eta \quad (6.136)$$

where $J(X_s)$ is the Jacobian matrix calculated at the equilibrium points. To calculate the natural frequencies of the beam for a given voltage, the stable static solution X_s is substituted into the matrix $M^{-1}J$ and then its corresponding eigenvalues are determined. This is equivalent to solving the below algebraic equation in terms of the eigenvalue λ :

$$Det(M^{-1}(X_s)J(X_s) - \lambda I) = 0$$

where Det is the matrix determinant and I is the identity matrix. Then by taking the square-root of each individual eigenvalue, the natural frequencies of the beam are

obtained. Solving for the eigenfunctions for each eigenvalue yields the modeshapes of the beam.

One can note that the above method has the complication of dealing with the matrix M (which is a consequence of the multiplication by the coefficient $(1 - w)^2$ of the electrostatic force term.) Next, we illustrate a modified approach that is easier to implement, which is also based on solving the beam equation linearized around its equilibrium position using the Galerkin method. This method is accurate and computationally efficient.

For this, consider the original beam equation, Eq. (6.123). Next, the deflection of the beam is split into a static component, due to the actuation of the DC voltage, $w_s(x)$ and a dynamic component $w_d(x, t)$:

$$w(x, t) = w_s(x) + w_d(x, t). \quad (6.137)$$

Substituting Eq. (6.137) into Eq. (6.123), dropping the damping and the higher order terms, and retaining only the linear terms in w_d yield the below linearized equation:

$$\begin{aligned} \frac{\partial^4 w_d}{\partial x^4} + \frac{\partial^2 w_d}{\partial t^2} = & \left[2\alpha_1 \int_0^1 \left(\frac{\partial w_d}{\partial x} \frac{\partial w_s}{\partial x} \right) dx \right] \frac{\partial^2 w_s}{\partial x^2} \\ & + N_{\text{non}} \frac{\partial^2 w_d}{\partial x^2} + \alpha_1 \int_0^1 \left(\frac{\partial w_s}{\partial x} \right)^2 dx \frac{\partial^2 w_d}{\partial x^2} + \frac{2\alpha_2 V_{\text{DC}}^2}{(1 - w_s)^3} w_d. \end{aligned} \quad (6.138)$$

Solving the eigenvalue problem associated with this linearized equation yields the natural frequencies of the beams. Toward this, we use the Galerkin method and assume

$$w_d(x, t) = \sum_{i=1}^n u_i(t) \phi_i(x). \quad (6.139)$$

Subsequently, Eq. (6.139) is substituted into Eq. (6.138) and ϕ_i'''' is replaced with $N_{\text{non}} \phi_i'' + \omega_{\text{non},i}^2 \phi_i$. The outcome is then multiplied by the modeshape ϕ_j and is integrated over the beam domain from 0 to 1, which yields

$$\begin{aligned} \ddot{u}_j + u_j \omega_{\text{non},j}^2 = & \left[2\alpha_1 \int_0^1 \phi_j \frac{\partial^2 w_s}{\partial x^2} dx \int_0^1 \left(\sum_{i=1}^n u_i \phi_i' \frac{\partial w_s}{\partial x} \right) dx \right] \\ & + \left[\alpha_1 \int_0^1 \left(\frac{\partial w_s}{\partial x} \right)^2 dx \right] \int_0^1 \phi_j \sum_{i=1}^n u_i \phi_i'' dx \\ & + \int_0^1 \left[\phi_j \frac{2\alpha_2 V_{\text{DC}}^2}{(1 - w_s)^3} \sum_{i=1}^n u_i \phi_i \right] dx. \end{aligned} \quad (6.140)$$

Equation (6.140) represents a system of linearly coupled ordinary differential equations in terms of the modal coordinates u_j . Solving the eigenvalue problem associated with this system, similar to the method of Sect. 2.7.1, gives the first n natural frequencies of the beam. Example 6.14 gives more details on the method.

Example 6.14: Consider a clamped–clamped microbeam actuated by electrostatic forces. Assuming three symmetric modes in the ROM, derive and formulate the eigenvalue problem. Then, consider a microbeam of length $l = 210 \mu\text{m}$, thickness $h = 1.5 \mu\text{m}$, width $b = 100 \mu\text{m}$, air-gap width $d = 1.18 \mu\text{m}$, effective Young's modulus $E = 169 \text{ GPa}$, and density $\rho = 2,332 \text{ kg/m}^3$. Calculate and plot the first nondimensional natural frequency of the microbeam up to the pull-in instability for the below cases:

- (a) Assuming zero axial force
- (b) Assuming an axial force of 0.0009 N
- (c) Assuming zero axial force with the thickness reduced to $h = 0.6 \mu\text{m}$

Solution: For $n = 3$ (three modes), Eq. (6.140) can be expanded into the following three modal equations:

$$\begin{aligned} \ddot{u}_1 + u_1 \omega_{\text{non},1}^2 = & \left[2\alpha_1 \int_0^1 \phi_1 \frac{\partial^2 w_s}{\partial x^2} dx \int_0^1 \left((u_1 \phi_1' + u_2 \phi_2' + u_3 \phi_3') \frac{\partial w_s}{\partial x} \right) dx \right] \\ & + \left[\alpha_1 \int_0^1 \left(\frac{\partial w_s}{\partial x} \right)^2 dx \right] \int_0^1 \phi_1 (u_1 \phi_1'' + u_2 \phi_2'' + u_3 \phi_3'') dx \\ & + \int_0^1 (\phi_1 \frac{2\alpha_2 V_{\text{DC}}^2}{(1 - w_s)^3} [u_1 \phi_1 + u_2 \phi_2 + u_3 \phi_3]) dx \end{aligned} \quad (\text{a})$$

$$\begin{aligned} \ddot{u}_2 + u_2 \omega_{\text{non},2}^2 = & \left[2\alpha_1 \int_0^1 \phi_2 \frac{\partial^2 w_s}{\partial x^2} dx \int_0^1 \left((u_1 \phi_1' + u_2 \phi_2' + u_3 \phi_3') \frac{\partial w_s}{\partial x} \right) dx \right] \\ & + \left[\alpha_1 \int_0^1 \left(\frac{\partial w_s}{\partial x} \right)^2 dx \right] \int_0^1 \phi_2 (u_1 \phi_1'' + u_2 \phi_2'' + u_3 \phi_3'') dx \\ & + \int_0^1 (\phi_2 \frac{2\alpha_2 V_{\text{DC}}^2}{(1 - w_s)^3} [u_1 \phi_1 + u_2 \phi_2 + u_3 \phi_3]) dx \end{aligned} \quad (\text{b})$$

$$\begin{aligned} \ddot{u}_3 + u_3 \omega_{\text{non},3}^2 = & \left[2\alpha_1 \int_0^1 \phi_3 \frac{\partial^2 w_s}{\partial x^2} dx \int_0^1 \left((u_1 \phi_1' + u_2 \phi_2' + u_3 \phi_3') \frac{\partial w_s}{\partial x} \right) dx \right] \\ & + \left[\alpha_1 \int_0^1 \left(\frac{\partial w_s}{\partial x} \right)^2 dx \right] \int_0^1 \phi_3 (u_1 \phi_1'' + u_2 \phi_2'' + u_3 \phi_3'') dx \\ & + \int_0^1 (\phi_3 \frac{2\alpha_2 V_{\text{DC}}^2}{(1 - w_s)^3} [u_1 \phi_1 + u_2 \phi_2 + u_3 \phi_3]) dx. \end{aligned} \quad (\text{c})$$

Equations (a)–(c) can be rewritten in a matrix format as

$$\begin{Bmatrix} \ddot{u}_1 \\ \ddot{u}_2 \\ \ddot{u}_3 \end{Bmatrix} + \underbrace{\begin{bmatrix} -c_{11} & -c_{12} & -c_{13} \\ -c_{21} & -c_{22} & -c_{23} \\ -c_{31} & -c_{32} & -c_{33} \end{bmatrix}}_{[c_{ij}]} \begin{Bmatrix} u_1 \\ u_2 \\ u_3 \end{Bmatrix} = 0 \quad (\text{d})$$

where the constant coefficients c_{ij} are defined as below:

$$\begin{aligned}
 c_{11} &= \lambda_{11}\lambda_{12} + \lambda_{15}\lambda_{16} + \lambda_{19} - \omega_{\text{non},1}^2 \\
 c_{12} &= \lambda_{11}\lambda_{13} + \lambda_{15}\lambda_{17} + \lambda_{110} \\
 c_{13} &= \lambda_{11}\lambda_{14} + \lambda_{15}\lambda_{18} + \lambda_{111} \\
 c_{21} &= \lambda_{21}\lambda_{12} + \lambda_{15}\lambda_{26} + \lambda_{29} \\
 c_{22} &= \lambda_{21}\lambda_{13} + \lambda_{15}\lambda_{27} + \lambda_{210} - \omega_{\text{non},2}^2 \\
 c_{23} &= \lambda_{21}\lambda_{14} + \lambda_{15}\lambda_{28} + \lambda_{211} \\
 c_{31} &= \lambda_{31}\lambda_{12} + \lambda_{15}\lambda_{36} + \lambda_{39} \\
 c_{32} &= \lambda_{31}\lambda_{13} + \lambda_{15}\lambda_{37} + \lambda_{310} \\
 c_{33} &= \lambda_{31}\lambda_{14} + \lambda_{15}\lambda_{38} + \lambda_{311} - \omega_{\text{non},3}^2
 \end{aligned} \tag{e}$$

and the coefficients λ_{ij} are defined as

$$\begin{aligned}
 \lambda_{11} &= 2\alpha_1 \int_0^1 \phi_1 \frac{\partial^2 w_s}{\partial x^2} dx; \quad \lambda_{21} = 2\alpha_1 \int_0^1 \phi_2 \frac{\partial^2 w_s}{\partial x^2} dx; \quad \lambda_{31} = 2\alpha_1 \int_0^1 \phi_3 \frac{\partial^2 w_s}{\partial x^2} dx; \\
 \lambda_{12} &= \int_0^1 \left(\phi_1' \frac{\partial w_s}{\partial x} \right) dx; \quad \lambda_{13} = \int_0^1 \left(\phi_2' \frac{\partial w_s}{\partial x} \right) dx; \quad \lambda_{14} = \int_0^1 \left(\phi_3' \frac{\partial w_s}{\partial x} \right) dx; \\
 \lambda_{15} &= \alpha_1 \int_0^1 \left(\frac{\partial w_s}{\partial x} \right)^2 dx; \quad \lambda_{16} = \int_0^1 \phi_1 \phi_1'' dx; \quad \lambda_{17} = \int_0^1 \phi_1 \phi_2'' dx; \\
 \lambda_{18} &= \int_0^1 \phi_1 \phi_3'' dx; \quad \lambda_{19} = \int_0^1 \left[\frac{2\alpha_2 V_{\text{DC}}^2}{(1-w_s)^3} \phi_1 \phi_1 \right] dx; \\
 \lambda_{110} &= \int_0^1 \left[\frac{2\alpha_2 V_{\text{DC}}^2}{(1-w_s)^3} \phi_1 \phi_2 \right] dx; \quad \lambda_{111} = \int_0^1 \left[\frac{2\alpha_2 V_{\text{DC}}^2}{(1-w_s)^3} \phi_1 \phi_3 \right] dx \\
 \lambda_{26} &= \int_0^1 \phi_2 \phi_1'' dx; \quad \lambda_{27} = \int_0^1 \phi_2 \phi_2'' dx; \quad \lambda_{28} = \int_0^1 \phi_2 \phi_3'' dx; \\
 \lambda_{29} &= \int_0^1 \left[\frac{2\alpha_2 V_{\text{DC}}^2}{(1-w_s)^3} \phi_2 \phi_1 \right] dx; \quad \lambda_{210} = \int_0^1 \left[\frac{2\alpha_2 V_{\text{DC}}^2}{(1-w_s)^3} \phi_2 \phi_2 \right] dx; \\
 \lambda_{211} &= \int_0^1 \left[\frac{2\alpha_2 V_{\text{DC}}^2}{(1-w_s)^3} \phi_2 \phi_3 \right] dx \quad \lambda_{36} = \int_0^1 \phi_3 \phi_1'' dx; \\
 \lambda_{37} &= \int_0^1 \phi_3 \phi_2'' dx; \quad \lambda_{38} = \int_0^1 \phi_3 \phi_3'' dx; \quad \lambda_{39} = \int_0^1 \left[\frac{2\alpha_2 V_{\text{DC}}^2}{(1-w_s)^3} \phi_3 \phi_1 \right] dx; \\
 \lambda_{310} &= \int_0^1 \left[\frac{2\alpha_2 V_{\text{DC}}^2}{(1-w_s)^3} \phi_3 \phi_2 \right] dx; \quad \lambda_{311} = \int_0^1 \left[\frac{2\alpha_2 V_{\text{DC}}^2}{(1-w_s)^3} \phi_3 \phi_3 \right] dx.
 \end{aligned} \tag{f}$$

The solution procedure is then as follows. For a given value of voltage, the static deflection of the microbeam w_s is evaluated, as in Sect. 6.12.2. Then, the results are substituted into Eq. (f) and the coefficients λ_{ij} , and hence c_{ij} , are calculated. The integrals of Eq. (f) can be easily computed using numerical integration methods,

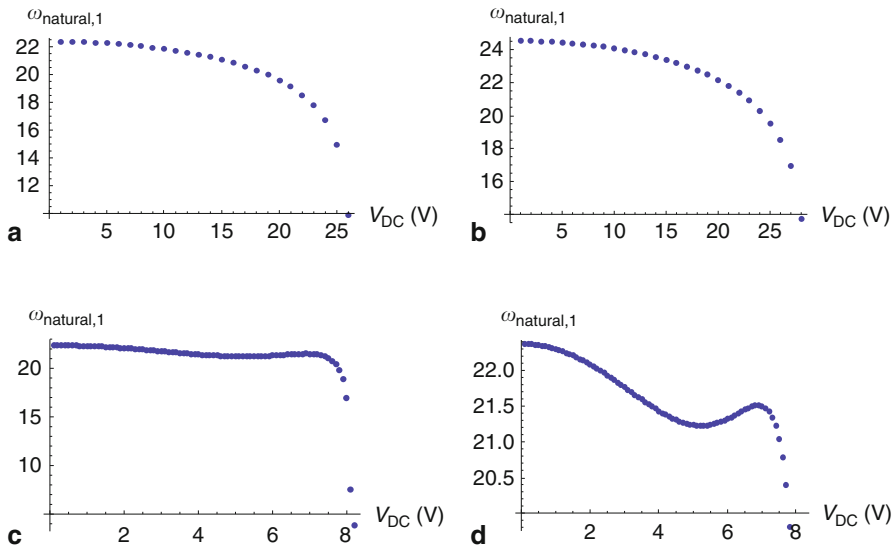


Fig. 6.36 The variation of the first natural frequency of a clamped–clamped beam versus the DC voltage. Figure part **a** is for zero axial force, **b** is for 0.0009 axial force, **c** is for zero axial force with reduced thickness, and **d** is a zoomed view of **c**

such as the Trapezoidal method. After that, the eigenvalue of the matrix $[c_{ij}]$ of Eq. (d) is calculated. In Matlab, one can use the command “eig” and in Mathematica the command “Eigenvalues.” By taking the square roots of the individual eigenvalues, the first three natural frequencies are obtained.

The results of parts (a)–(c) are depicted in Fig. 6.36. Recall here that to obtain the dimensional natural frequencies, the nondimensional frequencies are multiplied by $1/T = \sqrt{EI/(\rho b h l^4)}$. One can see that the axial force has increased the initial natural frequency of the beam and extended the pull-in range. Decreasing the thickness makes the beam more compliant. This increases the parameter α_1 making the effect of midplane stretching more pronounced. As seen in Figs. 6.36c and 6.36d, this can lead to an increase in the natural frequency for some range of voltages (hardening effect due to the midplane stretching) before the softening effect of the electrostatic force dominates again leading to pull-in.

6.14 Pull-in Time of RF Switches

As explained in Sect. 5.6, estimating the pull-in time is crucial for RF switches. The developed ROM of Eq. (6.127) can be used to estimate numerically this parameter. This can be done by integrating numerically the modal equations in time and

monitoring the beam transient response during pull-in until it reaches the stationary electrode (or the dielectric layer if any). Example 6.15 next demonstrates this method.

Example 6.15: Consider the switch of Hung and Senturia [34], which is made of a clamped–clamped microbeam of length $l = 610\text{ }\mu\text{m}$, thickness $h = 2.015\text{ }\mu\text{m}$, width $b = 40\text{ }\mu\text{m}$, air-gap width $d = 2.3\text{ }\mu\text{m}$, Young’s modulus $E = 149\text{ GPa}$, and density $\rho = 2,332\text{ kg/m}^3$. The beam is subjected to a compressive axial force, which is estimated to be near 3.7 MPa . Calculate the pull-in time for the actuation voltages of 8.76, 9, 9.33, 9.5, 10, and 10.3 V . Assume a nondimensional damping coefficient $c_{\text{non}} = 260$.

Solution: First, we need to investigate the convergence of the ROM of Eq. (6.127) for calculating the pull-in time t_{pull} . It turns out that five symmetric modes need to be used at least for accurate results. Using three or four modes, for instance, predicts stable response at $V_{\text{DC}} = 8.76\text{ V}$. Next, we integrate the equations of motion and monitor the response for the time instant at which the beam reaches the other electrode ($W_{\text{Max}} = 1$). This nondimensional time is recorded as the pull-in time [27]. To transform to dimensional time, the nondimensional time is multiplied by $T = \sqrt{\rho b h l^4 / (E I)}$. Figure 6.37 depicts an example of the obtained transient response during pull-in. From the figure, t_{pull} of this case is calculated as $t_{\text{pull}} = 52.5 \times T = 4.2\text{ ms}$. Table 6.5 shows the obtained simulation results along with the measured experimental data [34].

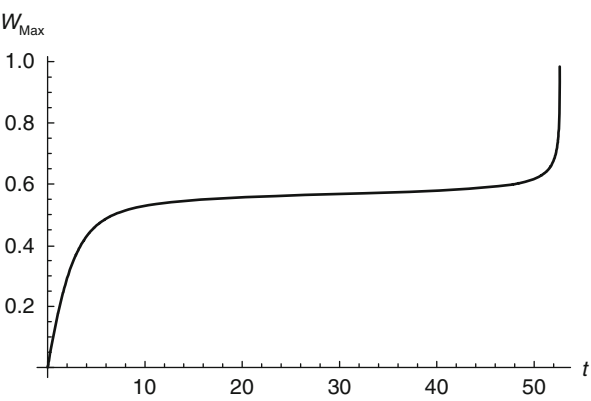


Fig. 6.37 The switch response for $V_{\text{DC}} = 8.76\text{ V}$ showing the onset of pull-in

Table 6.5 The pull-in time versus the actuation voltage as measured experimentally [34] and obtained by simulation using the ROM

$V_{\text{DC}}\text{ (V)}$	8.76	9	9.33	9.5	10	10.3
$t_{\text{pull}}\text{ (ms), Exp}$	3.5	0.75	0.5	0.36	0.25	0.2
$t_{\text{pull}}\text{ (ms), Sim}$	4.2	0.685	0.435	0.374	0.272	0.235

6.15 Resonators Under AC + DC Excitation

In Sect. 5.8.3, the nonlinear vibration of mechanical oscillators due to external forcing has been discussed. Examples of oscillators of cubic and quadratic nonlinearities have been studied in details. Also, the nonlinear oscillation of single-sided capacitor has been investigated. Next, a more accurate beam model combined with the ROM is utilized for the dynamic response of microbeams to a combined load of AC and DC excitation. As a case study, we consider clamped–clamped microbeams. We will demonstrate that, when actuated by parallel-plate electrostatic force, the dynamic of the microbeam is influenced by both the cubic nonlinearity due to midplane stretching and the quadratic nonlinearities due to the initial deflection of the beam and the electrostatic force. Primary, subharmonic, and superharmonic resonances and dynamic pull-in will be shown. Hence, the discussions of Sect. 5.8.3 are all relevant here.

Example 6.16: We consider the same microbeam of Example 6.12 of length $l = 510 \mu\text{m}$, thickness $h = 1.5 \mu\text{m}$, width $b = 100 \mu\text{m}$, and air-gap width $d = 1.18 \mu\text{m}$. The microbeam is excited by a voltage load of the form $V_{\text{DC}} + V_{\text{AC}} \cos(\Omega t)$. Assume the beam is subjected to an axial force of 0.0009 N and of a quality factor of 100. Consider $E = 154 \text{ GPa}$ and $\rho = 2,330 \text{ kg/m}^3$. Calculate and plot the nondimensional frequency–response curves for the following cases:

- (a) $V_{\text{DC}} = 2 \text{ V}$ and $V_{\text{AC}} = 0.1 \text{ V}$ near the fundamental natural frequency
- (b) $V_{\text{DC}} = 3.4 \text{ V}$ and $V_{\text{AC}} = 0.05 \text{ V}$ near the fundamental natural frequency
- (c) $V_{\text{DC}} = 2 \text{ V}$ and $V_{\text{AC}} = 0.2 \text{ V}$ near the fundamental natural frequency
- (d) $V_{\text{DC}} = 2 \text{ V}$ and $V_{\text{AC}} = 0.3 \text{ V}$ near the fundamental natural frequency
- (e) $V_{\text{DC}} = 2 \text{ V}$ and $V_{\text{AC}} = 0.6 \text{ V}$ near half the fundamental natural frequency
- (f) $V_{\text{DC}} = 2 \text{ V}$ and $V_{\text{AC}} = 0.6 \text{ V}$ near twice the fundamental natural frequency

Solution: The method of solution is based on integrating the equation of motion of the ROM of Eq. (6.127) for a long period of time until a steady-state response is reached. Continuation of the initial conditions is used as explained in Example 5.21. For this beam, the static pull-in voltage is estimated to be 4.8 V . The dynamic response of the loading cases of (a)–(f) are depicted in Fig. 6.38. For the loading case of (a), one can see a hardening behavior. This figure was obtained using a forward sweep of the excitation frequency Ω . On the other hand, the loading case of (b) yields a softening behavior as seen in Fig. 6.38b, which was generated using a backward sweep. The reason of this is that for case (a), the cubic nonlinearity due to midplane stretching of hardening effect dominates the electrostatic nonlinearity of softening effect. Increasing V_{DC} enhances the electrostatic nonlinearity. This continues until its effect dominates the cubic nonlinearity, as in case (b). The impacts of the various nonlinearities can be lumped into a single parameter, which is called the effective nonlinearity [35]. In a previous study, it was found that this effective nonlinearity changes sign from positive indicating hardening effect to softening indicating softening effect as V_{DC} is changed [35].

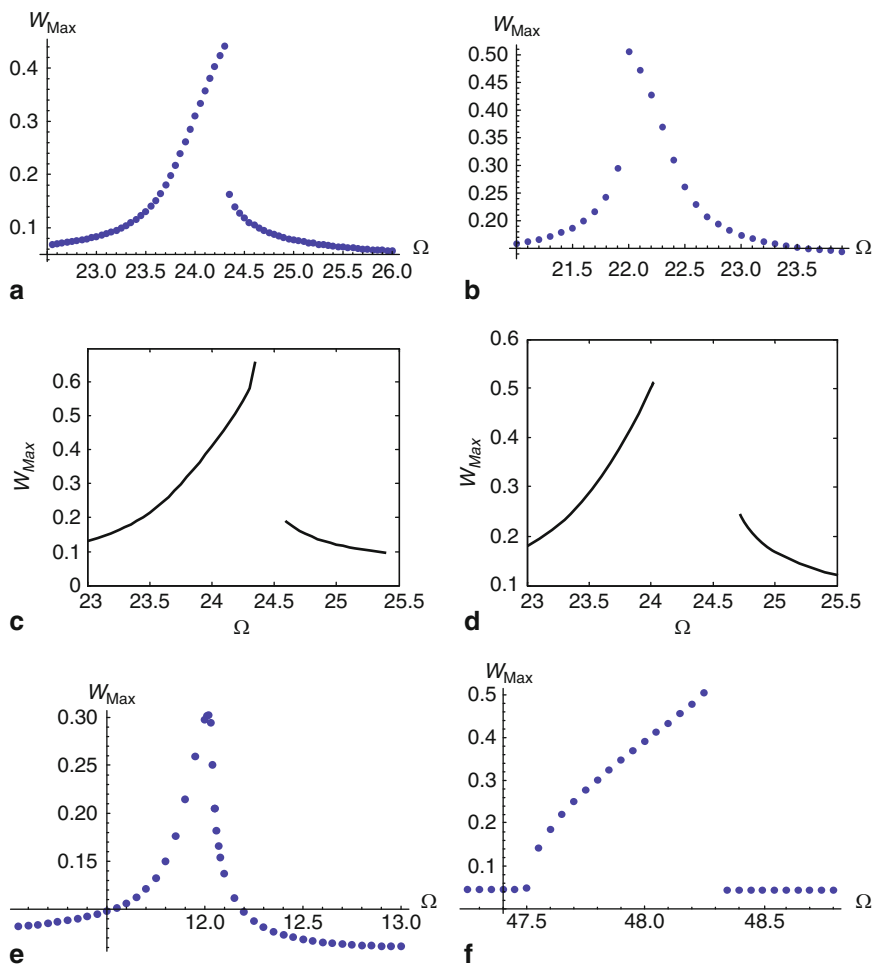


Fig. 6.38 Frequency–response curves of a clamped–clamped beam for the loading cases of **a–f** of Example 6.16. **a** Hardening behavior. **b** Softening behavior. **c** Dynamic pull-in. **d** Pull-in band. **e** Superharmonic resonance. **f** Subharmonic resonance

Figure 6.38c indicates a frequency–response curve of hardening type with the slope of the upper branch approaching infinity. This is an indication of the phenomenon of dynamic pull-in [36–39]. This instability occurs at a voltage load much lower than the static pull-in threshold. Therefore, resonators designers need to be aware of its presence. Increasing V_{AC} further, Fig. 6.38d, creates a band of frequencies where the resonator is forced to pull-in if it is operated inside it (pull-in band [38, 39]). Figure 6.39 shows the time-history responses of the beam just before the pull-in band and inside the pull-in band. Such a behavior has been proposed to realize smart switches triggered by the detection of mass [40]. It is worth to mention that there exists another stable solution (not shown) of high amplitude (W_{Max} near 0.8)

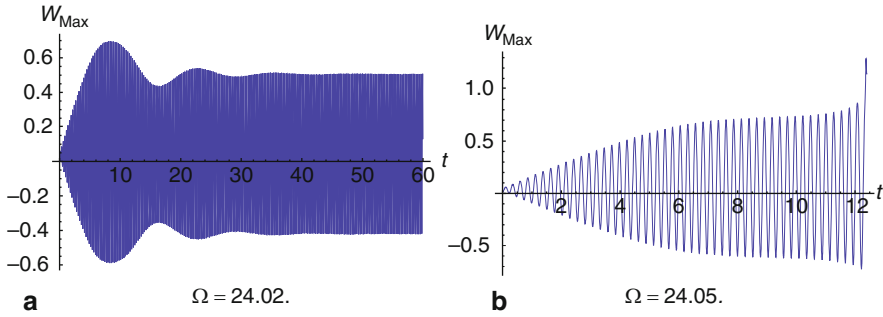


Fig. 6.39 Time-history responses for the loading of case (d). **a** before the pull-in band and **b** inside the pull-in band

above this pull-in band, where in theory the beam may land on. Practically, the basin of attraction of this attractor is too weak to be realized physically [36]. More details on dynamic pull-in and the basin of attraction are in Chap. 7.

Figure 6.38d, e shows superharmonic resonance of order two and subharmonic resonance of order half, respectively. These are consequences of the quadratic effect of the electrostatic forces. In addition to these, secondary resonances of order one third and three exist (not shown) due to the cubic geometric nonlinearity. However these are of weaker effect. Increasing the level of voltages can lead to dynamic pull-in phenomenon in the case of secondary resonances also [37].

6.16 Atomic Force Microscopes

6.16.1 Introduction

The atomic force microscope (AFM) was invented by Bining, Quate, and Gerber in 1986 [41]. It is a very powerful tool for imaging surfaces of materials, conductive and nonconductive, soft and hard, metals and biomaterials, in vacuum, air, or liquid [42–91]. It has been increasingly implemented for nanomanipulation, nanoassembly, and nanofabrication. The AFM overcomes the limitations of the older version of microscopy, the scanning tunneling microscope (STM), which requires electrical conduction of the sample material limiting it to conducting materials, such as metals and semiconductors.

The main core of an AFM consists of a microcantilever with a very sharp tip at its end, Fig. 6.40. Typical dimensions of the cantilevers are few hundred μm in length, tens of μm in width, and 1–2 μm in thickness. The motion of the cantilever is detected by shining a laser beam to its end, which is reflected back to a photo detector. This provides a feedback signal of the cantilever motion. The feedback signal is transmitted to a controller, which either adjusts the distance between the

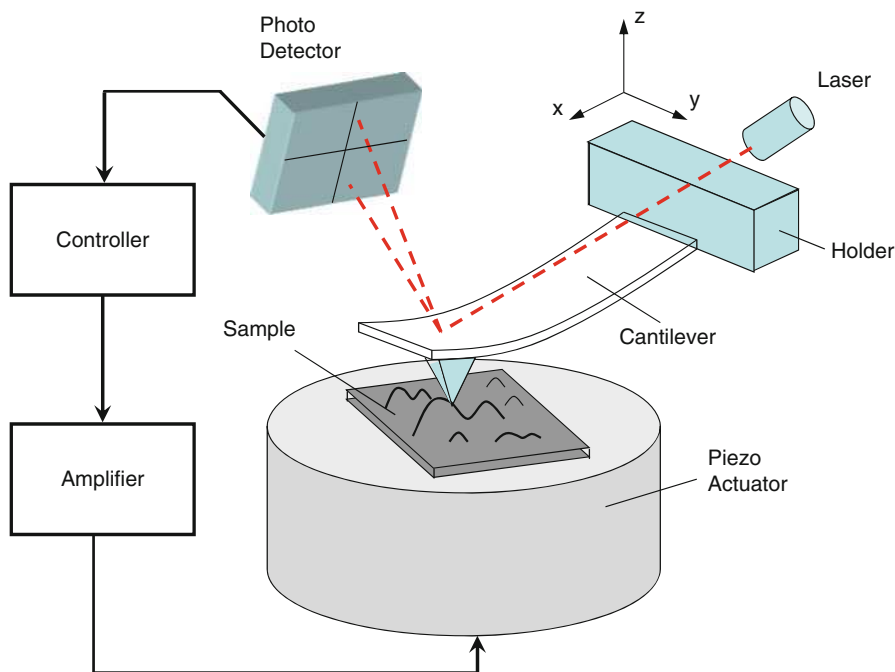


Fig. 6.40 Schematic of an atomic force microscope (AFM)

cantilever tip and the sample or adjusts the amplitude, phase, or operating frequency of the cantilever in the case of a dynamic AFM. This adjustment can be achieved, for example, using a piezoelectric actuator. A piezoelectric actuator is also used to move the sample horizontally in the x - y direction for scanning purposes.

There are two major modes of operation of an AFM: The static mode and the dynamic mode. In the static mode, also sometimes called the contact mode, the tip is made to be constantly in contact with the sample surface. A feedback loop is used to minimize the deflection of the cantilever away from its nominal position so that the deflection of the cantilever is kept constant (controlling the deflection means controlling the force of interaction between the beam tip and the sample surface). This feedback control signal maps the topology of the surface. The beams of a contact mode AFM are designed to be very compliant so that they can deflect significantly allowing precise mapping of any small feature on the surface of the sample they are in contact with. The experimental realization of this mode is difficult; however, its physical interpretation is simple. The static mode AFM is used for materials that are not affected by the shear of the sharp tip during scanning. Hence, it is not suitable for polymers and biological materials, such as cells.

In the dynamic mode AFM, the cantilever is deliberately vibrated. Because of the interaction force between the cantilever tip and the sample, the vibration properties of the beam (resonance frequency, amplitude, and phase) vary as the cantilever is scanned over the surface. By measuring the variation in either of these parameters,

information about the topology of the surface is obtained. Dynamic mode AFM offers higher resolution compared to the static one. It also minimizes the degradation of the tip and allows the testing of soft materials.

There are two major categories of dynamic AFM: amplitude-modulation (AM) and frequency-modulation (FM) [59]. The AM-AFM is also called intermittent contact or tapping mode AFM, since in this mode the cantilever tip makes a brief contact with the sample while being vibrated over a small portion of each vibration cycle. The idea of vibrating the cantilever intentionally was first introduced by Martin et al., [73] with the intention of making a noncontact AFM. Later, in 1993 Zhong et al., [91] proposed the tapping mode AFM [59]. In AM-AFM, the cantilever is excited at a fixed frequency near its fundamental natural frequency. Due to the contact and the tip-sample interaction, the oscillation amplitude (and also the phase) changes, which is used as feedback parameter to image the sample topography. The phase change reflects information about the composition and viscoelastic property of the sample. Hence, the AM-AFM allows measuring simultaneously the topographic and compositional contrast of a sample through amplitude and phase monitoring. The tapping mode AFM can be used in air or liquid and suits soft material, such as biological materials and polymers. The excitation of the cantilever can be achieved by a piezoelectric or a magnetic actuator.

A FM-AFM, also called a noncontact (NC) AFM, was introduced by Albrecht et al. [44] in 1991. The cantilever in this case is operated at constant amplitude and is made to track its resonance frequency, which varies during scanning due to the interaction between the tip and the surface, through a self-driven (self-excited) oscillator. This resonance-frequency shift of the cantilever is measured and used as the feedback signal to map the topology of the surface. Typically, ultra high vacuum UHV is needed for this mode. NC-AFMs are used to probe electric, magnetic, and atomic forces. They can achieve true atomic resolution and enhanced sensitivity with the high quality factor without any restriction on the bandwidth of device. They are suitable for soft materials and provide very high resolution.

Whether it is static or dynamic mode, the core principle of AFM relies primarily on the motion of its cantilever beam and how its tip interacts with the sample through the nonlinear interaction forces. Understanding the dynamics of the AFM is crucial to ensure proper operation, calibration, and interpretation of the transmitted images. Indeed, several artifacts and strange results have been reported when recording images using AFMs, such as strange contours, unexpected high shifts, and sudden changes of the image resolution [52, 70, 72]. These artifacts have been attributed to the dynamic behavior of the AFM and its interaction between its tip and the surface of the sample.

6.16.2 Interaction Forces

All versions of the AFM depend on the forces of interaction between the tip and the sample. There are several models that have been proposed to model these forces.

A common fact among all the models is that the interaction forces are inherently nonlinear. These forces can be classified into short and long-range forces. The short range forces are repulsive chemical forces active in the range of fraction of nano meters (nm). The long-range forces are attractive forces. They are effective to a range up to 100 nm. In the absence of liquid and electrostatic charges and with a properly controlled environment, van der Waals forces become the most critical force. By approximating the tip of the sample as a sphere and the surface of the sample as a flat surface, the van der Waals forces F_{van} can be expressed as

$$F_{\text{van}} = \frac{-HR}{6d^2} \quad (6.141)$$

where H is the Hamaker constant, R is the tip radius, d is the instantaneous tip-surface separation (Fig. 6.41), and the negative sign to indicate an attractive force.

For short-range forces, two approaches have been utilized to model their effect in AFM applications. One approach is based on the molecular interactions due to the Paulis and ionic repulsion forces among the atoms on the AFM tip and the sample. Examples of such models are the Morse potential [60], the Lennard–Jones (L–J) potential, and the Stillinger–Weber potential models [63]. Of these models, the L–J potential model is the most commonly used. The L–J potential derivation starts from the interaction potential between two molecules (6–12 potential) [49]. Then, the interaction potential between a single molecule on the tip and that of the sample is calculated. The results are then integrated over the surface of the tip (sphere) and the sample (flat surface), which yields the tip-sample interaction potential. The result contains both an attractive component due to van der Waals force and a repulsive component due to the Pauli principle. The L–J potential $V_{\text{L–J}}$ in this case can be expressed as

$$V_{\text{L–J}} = \frac{R}{6} \left[\frac{A_1}{210d^7} - \frac{A_2}{d} \right] \quad (6.142)$$

where A_1 is the Hamacker constant for the repulsive potential and A_2 is the Hamacker constant for the attraction potential ($A_2 = H$). Taking the derivative of $V_{\text{L–J}}$ yields

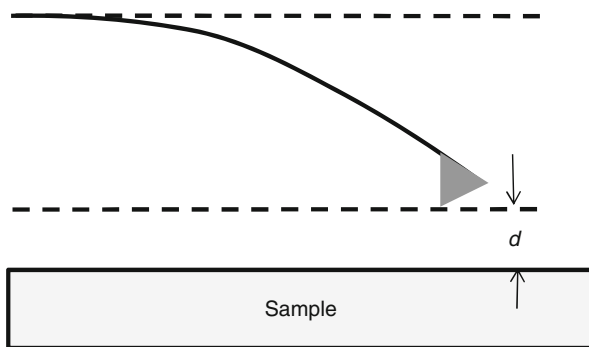


Fig. 6.41 Schematic of an AFM cantilever beam suspended above a sample

the L-J force F_{L-J} :

$$F_{L-J} = \frac{R}{6} \left[\frac{A_1}{30d^8} - \frac{A_2}{d^2} \right]. \quad (6.143)$$

The force can also be written as

$$F_{L-J} = \frac{A_2 R}{6\sigma^2} \left[\frac{1}{30} \left(\frac{\sigma}{d} \right)^8 - \left(\frac{\sigma}{d} \right)^2 \right] \quad (6.144)$$

where σ is the atomic size of the tip and flat surface (typical value equal to 0.3 Å [49]).

The second approach is based on continuum mechanics laws of contacts instead of considering the molecular forces directly with the justification that the interaction between the sample and tip during contact involves hundreds of atoms [59]. Among the used continuum mechanics laws are these of Hertz, Derjagin–Muller–Toropov (DMT), and Johnson–Kendall–Robert (JKR) (suitable for highly adhesive surface with low stiffness) [59, 64]. The DMT model is suitable for stiff contact with low adhesion forces. The DMT and Hertz models are commonly used in the AFM literature. The contact force based on the Hertz model F_{HZ} can be expressed as

$$F_{HZ} = \frac{4E^* \sqrt{R}}{3} (a_0 - d)^{3/2} \quad (6.145)$$

where E^* is an effective modulus of elasticity of the tip and sample given by

$$\frac{1}{E^*} = \frac{1 - \nu_t^2}{E_t} + \frac{1 - \nu_s^2}{E_s}$$

where ν is the Poisson's ratio, a_0 is the intermolecular distance (where the contact is assumed to start for tapping AFM), and the subscripts t and s indicate tip and sample, respectively. In the DMT model, in addition to the Hertzian contact force, an adhesion force is assumed, which is expressed by

$$F_{Adh} = 4\pi R\gamma \quad (6.146)$$

where γ is the surface energy.

6.16.3 AFM Models

Various models have been utilized to analyze the dynamic response of the AFM cantilevers with their tip interaction with a sample. Several models have been based on a single-degree-of-freedom system, which models the AFM cantilever as a lumped spring–mass–damper system. Other models have been based on the Euler–Bernoulli beam theory [42, 45, 64, 65, 75–78, 85, 87–89]. The nonlinear interaction force between the tip and the sample has been imposed on the beam model through using a

spring, spring–mass, or spring–mass–damper system or through assigning a localized force at the beam tip. Next, we outline some of the models that have been used so far for AFMs. For more comprehensive reviews of the contributions in this field, we refer to these excellent review papers [43, 59, 63, 67, 85].

For **contact** AFMs, the Hertzian contact force has been extensively used to model the interaction of the cantilever tip with the sample. For example, in the works of [76] a beam model is utilized, in which one end of the beam is fixed and the other end is attached to a spring to represent the contact effect with the sample. The spring constant is extracted from the gradient of the Hertzian contact force at the equilibrium position of the tip (this is similar to linearizing the force around the equilibrium position or taking the Jacobian of the force at the equilibrium position). Turner [88], Abdel-Rahman and Nayfeh [42], and Arafat et al. [45] assumed a nonlinear spring and a damper at the tip of the AFM cantilever. The nonlinear spring coefficients were extracted by expanding the Hertzian force into Taylor series and equating the outcome to a nonlinear spring with nonlinearities up to the third order. The method of multiple scales, a perturbation technique, has been used then to simulate the dynamic response of the AFM.

In a contact AFM, the tip of the cantilever in the initial static position penetrates the sample by a distance δ_0 . Due to this indentation, the equation governing the static deflection of the cantilever beam w_s of a contact AFM and boundary conditions can be written as [42, 45]

$$EI \frac{d^4 w_s}{dx^4} = 0 \quad (6.147a)$$

$$w_s = 0; \quad \frac{dw_s}{dx} = 0; \quad \text{at } x = 0 \quad (6.147b)$$

$$\frac{d^2 w_s}{dx^2} = 0; \quad EI \frac{d^3 w_s}{dx^3} = F_0; \quad \text{at } x = l \quad (6.147c)$$

where $F_0 = \frac{4}{3} E^* \sqrt{R \delta_0^3}$, which is the zeroth-order component coming from expanding the Hertzian force into a Taylor series [88] or from parameter extraction techniques [42]. Equations (6.147a)–(6.147c) are solved analytically as in Sect. 6.2 to yield the equilibrium position of the beam and its tip (this will be left as an exercise).

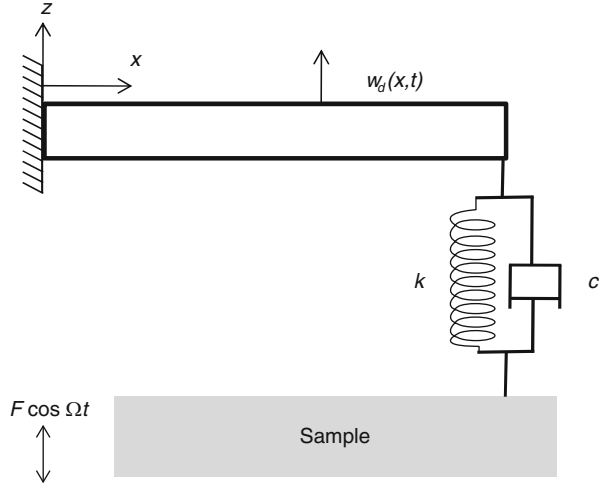
The equation of motion governing the cantilever dynamic deflection w_d around the static position (see Fig. 6.42) and its boundary conditions can be written as [42, 45]

$$EI \frac{\partial^4 w_d}{\partial x^4} + \rho A \frac{\partial^2 w_d}{\partial t^2} = 0 \quad (6.148a)$$

$$w_d = 0; \quad \frac{\partial w_d}{\partial x} = 0; \quad \text{at } x = 0 \quad (6.148b)$$

$$\frac{\partial^2 w_d}{\partial x^2} = 0; \quad \text{at } x = l \quad (6.148c)$$

Fig. 6.42 A beam model of a contact AFM



$$EI \frac{\partial^3 w_d}{\partial x^3} = \mu \frac{\partial w_d}{\partial t} + \alpha_1 \left(\frac{w_d}{\delta_0} \right) - \alpha_2 \left(\frac{w_d}{\delta_0} \right)^2 - \alpha_3 \left(\frac{w_d}{\delta_0} \right)^3 + F \cos(\Omega t); \quad \text{at } x = l \quad (6.148d)$$

where α_1 , α_2 , and α_3 are Hertzian contact coefficients defined as

$$\alpha_1 = 2E^* \sqrt{R\delta_0^3}; \quad \alpha_2 = \frac{\alpha_1}{4}; \quad \alpha_3 = \frac{\alpha_1}{24}.$$

The parameters F and Ω are the amplitude and frequency of the excitation force applied from the sample to the beam, respectively, and μ is an assumed damping coefficient representing the dissipation of energy of the beam during its contact with the sample. Equation (6.148d) represents a force balance at the tip of the beam between the internal shear force, the damping force, the nonlinear restoring force from the contact, and the excitation force from the sample. Equations (6.148a)–(6.148d) form the starting point for simulating the dynamic response of the AFM. As a first step, the linear undamped eigenvalue problem is solved to determine the natural frequency of the beam during contact. In this case, the coefficients α_2 , α_3 , and μ are set equal to zero in Eq. (6.148d). Thus, the problem is reduced to solving the eigenvalue problem of a beam with a linear spring at the tip with a coefficient α_1 .

Models of **NC-AFM** have mainly considered the interaction between the tip and the sample through either the van der Waals force alone [48, 53], the L–J force alone [49, 89], or both the van der Waals and L–J forces [61]. The Morse potential has been also utilized [60]. A major goal in many of these models is to calculate the shift of the resonance frequency of the AFM as a function of the tip-sample distance (see for example [60, 61]). The linear shift in the natural frequency of the beam in this case can be calculated by linearizing the nonlinear force and then solving the resulting

eigenvalue problem. To obtain the nonlinear shift in the resonance frequency (backbone curve), perturbation techniques can be utilized, such as the method of multiple scales or the averaging method.

Several approaches have been used to model tapping-mode AFM. These include the L–J force [46, 49, 50, 69, 65, 74, 79, 90], an impact model [86], a piecewise linear sample interaction model [54, 55, 83, 84], a van der Waals force combined with the DMT model [56–58, 58, 71], and an L–J force combined with the Hertzian model [81, 82]. With the exception of the van der Waals force and the L–J force models, all other models assume discrete forms of the forces in the attractive and repulsive (or contact) regimes. As an example, the model of Garcia and Paulo [57, 58] approximates the interaction forces as

$$F_{\text{tip}} = \begin{cases} F_{\text{van}} = \frac{-HR}{6d^2}; & d > a_0 \\ F_{\text{Adh}} + F_{\text{HZ}} = \frac{-HR}{6a_0^2} + \frac{4E^*\sqrt{R}}{3}(a_0 - d)^{3/2}; & d \leq a_0 \end{cases} \quad (6.149)$$

where a_0 is an intermolecular distance that is introduced to avoid the divergence of the first part of Eq. (6.149) when d approaches zero (when there is penetration). Note that in the second part of Eq. (6.149), the adhesion force is assumed equal to that of the van der Waals force at a_0 .

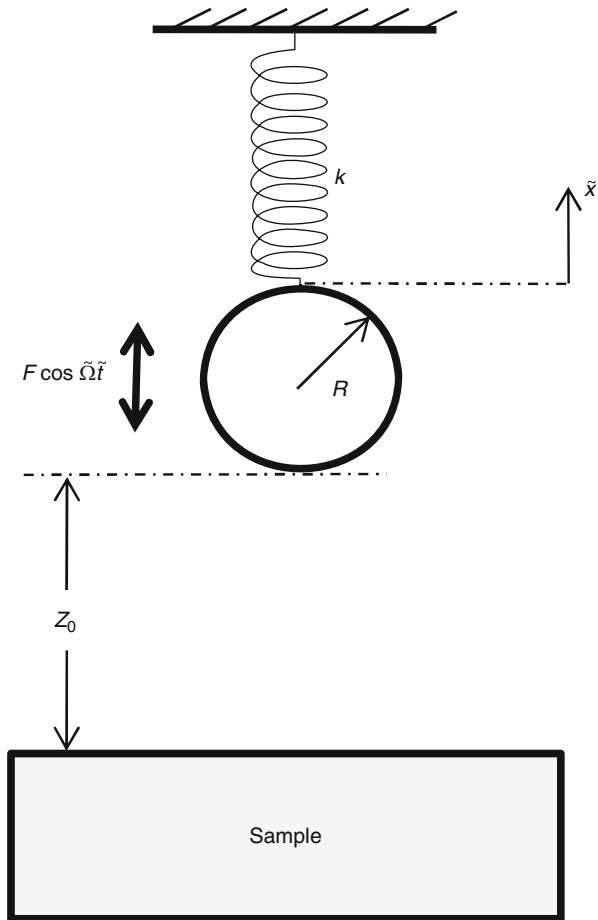
The various tapping AFM models have revealed the existence of more than one stable state of the cantilever, which creates complex dynamical phenomena including hysteresis, jumps, and sensitivity to initial conditions [72]. Chaotic behaviors due to the presence of the double-well potential formed of the long-range attractive and short-range repulsive forces have been reported numerous in the literature both theoretically and experimentally through subharmonic and period-doubling bifurcations [50, 51, 66, 74, 90]. Complex and global dynamical behavior concerning the cross-well motion of the AFM within the framework of the escape from potential well theory has been investigated in several other works [46, 49, 65, 65, 68, 79].

6.16.4 AFM Under Lennard–Jones Force

In this section, we consider as a case study the behavior of an AFM cantilever under the influence of the L–J force. As mentioned earlier, this model can be used to represent a NC-AFM and can serve as a good approximation to understand the behavior of a tapping-mode AFM. To explain several key concepts of the AFM without the distractions of the computational complications of sophisticated models, we utilize a lumped-parameters model. Later on, we shed light on the use of a distributed-parameter model.

To proceed, consider the spring–mass model of the AFM cantilever shown in Fig. 6.43 [49]. Damping is neglected here to simplify the analysis. The beam has an effective mass m and an effective stiffness k . The tip of the cantilever beam is modeled as a sphere of radius R . The cantilever tip is assumed to be placed initially

Fig. 6.43 A lumped-parameter model of a noncontact AFM



above the sample a distance Z_0 . This distance represents the tip-sample separation in the absence of any interaction among them. The cantilever is assumed to be excited harmonically with the force $F \cos \tilde{\Omega} \tilde{t}$, where F and $\tilde{\Omega}$ are the force amplitude and frequency, respectively, and \tilde{t} is the time. The displacement of the cantilever tip with respect to Z_0 is labeled \tilde{x} . Accordingly, the equation of motion governing the displacement of the cantilever tip under the influence of the L-J force is written as

$$m\ddot{\tilde{x}} + k\tilde{x} = F \cos \tilde{\Omega} \tilde{t} + \frac{A_1 R}{180(Z_0 + \tilde{x})^8} - \frac{A_2 R}{6(Z_0 + \tilde{x})^2}. \quad (6.150)$$

Next, the following normalized quantities are introduced:

$$\tilde{x} = \frac{x}{Z_s}; \quad \tilde{t} = \frac{t}{T} \quad (6.151)$$

where T is a time scale and Z_s is a critical displacement (see explanation below), both defined as

$$T = \sqrt{\frac{m}{k}}; \quad Z_s = \frac{3}{2} \left(\frac{A_2 R}{3k} \right)^{1/3}.$$

Substituting Eq. (6.151) into Eq. (6.150) yields the following nondimensional equation of motion:

$$\ddot{x} + x = F_{\text{non}} \cos \Omega t + \frac{\beta_1}{(\alpha + x)^8} - \frac{\beta_2}{(\alpha + x)^2} \quad (6.152)$$

where

$$F_{\text{non}} = \frac{F}{kZ_s}; \quad \beta_1 = \frac{A_1 R}{180 k Z_s^9}; \quad \beta_2 = \frac{A_2 R}{6 k Z_s^3}; \quad \alpha = \frac{Z_0}{Z_s}; \quad \Omega = \tilde{\Omega} T. \quad (6.153)$$

It is fruitful at this juncture to consider the special case of Eq. (6.152) for a beam under the influence of **van der Waals** force only [48]:

$$\ddot{x} + x = \frac{\beta_2}{(\alpha + x)^2}. \quad (6.154)$$

Writing Eq. (6.154) into state-space representation gives

$$\dot{x}_1 = x_2 \quad (6.155a)$$

$$\dot{x}_2 = \frac{\beta_2}{(\alpha + x)^2} - x. \quad (6.155b)$$

Setting the right hand side of Eq. (6.155b) equal to zero yields a third-order algebraic equilibrium equation:

$$x = \frac{\beta_2}{(\alpha + x)^2}. \quad (6.156a)$$

Equation (6.156a) predicts three solutions. Of these, two are physical, of which one turns out to be stable and the other is unstable (the details will be left as an exercise). Both meet at a saddle-node bifurcation in the x - α space corresponding to the point at which the beam collapses into the sample (similar to the pull-in collapse). Taking the Jacobian of Eq. (6.155a) and (6.155b) and solving for the eigenvalue equation gives

$$\lambda^2 = -1 - \frac{2\beta_2}{(\alpha + x)^3}. \quad (6.156b)$$

At the saddle-node bifurcation point, the eigenvalue λ vanishes. Setting Eq. (6.156b) equal to zero and solving for the critical value of x , x_c , yield

$$x_c = -\alpha + 2^{1/3} \beta_2^{1/3}.$$

Recalling that this point is also an equilibrium solution, substituting this value into Eq. (6.156a), and solving for the corresponding critical α give $\alpha = 3\beta_2^{1/3}/2^{2/3}$. Recalling the definitions of α and β_2 from Eq. (6.153) and solving for the critical Z_0 yield $Z_0 = \frac{3}{2} \left(\frac{A_2 R}{3k} \right)^{1/3}$.

Note that this value of critical Z_0 is the same as Z_s . Hence, the normalization of x with respect to Z_s is actually normalization with respect to the critical tip-sample separation at which the beam collapses into the sample assuming only van der Waals forces [48].

Now back to Eq. (6.152) and the case of a beam under L–J force. For numerical calculations, consider the AFM cantilever of Rützel et al. [79] with the parameters shown in Table 6.6. The equation governing the static response of the beam is obtained by setting the forcing and inertia terms of Eq. (6.152) equal to zero

$$x = \frac{\beta_1}{(\alpha + x)^8} - \frac{\beta_2}{(\alpha + x)^2}. \quad (6.157)$$

Solving Eq. (6.157) for a given value of Z_0 , and hence α , yields nine solutions. The majority of these are complex. Depending on the value of Z_0 , the real values of x can be one or three. In the case of three solutions, it is necessary to screen whether a solution is realistic for this model or not. For some ranges of Z_0 , x can come out negative with an absolute value exceeding that of Z_0 , which indicates penetration into the sample. Such a solution is excluded for this L–J model. For other cases, it turns out that there coexist three possible solutions. Analyzing the stability of these solutions, as explained in Chap. 5, reveals that two of them are stable and the third one is unstable. The equilibrium solutions of the considered case study are shown in Fig. 6.44a. As seen in the figure, there are two saddle-node bifurcations with possibility of jumps and hysteresis. Another representation of the results is depicted in Fig. 6.44b, which shows the equilibrium separation distance d between the tip and the sample versus Z_0 .

The following remarks can be made based on Fig. 6.44. As the cantilever is brought down near the surface of the sample at point A, it starts to deflect downward due to the attractive van der Waals force, as reflected in the negative x in Fig. 6.44a and the decreasing value of the equilibrium gap $d = Z_0 + \tilde{x}$ in Fig. 6.44b. Moving the

Table 6.6 Properties of the case study of the AFM cantilever of Rützel et al. [79]

Symbol	Value
l	449 μm
b	46 μm
h	1.7 μm
R	150 μm
ρ	2,330 kg/m^3
k	0.11 N/m^{-1}
E	176 GPa
f_1	11.804 kHz
Q	100
A_1	$1.3596 \times 10^{-70} \text{ J m}^6$
A_2	$1.865 \times 10^{-19} \text{ J}$

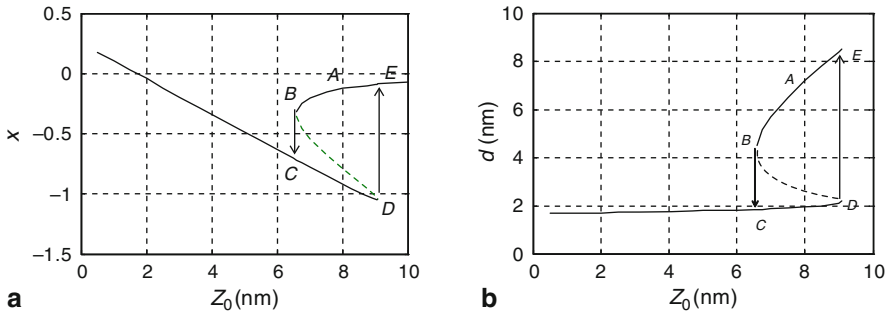


Fig. 6.44 The equilibrium solutions of an AFM cantilever under L-J force. Stable (solid), unstable (dashed)

cantilever closer to the sample (decreasing Z_0) leads to further downward deflection up to point B, where it loses stability and snaps down into the sample to point C. This point represents a saddle-node bifurcation and is known as the **jump-to-contact** instability. It is the point at which the nonlinear attractive van der Waals force overcomes the restoring force of the cantilever. Decreasing Z_0 further makes the cantilever tip deflects less downward as the repulsive forces starts to come into play until they dominate and cause an upward deflection (positive x). On the other hand, if the cantilever is pulled back from the sample (moving from point C to D) the cantilever tip deflection downward increases until the attractive forces get strong enough to balance the other repulsive and restoring force of the microbeam at point D. This point represents another saddle-node bifurcation, where the cantilever loses stability again and snaps back off the sample to point E.

Figure 6.45 shows plots of the L-J force, the L-J potential, and the corresponding phase portrait of the beam for three representative values of Z_0 . In all the three cases, the L-J force shows qualitatively similar behavior. It is positive for small values of x , indicating repulsive forces, and negative for larger values of x , indicating attractive forces. The potential well $V(x)$ and the corresponding phase portrait vary however for each value of Z_0 . For $Z_0 = 10$ nm and $Z_0 = 4$ nm, the potential function is of a single-well type with the stable center is the only possible equilibrium solution. On the other hand, in the case of $Z_0 = 8$ nm, the potential function is of a double-well type with two possible stable centers and one saddle. The bi-stable state of the system in this case, as reflected from Fig 6.44 or Fig. 6.45b, is the main cause of the complicated dynamical behavior reported for tapping mode AFM that includes jumps, hysteresis, and possible chaotic behavior.

The natural frequencies of the cantilever beam associated with each equilibrium solution can be found by first linearizing the force in the equation of motion, Eq. (6.152), by expanding it into Taylor series. Then by taking the square root of the coefficient of x (the effective stiffness) evaluated at the equilibrium point divided by the effective mass, the natural frequency is determined. Alternatively, one can write Eq. (6.152) into state-space form, take its Jacobian A at the equilibrium point, and solve the eigenvalue problem $|A - \lambda I| = 0$ to yield the eigenvalue λ , which has the

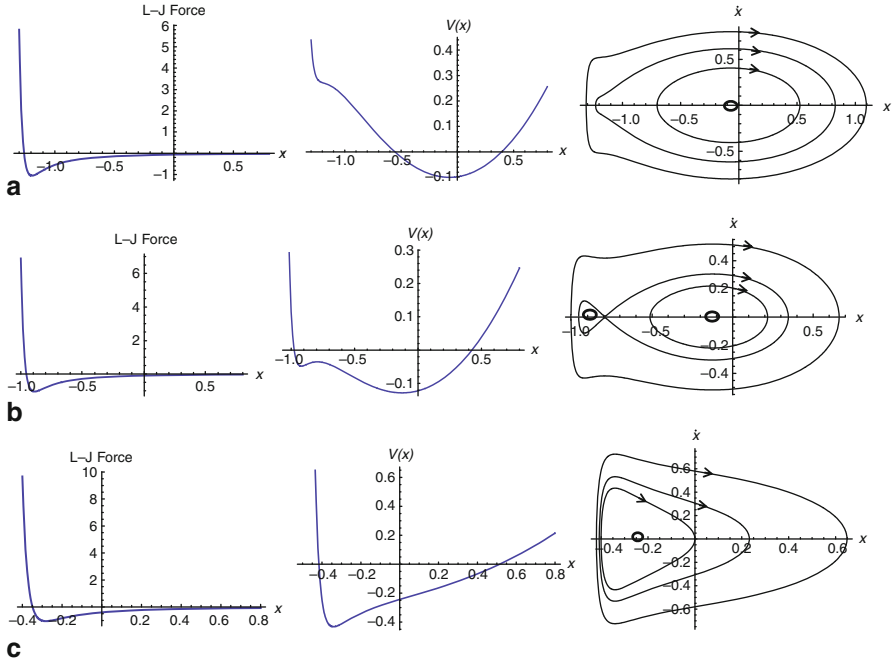


Fig. 6.45 Plots of the L-J force, the L-J potential, and the corresponding phase portrait of an AFM cantilever for **a** $Z_0 = 10$ nm, **b** $Z_0 = 8$ nm, and **c** $Z_0 = 4$ nm

same magnitude as the natural frequency. Either way leads to the below expression of the nondimensional natural frequency ω

$$\omega = \sqrt{1 + \frac{8\beta_1}{(\alpha + x)^9} - \frac{2\beta_2}{(\alpha + x)^3}} \quad (6.158)$$

Figure 6.46 shows ω evaluated at the upper and lower stable branches of Fig. 6.44a. One can see that the natural frequency at the upper stable branch approaches zero at the bifurcation point B whereas the natural frequency at the lower stable branch approaches zero at the bifurcation point D.

The next level of simulations is to consider the forced vibration response of the cantilever when subjected to periodic excitation in the presence of L-J force. The starting point of this is to use numerical long-time integration of Eq. (6.152) along with either a continuation scheme or a shooting technique to capture periodic motion (more on this technique in Chap. 7).

For more accurate dynamic analysis, a beam model needs to be utilized. A beam model provides more accurate results, can capture the participation of the various higher order modes in the response, and enables deeper dynamic analysis of sophisticated nonlinear phenomena, such as nonlinear interactions among the various modes. An example of such a model is that of Rützel et al. [79], Fig. 6.47. In this model,

Fig. 6.46 Variation of the nondimensional natural frequency of the cantilever beam at the upper branch equilibrium position of Fig. 6.44 (*thick*) and the lower branch solution (*thin*)

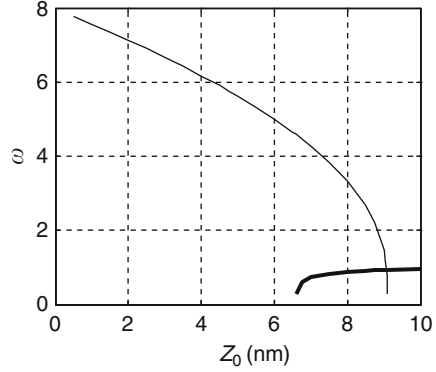
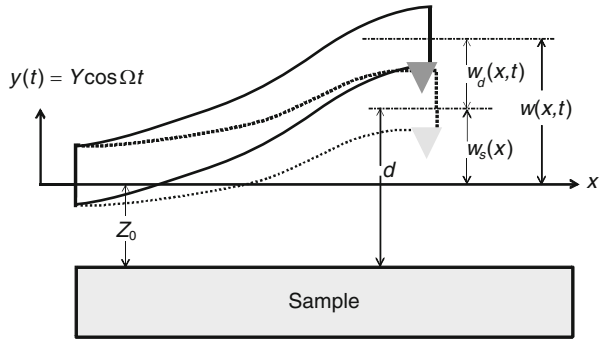


Fig. 6.47 A schematic of a beam model of a cantilever AFM under L-J force



the L-J force is modeled as a concentrated force at the tip of the beam. The beam is assumed to be excited from the base with a harmonic displacement $y(t) = Y \cos \Omega t$, where Y is the amplitude displacement and Ω is the driving frequency. Accordingly, the displacement of the beam $w(x, t)$, measured relative to $y(t)$, is governed by the following equation:

$$EI w'''' + \rho A \ddot{w} = \rho A Y \Omega^2 \cos \Omega t + \left[\frac{A_1 R}{180(Z_0 + w + y)^8} - \frac{A_2 R}{6(Z_0 + w + y)^2} \right] \delta(x - l). \quad (6.159)$$

Following Rützel et al. [79], $w(x, t)$ can be split into a static component $w_s(x, t)$ and a dynamic component $w_d(x, t)$, that is

$$w(x, t) = w_s(x) + w_d(x, t). \quad (6.160)$$

The static equation can be obtained by setting the forcing, damping, and time dependent terms equal to zero, which yields

$$EI w_s'''' = \left[\frac{A_1 R}{180(Z_0 + w_s)^8} - \frac{A_2 R}{6(Z_0 + w_s)^2} \right] \delta(x - l). \quad (6.161)$$

Before proceeding further, Eq. (6.161) is nondimensionalized by introducing the following variables:

$$\hat{x} = \frac{x}{l}; \quad \hat{w}_s = \frac{w_s}{Z_s}. \quad (6.162)$$

Substituting Eq. (6.162) into Eq. (6.161) and omitting the hats yield the nondimensional equation

$$w_s'''' = \left[\frac{\Gamma_1}{(\alpha + w_s)^8} - \frac{\Gamma_2}{(\alpha + w_s)^2} \right] \delta(x - 1) \quad (6.163)$$

where

$$\Gamma_1 = \frac{A_1 R l^3}{180 E I Z_s^9}; \quad \Gamma_2 = \frac{A_2 R l^3}{6 E I Z_s^3}. \quad (6.164)$$

One approach to solve Eq. (6.163) using a reduced-order model is to expand the L–J force into a Taylor series. To guarantee accurate results, the magnitude of the expanded L–J force needs to be checked by including enough number of terms of the Taylor series until its result matches that of the force in the original expression. Figure 6.48 shows an example of such a comparison check. The figure indicates that at least forty terms need to be retained in the Taylor series to represent the force accurately.

Because of the attractive property of the Delta function in Eq. (6.163), one can work on the L–J force directly without Taylor series expansion. When multiplying the L–J force by the modeshape ϕ_j and integrating from 0 to 1, the following property of the Delta function is utilized:

$$\int_0^1 [F_{L-J}(x) \phi_j(x) \delta(x - 1)] dx = F_{L-J}(1) \phi_j(1). \quad (6.165)$$

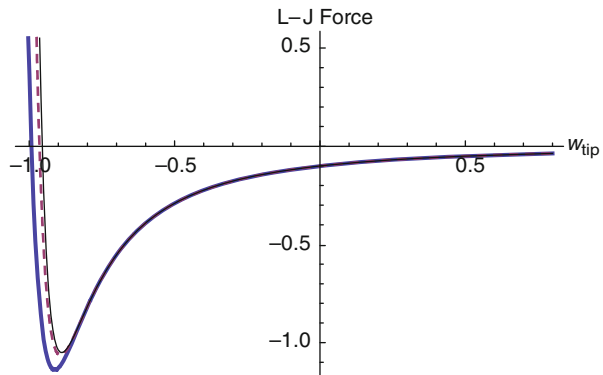
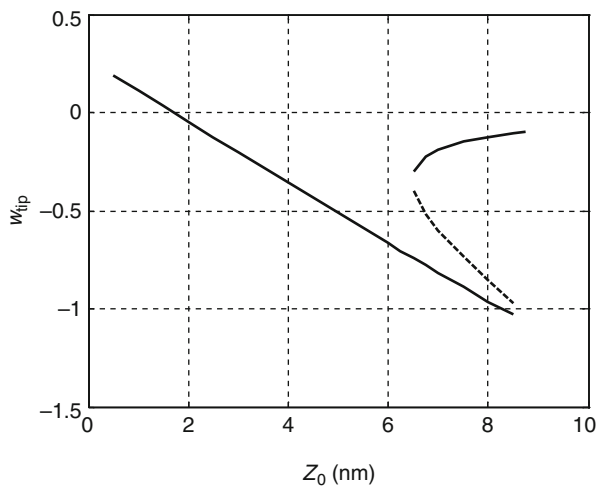


Fig. 6.48 The L–J force versus the tip displacement w_{tip} calculated using a 40-term (*dashed*), a 20-term (*thick*) Taylor series expansion of the force, and the original L–J force form (*thin*) for $Z_0 = 8$ nm

Fig. 6.49 The normalized cantilever tip deflection versus the initial gap space obtained using a three-mode reduced-order model



For example, in the case of a one-mode approximation of the displacement, $w_s(x) = C_1\phi_1(x)$, the result becomes

$$\begin{aligned} & \int_0^1 \left\{ \left[\frac{\Gamma_1}{(\alpha + \phi_1(x)C_1)^8} - \frac{\Gamma_2}{(\alpha + \phi_1(x)C_1)^2} \right] \phi_1(x)\delta(x-1) \right\} dx \\ &= \left[\frac{\Gamma_1}{(\alpha + \phi_1(1)C_1)^8} - \frac{\Gamma_2}{(\alpha + \phi_1(1)C_1)^2} \right] \phi_1(1) \end{aligned} \quad (6.166)$$

where C_1 is the unknown modal coefficient to be determined. One can use the lumped-parameter model results to provide good initial guesses for C_1 while solving the nonlinear algebraic equation obtained from the reduced-order model. As always, the minimum number of modes needs to be tested for convergence, which for this case turns out to be three modes. Figure 6.49 shows the static equilibrium solutions obtained using a three-mode reduced-order model.

To obtain the natural frequencies of the cantilever at its static equilibrium position, the beam equation is linearized around the equilibrium position. Then, the linearized system is discretized using the Galerkin procedure and the associated eigenvalue problem is solved, as done for the electrostatic problem in Sect. 6.13. The reader is referred to [79] for more details.

6.17 Beams Under Capillary Forces

In this section, we study the collapse problem of a clamped–clamped microbeam with a droplet of liquid trapped underneath it, Fig. 6.50 [92–98]. This induces a capillary force, which is assumed generally to be partially distributed underneath

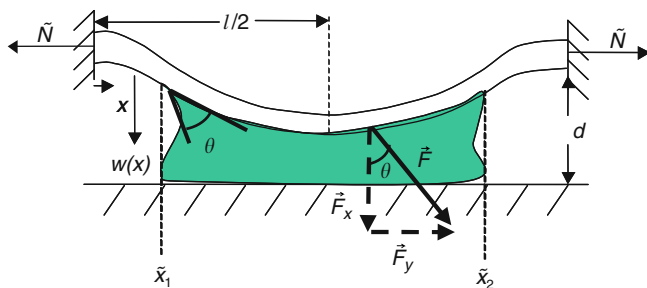


Fig. 6.50 Schematic of a clamped-clamped microbeam under the effect of capillary forces

the beam over its length between \tilde{x}_1 and \tilde{x}_2 . The fluid has a surface tension γ and it forms an angle θ with both the beam and the substrate. Both the beam and the substrate are assumed to be made of the same material, hence are considered to be highly hydrophilic surfaces with θ equal to zero for the beam-fluid and fluid-substrate interfaces (perfect wetting condition). The initial distance separating the microbeam from the substrate is d . The beam is assumed to be generally under an axial load \tilde{N} . The meniscus effect is neglected in this model.

For a given point on the beam-liquid and the liquid-substrate interface, there exists a local capillary force F_{cap} of a magnitude proportional to $\gamma \cos(\theta)$ (Young-Dupré equation), and a direction perpendicular to the beam width z [99]. Assuming the microbeam and the underneath substrate can be treated as two parallel rigid plates, the capillary force per unit length acting on the microbeam can be expressed as $\vec{F} = \int_0^b F_{\text{cap}} d\vec{z}$. In addition, the capillary force is assumed to satisfy the following [99]:

- The capillary force makes an angle θ with the unit vector that is normal to the surface of the fluid, where θ is the contact angle as shown in Fig. 6.50.
- The magnitude of the force $|\vec{F}|$ is equal $\gamma A_c / r$, where r is the distance between the microbeam and the substrate and A_c is the area of contact between the microbeam and the fluid. Under the action of capillary forces, the microbeam deflects changing the distance r , which in turns changes the magnitude of the capillary force. This will cause further deflection of the microbeam. This pattern continues until equilibrium is reached between the microbeam and the capillary force. To account for the change in r , we follow Legtenberg et al. [97] and modify the capillary force expression as $F = 2\gamma b \cos(\theta) / (d - w)$.

In addition to these assumptions, the volume of fluid trapped underneath the beam is assumed constant while the beam is being deflected. This implies that there is some leakage of fluid across the beam width during its deflection. Based on this, the equation of motion and associated boundary conditions of the microbeam shown in Fig. 6.50 can be expressed as

$$EI \frac{d^4 w}{dx^4} = \left[\frac{EA}{2l} \int_0^l \left(\frac{\partial w}{\partial x} \right)^2 dx + \tilde{N} \right] \frac{d^2 w}{dx^2}$$

$$+ \frac{2\gamma b \cos \theta}{(d-w)} [u(x - \tilde{x}_1) - u(x - \tilde{x}_2)] \quad (6.167a)$$

$$w(0) = w(l) = 0; \quad \frac{dw}{dx}(0) = \frac{dw}{dx}(l) = 0 \quad (6.167b)$$

where u is the Heaviside function. For convenience, the following nondimensional variables are introduced:

$$\hat{w} = \frac{w}{d}; \quad \hat{x} = \frac{x}{l}. \quad (6.168)$$

In nondimensional forms, after dropping the hats, Eq. (6.167a) and Eq. (6.167b) become

$$\frac{d^4 w}{dx^4} = \left[\alpha_1 \int_0^1 \left(\frac{dw}{dx} \right)^2 dx + N \right] \frac{d^2 w}{dx^2} + \frac{\alpha_2}{(1-w)} [u(x - x_1) - u(x - x_2)] \quad (6.169a)$$

$$w(0) = 0; \quad w(1) = 0; \quad \frac{\partial w}{\partial x}(0) = 0; \quad \frac{\partial w}{\partial x}(1) = 0 \quad (6.169b)$$

where

$$\alpha_1 = 6 \left(\frac{d}{h} \right)^2; \quad \alpha_2 = \frac{2\gamma b \cos(\theta) l^4}{EI d^2}; \quad N = \frac{\tilde{N} l^2}{EI}; \quad x_1 = \frac{\tilde{x}_1}{l}; \quad x_2 = \frac{\tilde{x}_2}{l}. \quad (6.170)$$

Equation (6.169a) is discretized using the Galerkin procedure. The capillary force in this case is treated by either expanding it into sufficient number of terms in a Taylor series or by premultiplying the whole equation by $(1-w)$. Here we follow the second approach. Then, the microbeam deflection is approximated as

$$w(x) = \sum_{i=1}^n a_i \phi_i(x) \quad (6.171)$$

where $\phi_i(x)$ ($i = 1, 2, \dots, n$) are the normalized modeshapes of the unforced microbeam and a_i ($i = 1, 2, \dots, n$) are nontime varying constant coefficients. Because of the symmetric nature of the clamped-clamped microbeam and the capillary forces, only symmetric (odd) modeshapes are used. Multiplying Eq. (6.169a) by $(1-w)$, substituting Eq. (6.171) into the outcome, multiplying by $\phi_j(x)$, using the orthogonality conditions of the modeshapes, and integrating numerically the outcome from 0 to 1 yield the following reduced-order model:

$$\int_0^1 \left\{ \left[1 - \sum_{i=1}^n a_i \phi_i(x) \right] \left[\sum_{i=1}^n u_i(t) \phi_i'''(x) \right] \phi_j(x) dx \right\}$$

$$\begin{aligned}
&= \alpha_2 \int_0^1 \phi_j(x) [u(x - x_1) - u(x - x_2)] dx \\
&\quad + \alpha_1 \left(\int_0^1 \left\{ \left[\sum_{i=1}^n a_i \phi'_i(x) \right]^2 \right\} dx + N \right) \\
&\quad \times \left(\int_0^1 \left\{ \left[1 - \sum_{i=1}^n a_i \phi_i(x) \right] \left[\sum_{i=1}^n a_i \phi''_i(x) \right] \phi_j(x) dx \right\} \right), \quad j = 1, \dots, n
\end{aligned} \tag{6.172}$$

The obtained ROM contains a system of nonlinear algebraic equations that can be solved numerically using the Newton–Raphson method to obtain a_i and hence the static deflection of the microbeam.

Next, the convergence of the ROM is examined as the number of modes is increased. For this, consider a microbeam of 100 μm length, 10 μm width, 1.5 μm thickness, and a gap width underneath equals to 1.18 μm . The Young’s modulus is assumed equal to 169 GPa. The applied axial load N and the angle formed by the fluid and the microbeam are set equal to zero. The fluid surface tension is assumed equal to 0.073 N/m. Figure 6.51 shows the normalized maximum deflection of the considered microbeam using the ROM for different number of modes (first few) and while varying the capillary force distribution for the case of $x_1 = x_2$. It follows that the use of three symmetric modes yields converged results. As seen from Fig. 6.51, the microbeam exhibits collapse instability at a specific threshold of liquid volume, where the slope of the curve approaches infinity.

Next, complete wetted area is assumed underneath the beam. Then, we calculate the minimum length, beyond which the microbeam undergoes the collapse instability (also called pull-in length). To estimate the pull-in length, the static deflection of the microbeam is calculated for various beam lengths starting from small values. When the slope of the maximum displacement–length curve approaches infinity, the length

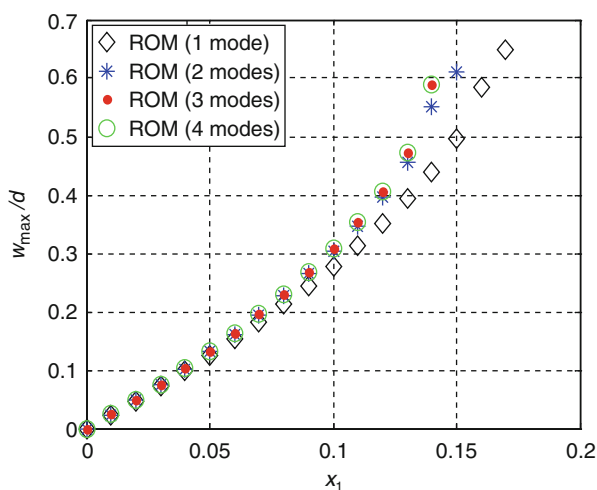
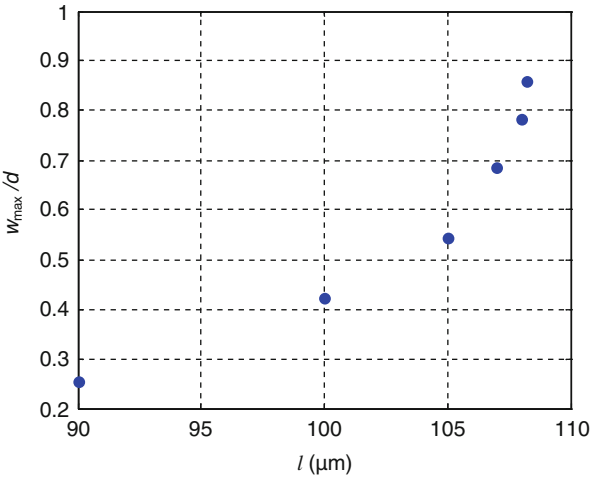


Fig. 6.51 The normalized maximum deflection of the clamped–clamped microbeam versus the normalized liquid distribution in the case of a symmetric distribution for the liquid with $\alpha_1 = 3.71$ and $\alpha_2 = 220$ [92]

Fig. 6.52 A deflection–length curve of completely wetted microbeams [92]. Based on this figure, a pull-in length can be identified as $l = 108 \mu\text{m}$



of the curve where it ends is identified as the pull-in length. Figure 6.52 shows an example of a displacement–length curve. Next, the pull-in length calculated using the ROM (with one and three modes) is compared to results obtained using the model of Mastrangelo et al. [95], which is based on the Ritz method. Figure 6.53 shows excellent agreement among the results of the model of Mastrangelo [95] and the ROM results.

6.18 Coupled-Field Damping of Beams

So far, we have considered the damping affecting the microbeams to be a simple linear viscous damping with a constant coefficient. As has been discussed in Chap. 4, this

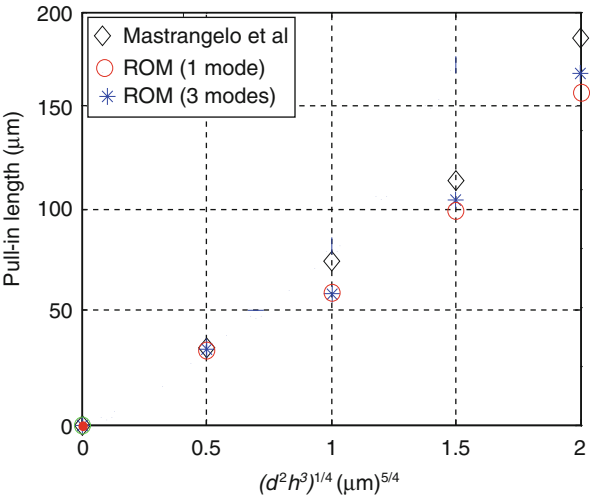


Fig. 6.53 The pull-in length of a clamped–clamped microbeam for $h = 1 \mu\text{m}$ [92]

may not be accurate. Next, we discuss two common damping models of microbeams representing both extrinsic and intrinsic dissipation mechanisms.

6.18.1 Squeeze-Film Damping

Quiet commonly, a beam that vibrates freely in air and in close proximity to another surface is subjected to squeeze-film damping. In this case, the equation of motion of the beam coupled with the Reynolds equation need to be solved simultaneously, for example using finite difference [100] or perturbation techniques [101]. However, under the assumption of incompressible fluid, a simplification can be made [102]. For this, we refer back to the nonlinear Reynolds equation, Eq. (4.27), of Chap. 4 and consider as an example the beam configuration shown in Fig. 6.26. We assume small displacement of the beam $w(x, t)$ compared to the original gap width d and small pressure change across the beam $\Delta p(x, y, t)$ compared to the original static pressure in the air gap P_a . Therefore, the total displacement and pressure are expressed, respectively, as

$$H(x, t) = d - w(x, t) \quad (6.173a)$$

$$P(x, y, t) = P_a + \Delta p(x, y, t). \quad (6.173b)$$

Substituting Eqs. (6.173a) and (6.173b) into Eq. (4.27), dropping the nonlinear terms, and setting the variation of pressure with time equal to zero (assuming incompressible fluid) yield

$$\frac{\partial^2(\Delta p)}{\partial x^2} + \frac{\partial^2(\Delta p)}{\partial y^2} = \frac{12\mu}{d^3} \frac{\partial w}{\partial t}. \quad (6.174)$$

If the beam length l is assumed much larger than its width b , then the pressure gradient across the width can be assumed more significant than that across the beam length, and hence the latter can be neglected. Hence, the equation is further simplified to

$$\frac{\partial^2(\Delta p)}{\partial y^2} = \frac{12\mu}{d^3} \frac{\partial w}{\partial t}. \quad (6.175)$$

Integrating for Δp twice and using $\Delta p = 0$ at $y = \pm b/2$ (open edges) yield

$$\Delta p = \frac{6\mu}{d^3} \frac{\partial w}{\partial t} \left[y^2 - \frac{b^2}{4} \right]. \quad (6.176)$$

Finally, the squeeze force per unit length of the beam can be calculated as

$$F_{\text{SQFD}} = \int_{-b/2}^{b/2} \Delta p dy = \int_{-b/2}^{b/2} \frac{6\mu}{d^3} \frac{\partial w}{\partial t} \left(y^2 - \frac{b^2}{4} \right) dy = -\frac{b^3\mu}{d^3} \frac{\partial w}{\partial t} \quad (6.177)$$

where the negative sign indicates that the force opposes the positive motion (resistive force). Hence, the damping coefficient in this case is given by

$$c = \frac{b^3 \mu}{d^3}. \quad (6.178)$$

To account for the nonlinearity of squeeze-film damping in the case of large beam deflection, d can be replaced by a time varying gap that depends on the beam deflection (see for example [4]). Hence the damping coefficient becomes

$$c = \frac{b^3 \mu}{[d - w(x, t)]^3}. \quad (6.179)$$

More generally, in the case of nonuniform geometry, the coefficient can be expressed as

$$c = \frac{\alpha_{sq}}{[d - w(x, t)]^3} \quad (6.180)$$

where α_{sq} can be estimated from fully coupled finite-element or finite-difference simulations or from experimental data.

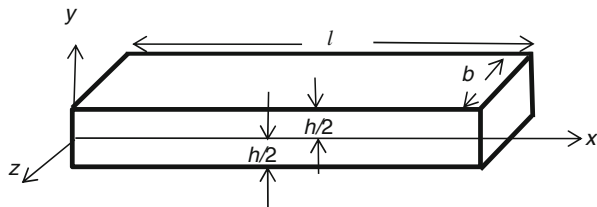
Treating either Eq. (6.179) or Eq. (6.180) in a reduced-order model can be done either by expanding the force into an adequate number of terms in a Taylor series expansion or by multiplying the whole equation by $[d - w(x, t)]^3$ if possible, as in the case of electrostatically actuated microbeams.

6.18.2 Thermoelastic Damping

As explained in Sect. 4.3.7, thermoelastic damping can limit the quality factor of MEMS resonators when operated in vacuum and in the absence of other extrinsic dissipation sources. To quantitatively study this effect in microbeams, we follow next the analysis of Lifshitz and Roukes [4] of the coupled-field model of a thermoelastic beam. The equation of motion of the thermoelastic beam, Fig. 6.54, can be written as

$$\rho A \frac{\partial^2 w}{\partial t^2} + \frac{\partial^2}{\partial x^2} \left(EI \frac{\partial^2 w}{\partial x^2} + M_T \right) = 0 \quad (6.181)$$

Fig. 6.54 Schematic of a thermoelastic beam



where M_T refers to the thermal moment defined as

$$M_T = E\alpha_t \int_A y\theta dydz = E\alpha_t b \int_{-h/2}^{h/2} y\theta dy \quad (6.182)$$

where α_t is the thermal expansion coefficient of the beam material and $\theta = T - T_0$, where T is the temperature distribution and T_0 is the stress free temperature. This beam equation is coupled with the heat conduction equation written as

$$k\nabla^2 T = \rho C_p \frac{\partial T}{\partial t} + \frac{E\alpha_t T}{1-2\nu} \frac{\partial e}{\partial t} \quad (6.183)$$

where ∇^2 is the Laplacian operator, k is the thermal conductivity, C_p is the heat capacity coefficient at a constant pressure, ρ is the material density, ν is the Poisson's ratio, and e is the dilatation strain including the thermal effect defined as [103]

$$e = (2\nu - 1) y \frac{\partial^2 w}{\partial x^2} + 2\alpha_t (1 + \nu) \theta. \quad (6.184)$$

Substituting Eq. (6.184) into Eq. (6.183) and dividing the whole equation by ρC_p yield

$$\chi \nabla^2 T = \left[1 + \frac{2E\alpha_t^2 T(1+\nu)}{(1-2\nu)\rho C_p} \right] \frac{\partial T}{\partial t} - \frac{E\alpha_t T}{\rho C_p} \frac{\partial}{\partial t} \left(\frac{\partial^2 w}{\partial x^2} \right) \quad (6.185)$$

where χ is the thermal diffusivity defined as $\chi = \frac{k}{\rho C_p}$. Next, we substitute for $T = T_0 + \theta$ in Eq. (6.185)

$$\chi \nabla^2 \theta = \left[1 + \frac{2E\alpha_t^2 (\theta + T_0)(1+\nu)}{(1-2\nu)\rho C_p} \right] \frac{\partial \theta}{\partial t} - \frac{E\alpha_t (\theta + T_0)}{\rho C_p} \frac{\partial}{\partial t} \left(\frac{\partial^2 w}{\partial x^2} \right). \quad (6.186)$$

Several simplifications can be made to Eq. (6.186). First, since $\theta \ll T_0$, Eq. (6.187) can be linearized as below

$$\chi \nabla^2 \theta = \left[1 + \frac{2E\alpha_t^2 T_0(1+\nu)}{(1-2\nu)\rho C_p} \right] \frac{\partial \theta}{\partial t} - \frac{y\Delta_E}{\alpha_t} \frac{\partial}{\partial t} \left(\frac{\partial^2 w}{\partial x^2} \right) \quad (6.187)$$

where $\Delta_E = \frac{E\alpha_t^2 T_0}{\rho C_p}$. Second, it turns out that the term $\frac{2E\alpha_t^2 T_0(1+\nu)}{(1-2\nu)\rho C_p} \ll 1$, hence it can be dropped out. Third, it is reasonably assumed that the thermal gradient across the beam's thickness (y direction) is much greater than that across its length or width. Hence, $\nabla^2 \theta$ in Eq. (6.187) is replaced by $\partial^2 \theta / \partial y^2$. Accordingly, Eq. (6.187) is simplified to

$$\chi \frac{\partial^2 \theta}{\partial y^2} = \frac{\partial \theta}{\partial t} - \frac{y\Delta_E}{\alpha_t} \frac{\partial}{\partial t} \left(\frac{\partial^2 w}{\partial x^2} \right). \quad (6.188)$$

Next, the linear damped eigenvalue problem of the coupled equations, Eq. (6.181) and Eq. (6.188) are solved by assuming harmonic variations in the beam displacement and temperature difference, that is

$$\begin{aligned} w(x, t) &= \phi(x)e^{i\omega t} \\ \theta(x, y, t) &= \theta_0(x, y)e^{i\omega t} \end{aligned} \quad (6.189)$$

where ϕ and θ_0 are the beam modeshape and the associated spatial temperature variation, respectively, and ω is the complex eigenvalue (it is complex because of the damping). Substituting Eq. (6.189) into Eq. (6.188) gives

$$\chi \frac{\partial^2 \theta_0}{\partial y^2} = i\omega \left(\theta_0 - \frac{\Delta_E y}{\alpha_t} \frac{\partial^2 \phi}{\partial x^2} \right). \quad (6.190)$$

The temperature conditions are zero heat flux from the beam to the ambient, that is

$$\frac{\partial \theta_0}{\partial y} = 0 \quad \text{at} \quad y = h/2 \quad \text{and} \quad y = -h/2. \quad (6.191)$$

Solving for the homogenous and particular solution of Eq. (6.190) and applying the boundary conditions of Eq. (6.191) give

$$\theta_0 = \frac{\Delta_E}{\alpha_t} \frac{\partial^2 \phi}{\partial x^2} \left[y - \frac{\sin(Ky)}{K \cos(\frac{bK}{2})} \right] \quad (6.192)$$

where $K = (1 + i)\sqrt{\frac{\omega}{2\chi}}$.

Equation (6.192) describes the temperature profile for a given frequency and modeshape. Substituting Eq. (6.192) into Eq. (6.182) and then the result along with Eq. (6.189) into Eq. (6.181) yield the modeshape equation of the beam

$$\omega^2 \phi = \frac{EI}{\rho A} \{1 + \Delta_E [1 + f(\omega)]\} \frac{\partial^4 \phi}{\partial x^4} \quad (6.193)$$

where

$$f(\omega) = \frac{24}{h^3 K^3} \left[\frac{Kh}{2} - \tan\left(\frac{Kh}{2}\right) \right].$$

It is noted that Eq. (6.193) is similar to that of an isothermal beam with no thermoelastic effect except that the Young's modulus E is replaced by a frequency-dependent modulus $E_\omega = E \{1 + \Delta_E [1 + f(\omega)]\}$.

Thus, the natural frequency of the beam in this case is governed by the same expression of that of an isothermal beam, except that E is replaced with E_ω . Hence

$$\omega = \sqrt{\frac{E_\omega I}{\rho A}} \omega_{\text{non}} = \omega_0 \sqrt{1 + \Delta_E [1 + f(\omega)]} \quad (6.194)$$

where ω_0 is the isothermal natural frequency of the beam. Expanding the under-square-root term in Eq. (6.194) and keeping only a linear term in Δ_E gives:

$$\omega = \omega_0 \left[1 + \frac{\Delta_E}{2} [1 + f(\omega_0)] \right]. \quad (6.195)$$

Equation (6.195) describes the complex eigen-frequency of a thermoelastic beam. As a matter of fact, this complex eigen-frequency can be thought to be similar to λ of Eq. (2.20) of a damped free oscillator (particularly $\lambda = i\omega$). The real part Re of ω represents the modified natural frequency of the beam due to thermoelasticity (similar to $\omega_n \sqrt{\zeta^2 - 1}$) and the imaginary part Im represents the damping rate coefficient of the beam (similar to $-\zeta \omega_n$). Hence, the quality factor Q of the beam is given by [103]

$$Q^{-1} = 2 \left| \frac{\text{Im}(\omega)}{\text{Re}(\omega)} \right| = \frac{E \alpha_t^2 T_0}{\rho C_p} \left(\frac{6}{\xi^2} - \frac{6}{\xi^3} \frac{\sinh \xi + \sin \xi}{\cosh \xi + \cos \xi} \right) \quad (6.196)$$

where $\xi = h \sqrt{\frac{\omega_0}{2\chi}}$.

Example 6.17: Consider a clamped–clamped microbeam of length $l = 200 \mu\text{m}$, thickness $h = 2 \mu\text{m}$, and width $b = 20 \mu\text{m}$. Consider the beam made of silicon with $E = 160 \text{ GPa}$, $\rho = 2,330 \text{ kg/m}^3$, $\alpha_t = 2.6 \times 10^{-6} \text{ K}^{-1}$, $C_p = 711 \text{ J/kg K}$, and $k = 1.7 \text{ W/m K}$. Calculate and plot the variation of its thermoelastic quality factor for a temperature range from 100 to 400 K.

Solution: First, the ratios χ and ξ and the isothermal natural frequency ω_0 are calculated. Then, the outcomes are plugged into Eq. (6.196). The results are shown in Fig. 6.55. The figure clearly indicates the significant effect of temperature in reducing the quality factor.

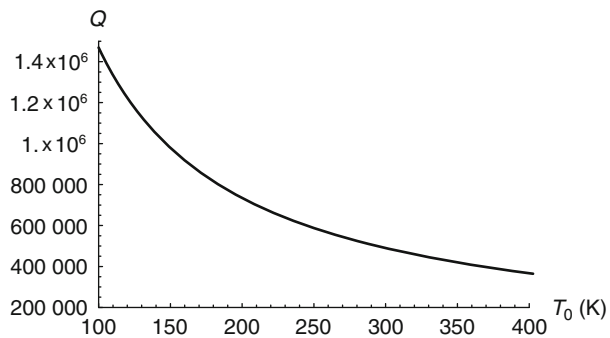


Fig. 6.55 The variation of the quality factor versus temperature due to thermoelastic effect for a clamped–clamped microbeam

Problems

1. Write the boundary conditions of the beam edges shown in Fig. 6.56.

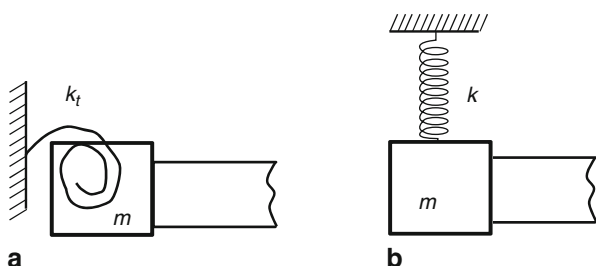


Fig. 6.56 **a** a rotational spring and a lumped mass, **b** a translational spring and a lumped mass

2. Shown in Fig. 6.57 a schematic of a cantilever beam stuck to the substrate at the tip. Solve analytically for the beam deflection (profile) and plot $w(x)/d$ versus x assuming the stuck tip (a) pinned and (b) clamped.

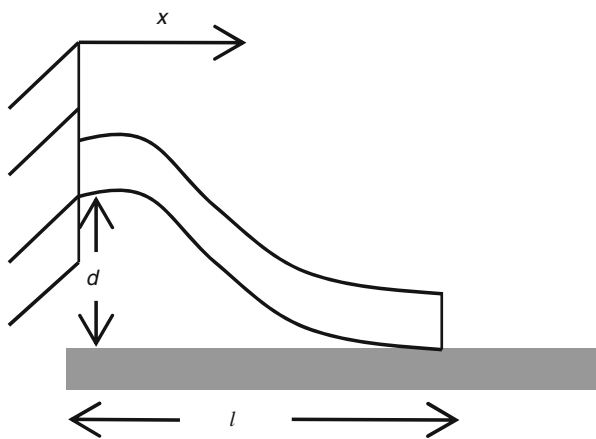


Fig. 6.57 A cantilever beam stuck to the substrate at the tip

3. Repeat Problem 2 by replacing the clamped edge of the beam with a torsional and transversal springs representing a nonideal clamping.
4. Determine the deflection profile of a clamped–clamped beam subjected to a constant distributed force per unit length F_0 . Assume EI to be constant.
5. Repeat Problem 4 for the beam with springs at the boundaries shown in Fig. 6.14.
6. Consider the beam of Fig. 6.14, which is connected with rotational and transversal springs at its both ends. Assume symmetric stiffness properties of the springs at both ends and that they are being varied at the same time by the same amount.

- (a) Assuming infinite rotational stiffness coefficient, investigate the effect of reducing the translational spring stiffness coefficients on both sides of the beam from very large to very small values on its first four natural frequencies.
 - (b) Assuming infinite translational stiffness coefficient, investigate the effect of reducing the rotational spring stiffness coefficients on both sides of the beam from very large to very small values on its first four natural frequencies.
7. Consider the cantilever beam with a lumped mass of mass m at its tip of Fig. 6.19. Determine the first four natural frequencies and plot the corresponding mode-shapes for the cases of (a) $m = 0.2$ of the beam's mass, (b) $m = 50$ times the beam mass.
 8. Consider a cantilever beam with a lumped mass of mass m at its tip and nonideal support, Fig. 6.58. Determine the first four natural frequencies for the cases when $m =$ (a) 0.01 of the beam's mass, (b) the beam's mass, and (c) 100 that of the beam's mass. Investigate the effect of reducing the spring stiffness coefficients from very large to very small values.

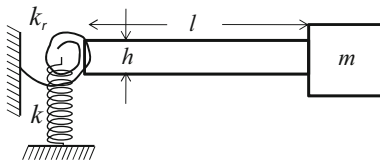


Fig. 6.58 A cantilever beam with a lumped mass at the tip and of a nonideal support

9. Consider a cantilever beam with a lumped mass of Fig. 6.19. By modeling the cantilever beam as a lumped-spring element, determine the first four natural frequencies and show their variations with the ratio of the tip mass to that of the beam. Compare to the results of Example 6.7 and draw conclusion on when it is accurate to model the cantilever as a lumped-spring element.
10. Determine the steady-state response of a clamped-clamped beam subjected to a fully distributed harmonic force over the length of the beam of amplitude F_0 . Evaluate the response of the beam at its midpoint when driven at a frequency equal half its fundamental natural frequency. Discuss the convergence of the solution and how many modes are needed.
11. Consider a cantilever microbeam made of silicon with $\rho = 2,332 \text{ kg/m}^3$ and $E = 169.0 \text{ GPa}$. The dimensions of the microbeam are $l = 100 \text{ }\mu\text{m}$, $h = 1.5 \text{ }\mu\text{m}$, and $b = 20 \text{ }\mu\text{m}$. Using a one mode in the Galerkin expansion, determine the maximum transient dynamic response of the microbeam at its midpoint when subjected to a spatially distributed shock force $F_0 = \alpha \rho b h \tilde{g}(t)$, where α is an acceleration magnitude and $\tilde{g}(t)$ is a half-sine pulse expressed as

$$\tilde{g}(t) = \sin\left(\frac{\pi}{T}t\right) u(t) + \sin\left[\frac{\pi}{T}(t - T)\right] u(t - T)$$

where T is the pulse duration and $u(t)$ is the unit step function. Consider $T = 0.1 \text{ ms}$ and $\alpha = 1,000g$, where g is the constant of gravity.

12. Solve the eigenvalue problem of a clamped–clamped beam under axial force and derive the Euler buckling limit expression of Table 6.3 of this case. Plot the first three natural frequencies versus the axial force.
13. Calculate the pull-in voltage of a cantilever microbeam switch made of aluminum with $\rho = 2,700 \text{ kg/m}^3$ and $E = 160.0 \text{ GPa}$ with
 - (a) $l = 300 \text{ }\mu\text{m}$, $h = 2 \text{ }\mu\text{m}$, $b = 20 \text{ }\mu\text{m}$, and $d = 2 \text{ }\mu\text{m}$.
 - (b) $l = 500 \text{ }\mu\text{m}$, $h = 2 \text{ }\mu\text{m}$, $b = 20 \text{ }\mu\text{m}$, and $d = 3 \text{ }\mu\text{m}$.
 - (c) Repeat (a) assuming the switch is made of gold with $\rho = 19,000 \text{ kg/m}^3$ and $E = 79.0 \text{ GPa}$.
14. Calculate the pull-in voltage of the below clamped–clamped microbeams assuming no axial load and assuming $E = 154 \text{ GPa}$ and $\rho = 2,330 \text{ kg/m}^3$.
 - (a) $l = 200 \text{ }\mu\text{m}$, $h = 2 \text{ }\mu\text{m}$, $b = 10 \text{ }\mu\text{m}$, and $d = 1 \text{ }\mu\text{m}$
 - (b) $l = 200 \text{ }\mu\text{m}$, $h = 1.5 \text{ }\mu\text{m}$, $b = 100 \text{ }\mu\text{m}$, and $d = 2 \text{ }\mu\text{m}$
15. Consider a microbeam of length $l = 500 \text{ }\mu\text{m}$, thickness $h = 1 \text{ }\mu\text{m}$, width $b = 10 \text{ }\mu\text{m}$, and air-gap width $d = 1.0 \text{ }\mu\text{m}$. Consider $E = 124 \text{ GPa}$ and $\rho = 2,332 \text{ kg/m}^3$. Calculate and plot the deflection of the microbeam up to the pull-in instability for the below cases:
 - (a) Assuming a cantilever microbeam with partial electrode as in Fig. 6.33a with $x_1 = 0.25l$ and $x_2 = 0.75l$. Compare the results with that of a full electrode.
 - (b) Assuming a clamped–clamped microbeam with partial electrode as in Fig. 6.33b with $x_1 = 0.125l$, $x_2 = 0.375l$, $x_3 = 0.625l$, and $x_4 = 0.875l$. Compare the results with that of a full electrode.
 - (c) Assuming a cantilever microbeam with full electrode curled upward initially with a tip deflection of $0.5 \text{ }\mu\text{m}$.
 - (d) Assuming a cantilever microbeam with full electrode curled downward initially with a tip deflection of $0.2 \text{ }\mu\text{m}$.
 - (e) Assuming a cantilever microbeam with partial electrodes with $x_1 = 0.25l$ and $x_2 = 0.75l$ curled downward initially with a tip deflection of $0.2 \text{ }\mu\text{m}$.
 - (f) Assuming a clamped–clamped microbeam with full electrode concaved upward initially with a maximum deflection of $0.5 \text{ }\mu\text{m}$.
 - (g) Assuming a clamped–clamped microbeam with full electrode concaved downward initially with a maximum deflection of $0.2 \text{ }\mu\text{m}$.
16. For Problem 15, calculate the pull-in time of each beam assuming actuation voltages equal the pull-in voltage and assuming a damping ratio equal 0.05.
17. Consider a cantilever microbeam of length $l = 200 \text{ }\mu\text{m}$, thickness $h = 2 \text{ }\mu\text{m}$, width $b = 20 \text{ }\mu\text{m}$, air-gap width $d = 1.5 \text{ }\mu\text{m}$, Young's modulus $E = 70 \text{ GPa}$, and density $\rho = 2,700 \text{ kg/m}^3$. Assume three symmetric modes in the ROM, derive and formulate the eigenvalue problem. Then, calculate and plot the first nondimensional natural frequency of the microbeam up to the pull-in instability.

18. Consider the microbeam of Problem 17 excited by a voltage load of the form $V_{DC} + V_{AC} \cos \Omega t$. Calculate and plot the nondimensional frequency–response curves for the following cases:
- $V_{DC} = 2 \text{ V}$ and $V_{AC} = 0.1 \text{ V}$ near the fundamental natural frequency
 - $V_{DC} = 4 \text{ V}$ and $V_{AC} = 0.05 \text{ V}$ near the fundamental natural frequency
 - $V_{DC} = 2 \text{ V}$ and $V_{AC} = 0.2 \text{ V}$ near the fundamental natural frequency
 - $V_{DC} = 2 \text{ V}$ and $V_{AC} = 0.3 \text{ V}$ near the fundamental natural frequency
 - $V_{DC} = 2 \text{ V}$ and $V_{AC} = 0.6 \text{ V}$ near half the fundamental natural frequency
 - $V_{DC} = 2 \text{ V}$ and $V_{AC} = 0.6 \text{ V}$ near twice the fundamental natural frequency
19. Consider the AFM cantilever microbeam of Lee et al. [71] with the properties of Table 6.7. For parts (a)–(c), use the spring-mass model of the AFM under L–J force of Fig. 6.43.
- Determine the equilibrium solutions and their stability of the cantilever beam for various values of Z_0 .
 - Show plots of the L–J force, the L–J potential, and the corresponding phase portrait for $Z_0 = 2 \text{ nm}$ and $Z_0 = 5 \text{ nm}$.
 - Calculate and plot the nondimensional natural frequency of the cantilever beam of the upper and lower branches of equilibrium position versus Z_0 .
 - Repeat (a) using a reduced-order model with one mode and then with three modes.

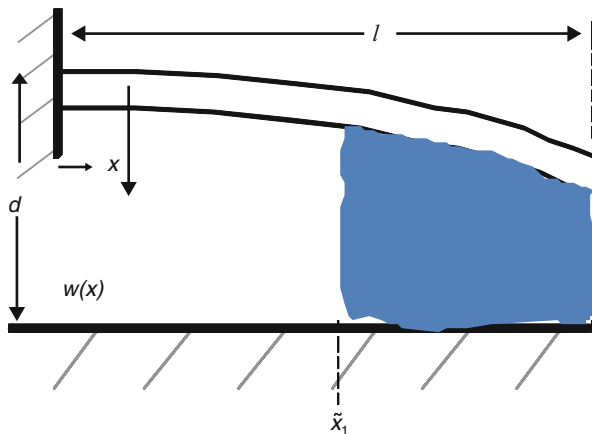


Fig. 6.59 A cantilever microbeam with a droplet of water trapped underneath

20. Consider a cantilever microbeam with a droplet of water trapped underneath it, Fig. 6.59. The microbeam is assumed to be of $80 \mu\text{m}$ length, $10 \mu\text{m}$ width, $2.5 \mu\text{m}$ thickness, and a gap width underneath equals to $1 \mu\text{m}$. The nondimensional static equation of the microbeam under the effect of the capillary force

Table 6.7 Properties of the AFM cantilever of Lee et al. [71]

Symbol	Value
A (cross section area)	$8.09 \times 10^{-11} \text{ m}^2$
I (area moment of inertia)	$3.57 \times 10^{-23} \text{ m}^4$
R	10 nm
ρ	$2,330 \text{ kg/m}^3$
k	0.87 N/m
E	130 GPa
f_1	44.0 kHz
Q	33.3
A_1	$1.3596 \times 10^{-70} \text{ J m}^6$
A_2	$2.96 \times 10^{-19} \text{ J}$

can be written as [92]

$$\frac{d^4 w}{dx^4} = \frac{\alpha_2}{(1-w)} u[x - (1-x_1)] \quad (\text{a})$$

where $\alpha_2 = \frac{2\gamma b l^4}{E I d^2}$ and $x_1 = 1 - \tilde{x}_1/l$.

Develop a reduced-order model ROM of this problem. Then, calculate and plot the normalized maximum deflection of the cantilever microbeam versus the normalized liquid distribution underneath it, x_1 , starting from $x_1 = 0$ up to the collapse limit using the ROM for different number of modes. Investigate how many modes are needed for convergence.

21. Repeat Problem 16 assuming squeeze-film damping of the form of Eq. (6.179) for values of gas pressure equal (a) the atmospheric pressure, (b) 1% of the atmospheric pressure.
22. Consider the microbeam of Example 6.17. Study the effect of changing the thickness of the beam on the thermoelastic quality factor by calculating and plotting Q versus h for $T_0 = 200 \text{ K}$ and $T_0 = 400 \text{ K}$.

References

- [1] Meirovitch L (2001) Fundamentals of Vibrations. McGraw Hill, New York
- [2] Rao S S (2004) Mechanical Vibrations. Fourth Edition, Prentice Hall, New Jersey
- [3] Beer F, Johnston R, DeWolf J, and Mazurek D (2008) Mechanics of materials. McGraw-Hill, New York
- [4] Krylov S, and Maimon R (2004) Pull-in dynamics of an elastic beam actuated by continuously distributed electrostatic force, ASME Journal of Vibrations and Acoustics, 126(3):332–342
- [5] Timoshenko S (1983) Strength of materials, Third edition, Krieger Pub Co, Malabar, Florida
- [6] Shames I H and Pitarresi J M (1999) Introduction to solid mechanics. Third Edition, Prentice Hall, New Jersey
- [7] Senturia S D (2001) Microsystem design. Springer, New York
- [8] Fang W and Wickert J A (1996) Determining mean and gradient residual stresses in thin films using micromachined cantilevers. Journal of Micromechanics and Microengineering. 6:301–309
- [9] Chu W H and Mehregany M (1993) A study of residual stress distribution through the thickness of p^+ silicon films. IEEE Transactions on Electron Devices, 40 (7):1245–1250

- [10] Madou M J (2002) *Fundamentals of Microfabrication: The Science of Miniaturization*. CRC, Boston
- [11] Bouwstra S and Geijselaers B (1991) On the resonance frequencies of microbridges," in *Proceedings of the 6th International Conference on Solid-State Sensors and Actuators (TRANSDUCERS '91)*, San Francisco, CA, IEEE, New York, 2: 1141–1144
- [12] Meng Q, Mehregany M and Mullen R (1993) Theoretical modeling of microfabricated beams with elastically restrained supports. *Journal of Microelectromechanical Systems* 2:128–137
- [13] Jensen B D, Bitsie F, and de Boer M P (1991) Interferometric measurement for improved understanding of boundary effects in micromachined beams. in *proceedings of. SPIE Measurement Techniques II*, Vol. 3875, doi:10.1117/12.360480, Santa Clara, CA, USA
- [14] Kobrinsky M J, Deutsch E R, and Senturia S D (2000) Effect of support compliance and residual stress on the shape of doubly supported surface-micromachined beams. *Journal of Microelectromechanical Systems*, 9:361–369
- [15] Lishchynska M, Cordero N, Slattery O, and O'Mahony C (2005) Modelling electrostatic behaviour of microcantilevers incorporating residual stress gradient and non-ideal anchors. *Journal of Micromechanics and Microengineering*, 15(7): S10, doi: 10.1088/0960-1317/15/7/002
- [16] Rinaldi G, Packirisamy M, and Stiharu I (2006) Boundary characterization of microstructures through thermo-mechanical testing. *Journal of Micromechanics and Microengineering*, 16:549–556
- [17] Balachandran B, Magrab E (2009) *Vibrations*. Second Edition, Cengage Learning, Toronto
- [18] Chiao M and Lin L (2000) Self-buckling of micromachined beams under resistive heating. *Journal of Microelectromechanical Systems*, 9(1):146–151
- [19] Abu-Salih S and Elata D (2006) Experimental validation of electromechanical buckling. *Journal of Microelectromechanical Systems*, 15(6):1656–1662.
- [20] Fang W and Wickert J A (1994) Post-buckling of micromachined beams. *Journal of Micromechanics and Microengineering*, 4:116–22
- [21] Shaker F J (1975) Effect of axial load on mode shapes and frequencies of beams. NASA Lewis Research Center Report NASA-TN-7098
- [22] Bokaian A (1988) Natural frequencies of beams under compressive axial loads. *Journal of Sound and Vibration* 126:49–56
- [23] Inman D J (2008) *Engineering Vibration*. Prentice Hall, New Jersey, Third Edition
- [24] Nayfeh A and Pai F (2004) *Linear and Nonlinear Structural Mechanics*. Wiley and Sons, New York
- [25] Reddy J N (2002) *Energy Principles and Variational Methods in Applied Mechanics*. Wiley and Sons, New York
- [26] Nayfeh A H, Younis M I, and Abdel-Rahman E M (2005) Reduced-order models for MEMS applications. *Nonlinear Dynamics*, 41:211–236
- [27] Younis M I, Abdel-Rahman E M, and Nayfeh A H (2003) A reduced-order model for electrically actuated microbeam-based MEMS. *Journal of Microelectromechanical Systems*, 12:672–680
- [28] Tilmans H A, Elwespoek M and Fluitman J H (1992) Microresonant force gauges. *Sensors Actuators A* 30:35–53
- [29] Zook J D and Burns D W (1992) Characteristics of polysilicon resonant microbeams. *Sensors Actuators A* 35:51–9
- [30] Ijntema D J and Tilmans H A (1992) Static and dynamic aspects of an air-gap capacitor. *Sensors Actuators A* 35:121–8
- [31] Tilmans H A and Legtenberg R (1994) Electrostatically driven vacuum-encapsulated polysilicon resonators: Part II. Theory and performance. *Sensors Actuators A* 45:67–84
- [32] Ahn Y, Guckel H and Zook J D (2001) Capacitive microbeam resonator design. *Journal of Micromechanics and Microengineering*, 11:70–80
- [33] Abdel-Rahman E M, Younis M, and Nayfeh A H (2002) Characterization of the mechanical behavior of an electrically actuated microbeam. *Journal of Micromechanics and Microengineering*, 12:759–766

- [34] Hung E S and Senturia S D (1991) Generating efficient dynamical models for microelectromechanical systems from a few finite-element simulations runs. *Journal of Microelectromechanical Systems*, 8:280–289
- [35] Younis M I and Nayfeh A H (2003) A study of the nonlinear response of a resonant microbeam to an electric actuation. *Journal of Nonlinear Dynamics*, 91:117
- [36] Nayfeh A H, Younis M I, and Abdel-Rahman E M (2007) Dynamic pull-in phenomenon in MEMS resonators. *Nonlinear Dynamics*, 48:153–163
- [37] Nayfeh A H and Younis M I (2005) Dynamics of MEMS resonators under superharmonic and subharmonic excitations. *Journal of Micromechanics and Microengineering*, 15:1840–1847
- [38] Alsaleem F, Younis M I, Ouakad H (2009) On the nonlinear resonances and dynamic pull-in of electrostatically actuated resonators. *Journal of Micromechanics and Microengineering*, 19:045013(1-14)
- [39] Alsaleem F M, Younis M I, and Ruzziconi L (2010) An experimental and theoretical investigation of dynamic pull-in in MEMS resonators actuated electrostatically. *Journal of Microelectromechanical Systems*, 19(4):1–13
- [40] Younis M I, and Alsaleem F M (2009) Exploration of new concepts for mass detection in electrostatically-actuated structures based on nonlinear phenomena. *Journal of Computational and Nonlinear Dynamics*, 4(2), doi:10.1115/1.3079785, 15 pages
- [41] Binning G, Quate C F, and Gerber C (1986) Atomic force microscope. *Physical Review Letters* 56:930–933.
- [42] Abdel-Rahman E M, and Nayfeh A H (2005) Contact force identification using the subharmonic resonance of a contact-mode atomic force microscopy. *Nanotechnology*, 16:199–207
- [43] Abramovitch D Y, Andersson S B, Lucy Y P, and Schitter G (2007) A tutorial on the mechanisms, dynamics, and control of atomic force microscopes. proceedings of the 2007 American Control Conference, Marriott Marquis Hotel at Times Square, New York City, 11–13, 2007.
- [44] Albrecht T R, Grutter P, Horne D, and Rugar D (1991) Frequency modulation detection using high-Q cantilevers for enhanced force microscope sensitivity. *Journal of Applied Physics*, 69(2)
- [45] Arafat H N, Nayfeh A H, and Abdel-Rahman E M (2008) Modal interactions in contact-mode atomic force microscopes. *Nonlinear Dynamics*, 54(1,2):151–166
- [46] Arjmand M T, Sadeghian H, Salarieh H, and Alasty A (2008) Chaos control in AFM systems using nonlinear delayed feedback via sliding mode control. *Nonlinear Analysis: Hybrid systems*, 2:993–1001
- [47] Ashhab M, Salapaka M V, Dahleh M, and Mezic I (1997) Control of chaos in atomic force microscopes. proceedings of the American Control Conference, Albuquerque, New Mexico, June 1997
- [48] Ashhab M, Salapaka M V, Dahleh M, and Mezic I (1991) Dynamical analysis and control of microcantilevers. *Automatica*, 35:1663–1670
- [49] Ashhab M, Salapaka M V, Dahleh M, and Mezic I (1999) Melnikov-based dynamical analysis of microcantilevers in scanning probe microscopy. *Nonlinear Dynamics*, 20:197–220
- [50] Basso M, Giarre L, Dahleh M, and Mezic I (2000) Complex dynamics in a harmonically excited Lennard-Jones oscillator: Microcantilever-sample interaction in scanning probe microscopes. *Journal of Dynamic Systems, Measurement, and Control*, 122:240–245
- [51] Burnham N A, Kulik A J, and Gremaud G (1995) Nanosubharmonics: The dynamics of small nonlinear contacts. *Physical Review Letters*, 74(25):5092–5095
- [52] Chen L, Yu X, and Wang D (2007) Cantilever dynamics and quality factor control in AC mode AFM height measurements. *Ultramicroscopy*, 107:275–280
- [53] Coururier G, Boisgard R, Nony L, and Aime J P (2003) Noncontact atomic force microscopy: Stability criterion and dynamical responses of the shift of frequency and damping signal. *Review of Scientific Instruments*, 74(5):2726–2734
- [54] Dankowicz H (2006) Nonlinear dynamics as an essential tool for non-destructive characterization of soft nanostructures using tapping-mode atomic force microscopy. *Philosophical Transaction of the Royal Society A.*, 364, 3505–3520 doi: 10.1098/rsta.2006.1907

- [55] Dankowicz H, Zhao X, and Misra S (2007) Near-grazing dynamics in tapping-mode atomic-force microscopy. *International Journal of Non-Linear Mechanics*, 42:697–709
- [56] Farrokhpayam A, and Fathipour M (2009) Modeling and dynamic analysis of atomic force microscope based on Euler-Bernoulli beam theory. *Digital Journal of Nanomaterials and Biostructures*, 4(4):789–801
- [57] Garcia R, and San Paulo A (1991) Attractive and repulsive tip-sample interaction regimes in tapping-mode atomic force microscopy. *Physical Review B*, 60(7):4961–4967
- [58] Garcia R, and San Paulo A (2000) Dynamics of a vibrating tip near or in intermittent contact with a surface. *Physical Review B*, 61(20):R13381–R13384
- [59] Garcia R, and Perez R (2001) Dynamic atomic force microscopy methods. *Surface Science Reports*, 47:197–301
- [60] Gauthier M, Sasaki N, and Tsukada M (2001) Dynamics of the cantilever in noncontact dynamic force microscopy: The steady-state approximation and beyond. *Physical Review B*, 64:085409
- [61] Giessibl F J (1997) Forces and frequency shifts in atomic-resolution dynamic-force microscopy. *Physical Review B*, 56(24):16010–16015
- [62] Giessibl F J (2001) A direct method to calculate tip-sample forces from frequency shifts in frequency-modulation atomic force microscopy. *Applied Physics Letters*, 78(1):123–125
- [63] Giessibl F J (2003) Advances in atomic force microscopy. *Reviews of Modern Physics*, 75:949–984
- [64] Ha J, Fung K, and Chen Y (2005) Dynamic responses of an atomic force microscope interacting with samples. *Journal of Dynamic systems, Measurement, and Control*, 127:705–709
- [65] Hornstein S and Gottlieb O (2008) Nonlinear dynamics, stability, and control of the scan process in noncontacting atomic force microscopy. *Nonlinear Dynamics*, 54:93–122
- [66] Hu S and Raman A (2006) Chaos in atomic force microscopy. *Physical Review Letters*, 96, doi:10.1103/96.036107
- [67] Jalili N and Laxminarayana k, (2004) A review of atomic force microscopy imaging systems: application to molecular metrology and biological sciences. *Mechatronics*, 14:907–945
- [68] Jamitzky F and Stark R W (2010) Intermittency in amplitude modulated dynamic atomic force microscopy. *Ultramicroscopy*, 110:618–621
- [69] Korayem M H, Zafari S, Amanati A, Damircheli M, and Ebrahimi, N (2010) Analysis and control of micro-cantilever in dynamic mode AFM. *The International Journal of Advanced Manufacturing Technology*, doi:1007/s00170-010-2588-4
- [70] Kühle A, Sorenson A H, Zandbergen J B, and Bohr J (1998) Contrast artifacts in tapping tip atomic force microscopy. *Applied Physics A* 66:S329–S33.
- [71] Lee S I, Howell S W, Raman A, and Reifengerger R (2002) Nonlinear dynamics of micro-cantilevers in tapping mode atomic force microscopy: A comparison between theory and experiment. *Physical Review B*, 66: 115409, 2002
- [72] Marth M, Maier D, Honerkamp J, Brandsch R, and Bar G (1991) A unifying view on some experimental effects in tapping-mode atomic force microscopy. *Journal of Applied Physics*, 85(10):7030–7036
- [73] Martin Y, Williams C C, and Wickramasinghe H K (1987) Atomic force microscope—force mapping and profiling on a sub 100-Å scale. *Journal of Applied Physics*, 61:4723–4729
- [74] Pai N, Wang C, and Lin D T (2010) Bifurcation analysis of a microcantilever in AFM system. *Journal of Franklin Institute*, 347:1353–1367
- [75] Payam A F and Fathipour M (2009) Modeling and dynamic analysis of atomic force microscope based on Euler-Bernoulli beam theory. *Digest Journal of Nanomaterial and Biostructures*, 4:789–801
- [76] Rabe U, Janser K, and Arnold W (1996) Vibrations of free and surface-coupled atomic force microscope cantilevers: Theory and experiment. *Review of Scientific Instruments*, 67(9):3281–3293
- [77] Rabe U, Turner J, and Arnold W (1998) Analysis of the high-frequency response of atomic force microscope cantilever. *Applied Physics A*, 66:S277–S282

- [78] Rodriguez T R and Garcia R (2002) Tip motion in amplitude modulation (tapping-mode) atomic-force microscopy: Comparison between continuous and point-mass models. *Applied Physics Letters*, 80(9):1646–1648
- [79] Rützel S, Lee S I, and Raman A (2003) Nonlinear dynamics of atomic-force-microscope probes driven in Lennard-Jones potentials. *Proceedings of the Royal Society A*, 459:1925–1948
- [80] Santos S, Barcons V, Font J, and Thomson, N H (2010) Cantilever dynamics in amplitude modulation AFM: continuous and discontinuous transitions. *Journal of Physics D: Applied Physics*, 43:275401, doi: 10.1088/0022-3727/43/27/275401
- [81] Sarid D, Ruskell T G, Workman R K, and Chen D (1996) Driven nonlinear atomic force microscopy cantilevers: From noncontact to tapping modes of operation. *Journal of Vacuum Science & Technology B*, 14(2):864–867
- [82] Schitter G, Menold P, Knapp H F, Allgower F, and Stemmer A (2001) High performance feedback for fast scanning atomic force microscopes. *Review of Scientific Instruments*, 72(8):3320–3327
- [83] Sebastian A, Salapaka M V, and Chen D J (2001) Harmonic and power balance tools for tapping-mode atomic force microscope. *Journal of Applied Physics*, 89(11):6473–6480
- [84] Sebastian A, Salapaka M V, Chen D J, and Cleveland J P (1991) Harmonic analysis based modeling of tapping-mode AFM. *Proceedings of the American Control Conference*, San Diego, California
- [85] Song Y and Bhushan B (2008) Atomic force microscopy dynamic modes: modeling and applications. *Journal of Physics: Condensed Matter*, Vol. 20, doi: 10.1088/0953-8984/20/22/225012
- [86] Stark R W, and Heckl W M (2000) Fourier transformed atomic force microscopy: tapping mode atomic force microscopy beyond the Hookian approximation. *Surface Science*, 457:219–228
- [87] Turner J A, Hirsekorn S, Rabe U, and Arnold W (1997) High-frequency response of atomic-force microscope cantilevers. *Journal of Applied Physics*, 82(3):966–979
- [88] Turner J A (2004) Non-linear vibrations of a beam with cantilever-Hertzian contact boundary conditions. *Journal of sound and Vibration*, 275:177–191
- [89] Wolf K, and Gottlieb O (2002) Nonlinear dynamics of a noncontacting atomic force microscope cantilever actuated by a piezoelectric layer. *Journal of Applied Physics*, 91(7):4701–4709
- [90] Zhang W, Meng G, Zhou J, and Chen J (2009) Nonlinear dynamics and chaos of microcantilever-based TM-AFMs with squeeze film damping effects. *Sensors*, 9:3854–3874
- [91] Zhong Q, Innis D, Kjoller K, and Elings V B (1993) Fractured polymer silica fiber surface studied by tapping mode atomic-force microscopy,” *Surface Science*. 290:L688–L692
- [92] Ouakad H and Younis M I (2009) Modeling and simulations of collapse instabilities of microbeams due to capillary forces. *Mathematical Problems in Engineering*, Article ID 871902, 16 pages, doi:10.1155/2009/871902
- [93] de Boer M P, Clews P J, Smith B K, and Michalske T A (1997) Adhesion of polysilicon microbeams in controlled humidity ambient. *Materials Research Society*, 518:131–136
- [94] de Boer M P, and Michalske T A (1999) Accurate method for determining adhesion of cantilever beams. *Journal of applied physics*, 86(2):817–827
- [95] Mastrangelo C H and Hsu C H (1993) Mechanical stability and adhesion of microstructures under capillary forces. I. Basic theory. *Journal of Microelectromechanical Systems*, 2:33–43
- [96] Mastrangelo C H and Hsu C H (1993) Mechanical stability and adhesion of microstructures under capillary forces. II. Experiments. *Journal of Microelectromechanical Systems*, 2:44–55
- [97] Legtenberg R, Tilmans H A C, Elders J, and Elwenspoek M (1994) Stiction of surface micromachined structures after rinsing and drying: model and investigation of adhesion mechanisms. *Sensors and Actuators*, 43:230–238
- [98] Tas N, Sonnenberg T, Jansen H, Legtenberg R, and Elwenspoek M (1996) Stiction in surface micromachining. *Journal of Micromechanics and Microengineering*, 6:385–397

- [99] Lambert P (2007) *Capillary Forces in Microassembly: Modeling, Simulation, Experiments, and Case Study*", Springer, New York
- [100] Hung E S and Senturia S D (1991) Generating efficient dynamical models for microelectromechanical systems from a few finite-element simulations runs. *Journal of Microelectromechanical Systems*, 8:280–289
- [101] Nayfeh A H and Younis M I (2004) A new approach to the modeling and simulation of flexible microstructures under the effect of squeeze-film damping. *Journal of Micromechanics and Microengineering*, 14:170–181
- [102] Hosaka H, Itao K, and Kuroda S (1995) Damping characteristics of beam-shaped micro-oscillators. *Sensors and Actuators A*, 49:87–95
- [103] Lifshitz R and Roukes M L (2000) Thermoelastic damping in micro-and nanomechanical systems. *Physical Review B*, 61:5600–5609
- [104] Nayfeh A H and Younis M I (2004) Modeling and simulations of thermoelastic damping in microplates. *Journal of Micromechanics and Microengineering*, 14:1711–1717

Chapter 7

Nonlinear Dynamics of an Electrically Actuated Resonator

This chapter discusses the nonlinear dynamics of an electrically actuated resonator as a case study in some depth. Several experimental data of the static and dynamic responses will be shown. After that, we discuss several modeling and simulation techniques to explain the measurements, particularly, the measured pull-in data. A shooting technique to find periodic motion and a basin-of-attraction technique will be illustrated and demonstrated. These are used to shed light on the fractal or chaotic-like nature of the dynamic behavior near the pull-in regime. Bifurcation analysis will be conducted based on the so-called Dover-Cliff integrity curves, which help justify the experimental measurements. This complicated behavior of the resonator will be then proposed to realize a new class of devices that combines the functionality of a mass detector and a switch. Finally, delayed-feedback control technique will be demonstrated as a powerful method to enhance the stability of the resonator.

7.1 The Device and Experimental Setup

The device under investigation is a capacitive sensor shown previously in Fig. 3.17 and which behavior has been discussed briefly in various places in the previous chapters. Figure 7.1 shows a picture of the device, which is essentially an accelerometer, fabricated by Sensata Technologies [1]. It is made of two long cantilever beams with a proof mass attached to their tips. The proof mass forms one side of the capacitive electrode used for detection. The accelerometer's proof mass and cantilever beams are made of an alloy 42 metal of thickness 150 μm . The proof mass has an approximate length of 9 mm and width of 5.32 mm. The experimental setup used for testing is shown in Fig. 7.2. It consists of a laser Doppler vibrometer, which is equipped with a displacement encoder to measure the deflection of the proof mass, an AC and DC power sources, a LabView data acquisition system, and a vacuum chamber hooked up to a vacuum pump. The vacuum chamber is equipped with ports for electrical connections and a viewport window made of a quartz glass that enables the laser to penetrate without distortion. The use of the vacuum chamber is to reduce the high damping that the proof mass experiences due to squeeze-film effect.

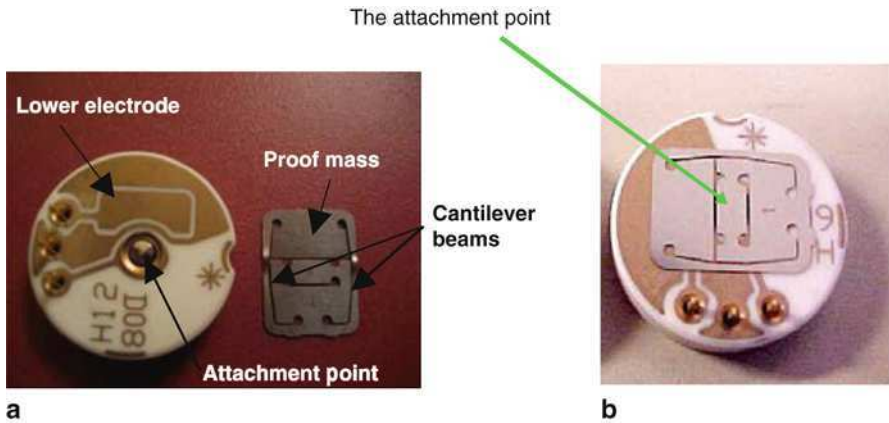


Fig. 7.1 **a** A top view picture for the tested capacitive sensor (taken apart). **b** A top view of the assembled part. When excited electrostatically, the proof mass oscillates in the out of plane direction. (Reprinted with permission. Copyright 2009, IOP Publishing Ltd [2])

7.2 Initial Characterization and Parameters Extraction

Experimental characterization of the device has been conducted to extract the parameters needed to be used in a lumped spring–mass model. First the device is biased with different DC voltages and the static deflection of the proof mass is measured using the laser Doppler vibrometer. Figure 7.3a shows the transient response of the proof mass for different step DC voltages. According to the measurements, the pull-in voltage of the device is 115.3 V and the gap width separating the proof mass from the substrate is 42 μm . Using the curve fitting procedure of Sect. 4.1.1 and Eq. (4.3), the stiffness coefficient is estimated to be $k = 215 \text{ N/m}$. This value yields the best match with the experimental data (Fig. 7.3b). Figure 7.3b shows also the simulated unstable equilibrium solution.

The next step in characterization is to measure the linear natural frequency of the device and to investigate the effect of pressure variation on the response. Toward this, the device is excited using a small DC voltage V_{DC} superimposed to a small AC voltage V_{AC} , such that a linear response is generated, Fig. 7.4. In this figure only the dynamic part of the proof mass deflection is shown (i.e., the static deflection due to the DC load is not shown since the laser Doppler vibrometer cannot read it while measuring the dynamic deflection). The figure indicates that the fundamental natural frequency of the cantilevers–mass system is approximately equal to 192.5 Hz. This value and the measured stiffness are used to calculate the effective mass of the proof mass to be used in the lumped model. Figure 7.4 indicates that the pressure value inside the chamber has significant effect on the amplitude of the response and the sharpness of the resonance. This implies that any variation in the pressure inside the chamber while taking measurements may affect the quality of the obtained data. On

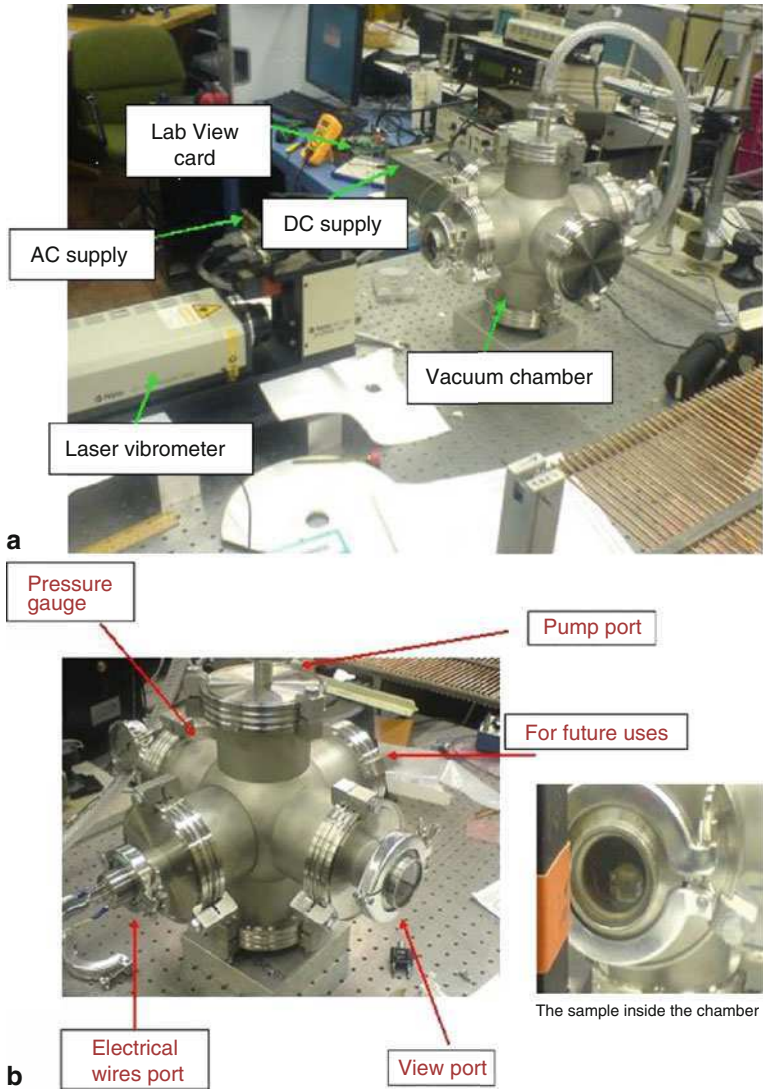


Fig. 7.2 **a** The experimental setup used for testing the capacitive accelerometers. **b** The vacuum chamber. (Reprinted with permission. Copyright 2009, IOP Publishing Ltd [2])

the other hand, the figure shows that the variation in the pressure value has negligible effect on changing the natural frequency of the device. This is because the resonator is operated at low excitation frequency. Therefore, the squeeze number is low, and hence the effect of the squeeze-film damping on shifting the natural frequency of the resonator (the stiffness effect of squeeze-film damping) is very small.

Fig. 7.3 a Experimentally measured transient response for different step V_{DC} inputs. **b** Experimental data versus simulation results (*stable* and *unstable*) for the static deflection of the proof mass due to different V_{DC} values. (Reprinted with permission. Copyright 2009, IOP Publishing Ltd [2])

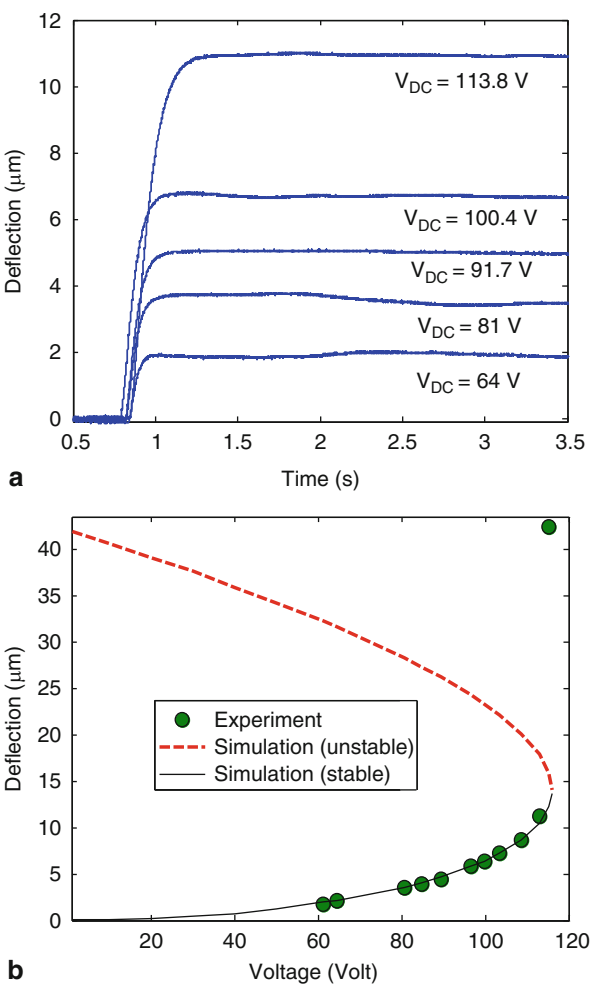
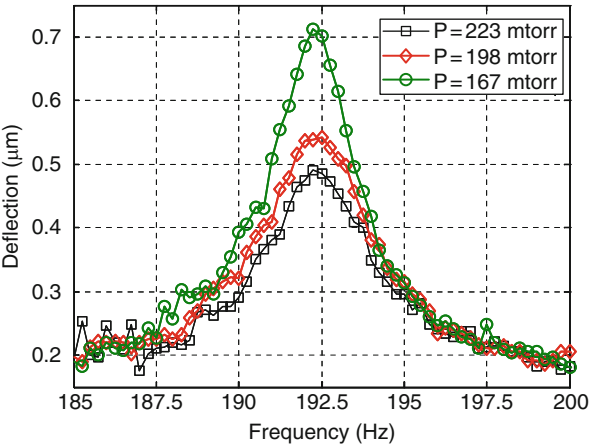


Fig. 7.4 Experimentally measured frequency–response curves for different pressure values for $V_{DC} = 2 \text{ V}$ and $V_{AC} = 4.2 \text{ V}$. (Reprinted with permission. Copyright 2009, IOP Publishing Ltd [2])



7.3 Experimental Data for Large DC and AC Excitations

Next, experimental data are presented for the response of the capacitive device to large AC and DC electric loads. Such strong excitation results in multitude of non-linear phenomena and bifurcations. Focus is given here for actuation at an excitation frequency near the fundamental natural frequency of the device (primary resonance) and also near twice the natural frequency (subharmonic resonance).

7.3.1 Primary Resonance

As noted from Fig. 7.4, the resonator responds linearly to low level of excitation loads near its primary resonance. Raising the excitation level to $V_{DC} = 19.4$ V and $V_{AC} = 15.3$ V, while keeping low air pressure near 150 mtorr, leads to the softening behavior shown in Fig. 7.5a, which is marked by the bending of the frequency–response curve to the left. The response of this figure was obtained by running both forward and backward frequency-sweep tests. This softening behavior can cause jumps in the response from lower to higher response and vice versa where there are coexisting states.

The softening behavior of Fig. 7.5a is considered a local bifurcation phenomenon in the sense that the dynamic behavior is inside the potential well in the neighborhood of the equilibrium solutions of the system. Global behavior on the other hand refers to the dynamics away from the equilibrium solutions and can exceed the boundaries of the potential well, which is the case of dynamic pull-in. Increasing the voltage load to $V_{DC} = 40.1$ V and $V_{AC} = 18.4$ V shows an example of this global behavior, Fig. 7.5b. The figure indicates dynamic pull-in, where the frequency–response curves are terminated with slopes approaching infinity. Also, the figure shows what appears to be a band of frequencies, wherein the resonator is forced to exhibit dynamic pull-in

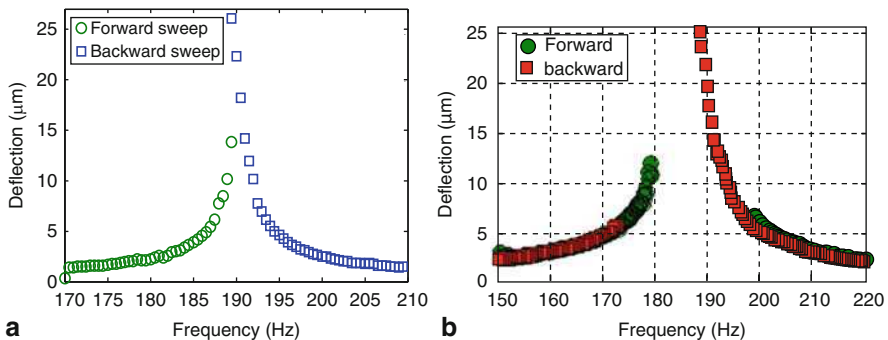


Fig. 7.5 Experimentally measured frequency–response curves for a load of **a** $V_{DC} = 19.4$ V and $V_{AC} = 15.3$ V and **b** $V_{DC} = 40.1$ V and $V_{AC} = 18.4$ V. A sampling rate of 0.1 Hz/s was used in this experiment. (Reprinted with permission. Copyright 2009, IOP Publishing Ltd [2])

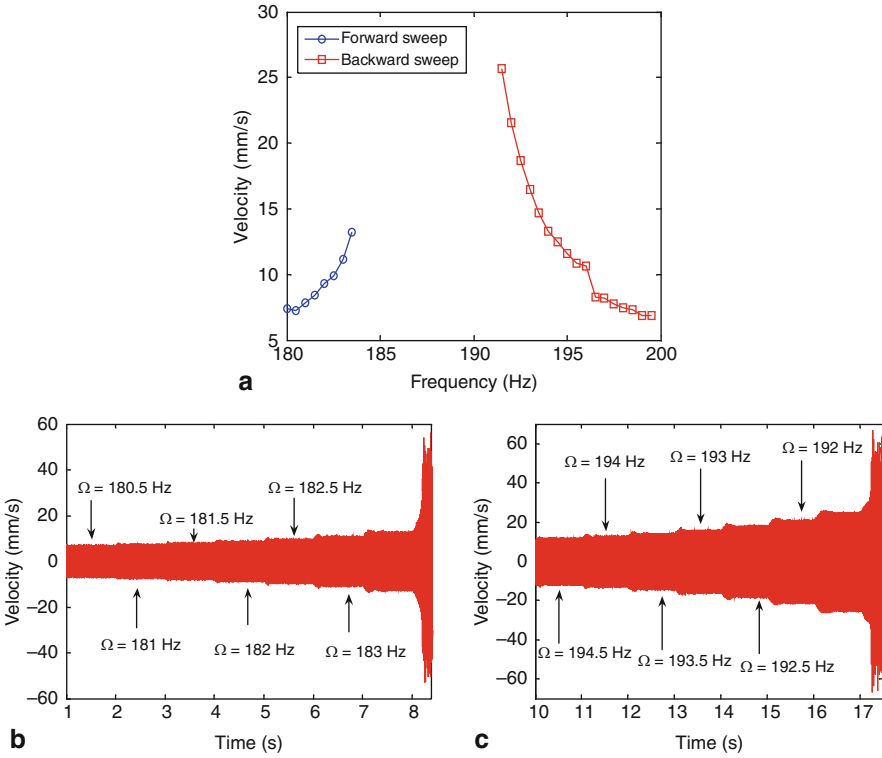


Fig. 7.6 The experimental data of the frequency-sweep method for $V_{DC} = 19.4$ V and $V_{AC} = 32.4$ V. Figure part **a** shows the frequency–response, **b** the time history of a forward sweep, and **c** the time history of a backward sweep. (Reprinted with permission. Copyright 2010, IEEE [3])

instability. We recall here that the static pull-in voltage of the device is 115 V, so dynamic pull-in is triggered at a voltage load much lower than the static value.

Figure 7.6a shows another example of a frequency–response curve with a pull-in band. Figures 7.6b and c show the time responses of the resonator during the forward and backward frequency-sweeps, respectively, illustrating the method of obtaining Fig. 7.6a. By running several experiments similar to Fig. 7.6 at a constant value of V_{DC} and for various levels of V_{AC} , an instability tongue is obtained indicating the zone wherein the resonator is experimentally forced to pull-in, Fig. 7.7. As seen from Fig. 7.7, the higher the AC voltage is the wider this band of frequency becomes. This V-shape instability tongue of Fig. 7.7 is typical of electrostatically actuated structures. The reader is referred to [3] for further experimental data showing such V zones for other micromachined structures.

It turns out that one can also run a force-sweep test at a constant excitation frequency to generate the same data (provided that both sweep tests are conducted quasi-statically, i.e., the transient effects in both tests are almost the same). This force-sweep method can be easier to implement. Figure 7.8 depicts a time history

Fig. 7.7 Experimentally measured pull-in zone for $V_{DC} = 40.1$ V using two methods of sweeping. (Reprinted with permission. Copyright 2010, IEEE [3])

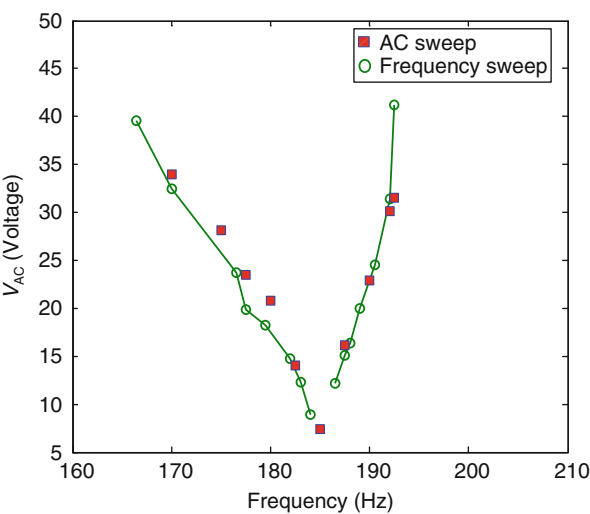
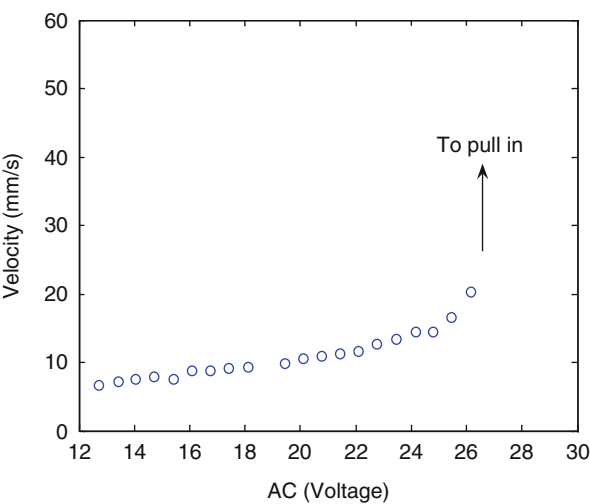


Fig. 7.8 Experimentally measured AC amplitude sweep at an excitation frequency of 175 Hz. (Reprinted with permission. Copyright 2010, IEEE [3])



response as an example of a force-sweep test used to generate one data point of Fig. 7.7. As noted from Fig. 7.7, both sweeping types generate close results.

7.3.2 Subharmonic Resonance

Next, experimental data are shown for the subharmonic resonance of order one-half (excitation at a frequency close to twice the fundamental natural frequency of the resonator). Figure 7.9 shows two frequency–response curves for $V_{DC} = 40.1$ V

Fig. 7.9 Experimentally measured forward sweep response showing subharmonic resonance for $V_{DC} = 40.1$ V. (Reprinted with permission. Copyright 2009, IOP Publishing Ltd [2])

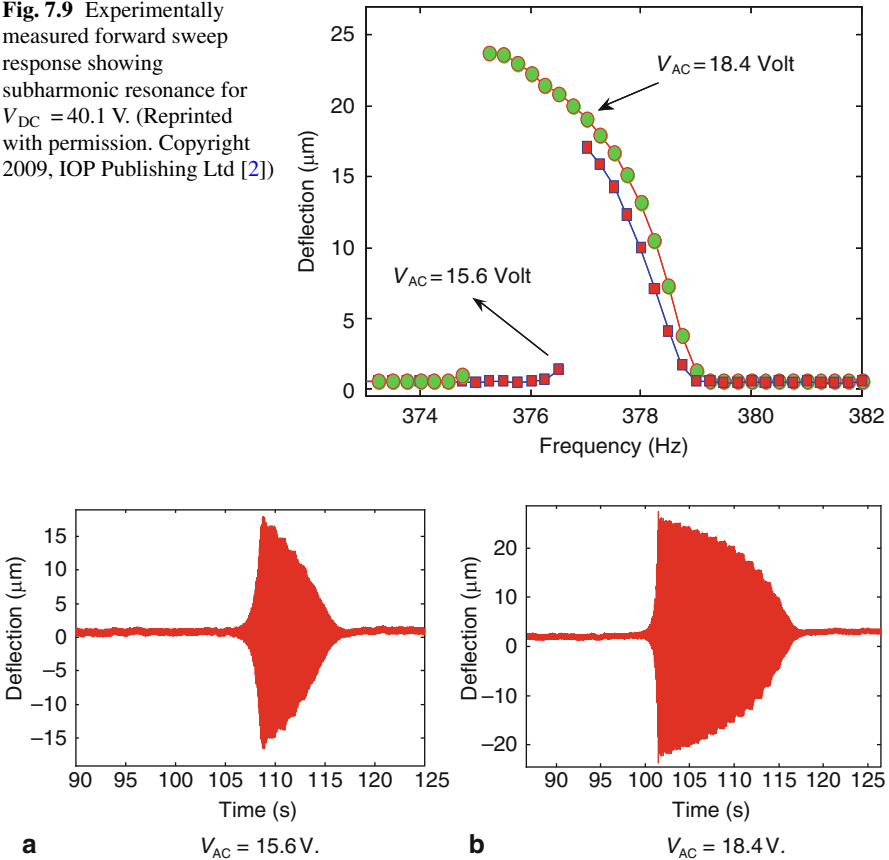


Fig. 7.10 Experimentally measured time history response of the resonator during a forward frequency-sweep for the cases of Fig. 7.9. The excitation frequency is 372.5 Hz. The excitation frequency was increased by 0.25 Hz every one second. (Reprinted with permission. Copyright 2009, IOP Publishing Ltd [2])

and $V_{AC} = 15.6$ V and $V_{AC} = 18.4$ V. The figure indicates significant sensitivity of the subharmonic resonance when increasing V_{AC} . This is further highlighted in Fig. 7.10, which shows time histories of the frequency-sweep for the two loading cases of Fig. 7.9 demonstrating sharp transition for the resonator response before and after the activation of subharmonic resonance. Both Fig. 7.9 and Fig. 7.10 do not show any sign of dynamic pull-in for these loading cases. Increasing V_{AC} slightly however to 21.1 V results in dynamic pull-in as seen in Fig. 7.11. The figure shows that there is an apparent pull-in band starting at a frequency of 373.5 Hz. Exceeding this frequency, the response of the resonator increases unboundedly until it hits the substrate (dynamic pull-in). Experimentally, after entering the pull-in band the laser signal jumps to a high value, Fig. 7.11b. One can note from Fig. 7.11b the dramatic increase in the deflection of the resonator from very small value before the activation

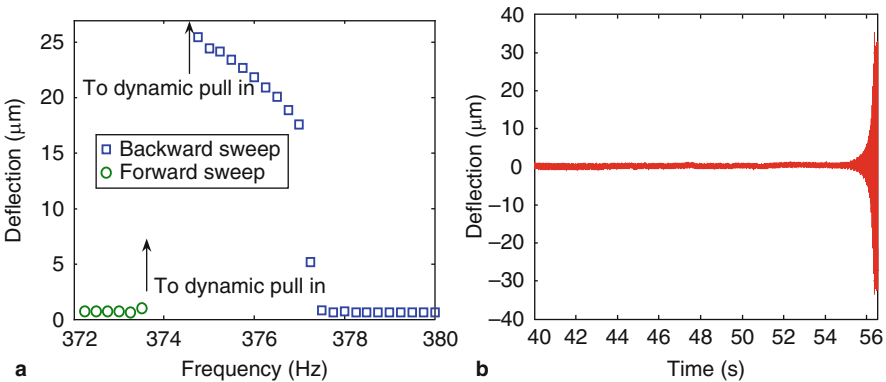


Fig. 7.11 **a** Experimentally measured frequency–response curve in the case of subharmonic resonance (*forward* and *backward* sweep) showing a dynamic pull-in band of frequencies. Results are shown for $V_{\text{DC}} = 40.1 \text{ V}$ and $V_{\text{AC}} = 21.1 \text{ V}$. **b** The corresponding time history of the response for the forward frequency-sweep showing dynamic pull-in when the excitation frequency reaches 373.5 Hz at time = 55 s. (Reprinted with permission. Copyright 2009, IOP Publishing Ltd [2])

of subharmonic resonance to a very large value leading to pull-in upon the activation of the subharmonic resonance. Because of this feature, subharmonic excitation can be very promising for designing sensitive sensors as explained later in the chapter.

Increasing the AC voltage further creates a dynamic pull-in band near the subharmonic resonance as depicted in Fig. 7.12. The figure shows experimental data for the pull-in bands as a function of the AC amplitude for two different DC values. The figure indicates that increasing the DC voltage has the effects of widening the pull-in zones and lowering the AC threshold needed for triggering pull-in.

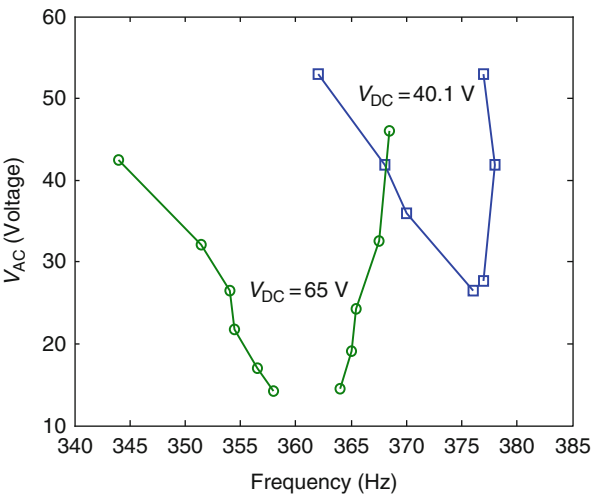


Fig. 7.12 Experimentally measured pull-in bands near subharmonic excitation. (Reprinted with permission. Copyright 2010, IEEE [3])

7.4 Simulations Using Long-Time Integration

To understand the experimentally measured nonlinear phenomena, dynamic pull-in, and pull-in band, theoretical modeling and analysis of the resonator dynamics are needed. Toward this, a nonlinear single-degree-of-freedom model is used of the equation

$$m\ddot{x} + c\dot{x} + kx = \frac{\varepsilon A [V_{DC} + V_{AC} \cos(\Omega t)]^2}{2(d - x)^2} \quad (7.1)$$

where x is the tip deflection of the proof mass of the resonator, Ω is the AC voltage frequency, A is the electrode area of the capacitor, d is the capacitor gap width, c is the viscous damping coefficient, k is the effective stiffness of the cantilever beams, m is the effective mass, ε is the dielectric constant of the gap medium, and the superscript dot denotes time derivative.

One approach to simulate the response is to integrate Eq. (7.1) numerically for a long-time until reaching steady state using Runge–Kutta scheme, similar to Example 5.23. While this approach is easy to implement, it suffers convergence problems near bifurcation points, pull-in, and where the domain of attraction (basin of attraction) of the periodic solution is too small. Figure 7.13 depicts an example of a comparison between measurements and simulations for primary and subharmonic resonance using long-time integration. The simulation results show generally good agreement with the experimental data, except for slight deviation, which might be attributed to the variation of air pressure inside the chamber during the frequency-sweep. In the case of primary resonance, simulations were conducted for the left and right branches of the frequency–response curves using a continuation approach (loading the initial conditions of the previous frequency step) up to the point where the numerical integrator experiences divergence. This numerical divergence might be an indication that the system is losing stability due to pull-in or it can be just due to poor numerical convergence of the Runge–Kutta scheme. To seek more robust understanding and

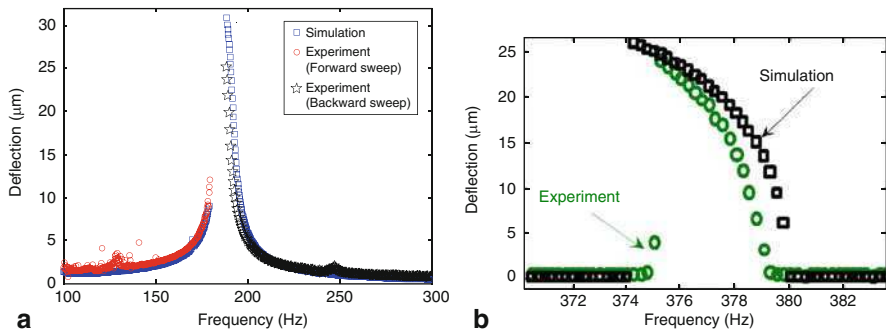


Fig. 7.13 Experimental data versus simulation results obtained using long-time integration for **a** primary resonance and **b** subharmonic resonance for $V_{DC} = 40.1$ V and $V_{AC} = 18.4$ V. (Reprinted with permission. Copyright 2009, IOP Publishing Ltd [2])

analysis of the behavior of the resonator in this regime, other numerical techniques need to be used.

7.5 Simulations Using the Shooting Technique

As noted previously, the long-time integration technique may not predict accurately when exactly a stable state/solution of the system exists or not since it depends on the domain of attraction of the solutions. If the domain is big, long-time integration converges to a periodic solution easily. If the domain is not robust, as the case near termination and bifurcation points, the integration scheme diverges, which may or may not indicate reaching an unstable state. In another word, it is hard to tell using this approach whether the divergence of the scheme is due to reaching physically unstable state or because of the divergence of the numerical scheme. In such cases, other numerical methods to find periodic solutions and analyze their stability should be used, such as the finite difference method and the shooting techniques [4]. Here, we utilize the shooting method in conjunction with the Floquet theory to analyze the stability of the captured periodic solution.

7.5.1 The Shooting Method

The shooting method is a powerful technique for capturing periodic motion and analyzing their stability for nonlinear systems. Hence, it is capable of predicting both stable and unstable solutions. The shooting technique captures a periodic solution (orbit) of period $T = 2\pi/\Omega$, where Ω is the excitation frequency. It is called shooting because it is based on searching (shooting) for an appropriate set of initial conditions that can result in a periodic motion for the system. In this technique, initial guesses for the initial conditions are first supplied to the scheme and then they are corrected using a Newton–Raphson method. Convergence is achieved when the difference between the newly corrected set of initial guesses and the previous ones diminishes to very small values. Once a periodic motion is captured, its stability is determined using the so-called Floquet theory [4].

Next, we illustrate the method for a nonautonomous dynamical system (systems with explicit dependence on time). Toward this, consider the equations of motion of the system written in state-space form as

$$\dot{\vec{x}} = \vec{F}(\vec{x}, t) \quad (7.2)$$

where \vec{x} is the state vector and \vec{F} represents a vector of the right hand sides of the state-space equations. For Eq. (7.2), we seek a vector of initial conditions

$$\vec{x}(0) = \vec{\eta} \quad (7.3)$$

such that the solution is periodic with a period T , that is

$$\vec{x}(T, \vec{\eta}) = \vec{\eta}. \quad (7.4)$$

This method starts by searching or “shooting” for an initial guess $\vec{\eta}_0$ for the initial conditions, which generally deviates from the exact one by an error or correction $\delta\vec{\eta}$. Hence,

$$\vec{\eta} = \vec{\eta}_0 + \delta\vec{\eta}. \quad (7.5)$$

Substituting Eq. (7.5) into Eq. (7.4):

$$\vec{x}(T, \vec{\eta}_0 + \delta\vec{\eta}) = \vec{\eta}_0 + \delta\vec{\eta}. \quad (7.6)$$

Expanding Eq. (7.6) in a Taylor series and keeping only linear terms yield:

$$\vec{x}(T, \vec{\eta}_0) + \frac{\partial \vec{x}(T, \vec{\eta}_0)}{\partial \vec{\eta}} \delta\vec{\eta} = \vec{\eta}_0 + \delta\vec{\eta} \Rightarrow \left(\frac{\partial \vec{x}(T, \vec{\eta}_0)}{\partial \vec{\eta}} - I \right) \delta\vec{\eta} = \vec{\eta}_0 - \vec{x}(T, \vec{\eta}_0). \quad (7.7)$$

This method seeks to solve Eq. (7.7) for the correction vector using the Newton–Raphson scheme. To proceed, we need to evaluate $\frac{\partial \vec{x}(T, \vec{\eta}_0)}{\partial \vec{\eta}}$, toward this, Eq. (7.2) is differentiated with respect to $\vec{\eta}$

$$\frac{\partial}{\partial \vec{\eta}} \left(\frac{\partial \vec{x}}{\partial t} \right) = \frac{\partial \vec{F}}{\partial \vec{\eta}} \Rightarrow \frac{d}{dt} \left(\frac{\partial \vec{x}}{\partial \vec{\eta}} \right) = \frac{\partial \vec{F}}{\partial \vec{x}} \frac{\partial \vec{x}}{\partial \vec{\eta}}. \quad (7.8)$$

Equation (7.8) provides a system of differential equations that describes the evolution of the variables $\frac{\partial \vec{x}}{\partial \vec{\eta}}$ in time. To find the initial conditions of this system, Eq. (7.3) is derived with respect to $\vec{\eta}$, which gives

$$\frac{\partial \vec{x}(0)}{\partial \vec{\eta}} = I \quad (7.9)$$

where I is the identity matrix.

The procedure of solution is then goes as follows: Using the initial guess $\vec{\eta}_0$, the system of differential equations, Eqs. (7.2), (7.3), (7.8), and (7.9) are integrated simultaneously over one-period T using Runge–Kutta technique for the variables \vec{x} and $\frac{\partial \vec{x}}{\partial \vec{\eta}}$. The results are then substituted into Eq. (7.7) to yield an algebraic system of equations for the correction vector $\delta\vec{\eta}$. This system is solved using the Newton–Raphson method. Then, the initial guesses are corrected according to Eq. (7.5) and the procedure is repeated until the values of $\delta\vec{\eta}$ reach very small numbers.

Next, we demonstrate the procedure as it is applied to the equation of motion of the resonator studied here. For convenience, we first normalize Eq. (7.1) by introducing nondimensional variables (denoted by superscript \wedge) as below

$$\hat{x} = \frac{x}{d}; \quad \hat{t} = \frac{t}{T} \quad (7.10)$$

where $T = 2\pi/\omega_n$ and $\omega_n = \sqrt{k/m}$. Substituting Eq. (7.10) into Eq. (7.1) yields the nondimensional equation of motion

$$\hat{\ddot{x}} + \hat{c}\hat{\dot{x}} + \hat{x} = \alpha \frac{[V_{DC} + V_{AC} \cos(\Omega\hat{t})]^2}{(1 - \hat{x})^2} \quad (7.11)$$

where

$$\hat{c} = 2\zeta\omega_n = \frac{c}{\sqrt{km}}, \quad \alpha = \frac{\varepsilon A}{2m\omega_n^2 d^3}.$$

Next, Eq. (7.11) is written in state-space representation, hence we let $X_1 = \hat{x}$ and $X_2 = \hat{\dot{x}}$, which yields

$$\dot{X}_1 = X_2 \quad (7.12)$$

$$\dot{X}_2 = -X_1 - \hat{c}X_2 + \alpha \frac{[V_{DC} + V_{AC} \cos(\Omega\hat{t})]^2}{(1 - X_1)^2}. \quad (7.13)$$

For this second-order system, we need to search for an appropriate set of initial conditions (η_1, η_2) that yields periodic solution for Eqs. (7.12) and (7.13). To proceed with the shooting technique, for convenience, we define the following variables:

$$X_3 = \frac{\partial X_1}{\partial \eta_1}; \quad X_4 = \frac{\partial X_1}{\partial \eta_2}; \quad X_5 = \frac{\partial X_2}{\partial \eta_1}; \quad X_6 = \frac{\partial X_2}{\partial \eta_2}.$$

The shooting technique requires integrating Eqs. (7.12) and (7.13) in time for one-period simultaneously with the below system of differential equations

$$\dot{X}_3 = X_5 \quad (7.14)$$

$$\dot{X}_4 = X_6 \quad (7.15)$$

$$\dot{X}_5 = -X_3 - \hat{c}X_5 + 2X_3\alpha \frac{[V_{DC} + V_{AC} \cos(\Omega\hat{t})]^2}{(1 - X_1)^3} \quad (7.16)$$

$$\dot{X}_6 = -X_4 - \hat{c}X_6 + 2X_4\alpha \frac{[V_{DC} + V_{AC} \cos(\Omega\hat{t})]^2}{(1 - X_1)^3}. \quad (7.17)$$

The initial conditions of Eqs. (7.12)–(7.17) are

$$\begin{aligned} X_1(0) &= \eta_{10} \\ X_2(0) &= \eta_{20} \\ X_3(0) &= 1 \\ X_4(0) &= 0 \\ X_5(0) &= 0 \\ X_6(0) &= 1 \end{aligned} \quad (7.18)$$

where (η_{10}, η_{20}) are the initial guesses for the initial conditions that lead to periodic motion. Then, Eqs. (7.12)–(7.17) are integrated numerically subjected to the initial conditions of Eq. (7.18) over the duration of one-period T . Subsequently, we calculate the values of X_3 – X_6 at time T , substitute them in the below algebraic system of equations, and solve for the error in the initial conditions $(\partial\eta_1, \partial\eta_2)$:

$$\left\{ \begin{pmatrix} X_3 & X_4 \\ X_5 & X_6 \end{pmatrix} - [I] \right\} \begin{Bmatrix} \partial\eta_1 \\ \partial\eta_2 \end{Bmatrix} = \begin{Bmatrix} \eta_{10} - X_1(T, \eta_{10}, \eta_{20}) \\ \eta_{20} - X_2(T, \eta_{10}, \eta_{20}) \end{Bmatrix}. \quad (7.19)$$

The procedure is repeated until the errors are minimized and a convergence is achieved. The next step after obtaining the periodic motion is to analyze its stability. This can be done by solving for the eigenvalues of the so-called monodromy matrix, which is composed of the variables X_3 – X_6 calculated at time T as

$$\begin{pmatrix} X_3(T) & X_4(T) \\ X_5(T) & X_6(T) \end{pmatrix}.$$

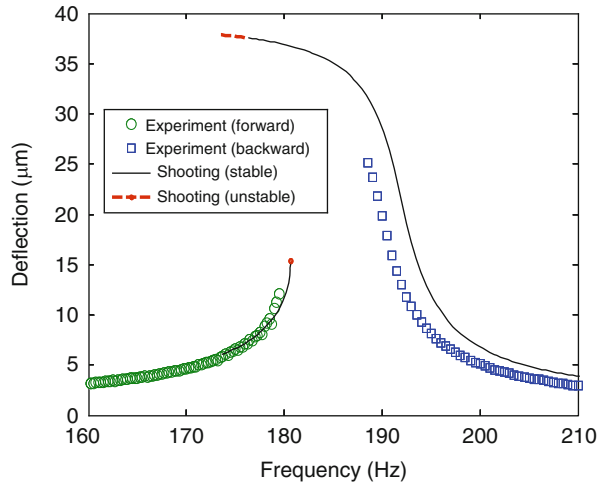
This yields two eigenvalues called Floquet multipliers. If the absolute values of both Floquet multipliers are less than unity then the periodic motion is stable, otherwise it is considered unstable, which is equivalent to exiting the unit circle in the complex plane.

If the Floquet multipliers are monitored while changing a bifurcation or a control parameter, such as the voltage load, then bifurcations of the periodic solutions can be identified. If, while varying the control parameter, a Floquet multiplier exists the unit circle through negative one, then the bifurcation is called period-doubling or flip bifurcation since the new periodic motions are born with period twice the period before the bifurcation point. Hence, in order to track the bifurcation on the newborn periodic solution, one needs to change the period in the shooting scheme from T to $2T$. If a Floquet multiplier exists the unit circle through positive one, then the bifurcation can be either symmetry breaking or pitchfork (if the symmetry of the periodic solutions is broken beyond the bifurcation point), cyclic fold (if stable and unstable periodic motions collide at the bifurcation point leading to their destruction), or transcritical (in the case of exchange of stability) [4]. If a pair of complex Floquet multipliers exist the unit circle away from the real axis, the bifurcation is called secondary Hopf or Neimark bifurcation.

7.5.2 Results

Figure 7.14 compares the frequency–response obtained using the shooting technique for $V_{DC} = 40.1$ V and $V_{AC} = 18.4$ V to that obtained experimentally near primary resonance. In the figure, the stable solution is plotted as a solid line and the unstable solution is plotted as a dashed line. Only small portion of the unstable solution is calculated and shown. It should be remarked that the stable solution of the upper branch of the frequency–response curve loses stability through a period-doubling

Fig. 7.14 A comparison between the simulated frequency–response using the shooting method to that obtained experimentally for $V_{DC} = 40.1$ V and $V_{AC} = 18.4$ V. (Reprinted with permission. Copyright 2009, IOP Publishing Ltd [2])

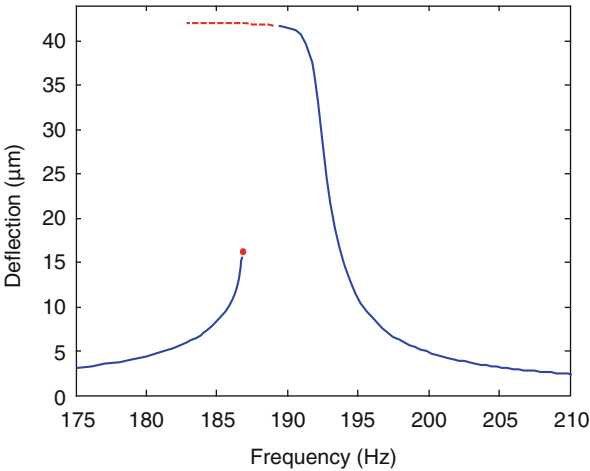


bifurcation, where a Floquet multiplier exits the unit circle through negative one. It is noted from the figure that there is a slight deviation between theory and experiment in the right branch of the frequency–response curve, which might be because of the variation in damping during the experiment. Interestingly, the figure shows that for each excitation frequency there is at least one stable solution exists. This is contrary to what one would expect from the experimental data of Fig. 7.14, which show a pull-in band of frequencies approximately from 180 to 188 Hz. Therefore, the conclusion of this is that dynamic pull-in due to AC + DC excitation (resonant dynamic pull-in) does not occur necessary due to the disappearance of stable solutions. There should be another cause, which is explained in the next section.

Figure 7.15 shows an example of a simulated frequency–response curve with unstable band of frequencies (approximately from 187 to 191 Hz). One can note that the left or lower branch of the frequency–response curve is terminated by a cyclic fold bifurcation with a Floquet multiplier exiting the unit circle through positive one. The right or upper branch on the other hand loses stability through a period-doubling bifurcation with a Floquet multiplier exiting the unit circle through negative one. Either one of these bifurcations leads to pull-in. If a resonator is operated within the band of unstable frequencies then it must exhibit dynamic pull-in since there is no stable state elsewhere that it can settle on. Such a band of frequencies where the resonator must pull-in is called inevitable escape band since an oscillator is forced to escape its potential well [5].

The shooting technique can be used to track the disappearance of the lower (left) branch and the loss of stability of the upper (right) branch of the frequency–response curve for several values of V_{AC} . This yields the band of frequencies where in theory the resonator has zero chance of vibrating in a stable state. Figure 7.16 depicts the results as compared to the experimental measurements of Fig. 7.12 for $V_{DC} = 40.1$ V. As observed from the figure, the theoretical concept of inevitable escape does not help much in predicting the practical pull-in band that is obtained experimentally.

Fig. 7.15 Simulated frequency–response obtained using the shooting method showing inevitable escape band of frequencies for $V_{DC} = 19.4\text{ V}$ and $V_{AC} = 24\text{ V}$ (solid: stable, dashed: unstable). (Reprinted with permission. Copyright 2009, IOP Publishing Ltd [2])



In another word, the correlation between the pull-in band of the experiment and the inevitable escape band from theory is weak. To further understand these results, another simulation tool needs to be utilized, which is explained in the next section.

Next, the shooting method is used to gain deeper understanding of the dynamics and the possible bifurcations for the case of subharmonic resonance. Figure 7.17 depicts an example of a frequency–response curve generated using the shooting method. It turns out for this example that while sweeping the frequency from low to high values, the lower branch of the response loses stability through a subcritical pitchfork or symmetry breaking bifurcation with a Floquet multiplier exiting the unit circle through positive one. This occurs at a frequency near 366 Hz. The new unstable lower branch regains stability again through a supercritical pitchfork bifurcation near a frequency of 381 Hz. At this point, a new upper-branch stable solution is born, which

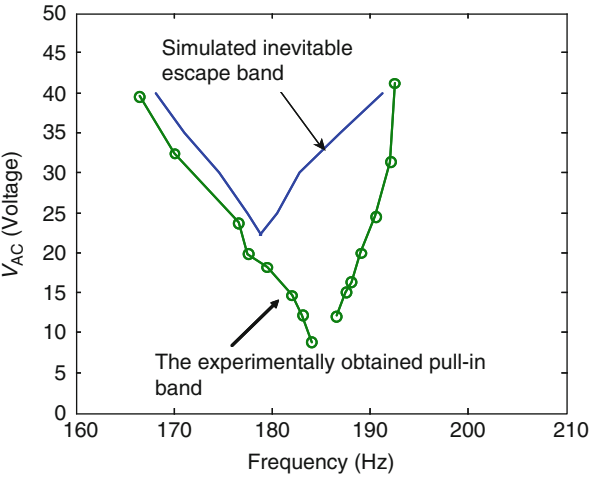
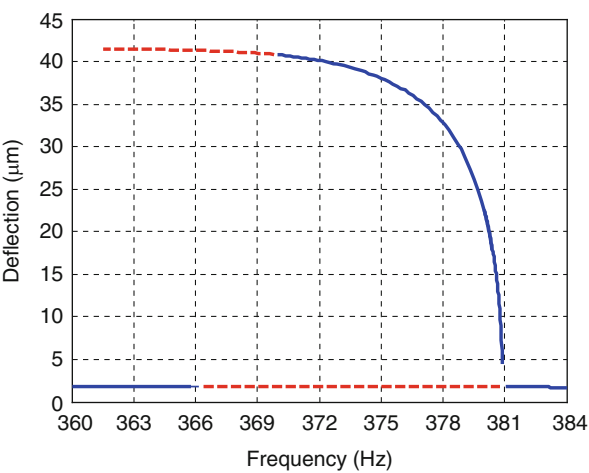


Fig. 7.16 The simulated inevitable escape band versus the experimentally measured pull-in band for the case of primary resonance for $V_{DC} = 40.1\text{ V}$. (Reprinted with permission. Copyright 2010, IEEE [3])

Fig. 7.17 A frequency–response curve obtained using the shooting method near subharmonic resonance for $V_{DC} = 40.1$ V and $V_{AC} = 42.4$ V



is essentially an indication of the activation of the subharmonic resonance. We recall here that that newborn upper solution is of period double that of the lower branch (see Eq. (5.89)). Thus, the period needs to be doubled in the shooting program when tracking the stability of the upper branch. Also, the initial conditions need to be changed to reflect a higher amplitude response. When sweeping backward the values of the frequencies while tracking the upper branch, it turns out that it loses stability through a period-doubling bifurcation with a Floquet multiplier exiting the unit circle through negative one. This occurs near a frequency of 370 Hz. The resonator at this frequency reaches pull-in. Below this frequency and up to 366 Hz, both upper and lower solutions are unstable. This means a must pull-in band, inevitable escape band, since there is no chance for the resonator to have a stable state.

By generating several plots such as Fig. 7.17 for various values of V_{AC} , the inevitable escape band of frequencies are obtained, Fig. 7.18. When comparing

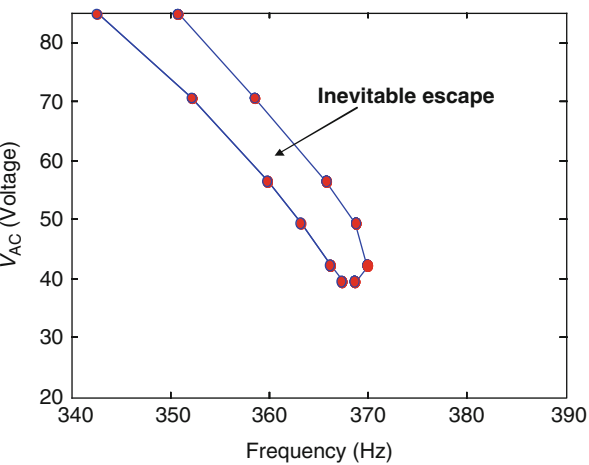


Fig. 7.18 Inevitable escape band using the shooting method near subharmonic resonance for $V_{DC} = 40.1$ V

Fig. 7.18 to the experimental data of Fig. 7.12, one can see that the pull-in band starts at lower values of V_{AC} compared to the inevitable escape band. This indicates again that the shooting method by itself is not sufficient to predict dynamic pull-in.

7.6 Basin of Attraction Analysis

A useful tool to analyze the dynamic response of an oscillator is the basin of attraction analysis. Basin of attraction, also called domain of attraction, is defined as a set of initial conditions in phase space (velocity versus displacement plane), which leads to a long-time motion or an attractor. An attractor is a set of points in phase space toward which a time history approaches after transients die out. Examples of attractors are equilibrium points and periodic motions or limit cycles. For a resonator, the basin of attraction represents the set of initial conditions (velocity, displacement) that leads the resonator to a stable state of oscillation. This is also called “safe” basin since it leads to a stable oscillation as opposed to the “unsafe” zones, which lead to unstable oscillation (escape from the potential well or pull-in in this case study).

The basin of attraction of an oscillator can be calculated by integrating its equation of motion in time for various grid points of initial velocity and displacement. If a point of an initial displacement and velocity leads to a stable solution, it is represented with a specific color in the phase plane. The collection of these points forms an area of the safe basin. If however the point of initial conditions leads to unstable response, it is represented using a different color on the phase space. The collection of these forms the unsafe zone. Therefore, the phase space is divided into safe and unsafe zones.

In order to gain deeper insight into the experimental data of the previous sections and how they are related to the simulation results, we calculate next the basin of attraction of the stable solutions obtained by the shooting method near the pull-in band of frequencies. Here, we adopt 500×500 grid points for each case of an excitation frequency. At each point (x_0, \dot{x}_0) , the equation of motion, Eq. (7.1), is integrated numerically over a sufficiently long period of time. The points leading to stable state are represented as white points in the phase plane; otherwise, they are represented as black points. The collection of white points composes the safe zone/basin of attraction and the black points compose the unsafe zone.

Figures 7.19 and 7.20 show pictures of various basins of attraction for excitation frequencies before, near, and after primary resonance for the loading case of Fig. 7.14. Away from primary resonance, we can observe a relatively large safe basin. As the excitation frequency is increased toward primary resonance, one can observe the erosion of the basin of attractions with the white region shrinking due to the appearance of black instability fingers. Near primary resonance, the basins of attraction become too small with more instability fingers penetrating making the boundaries between the safe and unsafe zone unclear or unsmooth; the so-called fractal boundaries. The fractal behavior causes unpredictability of the response and results in the loss of the

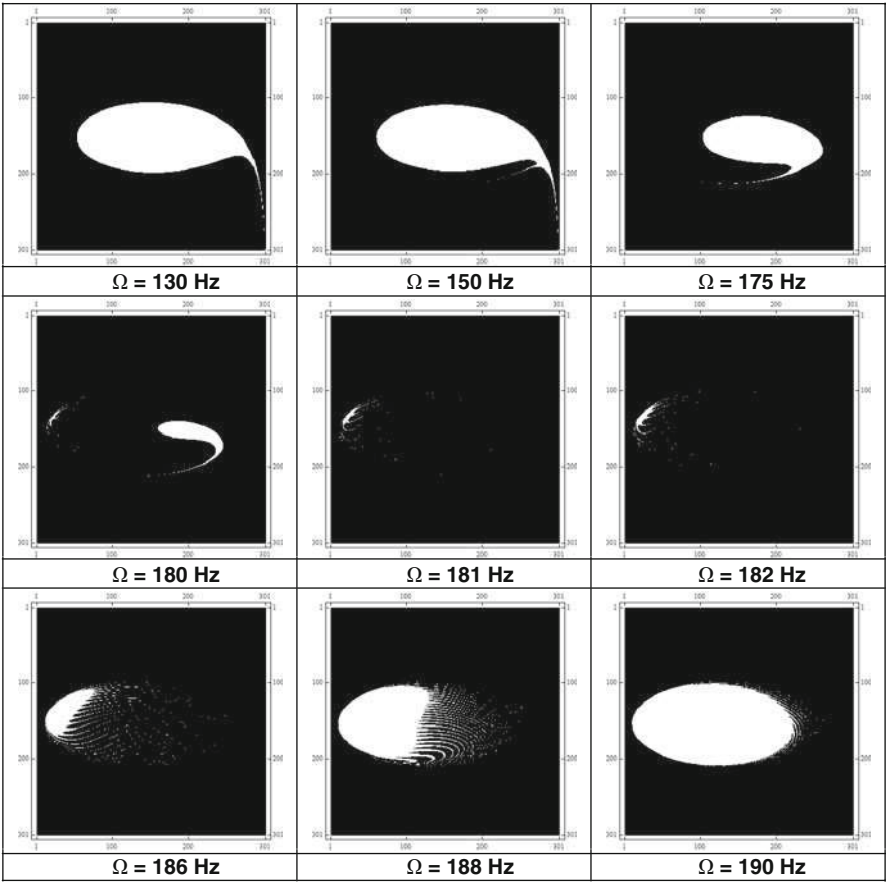


Fig. 7.19 The calculated basin of attractions of the resonator for various excitation frequencies for $V_{DC} = 40.1 \text{ V}$ and $V_{AC} = 18.4 \text{ V}$

engineering integrity of the system from stability point of view. Practically, in the fractal regime, it is very hard for the system to reach a steady-state stable oscillation. This explains the experimental data of Fig. 7.14. Hence, the conclusion here that there is a band of frequency, pull-in band, where the basin of attraction is severely weak and wherein the system is most likely to experience dynamic pull-in. Theoretically speaking, the pull-in band is not necessary the same as the inevitable escape band, since there is still a slight possibility for the system to oscillate in a stable state under some initial conditions. Practically speaking however, the resonator is most likely to experience pull-in if operated in this regime.

To quantify the erosion of the basin of attraction and relate it to the safety and integrity of the system, the variation in the safe area is tracked while sweeping the frequency of excitation near primary resonance. This is similar to the so-called

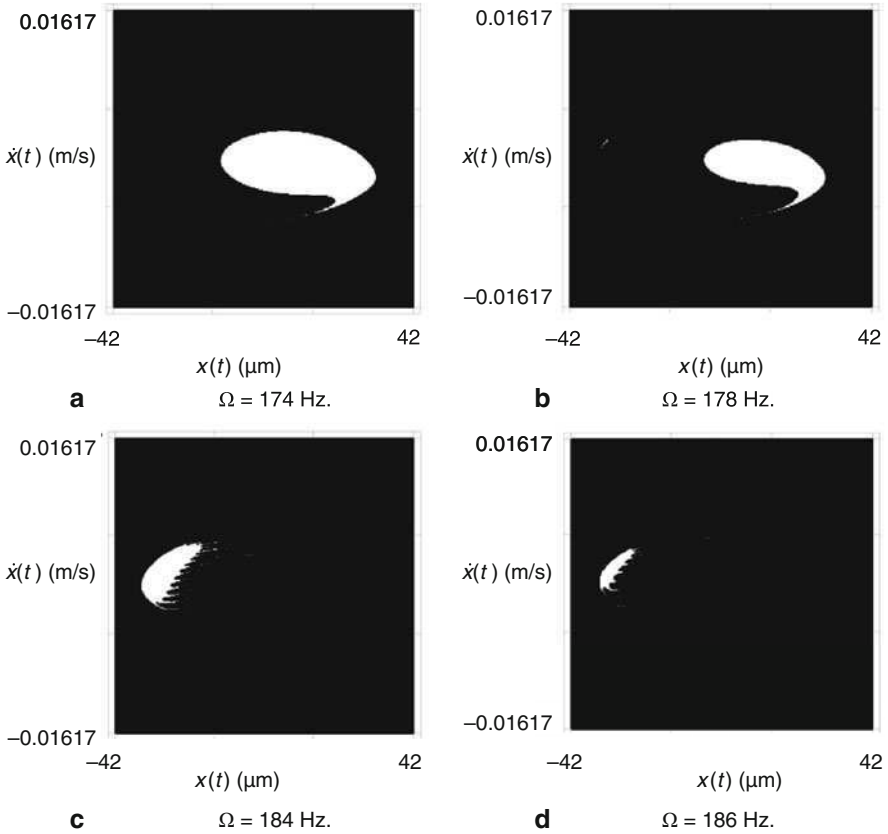
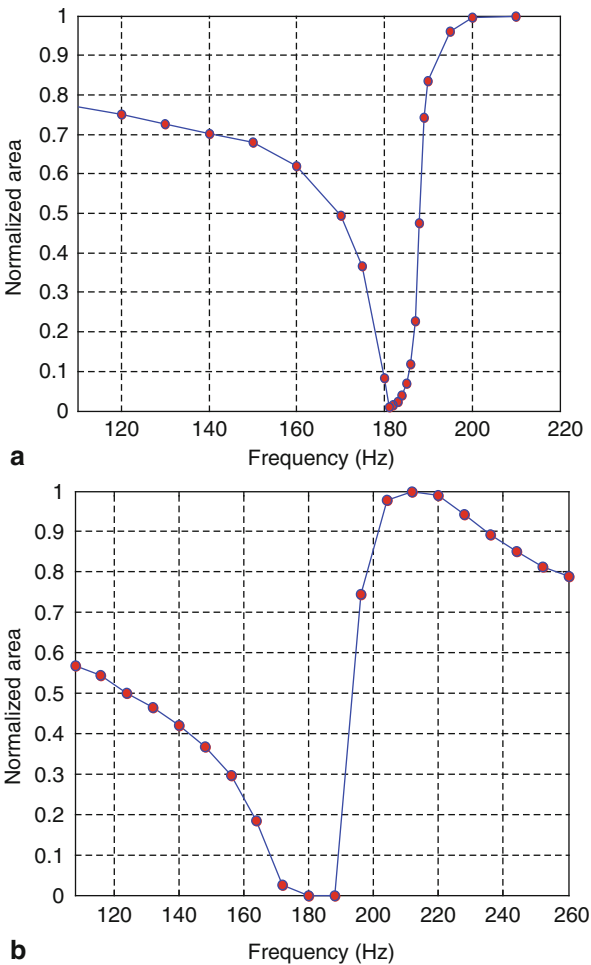


Fig. 7.20 Enlarged view of the basin of attraction for selected excitation frequencies for $V_{DC} = 40.1$ V and $V_{AC} = 18.4$ V. (Reprinted with permission. Copyright 2009, IOP Publishing Ltd [2])

Dover-Cliff integrity curves [4, 5], except that here the excitation frequency is varied while keeping the forcing level constant. The area can be calculated by counting the stable points. It can be normalized, for instance, with respect to an area that is away from primary resonance. Figure 7.21a shows the variation of the safe basin area while varying the excitation frequency passing primary resonance for the loading case of Fig. 7.14. One can see the dramatic drop in the safe area near 180 Hz. Also shown in Fig. 7.21b another simulation example for a higher value of V_{AC} . Based on these figures, it is possible to draw conclusions about the safety of the system and the range of frequencies it becomes dangerous and unreliable. One can note for example in Fig. 7.21a that the most dangerous band of frequencies is between 170 and 190 Hz where the safe area drops below 50%. Due to noise and uncertainty of the system parameters, there is a good chance for the resonator to experience dynamic pull-in near this regime. One can note that at $V_{AC} = 35$ V (Fig. 7.21b) the safe area reaches zero for some frequency band and the 50%-below band gets much wider.

Fig. 7.21 The simulated integrity curves showing the variation of the area of the safe basin versus the excitation frequencies for $V_{DC}=40.1$ V and **a** $V_{AC}=18.4$ V and **b** $V_{AC}=35$ V. (Reprinted with permission. Copyright 2009, IOP Publishing Ltd [2])



Operating the resonator outside these bands can be considered relatively safe since it will require a big jump in velocity, due to shock or dynamic disturbances, before the system gets to the dark unstable area.

Figure 7.22 demonstrates a basin-of-attraction analysis for the case of subharmonic resonance of the loading case of Fig. 7.17. As expected, the area of the basin reaches zero for some frequency range indicating an inevitable escape band.

7.7 Attractors Tracking and the Integrity Factor

A more insightful analysis of the basin of attraction considers the erosion of each individual branch of the frequency–response curve, which represents a steady-state solution or an attractor. This is opposed to analyzing the whole phase space without

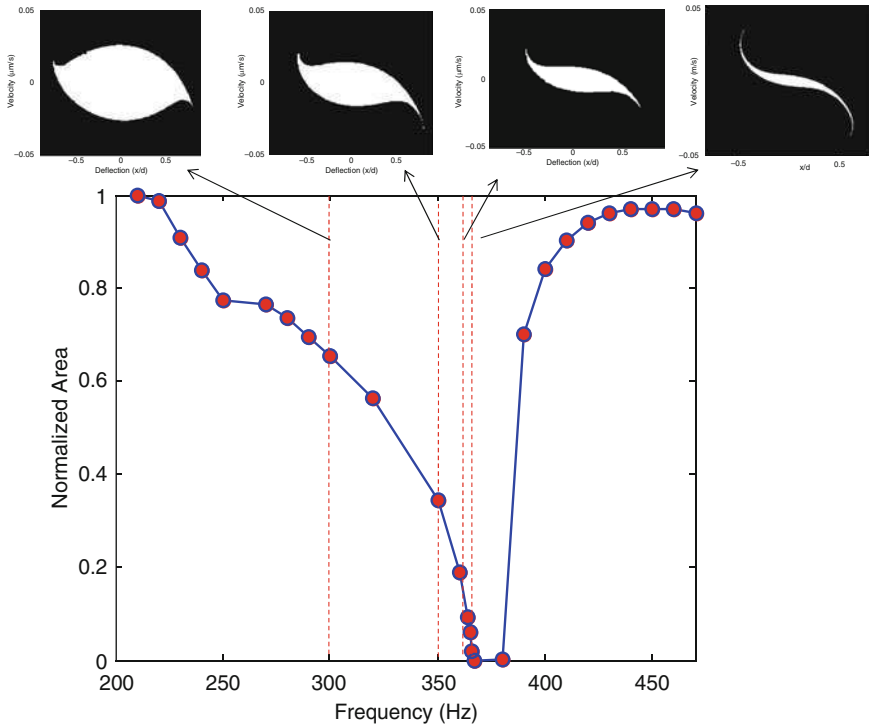


Fig. 7.22 The simulated integrity curve along with samples of the basin of attraction near subharmonic resonance for $V_{DC} = 40.1$ V and $V_{AC} = 42.4$ V

consideration of the integrity and stability of each attractor being captured, as in the previous section. To explain the motivation of this approach, consider the basin of attractions for two excitation frequencies and a constant V_{AC} , Fig. 7.23. The colored points in the figure indicate stable zones and the white regions indicate unstable zones. Figure 7.23a indicates a small safe basin of the lower solution (attractor) and an extremely weak and fractal basin of the upper attractor (shown on the top corner to the left of the figure). The phase space of Fig. 7.23b is generated at another excitation frequency indicating the presence of the basin of attraction of the upper attractor only. It is concluded from these figures that in the phase space, either the two attractors do not coexist (Fig. 7.23b) or they coexist, but with the upper one has very weak basin (Fig. 7.23a). As a consequence, it is more meaningful to study the erosion of the basin of attraction of each attractor separately as the frequency of excitation is changed rather than studying the erosion of the basin of attractions of the whole system, which may contain more than one attractor.

An efficient tool to study and track the erosion of the basin of attraction of each individual attractor in the phase space is the so-called integrity factor (IF), which was pioneered by Rega and Lenci in a series of papers (see for example [6–8]). It is

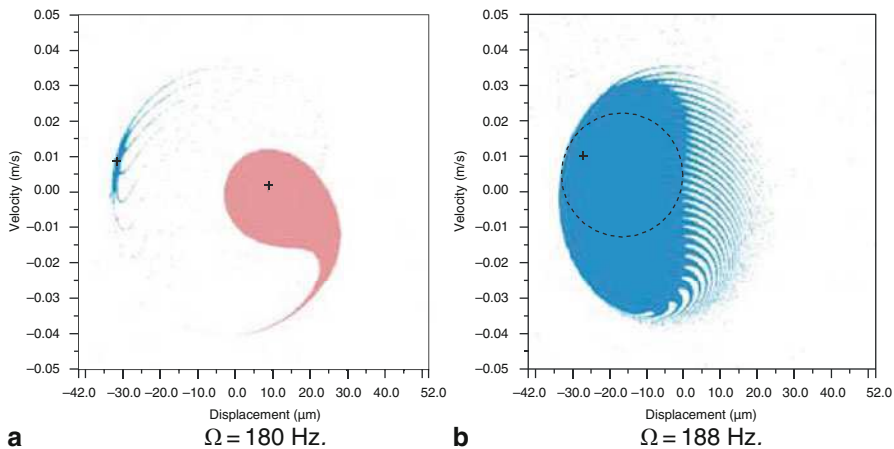


Fig. 7.23 Basin of attractions of the resonator for $V_{DC} = 40.1$ V and $V_{AC} = 15$ V. The colored points in the figure indicate stable zones and the white regions indicate unstable zones. (Reprinted with permission. Copyright 2010, IEEE [3])

defined as the normalized radius of the largest circle contained in the safe basin. An example of such is shown as the dashed line circle drawn in Fig. 7.23b. The radius of this circle is normalized to that of another circle that is chosen way from resonance with no erosion or contractions in the nearby range of frequencies.

Based on the IF, the erosion profile of the basin with the frequency of excitation can be constructed. Examples of these are depicted in Fig. 7.24 along with the frequency–response curves. In the figure, the dotted lines represent the IF and the solid lines represent the simulated stable frequency–response curves using the shooting method. The radius of the circles used to normalize IF are evaluated at $\Omega = 215$ Hz and $\Omega = 80$ Hz for the upper and lower branches, respectively. Figure 7.24b shows an example of a frequency–response curve with an inevitable escape band. Hence, the IF values drop to zero for some band of Ω , meaning the basin of attraction vanishes for this range. Figure 7.24a on the other hand shows an example of a frequency–response curve where for each Ω there is a stable state/solution of the system. However, by noting the IF curve, one can see that the basins of attraction of both upper and lower attractors drop sharply and suddenly as it approaches the range of $180 \text{ Hz} < \Omega < 187 \text{ Hz}$ and become too small. As concluded previously, the existence of an attractor does not mean the system is “safe” from pull-in, because the attractor may not be robust enough to tolerate the perturbations encountered in practice. Hence, pull-in may be anticipated in such conditions. It is more meaningful to relate these observations to the values of IF rather than Ω to make the results generic. For this frequency–response curve, it seems that below $IF = 0.5$ the curve starts to erode fast. It would be beneficial also to establish such rules for a range of V_{AC} and not only for one single case. This is discussed next.

Based on curves, such as in Fig. 7.24, a bifurcation diagram of V_{AC} – Ω is established, which is shown in Fig. 7.25 for the same loading cases of Fig. 7.7. The

Fig. 7.24 Frequency–response curves (*solid lines*) and erosion profiles (*dotted lines*) in the case of primary resonance for $V_{DC} = 40.1$ V and **a** $V_{AC} = 15$ V and **b** $V_{AC} = 30$ V. (Reprinted with permission. Copyright 2010, IEEE [3])

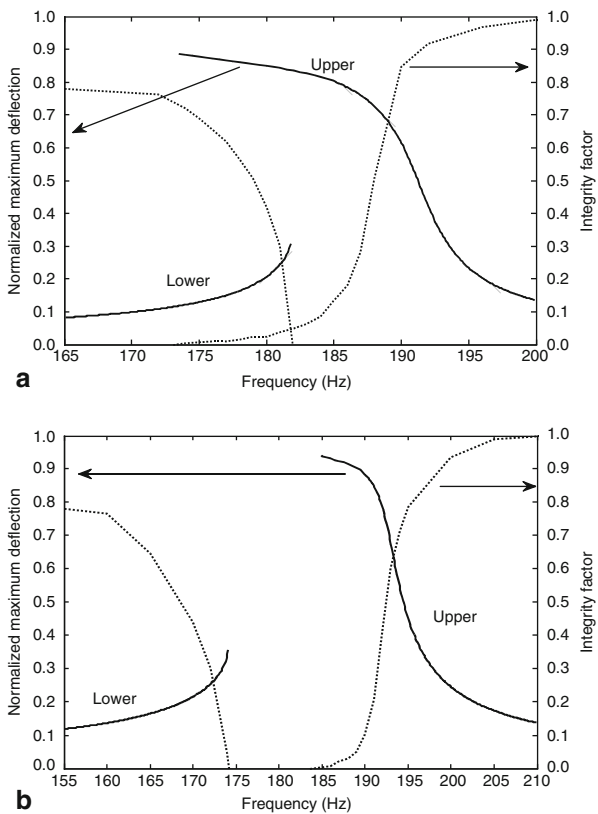
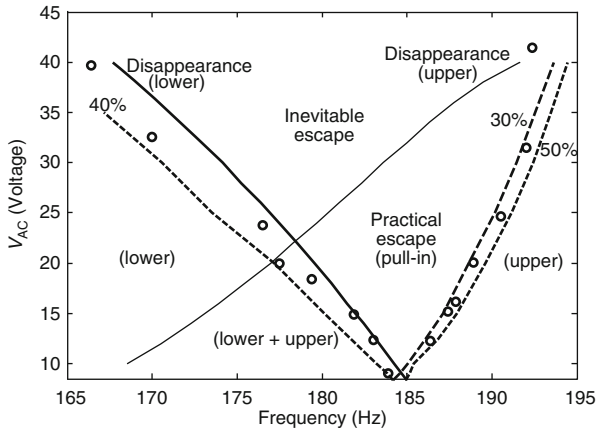


Fig. 7.25 A bifurcation diagram of the resonator near primary resonance for the loading cases of Fig. 7.7 ($V_{DC} = 40.1$ V). The *solid lines* indicate the disappearance of the *lower* and *upper* branches of the frequency–response curves (attractors). The *dashed lines* show the percentage of the remaining fraction of the safe basin of the nearby attractor. The *discrete points* are experimental data. (Reprinted with permission. Copyright 2010, IEEE [3])



solid lines in the figure represent points where the upper and lower stable solutions disappear. Above the thick solid line to the left, the lower solution disappears in a cyclic-fold bifurcation and above the thin solid line to the right the upper solution disappears due to a period-doubling bifurcation. Note that the upper “V” shape that these lines form is the inevitable escape band, where both solutions disappear. The below “ Δ ” shape formed by the two solid lines, referred in the figure as (lower + upper), is the regime where both the lower and upper solution coexist. Also written in brackets are the solutions that exist below the solid lines. In addition, shown on the figure are dashed lines for constant values of IF. These represent percentages of the remaining part of the eroded safe basin of the lower (left) and upper (right) solutions. They have been obtained by generating several figures, such as Fig. 7.24, for various values of V_{AC} . Also shown in the figure as discrete data points are the experimentally measured pull-in band of Fig. 7.7. By comparing the experimental data to the simulation results, rules for predicting pull-in bands become clear. Essentially, the fractal pull-in occurs when IF drops below 30–40%. Hence, this regime in the bifurcation diagram is called “practical escape or practical pull-in” since practically, pull-in occurs definitely in this regime. It is concluded that to ensure stable operation of electrostatic MEMS resonators against disturbances and noises, IF must be at least above 50%. Below this, the resonator becomes vulnerable to pull-in.

A similar analysis is made to understand the resonant pull-in for the case of subharmonic resonance. Figure 7.26 shows two examples of the basin of attractions of the solutions of this case. Figure 7.26a shows the coexistence of the upper and lower attractors with a very weak basin of the upper one. Figure 7.26b indicates the presence of the safe basin of the upper attractor only. Figure 7.27 shows examples of the erosion profiles for the case of a weak basin of attraction for some range of Ω , Fig. 7.27a, and for the case of an inevitable escape band, Fig. 7.27b. The normalizing radii are taken at $\Omega = 300$ Hz for the lower solution and $\Omega = 420$ Hz for the upper solution. It is worth to note from Fig. 7.27 that the IF curve of the upper

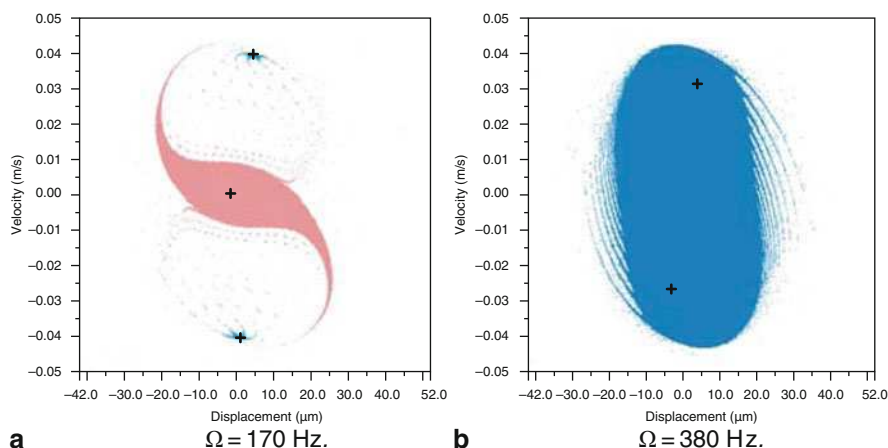
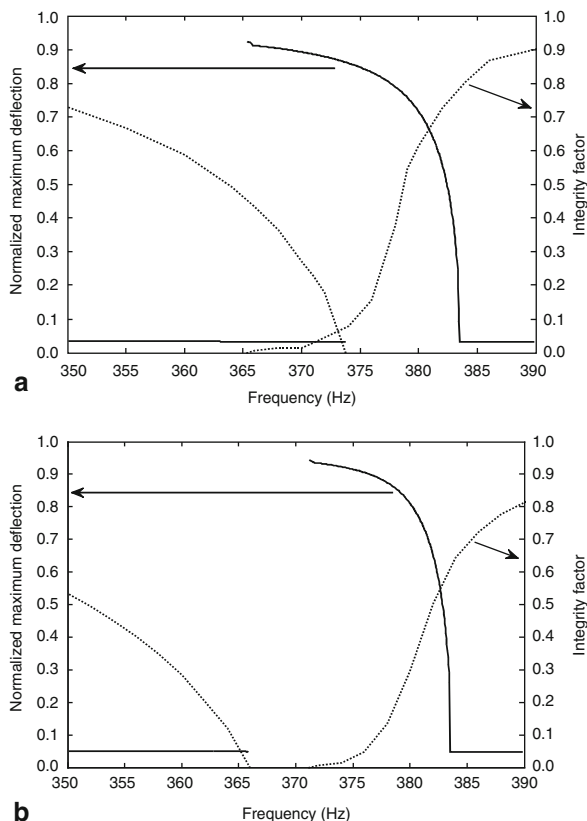


Fig. 7.26 Basin of attractions of the resonator at subharmonic resonance for $V_{DC} = 40.1$ V and $V_{AC} = 30$ V. (Reprinted with permission. Copyright 2010, IEEE [3])

Fig. 7.27 Frequency–response curves (*solid lines*) and erosion profiles (*dashed lines*) in the case of subharmonic resonance for $V_{DC} = 40.1$ V and **a** $V_{AC} = 30$ V and **b** $V_{AC} = 50$ V. (Reprinted with permission. Copyright 2010, IEEE [3])



branch drops sharply to a significantly low value, after which it declines very slowly over some range of Ω . Practically however, the system is anticipated to pull-in within this range of weak basin of attraction.

Using such curves, a bifurcation diagram of $V_{AC}-\Omega$ is established for the subharmonic resonance case, Fig. 7.28. Curves are generated to show the disappearance of the upper and lower branches and also showing lines of constant values of IF. It is concluded from the figure that, for subharmonic excitation, the practical pull-in band, where experimentally pull-in is most likely to occur, is located between the 5–15% IF curves. It is noticeable that the 15% IF curve of the upper branch is located a considerable distance away from the curve where the upper branch disappears.

7.8 Remarks on Resonant Dynamic Pull-in

It is concluded from the previous sections that there are several mechanisms through which an electrostatic resonator can undergo dynamic pull-in. These include cyclic fold bifurcation, period-doubling bifurcation, pitchfork bifurcation in the case of subharmonic resonance, and the fractal behavior.

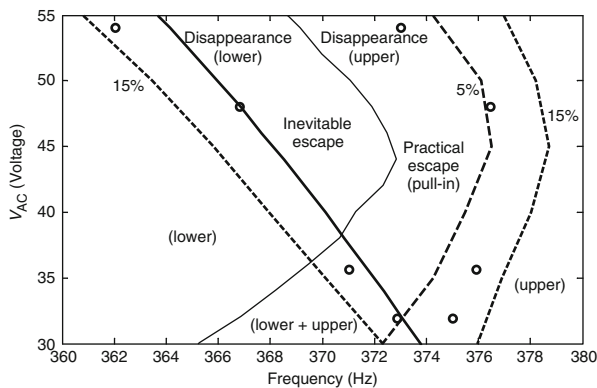


Fig. 7.28 A bifurcation diagram of the resonator near subharmonic resonance for $V_{DC} = 40.1$ V. The *solid lines* show the disappearance of the *lower* and *upper* branches of the frequency–response curves (attractors). The *dashed lines* show the percentage of the remaining fraction of the safe basin of the nearby attractor. The *discrete points* are experimental data of Fig. 7.12. (Reprinted with permission. Copyright 2010, IEEE [3])

All these mechanisms lead to the escape of the resonator from its local vibration within its potential well to pull-in. Below we make some remarks based on the results of the previous sections:

- Figure 7.14 demonstrates an example of a frequency–response curve with possibilities of dynamic pull-in through either a cyclic fold on the lower branch or a period-doubling bifurcation on the upper branch. It is not certain possibility because of the presence or the coexistence of more than one solution. Hence, there is a possibility that a jump from one solution leads the oscillator to land on the other solution. Whether this occurs or not depends on the initial conditions, level of fractality, and size of the basin of attraction of each attractor.
- Figure 7.15, also Fig. 7.17 in the case of subharmonic, represents an example of must pull-in scenarios upon reaching the bifurcation points (either the cyclic fold in the case of the lower branch solution or the period doubling in the case of the upper branch solution for the case of primary resonance). The thresholds of instability obtained based on catching these bifurcations, which is essentially the V-shape inevitable escape band, do not take into account the fractal behavior. They can be taken to indicate must pull-in scenarios only. Pull-in still can occur outside these bands as was demonstrated previously due to noise and disturbances.
- The initiation of the fractal behavior of the basin of attraction of the attractors is due to a global bifurcation called homoclinic tangling. To explain this, we refer to Fig. 5.26 of Chap. 5. One can see from the figure that the saddle is composed of two manifolds, one is stable (the separatrix) and the other is unstable. Both normally do not intersect outside the saddle. Exciting the system with a small V_{AC} leads to a stable periodic motion in the stable regime of the basin near the stable focus. As V_{AC} and thus the amplitude of the motion increases, the stable

manifold approaches the unstable manifold. Eventually, both manifolds intersect transversally (if they do it once they do it infinitely many times) resulting in the so-called homoclinic tangling bifurcation [4, 5]. This marks the beginning of the erosion of the basin of attraction. This event can be predicted analytically using the so-called Melnikov method [4, 5]. Discussing this method is beyond the scope of this book. However, the results of previous studies on electrostatic resonators have revealed that the threshold of tangling occurs at very low values of AC voltages [7, 9, 10]. Hence, it is impractical to limit the excitation force of resonators to this limit (it is too conservative). Increasing V_{AC} further leads to further erosion of the basin of attraction leading eventually to the fractal behavior and sensitivity of initial conditions demonstrated in Figs. 7.25 and 7.28.

Before closing, we should mention that the mechanisms of resonant dynamic pull-in in the case of systems with locally hardening behavior, such as clamped–clamped beams with mid-plane stretching, share many similarities with those of locally softening behavior, such as this case study. However, there are slight differences. For example, the upper branch solution in the hardening case reaches pull-in through a cyclic fold bifurcation instead of period-doubling bifurcation. The reader is referred to [11] and [12] for more information about this case.

7.9 Mass Detection Application

The theoretical and experimental results of the previous sections have revealed the creation of a pull-in band when operating a resonator above certain levels of V_{AC} and V_{DC} in low damping. One potential use of this phenomenon can be to realize resonant sensors that can act as switches when they detect significant change in the physical quantity they measure. The basic idea is to build a resonator operating at a constant frequency outside the pull-in band. Then upon the change of the natural frequency of the resonator, due to change in its mass or stiffness (for example due to temperature change), the pull-in band shifts toward the operating frequency of the resonator. Hence, the operating frequency of the resonator becomes inside the new pull-in band. This causes the resonator to dynamically pull-in. With a proper circuitry design, the pulled-in resonator can be made to close an electric circuit to pass a current as a switch.

As an example of an application that can make use of such an action is to design a switch that is triggered by the detection of a specific mass threshold (STMT) [13]. To illustrate the concept, consider a parallel plate capacitor employing a cantilever beam as its upper electrode of length $l = 100\ \mu\text{m}$, width $b = 10\ \mu\text{m}$, thickness $h = 0.1\ \mu\text{m}$, and a capacitor gap width $d = 2\ \mu\text{m}$. The microbeam is assumed actuated with $V_{DC} = 0.4\ \text{V}$ and $V_{AC} = 0.1\ \text{V}$ at a quality factor $Q = 100$. Using a reduced-order model with three-mode approximation and long-time integration, the frequency–response curve for the tip deflection of the beam W_{Max} is obtained, as shown in solid line in Fig. 7.29

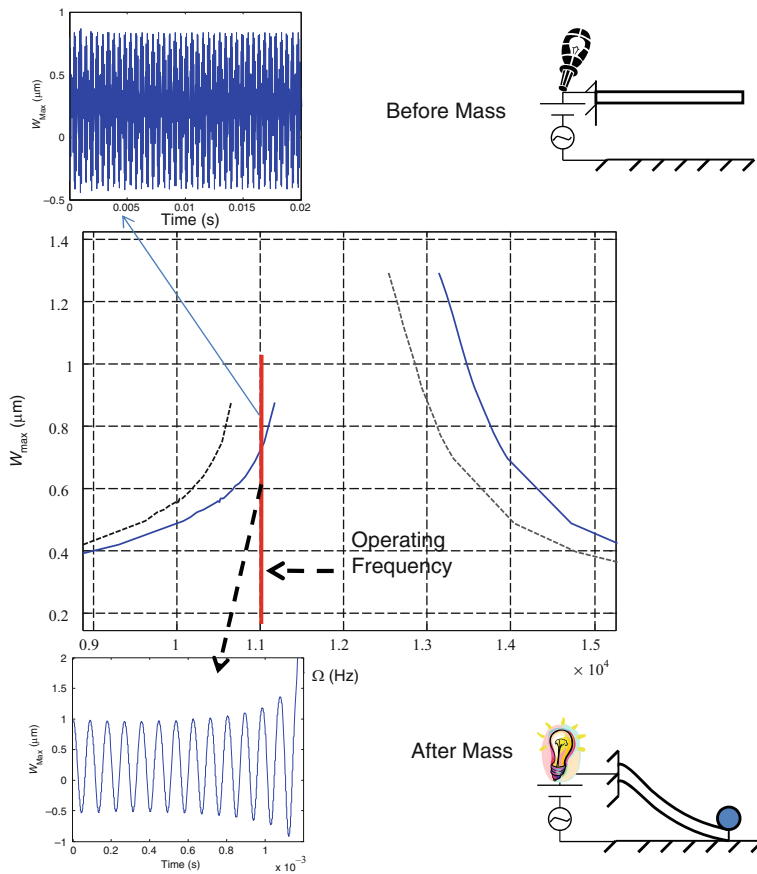


Fig. 7.29 A frequency–response curve of a cantilever microbeam excited near primary resonance before (solid) and after (dashed) mass detection. Shown in the figure also time histories for the response of the microbeam before (up) and after (down) mass detection illustrating the idea of a switch triggered by mass detection STMT operating at a fixed excitation frequency

[13]. It is clear that there is a pull-in band in the frequency–response curve. This band can be generally fractal or inevitable. From a practical point of view, and as was demonstrated in Fig. 7.25, this pull-in band is close to what is expected experimentally.

According to Fig. 7.29, if the microbeam is operated at a fixed excitation frequency to the left of the pull-in band, with a sufficiently safe basin, it will oscillate in a stable state. An example of the steady-state time response is shown on the upper left corner of the figure for an operating frequency of 11 kHz. Assuming the beam is coated uniformly with a material that can capture or absorb a chemical or biological substance (analyte), such some kinds of polymers [14], then upon the capturing of this substance in a sufficient quantity or concentration, the resonance frequency of

the beam will decrease. This means that the whole pull-in band will shift to the left leaving the microbeam that operates at the fixed frequency of oscillation, the 11 kHz in this example, to be located within the pull-in band. The new frequency–response curve is plotted in Fig. 7.29 as dashed lines. This means that the resonator will pull in to close or break an electric circuit as a sign for mass detection (a switch). The lower left corner of Fig. 7.29 shows the dynamic pull-in action due to the mass addition obtained using time integration.

The idea of a switch triggered by mass threshold STMT can offer many attractive features. The switch can serve as a regular resonant sensor if the detected mass is below the desired threshold. However, the idea can be especially attractive in applications where measuring the quantity of mass is not as important as doing an action upon detection, such as detecting explosives, hazardous and poisonous gases, and dangerous viruses and Bacteria. Such a switch can provide an electrical signal that can be functionalized directly to a useful action without the need to complicated circuitry, controllers, and decision units. The reliability of this device, its performance under thermal variations and other disturbances, and its reusability after switching (post-switching scenarios including stiction problems) are all issues that need further investigations.

Subharmonic excitation can also be utilized for the same purpose. Toward this, the AC load of this example is increased to $V_{AC} = 0.2$ V while keeping the DC bias fixed at $V_{DC} = 0.4$ V. Figure 7.30 shows the simulation result near subharmonic resonance of this loading case. The figure shows the response before and after adding a uniformly distributed mass, which is assumed to be 1% of the original beam mass. Also shown are the time histories of the response before and after the addition of mass. As noted, the microbeam experiences a dynamic pull-in after the mass is added, which can serve as a switch. One can see in this case the sharp transition for the beam response from a relatively small deflection to pull-in.

To verify the shift in the pull-in band experimentally, we refer back to the capacitive sensor of Sect. 7.1. To simulate the process of detecting an external mass, a small amount of epoxy has been applied to the proof mass of the sensor using a pipette as shown in Fig. 7.31. Initially, the sensor was excited near primary resonance using low values of AC and DC voltages ($V_{DC} = 8.0$ V and $V_{AC} = 9.76$ V) to guarantee linear response at a pressure value near 148 mtorr. The resonance frequency of the system was measured before and after the application of the added mass, Fig. 7.32a. The added mass causes a 0.7 Hz frequency shift in the fundamental natural frequency of the device corresponding to an added mass of 1.07 μ g compared to the original mass of 147 μ g. Next, the sensor was driven by large values of AC and DC voltages ($V_{DC} = 40.1$ V and $V_{AC} = 18.4$ V) to reach dynamic pull-in. Figure 7.32b shows the obtained pull-in band of frequencies. One can note a slight shift in this pull-in band due to the addition of mass.

Next, the system was excited near subharmonic resonance by applying a voltage load of $V_{DC} = 40.1$ V and $V_{AC} = 18.4$ V. These voltage values do not cause escape or dynamic pull-in near subharmonic resonance. Figure 7.33a demonstrates how subharmonic excitation can be utilized for detecting mass change. If we consider, for example, the excitation frequency of 374 Hz in the case of the no added mass

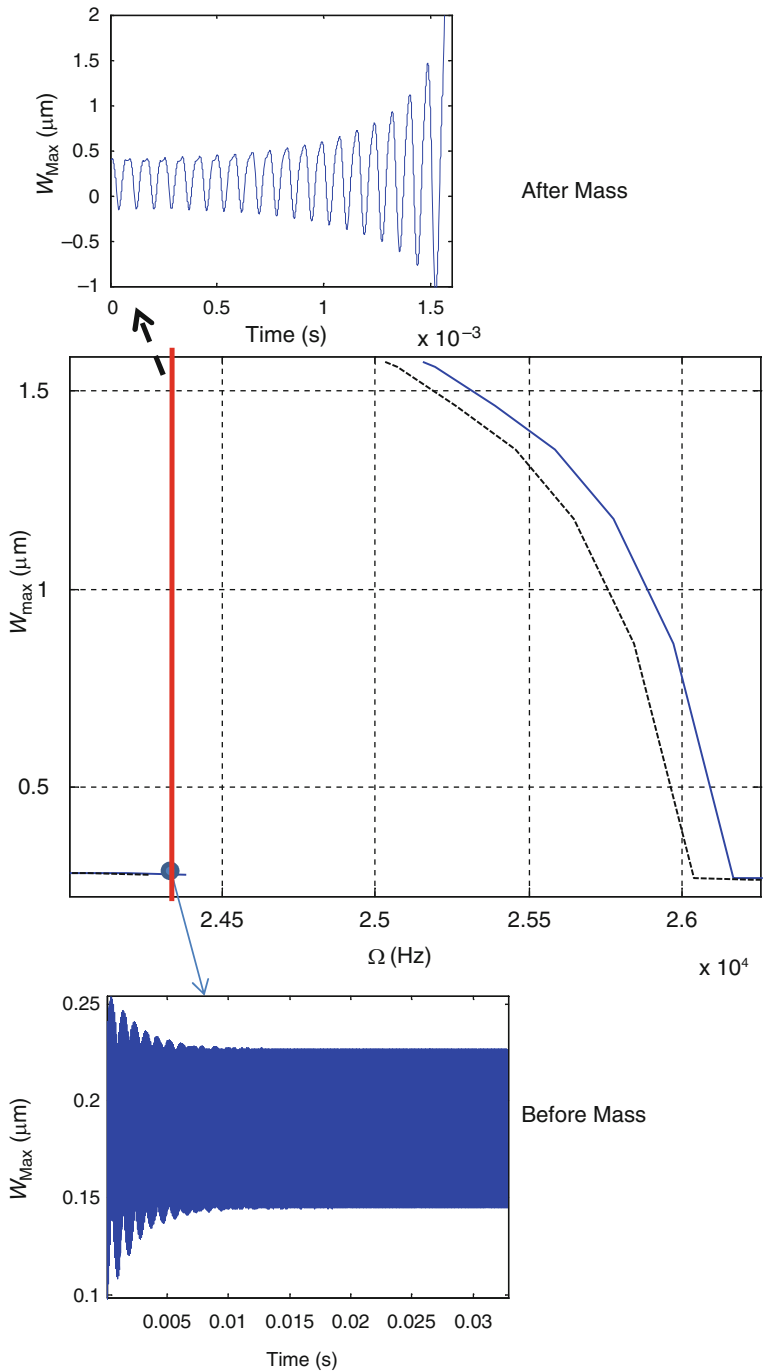


Fig. 7.30 A frequency–response curve of a cantilever microbeam excited near subharmonic resonance before (*solid*) and after (*dashed*) mass detection. Shown in the figure also time histories for the response of the microbeam before (*down*) and after (*up*) mass detection illustrating the idea of a STMT operating at a fixed excitation frequency

Fig. 7.31 A picture showing the capacitive sensor with the added mass on top of the proof mass of the device. (Reprinted with permission. Copyright 2009, ASME [13])

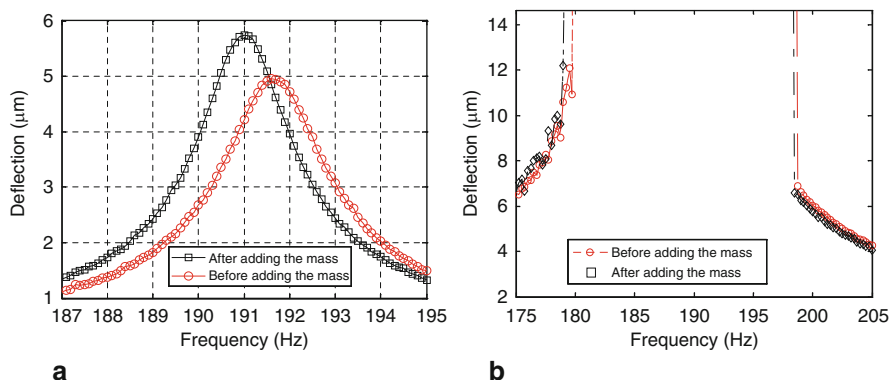


Fig. 7.32 Frequency–response of the capacitive sensor when excited near primary resonance before and after adding the mass for the case of **a** small linear response, **b** large nonlinear response with a pull-in band. (Reprinted with permission. Copyright 2009, ASME [13])

we notice that the sensor response is very small (near $0.6\ \mu\text{m}$). On the other hand, at the same excitation frequency the sensor response is very high (around $23.6\ \mu\text{m}$) after adding mass. Now, with a previous calibration, this drastic change of the sensor amplitude for the same excitation frequency can be used to determine the amount of the added mass.

Increasing the AC voltage further to $V_{AC} = 21.1\ \text{V}$ leads to dynamic pull-in, Fig. 7.33b. The figure demonstrates how subharmonic resonance can be utilized to design a switch that is activated by mass detection. If we consider, for example, the excitation frequency of $373\ \text{Hz}$ for the no added mass case we notice that the sensor response is very small (near $0.5\ \mu\text{m}$). On the other hand, at the same excitation frequency the sensor response becomes unstable and goes to pull-in when the mass is added.

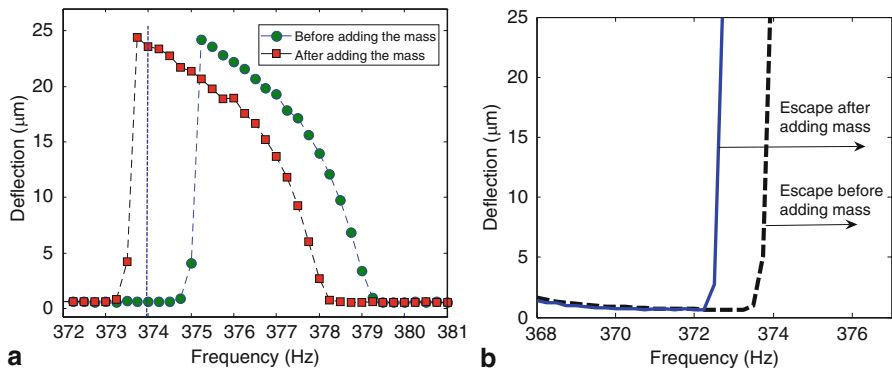


Fig. 7.33 Frequency–response of the capacitive sensor when excited near subharmonic resonance (twice the natural frequency) before and after adding the mass for the case of **a** small linear response, **b** large nonlinear response with pull-in. (Reprinted with permission. Copyright 2009, ASME [13])

7.10 Controlling Resonant Dynamic Pull-in

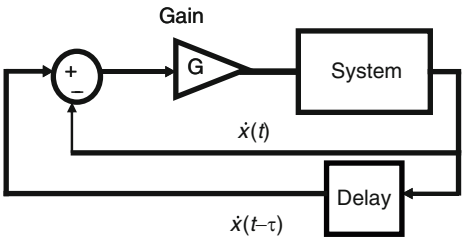
7.10.1 Introduction

With the increasing demand to push the limits of sensitivity of electrically actuated resonators, there is an obvious need to improve their stability to enable operating them at the highest possible amplitude without risking their integrity with the possibility of dynamic pull-in. In addition, the concept of a switch triggered by mass detection of the previous section relies on the ability to ensure a stable operation of the resonator just below the pull-in band without the danger of pulling-in accidentally due to noise or disturbances. This is particularly important since, as explained previously, the behavior close to the pull-in band is highly fractal. Hence, to lower the threshold of detectable mass that can trigger the switch, it needs to be operated as close as possible to the pull-in band without the danger of accidental pull-in.

Thus, there is a need of an active control technique that can improve the stability of resonators in such conditions and help them reject external disturbances. This section discusses a promising feedback control technique to achieve this goal. We will also demonstrate how this control scheme can help stabilize a resonator even if it is operated in the inevitable escape band.

The control scheme under focus is a delayed-feedback controller introduced by Pyragas [15]. This controller has been originally proposed to stabilize the unstable periodic orbits of a chaotic system. The output signal of this controller is a delayed value of the system output subtracted from it the current output of the system. The delayed value is suggested to be equal to either the same [15] or half of the period [16] of the unstable periodic orbit. The control output vanishes to zero as the system reaches its stable solution in the case of full period delay. Hence, the controller does not change the dynamics of the system in the steady-state operation. The system

Fig. 7.34 A schematic illustrating the principle of the delayed-feedback controller of Pyragas [15]



output can be either the system deflection or velocity [17]. Such a controller has been proven experimentally and theoretically to stabilize various systems including AFM resonators [18]. Figure 7.34 shows a schematic illustrating the principle of a velocity-based delayed controller.

7.10.2 Simulation and Experimental Results

Next, the control technique is demonstrated on the capacitive sensor of Fig. 7.1. First, the uncontrolled response is simulated for $V_{AC} = 20.1$ V and $V_{DC} = 40.2$ V assuming a damping ratio of 0.0026, Fig. 7.35. Three curves are shown in the figure. Two of them are obtained by numerically integrating the equation of motion, Eq. (7.1), using Runge–Kutta technique. Of the two, one curve is obtained assuming trivial initial conditions to simulate sudden application of the excitation force. The other one is generated to simulate a frequency-sweep test by using the response at a certain excitation frequency as an initial condition for the response of the system to

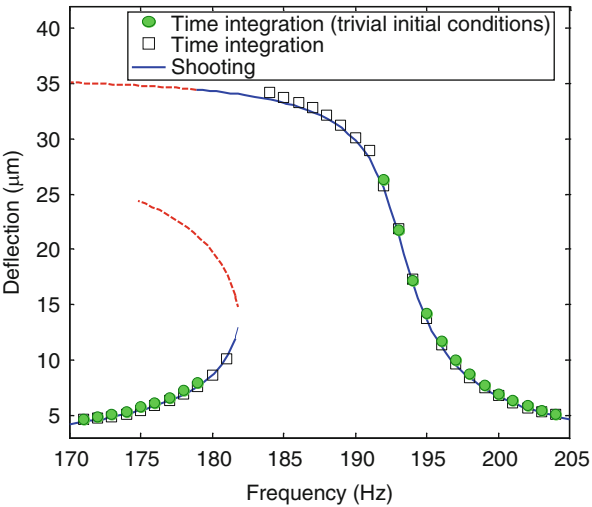


Fig. 7.35 Simulation results for the frequency–response of the capacitive sensor for $V_{AC} = 20.1$ V and $V_{DC} = 40.2$ V. (Reprinted with permission. Copyright 2010, IOP Publishing Ltd [19])

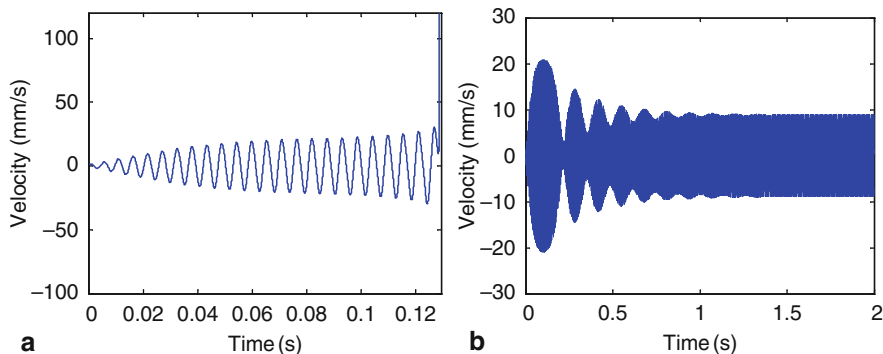


Fig. 7.36 Simulated time history responses of the capacitive sensor when actuated suddenly with $V_{DC} = 40.2$ V and $V_{AC} = 20.1$ V at $\Omega = 180$ Hz **a** without the delayed-feedback controller, **b** with the delayed-feedback controller of $G = 8$ Vs/m. (Reprinted with permission. Copyright 2010, IOP Publishing Ltd [19])

the next excitation frequency in the sweep (continuation approach). The third curve is obtained using the shooting technique.

Next, the delayed-feedback controller is applied on this system. As an example, consider exciting the system at a frequency of 180 Hz assuming a sudden application of the AC voltage. According to Fig. 7.35, and as also confirmed by the time history response of Fig. 7.36a, at this excitation frequency the device experiences dynamic pull-in. Next, the delayed-feedback controller is introduced to the system by modifying the voltage signal. A velocity feedback is used with the delayed time value τ equal to half the period of oscillation. Hence, the equation of motion becomes

$$m\ddot{x} + c\dot{x} + kx = \frac{\varepsilon A [V_{DC} + V_{AC} \cos(\Omega t) + G (\dot{x}(t - \tau) - \dot{x}(t))]^2}{2(d - x)^2} \quad (7.20)$$

where G is the controller gain. Applying this controller on the system with $G = 8$ Vs/m, the system regains its stability as shown in Fig. 7.36b. Another advantage is the low voltage requirement. Figure 7.37 shows that the controller maximum voltage needed to stabilize the system is near 0.3 V. This value represents only 0.5% of the excitation signal.

The experimental set up of Fig. 7.2 has been used to verify the above simulation results. A built-in A/D convertor in LabVIEW with sampling rate $f_s = 10$ kHz was used to acquire the laser measurement. A stack of shift registers was used to generate the required delay signal. Each shift register corresponds to a delay in time equals to $1/f_s = 0.1$ ms. For example, to generate a signal that has a delay of 2 ms, a stack of 20 shift registers should be used. Figure 7.38 shows the result of the experimental tests of the same loading conditions of Fig. 7.36, before and after the application of the controller. As noticed, the results are close to those predicted theoretically in Fig. 7.36.

Next, the sensitivity of mismatching the time delay from half the period of excitation $T/2$ is investigated. This mismatch can be practically due to some uncertainty

Fig. 7.37 The controller output voltage applied in Fig. 7.36b. (Reprinted with permission. Copyright 2010, IOP Publishing Ltd [19])

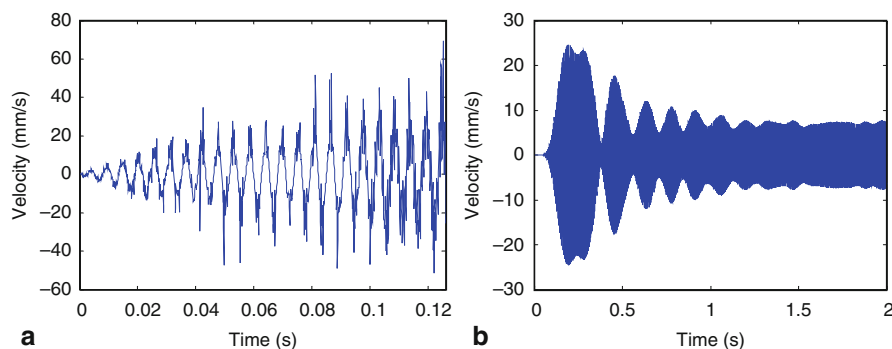
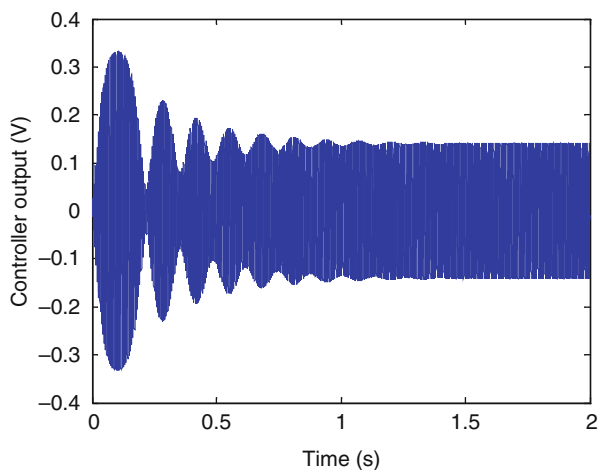


Fig. 7.38 Experimentally measured velocity response of the capacitive sensor for the loading of Fig. 7.36. Figure part a shows the uncontrolled response and b shows the controlled response. (Reprinted with permission. Copyright 2010, IOP Publishing Ltd [19])

in estimating the natural period of the system or due to some hardware errors in generating the exact excitation frequency. Figure 7.39 shows simulated results for the percentage of mismatch in the time delay versus the minimum control gain needed for stabilization. The figure shows that the higher the mismatch is the higher gain is needed. It is noted that for a mismatch value up to 10%, a small increase in the control gain is needed, which still results in a small voltage load. This indicates high robustness of the delayed-feedback controller in its tolerance to parameter variations.

Figure 7.36 demonstrates the ability of the controller to stabilize the resonator in the fractal regime. Next, we study its effects when the device is operated in the inevitable escape band at $V_{AC} = 30$ V, which represents the worst condition that this resonator can be operated at from a stability perspective. Referring back to Fig. 7.25, it is noted that the inevitable escape band starts at a frequency 177 Hz and ends at 185 Hz. For this simulation, the resonator is assumed operated at 180 Hz. According

Fig. 7.39 The effect of the mismatch of the applied delayed value from $T/2$. (Reprinted with permission. Copyright 2010, IOP Publishing Ltd [19])

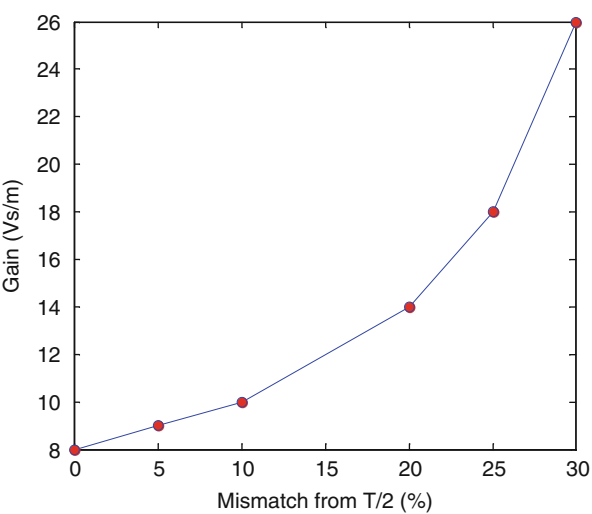
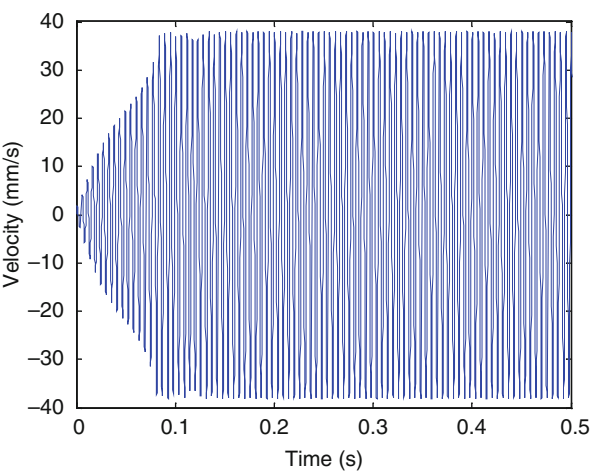


Fig. 7.40 The controlled response of the capacitive sensor when operated inside the inevitable escape band. (Reprinted with permission. Copyright 2010, IOP Publishing Ltd [19])



to the simulation, it turns out that a minimum gain of 300 Vs/m is needed for the stabilization at this extreme operating condition. The time history response of this case is depicted in Fig. 7.40.

7.10.3 Integrity Analysis

Here, we attempt to shed light on the influence of the delayed control scheme on the integrity and stability of the resonator by calculating its basin of attraction under various excitations and controlling conditions. In the following, white color is used to indicate stable response and black color to indicate unstable response. Figure 7.41 shows the effect of introducing the feedback controller on the basin of attraction of

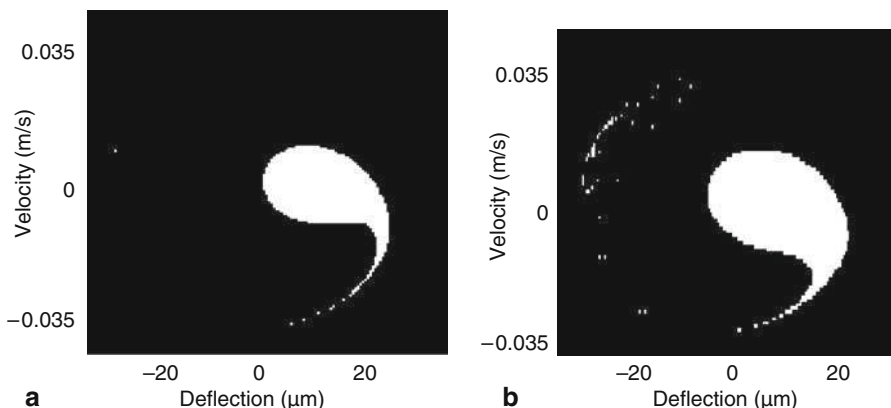


Fig. 7.41 The basin of attraction the resonator when operated at a voltage load of $V_{DC} = 40.2$ V and $V_{AC} = 20.1$ V at a frequency of 180 Hz. Figure part **a** shows the uncontrolled case and **b** shows the controlled case for $G = 70$ Vs/m. (Reprinted with permission. Copyright 2011, ASME [20])

the resonator for the same load of Fig. 7.36. Note that Fig. 7.41a shows a small basin of attraction, in which the initial conditions $(0, 0)$ are located in the unstable zone. However, after introducing the feedback controller, Fig. 7.41b, the area of the safe basin increases and the system regains stability with the zero initial conditions.

The shooting method and the Dover-Cliff integrity curves can be used together to better understand the effects of the delayed-feedback controller on the stability of the system. The results of these analytical tools are depicted in Fig. 7.42. The figure shows the erosion of the safe basin for positive, zero, and negative values of gain. For the uncontrolled case of $G = 0$, the frequency–response curve in the band 175–190 Hz shows that at least one stable state exists. However, by noting the Dover-Cliff curve for $G = 0$, it shows a weak region of stability for the same range of frequencies, which is indicated by the low values of normalized safe area (0.33 at 175 Hz and 0.24 at 190 Hz). Introducing the feedback controller with $G = 70$ Vs/m, the Dover-Cliff curve shifts upward to larger values (0.45 at 175 Hz and 0.89 at 190 Hz), indicating an increase in the safe basin. In the case of a negative sign ($G = -70$ Vs/m), the Dover-Cliff curve shifts significantly downward to smaller values (0.21 at 175 Hz and 0.0 at 190 Hz). This indicates a decrease in the stability of the system. Similar observation was made by Rega and Lenci in the case of using superharmonic signal to control the stability of thermoelastic MEMS devices [7]. This behavior can be desirable for applications such as RF switches, where losing the stability of the resonator yields a switch operated dynamically at reduced voltage.

Figure 7.43 further illustrates the effect of the feedback controller on increasing or decreasing the safe basin for the case of an excitation frequency of 190 Hz. For a zero gain, Fig. 7.43a shows a weak basin of attraction. Applying the feedback controller with a positive gain ($G = 70$ Vs/m), Fig. 7.43b, significantly increases the basin of attraction, indicating enhanced stable operation. On the other hand, introducing a gain value of -70 Vs/m, Fig. 7.43c, erodes the basin of attraction to the extent that the system has almost no stable solution.

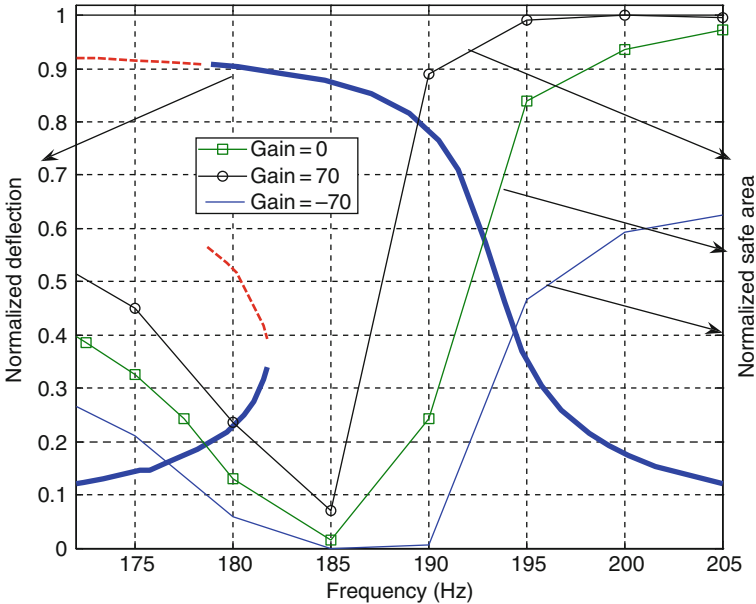


Fig. 7.42 The frequency–response of the resonator obtained using the shooting technique and the Dover-Cliff integrity curves at various values of gain. In the figure, $V_{DC} = 40.2$ V and $V_{AC} = 20.1$ V. The unit of Gain in the legend is Vs/m. (Reprinted with permission. Copyright 2011, ASME [20])

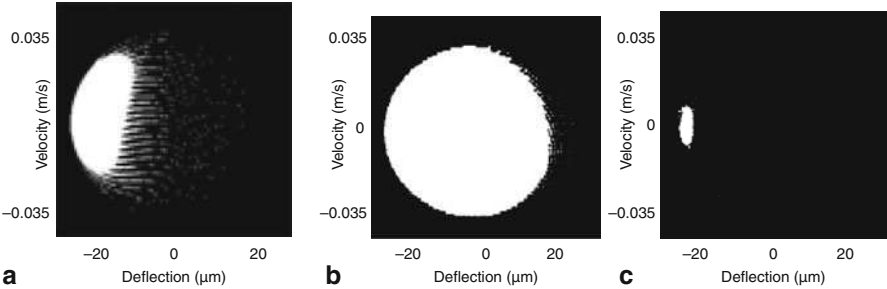


Fig. 7.43 The basin of attractions at an excitation frequency of 190 Hz for the case of **a** no control, **b** with control with a positive gain $G = 70$ Vs/m, and **c** with control with a negative gain $G = -70$ Vs/m. (Reprinted with permission. Copyright 2011, ASME [20])

Problems

1. Use the shooting technique to generate frequency–response curves for the case of primary resonance for $V_{DC} = 19.4$ V and $V_{AC} = 42.4$ V. Compare your results to Fig. 7.6.

2. Track the erosion of the basin of attraction of the frequency–response curves of the pervious question by generating a Dover-Cliff curve. Compare to the experimental data of Fig. 7.6 and the results of the shooting method.
3. Use the shooting technique to generate frequency–response curves for the case of subharmonic resonance for $V_{DC} = 40.1$ V and
 - (a) $V_{AC} = 15.6$ V, compare your results to Fig. 7.9.
 - (b) $V_{AC} = 18.4$ V, compare your results to Fig. 7.9.
 - (c) $V_{AC} = 21.1$ V, compare your results to Fig. 7.11.
4. Track the erosion of the basin of attraction of the frequency–response curves of the cases of question 3 by generating Dover-Cliff curves. Compare to the experimental data of Figs. 7.9 and 7.11 and the results of the shooting method.
5. Use the delayed-feedback controller to stabilize the response of the capacitive sensor at the loading case of Fig. 7.36 using a displacement feedback instead of velocity feedback. Choose an appropriate value of gain.
6. Generate a curve for the effect of the mismatch of the applied delayed value for the displacement feedback, similar to Fig. 7.39.
7. Generate Dover-Cliff integrity curves for the case of Fig. 7.42 using the gains of $G = 100$ Vs/m and $G = -100$ Vs/m.

References

- [1] www.sensata.com (Sensata Technologies; Attleboro, MA)
- [2] Alsaleem F, Younis M I, Ouakad H (2009) On the nonlinear resonances and dynamic pull-in of electrostatically actuated resonators. *Journal of Micromechanics and Microengineering*, 19:045013(1–14)
- [3] Alsaleem F M, Younis M I, and Ruzziconi L (2010) An experimental and theoretical investigation of dynamic pull-in in MEMS resonators actuated electrostatically. *Journal of Microelectromechanical Systems*, 19–4:794 - 806
- [4] Nayfeh A and Balachandran B (1995) *Applied nonlinear dynamics*. Wiley, New York
- [5] Thompson J and Stewart H (2001) *Nonlinear dynamics and chaos*. Wiley, New York
- [6] Lenci S and Rega G (2003) Optimal control of non-regular dynamics in a Duffing oscillator. *Nonlinear Dynamics*, 33:71–86
- [7] Lenci S and Rega, G (2006) Control of pull-in dynamics in a nonlinear thermoelastic electrically actuated microbeam. *Journal of Micromechanics and Microengineering*, 16:390–401
- [8] Lenci S and Rega G (2008) Dynamical integrity and control of nonlinear mechanical oscillators. *Journal of Vibration and Control*, 159–179; doi:10.1177/1077546307079403
- [9] Ruzziconi L, Younis M I, and Lenci S (2010) Dynamical integrity for interpreting experimental data and ensuring safety in electrostatic MEMS. *Proceedings of the IUTAM Symposium on Nonlinear Dynamics for Advanced Technologies and Engineering Design*, Aberdeen, Scotland, UK, pp: 27–30
- [10] Nayfeh A H, Ouakad H M, Najjar F, Choura S and Abdel-Rahman E M (2010) Nonlinear dynamics of a resonant gas sensor. *Nonlinear Dynamics*, 59–4:607–618
- [11] Nayfeh A, Younis M I, and Abdel-Rahman E (2007) Dynamic pull-in phenomenon in MEMS resonator. *Nonlinear Dynamics*, 48:153–163
- [12] Nayfeh A H and Younis M I (2005) Dynamics of MEMS resonators under superharmonic and subharmonic excitations. *Journal of Micromechanics and Microengineering*, 15:1840–1847

- [13] Younis M I and Al-saleem F M (2009) Exploration of new concepts for mass detection in electrostatically-actuated structures based on nonlinear phenomena. *Nonlinear Dynamics*. 4–2: doi:10.1115/1.3079785, 15 pages
- [14] Lange D, Brand O, and Baltes H (2002) CMOS cantilever sensor systems: atomic-force microscopy and gas sensing applications. Springer, Berlin
- [15] Pyragas K (1992) Continuous control of chaos by self-controlling feedback. *Physics Letters A*. 170:421–428
- [16] Nakajima H and Ueda Y (1998) Half-period delayed feedback control for dynamical systems with symmetries. *Physical Review E*. 58:1757–1763
- [17] Yamasue K and Hikiara T (2006) Persistence of chaos in a time-delayed-feedback controlled duffing system. *Physical Review E*. 73:036209–16
- [18] Yamasue K and Hikiara T (2006) Control of microcantilevers in dynamic force microscopy using time delayed feedback. *Review of Scientific Instruments*. 77:53703–16
- [19] Alsaleem F M and Younis M I (2010) Stabilization of electrostatic MEMS resonators using delayed feedback controller. *Smart Materials and Structures*. 19:035016
- [20] Alsaleem F M and Younis M I (2011) Integrity analysis of electrostatically actuated resonators with delayed feedback controller. *Dynamic Systems, Measurements, and Control*. 133:019101JD

Chapter 8

Mechanical Shock in MEMS

This chapter addresses a reliability issue of MEMS that is crucial for their commercialization, which is their survivability under mechanical shocks. Unlike conventional electronics of passive elements, MEMS contain flexible components that are deliberately designed to undergo some kind of motion. Thus, a natural question comes of how these microstructures respond when they are subjected to dynamic shock loads? What about short circuit and stiction when they make contacts with the substrate or stationary electrodes due to shock loads? These are some of the issues that are treated in this chapter. In addition, the impact of electrostatic forces on the dynamic response is illustrated. The interaction of the motion of microstructures with the printed circuit boards where they are mounted on is also discussed.

8.1 Introduction

With the rapid growth and maturity of the MEMS technology, many device concepts are ready to make the transition from research labs to consumer products. One of the critical issues affecting the commercialization of MEMS devices is their reliability and survivability under mechanical shock and impact. Several MEMS components have already made it to the market and being increasingly integrated and embedded into handheld devices and consumer products, such as the interactive motion-sensitive video games and smart phones. In such environments, there is an obvious need to ensure the durability and reliability of MEMS to sustain the various dynamic loads while being used by consumers.

MEMS generally can be exposed to shock during fabrication, deployment, shipping, and operation. Also, a crucial criterion for automotive and industrial applications is the survivability of portable devices containing MEMS when dropped on hard surfaces, which can induce significant shock loads. For some applications, MEMS are expected to survive severe dynamic loading, such as the harsh environments in military applications. In addition, aerospace applications rely on pyrotechnic devices, which generate dangerous shock waves of amplitude reaching hundreds of thousands of *gs*. MEMS sensors and devices in these applications are required to survive such severe environments.

Mechanical shock can induce highly dynamic loads on structures causing cracking, chipping, and fracture problems. In MEMS, shock can in addition cause functionality failures due to the induced large deflection of the moveable microstructures, such as suspended microbeams, which may lead to mechanical and/or electrical failure. Electrical failure can be due to the unaccounted-for contact between a moveable electrode and a stationary electrode, such as in resonators applications, resulting in circuit shorts. Mechanical failures can be due to stiction as a result also of the unaccounted-for contacts. Thus, unlike failure in large machines and printed circuit boards, failure in MEMS does not have to mean necessarily fracture of structures or solders due to high stresses. In fact, because the majority of microstructures are fabricated of silicon or polysilicon, they are very tough against bending stresses induced from shock acceleration. Hence, they are less likely to be directly broken due to high stresses. However, when they hit other parts or a substrate, they can be broken due to the severe contact stresses or their functionality becomes adversely affected due to changes in their mechanical or electrical characteristics. Therefore, our focus in this chapter is to investigate how to prevent such contacts rather than designing the parts to resist fracture or breakage from high stresses, since as explained this comes as a second concern in MEMS.

A number of investigations have been presented in recent years on mechanical shock in MEMS. These can be classified into experimental works, aiming to subject MEMS chips to shock and observe their failure modes, and theoretical works aiming to model and simulate the response of microstructures during shock. Among the experimental works, Béliveau et al. [1] tested commercial accelerometers under shock loads. Brown and coauthors subjected MEMS sensors, commercial accelerometers, and pressure sensors to high- g shock load in harsh environments [2–4]. Tanner et al. [5] tested MEMS microengines with comb-drive actuators against shock pulses of various time durations and amplitudes. Li and Shemansky [6] conducted experimental drop tests of MEMS accelerometers. Sheey et al. [7] investigated experimentally the response of cantilever microbeams to high- g mechanical shock using a modified Hopkinson pressure bar. Kelly et al. [8] presented several techniques to amplify the shock pulse due to a drop table or a Hopkinson pressure bar to reach high level of acceleration to be effective for testing stiff microstructures. Kimberley et al. [9] conducted several tests on RF MEMS switches when subjected to mechanical shock of various ranges. They tested the switches under shock loads in the range of few thousands of g s, due to drop-table test, hundreds of thousands of g s, due to Hopkinson pressure bar, and up to hundreds of millions of g s, which are due to pulsed-laser loading.

Other investigations have been also presented in the modeling of MEMS devices and structures under shock. Several works have been based on finite-element models, for example Cunningham et al. [10], Wagner et al. [11], Lim et al. [12], Atwell et al. [13], Jiang et al. [14], Fan and Shaw [15], and Mariani et al. [16, 17]. Other researchers modeled the shock problem of MEMS using lumped spring–mass–damper models, such as Srikar and Senturia [18], Li and Shemansky [6], Qian et al. [19], Coster et al. [20], Bao et al. [21], Khatami and Rezazadeh [22], and Ghisi et al. [23]. Also, a number of studies accounted for the flexibility of microstructures and treated

them as distributed parameters systems in analytical models including the works of Tas et al. [24], Fang et al. [25], Yee et al. [26], and Millet et al. [27].

Younis and coworkers have developed analytical and computational techniques to investigate shock in MEMS [28–39]. In [28–34] the response of microstructures under the combined effects of mechanical shock and electrostatic forces has been investigated theoretically and experimentally. Computationally efficient approaches to study shock in MEMS were presented in [35]. The effect of the PCB motion on the response of a microstructure has been studied theoretically and experimentally in [31, 36, 37]. The influence of squeeze-film damping in suppressing the dynamic response of microstructures has been analyzed in [30, 31, 33, 38, 39].

8.2 Mechanical Shock

Shock can be defined as a force applied suddenly over a short period of time relative to the natural period of the structure [40]. Also it can be defined as a rapid transfer of energy to a mechanical system leading to significant increase in its stress, velocity, acceleration, or displacement [41]. Because of the sudden change in velocity, which is translated into induced acceleration on the impacted structure, a shock force is commonly measured and expressed in terms of acceleration level in g s, where g is the gravitational constant.

The most common methods to induce mechanical shock to test MEMS and electronics equipments are electromagnetic shakers (range of sub g s-tens of g s), drop tests and drop-table machines (hundreds-few thousands of g s), pendulum hammers (thousands of g s), and Hopkinson pressure bars (tens of thousands of g s). Figure 8.1 shows pictures of an electromagnetic shaker and a drop table. These machines are



Fig. 8.1 Pictures of two experimental techniques to induce shock in MEMS and electronic equipments. **a** An electromagnetic shaker, **b** a hydraulic-driven Lansmont 23A drop table. (Vibration Lab, Department of Mechanical Engineering, SUNY Binghamton, courtesy of Prof. James Pitarresi)

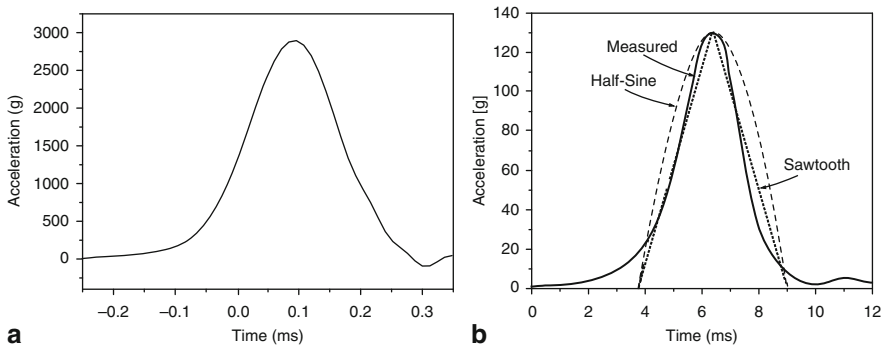


Fig. 8.2 Examples of shock pulses measured experimentally of a drop-table test. **a** A typical acceleration pulse of a drop table test, **b** A comparison of a measured acceleration pulse to idealized pulse models. (Pictures are courtesy of Prof. James Pitarresi, Department of Mechanical Engineering, SUNY Binghamton)

generally programmable to generate varieties of shock pulses in various shapes, amplitudes, and shock durations.

The profile of a shock force over time, the pulse shape, can take various forms depending on the source of the shock force and the material of the involved impacted bodies. For example, shock pulses due to explosions or blasts take profiles close to a right-angled triangle whereas a pulse due to a drop-table test looks more of a half-sine pulse, Fig. 8.2. A metal-to-metal impact, for example, results in shock pulses of very short durations compared to impacts involving softer materials, such as plastic or rubber. In general, a shock pulse is characterized by its maximum value, duration, and shape. To facilitate modeling these pulses, they are approximated as pulses of uniform shapes of simple analytical expressions, such as rectangular, triangular, and half-sine pulses, Fig. 8.3. Figure 8.2b compares a measured drop-table signal to a triangular and a half-sine pulse. One can see that using uniform pulses can be good approximation to the actual pulse. Particularly, the half-sine pulse seems to be the closest to the original pulse. Therefore it is not surprising that the half-sine pulse is by far the most common shape used to model shock for commercial, industrial, and military applications [41]. Hence, in this chapter, we adopt this pulse for simulation purposes.

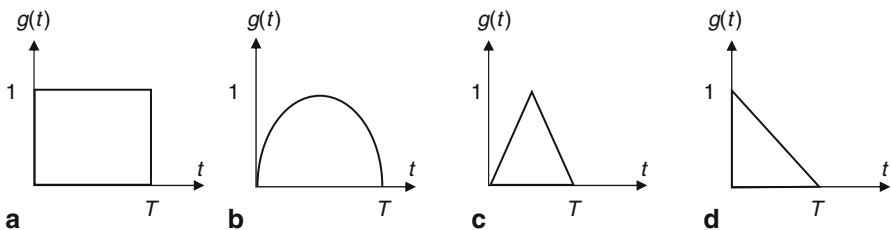


Fig. 8.3 Simple pulses used to model actual shock loads. Shown in the figure are **a** rectangular, **b** half-sine, **c** saw-tooth, and **d** initial-peak triangular pulses

8.3 Modeling Shock in Lumped-Parameter Models

The discussion of Sect. 2.5 indicates that a packaged MEMS device, such as an accelerometer, gets excited dynamically from its base when the package or the printed circuit board PCB carrying it vibrates. The equation of motion governing the dynamic behavior of a simple linear spring–mass–damper model of a packaged device, according to Fig. 2.16, is expressed in Eq. (2.42), which is rewritten here as

$$m\ddot{z} + c\dot{z} + kz = -m\ddot{y} \quad (8.1)$$

where z represents the relative motion of the mass to the base and \ddot{y} is the acceleration of the base. Equation (8.1) applies to any form of base motion, which is not necessarily harmonic. As discussed previously, the PCB or package experiences a finite-duration acceleration pulse during shock, similar to Fig. 8.2. Also, Example 2.7 shows using a simplified model of a free-fall drop test that the drop is translated into a base acceleration signal, according to Eq. (2.54), which is rewritten here as

$$m\ddot{z} + kz = -m\ddot{y} = mg. \quad (8.2)$$

In view of Eq. (8.1) and Eq. (8.2), the shock effect on MEMS devices, as transferred to them from their package or PCB, can be modeled as a point force $F(t)$, that is proportional to the base acceleration, i.e., $F(t) = (ma)g(t)$, where a is the maximum amplitude of the shock pulse acceleration and $g(t)$ is the shape function of the pulse. For a MEMS microstructure of spatial mass distribution, the equation of motion of the damped response can be written as

$$m_{\text{eff}}\ddot{z} + c\dot{z} + kz = m \times a \times g(t) \quad (8.3)$$

where m_{eff} is the effective mass of the microstructure. Note that m is replaced in the inertia term only; that associated with $g(t)$ remains unchanged. The acceleration input $ag(t)$ can be imported directly from experimental data if available and then the equation of motion is solved numerically. Alternatively, the pulse can be approximated to be of uniform shape with a simple analytical expression. For example, the analytical expressions of a rectangular, half-sine, saw-tooth, and an initial-peak triangular pulse can be written, respectively, as

$$g(t) = u(t) - u(t - T) \quad (8.4)$$

$$g(t) = \sin\left(\frac{\pi}{T}t\right)u(t) + \sin\left[\frac{\pi}{T}(t - T)\right]u(t - T) \quad (8.5)$$

$$g(t) = \frac{t}{T/2} - 2\left(\frac{t - T/2}{T/2}\right)u(t - T/2) + \left(\frac{t - T}{T/2}\right)u(t - T) \quad (8.6)$$

$$g(t) = 1 - \frac{t}{T} + \left(\frac{t - T}{T}\right)u(t - T) \quad (8.7)$$

where t is time, T is the shock duration, and $u(t)$ is the unit step function. Then, using the convolution integral approach, Eq. (8.3) is solved analytically. An illustration of this procedure is demonstrated in Example 2.8 for the case of a rectangular pulse. Also, one can use numerical integration of the equation of motion directly instead of dealing with convolution integrals. This is especially useful for systems of nonlinear equations of motions.

In the next sections, we focus our attention on the response to a half-sine pulse since, as indicated previously, it represents the closest approximation to several real-life shock pulses.

Example 8.1: Here we consider the cantilever microbeam of Example 4.4, which is made of silicon with density $\rho = 2,332 \text{ kg/m}^3$ and modulus of elasticity $E = 169 \text{ GPa}$ of length $l = 900 \text{ }\mu\text{m}$, thickness $h = 1.0 \text{ }\mu\text{m}$, and width $b = 100 \text{ }\mu\text{m}$. The microbeam is subjected to a drop test, which induces a base acceleration pulse of maximum amplitude $a = 100g$. Using a lumped-parameters model, determine and plot the response of the beam tip under the following shock conditions:

- Assuming a half-sine pulse of $T = 0.1 \text{ ms}$ and a damping ratio $\zeta = 0.05$.
- Assuming a half-sine pulse of $T = 0.6 \text{ ms}$ and a damping ratio $\zeta = 0.05$.
- Assuming a half-sine pulse of $T = 10 \text{ ms}$ and a damping ratio $\zeta = 0.05$.
- Repeat (a)–(c) for $\zeta = 0.5$.
- Repeat (a)–(c) assuming a saw-tooth pulse.

Solution: Since the beam is excited through its support, the support acceleration is translated into a uniformly distributed load equal the mass of the beam times the pulse acceleration (see Sect. 8.5). The effective mass of the beam in this case is $0.646m$, where m is the total mass, and its stiffness coefficient is $k = 8EI/l^3$. Hence, the undamped equation of motion governing the tip deflection x of the cantilever becomes

$$(0.646m)\ddot{x} + \left(\frac{8EI}{l^3}\right)x = mag(t). \quad (\text{a})$$

For parts (a)–(d), $g(t)$ is given by Eq. (8.5), and for part (e) it is given in Eq. (8.6). Dividing Eq. (a) by $0.646m$ gives

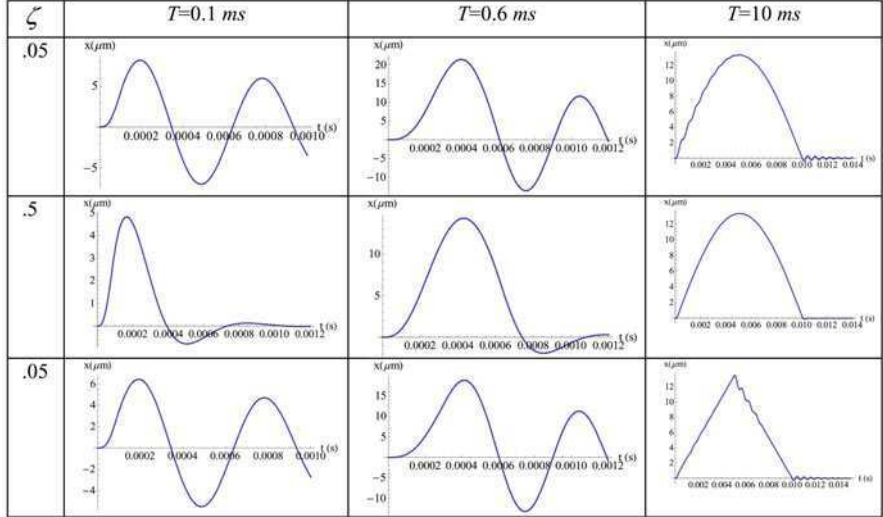
$$\ddot{x} + \omega_n^2 x = F_0 g(t) \quad (\text{b})$$

where $F_0 = 1.548a$ and $\omega_n = 3.52\sqrt{EI/ml^3}$. Adding proportional damping ($2\zeta\omega_n$) yields

$$\ddot{x} + 2\zeta\omega_n\dot{x} + \omega_n^2 x = F_0 g(t). \quad (\text{c})$$

Equation (c) can be solved using the convolution integral approach of Sect. 2.6 or it can be integrated numerically in time. The results are depicted in Table 8.1. The following observations can be made on the results. First, the maximum response is largest when $T = 0.6 \text{ ms}$. Then comes second in magnitude the case of $T = 0.1 \text{ ms}$

Table 8.1 Response to various shock conditions for parts (a)–(e) of Example 8.1

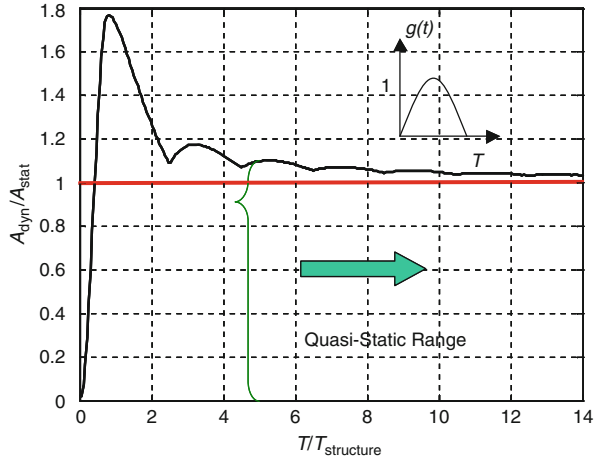


and comes last the case of $T = 10\text{ ms}$. However, for $\zeta = 0.5$, the maximum response of $T = 0.6\text{ ms}$ and $T = 10\text{ ms}$ are very close to each other. Another note worth to be observed is regarding the shape of the response. The responses at $T = 0.1\text{ ms}$ and $T = 0.6\text{ ms}$ show some sort of harmonic vibrations whereas the responses at $T = 10\text{ ms}$, third column, show shapes similar to the input pulse (half sine or triangular shape). One more note that the response at $T = 0.6\text{ ms}$ is very sensitive to the changes in damping and shape of the pulse. The conclusion of these results is that the response of a mechanical system to shock depends on the duration of the pulse, its shape, and damping conditions. To better understand the reason behind this variation in the response, we need to refer to the so-called shock-response spectrum (SRS), which is explained next.

8.4 The Shock-Response Spectrum

The SRS is a universal plot of the peak dynamic response A_{dyn} of a linearly behaving damped single-degree-of-freedom (SDOF) system, Eq. (8.3), to shock load as a function of the ratio between the shock duration T to the natural period of the structure $T_{\text{structure}}$. It is obtained by solving for the maximum transient response of the SDOF system while varying either the shock duration T while keeping $T_{\text{structure}}$ constant or vice versa. Hence, the horizontal axis in this plot is $T/T_{\text{structure}}$. The peak dynamic response is usually normalized to the peak response A_{stat} due to an equivalent static load of the same amplitude as the shock load. Hence, the vertical axis of this plot is $A_{\text{dyn}}/A_{\text{stat}}$. Other versions of the SRS exist, which show on the vertical axis the

Fig. 8.4 A shock-response spectrum of a spring–mass system under a half-sine shock pulse. (Reprinted with permission. Copyright 2007, IOP Publishing Ltd [30])

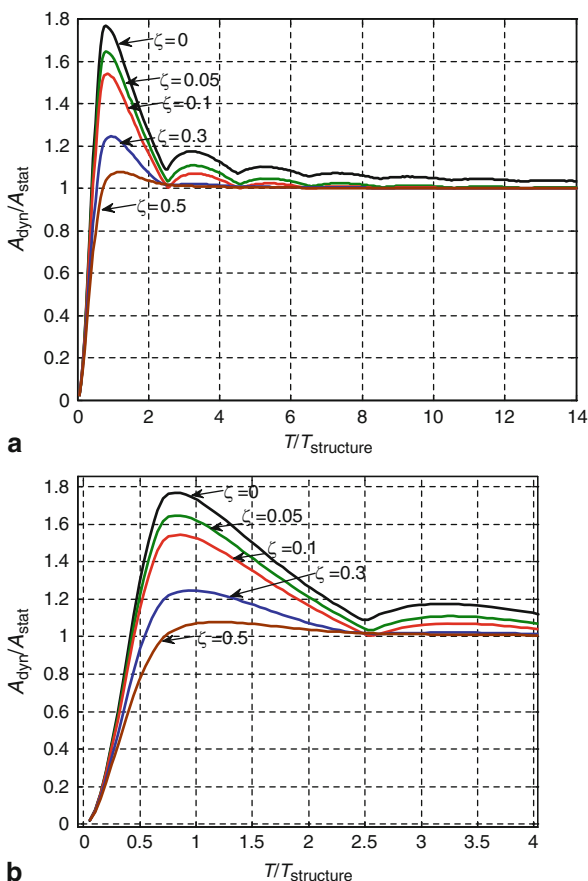


normalized peak velocity or acceleration of the system response. Also, the horizontal axis sometimes is written in terms of the inverse of the ratio $T/T_{\text{structure}}$, i.e., in terms of the frequency ratio of the natural frequency of the structure to that of the shock ($= 1/T$). The SRS is a well-established and common design tool that helps designers choose the appropriate parameters of a system to suppress its shock response for a certain range of durations.

The SRS can be established for various pulse shapes and damping ratios. Figure 8.4 shows an SRS for a half-sine pulse assuming zero damping. It is noted from the figure that when $T/T_{\text{structure}}$ gets large, $A_{\text{dyn}}/A_{\text{stat}}$ gets close to unity. This corresponds to the so-called quasi-static loading. In such cases, the shock duration is too big compared to the natural period of the structure. Hence, the structure experiences the shock as a sort of slow varying force rather than a fast time-varying force, which the classical definition of shock implies. In this regime, the response becomes less sensitive to variation in the shock durations and damping conditions. This can be seen clearly in Table 8.1 in the third column (note that the maximum amplitude is almost unchanged despite the change in damping and pulse shape). The natural period of the beam of Example 8.1 is $T_{\text{structure}} = 0.59$ ms. Hence, for $T = 10$ ms, $T/T_{\text{structure}} = 17$, which is clearly in the quasi-static regime. This point is further clarified in Fig. 8.5a, which shows various spectra for various values of damping ratio. Note that all the curves converge to the same values as $T/T_{\text{structure}}$ gets larger in the quasi-static regime. It is worth to mention that because of the high natural frequencies of many microstructures, such as clamped–clamped microbeams, a good portion of them experience shock loads due to drop tests (usually of duration 0.2–2.0 ms) as quasi-static loads.

When the ratio T/T_n is approximately in the range of 0.5–4.0, one can see that the response experiences large amplification. The peak of the response occurs when $T/T_n \approx 0.8$, at which the response due to shock peaks at $A_{\text{dyn}}/A_{\text{stat}} = 1.76$. This range represents the dynamic regime in the SRS. The response in this regime is highly sensitive to damping and pulse shape. This is clear in the second column of Table 8.1, which shows results for $T/T_n \approx 1.0$. Also, this point is further clarified

Fig. 8.5 a Shock-response spectra of a spring–mass–damper system under a half-sine shock pulse for various values of damping ratios. **b** A zoomed view of (a)



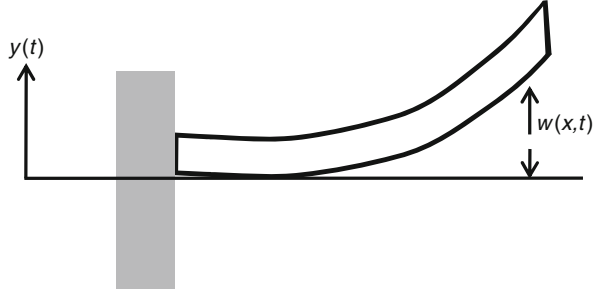
in Fig. 8.5b, which shows various spectra for various values of damping ratio in the dynamic regime. Note the significant reduction in the response as the damping ratio is changed.

The third regime of an SRS is for T/T_n approximately below 0.5. In this range, the response is suppressed with $A_{\text{dyn}}/A_{\text{stat}}$ below unity. This regime is called the shock-isolation regime. This is the case of the first column of Table 8.1. Damping and pulse shape here have some effect on the response, which is less than the dynamic regime but more than the quasi-static regime, as clarified in Fig. 8.5b.

8.5 Modeling Shock on Microbeams

When a MEMS package or a PCB carrying MEMS chips is subjected to shock of a drop or a drop-table test, the shock force is transferred to the suspended microstructures through their supports or anchors. Hence, shock affects microstructures including microbeams through supports, which is equivalent to base excitation.

Fig. 8.6 A microbeam driven dynamically from its support



To model the effect of shock in this case, consider, without the loss of generality, a cantilever beam driven from its support by a displacement input $y(t)$, Fig. 8.6. By following the derivation procedure of Sect. 6.1 and assuming $w(x, t)$ to be the displacement of the beam with respect to $y(t)$, one can note that the base motion affects the beam equation through the inertia term (or in Lagrangian dynamics it affects the kinetic energy term). Hence, the equation of the beam can be written as

$$EI \frac{\partial^4 w}{\partial x^4} + \rho A \left(\frac{\partial^2 w}{\partial t^2} + \frac{d^2 y}{dt^2} \right) + c \frac{\partial w}{\partial t} = 0. \quad (8.8)$$

Rearranging Eq. (8.8) we get

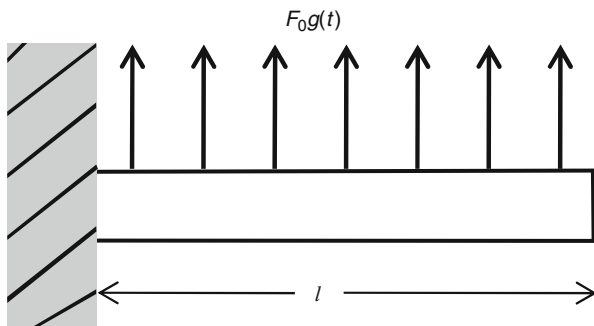
$$EI \frac{\partial^4 w}{\partial x^4} + \rho A \frac{\partial^2 w}{\partial t^2} + c \frac{\partial w}{\partial t} = -\rho A \frac{d^2 y}{dt^2} = F_0 g(t) \quad (8.9a)$$

where $F_0 = -(\rho A) a$, where a is the maximum acceleration and $g(t)$ is the acceleration pulse shape. If the microbeam has immovable edges, such as clamped-clamped microbeams, then mid-plane stretching needs to be accounted for. Accordingly, the nonlinear equation of motion of the beam in this case is written as

$$EI \frac{\partial^4 w}{\partial x^4} + \rho A \frac{\partial^2 w}{\partial t^2} + c \frac{\partial w}{\partial t} = \left[\frac{EA}{2I} \int_0^l \left(\frac{\partial w}{\partial x} \right)^2 dx + N_1 \right] \frac{\partial^2 w}{\partial x^2} - \rho A \frac{d^2 y}{dt^2} \quad (8.9b)$$

where N_1 is a tensile axial force. Equations (8.9a) and (8.9b) indicate clearly that the beam experiences the base motion as a distributed force, which is proportional to the base acceleration. Hence, shock in microstructures, such as microbeams, can be viewed and modeled as a distributed force, Fig. 8.7. Typically in drop-table tests, an accelerometer is mounted on the drop table, which records the amount of induced acceleration during shock, similar to Fig. 8.2. For simulation purposes, assuming no amplification of the shock signal due to the PCB motion or other effects, this recorded signal can be approximated in terms of a uniform pulse as explained in Sect. 8.3. Then, a multi-mode reduced-order model is derived and utilized, similar to the procedure of Sect. 6.10, to obtain the dynamic response of the microbeam in time. Example 6.10 of Chap. 6 demonstrates this procedure.

Fig. 8.7 A microbeam subjected to a shock force modeled as a distributed force



8.6 Computationally Efficient Approach for Microstructures

Because shock is a transient dynamic phenomenon, modeling its effect on microstructures accurately, for example using finite-element methods, can be computationally challenging. It turns out that one can use the SRS of a SDOF system combined with an accurate simulation of the static response of a microstructure to gain information about its maximum dynamic response when subjected to shock. The reduction in the computational cost comes from the fact that static simulation is computationally cheap and easier compared to dynamic simulation.

The procedure goes as follows. First, the natural frequency of the microstructure and its natural period $T_{\text{structure}}$ are calculated. Then, an estimate of $T/T_{\text{structure}}$, or a range of values, needs to be calculated based on the expected duration of the mechanical shock. For instance, a drop on a hard floor surface causes a shock force of duration ranges from 0.1–2 ms (depending on the hardness of the floor). Blast loading can result in smaller shock durations. Based on the calculated $T/T_{\text{structure}}$, a judgment can be made on the nature of the shock force whether it is quasi-static or dynamic. If it is quasi-static, then the response of the microstructure can be approximated as a response to a spatially distributed static load of magnitude equal to the maximum amplitude of the shock force. If the microstructure has a regular geometry or shape, then available analytical expressions of its static response can be utilized. Otherwise, a simple finite-element model of the structure under a spatially uniform constant force is built and utilized. This again is favorable computationally compared to building a transient dynamic finite-element model.

If the ratio $T/T_{\text{structure}}$ turns out to be in the dynamic, or even in the isolation, regime, then the analytical static-response formula, if available, or the static finite-element results needs to be corrected by multiplying them by the amplification factor $A_{\text{dyn}}/A_{\text{stat}}$. This factor is read directly from the SRS corresponding to the calculated $T/T_{\text{structure}}$ at the operating damping ratio of the device. The next example illustrates this procedure for a case study of a cantilever microbeam.

The above approach works accurately for linearly behaving microstructures, such as cantilever microbeams [35]. For microstructures with geometric nonlinearities, such as clamped–clamped beams, the amplification factor $A_{\text{dyn}}/A_{\text{stat}}$ becomes less

accurate (since it is based on a linear SRS). However, if it turns out that $T/T_{\text{structure}}$ is in the quasi-static regime, meaning $A_{\text{dyn}}/A_{\text{stat}} = 1$, then accurate nonlinear static simulations of the response of microstructures to static load can be used.

Example 8.2: Consider the cantilever microbeam of Example 8.1, which is subjected to an acceleration pulse of maximum amplitude $a = 100g$. Calculate the maximum response of the microbeam for the below conditions based on the static-SRS method. Also, compare the results to those obtained using a multi-mode reduced-order model for the following cases:

- (a) Assuming a half-sine pulse of $T = 10$ ms and a damping ratio $\zeta = 0.05$.
- (b) Assuming a half-sine pulse of $T = 0.6$ ms and a damping ratio $\zeta = 0.05$.

Solution: The natural period of this microbeam is $T_{\text{structure}} = 0.59$ ms. For loading case (a), $T/T_{\text{structure}} = 17$, which is clearly a quasi-static loading case. Thus, the maximum response of the beam is taken to be the same as the tip deflection due to a distributed static force of amplitude equal the maximum amplitude of the shock force, which is according to Eq. (8.9a) is $F_0 = (\rho A) a$. Recall that for a cantilever beam under uniform constant force F_0 , the maximum tip deflection W_{Max} is expressed as [42]

$$W_{\text{Max}} = \frac{F_0 l^4}{8EI} = \frac{12F_0 l^4}{8Ebh^3}. \quad (\text{a})$$

For loading case (b), $T/T_{\text{structure}} \approx 1$, which is clearly a dynamic loading case. Reading from Fig. 8.5b at $T/T_{\text{structure}} = 1$ and $\zeta = 0.05$, we find that $A_{\text{dyn}}/A_{\text{stat}} \approx 1.65$. Accordingly, W_{Max} in this case is expressed as

$$W_{\text{Max}} = \frac{A}{A_0} \left(\frac{12F_0 l^4}{8Ebh^3} \right). \quad (\text{b})$$

Table 8.2 compares the static-SRS results obtained using Eq. (a) and Eq. (b) with results obtained using a multi-mode reduced-order model ROM of the cantilever beam. As noted, the analytical results are very close to the ROM results. Also, it seems for this loading case that a 1-mode ROM suffices. However, one should always check the convergence of the ROM since it depends on the loading and damping conditions.

Table 8.2 The maximum response of a cantilever microbeam using various solution methods

Method/shock duration	$T = 10$ ms (μm)	$T = 0.6$ ms (μm)
Static + SRS	13.322	21.981
ROM using 1 mode	13.526	21.799
ROM using 4 modes	13.347	21.653
ROM using 6 modes	13.348	21.653

8.7 High-g Shock Response

There is a greater need to develop computationally efficient approaches that are capable of tackling high-g loading cases, such as in military and aerospace applications. In such cases, microstructures can be subjected to shock loads in the order of hundreds of thousands of *gs*. Such high level of shock loads can induce complex dynamical responses. From a computational point of view, modeling such problems using finite-element techniques is very cumbersome [35].

To illustrate the impact of high-g shock loads, consider next as a case study a silicon clamped–clamped microbeam of $l = 900 \mu\text{m}$, $h = 1.5 \mu\text{m}$, and $b = 100 \mu\text{m}$. Assume zero damping and the beam subjected to a half-sine shock pulse of amplitude ranging from very small to very large values. Using a nonlinear ROM of the microbeam, similar to Eq. (6.112), the maximum values of the first six symmetric modal coordinates, u_1 – u_6 of Eq. (6.115), of the beam response are calculated as the shock amplitude is varied from small to large values, Fig. 8.8. As seen in the figure, for small shock values, the higher order coefficients have much lower magnitudes than the smaller coefficients. For example, there is more than four order of magnitude difference between u_1 and u_6 . Therefore, dropping the higher order terms in the ROM in this case does not affect much the accuracy of the results. On the other hand, we note that for large values of shock, there is significant increase in the magnitude of the modal coordinates with the difference among their values shrinking. The difference between u_1 and u_6 , for instance, becomes within two orders of magnitude. Hence, unlike the case of Example 8.2, neglecting the higher order terms in the ROM in such cases affects the accuracy of the predicted behavior. Figure 8.9a, b shows the time response of the clamped–clamped microbeam when subjected to a shock pulse of amplitude 200,000 *g* for quasi-static and dynamic loading cases, respectively. We note from the figure the participation of the higher order modes in the response and the existence of multiple frequencies.

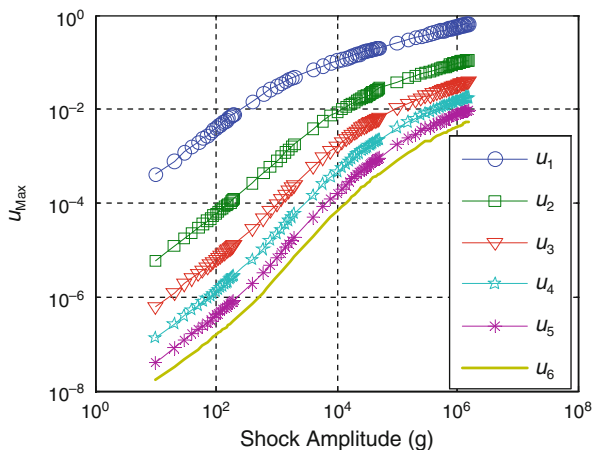


Fig. 8.8 Comparison of the normalized values of the first six symmetric modal coordinates used in the ROM for a clamped–clamped microbeam. (Reprinted with permission. Copyright 2007, IEEE [35])

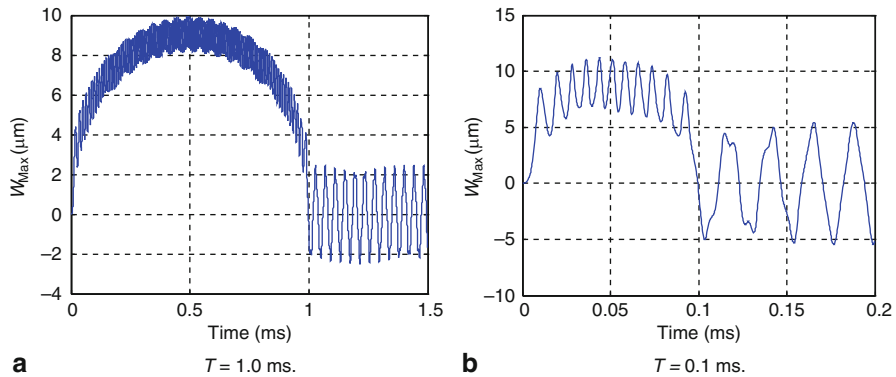


Fig. 8.9 Time history of the undamped response of a clamped-clamped microbeam subjected to a shock pulse of amplitude 200,000g. (Reprinted with permission. Copyright 2007, IEEE [35])

8.8 The Combined Effect of Shock and Electrostatic Forces

Because of the fact that many microstructures are biased by voltage loads for actuation and detection purposes, it is unrealistic to ignore the effect of electrostatic forces when modeling the response of these microstructures under mechanical shock. One would expect that electrostatic forces weaken the stiffness of microstructures making them more susceptible to large motion under shock. If the energy induced due to shock is sufficiently large, microstructures can escape their potential well leading to dynamic pull-in collapse. Even in comb-drive actuators, the individual fingers may stick to each other under the combined effect of shock and electrostatic forces. Next, we discuss the combined effect of shock and electrostatic forces on SDOF systems and then on microbeams. After that, experimental data are shown verifying the theoretical conclusions.

8.8.1 Single-Degree-of-Freedom Model

To model an electrostatically actuated microstructure under mechanical shock, for example of a drop test, we use a model similar to Fig. 5.8 and subject it to base motion, Fig. 8.10a. The sign convention is taken to be positive for upward motion or forces. In the figure, z refers to the relative motion of the microstructure to the base motion y and x represents the absolute motion of the microstructure to an inertial frame of reference. The free-body diagram of the mass in this case is depicted in Fig. 8.10b. Based on this figure, the equation of motion is written as

$$m\ddot{z} + c\dot{z} + kz = \frac{-\varepsilon AV_{DC}^2}{2(d+z)^2} - m\ddot{y}. \quad (8.10)$$

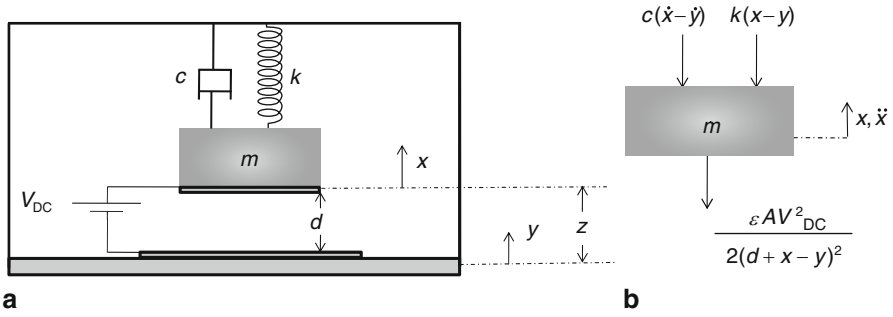


Fig. 8.10 **a** A single-degree-of-freedom model of an electrostatically actuated microstructure inside a package subjected to base motion. **b** A free-body diagram of the microstructure

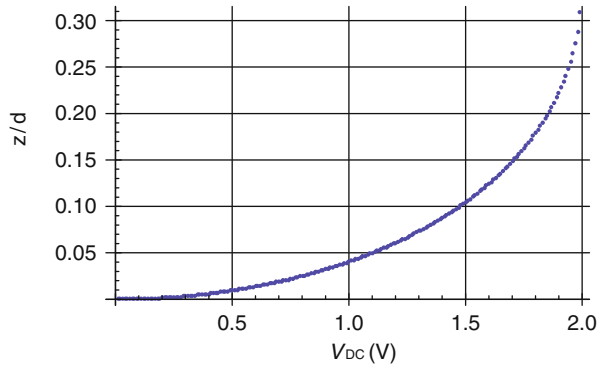
For spatially distributed microstructures, the mass coefficient in the inertia term is replaced with an effective mass m_{eff} , that is

$$m_{\text{eff}}\ddot{z} + c\dot{z} + kz = \frac{-\epsilon A V_{DC}^2}{2(d+z)^2} - m\ddot{y}. \quad (8.11)$$

Equation (8.11) can be utilized to simulate the dynamic response of an electrostatically actuated microstructure under shock. The first step in the simulation is to calculate the static (equilibrium) deflection of the microstructure under a DC voltage alone. This value is used for the solution of Eq. (8.11) as an initial condition for the displacement z along with a zero initial velocity. Equation (8.11) is then integrated numerically in time to reveal the dynamical response to shock. The loading of the initial conditions is equivalent to subjecting the microstructure to the step voltage load, which induces transient behavior, and waiting until the microstructure settles down to its new equilibrium position. This step makes the simulation more realistic to the scenario of already biased microstructure (in operation), which is suddenly subjected to the shock force. Not performing this step means applying the voltage load and shock simultaneously making the transient response due to the DC voltage contributes to the total response. This makes the response appear larger than what it would be in the more realistic scenario of shock while in operation. This factor however is of less importance for quasi-static pulses.

To illustrate the main dynamical features of an electrostatically actuated microstructure under shock, consider as a case study an air-gap capacitor with a cantilever microbeam as its upper electrode placed a distance $d = 3 \mu\text{m}$ from the stationary lower electrode. The microbeam is made of silicon with density $\rho = 2,332 \text{ kg/m}^3$ and modulus of elasticity $E = 169 \text{ GPa}$. The microbeam has length $l = 400 \mu\text{m}$, thickness $h = 1.0 \mu\text{m}$, and width $b = 100 \mu\text{m}$. The damping ratio is taken as $\zeta = 0.01$. We would like to use a lumped-parameter model to analyze the response of the cantilever microbeam for various shock and voltage loads. The effective mass of the beam in this case is $0.646m$, and its stiffness coefficient is $k = 8EI/l^3$. Calculating the natural period and pull-in voltage of this microbeam gives $T_{\text{structure}} = 0.116 \text{ ms}$

Fig. 8.11 The stable equilibrium positions of the cantilever microbeam tip



and $V_{\text{pull}} = 2 \text{ V}$, respectively. Figure 8.11 shows the calculated equilibrium position of the microbeam tip, as represented by z , for various values of V_{DC} (see Chap. 5 for details).

Next, the voltage load is set at $V_{\text{DC}} = 1 \text{ V}$. The equilibrium position at this V_{DC} is loaded as an initial condition of Eq. (8.11) for the subsequent simulations of the dynamic response under shock. The microbeam is then subjected to a half-sine shock load of $T = 2.0 \text{ ms}$ of maximum amplitude of $212g$, Fig. 8.12a. Figure 8.12a shows a typical quasi-static response with the amplitude peak near $z = -0.59d$, which is then settled down to the equilibrium position at $z = -0.04d$. Note here that the negative sign indicates deflection toward the electrode (see Fig. 8.10a). Increasing the shock load slightly to $213g$ leads to the collapse of the microstructure through dynamic pull-in, as revealed in Fig. 8.12b. Hence, the pair of ($V_{\text{DC}} = 1 \text{ V}$; $213g$) can be thought as a new instability threshold of the microstructure. In another word, the pull-in instability can be thought as a function of both the shock threshold and the voltage load.

Figure 8.13a shows simulation results for the maximum amplitude of the beam response, taken as an absolute value without consideration for the sign, when subjected to a wide range of shock loads for various values of V_{DC} . In the case of

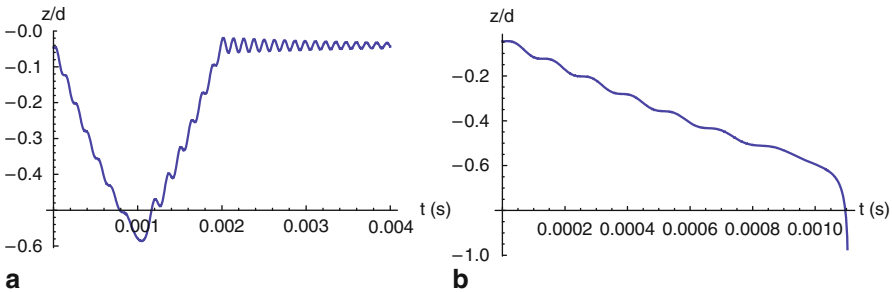


Fig. 8.12 The transient response of a cantilever microbeam actuated by $V_{\text{DC}} = 1 \text{ V}$ subjected to a half-sine shock pulse of $T = 2 \text{ ms}$ and maximum amplitude of **a** $212g$ and **b** $213g$

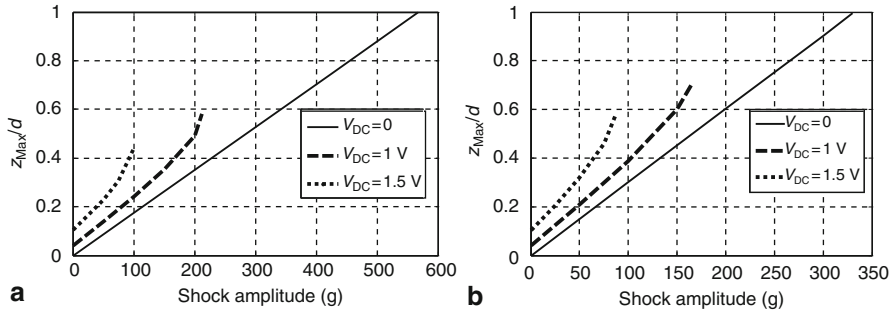


Fig. 8.13 The maximum transient response of a cantilever microbeam actuated by various V_{DC} and subjected to a half-sine shock pulse of **a** $T = 2$ ms and **b** $T = 0.1$ ms

$V_{DC} = 0$ V, one can see a linear relationship between the shock amplitude and the beam response, which is expected considering that both the stiffness and forcing are linear in this case. The solid line is terminated at shock amplitude of 570g. This is the value at which the microstructure hits the substrate ($z_{Max} = 1$) when not biased. The other dashed and dotted lines of this figure are for nonzero V_{DC} . Both start as linear curves and then turn into nonlinear toward their end. Both are terminated by the dynamic pull-in instability, at which the slope of each curve approaches infinity. The shock amplitude threshold-to-pull-in, as expected, decreases with the increase of V_{DC} (213 g for $V_{DC} = 1$ V and 89g for $V_{DC} = 1.5$ V.)

Figure 8.13b displays another family of curves similar to Fig. 8.13a for $T = 0.1$ ms. This makes the shock pulses in the dynamic range. Thus, we can see that the thresholds at which the microstructure hits the substrate, through pull-in when biased or though reaching $z_{Max} = 1$ when $V_{DC} = 0$ V, are significantly lower than the values of Fig. 8.13a. This emphasizes the importance of estimating the expected shock duration accurately in this kind of problems.

By generating several curves, such as Fig. 8.13, stability plots can be established that determine V_{DC} –shock safety zones. Figure 8.14 shows such curves for the two

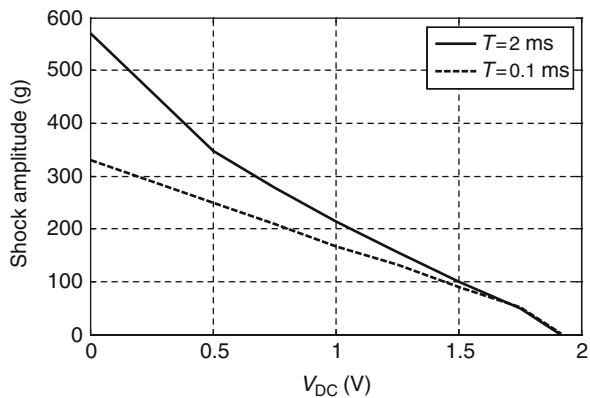


Fig. 8.14 Stability curves. Any point of (V_{DC} ; shock amplitude) above a line results in pull-in

considered shock durations. In the figure, any operating point (V_{DC} ; shock amplitude) above the line results in pull-in whereas any point below the line yields stable operation. In the case that there is uncertainty in the value of the expected shock duration, the worst-case-scenario curve is adopted for safety conclusions (in this case it is the curve of $T = 0.1$ ms). Note that these curves are established for $\zeta = 0.01$. For higher damping ratios, the dynamic duration becomes more sensitive to damping and then the curve of $T = 2$ ms may represent the worst scenario in terms of stability.

8.8.2 Beam Model

Distributed-parameter models provide more accurate results compared to lumped-parameter models. Next, we discuss a beam model for the shock and electrostatic force problem in microbeams. For this, we refer to Fig. 8.15, which shows a biased beam being excited from its support by a displacement $y(t)$. The equation of motion governing the relative deflection of the microbeam to the support $w(x,t)$ is written as

$$EI \frac{\partial^4 w}{\partial x^4} + \rho A \frac{\partial^2 w}{\partial t^2} + c \frac{\partial w}{\partial t} = \frac{-\varepsilon A V_{DC}^2}{2(d+w)^2} - \rho A \frac{d^2 y}{dt^2}. \quad (8.12)$$

Equation (8.12) is discretized using the Galerkin method and the outcome equations are integrated numerically in time, similar to the procedure of Example 6.10. As an example, consider the case study of the cantilever microbeam of Sect. 8.8.1. Using Eq. (6.131), the pull-in voltage in this case is predicted near 2.4 V. Using a 4-mode ROM, pull-in is found to be 2.38 V. Comparing this to the results based on the lumped-parameter model ($V_{pull} = 2$ V), one can see a clear difference in the results. Figure 8.16 shows the shock- V_{DC} instability curve for the case of $T = 2$ ms as compared to the results in Fig. 8.14 using a SDOF model. It is clear that the SDOF model can provide qualitative picture only. For more accurate results, a beam model needs to be utilized. It is noted in the figure that the ROM curve starts with slight decrease in magnitude. This regime is called the shock-dominated regime, where the electrostatic force has very slight magnitude and hence influence compared to the magnitude of the shock force [28]. Typically the ROM in this regime requires using at least six modes to yield accurate results.

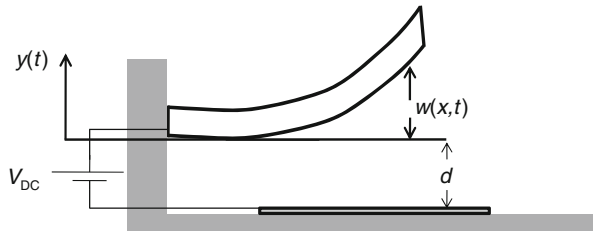


Fig. 8.15 An electrostatically actuated microbeam subjected to base motion

Fig. 8.16 Stability curves for a cantilever microbeam obtained using a lumped and a beam model

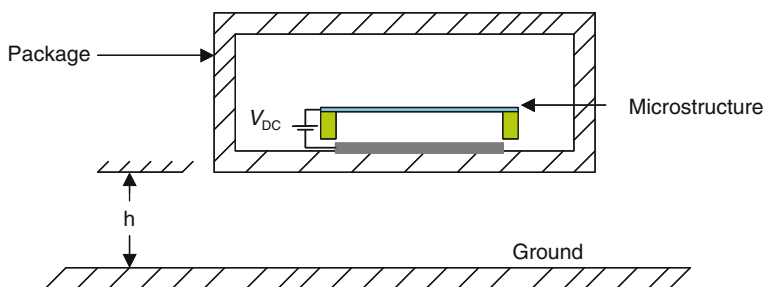
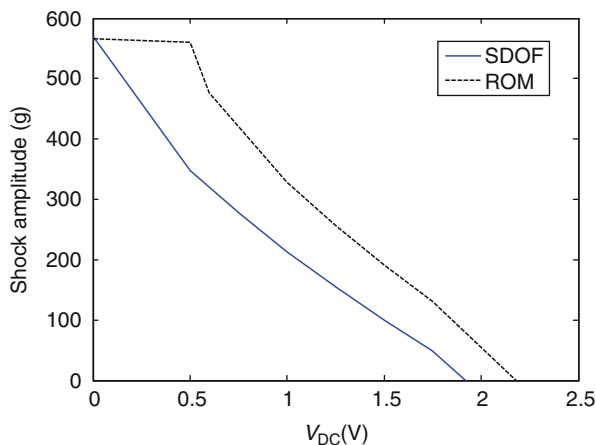


Fig. 8.17 Schematic of a packaged MEMS device being dropped on the ground. (Reprinted with permission. Copyright 2007, Elsevier [29])

In the case of a clamped–clamped microbeam under shock, Fig. 8.17, the nonlinear equation of motion needs to be used, which is written as

$$EI \frac{\partial^4 w}{\partial x^4} + \rho A \frac{\partial^2 w}{\partial t^2} + c \frac{\partial w}{\partial t} = \left[\frac{EA}{2l} \int_0^l \left(\frac{\partial w}{\partial x} \right)^2 dx + N_1 \right] \frac{\partial^2 w}{\partial x^2} + \frac{-\epsilon A V_{DC}^2}{2(d+w)^2} - \rho A \frac{d^2 y}{dt^2}. \quad (8.13)$$

As an example of this case, consider a silicon clamped–clamped beam of $l = 900 \mu\text{m}$, $h = 1.5 \mu\text{m}$, $b = 100 \mu\text{m}$, and $d = 2.0 \mu\text{m}$. Assume the microbeam to be placed in near vacuum conditions (no damping). The pull-in voltage of this microbeam is 3.38 V, and accounting for the transient effect is 3.11 V. Calculating the fundamental natural period of this microbeam, it is found near 0.1 ms. Hence, the microbeam experiences the mechanical shock load of $T = 1.0 \text{ ms}$ as a quasi-static load and of $T = 0.1 \text{ ms}$ as a dynamic load. Because of the symmetry of the load and boundary conditions of

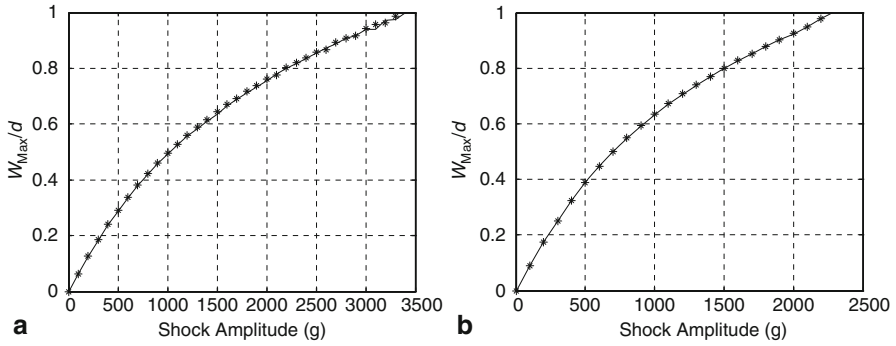


Fig. 8.18 The response of a clamped–clamped microbeam generated using a dynamic nonlinear finite-element model (*) and a reduced-order model (*solid*) for **a** $T = 1.0$ ms and **b** $T = 0.1$ ms. (Reprinted with permission. Copyright 2007, Elsevier [29])

the microbeam, the symmetric modes are the only modes that participate in the response. Hence, only those are used in the reduced-order model. Figure 8.18 shows the simulated results of the ROM using the first symmetric four modes as compared to results generated using a nonlinear multi-physics finite-element model [29]. It is noted from Fig. 8.18 that the microbeam deflection changes nonlinearly with the shock amplitude. Using a linear beam model in this case yields inaccurate results. We can note full agreement among the ROM and finite-element results. According to the figure, the unbiased microbeam is likely to hit the substrate under a shock load of amplitude 2,300–3,400g.

Next, we study the effect of the electrostatic force on the stability of the microbeam. Figure 8.19 shows comparisons between the results of the reduced-order model employing four and six modes to the results of a nonlinear multi-physics finite-element model for the cases of $T = 1$ ms and $T = 0.1$ ms. It is clear that using

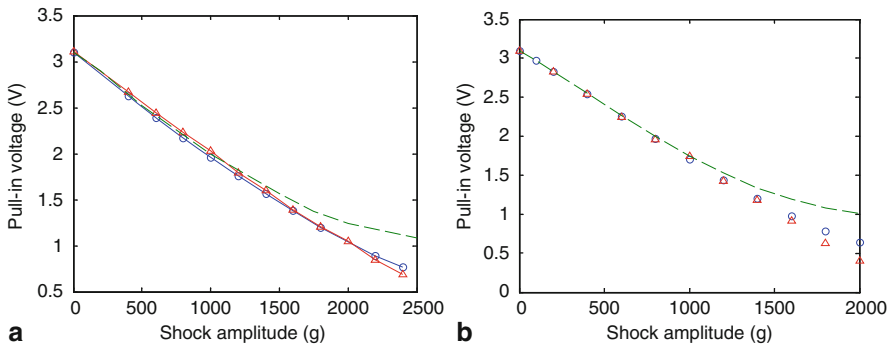


Fig. 8.19 Clamped–clamped beam stability curves generated using a dynamic finite-element model (*triangles*), a ROM employing four (*dashed*) and six (*circles*) modes for **a** $T = 1.0$ ms and **b** $T = 0.1$ ms. (Reprinted with permission. Copyright 2007, Elsevier [29])

at least six modes are required to capture accurately the instability curves in this case. This is computationally still much cheaper than using the multi-physics nonlinear finite-element model.

8.8.3 *Switch Application*

One can take advantage of the instability induced by the combined effect of shock and electrostatic force for the development of a switch triggered above a certain level of acceleration. Such a device consists of a biased microstructure, such as that of Fig. 8.15 or Fig. 8.17, where the applied DC voltage is used to set the acceleration level where instability occurs. One could tune the DC voltage on the microbeam so that it collapses when the device experiences acceleration beyond a specific threshold. Below the threshold, the beam only deflects slightly due to acceleration. If the acceleration exceeds a specific threshold, the microbeam snaps down to close an electric circuit as a switch. This switching mechanism is very desirable in many applications, such as to trigger airbags in vehicles and to protect portable devices upon impact.

To illustrate the principle of the switch, consider the cantilever microbeam of the instability curve of Fig. 8.16. Assume that the expected shock duration on the microbeam is in the quasi-static regime. If it is desired to induce an action and close a switch at a shock level of 350g or beyond, one can bias the microbeam by $V_{DC} = 1$ V, for instance. As seen from the figure, above this shock range, the microbeam should collapse by pull-in. Below this shock level, the microbeam should deflect slightly during shock without any contact with the lower electrode (maintain the open circuit position). By employing stiffer microstructures as the switching element, the range of detected acceleration can be made higher. For example, the clamped-clamped microbeam of instability curves of Fig. 8.19 can be made to detect acceleration level of 1,000g or more. Also, the threshold of acceleration detection can be made lower by designing more compliant microstructures as the switching elements.

8.8.4 *Experiments*

In this section, we present experimental data on the combined effect of shock and electrostatic forces. Two case studies are discussed, one of very compliant structure that is sensitive to very low g levels and the other of a very stiff microstructure that requires hundreds of thousands of g s to be brought down to the substrate.

8.8.4.1 *Capacitive Sensor*

The capacitive sensor, which is the subject of investigation in Chap. 7, is considered as the first case study [30] (see Sect. 7.1 for details about the device). This device is

intended originally to be used as a low- g accelerometer. Hence, it is very sensitive to low levels of acceleration. The device was mounted on the head of a programmable electromagnetic shaker that can produce low acceleration pulses. Also, the device was electrically connected to a DC power supply. A laser Doppler vibrometer was used to monitor the time domain response of the accelerometer's proof mass. A reference accelerometer was mounted on the head of the shaker to measure its acceleration. The LabView software was used to generate the required output signals and to read the input signals. Figure 8.20 shows the experimental set up and data acquisition system used in the experimental investigation.

To determine the onset of pull-in, a simple electric circuit was used, which consists of a current-limiting resistor and a small resistor ($470\ \Omega$) that was added to monitor the induced voltage V_0 across it with an A/D LabVIEW input channel. If the measured voltage V_0 is greater than zero, then this indicates pull-in. The pull-in voltage was found for the considered device to be approximately 169.7 V. Figure 8.21 shows the measured transient response of the proof mass of the device for step voltage loads below and at the pull-in voltage.

Figure 8.22 shows the measured transient response of the proof mass of the device when subjected to an acceleration pulse, of sine shape, of magnitude 13.0g and

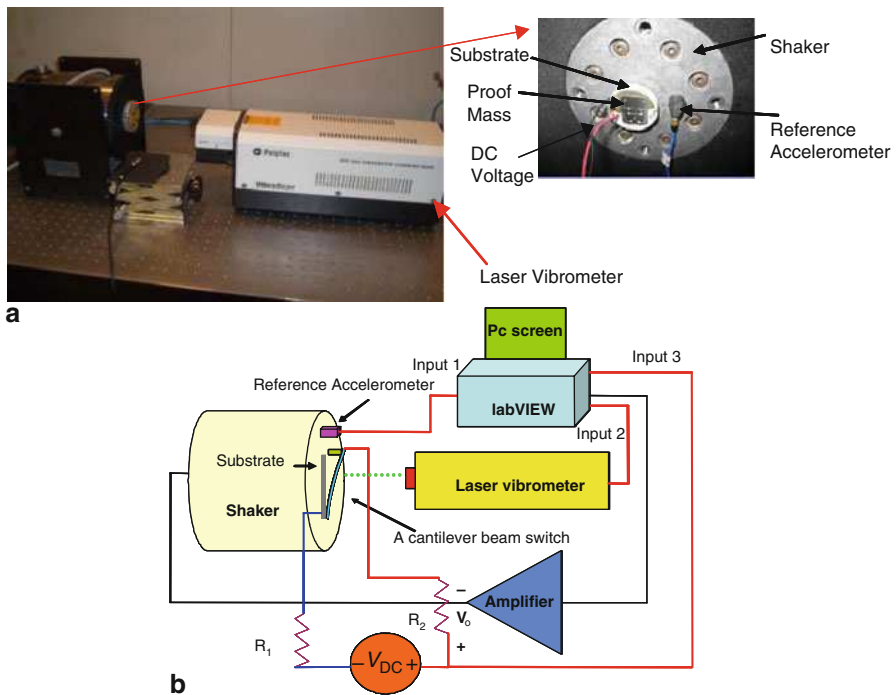


Fig. 8.20 **a** A picture of the experimental set up used for testing. **b** Schematic of the experimental setup and the data acquisition system. (Reprinted with permission. Copyright 2007, IOP Publishing Ltd [30])

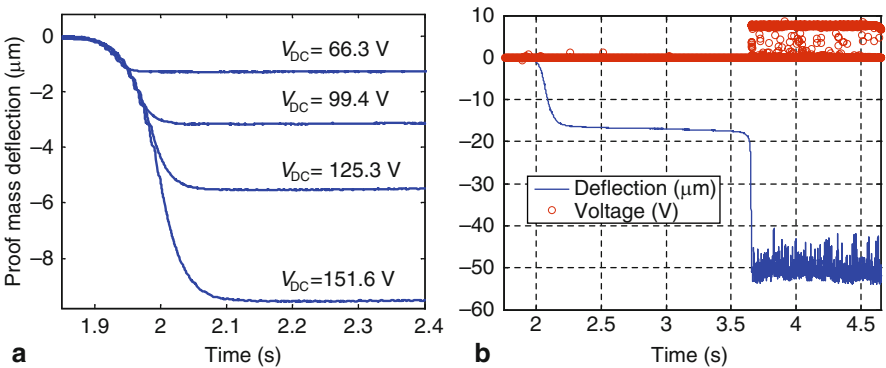


Fig. 8.21 **a** The transient response of the proof mass for different voltages below pull-in. **b** The transient response of the proof mass at the pull-in voltage at $V_{DC} = 169.7\text{ V}$. Also shown in **(b)** is the reading of the induced voltage across the current-limiting resistor. (Reprinted with permission. Copyright 2007, IOP Publishing Ltd [30])

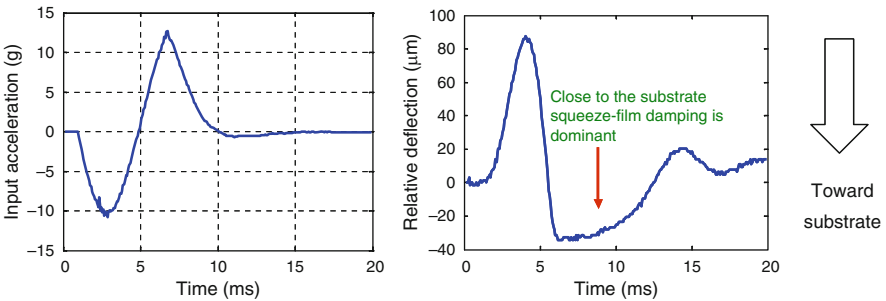
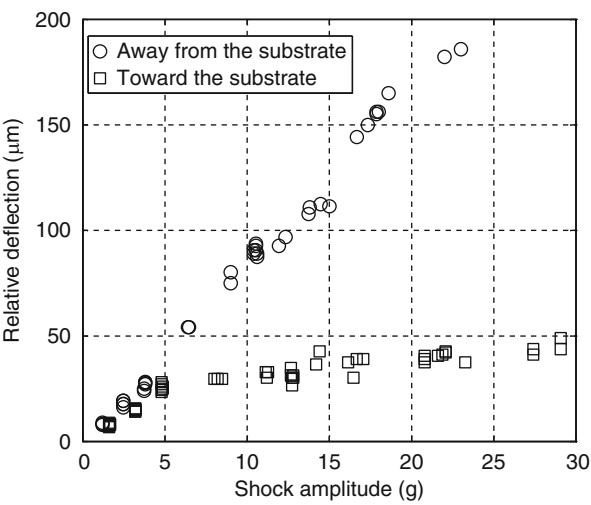


Fig. 8.22 The transient response of the proof mass when subjected to mechanical shock only as monitored through a laser Doppler vibrometer. (Reprinted with permission. Copyright 2007, IOP Publishing Ltd [30])

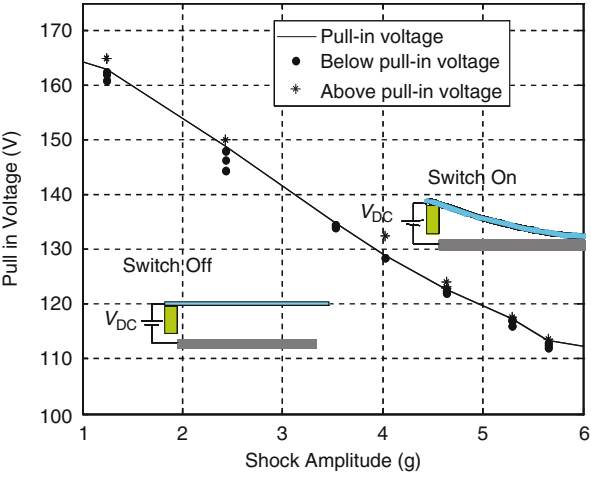
duration $T = 5.0\text{ ms}$, which is close to the natural period of the beams carrying the proof mass of 5.3 ms . It can be seen that the response is asymmetric due to the effect of squeeze-film damping, which becomes more significant when the proof mass moves down toward the substrate (note here that the device is operated at ambient pressure, unlike the case of Chap. 7). This asymmetric response is illustrated further in Fig. 8.23, which shows the measured relative deflection versus the shock amplitudes. The figure shows the deflection of the proof mass in both directions, toward the substrate and away from the substrate. For small values of mechanical shock, both deflection curves (toward and away from the substrate) are on top of each other indicating that the damping mechanism in both directions affects the proof mass linearly. However, as the value of the shock amplitude increases, both curves deviate from each other significantly. This is because of the increasing effect of the nonlinear squeeze-film damping that becomes dominant as the proof mass approaches the substrate.

Fig. 8.23 The maximum deflection of the proof mass at different shock levels for the cases when the proof mass moves toward and away from the substrate. (Reprinted with permission. Copyright 2007, IOP Publishing Ltd [30])



Next, the proof mass was excited by both electrostatic force and mechanical shock. Figure 8.24 shows the experimentally measured instability curve of the pull-in voltage versus the shock amplitude. As seen from the figures, the pull-in voltage is dropped from 169.7 V at 0.0g to 110.0 V at shock amplitude of 6.75g. This verifies the conclusions of the previous sections about the possibility of inducing early dynamic pull-in due to shock. Also, the basic idea of the switch triggered by acceleration of Sect. 8.8.3 can be understood here by observing Fig. 8.24. One can tune the desirable threshold of actuation for the switch by adjusting the DC bias. If the acceleration exceeds the threshold value, the microbeam snaps down to close an electric circuit as a switch (ON state); otherwise the switch will remain open (OFF state).

Fig. 8.24 The experimentally measured pull-in voltage of the device versus the shock amplitude of a sine pulse of duration $T = 5.0$ ms. Points below the solid line represent the switch in the off-position while points on or above the solid line represent the switch in the on-position. (Reprinted with permission. Copyright 2007, IOP Publishing Ltd [30])



8.8.4.2 Cantilever Microbeams

Next, a cantilever microbeam made of gold of length $50\text{ }\mu\text{m}$, thickness $1.5\text{ }\mu\text{m}$, and an estimated gap width of $1.5\text{ }\mu\text{m}$ is subjected to a drop table test. Since this microbeam is too short, it requires very high level of g s to be brought down to touch the substrate (more than $200,000g$) [34]. Such a high level of g is hard to be generated experimentally. Hence, one way to overcome this issue is by biasing the beam by a voltage load close to pull-in, which enables testing its collapse under lower level of shock force using available in-house shock equipments. While this does not eliminate the need to test the beam under very high- g level, it represents an intermediate testing step.

The experimental set-up of this investigation, shown in Fig. 8.25, consists of a drop-table machine, a DC power supply, and a LabView card. The tested microbeam is wire-bonded to a chip, which is then hooked up to a DC power supply to actuate the microbeam with an electrostatic force. The chip is mounted on top of the table of a drop-table machine (a Lansmont Model 23). A reference accelerometer is mounted on the table of the drop-table machine to measure its acceleration. The chip was hooked up to a data acquisition system to monitor the resistance of the capacitor circuit of the microbeam during the drop test, and hence enable live monitoring of the collapse of the microbeam during the test. The LabView acquisition system is used to measure the voltage V_0 across the resistor R_2 shown in Fig. 8.26. The resistors

Fig. 8.25 The experimental set up showing a MEMS chip mounted on a drop-table test while being biased by a DC voltage. (Reprinted with permission. Copyright 2010, IEEE [34])

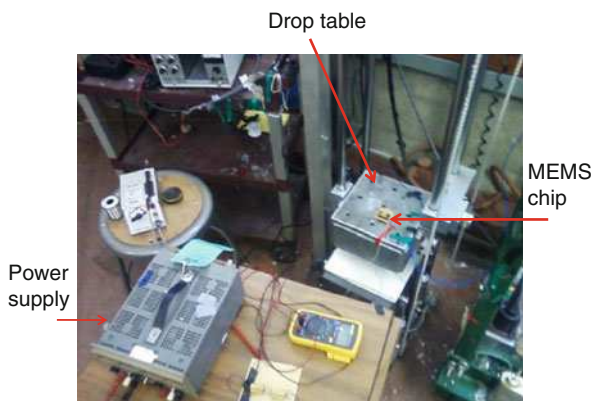


Fig. 8.26 Schematic of the experimental set up. (Reprinted with permission. Copyright 2010, IEEE [34])

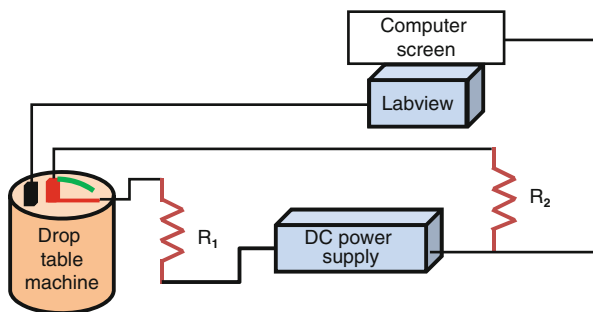


Table 8.3 The results of a drop-table test of an electrostatically actuated microbeam [34]

Applied voltage (V)	Applied shock load (g)	Test result
75	1,500	No pull-in
80	1,500	No pull-in
83.1	1,500	Pulled-in
82.5	1,500	Pulled-in
80.1	1,500	No pull-in
80.1	1,924	No pull-in
80.1	2,363	Pulled-in

R_1 and R_2 are designed so that $V_0 \neq 0$ V when the device experiences pull-in and $V_0 = 0$ V otherwise.

The pull-in of the microbeam was first measured experimentally without shock and found to be near 84 V. Then, the drop table is used to produce shock loads of duration near 1.8 ms while the microbeam was biased by large voltages below pull-in. The results are shown in Table 8.3. The obtained results demonstrate sensitivity of the microbeam to slight variations in shock or electrostatic force, as predicted theoretically in the previous sections. As noted, by biasing the microbeam with a DC load near its static pull-in voltage, the threshold of collapse can be brought down considerably to a range of acceleration that enables conducting a drop-table test on the device.

8.9 Resonators Under Shock

Resonators are commonly employed in resonant sensors, where they are operated at low pressure for enhanced sensitivity making their response to external disturbances such as shock a critical issue. In this section, we investigate the response of resonators, actuated electrically by a DC load superimposed to an AC harmonic load, when subjected to mechanical shock [32]. For simplicity, a SDOF system is used to model the resonator. Experimental work is then shown.

8.9.1 Simulations

We shall use the model of Fig. 8.10 with the addition of the AC harmonic load. Accordingly, the equation of motion of the resonator is written as

$$m_{\text{eff}}\ddot{z} + c\dot{z} + kz = \frac{-\varepsilon A[V_{\text{DC}} + V_{\text{AC}} \cos(\Omega t)]^2}{2(d+z)^2} - m\ddot{y}. \quad (8.14)$$

Equation (8.14) is integrated numerically in time using the Runge–Kutta scheme to obtain the resonator response for various loading conditions. As a case study, we investigate the response of the capacitive sensor of Chap. 7 when operated as

a resonator. For the considered sample of this investigation, the cantilever beams carrying the proof mass has a stiffness coefficient $k = 124 \text{ N/m}$ and a fundamental natural frequency of 187 Hz . The gap size d is measured as $47.5 \mu\text{m}$. The pull-in voltage of the accelerometer is measured as 112 V under zero shock loading. When operated at reduced pressure, an acceleration of $3g$ is sufficient to bring the poof mass down to the substrate. Thus, in the following, low levels of acceleration will be assumed in the simulation. The resonator is assumed to have a linear damping ratio of $\zeta = c/(2m\omega_n) = 0.006$, where ω_n is the fundamental natural frequency of the device. This value of low damping ratio is typical for a resonator operating at reduced pressure.

Predicting the effect of shock on the dynamic response of a resonator can be challenging due to the oscillatory motion of the resonator and how it interacts with the shock load. This is especially important when the excitation frequency and the shock frequency (inverse of shock duration) are of comparable magnitude. At the time instant when shock hits the resonator, T_{AP} , the resonator can be either moving in the direction or opposite direction of the shock force. Hence, the effect of the shock can either add to the influence of the AC force or reduce it depending on the direction of motion compared to the shock pulse at the moment of impact.

Figure 8.27 shows examples of the simulated response of the electrically actuated resonator when a $1g$ shock pulse applied at two different time instances. In the figure, the excitation frequency is assumed to be equal the natural frequency. In Fig. 8.27a, shock amplifies the resonator response, which reaches a peak value near $25 \mu\text{m}$. In Fig. 8.27b, with shock being applied just 2.3 ms latter, the response of the resonator is attenuated to be less than $4 \mu\text{m}$ before it goes back to the steady-state level of vibrations before shock.

Next, we illustrate the procedure for calculating the SRS of the resonator. In order to ensure covering all the possibilities of the dynamic response for a given shock pulse duration T , the shock is applied at various time instances (T_{AP}) during one full steady-state oscillation of the resonator. In other words, if the resonator oscillation period is T_{AC} , the shock is applied at various fractions of T_{AC} . For each time instance of the applied shock, the maximum displacement of the resonator is calculated. To capture the worst case scenario of the response, the maximum displacement is calculated by comparing the results of all the time instances. Figure 8.28 shows a plot of the resonator maximum response to an applied shock of amplitude $1g$, applied at different T_{AP} during two full cycles of oscillations. Curves, similar to Fig. 8.28, are generated for various values of shock duration. Of each curve, the maximum response is extracted. The ensemble of these data points yields the SRS. Figure 8.29 shows an example of the SRS of the resonator due to shock, DC load, and an AC load for the case when the resonator is excited at its fundamental natural frequency. The results are normalized by the gap width d .

Figure 8.30a, b depicts the shock spectrum for various AC loads when subjected to a shock load of amplitude $1g$ while biased by $V_{DC} = 20 \text{ V}$ and 30 V , respectively. The frequency of the AC load is set at $\Omega = \omega_n$. To emphasize the dynamic amplification due to shock when varying V_{AC} , without mixing the contribution of V_{AC} itself in the amplification, the maximum response of the resonator due to the DC and AC

Fig. 8.27 Time history response of the resonator at $V_{DC} = 30\text{ V}$ and $V_{AC} = 15\text{ V}$ when subjected to a shock pulse of amplitude $1g$ and $T = 5\text{ ms}$. (Reprinted with permission. Copyright 2010, IOP Publishing Ltd [32])

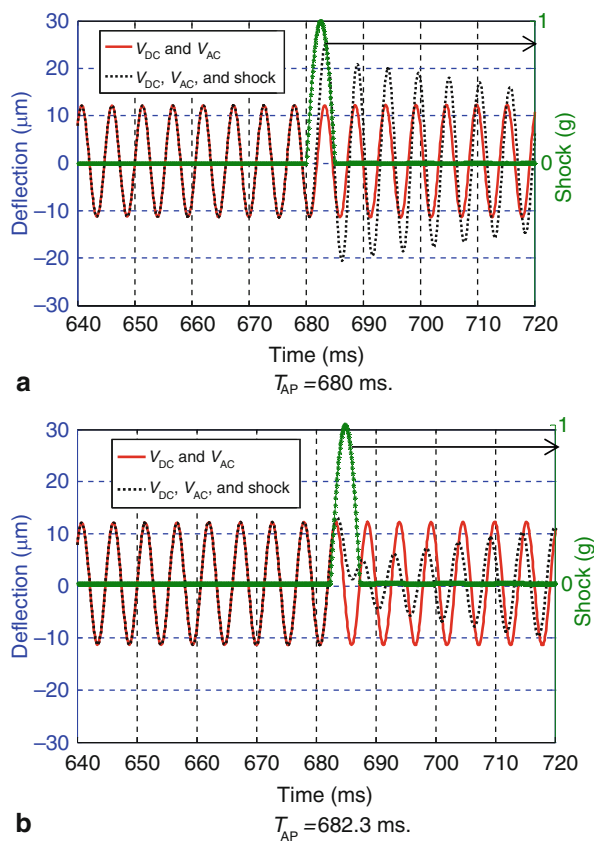


Fig. 8.28 The maximum response of the resonator for the parameters of Fig. 8.27. (Reprinted with permission. Copyright 2010, IOP Publishing Ltd [32])

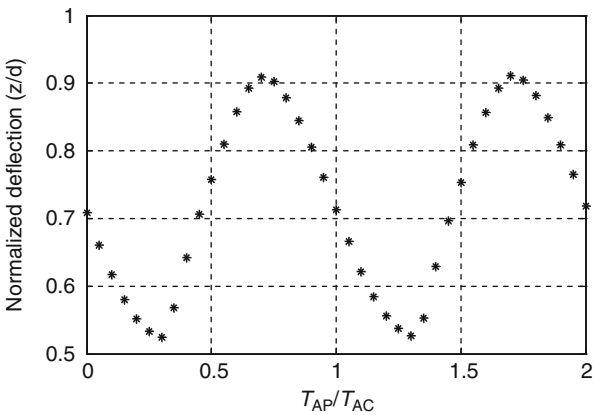
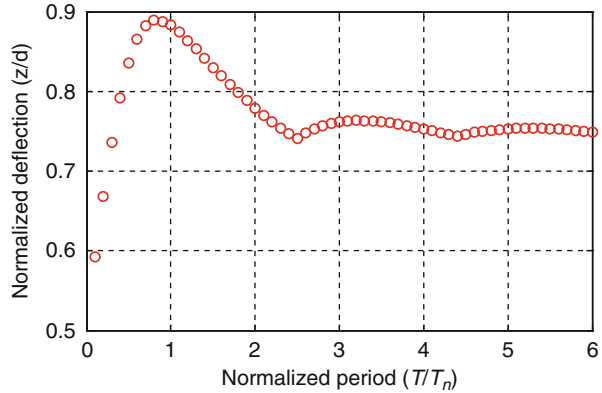


Fig. 8.29 The shock-response spectrum of the resonator for the parameters of Fig. 8.27. (Reprinted with permission. Copyright 2010, IOP Publishing Ltd [32])



harmonic load is subtracted from the total dynamic response due to the AC, DC, and shock loads. Before discussing the AC effect, it is worth to note the effect of the DC load alone on the shock spectrum. By comparing the SRS of the two figures for the case of zero AC load (solid lines), one can see that a higher DC load softens the structure and raises its dynamic response. This softening influence is mainly linear (V_{DC} reduces the total linear stiffness of the system), and hence it affects the spectrum regardless of the magnitude of the shock amplitude. More on the effect of V_{DC} on the SRS can be found in [33].

Next, we compare the several spectrum curves for various AC loads while keeping the DC load constant. Considering Fig. 8.30a, it is noted that as V_{AC} increases, the dynamic response increases until reaching pull-in, as seen from the open zones in the spectrum in the cases of $V_{AC} = 17$ V and $V_{AC} = 20$ V. Within these “pull-in bands” in the spectrum, the resonator is forced to pull-in if it is subjected to a shock pulse of duration within these bands. This clearly shows that accounting for the effects of the AC harmonic load and the DC voltage when studying the reliability of the resonator under mechanical shock is crucial. Figure 8.30b shows similar behavior. However, one can see that despite raising the total electric load ($V_{AC} + V_{DC}$), the dynamic response seems to be less sensitive to shock compared to Fig. 8.30a. Compare for example the case of $V_{DC} = 20$ V and $V_{AC} = 10$ V to the curve of $V_{DC} = 30$ V and $V_{AC} = 10$ V, where the maximum response in the latter case is lower than that of the first case. The reason for this is due to the fact that as V_{DC} is increased, the quadratic nonlinearity of the electrostatic force gets stronger. This in turn weakens the dynamic response, since the nonlinearity tends to cap or suppress the response.

8.9.2 Experimental Results and Comparison with Simulations

This section discusses some of the experimental results generated to verify the theoretical findings. Comparison with the simulation results is also made. Figure 8.31 shows the experimental setup used in this work. The device was mounted on a shaker

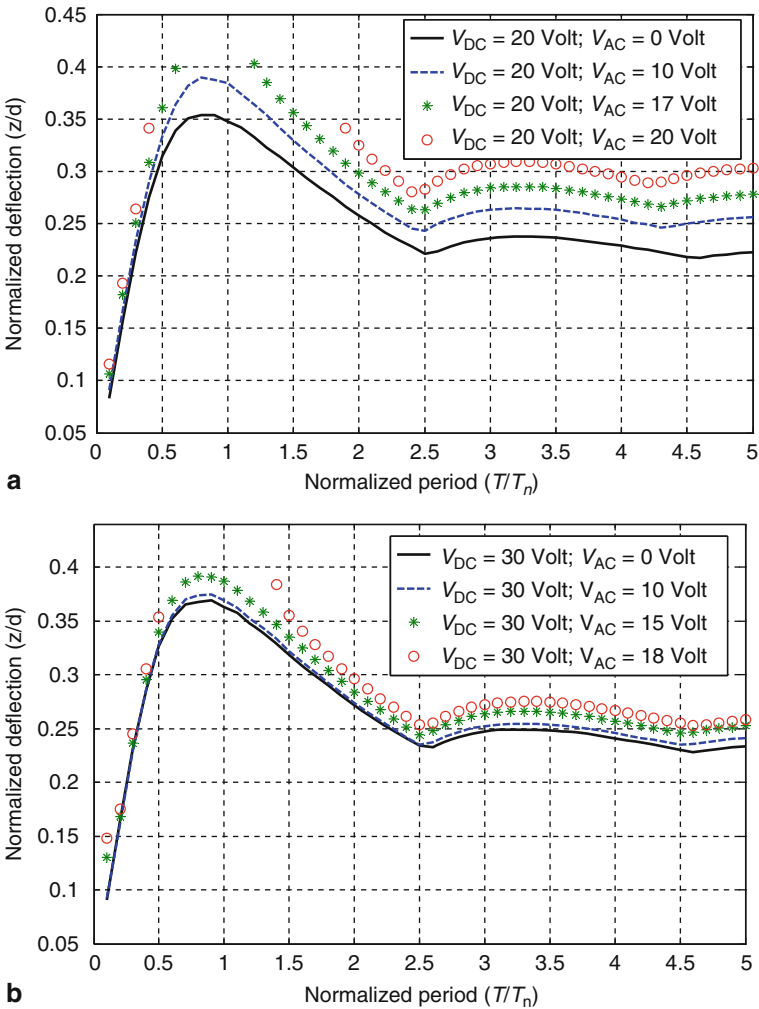


Fig. 8.30 The shock-response spectra of the resonator for various V_{AC} for an applied shock load of amplitude $1g$ and **a** $V_{DC} = 20$ V and **b** $V_{DC} = 30$ V. (Reprinted with permission. Copyright 2010, IOP Publishing Ltd [32])

head and connected to a DC and AC voltage power supply. Current limiting resistors were used in the circuit to avoid failure of the device in the case of pull-in. The shaker was placed inside a vacuum chamber with a quartz glass window. A reference accelerometer was also mounted on the shaker head to monitor the value of shock applied to the device. A laser vibrometer was used to monitor the response of the device proof mass. All input and output signals were controlled through the LabView software through a data acquisition card.

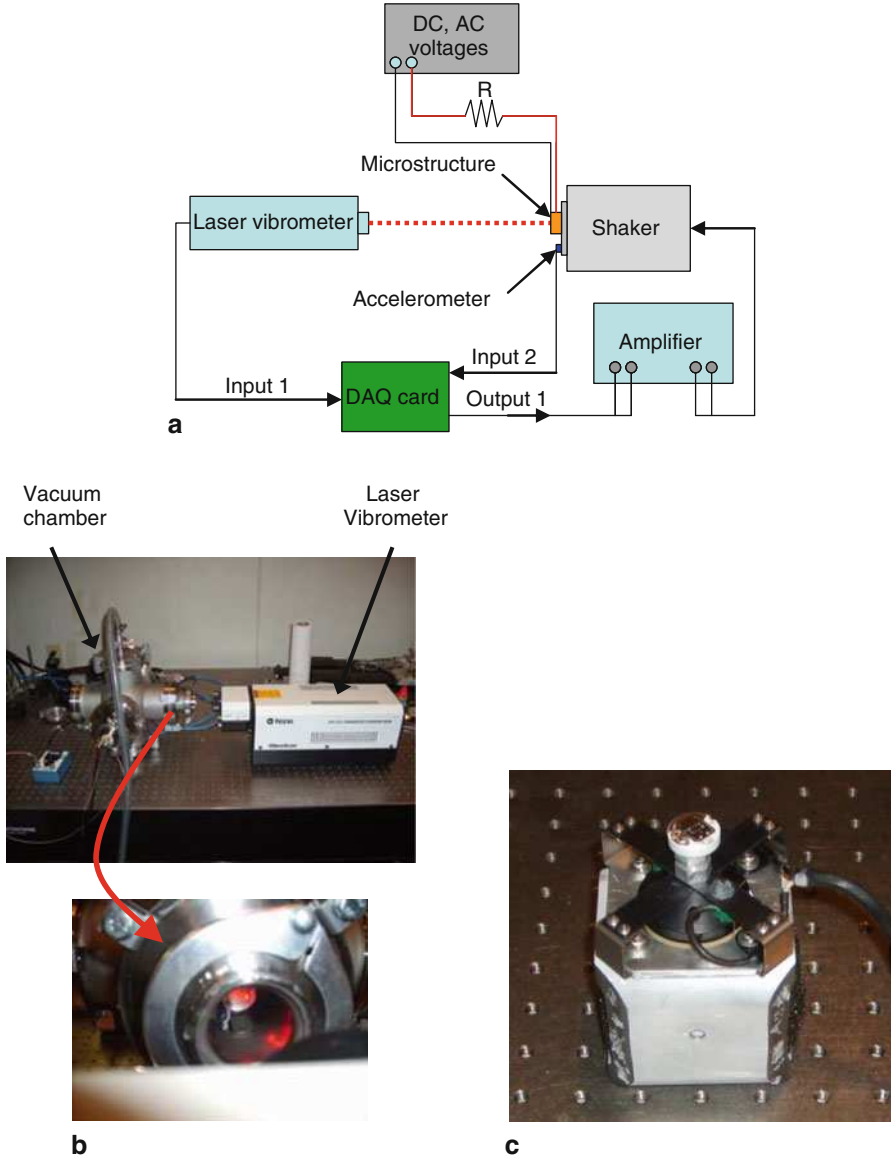
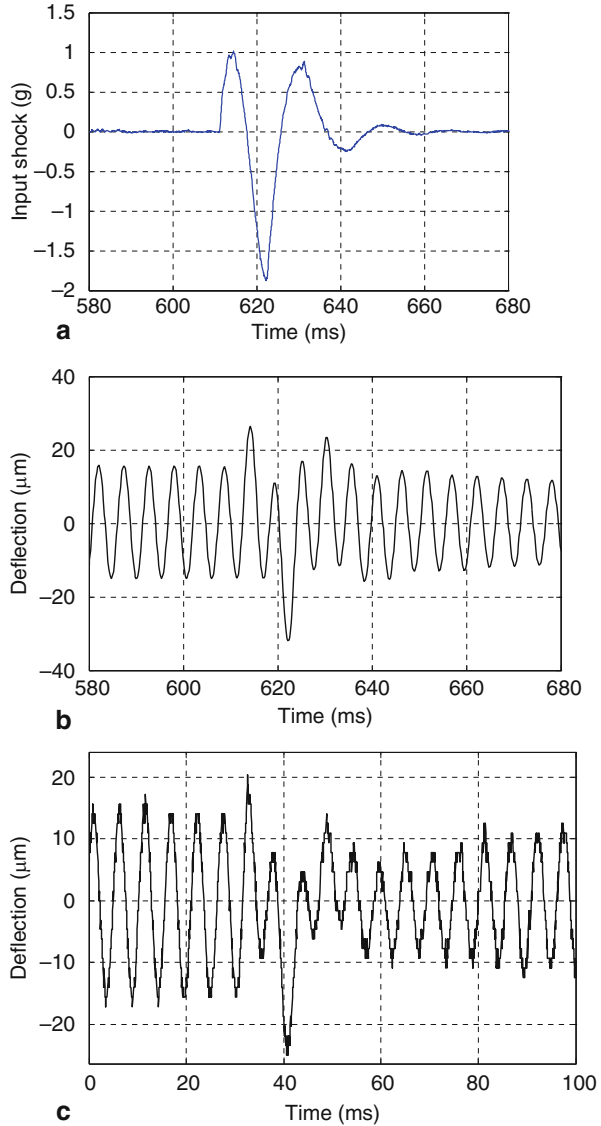


Fig. 8.31 **a** Schematic of the experimental setup. **b** A picture of the experimental setup. **c** A picture of the shaker, which is used inside the vacuum chamber to generate shock pulses. (Reprinted with permission. Copyright 2010, IOP Publishing Ltd [32])

To facilitate the comparison between simulations and experiments, the input shock profile is imported directly from the experiment to be used in the simulation model. The parameter T_{AP} is approximated by carefully looking at the time history of the

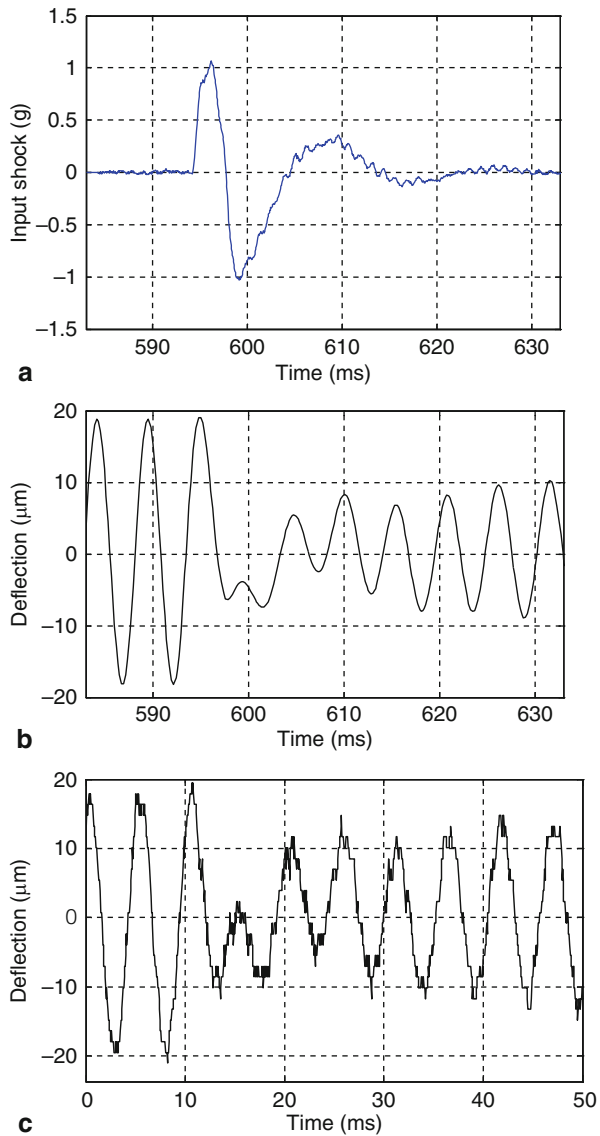
Fig. 8.32 Theoretical and experimental results of the resonator demonstrating amplification of the response due to shock. **a** The experimental pulse input of duration $T = 20$ ms. **b** The simulated time history response. **c** The measured time history response. (Reprinted with permission. Copyright 2010, IOP Publishing Ltd [32])



resonator response and the input shock. The rest of parameters are imported directly from the experiment to the model.

Next, three different cases are generated and compared theoretically and experimentally, where the resonator response is amplified, attenuated, and pulled-in. First, the resonator was actuated with $V_{DC} = 24.3$ V, $V_{AC} = 18.9$ V, and $\Omega = 189$ Hz. The resonator was operated at a reduced pressure of 180 mtorr. The resonator was subjected to the acceleration pulse of Fig. 8.32a. Figure 8.32b shows the theoretical results and Fig. 8.32c shows the experimental measurement for the same studied

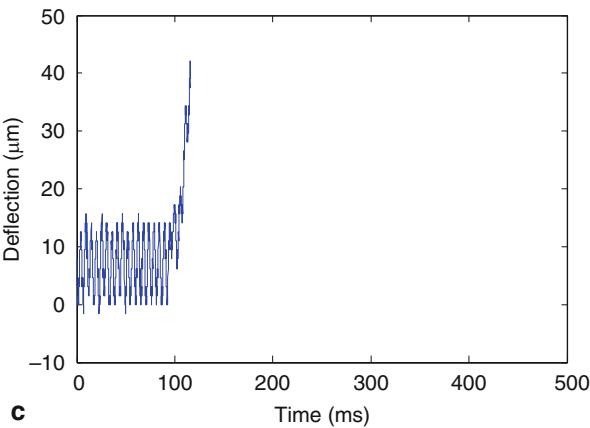
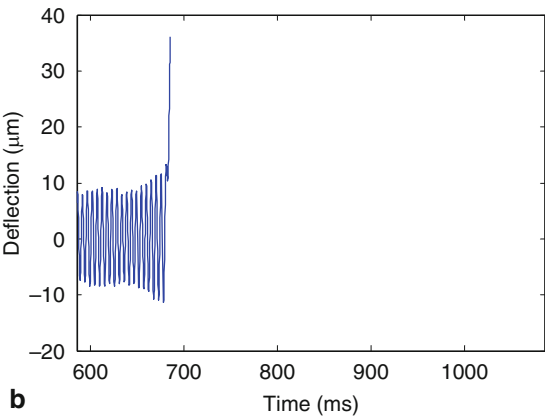
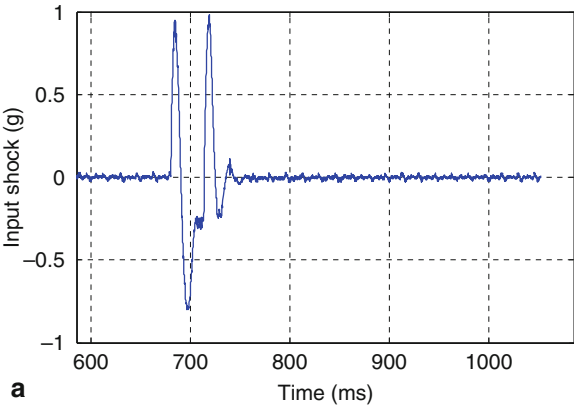
Fig. 8.33 Theoretical and experimental results of the resonator demonstrating amplification of the response due to shock. **a** The experimental pulse input of duration $T = 10$ ms. **b** The simulated time history response. **c** The measured time history response. (Reprinted with permission. Copyright 2010, IOP Publishing Ltd [32])



case. Both simulation and experimental results indicate that the dynamic response amplitude is amplified compared to the steady-state response without shock. The simulation and experimental results are in good agreement.

In the second case, the resonator was actuated with $V_{DC} = 25$ V, $V_{AC} = 18.0$ V, and $\Omega = 188$ Hz. The acceleration pulse, the simulated response, and the measured experimental response are depicted in Fig. 8.33. Both the theoretical and experimental results show that the resonator response is attenuated. In the third case, the resonator

Fig. 8.34 Theoretical and experimental results of the resonator demonstrating dynamic pull-in due to shock. **a** The experimental pulse input of duration $T = 45$ ms. **b** The simulated time history response. **c** The measured time history response. (Reprinted with permission. Copyright 2010, IOP Publishing Ltd [32])



was actuated with $V_{DC} = 19.2$ V, $V_{AC} = 21.2$ V, and $\Omega = 187$ Hz. The acceleration pulse, the simulated response, and the measured experimental response are depicted in Fig. 8.34. Both theory and experiment show that the resonator reaches an early dynamic instability and pulls-in.

8.10 The Effect of the PCB Motion

Thus far, we have assumed that the shock load is transmitted directly to the MEMS device without any attenuation or amplification through its package or mounting mechanism. In commercial devices and electronics, MEMS devices are likely to be placed on top of a printed circuit board (PCB) to facilitate the electrical interconnections and the structural support, Fig. 8.35. From a structural point of view, a PCB can be viewed as a flexible structure, such as a plate or a beam. Hence, when subjected to shock, it can amplify the shock pulse or attenuate it. With the quest for minimizing the size and thickness of hand-held devices, there is an increasing trend in the electronics and IC industry to manufacture PCBs as thin and flexible as possible. This means that the PCB is now more susceptible to experience considerable bending motion when subjected to mechanical shock and vibration. This motion can be transmitted to the microstructure leading to either its collapse or false functionality. In addition, a possible coupling in the response of PCBs with microstructures may occur when their natural frequencies get close to each other, which causes resonance-like effect amplifying the shock influence significantly. In this section, we illustrate some of these issues using a two-degree-of-freedom (2-DOF) model of a microstructure mounted over a PCB [31].

Figure 8.36 shows the 2-DOF model that is utilized. The first DOF accounts for the PCB motion, x_2 . The second DOF represents the motion of the microstructure, x_1 , which is mounted over the PCB. The rest of variables in Fig. 8.36 are defined as k_m : microstructure stiffness, k_{PC} : PCB stiffness, c_m : microstructure damping, c_{PC} : PCB damping, m_m : microstructure mass, and m_{PC} : PCB mass. Based on this model, the coupled equations of motion of the microstructure and PCB can be written, respectively, as

$$m_m \ddot{x}_1 + k_m(x_1 - x_2) + c_m(\dot{x}_1 - \dot{x}_2) = 0 \quad (8.15)$$

$$m_{PC} \ddot{x}_2 - k_m(x_1 - x_2) - c_m(\dot{x}_1 - \dot{x}_2) + k_{PC}x_2 + c_{PC}\dot{x}_2 = k_{PC}y + c_{PC}\dot{y} \quad (8.16)$$

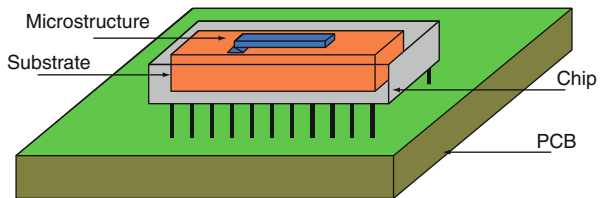
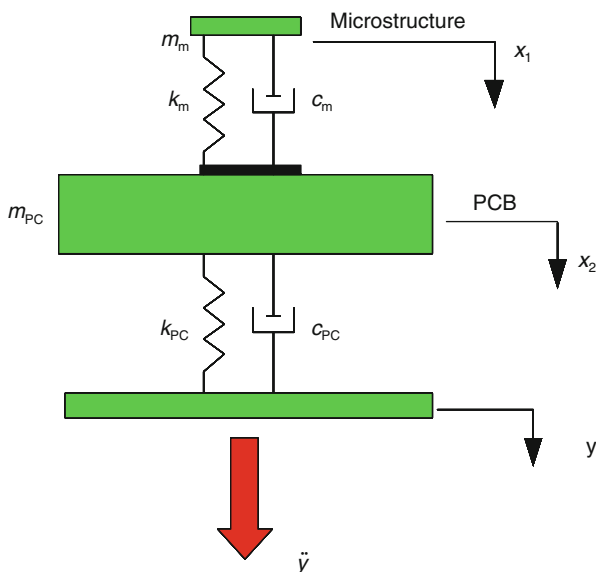


Fig. 8.35 Schematic of a MEMS chip placed on top of a PCB

Fig. 8.36 A 2-DOF model of a microstructure mounted on a PCB subjected to a base acceleration input. (Reprinted with permission. Copyright 2009, IEEE [31])



where y and \dot{y} are the displacement and velocity of the assembly base, respectively. The base acceleration \ddot{y} is assumed to be the input to this model, in the form of a half-sine pulse, which is integrated numerically in time to yield y and \dot{y} . Equations (8.15) and (8.16) can be solved analytically using modal analysis as explained in Sect. 2.7.2.

As a case study, the behavior of a microstructure of a fundamental natural frequency of 24 kHz is considered. Figure 8.37a, b shows the maximum relative amplitude of the microstructure with respect to the PCB ($x_1 - x_2$). The response in this figure and all subsequent ones is normalized with respect to the static deflection

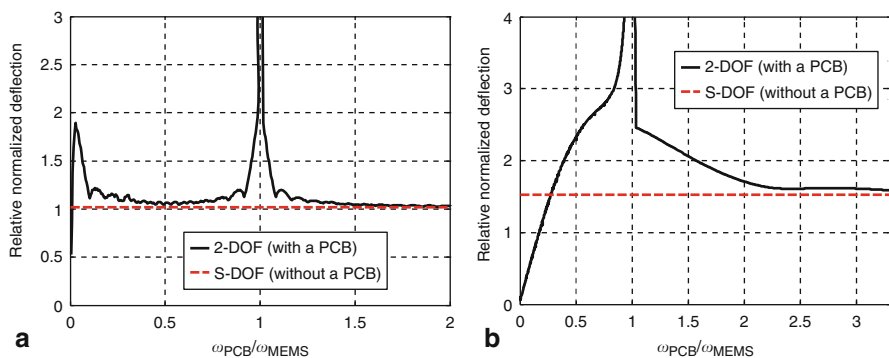


Fig. 8.37 The undamped 2-DOF response spectrum of a microstructure subjected to a base shock load of **a** $T = 1.0$ ms and **b** $T = 60 \mu\text{s}$. Shown in *dashed lines* are the responses of the microstructure without a PCB. (Reprinted with permission. Copyright 2009, IEEE [31])

of the microstructure to an equivalent static load. Results are shown for a range of the natural frequency of the PCB ω_{PCB} with two values of shock duration $T = 1.0$ ms and $T = 60$ μ s. In the figures, the damping ratio is assumed zero, considering the worst-case scenario for a shock response. The figures show that the MEMS response is always amplified due to the presence of the PCB except for the zones where the natural frequency of the PCB is very low (the response is attenuated) and very high (the response is the same as if there is no PCB). Moreover, as the shock duration decreases the amplification amplitude increases.

One can note that in Fig. 8.37a the response is amplified in two zones. The first zone is defined when the PCB experiences the shock load as a dynamic load (its natural period is close to the shock duration). Note that the first amplification occurs near $\omega_{\text{PCB}}/\omega_{\text{MEMS}} \approx 0.05$, hence in this case $\omega_{\text{PCB}} \approx 1.2$ kHz, which means a natural period very close to the shock duration $T = 1.0$ ms. The second zone is defined when the fundamental natural frequency of the PCB coincides with that of the microstructure, which causes a resonance-like effect. On the other hand, Fig. 8.37b shows only one amplification zone near $\omega_{\text{PCB}}/\omega_{\text{MEMS}} \approx 1$ with wider bandwidth compared to Fig. 8.37a (in this case $\omega_{\text{PCB}} \approx \omega_{\text{MEMS}} \approx 1/T$).

The conclusion of Fig. 8.37 that the response is determined through three parameters ω_{PCB} , ω_{MEMS} , and T , or its inverse in the frequency language $\omega_{\text{pulse}} = 1/T$. Hence, 3-D response spectra as a function of these three parameters can be established. Figure 8.38 shows two examples of such for two different damping ratios. These are considered universal plots for the normalized deflection of any microstructure as a function of the shock frequency, the PCB natural frequency, and the natural frequency of the microstructure. Such plots can serve as a guideline for MEMS designers to ensure reliable operation of their various MEMS devices when mounted over a PCB.

The effect of PCBs in amplifying the shock response has been investigated experimentally in [31]. In this investigation, the capacitive accelerometer of Chap. 7 has been placed on top of a PCB of a fundamental natural frequency 230 Hz, which is close to that of the accelerometer (the ratio of the natural frequency of PCB to the that of the accelerometer is 1.23). The PCB was mounted on top of a shaker, Fig. 8.39, and then the capacitive accelerometer was mounted on top of the PCB. The whole assembly was then subjected to acceleration pulses from the shaker. The response of the accelerometer proof mass was monitored using a laser Doppler vibrometer. Also, in a separate experiment, the device was mounted directly on the shaker to compare its dynamical response to that with the PCB effect. Figure 8.40 shows a comparison of the measured transient response of the proof mass with and without the PCB. It is clear that the PCB has significant effect in amplifying the response of the sensor. Note that without a PCB, the device responds quasi-statically to shock load. Hence, the PCB here has adverse effect on the performance of the device.

Figure 8.41 shows the SRS of the device without a PCB (Fig. 8.41a) and with the PCB (Fig. 8.41b) as measured experimentally and simulated theoretically using the model of Eq. (8.15) and Eq. (8.16). It is clear again here that a poor-designed PCB, such as the considered one, leads to amplification of the MEMS structure response.

Fig. 8.38 Universal 3-D plots of the normalized relative amplitude of a microstructure for different ω_{PCB} and ω_{Pulse} for **a** $\zeta_{MEMS} = 0.05$ and **b** $\zeta_{MEMS} = 0.5$. (Reprinted with permission. Copyright 2009, IEEE [31])

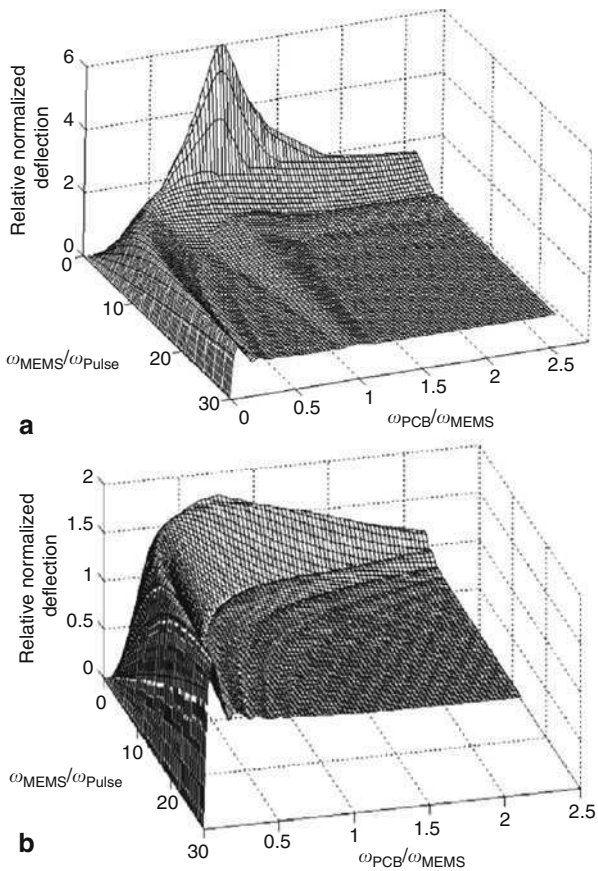


Fig. 8.39 A picture of a PCB mounted on top of a shaker. (Reprinted with permission. Copyright 2009, IEEE [31])

Fig. 8.40 Transient response of the proof mass with and without a PCB when subjected to a mechanical shock of $T = 5.0$ ms as monitored through a laser Doppler vibrometer. (Reprinted with permission. Copyright 2009, IEEE [31])

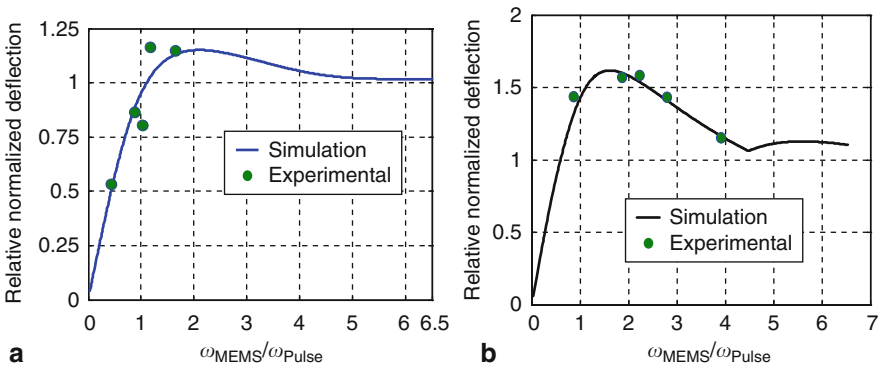
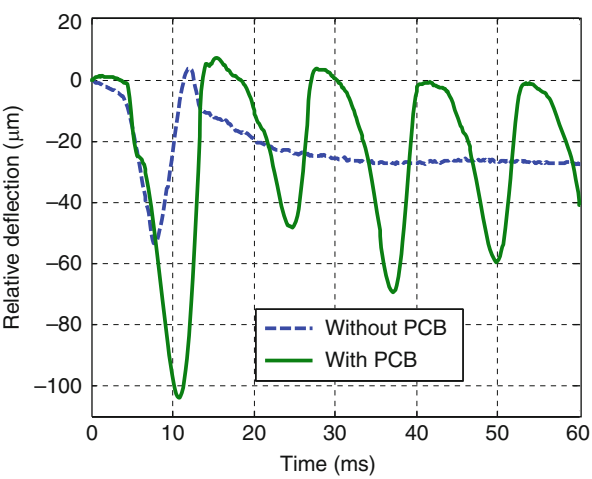


Fig. 8.41 **a** The simulated and measured SRS of the capacitive accelerometer when it is mounted directly on the shaker and **b** when it is mounted over a PCB and then on the shaker. The damping ratio is assumed in the simulations to be 0.05. (Reprinted with permission. Copyright 2009, IEEE [31])

Problems

1. Repeat Example 8.1 for the case of a rectangular shock pulse. Compare results to those of a half-sine and triangular pulse in the example.
2. Generate a family of SRS curves, similar to Fig. 8.5, for the cases of
 - (a) Rectangular shock pulse
 - (b) Triangular shock pulse
3. Consider a silicon cantilever microbeam of $l = 100\text{ }\mu\text{m}$, $h = 0.1\text{ }\mu\text{m}$, and $b = 10\text{ }\mu\text{m}$. Assume the microbeam is subjected to a half-sine acceleration pulse of a drop test of maximum amplitude $400g$. Assume no damping. Determine the

maximum tip deflection of the cantilever microbeam assuming $T = 1.0$ ms and $T = 0.1$ ms:

- (a) Using a reduced-order model. Determine the minimum number of modes needed for convergence.
 - (b) Using a combination of a static analytical formula for the beam tip deflection and the SRS.
4. For the beam of Problem 3, determine the maximum acceleration that is needed for the beam tip to hit the substrate underneath at a distance $2\text{ }\mu\text{m}$ for both cases of $T = 1.0$ ms and $T = 0.1$ ms.
 5. Assume that the beam of Problem 3 forms one side of a capacitor with the other electrode placed a distance $d = 2\text{ }\mu\text{m}$ underneath. Using a reduced-order model:
 - (a) Calculate the pull-in voltage of the beam.
 - (b) Calculate the maximum acceleration amplitude before the beam hits the substrate without considering the effect of the electrostatic force.
 - (c) Now considering both the electrostatic and shock effects, generate the shock-acceleration stability curves for this beam, similar to Fig. 8.19, for both cases $T = 1.0$ ms and $T = 0.1$ ms.
 6. Regenerate the stability curves of Fig. 8.16 by changing the shock duration to $T = 0.1$ ms.
 7. Consider the capacitive sensor of Sect. 8.9.1, operated as a resonator, of a stiffness coefficient $k = 124$ N/m, a fundamental natural frequency of 187 Hz, a gap size $d = 47.5\text{ }\mu\text{m}$, and a pull-in voltage of 112 V. Assume a linear damping ratio of $\zeta = 0.006$. Assume the device is actuated by $V_{\text{DC}} = 20$ V and $V_{\text{AC}} = 15$ V and then subjected to an acceleration pulse of amplitude $1g$. Calculate the SRS of the device, similar to Fig. 8.30, for the following cases:
 - (a) Assuming $\Omega = \omega_n$
 - (b) Assuming $\Omega = 0.5\omega_n$
 8. Assume the same parameters of the capacitive sensor of Problem 7. Also, assume the capacitive sensor placed on top of a PCB of $\omega_{\text{PCB}} = 6$ kHz. Generate an SRS, similar to Fig. 8.41 of this case. Justify your results.

References

- [1] Béliveau A, Spencer G T, Thomas K A, and Roberson S L (1999) Evaluation of MEMS capacitive accelerometers. *Design & Test of Computers*. 16:48–56
- [2] Brown T G (2003) Harsh military environments and microelectromechanical (MEMS) devices. *Proceeding of IEEE Sensors*, 753–760
- [3] Brown T G and Davis B S (1998) Dynamic high-g loading of MEMS sensors: Ground and flight testing. *Proceeding. SPIE - The Int. Society for Optical Engineering*, Bellingham WA, 228–235

- [4] Brown T G, Davis B S, Hepner D, Faust J, Myers C, Muller C, Harkins T, Hollis M, Miller C, and Placzankis B (2001) Strap-down microelectromechanical (MEMS) sensors for high-G munition applications. *IEEE Transactions on Magnetics*. 37:336–342
- [5] Tanner D M, Walraven J A, Helgesen K, Irwin L W, Smith N F, and Masters N (2000) MEMS reliability in shock environments. *Proceeding IEEE International Reliability Physics Symposium*, 129–138
- [6] Li G X, and Shemansky J R (2000) Drop test and analysis on micro-machined structures. *Sensors Actuators A*. 85:280–286
- [7] Sheehey M, Punch J, Goyal S, Reid M, Lishchynska M, and Kelly G (2009) The Failure mechanisms of micro-scale cantilevers in shock and vibration stimuli. *Journal Strain*. 45–3:283–294
- [8] Kelly G, Punch J, Goyal S, and Sheehy M (2008) Analysis of shock pulses from a small velocity amplifier. *Proceedings of the SEM XI International Congress & Exposition on Experimental and Applied Mechanics*, Orlando, Florida
- [9] Kimberley J, Cooney R S, Lambros J, Chasiotis I, and Barker N S (2009) Failure of Au RF-MEMS switches subjected to dynamic loading *Sensors and Actuators A*. doi: 10.1016/j.sna.2009.06.004, (9 pages)
- [10] Cunningham S, McIntyre S, Carper J, Jaramillo J, and Tang W C (1996) Microstructures designed for shock robustness. *Proceeding of SPIE - The Int. Society for Optical Engineering*, 99–107
- [11] Wagner U, Franz J, Schweiker M, Bernhard W, Muller-Fiedler R, Michel B, and Paul B (2001) Mechanical reliability of MEMS-structures under shock load. *Microelectronic Reliability*. 41:1657–1662
- [12] Lim B B, Yang J P, Chen S X, Mou J Q, and Lu Y (2002) Shock analysis of MEMS actuator integrated with HGA for operational and non-operational HDD. *Digest of the Asia-Pacific Magnetic Recording Conference*, WE-P-18-01-WE-P-18-02
- [13] Atwell A R, Okojie R S, Kornegay K T, Roberson S L, and Beliveau A (2003) Simulation, fabrication and testing of bulk micromachined 6H-SiC high-g piezoresistive accelerometers. *Sensors Actuators A*. 104:11–18
- [14] Jiang Y, Du M, Huang W, Xu W, and Luo L (2003) Simulation on the encapsulation effect of the high-G shock MEMS accelerometer. *Proceeding of the 5th Int. Conf. on Electronics Packaging Technology*, Shanghai, pp: 52–55
- [15] Fan M S and Shaw H C (2001) Dynamic response assessment for the MEMS accelerometer under severe shock loads. *National Aeronautics and Space Administration NASA*, Washington, DC TP—2001–209978, Washington, DC
- [16] Mariani S, Ghisi A, Corigliano A, and Zerbini S (2007) Multi-scale analysis of MEMS sensors subject to drop impacts. *Sensors*. 7:1817–1833
- [17] Mariani S, Ghisi A, Corigliano A, and Zerbini S (2009) Modeling impact-induced failure of polysilicon MEMS: a multi-scale approach. *Sensors*. 9:556–567
- [18] Srikar V T and Senturia S D (2002) The reliability of microelectromechanical systems (MEMS) in shock environments. *Journal of Micromechanics and Microengineering*. 11:206–214
- [19] Qian Z, Tomase J, Lian K (2004) Mechanical simulation for the robust design of RF-MEMS switches. *Proceedings of the ASME Intl. Conf. of Mechanical Engineering Congress and Exposition (MEMS)*, Anaheim, CA, IMECE2004-60112
- [20] Coster J D, Tilmans H C, van Beek J T M, Rijks T G S M, and Puers R (2004) The influence of mechanical shock on the operation of electrostatically driven RF-MEMS switches. *Journal of Micromechanics and Microengineering*. 14:S49–S54
- [21] Bao M, Huang Y, Yang H, and Wang Y (2004) Reliable operation conditions of capacitive inertial sensor for step and shock signals. *Sensors and Actuators A*. 114:41–48
- [22] Khatami F and Rezazadeh G (2008) Dynamic response of a torsional micromirror to electrostatic force and mechanical shock. *Microsystem Technology*. 15:535–545
- [23] Ghisi A, Kalicinski S, Mariani S, De Wolf I, and Corigliano A (2009) Polysilicon MEMS accelerometers exposed to shocks: numerical-experimental investigation. *Journal of Micromechanics and Microengineering*. 19: 035023

- [24] Tas N, Sonnenberg T, Jansen H, Legtenberg R, and Elwenspoek M (1996) Stiction in surface micromachining. *Journal of Micromechanics and Microengineering*. 6:385–397
- [25] Fang X W, Huang Q A, and Tang J Y (2004) Modeling of MEMS reliability in shock environments. *Proceeding of 7th Int. Conf. on Solid-State and Integrated Circuits Technology*, Beijing, 860–863
- [26] Yee J K, Yang H H, Judy J W (2003) Shock resistance of ferromagnetic micromechanical magnetometers. *Sensors Actuators A*. 103:242–52
- [27] Millet O, Collard D, and Buchaillet L (2002) Reliability of packaged MEMS in shock environments: crack and stiction modeling. *Design, Test, Integration and Packaging of MEMS/MOEMS*, Cannes, 696–703
- [28] Younis M I, Miles R, and Jordy D (2006) Investigation of the response of microstructures under the combined effect of mechanical shock and electrostatic forces. *Journal of Micromechanics and Microengineering*. 16:2463–2474
- [29] Younis M I, Alsaleem F, and Jordy D (2007) The Response of clamped-clamped microbeams under mechanical shock. *International Journal of Nonlinear Mechanics*. 42:643–657
- [30] Younis M I, Alsaleem F M, Miles R., and Su Q (2007) Characterization for the performance of capacitive switches activated by mechanical shock. *Journal of Micromechanics and Microengineering*. 17:1360–1370
- [31] Alsaleem F M, Younis M I, and Ibrahim M (2009) A study for the effect of the PCB motion and electrostatic force on the dynamics of MEMS devices under mechanical shock. *Journal of Micromechanics and Microengineering*. 18-3:597–609
- [32] Ibrahim M and Younis M I (2010) The dynamic response of electrostatically driven resonators under mechanical shock. *Journal of Micromechanics and Microengineering*. 20: doi: 025006
- [33] Ibrahim M, Younis M I, and Alsaleem F M (2010) An Investigation into the Effects of Electrostatic and Squeeze-Film Nonlinearities on the Shock Spectrum of Microstructures. *International Journal of Nonlinear Mechanics*. 45–8: doi:10.1016/j.ijnonlinmec.2010.05.005
- [34] Ouakad H, Alsaleem F A, Younis M I, Levo T, and Pitarresi J (2010) Response of an electrostatically actuated microbeam to drop-table test. *IEEE Thermal, Mechanical & Multiphysics Simulation and Experiments in Micro/Nano-Electronics and Microsystems Conference*, Eurosime 2010, Bordeaux, France, April, doi: 0.1109/ESIME.2010.5464602
- [35] Younis M I, Jordy D, and Pitarresi J (2007) Computationally efficient approaches to characterize the dynamic response of microstructures under mechanical shock. *Journal of Microelectromechanical Systems*. 16:628–638
- [36] Alsaleem M, Younis M I, and Miles R (2008) An investigation into the effect of the PCB motion on the dynamic response of MEMS devices under mechanical shock loads. *Journal of Electronic Packaging*, 130: 31002–31011, doi: 10.1115/1.2957319
- [37] Ramini A H, Younis M I, Miles R, and Pitarresi J (2010) Modeling the effects of PCB motion on the response of microstructures under mechanical shock. *IEEE Thermal, Mechanical & Multiphysics Simulation and Experiments in Micro/Nano-Electronics and Microsystems Conference*, Eurosime 2010, Bordeaux, France, doi: 10.1109/ESIME.2010.5464602
- [38] Jordy D and Younis M I (2008) Characterization of the dynamical response of a micromachined G-sensor to mechanical shock loading under the influence of squeeze-film damping. *Journal of Dynamic Systems, Measurement, and Control*. 130: doi: 10.1115/1.2936849
- [39] Yagubzade H, Younis M I, Rezazadeh G (2009) The effect of squeeze-film damping on suppressing the shock response of MEMS. *Proceedings of IMECE2009 2009 ASME International Mechanical Engineering Congress and Exposition*, Lake Buena Vista, Florida, USA, paper #IMECE2009-12433
- [40] Meirovitch L (2001) *Fundamentals of Vibrations*. McGraw-Hill, New York
- [41] Steinberg D S (2000) *Vibration Analysis for Electronic Equipment*, 3rd edition. Wiley, New York
- [42] Shigley J, Mischke J, Budynas R (2004) *Mechanical Engineering Design*. McGraw-Hill, New York

Appendix A

This section provides derivation of the equations of motion of a beam in bending subjected to midplane stretching using Hamilton's principle, which is a variational-mechanics energy-based approach. This presents an alternative technique to the Newtonian or vectorian method used in the derivations of Sect. 6.8. Hamilton's principle is considered very powerful for deriving the equation of motion, along with the associated boundary conditions, of complicated distributed-parameter systems of multiple bodies and complicated boundary conditions.

Here we shall adopt the same assumptions of Sect. 6.8 and consider a beam that is clamped to a fixed wall in one end and clamped to a roller that can move axially on the other end, where it is subjected to an axial force P , Fig. A.1. We start by recalling the linear Euler–Bernoulli beam theory and consider a segment on the beam before and after bending, Fig. A.2. Under the Euler–Bernoulli beam theory, the beam cross section remains plane and perpendicular to the beam's centerline. Note that the centerline is the same line of Fig. 6.24a. Hence, the axial strain of a fiber on the centerline is as expressed in Eq. (6.92b). In addition, we need to determine the axial strain of point B on the cross section of the beam, which is a distance y from the centerline, Fig. A.2. According to the figure, the axial displacement of point B due to pure bending u_b is given by [1]

$$u_b = -yw'. \quad (\text{A.1})$$

The corresponding axial strain ε_b is expressed as

$$\varepsilon_b = \frac{\partial u_b}{\partial x} = -yw''. \quad (\text{A.2})$$

The total axial strain of point B is that due to pure bending plus the axial strain of the centerline due to stretching. Hence, adding the centerline strain ε of Eq. (6.92b) to the pure bending strain of Eq. (A.2) yields the total strain ε_T

$$\varepsilon_T = \varepsilon - yw'' = u' + \frac{w'^2}{2} - yw'' \quad (\text{A.3})$$

The potential energy PE of the beam due to this strain is expressed as

$$PE = \frac{1}{2} \int_V \sigma \varepsilon_T dV \quad (\text{A.4})$$

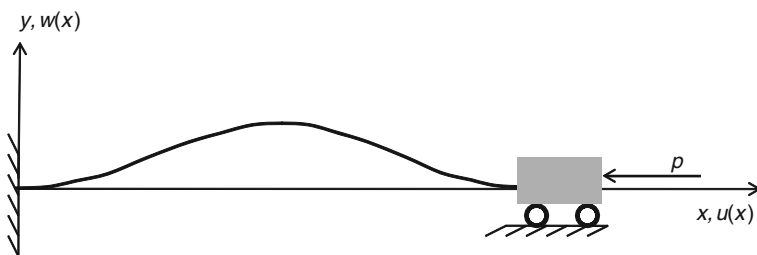


Fig. A.1 A schematic of a beam in bending under a compressive axial force

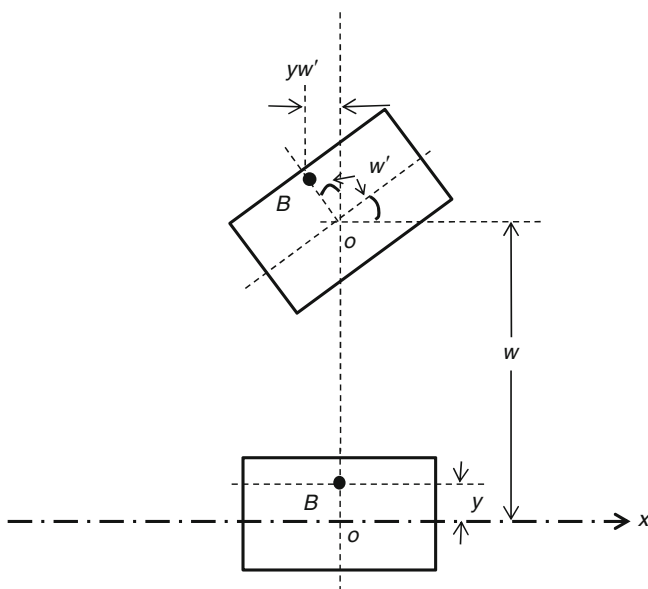


Fig. A.2 A segment of a beam in bending before and after deformation

where V is the beam's volume and σ is the axial stress. Using Hooke's law ($\sigma = E\varepsilon_T$), where E is Young's modulus, in Eq. (A.4) gives

$$PE = \frac{1}{2} \int_0^l \int_A E \varepsilon_T^2 dA dx = \frac{1}{2} \int_0^l \int_A E \varepsilon_T^2 dA dx \quad (\text{A.5})$$

where A is the beam's cross-sectional area and l is the beam's length. Substituting for ε_T from Eq. (A.3) into Eq. (A.5) yields

$$PE = \frac{1}{2} \int_0^l \int_A E (\varepsilon - yw'')^2 dA dx. \quad (\text{A.6})$$

Expanding Eq. (A.6) and distributing the integrals give

$$\begin{aligned}
 PE = & \frac{1}{2} \int_0^l \int_A E[\varepsilon^2 - 2\varepsilon y w'' + (y w'')^2] dA dx = - \int_0^l E \varepsilon w'' \left(\int_A y dA \right) dx \\
 & + \frac{1}{2} \int_0^l E w''^2 \left(\int_A y^2 dA \right) dx + \frac{1}{2} \int_0^l \int_A E \varepsilon^2 dA dx. \quad (A.7)
 \end{aligned}$$

Assuming the centerline of the beam passes through the centroid of the cross section, the first integral in the bracket in Eq. (A.7) vanishes. On the other hand, the second integral in brackets is reduced to the moment of inertia of the cross section I . Based on these simplifications, recalling ε from Eq. (6.92b), and assuming constant material and geometric properties E , I , and A , the potential energy of the beam is written as

$$PE = \frac{EI}{2} \int_0^l w''^2 dx + \frac{EA}{2} \int_0^l \left(u' + \frac{w'^2}{2} \right)^2 dx. \quad (A.8)$$

The kinetic energy KE of the beam due to its bending motion is expressed as

$$KE = \frac{\rho A}{2} \int_0^l \dot{w}^2 dx \quad (A.9)$$

where ρ is the material density. Note that the contribution of the axial inertia in the kinetic energy is negligible, and hence, is not included.

Assuming a distributed non-conservative force acting on the beam $F(x, t)$, the work of the nonconservative forces W_{NC} due to this force and the axial load at the end $x = l$ is expressed as

$$W_{NC} = \int_0^l (Fw) dx - pu(l) \quad (A.10)$$

where $u(l)$ is the axial displacement at $x = l$.

To derive the equation of motion of the beam and the associated boundary conditions, the extended Hamilton's principle needs to be utilized, which is written as

$$\int_{t_1}^{t_2} [\delta KE - \delta PE + \delta W_{NC}] dt = 0 \quad (A.11)$$

where t_1 and t_2 refer to two instants of time in which the system undergoes the variation and δ refers to the virtual or variation operator (similar to the differential

operator but occurs instantaneously, i.e., does not allow changes in time). In preparation to Eq. (A.11), the variation of the kinetic energy δKE , potential energy δPE , and the work of the nonconservative forces δW_{NC} need to be calculated. The results need to be simplified such that the final expressions in the integral terms contain only variations in terms of the virtual displacements δw and δu . This usually requires the use of integration by parts. We start by calculating δW_{NC} , which is based on Eq. (A.10) and expressed as

$$\delta W_{NC} = \int_0^l (F \delta w) dx - p \delta u(l). \quad (\text{A.12})$$

Also, the variation in the kinetic energy δKE is calculated based on Eq. (A.9) as

$$\delta KE = \rho A \int_0^l \dot{w} \delta \dot{w} dx. \quad (\text{A.13})$$

In preparation for Eq. (A.11), Eq. (A.13) is integrated from t_1 and t_2 and then integrated by parts to yield an expression in terms of δw as below

$$\begin{aligned} \int_{t_1}^{t_2} [\delta KE] dt &= \int_{t_1}^{t_2} \left[\rho A \int_0^l \dot{w} \delta \dot{w} dx \right] dt = \rho A \int_0^l \left[\int_{t_1}^{t_2} \dot{w} \delta \dot{w} dt \right] dx \\ &= \rho A \int_0^l \left[\underbrace{\dot{w} \delta w}_{=0} \Big|_{t_1}^{t_2} - \int_{t_1}^{t_2} \ddot{w} \delta w dt \right] dx \\ &= \rho A \int_0^l \left[- \int_{t_1}^{t_2} \ddot{w} \delta w dt \right] dx. \end{aligned} \quad (\text{A.14})$$

Note that the boundary term in time vanishes since by the definition of the virtual displacement, $\delta w(t_1) = \delta w(t_2) = 0$.

The variation in the potential energy δPE is calculated based on Eq. (A.8) as

$$\delta PE = EI \int_0^l w'' \delta w'' dx + EA \int_0^l \left(u' + \frac{w'^2}{2} \right) (\delta u' + w' \delta w') dx \quad (\text{A.15})$$

Several integrations by parts are needed for the integrals of Eq. (A.15) to yield expressions in terms of virtual displacements (δw and δu), which are illustrated below

$$EI \int_0^l w'' \delta w'' dx = EI w'' \delta w' \Big|_0^l - EI w''' \delta w \Big|_0^l + EI \int_0^l w''' \delta w dx \quad (\text{A.16})$$

$$EA \int_0^l \left(u' + \frac{w'^2}{2} \right) \delta u' dx = EA \left(u' + \frac{w'^2}{2} \right) \delta u|_0^l - EA \int_0^l \left(u' + \frac{w'^2}{2} \right)' \delta u dx \quad (\text{A.17})$$

$$EA \int_0^l \left(u' + \frac{w'^2}{2} \right) (w' \delta w') dx = EA \left(u' + \frac{w'^2}{2} \right) w' \delta w|_0^l - EA \int_0^l \left(\left[u' + \frac{w'^2}{2} \right] w' \right)' \delta w dx \quad (\text{A.18})$$

Next, Eqs. (A.12), (A.14), and (A.16)–(A.18) are substituted into Eq. (A.11):

$$\begin{aligned} \rho A \int_0^l \left[- \int_{t_1}^{t_2} \ddot{w} \delta w dt \right] dx + \int_0^l (F \delta w) dx - p \delta u(l) - \left\{ EI w'' \delta w'|_0^l - EI w''' \delta w|_0^l \right. \\ + EI \int_0^l w'''' \delta w dx + EA \left(u' + \frac{w'^2}{2} \right) \delta u|_0^l - EA \int_0^l \left(u' + \frac{w'^2}{2} \right)' \delta u dx \\ \left. + EA \left(u' + \frac{w'^2}{2} \right) w' \delta w|_0^l - EA \int_0^l \left(\left[u' + \frac{w'^2}{2} \right] w' \right)' \delta w dx \right\} \end{aligned} \quad (\text{A.19})$$

Rearranging and grouping terms give

$$\begin{aligned} \int_{t_1}^{t_2} \left\{ \int_0^l \left[-\rho A \ddot{w} - EI w'''' + EA \left(\left[u' + \frac{w'^2}{2} \right] w' \right)' + F \right] \delta w dx \right. \\ + \int_0^l EA \left(u' + \frac{w'^2}{2} \right)' \delta u dx \left[-p - EA \left(u' + \frac{w'^2}{2} \right) \right] \delta u(l) \\ + \left[EA \left(u' + \frac{w'^2}{2} \right) \right] \delta u(0) \left(-EA \left(u' + \frac{w'^2}{2} \right) w' + EI w''' \right) \delta w|_0^l \\ \left. - EI w'' \delta w'|_0^l \right\} dt = 0 \end{aligned} \quad (\text{A.20})$$

Since the variation of each virtual displacement is by definition arbitrary, for Eq. (A.20) to be satisfied, each individual group of terms in Eq. (A.20) must vanish. This yields the following equations of motion and boundary conditions:

$$\rho A \ddot{w} + EI w'''' = EA \left(\left[u' + \frac{w'^2}{2} \right] w' \right)' + F \quad (\text{A.21})$$

$$EA \left(u' + \frac{w'^2}{2} \right)' = 0 \quad (\text{A.22})$$

$$-EA \left(u' + \frac{w'^2}{2} \right) = 0; \quad \text{or} \quad \delta u = 0; \quad \text{at } x = 0 \quad (\text{A.23})$$

$$-EA \left(u' + \frac{w'^2}{2} \right) - p = 0; \quad \text{or} \quad \delta u = 0; \quad \text{at } x = l \quad (\text{A.24})$$

$$\left(-EA \left(u' + \frac{w'^2}{2} \right) w' + EIw''' \right) = 0; \quad \text{or} \quad \delta w = 0; \quad \text{at } x = 0, l \quad (\text{A.25})$$

$$-EIw'' = 0; \quad \text{or} \quad \delta w' = 0; \quad \text{at } x = 0, l \quad (\text{A.26})$$

Equations (A.21) and (A.22) are similar to Eq. (6.98a) and Eq. (6.98b) obtained using the Newtonian method (after neglecting the axial inertia). For the particular beam under consideration of Fig. A.1, the boundary conditions are as below

$$u = 0; \quad \text{at } x = 0 \quad (\text{A.27})$$

(Since the beam end is fixed axially).

$$-EA \left(u' + \frac{w'^2}{2} \right) - p = 0; \quad \text{at } x = l \quad (\text{A.28})$$

(Since the beam end is not fixed axially, but subjected to an axial force, which effect needs to be balanced by the internal axial force of the beam at this end).

$$w = 0; \quad \text{at } x = 0, l \quad (\text{A.29})$$

$$w' = 0; \quad \text{at } x = 0, l \quad (\text{A.30})$$

(Since the beam is not allowed to move transversally and is not free to rotate at both ends).

The coupled equations of motion, Eq. (A.21) and Eq. (A.22), can be further simplified by noting that Eq. (A.22) represents a constrain indicating that the axial strain of the beam remains constant in space. Hence dividing by Eq. (A.22) EA and integrating it in space yield

$$u' + \frac{w'^2}{2} = c_1(t) \quad (\text{A.31})$$

where $c_1(t)$ is a constant of integration in space (can be generally variable in time). Equation (A.31) can be rewritten as

$$u' = \frac{\partial u}{\partial x} = c_1(t) - \frac{w'^2}{2}. \quad (\text{A.32})$$

Integrating Eq. (A.32) gives

$$u = -\frac{1}{2} \int_0^x w'^2 dx + c_1(t)x + c_2(t). \quad (\text{A.33})$$

For simplicity, the nonlinear term in Eq. (A.28) is neglected, which simplifies the boundary condition to

$$-EA \frac{\partial u(l)}{\partial x} = p \Rightarrow u(l) = \frac{-pl}{EA}. \quad (\text{A.34})$$

Applying the boundary conditions, Eq. (A.27) and Eq. (A.34), on Eq. (A.33) yields

$$u(0) = 0 \Rightarrow c_2(t) = 0 \quad (\text{A.35})$$

$$\begin{aligned} u(l) = \frac{-pl}{EA} &\Rightarrow -\frac{1}{2} \int_0^l w'^2 dx + c_1(t)l = \frac{-pl}{EA} \\ &\Rightarrow c_1(t) = \frac{1}{2l} \int_0^l w'^2 dx - \frac{p}{EA}. \end{aligned} \quad (\text{A.36})$$

Next, Eq. (A.36) is substituted into Eq. (A.31) and then the outcome into Eq. (A.21), which gives

$$\begin{aligned} \rho A \ddot{w} + EI w'''' &= EA(c(t)w')' + F \Rightarrow \rho A \ddot{w} + EI w'''' \\ &= EA \left[\frac{1}{l} \int_0^l \left[\frac{w'^2}{2} \right] dx - \frac{p}{EA} \right] w'' + F. \end{aligned} \quad (\text{A.37})$$

Equation (A.37) can be used along with the boundary conditions of Eq. (A.29) and Eq. (A.30) to model the nonlinear beam behavior including the effect of midplane stretching.

It is worth to note that the boundary condition of Eq. (A.25) at $x = l$ can be further simplified by using Eq. (A.28) to replace $u' + w'^2/2$ in terms of p , which yields

$$pw' + EI w''' = 0; \quad \text{or} \quad \delta w = 0; \quad \text{at } x = l. \quad (\text{A.38})$$

The first part of Eq. (A.38) is similar to Eq. (d) of Example 6.8 obtained using the Newtonian method (after setting $k = 0$ and $N = -p$).

References

- [1] Rao S S, *Vibration of Continuous Systems* (2007) Wiley, New Jersey

Index

A

Accelerometer, 63, 64, 74, 75, 84, 91, 359, 405, 410, 422, 425, 427, 430, 437, 439
Actuation, 13, 22, 57, 61, 65, 70, 197
 Electromagnetic, 33, 65–67
 Electrostatic, 22, 70, 88, 225, 302, 306, 314, 383, 401, 414, 440
 Electrothermal, 57
 Magnetic, 33, 34, 65
 Piezoelectric, 22, 33–35, 61, 63
Actuator, 58–60
 Bimorph, 60
 Comb-drive, 82, 402, 414
 Torsional, 14, 78, 201
 U-Shaped, 58
 V-Beam, 59
AFM, 13, 32, 98, 237, 239, 251, 323, 351, 392
Atomic force, 13
Attractor, 376, 379–383, 385
Axial load, 108, 178, 230, 255, 281, 282, 286, 290, 294

B

Bandwidth, 26, 27, 52, 54, 437
Basin of attraction, 368, 376–381, 383–386, 395–398
Bifurcations, 168
 Hopf, 169, 182, 183, 301, 372
 Neimark, 372
 Pitchfork, 178, 372, 374, 385
 Saddle-node, 169
 Tangent, 169, 219
 Transcritical, 177, 372
Buckling, 280

C

Cantilever, 32, 111, 262, 277, 306, 359, 368, 386, 402, 439
Capillary forces, 5, 9, 155, 174, 176, 190, 201, 339, 340
Chaos, 239, 240
Clamped-clamped, 5, 59, 60, 63, 65, 87, 89, 98, 99, 105
Comb-drive devices, 82
Continuation, 321, 368, 393
Cut-off frequency, 128

D

Damped motion, 20
 Critically damped, 20, 21
 Overdamped, 19–21
 Underdamped, 20–22, 36
Damping, 14, 18, 32, 45, 51, 111, 131, 137, 291, 330, 343
 Intrinsic, 112, 142
 Slide-Film, 139
 Squeeze-film, 36, 118, 137, 343, 359, 361, 403, 423
 Thermoelastic, 143, 344, 396
Delayed-feedback controller, 391–394, 396, 398
Dielectric, 172, 368
Double-sided capacitor, 181, 194, 224
Dover cliff, 359, 378, 396, 398
Duffing, 217, 218, 220–224, 301
Dynamic pull-in, 228, 322, 363, 373, 384, 390, 414, 416, 417, 424, 434

E

Effective mass, 360, 368, 405, 406, 415
Eigenvalue, 40, 42
Entrainment, 239

Escape, 373, 376, 383, 385, 388, 414
 Excitation, 13, 21–27, 32, 33, 36, 38, 49, 54,
 55, 230, 321
 Arbitrary, 13, 36–38, 43, 48, 71, 121, 270
 Base, 405, 406, 409, 410, 414, 415, 418,
 436

F

Filter (band-pass), 13, 27, 52–55, 70, 237
 Fixed points, 161, 166, 169, 170, 177, 178,
 182, 183, 185, 219
 Floquet theory, 218, 233, 369
 Focus, 363, 386, 391, 402, 406
 Fractal, 239, 241, 359, 376, 377, 380, 383, 385,
 391, 394

G

Galerkin, 97, 107, 121, 231, 286, 297, 299,
 301, 304, 316, 338, 340, 349, 418
 Gyroscope, 1, 13, 28, 29, 31, 277,

H

Heteroclinic, 240
 Homoclinic, 240, 385, 386
 Hysteresis, 2, 156, 173, 211, 219, 236, 237,
 330

I

Inevitable escape, 373–377, 379, 381, 383,
 385, 391, 394, 395
 Integrity Factor, 379
 Internal resonance, 239
 Isolation, 411
 Insertion loss, 3, 53, 74, 197

J

Jacobian matrix, 163, 315
 Jump-to-contact instability, 7

K

Knudsen number, 115, 124, 128, 133, 134,
 146, 229

L

Lennard-Jones Force
 Limit cycle, 238, 376
 Linearization, 161
 Logarithmic decrement, 144, 145

M

Mass Detection, 386–391
 Mass sensor, 89, 90, 92, 230, 239
 Mathieu equation, 233–237
 Mean free path, 115, 133, 146

Micromirror, 1, 62, 70, 75, 82, 129, 149, 201,
 209, 243
 DMD, 70, 76, 78
 Torsional, 78, 129, 201, 209
 Mid-plane stretching, 386, 410
 Modal analysis, 436
 Modeshape, 42, 107, 121, 251, 267, 268, 270,
 274, 278, 279

N

Natural frequencies, 408, 435
 Node, 169
 Nondimensionalization, 157, 272
 Nonideal supports, 264, 283
 Nonlinear oscillations, 121

P

Parametric, 230, 231
 Partial electrodes, 312, 313, 350
 PCB, 403, 405, 409, 410, 435–440
 Piezoresistive detection
 Phase plane, 376
 Phase portraits, 190
 Pull-in, 74, 170, 190, 319, 322, 359, 360, 364,
 373, 381, 415, 440
 Time, 235, 319, 323, 364, 366–372, 376,
 387, 393–395, 402, 431
 Voltage, 87, 170, 172, 360, 388, 390, 414,
 440

Q

Quality factor, 386

R

Rayleigh's method, 110, 111, 315
 Rayleigh's oscillator, 237, 238
 Reduced-order model, 386, 410, 412, 420, 440
 Resonance, 217, 360, 363, 365–368, 372,
 374–385, 387–391, 397, 398
 Primary, 217, 225, 321, 363, 368, 372, 382,
 385, 397
 Secondary, 217, 221, 225, 372
 Subcritical, 374
 Supercritical, 374
 Release voltage, 172, 173, 198, 242
 Residual stresses, 98, 251, 262–264, 280, 312,
 313
 Resonant sensors, 87, 386, 426
 Resonator, 359, 381, 391, 394–397, 426–430,
 432–435, 440
 Reynolds equation, 120–125, 129, 130, 137,
 138, 147, 343
 Reynolds number, 114, 157

RF switches, 65, 70, 71, 74, 172, 173, 251,
319, 396

S

Saddle, 169, 385

Separatrix, 189, 190, 191, 192, 193, 198, 199,
211

Self-excited oscillators, 237

Side-instability, 190

Sink, 164

Shock, 379, 401–421, 423–437, 439, 440

Shock response spectrum, 407, 408, 429

Shooting, 359, 369–376, 381, 393, 396–398

Source, 404

Squeeze number, 361

Step voltage, 100, 193, 415, 422

Stiction, 388, 401, 402

Stiffness of Microstructures, 97

Stokes model, 139–141

Support losses, 113, 142

Switch, 359, 386–388, 390, 391, 396, 421, 424

T

Trajectory, 185–189, 193

Two-degree-of-freedom, 435

V

van der Pol oscillator, 183, 184, 237, 245

van der Waals force, 326, 329, 330, 332–334

Viscosity coefficient, 117, 121, 123, 124, 131,
133, 134, 146, 147, 229